Utilising High Throughput Screening Techniques to Identify Small Molecule Activators of the Epicardium

Thesis submitted for the degree of Doctor of Philosophy (D.Phil.)



Caitlin Clunie-O'Connor

St John's College

University of Oxford

Author's Declaration

The work presented in this thesis was conducted under the joint supervision of Prof. Paul R. Riley and Prof. Angela Russell, and carried out at the Department of Physiology, Anatomy and Genetics or the Chemistry Research Laboratory, University of Oxford, unless otherwise specified. All the work is my own, except where otherwise stated, and has not been submitted for any other degree at this or any other university.

Caitlin Clunie-O'Connor

7th October 2016

Acknowledgements

I must first thank my supervisors Professor Paul Riley and Professor Angela Russell.

Particular thanks must be extended to Alison Howarth and Daniel Ebner from the Target Discovery Institute for allowing me to use their wonderful facility and for all of the help they have given me over the past three years. It is fair to say this thesis would not exist without their input.

I must also thank Dr Nicola Smart for kindly reading over my thesis and for the help and advice she has given me throughout my time in the Riley lab.

I would like to thanks the lab of professor Derek Yellon at The Hatter Cardiovascular Institute, University College London, and the lab of Charalambos Antoniades at the Cardiovascular Medicine Radcliffe Department of Medicine, Oxford, for allowing me access to biopsy samples. Thanks to Dr Abdul Malik, Dr John McGowan, Ioannis Akoumianakis and Akansha Tarun for patient recruitment and sample preparation. I must also thanks Dr Anke Smits for her help in establishing the hEPDC derivation protocol.

Finally, I must thank of the people both past and present that make up the Riley and Russell labs for the help, support and advice over these four years, for being such wonderful colleagues and for making this process so much more fun!

Dedications

“Life is a journey, not a destination.”

- Ralf Waldo

This thesis is dedicated to all the people who have made this journey possible.

To Maggie Clunie; Takki Sulaiman; David, Joe and Meghan O’Connor; Fiona Wilson; Agnes, Matt, Nancy, Michele, Brian, Lorna, Eve and Erin Clunie; May Wilson; Maria Hatzipetrou and Ken Beasley. I have been shaped by your love and support and I will never be able to express eloquently enough how grateful I am to you all. This achievement is as much yours as it is mine.

I must also take this opportunity to thank the people who have helped to make this journey so much fun! With an attempt at reverse chronology I’d like to thank:

<u>From Oxford</u>
Flora Kennedy, Adam Gammack, Rory Beard, Sam Calderwood, Ant Hibbs, Sam Dockree, Emma Claussen, Wahbi El-Bouri, Megan Masters, Sophie Norman, Katherine Fender, Rebecca Hancock, Amy Varney, James Egleton, Aini Vuorinen, Carole Bataille, Laurence Silpa, Tim Bourns, Jack Seddon, Damien Barnette, Cristina Villa Del Campo, Matt Lewis and finally Adrastos, Chloé, Leo, Milo and soon to be baby Omissi.

<u>From Manchester</u>
Faye Alexander, Claire Whittaker, Nathan Galilee, Jen Aref, James Whitaker, Max Roebuck, Andrew Boyd, Adam Stylianou, Emily Lewis, Jamie King, Kate Groves, Flora Evans, Jessie Griffiths, Hazel Anderson and Hannah Moss.

<u>From London</u>
Katie Macmillan, Anna Bidmead, Jemima Greaves, Will Dunford, Anil Douglas, Shane Cullen, James Sheen, Tom Sweetman, Will Hawkins, Patrick Abrahart, Leon Geis and Jane Goldberg.

Natasha Mosienko and Amina Bhuiyan.

And finally, Oonagh, Anne and Niall O’Connor.

Your friendship and words of encouragement over the years mean more than I can possibly express. Charles Darwin once said ‘A man's friendships are one of the best measures of his worth’ which means, if true, that I am valuable indeed!

Abstract

The epicardium, the mesothelial layer covering the surface of the heart, plays an essential role during heart development. Epicardium derived cells (EPDCs) contribute essential cardiovascular cell types including vascular smooth muscle, interstitial fibroblasts and cardiomyocytes via the process of epithelial to mesenchymal transition (EMT) and EPDC paracrine signalling is critical for proper organ formation.

Whilst dormant in the adult heart, the epicardium is reactivated in response to injury in both mouse and zebrafish. Activation is characterised by epicardial expansion, EMT, EPDC migration and re-expression of embryonic transcription factors including WT1. Moreover, priming the mouse heart with thymosin β4 (Tβ4) increases the number of *Wt1*+ EPDCs *in vivo* following myocardial infarction. Subsequently, small numbers of Tβ4 activated *Wt1*+ cells migrate into the wound forming functional cardiomyocytes. Unfortunately, the number of functional EPDC-derived cardiomyocytes is suboptimal to restore the lost heart muscle; therefore, the aim of this project was to augment the process using chemical or genetic modulation.

To realise this aim, a high throughput phenotypic screen utilising primary human epicardium derived cells (hEPDCs) was developed in collaboration with the Target Discovery Institute. Recombinant transforming growth factor beta (TGFβ) was used to induce EMT in hEPDC cultures; morphological changes indicative of EMT were used as a surrogate read out for hEPDC activation. A rigorous analysis protocol was successfully developed, however, ongoing issues with access to primary human tissue led to investigation of alternate *in vitro* models of epicardial EMT.

Preliminary investigations into an EPDC line derived from rat proved problematic and due to numerous inconsistencies in the model an alternate cell line was sought. Success was found with an immortalised EPDC line derived from mouse (mEPDC), which reproducibly underwent EMT in response to TGFβ treatment. However, mEPDC EMT was not accompanied by morphological changes as pronounced as in hEPDC cultures, thus the mouse line was deemed unsuitable for the previously described phenotypic screen.

Moving forward, a high throughput scratch assay was developed which utilised migration as a surrogate read out for mEPDC activation. Upon screening of a small candidate library, two Bromodomain and Extra-Terminal motif (BET) inhibitors were found to reproducibly increase the speed of mEPDC wound closure. Screening a wider panel of BET inhibitors yielded several candidates that increased the rate of closure in a dose-responsive manner. To determine whether increased migration was correlated with a change in mEPDC phenotype the cells were cultured with an 'effective' dose of inhibitor and probed for a panel of differentiation markers. Several BET inhibitors were found to significantly upregulate expression of the EMT associated transcription factor *Snai2* after 24 hours of treatment compared with the control. Together, the observed increase in cell migration and expression of the *Snai2* transcription factor suggest a role for the BET bromodomains in epicardial activation and EMT.

Table of Contents

Abbreviations **5**

Chapter 1 ..... **9**

General introduction **9**

1.1 Cardiovascular disease: the biggest killer of the modern age **11**
1.2 With great success comes great burden **12**
1.3 Stem cells: the key to cardiac regeneration? **13**
1.4 The mammalian heart has regenerative potential **20**
1.5 Stem and progenitor populations residing in the adult heart **20**
1.6 The role of the epicardium in development **23**
1.7 The role of the epicardium in injury **29**
1.8 Small molecules in drug discovery and design **35**
1.9 High Throughput Screening and Hit to Lead development **37**
1.10 Target based drug discovery **40**
1.11 Phenotypic drug discovery **42**
1.12 Phenotypic screening in cardiac regeneration **45**
1.13 Generating cardiomyocytes from stem cells **45**
1.14 Recruiting resident cells for repair with small molecule compounds **51**
1.14.1 Cardiomyocyte proliferation 51
1.14.2 Cardiac fibroblast reprogramming 52
1.14.3 Recruiting epicardial progenitors 54
1.15 Patient derived human epicardium **55**
1.16 The role and characteristics of epithelial tissues **56**
1.17 Epithelial to Mesenchymal Transition **59**
1.18 hEPDC undergo spontaneous EMT **64**
1.19 High Throughput Phenotypic Screening in human EPDCs: Pilot Work **65**
1.20 Hypothesis **67**
1.21 Thesis aims **67**
1.22 Chapter synopsis **68**

Chapter 2 ..... **71**

General Materials and Methods **71**

2.1 Cell culture **73**
2.1.1 Protocol for the isolation of epicardial tissue from RAA biopsies 73
2.1.2 hEPDC passage and culture 76
2.1.3 Culture of rEPDCs 76
2.1.4 Culture of mEPDCs 77
2.2 EPDC EMT and differentiation protocol **77**
2.2.1 HEPDC EMT and differentiation 77
2.2.2 REPDC EMT and differentiation 77
2.2.3 MEPDC EMT and differentiation: differentiation media 78
2.2.4 MEPDC EMT and differentiation in IM 78
2.3 Molecular techniques **78**
2.3.1 RNA Extraction 78
2.3.2 cDNA synthesis 79

2.3.3 RT-PCR 80
2.3.4 QPCR analysis 80
2.3.5 Immunostaining 82
2.3.5 Western blot 83
2.4 SMAD3 Phosphorylation assay 84
2.5 High Throughput Screening protocols 84
2.5.1 Original hEPDC phenotypic screening protocol 84
2.5.2 rEPDC and mEPDC original phenotypic screening protocol 84
2.5.3 mEPDC automated scratch assay protocol 85
2.6 Data analysis 85
2.7 Compound purchase 85

Chapter 3 87

High Throughput Screening in primary human EPDCs 87

3.1. Establishing and characterising hEPDC cultures 89
3.1.1 Protocol for the isolation of epicardial tissue from RAA biopsies 89
3.1.2 Characterising hEPDCs 92
3.1.3 Characterising hEPDC EMT 95
3.1.4 Dynamic nuclear WT1 distribution 99
3.1.5 Punctate WT1 is localised to the nucleolus in hEPDCs 101
3.2 Using hEPDCs for high throughput phenotypic screening 105
3.2.1 Analysis of the pilot screen data 105
3.2.2 HEPDC validation screen 112
3.3 Summary and discussion 115
3.3.1 Establishing hEPDC cultures and modelling EMT 115
3.3.2 Dynamic WT1 nuclear distribution 116
3.3.3 High throughput phenotypic screening 118
3.3.4 Access to RAA biopsy samples 120
3.3.5 Future work 121

Chapter 4 123

High Throughput Screening in rat EPDCs 123

4.0 Introduction: immortal rat EPDC cell line 125
4.1 Model development 126
4.2 Utilising rEPDCs for high throughput phenotypic screening 139
4.2.1 REPDCs are not suitable for the previously established HTPS protocol 139
4.2.2 Quantifying VINCULIN ‘speckles’ 142
4.2.3 Quantifying α-SMA+ rEPDCs 146
4.3 Summary and discussion 147

Chapter 5 151

High Throughput Screening in mouse EPDCs 151

5.0 Introduction: immortalised mouse EPDCs 153
5.1. Model development 154
5.2 Utilising mEPDCs for high throughput screening 165
5.3 Developing an mEPDC Scratch Assay 168
5.3.1 Investigating mEPDC migration in low throughput 168

5.3.2 Developing an automated Scratch Assay 173
5.4 Summary and discussion 180
5.4.1 Establishing an EMT model in immortalised mEPDCs 180
5.4.2 High throughput screening with immortalised mEPDCs 181

Chapter 6 185

Small molecule library design and synthesis 185

6.0 Introduction: small molecule selection 187
6.1 TGFβ mimetic synthesis 188
6.2 Synthesis of small molecule sulfatase inhibitors 189
6.3 Isoxasole synthesis 191
6.4 Readily available compound selection 192

Chapter 7 199

Screening a small molecule library in the automated mEPDC scratch assay 199

7.1 Pilot mEPDC automated scratch assay 201
7.1.1 Assay protocol 201
7.1.2 Data analysis 202
7.1.3 Z-score calculation and identification of positive hits 205
7.2 Validation of primary 'hits' 210
7.3 Summary and discussion 219
7.3.1 Pilot mEPDC scratch assay 219
7.3.2 MEPDC validation screen 221

Chapter 8 225

Exploring the role of the BET bromodomains in mEPDC migration 225

8.0 Introduction to the BET bromodomains 227
8.1 Compound selection for the BET inhibitor screen 230
8.2 Screening the panel of BRD inhibitors 233
8.3 Investigating mEPDC EMT and differentiation 243
8.3.1 Morphology and gene expression of DMSO and TGFβ controls 244
8.3.2 Morphology and gene expression of PFI-1 treated mEPDCs 250
8.3.3 Morphology and gene expression of (+)-JQ1 treated mEPDCs 255
8.3.4 Morphology and gene expression of CPI203 treated mEPDCs 258
8.2.5 Morphology and gene expression of Bromosporine treated mEPDCs 263
8.2.6 Morphology and gene expression of OXF BD 02 treated mEPDCs 266
8.2.7 Morphology and gene expression of A-161906 treated mEPDCs 270
8.4 Summary and Discussion 274
8.4.1 Screening a panel of BET inhibitors in the automated mEPDC scratch assay 274
8.4.2 Exploring the role of BET bromodomains mEPDC EMT and differentiation 276

Chapter 9 291

Final Summary 291

9.1 Final Summary 293

Chapter 10 299

Experimental **299**

General procedure 1: Synthesis of 4-substituted ethyl-2,4-dioxobutanoates 302
General procedure 2: Synthesis of isoxazole-3-carboxylates 302
General procedure 3: Ester hydrolysis 303
General procedure 4: Amide coupling 303
Ethyl 7-((4'-cyano-[1,1'-biphenyl]-4-yl)oxy)heptanoate (4) 303
7-((4'-cyano-[1,1'-biphenyl]-4-yl)oxy)heptanoic acid (5) 304
7-((4'-cyano-[1,1'-biphenyl]-4-yl)oxy)-*N*-hydroxyheptanamide (1) 304
Benzyl ((3R,4R,5S,6R)-2,4,5-trihydroxy-6-(hydroxymethyl)tetrahydro-2H-pyran-3-yl)carbamate (8) 305
Benzyl ((2S,3R,4R,5S,6R)-4,5-dihydroxy-6-(hydroxymethyl)-2-methoxytetrahydro-2H-pyran-3-yl)carbamate (9) 306
((2R,3S,4R,5R,6S)-5-(((Benzyloxy)carbonyl)amino)-3,4-dihydroxy-6-methoxytetrahydro-2H-pyran-2-yl)methyl sulfamate (10) 306
((2R,3S,4R,5R,6S)-5-Amino-3,4-dihydroxy-6-methoxytetrahydro-2H-pyran-2-yl)methyl sulfamate (11) 307
((2*S*,3*R*,4*R*,5*S*,6*R*)-4,5-Dihydroxy-2-methoxy-6-((sulfamoyloxy)methyl) tetrahydro-2*H*-pyran-3-yl)sulfamic acid (6) 307
Ethyl 2,4-dioxo-4-(thiophen-2-yl)butanoate (19) 308
Ethyl 5-(thiophen-2-yl)isoxazole-3-carboxylate (20) 308
5-(thiophen-2-yl)isoxazole-3-carboxylic acid (21) 309
N-cyclopropyl-5-(thiophen-2-yl)isoxazole-3-carboxamide (12) 309
Ethyl 4-(furan-2-yl)-2,4-dioxobutanoate (22) 309
Ethyl 5-(furan-2-yl)isoxazole-3-carboxylate (23) 310
5-(furan-2-yl)isoxazole-3-carboxylic acid (24) 310
N-cyclopropyl-5-(furan-2-yl)isoxazole-3-carboxamide (13) 310
5-(furan-2-yl)-N-(2-methoxyethyl)isoxazole-3-carboxamide (15) 311
Ethyl 5-phenylisoxazole-3-*c*arboxylate (25) 311
N-cyclopropyl-5-phenylisoxazole-3-carboxamide (14) 312

Chapter 11 ..... **313**

Appendix **313**

A.1 Figures **314**
A.2 Tables **323**

References **335**

Abbreviations

10% FBS	10% fetal bovine serum.
4% PFA	4% paraformaldehyde in PBS
ADME	absorption, distribution, metabolism and excretion properties
Alpha Screen	amplified luminescence proximity homogeneous assay
BET	bromodomain and extra terminal domain
bHLH	basic helix-loop-helix
BMCs	bone marrow stem cells
BMPs	bone morphogenetic proteins
BRDs	bromodomains
BrdU	bromodeoxyuridine
BSA	10% bovine serum albumin
BVES	blood vessel epicardial substance
CBP	CREB binding protein
CABG	coronary artery bypass graft surgery
CERC2	cat eye syndrome critical region protein 2
CHD	coronary heart disease
CMLC2	cardiac myosin light chain 2
Cre	Cre recombinase
CTN1	cardiac troponin 1
CTNT	cardiac troponin t
CV	cardiovascular
CVD	cardiovascular disease
DKK1	dickkopf-related protein 1
DM	differentiation media
DMEM	dulbecco's modified eagles's medium
DPBS	dulbecco’s phosphate buffered saline
E 'X'	embryonic day 'x'
ECM	extra cellular matrix
EGFs	epidermal growth factors
ELISA	enzyme-linked immunosorbent assay
EMT	epithelial to mesenchymal transition
EPDCs	epicardium derived cells
Epo	erythropoietin
EpoR	erythropoietin receptor
ERK	extracellular signal-regulated kinases
ESCs	embryonic stem cells
FACS	fluorescence activated cell sorting
FGF	fibroblast growth factor
FGF2	fibroblast growth factor 2
FHF	first heart field
FRAP	fluorescence recovery after photobleaching
FSP1	fibroblast-specific protein 1
GATA-4	GATA binding protein 4
GATA-5	GATA binding protein 5
GFP	green fluorescent protein
GPCR 68	g protein coupled receptor 68

HAND1	heart and neural crest derivatives-expressed protein 1
HAND2	heart and neural crest derivatives-expressed protein 2
HDAC	histone deacetylases
hEPDCs	human epicardium derived cells
hESC	human embryonic stem cells
hIPS	human induced pluripotent stem cells
HTPS	high throughput phenotypic screening
HTS	high throughput screening
IC_{50}	half maximal inhibitory concentration
ICC	immunocytochemistry
IHC	immunohistochemistry
IL-6	interleukin 6
IL1	interleukin 1
IM	immortalisation media
IPS	induced pluripotent stem cells
ISO	isoproterenol
K	lysine
Kac	acetyl lysine
Kac site	acetyl lysine binding site
K_d	differentiation constant
K_i	inhibitory constant
KLF4	kruppel-like factor 4
LA	left atria
LAD	left anterior descending
LEF 1	lymphoid enhancer binding factor 1
LG-DMEM	low glucose DMEM
LHS	left hand side
LRP	low-density lipoprotein receptor–related protein
LV	left ventricle
LVEF	left ventricular ejection fraction
M-PBMCs	Mobilised peripheral blood mononuclear cells
MAPK	mitogen activates protein kinase
MEF2C	myocyte enhancer factor 2c
MESP1	moseoderm posterior 1
MI	myocardial infarction
MLC3F	muscle-specific myosin light chain 3f
MOA	mechanism of action
MSCs	mesenchymal stem cells
MW	molecular weight
MYC	myc proto-oncogene protein
MYOCD	myocardin
NEC	notch activated EPDC
Nkx 2.5	nk2 homobox 5
OCT4	octamer-binding transcription factor 4
OFT	outflow tract
P 'X'	postnatal day 'x'
P-SMAD3	phospho-smad3
PAI-1	plasminogen activator inhibitor-1
PAINS	pan-assay interference compounds

PBT	0.1% triton-x in PBS
PDGFs	platelet-derived growth factors
PE	proepicardium
PECAM-1	platelet endothelial cell adhesion molecule
pen/strep	100u/ml penicillin with 100µg/ml streptomycin
PHH3	phosphohistone-H3
PI3K	phosphatidylinositol-4,5-bisphosphate 3-kinase
PKC	protein kinase c
Q-PCR	quantitative real time PCR
RA	retinoic acid
RA	right atria
RAA	right atrial appendage
RALDH2	retinaldehyde dehydrogenase
RAR	retinoic acid receptor
rEPDCs	rat epicardial derived cells
RHD	right hand side
ROCK	rho-associated kinases
RTKs	receptor tyrosine kinases
RV	right ventricle
SAR	structure activity relationship
SB	SB-435142
SDF-1	asstromal cell–derived factor 1
SHF	second heart field
SNAI1/2	snail family zing finger 1/2
SM-MHC	smooth muscle myosin heavy chain
SM22-α	smooth muscle protein 2 alpha (gene *TAGLN*)
SMAD2/3	mothers against decapentaplegic homologs 2 and 3
SOX2	(sex determining region y)-box 2
T/BRA	t/brachyury
Tbx18	t-box 18
TBX5	t box 5
Tcf21	transcription factor 21
TCF7	transcription factor 7
TEM	transition electron microscopy
TGFβ	transforming growth factor beta
TIE-2	tek receptor tyrosine kinase
Trypsin	0.05% trypsin-EDTA solution
Tβ4	thymosin β4
VEGF	vascular endothelial growth factor
VEGFC	vascular endothelial growth factor c
WT1	wilms tumour 1
X-Gal	5-bromo-4-chloro-3-indolyl-beta-d-galactopyranoside
ZEB1/2	zinc finger e-box-binding homobox 1 and 2
α-MHC	α-myosin heavy chain (gene *Tnnt2*)
α-SMA	α-smooth muscle actin (gene *Acta2*)
β-GAL	β-GALACTOSIDASE

Chapter 1

General introduction

1.1 Cardiovascular disease: the biggest killer of the modern age

The prevalence of cardiovascular disease (CVD) in the global population is a relatively recent development in the history of human health. In the First Annual Report of the Registrar-General on Births, Deaths, and Marriages in England, published in 1839, the leading cause of death was attributed to infectious disease, with phthisis miliaris (tuberculosis) reported to be the biggest killer (Journal of the Statistical Society of London, 1839). A century later improved understanding of human disease and in particular the multinational, collaborative effort that established mass production of penicillin during the second world war resulted in dramatic improvements in public health and a near doubling of life expectancy (Quinn, 2013; The Longevity Science Advisory Panel, 2012). These developments, however, were coupled with the emergence of a new era of disease and by 1950 degenerative heart disease and cancer were ranked as the first and second most common causes of mortality (NISRA, 1950).

CVDs are currently the number one cause of death worldwide: in 2012, of the 17.5 million deaths attributed to CVD globally, 7.4 million were a result of coronary heart disease (CHD) (http://www.who.int/mediacentre/factsheets/fs317/en/). CHD is characterised as a disease of the blood vessels that supply blood to the heart: build-up of cholesterol rich plaques on the artery wall causes a gradual narrowing of the vasculature that restricts blood flow (Pjanic et al., 2016). Plaque rupture triggers the release of thrombotic and vasoconstrictive signals that can result in the formation of a blood clot that partially or fully occludes the blood vessel (Ashley and Niebauer, 2004). Total occlusion of the coronary artery and subsequent cessation of blood flow to the heart muscle is termed a ‘myocardial infarction’ (MI), more commonly known as a heart attack.

1.2 With great success comes great burden

At present, seven of every ten patients that suffer a MI will survive the initial injury, as compared to the three in ten chance of survival recorded in the 1960's (British Heart Foundation). This increased survival is due to improved primary intervention; acute MI can be treated via a number of clinical interventions including thrombolysis, the administration of drugs that dissolve blood clots, or by percutaneous transluminal coronary angioplasty in which a catheter balloon is delivered to the site of blockage through the femoral artery and inflated gently at the occlusion to restore blood flow (Ryan et al., 1996). Unfortunately, coronary reperfusion itself causes further injury and is the first in a series of pathological changes that will subsequently impact a patients' prognosis.

Cardiomyocytes, the contractile cells that make up the heart muscle, are for the most part terminally differentiated and unable to undergo mitosis. Therefore, the major mechanisms of repair in the mammalian heart are directed towards formation of a thick fibrotic scar. There are four distinct phases of cardiac wound healing (Cleutjens et al., 1999): first, approximately 6–8 hours after induction of ischemic injury, millions of oxygen deprived cardiomyocytes begin to die either by necrotic or apoptotic mechanisms. This triggers phase two, occurring 24–48 hours after the infarct, in which a cascade of inflammatory cells including neutrophils, granulocytes and macrophages help to clear away the dead tissue. Next the 'wound healing' phase begins: the extra cellular matrix (ECM) components fibrin and fibronectin, deposited early in the injury cascade, are replaced by collagens that are secreted by myofibroblasts. The myofibroblasts are arranged around the border of the injury zone and use contractile machinery to pull the edges of the wound closer together (van den Borne et al., 2010; Willems et al., 1996). Interstitial collagens are later replaced by collagen 1 and the interlinking of the collagen 1 strands further strengthens the scar, known as 'granulation tissue', which is also perfused with blood vessels.

Finally, after 2–3 weeks, cells begin to disappear from the scar region with the exception of the myofibroblasts, which have been found resident in human scars up to 17 years after the initial injury (Willems et al., 1994).

Formation of the collagen scar is essential for conservation of cardiac structural integrity, preventing rupture and maintaining blood flow around the body. However, the non-contractile nature of the scar tissue results in an overload of pressure on the remaining viable muscle that results in the abnormal growth of the remaining cardiomyocytes: 'hypertrophy' (Katz, 1995). Several animal models have demonstrated that increased haemodynamic pressure increases both cardiomyocyte size and rate of protein synthesis (Cooper et al., 1985; Kent et al., 1989; Kira et al., 1984). The hypertrophic response progressively weakens the heart leading to development of congestive heart failure, in which the organ is no longer able to effectively pump blood around the body. A recent study found that that the risk of a subsequent MI, stroke or other CV related death increases by an average of 3.5% every year for the first four years after a primary MI event, further highlighting the progressive and debilitating nature of this disease (Abtan et al., 2016). Transplantation is currently the only available 'cure' for heart failure; however, the limited number of donors and problems with immunocompatibility present a major bottleneck to treatment and current medication serves only to prevent a further decline in function (Smart et al., 2012).

1.3 Stem cells: the key to cardiac regeneration?

The broad definition of a stem cell is an unspecialised cell of a multicellular organism capable of unlimited proliferation to produce more stem cells and also of differentiation into specialised cell types (Jaenisch and Young, 2008). Numerous sub-categories of stem cells exist (**Figure 1.1**): 'totipotent' stem cells are capable of forming all cell lineages of an organism including

embryonic tissues. Only the zygote and blastomeres, the collection of cells formed from initial division of the zygote, are totipotent. Embryonic stem cells (ESCs) are an example of pluripotent stem cells, which can differentiate into all the cell lineages of the body (Evans, 2011). Multipotent stem cells can differentiate into multiple cell types but are committed to one lineage, such a neural stem cells that reside in the central nervous system and differentiate in to neurons and glial cells (Rhee et al., 2016). Unipotent stem cells can only differentiate into one cell type: spermatogonial stem cells are an example of unipotent stem cells (Jaenisch and Young, 2008).

A closely related but distinct concept is that of progenitor cells (Seaberg and van der Kooy, 2003). Unlike stem cells, progenitor cells have limited ability to self-renew and are often unipotent, or are more specialised with a tendency only to differentiate into specific cell types (**Figure 1.1**). For example, hematopoietic stem cells are multipotent with the ability to differentiate into all mature components of the blood; however, they then differentiate into subpopulations of progenitor cells that are multipotent but can only develop into a subset of specific cell lineages (Seaberg and van der Kooy, 2003).

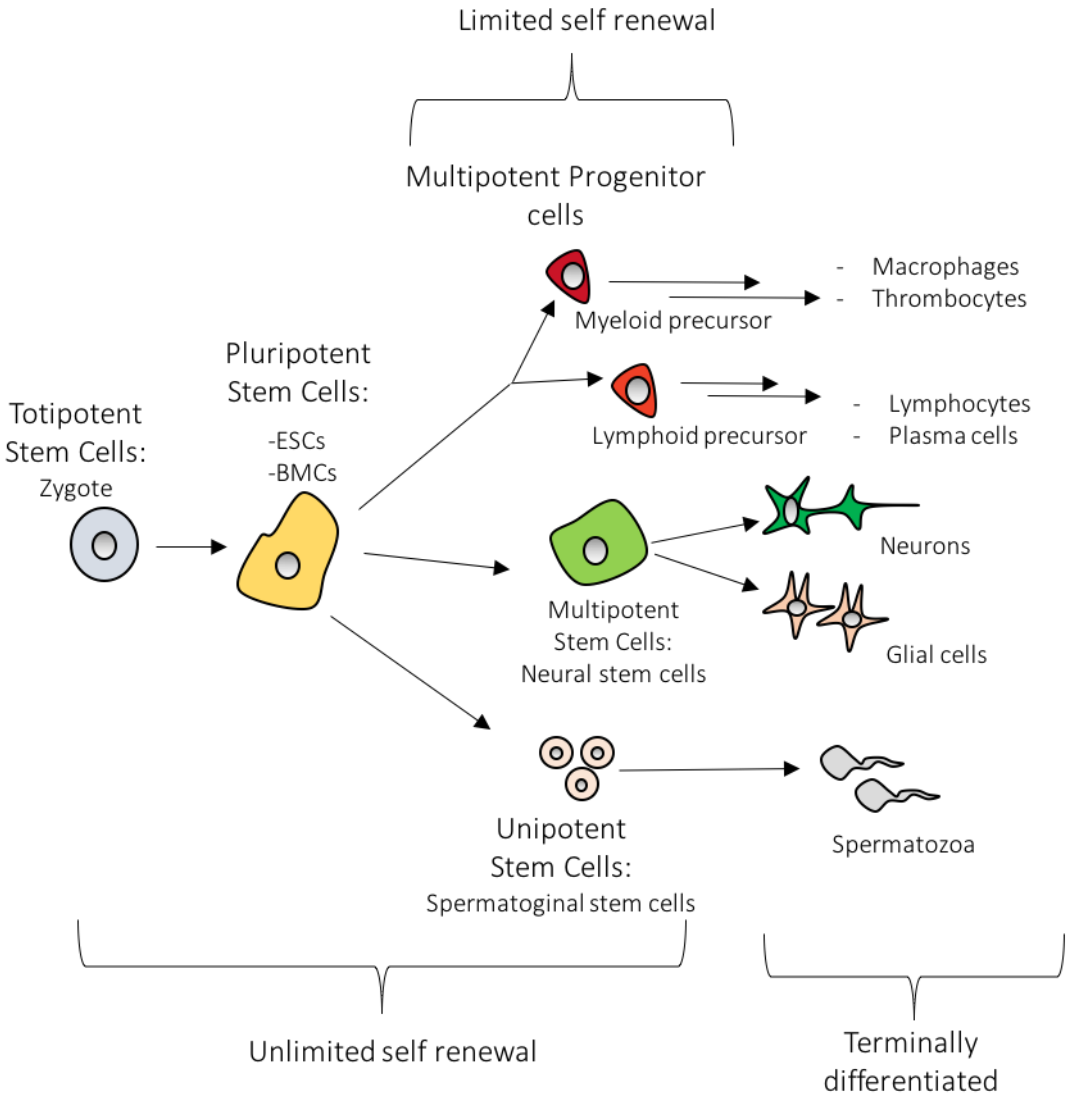


Figure 1.1 Simplified schematic demonstrating stem and progenitor cell differentiation. Stem cells have unlimited ability to self-renew and differentiate in to specialised cell types. Several kinds of stem cell exist: totipotent stem cells can differentiate into any cell lineage including embryonic tissues; pluripotent stem cells can differentiate into any cell of an organism; multipotent stem cells can differentiate into multiple cell types; unipotent stem cells can only differentiate into on cell type. Progenitor cells are multipotent and can differentiate into several cell types however they have limited renewal capacity.

In the case of skeletal muscle, endogenous repair is mediated by two cell sources: firstly, mononucleated satellite cells, a population of progenitor cells residing in the muscle, can divide and form young myotubes in response to injury (Ferrari et al., 1998; Grounds et al., 1992). There is also an added contribution from a non-satellite cell population: circulating bone marrow derived stem cells. Bone marrow (hematopoietic) stem cells (BMCs) derived from a transgenic

mouse line were injected in to immune deficient mice with skeletal muscle injury. These BMCs contained the MLC3F-nlacZ transgene in which the *lacZ* gene and consequent nuclear expression of the β-GALACTOSIDASE (β-GAL) enzyme is controlled by the promoter of muscle-specific myosin light chain 3F (MLC3F). β-GAL activity can be detected with immunohistochemistry (IHC) using 5-bromo-4-chloro-3-indolyl-β-D-galactopyranoside (X-gal) as a substrate, which is hydrolysed and then oxidised to 5,5'-dibromo-4,4'-dichloro-indigo which is dark blue in colour (Burn, 2012). Any BMCs that differentiate into muscle and express MLC3F will also co-express β-GAL. Between two and three weeks after transplantation, both mature and immature β-GAL+ muscle fibres were found in regenerating muscle, confirming a contribution from circulating bone marrow (Ferrari et al., 1998). BMCs have also been reported to contribute to regeneration of the liver and the brain (Eglitis and Mezey, 1997; Theise et al., 2000).

These studies inspired investigation into whether BMCs could contribute to repair in the injured myocardium. A seminal finding in the development of this field was published in 2001 (Orlic et al., 2001): lineage negative BMCs were isolated by fluorescence-activated cell sorting (FACS), based upon expression of the stem cell marker C-KIT. Injection of C-KIT+ BMCs into the infarcted myocardium of mice that had been subject to coronary artery ligation was reported to induce regeneration in 68% of the infarct area, and consequently conferred significant improvement in cardiac function. Furthermore, cytokine mediated activation of resident C-KIT+ BMCs was reported to decrease mortality by 68% and reduce infarct size by 40% in mice with acute MI (Orlic et al., 2001). The exciting nature of this discovery initiated a flurry of similar studies including a report in which Y-chromosome cardiomyocytes were identified in human females who had undergone under sex-mismatched bone marrow transplantation (Deb et al., 2003). Following this finding, human mesenchymal stem cells isolated from bone marrow were

also reported to form *de novo* cardiomyocytes when injected into infarcted mouse myocardium (Ngo et al., 2014).

These discoveries have been shrouded with controversy; two leading stem cell laboratories collaboratively attempted to replicate these findings (Murry et al., 2004), however, both them and other groups unanimously reported that injected BMCs do not develop a cardiac phenotype *in vivo*, and instead develop mature hematopoietic fates (Balsam et al., 2004; Murry et al., 2004; Wagers et al., 2002). Furthermore, recently published data from human clinical trials that were initiated as a result of this work did little to clarify the situation. Administration of BMCs into ischemic hearts by both intracoronary, induction through the coronary artery, and transendocardial, direct injection into the wall of the heart, methods were reported to show no observable benefits four and six months after treatment (Perin et al., 2012; Sürder et al., 2013). However, a meta-analysis that combined the results of 50 independent studies reported that transplantation of BMCs improved ventricular function and reduced both infarct size and incidences of death in patients with ischemic heart disease (Jeevanantham et al., 2012), although the methods used in this analysis have come under criticism for the omission of several key studies (Delewi et al., 2013). From these data it would appear that

In light of these findings it was postulated that poor efficacy of treatment may arise from failed homing of the BMCs to site of injury or due to injection of ineffective cell populations of. A number of cytokine attractants such as asstromal cell–derived factor 1 (SDF-1) and vascular endothelial growth factors (VEGF) are transiently released in the myocardium after injury which recruit BMC localisation (Assmus et al., 2013). Intracoronary administration of BMCs along with a low energy shock wave that prolonged myocardial cytokine release was found to result in modest but significant improvements in left ventricular ejection fraction (LVEF), and

reduction in subsequent cardiac events after four months. In another study administration of BMCs that had first been exposed to a 'cardiogenic cocktail' of growth factors *in vitro* were found to improve LVEF and six-minute walking distance six months after treatment (Bartunek et al., 2013). Ixymylocel-T' is a patient derived cocktail of bone marrow cell types that has been enriched for M2 macrophages, which are involved in extracellular matrix deposition and remodelling, and cluster of differentiation 90 positive (CD90+) mesenchymal stem cells (MSCs) (Patel et al., 2016). Transendocardial delivery of ixymylocel-T to patients with ischemic dilated cardiomyopathy resulted in a reduction of subsequent cardiac events over the following 12 months.

The interpretation of these findings remains an area of intense debate (Leri and Anversa, 2013) however, these early studies pioneered the field that continues to explore whether stem or progenitor cell transplantation can be utilised for heart regeneration. Strategies employed in the generation of cardiomyocytes from alternative cell populations have been varied, as have the results. Autologous transplantation of skeletal myoblasts (satellite cells) into cryoinjured rabbit hearts, in which a liquid nitrogen cooled cooper probe is used to induce tissue damage to the ventricle to mimic MI, resulted in improved cardiac function but only when the transplanted cells had successfully engrafted (González-Rosa and Mercader, 2012; Taylor et al., 1998). However, in human patients that had suffered a MI this treatment was found to have no beneficial effect on cardiac function and increased the occurrence of post-operative arrhythmic events (Menasché et al., 2008). Cardiomyocytes have been successfully generated from both human embryonic stem cells (hESCs) and induced pluripotent stem cells (hIPS) *in vitro* (Discussed in detail in **Chapter 1.12**) (Kehat et al., 2001; Zhang et al., 2009). Grafting of these pluripotent cell-derived cardiomyocytes into the ischemic myocardium in animal models has been hampered by problems including failure to integrate into the muscle and apoptosis,

postulated to be a result of the ischemic and inflammatory environment of the post MI heart (Moon et al., 2013; Zhang et al., 2001). Several strategies including cell grafting alongside a cocktail of 'pro-survival' factors, such as z-VAD.fmk, a peptide that inhibits apoptotic caspase enzymes (Laflamme et al., 2007), and transplantation of purified cardiomyocyte aggregates (Moon et al., 2013) have been reported to increase cell survival and cardiac output in rodents. In 2014, transplantation of hESC derived cardiomyocytes to infarcted non–human primate hearts was found to extensively remuscularise ~40% of the infarct region generating functional and mechanically integrated muscle, although this was also paired with increased arrhythmic activity (Chong et al., 2014).

Hydrogels are 'water soluble polymer networks' that can be injected in liquid form and induced to form a crosslinked gel by chemical or physical stimuli such as body temperature (Hasan et al., 2015). In pig, injection of acellular hydrogels into infarcted heart tissue formed a porous scaffold for cell permeation that resulted in reduced fibrosis and neovascularization (Seif-Naraghi et al., 2013). Hydrogels have also been used to enhance the efficiency of growth factor and stem cell delivery to the injured myocardium (Wang et al., 2012; Wu et al., 2011). There has also been extensive research into the generation of 3D heart muscle (Hirt et al., 2014). A number of studies have documented production of electrically coupled myocardium by seeding myocardial cells on to preassembled matrices or decellularised heart scaffolds (Ott et al., 2008; Radisic et al., 2004). Recently, transplanted hIPS derived 3D tissue scaffolds consisting of cardiomyocytes, endothelial and vascular cells were found to survive *in vivo* and functionally integrate with the myocardium, conferring some functional recovery (Masumoto et al., 2016). The use of embryo-derived stem cells evokes much controversy, and the added concern that uncontrolled proliferation of transplanted pluripotent cells can result in tumour formation has

delayed clinical translation to patients (Jeong et al., 2011). In time, continued efforts in the fields of tissue engineering and cell transplantation may reveal the true potential of these studies.

1.4 The mammalian heart has regenerative potential

The previously established doctrine that the mammalian heart is a terminally differentiated organ was challenged in several reports that documented *de novo* cardiomyocyte formation. Identification of adult cardiomyocytes undergoing mitosis after MI and cardiac failure in human heart samples initially challenged this dogma (Beltrami et al., 2001; Kajstura et al., 1998). Conclusive evidence to support *de novo* cardiomyocyte formation in adult humans was provided using carbon dating (Bergmann et al., 2009). The concentration of the ^{14}C isotope in cellular DNA reflects the concentration in the atmosphere at the time of synthesis meaning it is possible to trace the birth date of the cell. An increase in the concentration of atmospheric ^{14}C was recorded in 1955 due to above ground nuclear testing that occurred during the cold war. In human patients born prior to the 1955, ^{14}C concentration in the DNA of FACS isolated cardiomyocytes was higher than the corresponding atmospheric concentration at their time of birth, indicating that new cardiomyocytes had formed during their lifetime. This study calculated a cardiomyocyte turnover of 1% per year at the age of 25 which declined to 0.45% by age 75; this equates to less than 50% of the total cardiomyocyte population being turned over during a normal life span (Bergmann et al., 2009).

1.5 Stem and progenitor populations residing in the adult heart

Whilst the mammalian heart does appear to retain some regenerative potential, it is clearly not sufficient to functionally replace lost heart tissue following MI. Furthermore, the source of these *de novo* cells was yet to be confirmed. Studies evaluating the chromosome content of human hearts transplanted from female donors to male recipients revealed presence of Y-chromosome positive cardiomyocytes, suggesting there may be a contribution from an extra cardiac stem or

progenitor cell population rather than from division of existing cardiomyocytes (Laflamme et al., 2002; Quaini et al., 2002).

In an attempt to identify the source of *de novo* cardiomyocytes cells a study was conducted using a *Cre/loxP* mouse model (Hsieh et al., 2007). In this line the *lac-Z* gene is flanked by two *loxP* sequences which are recognised and cleaved by the inducible Cre recombinase enzyme, which is under control of cardiomyocyte specific α-myosin heavy chain (α-MHC, gene *Myh7*). Treatment of mice with 4-OH tamoxifen induces Cre expression in α-MHC+ cells, which subsequently excises the *lacZ* gene and instead drives expression of green fluorescent protein (GFP). 'Pulse' labelling with 4-OH tamoxifen marks existing cardiomyocytes with GFP at the time of injection: any new cardiomyocytes that subsequently form from division of existing GFP+ cells would also express GFP. In contrast, any *de novo* cardiomyocytes generated from stem or progenitor cell populations would express the β-GAL protein. This study found negligible turnover of cardiomyocytes in the myocardium of control mice over the first year of life. However, three months after surgically induced MI approximately 20% of cardiomyocytes were found to be β-GAL+, suggesting a contribution from a non-myocyte progenitor pool (Hsieh et al., 2007).

In a more recent study another mouse line, in which administration of 4-OH tamoxifen pulse labels existing cardiomyocytes with GFP with about 80% efficiency, was used in combination with administration of ^{15}N[thymidine] which labels replicating DNA (Senyo et al., 2013). In normal tissue homeostasis ~80% of ^{15}N+ cardiomyocytes were GFP+ which was about equal to that of the background GFP signal, demonstrating that DNA synthesis was occurring in pre-existing cardiomyocytes and excluding a role of an alternate stem or progenitor cell population. Much like the previous study, a negligible annual cardiomyocyte turnover of 0.79% a year was calculated for normal tissue homeostasis in young adult mice. In the case of an injury, dilution

of GFP cardiomyocytes was observed in the injury zone. However, of the $^{15}N+$ population 71% of the population was GFP which was equal to the background measure of GFP in $^{15}N–$ cells. This again appeared to exclude a major contribution from a progenitor source: the study concluded that spontaneous division occurred in 3.2% of the cardiomyocytes adjacent to the site of infarct, however, the majority of $^{15}N+$ cardiomyocytes were found to be undergoing hypertrophy and unable to re-enter the cell cycle.

The presence of stem cell populations in the heart was first reported more than a decade ago when lineage negative C-KIT+ cells were isolated from rat hearts (Beltrami et al., 2003). These cells were found to be self-renewing and multipotent; injecting the cells into ischemic myocardium significantly reduced the size of the infarct and resulted in improved cardiac performance. Another group reported the isolation and expansion of adult stem cells from both human and mouse; in contrast to the report of Beltrami *et al.* transplantation of the human cardiac stem cells to injured mouse myocardium had little effect on the resulting infarct size but did appear to improve fractional shortening, a measure of the hearts ability to eject blood (Messina et al., 2004). In an attempt to clarify the therapeutic potential of cardiac C-KIT+ cells a novel mouse model was employed. Injection of these mice with isoproterenol (ISO) causes Takotsubo cardiomyopathy, non-ischemic weakening of the heart muscle, that kills 8–10% of the cardiomyocytes in the left ventricle (LV) but not the resident stem cells (Ellison et al., 2007, 2013). Maximum cardiomyocyte death is seen on day one but, remarkably, by day 28 heart failure is reversed and normal anatomical function is resumed. By ablating cardiac stem cell proliferation in ISO damaged hearts with the antimitotic agent 5-flurouracil, cardiac repair was inhibited. This indicated that remuscularization of hearts treated with ISO, but not 5-fluorouracil, was due to differentiation of resident cardiac progenitor cells. The plot thickened further still in 2014, when a report demonstrated minimal contribution of the C-KIT lineage to

cardiomyocyte formation (van Berlo et al., 2014). A mouse line in which GFP expression is under the control of the C-KIT promoter revealed that 0.03% of cardiomyocytes were derived from C-KIT+ cells in the developing heart: the majority of GFP+ cells were positive for endothelial, fibroblast or immune cell markers. Pulse labelling of the C-KIT population for six weeks in adult mice revealed 0.0055% of GFP+ cardiomyocytes, which increased to 0.016% when mice were subject to surgical MI. Furthermore, in response to ISO induced injury only 0.007% of cardiomyocytes were GFP+. Collectively this work demonstrated minimal cardiogenic potential of the C-KIT lineage. Although it is generally accepted that a population of stem cell resides in the heart, their exact role in tissue homeostasis and injury remain to be fully elucidated, and as of yet there is no consensus as to whether they will prove useful for therapy (Nadal-Ginard et al., 2014).

1.6 The role of the epicardium in development

In the search for a resident pool of progenitor cells, the epicardium has attracted significant interest. The epicardium is an epithelial layer covering the hearts surface that plays an important role in heart development. The heart is the first organ to function in the embryo; it is required by the fourth week of gestation in humans when diffusion of oxygen and nutrients from the placenta is no longer sufficient (UNSW Embryology). Cardiac morphogenesis is a complex developmental event: three major sources of cells contribute to the developing heart: cardiogenic mesoderm, cardiac neural crest and the proepicardium (**Figure 1.2**) (Laugwitz et al., 2008). On day 15 in human development (Embryonic day (E) 7.5 in mouse) (**Figure 1.2**) two bilateral heart fields are present containing two distinct cell types which are myocardial and endocardial progenitors (Wessels and Pérez-Pomares, 2004). The first heart field (FHF) contributes to the left ventricle (LV) and second heart field (SHF) to the right ventricle (RV) and later the right and left atria (RA/LA), outflow tract (OFT) and sinous venosus (Bruneau, 2008). By day 20

(E8) (**Figure 1.2**) fusion and rearrangement of the two heart fields forms a tubular heart consisting of two concentric layers of myocardium and endocardium which are separated by an ECM rich cardiac jelly (Markwald et al., 1996). Around day 28 (E9) (**Figure 1.2**) the heart tube begins to loop forming the four heart chambers: towards the end of cardiac looping around day 32 (E10) (**Figure 1.2**) progenitors from the neural crest migrate and contribute vascular smooth muscle cells to the outflow track (OFT) (Laugwitz et al., 2008). At this point another epithelial layer is formed across the top of the myocardium: the epicardium. Initially the epicardium was thought to arise from the myocardium itself, which was collectively referred to as the 'epimyocardium'. However, electron microscopy studies in chick showed that epicardial cells are in fact derived from a cluster of cells called the proepicardium (PE) that is formed dorsal, to the back of, the developing heart tube just above the primordial liver and have been described as having a 'cluster of grapes' appearance (**Figure 1.2**) (Ho and Shimada, 1978; Svensson, 2010). The mechanism of PE migration to the myocardium varies depending upon the species. In chick, the PE migrates over an ECM bridge and the epicardium spreads across the surface in a sheet like manner. However, it has been suggested that in mice PE aggregates are released that attach to the surface of the myocardium forming a series of "epicardial islands" that consequently expand to form the epicardial sheet (Komiyama et al.; Plavicki et al., 2014). The transcription factors T-box 18 (TBX18), Wilms tumour 1 (WT1) and Transcription Factor 21 (TCF21) are expressed in the PE and in migrating epicardial cells, which serve as genetic markers of the population and illustrate the inherent heterogeneity of the PE and subsequent epicardium (Bollini et al., 2014; Svensson, 2010).

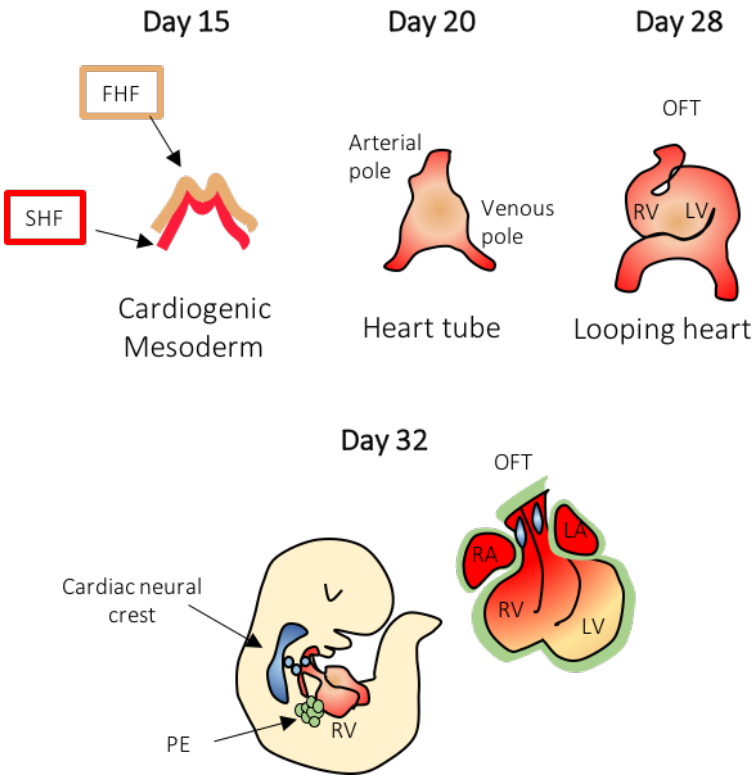


Figure 1.2 Embryonic heart development. On day 15 in human development two bilateral heart fields are present in the cardiac mesoderm: the first heart field (FHF) and second heart field (SHF). By day 20 fusion of the two heart fields forms a tubular heart. Around day 28 the heart tube begins to loop forming the four heart chambers: the left and right ventricles (LV/RV) and the left and right atria (LA/RA). Towards the end of cardiac looping, around day 32, progenitors from the neural crest migrate and contribute vascular smooth muscle cells to the outflow track (OFT). Coincidently cells from the proepicardium (PE) migrate over the surface of the heart forming the epicardial epithelial layer. Adapted from (Laugwitz et al., 2008)

After the epicardial sheet has formed it becomes separated from the underlying myocardium by an expanse of ECM termed the subepicardium. A subset of cells in the epicardium then undergo epithelial to mesenchymal transition (EMT) in which they lose epithelial characteristics, develop migratory and invasive capacity and subsequently populate the subepicardial space. Initiation of epicardial EMT and formation of epicardium derived cells (EPDCs) is thought to be stimulated by fibroblast growth factor (FGF) signalling from the underlying myocardium (Morabito et al., 2001a). The snail family zing finger 1/2 transcription factors 1 and 2 (SNAI1 and SNAI2) are involved in regulation of embryonic EMTs and are highly expressed in the developing epicardium (Carmona et al., 2010). The Snail family of proteins act as transcriptional repressors of the E-CADHERIN gene *Cdh1*, binding to the promoter region by recognising and binding specific regions named ‘E-boxes’ (De Herreros et al., 2010). The cell adhesion protein

E-CADHERIN is essential for the assembly and sealing of adherens junctions between epithelial cells, and is widely accepted as the defining characteristic of epithelia (Contreras et al., 2002; De Herreros et al., 2010). *Snai1* and *Cdh1* are under the transcriptional control of WT1, expression of which is essential for epicardial EMT and EPDC generation: genetic knock down of WT1 was found to decrease expression of mesenchymal markers and increase E-CADHERIN in immortalised epicardial cells and embryoid bodies *in vitro* (Martínez-Estrada et al., 2010).

The EPDC population plays a multitude of roles in cardiac development. EPDC paracrine signalling to the underlying myocardium is essential for correct differentiation and maturation of the heart muscle (Carmona et al., 2010). Studies of cardiomyocyte proliferation in development revealed a 'gradient' of cell replication that was greatest in the outer layers of cardiac tissue under the epicardium and lowest towards the endocardium (Sucov et al., 2009). Furthermore, in chick studies epicardial ablation resulted in thin, improperly formed ventricle walls and reduced cardiomyocyte proliferation (Pennisi et al., 2003; Stuckmann et al., 2003). A number of soluble factors have been reported to drive myocardial maturation including FGFs (Lavine et al., 2005; Pennisi et al., 2003) and platelet-derived growth factors (PDGFs) (Kang et al., 2008; Kim et al., 2010). More recently epicardial erythropoietin (Epo) and retinoic acid (RA) and their respective receptors (EpoR and RAR) have been implicated in regulating the growth of the forming myocardium. The Epo growth factor is essential for survival, proliferation and differentiation of several progenitor populations and genetic knock out of Epo or its receptor results in thin hypoplastic ventricles (Wu et al., 1999). The enzyme that generates retinoic acid: retinaldehyde dehydrogenase 2 (RALDH2): is highly expressed in the developing epicardium. RA is not thought to signal directly to the myocardium, as knock out of myocardial RAR has no effect on development of the muscle (Merki et al., 2005). However, knock out of RAR in the epicardium results in ventricular thinning, indicating a paracrine signalling effect that may then

stimulate production of FGFs and other direct myocardial signalling molecules (Merki et al., 2005).

In addition to essential paracrine signalling, EPDCs also populate the underlying myocardium with essential cardiovascular cell derivatives. The contribution of EPDCs to the developing coronary vasculature has been well established in several models. The importance of the epicardium in vascular development was first demonstrated in mouse when mutation of α-4 INTEGRIN, a membrane receptor expressed in the epicardium that controls ECM and cell-cell adhesion, resulted in incomplete formation of the epicardium and prohibited coronary vasculogenesis (Yang et al., 1995). In chick, EPDC invasive capacity was confirmed *in vitro* in cultures of quail epicardial cells which, when treated with fibroblast growth factor 2 (FGF2), underwent EMT and invaded collagen matrix gels (Dettman et al., 1998). Furthermore, β-GAL+ EPDCs grafted to the myocardial wall *in ovo* prior to formation of the epicardium migrated over the heart forming epithelia and subsequently invaded the myocardium, migrated toward the vasculature and differentiated into smooth muscle cells at the vascular wall. The smooth muscle phenotype was confirmed by expression of the markers α-smooth muscle actin (α-SMA) and CALDESMON (Dettman et al., 1998). β-GAL+ EPDC derivatives that were not associated with vessels did not express smooth muscle markers and were suggested to be perivascular and interstitial fibroblasts. Further fate mapping studies confirmed a significant EPDC contribution to the cardiac fibroblast population (Zhou et al., 2010).

In 2008, two reports of an epicardial contribution to the cardiomyocyte population were published. In one study a $Tbx18^{Cre}$ mouse was crossed with a *lacZ* line, generating a mouse in which all cells that expressed TBX18, and their progeny, were irreversibly labelled with β-GAL. Active TBX18 expression was restricted to the epicardium at embryonic day 11.5 (E11.5)

however, β-GAL+ cardiomyocytes were found to be located in the ventricular septum and in the walls of the atria and ventricles indicating epicardial contribution to the muscle (Cai et al., 2008). These data were later challenged in a conflicting study in which TBX18 was found to be expressed in cardiomyocytes from E10.5 onward, calling in to question the use of TBX18 as the appropriate Cre driver to fate map the contribution of the epicardium (Christoffels et al., 2009).

In a second study, GFPCre was knocked into the WT1 locus: WT1 and GFPCre expression were specifically located in the epicardium and PE from E9.5 to E15.5. Crossing $WT1^{GFPCre}$ with the Z/Red reporter line irreversibly labelled WT1+ cells and their progeny with β-GAL. β-GAL+, WT1-derived cardiomyocytes were found throughout the myocardium at E15.5 constituting 7–10% of ventricular and 18% of atrial myocytes, again suggesting that the EPDCs can contribute to the cardiomyocyte population in development (Zhou et al., 2008). Subsequently a $WT1^{GFPERT2}$ mice were crossed on to the $Rosa26^{fsLz}$ reporter line. In these mice Cre activity is activated by administration of 4-OH tamoxifen, inducing β-GAL+ activity in WT1 expressing cells. In this model, only 0.02±0.01% of cardiomyocytes were found to be derived from WT1+ precursors (Zhou et al., 2008). A later study that reviewed the specificity of the $WT1^{GFPCre}$ line found that sporadic recombination had induced GFP in cells throughout the myocardium that were not of epicardial origin (Rudat and Kispert, 2012). This demonstrated that the originally observed contribution of the epicardium to muscle was likely to be an overestimate.

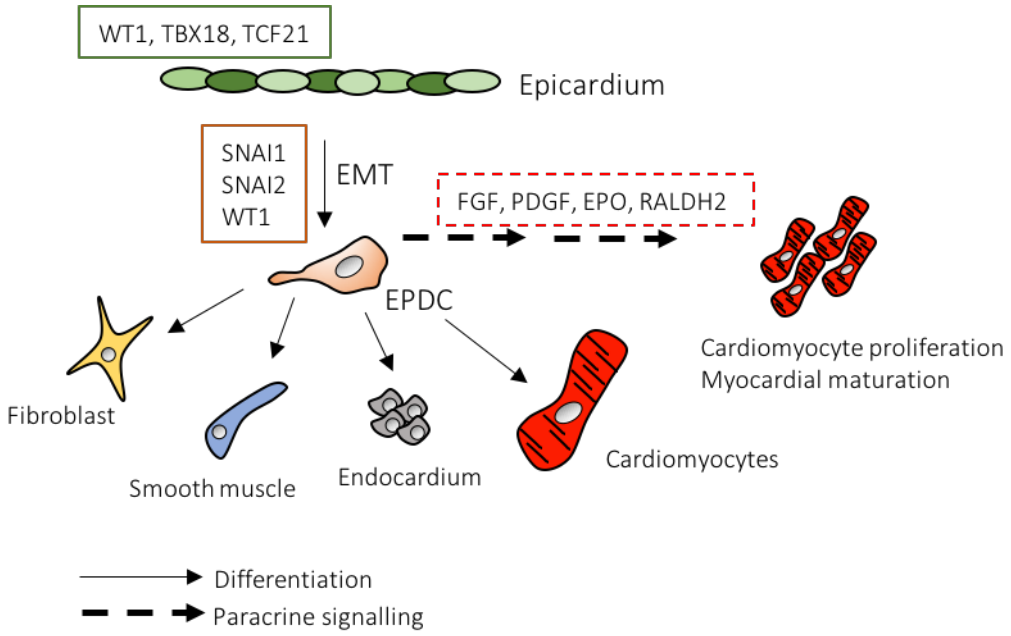


Figure 1.3 Summary of epicardial contribution in development. Embryonic epicardium expresses the transcription factors WT1, TBX18 and TCF21. After the epicardial sheet has formed over the surface of the heart a subset of cells undergo EMT characterised by expression of the transcription factors SNAI1 and SNAI2, which are under the control of WT1. The subsequently formed EPDCs are a progenitor population that migrate into the myocardium and differentiate into multiple cardiac lineages including fibroblast, smooth muscle, endocardium and small numbers of cardiomyocytes. EPDCs are also involved in essential paracrine signalling through FGF, PDGF EPO and RA that aids proper myocardial formation. Adapted from (Brade et al., 2013).

Despite these somewhat controversial findings, the phenotypic plasticity of EPDCs is generally accepted and they are widely thought of an as endogenous progenitor population (For overview see **Figure 1.3**). Furthermore, although TBX18 was shown not to be epicardium-specific, a subpopulation of TBX18+ cells isolated from the PE and differentiated *in vitro* expressed the cardiomyocyte marker cardiac troponin T (CTNT) and began beating spontaneously (Cai et al., 2008). Interestingly EPDCs isolated from adult epicardium did not exhibit the same plasticity.

1.7 The role of the epicardium in injury

Interest in the role of the epicardium in heart regeneration and in particular as a source of *de novo* cardiomyocytes stemmed from studies in zebrafish. In 2002, a study demonstrated that the

zebrafish heart can fully regenerate after resection of up to 20% of ventricular tissue (Poss et al., 2002). Histochemical analysis 30 days post resection revealed complete myocardium almost indistinguishable from that of pre-injury or sham-operated animals. Pulse labelling of regenerating hearts with Bromodeoxyuridine (BrdU), a synthetic nucleotide that can be incorporated into DNA during mitosis and subsequently identified by immunocytochemistry (ICC), indicated that existing cardiomyocytes proliferate and contribute cells to regenerating tissue. Interestingly, as seen in cardiac development, cardiomyocyte replication also occurred on a gradient with greatest proliferation seen at the outer myocardial surface beneath the epicardium.

More recently, the contribution of existing cardiomyocyte proliferation was confirmed by transition electron microscopy (TEM) in transgenic fish in which GFP expression is driven by the myocardial specific cardiac myosin light chain 2 (CMLC2) (Jopling et al., 2010). In fish treated with BrdU 7 days after ventriclar amputation, GFP+/BrdU+ cardiomyocytes were identified in regenerating myocardium at day 14. TEM revealed that at day 7 the cardiomyocytes had begun to detach from one another creating intercellular space, which was followed by disassembly of sarcomeric structure and consequent loss of characteristic z-lines as cells dedifferentiated and re-entered the cell cycle. Further genetic lineage studies demonstrated that a subset of cardiomyocytes re-express the embryonic cardiogenic marker GATA binding protein 4 (GATA4) after ventricular resection, which then proliferate and substantially contribute to the regenerating myocardium; GATA4+ cardiomyocytes were particularly prevalent in the subepicardial muscle (Kikuchi et al., 2010).

Interestingly, as well as inducing cardiomyocyte proliferation, partial resection of the zebrafish ventricle also induced organ wide epicardial activation (Lepilina et al., 2006). In the uninjured

adult fish heart the epicardium is generally quiescent: epicardial cells do not undergo EMT or differentiate and are found only to express low levels of the epicardial markers WT1, TBX18 and RALDH2 (Lepilina et al., 2006). However, in zebrafish the epicardium is reactivated shortly after ventricular resection strongly expressing both RALDH2 and TBX18 1–2 days after injury. The expression in activated cells was concentrated around the site of injury and similar patterning in BrdU incorporation was observed, indicating localised proliferation. TBX18+ cells exhibited invasive behaviour similar to that seen in the developing heart and it was proposed that these activated EPDCs contribute to vascularization of newly formed tissue via EMT (Lepilina et al., 2006).

Although an impressive response, ventricular resection is not representative of the ischemic injury that results from MI. An alternative model is cryoinjury: fish are anesthetised before a small incision is made in the chest and a copper probe, cooled in liquid nitrogen, is applied to the ventricle for a few seconds to induce damage in ~25% of the tissue. Cryoinjury-induced cardiomyocyte death throughout the myocardium is followed by scarring and then delayed regeneration, providing a more relevant model for study (González-Rosa and Mercader, 2012). Initially the repair process in fish mimics mammalian adult wound healing with an inflammatory response to remove debris followed by collagen scar formation and fibrosis (Chablais et al., 2011). However, unlike mammalian repair, the zebrafish scar is subsequently resorbed and replaced with muscle. In this case, cardiomyocyte proliferation and migration was accompanied by apoptosis of scar-forming cells (Chablais et al., 2011; González-Rosa et al., 2011). Hearts were almost completely regenerated by 90 days post injury and, with the exception of some minor morphological differences, were both histologically and electrophysiologically comparable to controls demonstrating functional integration of new muscle tissue. Cryoinjury was also found to stimulate re-expression of the embryonic epicardial transcription factor WT1

and extensive epicardial proliferation, which implicated the activation of the epicardium as a key event in zebrafish heart regeneration irrespective of the nature of the injury (González-Rosa et al., 2011).

As previously described, mammalian wound healing after MI results in formation of a fibrotic scar. Interestingly, the myocardial repair response seen in zebrafish appears to be conserved in neonatal mice during the first week of life. 15% of the ventricular apex can be resected from 1 day old mice and endogenously repaired within 21 days (Porrello et al., 2011). Permanent ligation of the left anterior descending (LAD) coronary artery in mice induces MI and ischemia. When performed in neonates at post-natal day one (P1) the resulting fibrosis is also repaired by resident cardiomyocyte dedifferentiation and proliferation, leaving only a small amount of residual scar tissue around the ligature (Porrello et al., 2013). This response in both models is reported to be lost by P7, at which point the repair mechanisms revert to scarring and default adult wound healing. This phenomenon has become known as the 'regenerative window' and has inspired research into the developmental mechanisms controlling regenerative potential (Porrello et al., 2013). However, a contrasting study reported that in over 400 surgically resected neonates no regenerative response was observed and instead the hearts developed signs of remodelling and fibrosis (Andersen et al., 2014). Differences in the way the ventricular resection was carried out between studies have since been suggested as underlying these contrasting observations (Bryant et al., 2015). Definitive proof of neonatal mouse regeneration requires implementation of novel techniques, such as magnetic resonance imaging, to conclusively demonstrate both the induction of an injury and subsequent regeneration.

Much like the zebrafish, the mammalian epicardium is reactivated in response to cardiac injury. Induction of MI in rats resulted in epicardial re-expression of the embryonic transcription factor

WT1. Consequently, WT1+ cells that also expressed α-SMA and Platelet Endothelial Cell Adhesion Molecule (PECAM-1), an endothelial marker, were found located in the coronary vasculature around the ischemic region suggesting epicardial contribution to revascularization (Wagner et al., 2007). In mice, coronary artery ligation results in epicardial expansion and expression of WT1, TBX18 and RALDH2 (Limana et al., 2010; van Wijk et al., 2012; Zhou et al., 2011). The role and fate of activated adult EPDCs is a topic of debate: in one study a population of activated EPDCs were reported to express the stem cell marker C-KIT and contribute myocardial, endocardial and smooth muscle cells in to the injury response (Limana et al., 2007, 2010). In $WT1^{GFPCre}$ mice, MI induced epicardial activation was paired with epicardial EMT, confirmed by increased expression of SNAI1 and SNAI2, and proliferation (van Wijk et al., 2012; Zhou et al., 2011). Contrary to the previous studies, EPDCs were unable to fully recapitulate fetal behaviour as they largely remained in the sub-epicardial region, failing to migrate into the underlying myocardium. Moreover, EPDCs gave rise exclusively to fibroblasts without evidence of differentiation in to other cardiac cell types such as coronary smooth muscle or cardiomyocytes. There was some, limited, evidence of epicardium derived 'cardiomyocyte-like' cells that stained positive for cardiac troponin I (CTNI) but failed to exhibit the characteristic sarcomeric structure of mature myocytes (van Wijk et al., 2012). However, adult EPDCs were found to release proangiogenic factors such as FGF2 and VEGFC, and EPDC conditioned media was found to have pro-angiogenic effects both *in vitro* and *in vivo* demonstrating a role of the epicardium in paracrine signalling after injury (Zhou et al., 2011).

Thymosin β4 (Tβ4) is an essential peptide for actin filament formation and both the maintenance of the cytoskeleton and subsequent cell migration (Nemolato et al., 2013). In mice, Tβ4 has been shown to induce myocardial and endothelial cell migration in the developing heart and minimise cardiomyocyte loss after injury (Bock-Marquette et al., 2004). Embryos with heart specific

knock down of Tβ4 exhibited improperly formed epicardium and haemorrhaging at E12.5 (Smart et al., 2007). At E14.5 embryos were found to have thin, non-compact myocardium and detached epicardium. Tβ4 knockdown was also shown to inhibit EPDC migration into the myocardium and subsequently prevented formation of the coronary vasculature. To further investigate the effect of Tβ4 on the developing epicardium, embryonic epicardial explants were established: at E10.5 explants produced extensive outgrowths positive for α-SMA+ and the TEK Receptor Tyrosine Kinase (TIE-2), an endothelial marker. Explant outgrowth was significantly increased by addition of Tβ4. The adult epicardium exhibited minimal outgrowth *in vitro*; however, treatment with Tβ4 induced explant outgrowth and differentiation towards fibroblast, smooth muscle and endocardial phenotypes (Smart et al., 2007). To further probe the effects of Tβ4 induced epicardial activation, mice were 'primed' with 7 days of intraperitoneal Tβ4 injections prior to surgically induced MI (Smart et al., 2011). Priming resulted in higher levels of WT1 re-expression *in vivo* after MI suggesting targeted epicardial activation. Subsequently activated WT1+ progenitors were identified within the area surrounding the infarct that expressed cardiomyocyte markers such as CTN1 and exhibited mature sarcomeric structure and calcium transients.

The epicardial response to injury in humans remains to be determined. However examination of donor hearts identified WT1, TBX18 and RALDH2 expression after MI and/or chronic heart failure suggesting some evolutionary conservation of an epicardial response to injury (Braitsch et al., 2013). Collectively, these studies illustrate that adult quiescent epicardium is activated by ischemic injury and that EPDCs retain characteristics of a progenitor population with potential to differentiate into numerous cardiac cell types including fibroblast, smooth muscle, endothelial are cardiac muscle. The Tβ4 study demonstrated that administration of exogenous agents, in this case a small peptide, augments this regenerative potential. In this model, only 0.59% of activated

progenitors formed *de novo* cardiomyocytes which is clearly an insufficient response to compensate for the millions of cardiomyocytes lost after a MI (Smart et al., 2011). Furthermore, a complementary study in mice found that no epicardium derived cardiomyocytes were formed in mice retrospectively treated with Tβ4 after MI (Zhou et al., 2012a). With regards to translating these findings to the clinic, prophylactic administration of epicardium 'activating' agents to patients predicted to be at risk of a heart attack is clearly not a viable therapeutic strategy. Therefore, further research is required to identify alternative biological or chemical agents that, unlike Tβ4 treatment, can amplify epicardial reactivation post MI. Optimising this response and enhancing the cardiovascular lineage potential represents a tractable therapeutic strategy towards resident cell-based repair in human patients; this objective forms the basis of this thesis.

1.8 Small molecules in drug discovery and design

Small molecules as therapeutic agents have been central to the management and treatment of disease since the beginning of documented human history. Recommended use of willow bark, which contains the active component of aspirin 'salicylic acid' (**Figure 1.4**), for its pain relieving and anti-inflammatory properties date back as far as 2000 BC. Hippocrates (460–370 BC), considered by many to be the father of medicine, recommended chewing the bark to relieve symptoms of fever and pain (Mahdi et al., 2006). However, it was not until 1838, nearly 4000 years later, that the precise structure of the active small molecule salicylic acid was elucidated. Administering salicylic acid itself was found to induce irritation and bleeding of the stomach: acetylation of the alcohol produced the prodrug acetylsalicyclic acid, which is transformed back to the active form in the liver and was registered as by its trade name 'Aspirin' by Bayer in 1899 and made available without prescription in 1915 (**Figure 1.4**) (Mahdi et al., 2006). Interestingly, it was another 72 years before the mechanisms of Aspirins anti-inflammatory properties were revealed (Vane, 1971). This is a classic example of 'forward' or 'phenotypic drug discovery'

(Discussed in **Chapter 1.11**) in which a substance identified as having functional activity and is then investigated to determine its pharmacology (Takenaka, 2001).

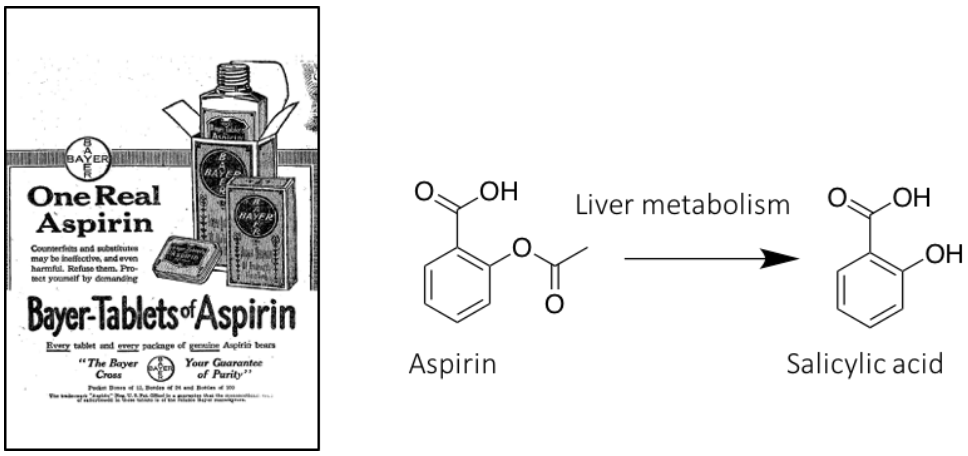


Figure 1.4 Aspirin The prodrug Aspirin is metabolised by the liver to the active component salicylic acid. Aspirin was made commercially available without prescription in 1899. Advert printed in the New York Times in February 1901.

Today, pharmaceutical sciences have evolved in ways unimaginable to ancient civilisations. In particular, the contribution of biopharmaceuticals to public health cannot be undervalued. A biopharmaceutical (or biologic) is a medical product extracted or semi-sythesised from biological sources. The most commonly used biologic is probably insulin, the peptide hormone that regulates blood glucose levels (Martínez et al., 2012). Originally purified from ox liver, synthetic human insulin can now be mass produced from recombinant DNA in bacteria and, more recently, yeast (Martínez et al., 2012). Biologics currently account for about 25% of commercial pharmaceutical sales (Martínez et al., 2012); however, small molecules remain a central and essential component in the quest to understand and treat disease. The central role of small molecules has persisted for several reasons. Firstly, inducing biological change with a small molecule compound is much easier than making genetic modifications both *in vitro* and *in vivo* and synthesis of relatively 'simple' compounds is much easier than the production, extraction or cultivation of biologics (Xu et al., 2008). Biologics are hard to manipulate, often unstable and tend to only modulate a single target (Ao et al., 2011). Small molecules on the

other hand are usually cheaper and easier to produce, they are well characterised and can be delivered in known quantities using a variety of administrative techniques (Willems et al., 2011). Small molecules with the correct properties will rapidly penetrate membranes and act in a time dependent, and often reversible, manner upon their target making them excellent tools to probe molecular pathways (Willems et al., 2009a). Finally, small drug-like molecules can be subjected to structural development to modulate activity and potentially provide hit or lead compounds for therapy.

1.9 High-Throughput Screening and Hit to Lead development

High-throughput screening (HTS) has remained a staple technique in the identification of 'hit' compounds for drug discovery since it was first conceptualised in the 1980's (Pereira and Williams, 2007). The principle of HTS is that vast numbers of structurally diverse compounds can be tested, in parallel, in a system of choice. Screening will generally employ a relatively simple experimental design in order to generate large volumes of data in a manner that is both fast and cost effective (Liu et al., 2004). To realise these aims HTS employs the use of robotic liquid handling platforms and automated data collection and analysis protocols. As well as increased efficiency, automated protocols allow the use of low experimental volumes thereby minimizing the costs of reagents. Original HTS experiments utilised 96 well plates with a 50-100 μL volume (Pereira and Williams, 2007), however dramatic improvements in the accuracy of low volume liquid dispensing means that assays can now been miniaturised to nL volumes (Macarron et al., 2011).

HTS is a multidisciplinary field and the technique has been applied to a number of experimental designs. In reductionist assays, libraries are be screened against purified recombinant proteins for direct measurement of molecular interactions. However, HTS has also been applied to cell-

based assays and those that utilise bacteria or other whole organisms (Fernandes, 1998; Lee et al., 2013). This flexibility of the approach means that HTS techniques can be applied both to traditional target based drug design (**Chapter 1.10**) and to phenotypic screening (**Chapter 1.11**). Irrespective of the experimental design, the assay read out must provide a means of quantitatively measuring the activity of the compounds being screened in the test system.

Compounds that induce a desired change in the assay system are referred to as 'hits': the hits are then reviewed to decide which are the most appropriate to take forward into lead development. Pan-Assay Interference Compounds (PAINS), are a group of promiscuous molecules known to flag up as false positives across numerous assays (Baell and Walters, 2014). To validate initial hits and weed out potential PAINS subsequent counter assays are employed to determine whether the observed effect is real. One method of doing so it so is to test for a dose response: dose response curves are a plot of activity against concentration; usually with activity on the y-axis against the $\log_{10}$ dose on the x axis (**Figure 1.5**). Biological responses induced by a small molecules are often complex and can be variable depending upon the system: however, in reductionist assays at least, the effect should be directly related to the concentration of the drug at its site of action. In theory, across an appropriate range of concentrations specific to drug potency, a sigmoidal dose response curve is observed. The curve represents minimal activity at low concentrations followed by an exponential increase in activity as the effective dose is reached; the slope then flattens out at higher concentrations as the system reaches saturation. An all or nothing response is not desirable and the compound is likely to be demonstrating off target effects (Hughes et al., 2011). Counter screens can be employed in parallel with or after the primary screen to identify compounds that interfere with the assay read-out irrespective of whether the target is present or not (Strovel et al., 2004). Orthogonal assays with hits from a primary screen can also be employed; these will use a different assay reporter

or format to confirm activity against the chosen target (Thorne et al., 2010). Another consideration when reviewing 'hit' compounds is which appear the most 'drug like', the criteria of which is often based upon Lipinski's famous 'rules of five' (Lipinski et al., 2001). The rules of five state that problematic absorption and permeation in the body would be predicted when a compound contains: more than five hydrogen bond donors, more than 10 hydrogen bond acceptors, a calculated LogP greater than five or a molecular weight (MW) greater than 500. Although these 'rules' are really more a set of guidelines, they are useful for encouraging medicinal chemists to consider not only a compounds activity but its suitability for clinical application.

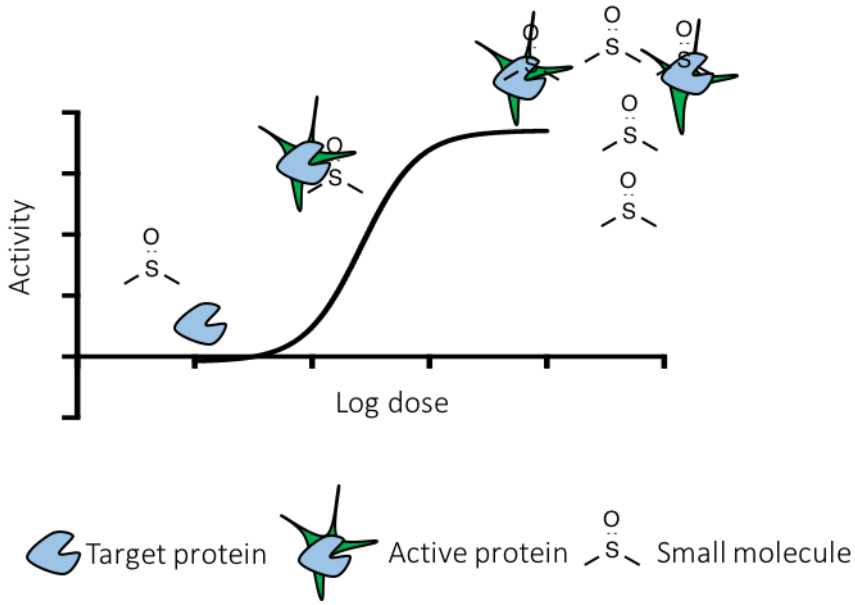


Figure 1.5 Sigmoidal dose response curve. Compound activity should, in theory, be directly related to its concentration at the target producing a sigmoidal dose response curve. Minimal activity is seen at low compound doses (LHS), followed by exponential increase in activity as the concentration reaches an effective dose. The curve plateaus at high concentrations as the system becomes saturated (RHS).

Low molecular weight (MW) of the hit compound is of particular importance for the subsequent step: study of the structure activity relationship (SAR). After a suitable compound or compound family has been chosen for further investigation the project enters the 'lead optimization' phase in which a series of sequential chemical modifications are made to the compound in order to

identify the pharmacophore, the compound 'fragment' essential for activity, and to ascertain which areas of the compound can be modified for improved specificity and activity (Bleicher et al., 2003). This stage will often involve the addition of extra functional groups resulting in increased MW which exemplifies why hit molecules with low molecular weights are a desirable starting point. Hit compounds and subsequent analogues will be tested *in vitro* in secondary assays for activity, which is often required to be in the low nanomolar range, and also for specificity against panels of known drug receptors. If a compound exhibits undesirable binding interactions this may be prevented by further SAR development (Hefti, 2008). Compounds with acceptable activity and specificity profiles may then be taken forward into animal studies to assess activity against the chosen target *in vivo* and also to determine toxicology profiles and well as absorption, distribution, metabolism and excretion properties (ADME). A potent molecule with appropriate physical properties will also be subject efficacy studies if a suitable disease model exists (Hughes et al., 2011). Finally, if a compound has met all of the relevant requirements it may then be taken forward in to clinical trials.

1.10 Target based drug discovery

Towards the end of the 20th century, the pharmaceutical industry was largely dominated by target based drug discovery (**Figure 1.6, LHS**). This was driven in part by advances in the field of molecular genetics and the successful mapping of the human genome (Lindsay, 2003). This approach is hypothesis driven: a 'target' is first identified which is often a gene, gene product, specific molecular mechanism or molecular pathway that is directly implicated in the manifestation of the disease. A number of methods have been employed for target identification that are commonly based upon assessing differential gene or protein expression between normal and diseased tissues (Lindsay, 2003). For success in this model there is a requirement that a) the target is expressed in the disease tissue and b) appropriate modification of the chosen target is

sufficient to ameliorate the disease state (Sams-Dodd, 2005). Once chosen the target must be validated for its physiological relevance. Initial proof of principle studies often employ small interfering RNA techniques to modulate target expression in the disease model. This can be further explored by use of the *Cre\loxP* system to determine the effect of tissue specific and time-dependant knock out of the target gene (Lindsay, 2003). Target validation is followed by development of a robust assay system for use in HTS so that large libraries of compounds can be screened for their ability to modulate the target in the desired fashion. After lead candidates have been identified and subject to SAR development, mechanism of action studies are undertaken to validate the candidate *in vitro* and *in vivo* (Schenone et al., 2013).

A classic example of success in target based drug discovery is the small molecule kinase inhibitor Gleevec (Imatinib) used for the treatment of chronic myeloid leukaemia (CML). CML is the result of a translocation between chromosomes 9 and 22; the resulting fusion gene encodes an aberrant tyrosine kinase that is improperly regulated causing uncontrolled proliferation of white blood cells. Kinases transfer phosphate groups from ATP to proteins which act as on or off switches for numerous cell functions including proliferation: the ATP-binding sites are highly conserved, however, slight variations in structural motifs allow for development of specific inhibitors (Robinson et al., 2000). Gleevec was identified from a screen of compounds that had been designed to specifically inhibit the known CML protein target; in the first clinical trial 100% of patients showed complete remission and at 60 months 98% of patients presented with a normal white blood cell count (Druker et al., 1996, 2006). Gleevec has since been approved for the treatment of several additional cancers that also stem from mutated tyrosine kinase expression including gastrointestinal stromal tumours and five separate haematological diseases (Joensuu, 2002; Verstovsek, 2007). This example clearly demonstrated the merits of targeted drug design; however, several diseases manifest through multiple mutations meaning

single target therapy is unlikely to prove successful. Furthermore, the general decrease in therapeutic output from big pharma that coincided with the increased use of targeted design, and numerous instances of inadequate target validation resulting in generation of inefficacious drug candidates have led some to question this approach (Sams-Dodd, 2005).

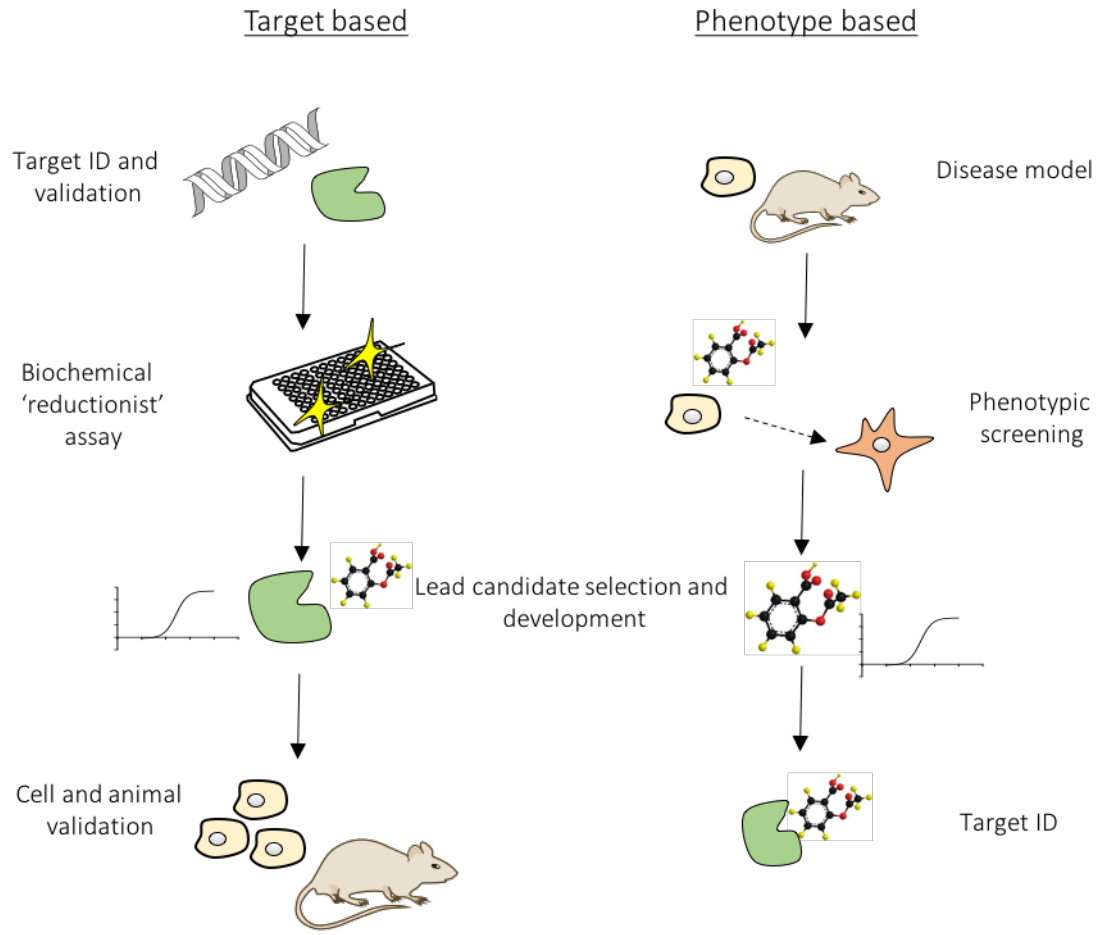


Figure 1.6 Target based vs phenotypic drug discovery: In target based drug discovery a target is first identified and validated. This is followed by HTS in 'reductionist' assays that measure the direct effect of the compound on the target. 'Hit' compounds are then subject to SAR development before the lead candidates are taken into cell and animal models for mechanism of action studies. In phenotypic drug discovery a disease model is first identified and a phenotypic screen with a relevant biological read out is designed. Hit compounds are also subject to SAR development after which studies to elucidate the MOA and target can be undertaken. Adapted from (Schenone et al., 2013).

1.11 Phenotypic drug discovery

An alternative approach to target based drug discovery is phenotypic drug discovery. Rather than identifying potential therapeutics by examining their effects at a molecular level, a

phenotypic approach assesses the effect of a small molecule by measuring observable changes in complex living systems (**Figure 1.6, RHS**) (Terstappen et al., 2007). In theory, direct *in vivo* study would bypass the issues of multiple targets and prevent development of compounds with unsuitable ADME or toxicology profiles. Clearly administering compounds of unknown effect to humans and animals is ethically questionable at best, but whole animal screening is feasible in model organisms such as worms, c. elegans and zebrafish (Priest and Erdemli, 2014). However, some question the relevance of these to human disease and, furthermore, this approach is generally poorly suited to large scale screening methods (Zheng et al., 2013a).

Cell based assays are generally favoured for identifying lead molecules and can usually be miniaturised for use on robotic screening platforms for HTS. The systems of study are highly variable and can include primary mammalian cells isolated from human patients or animals, or cells that have been immortalised to form permanent cell lines. Several biological read-outs can be utilised in cell-based phenotypic screening: one example is the use of reporter assays, in which a reporter gene such as GFP or luciferase is inserted after the promoter region of a target gene which is predicted to undergo a change in expression. Alternative read-outs can include changes in cell morphology, motility, proliferation or induction of cell death (Terstappen et al., 2007; Zheng et al., 2013a). This may seem a somewhat rudimentary approach as initially there is no understanding of the target or underlying pharmacology that leads to the phenotype of interest, which can be problematic when trying to optimise a molecular structure for improved activity. However, this approach offers several potential benefits: firstly, the observed effects could be a result of compound interaction with multiple targets or perturbation of signalling cascades which can only be observed at cell or organism level. Secondly, phenotypic screening should only identify hit compounds with therapeutically relevant mechanisms of action (MOA) (Moffat et al., 2014). Thirdly, phenotypic screening removes bias from the assay and by

assessing the effects of a compound on a complex system can allow for discovery of novel disease targets and first in class drugs (Swinney and Anthony, 2011). First in class drugs are those that use a new or unique mechanisms to treat a disease. In 2011 a report was published that compared the discovery strategy and MOA of all new FDA approved drugs between 1999-2008: it found that of all of the first in class small molecule drugs developed in that time, 28 were identified by phenotypic screening techniques compared with 17 from target based approaches (Swinney and Anthony, 2011). Considering this study focused on drug development during a period when the majority of pharmaceutical efforts were focused upon target based screening, it exemplified the utility of phenotypic screening in hit and lead discovery of novel therapies for areas of unmet clinical need (Swinney, 2013).

A limitation to phenotypic screening can be deciphering the target and MOA, which represents a significant challenge. The classical approach to target identification is based upon affinity chromatography: the compound of interest is modified in such a way that it can be attached to a solid support (Terstappen et al., 2007). The compound is then incubated in a cell lysate from the system of interest in the hope that the affinity of the protein target for the small molecule will cause them to bind together. Excess protein and debris can then be washed away and the protein of interest identified by mass spectrometry. Problems such as weak binding, steric hindrance from the solid support or insufficient protein expression can hinder this method of analysis, and development of alternative techniques remains a major area of study (Schenone et al., 2013). Interestingly, although it may seem counter intuitive, target identification is not always a necessary requirement for approval of a drug as long as it is proven to be safe and efficacious (Zheng et al., 2013a).

1.12 Phenotypic screening in cardiac regeneration

As the biological mechanisms of regenerative and fibrotic cardiac wound healing began to be elucidated, interest has arisen in the identification of small molecules that could be utilised for pro-regenerative therapies. The search for regenerative medicines has been described as a 'new-era' of drug discovery. The broad definition of a regenerative medicine is one that replaces cells, tissues or organs to restore normal function (Mason and Dunnill, 2008). In the case of MI and ischemic injury, the requirements of a regenerative therapy not only include replenishing the lost cardiomyocytes but also the reconstitution of vasculature and prevention of chronic inflammation or excessive cardiac fibrosis and remodelling: this is likely to require combined therapies against several targets rather than just one. Given that the potential therapeutic targets to instigate cardiac regeneration are relatively unknown, phenotypic screening methods have emerged at the forefront of the search for small molecule activators of the process.

Thus far, the majority of efforts have been focused upon the generation of new cardiomyocytes for repair and can be broadly divided into two main strategies. Firstly, the identification of compounds that direct stem cell fate for the purpose of generating cardiac progenitors or fully differentiated cells for transplantation; secondly, identification of compounds that drive proliferation of resident stem or progenitor cell populations that could in turn contribute to a regenerative response. This area of research is vast and has been expertly reviewed elsewhere (Schade and Plowright, 2015), however, an overview supplemented with a few notable examples will be presented in **Chapter 1.13** and **1.14**.

1.13 Generating cardiomyocytes from stem cells

There has been significant interest in driving stem cell differentiation towards a cardiac fate due to their potential use as a regenerative therapy but also because establishing human

cardiomyocyte cultures that mimic *in vivo* functionality could be invaluable for pre-clinical toxicology testing of drug candidates (Asai et al., 2010). Since the first publications that documented generation of beating cardiac tissue from ESCs *in vitro*, various methods have been used to direct the fate of uncommitted stem cells including treatment with growth factors and genetic reprogramming which have been extensively reviewed elsewhere (Mummery et al., 2012); the focus here will be the contribution of small molecules.

Embryonic cardiomyogenesis has been well characterised. There are four steps required for the generation of cardiomyocytes from uncommitted ES cells and several genetic markers that can be used to map progression: (1) formation of mesoderm, one of the three basic germ layers that includes muscle and bone, which can be characterised by expression of T/Brachyury (T/BRA); (2) formation of cardiogenic mesoderm characterised by Mesoderm posterior-1 (MESP1) expression; (3) formation of cardiac mesoderm which can be characterised by transcription factors such as NK2 homeobox 5 (NKX2.5), GATA4 and myocyte enhancer factor 2C (MEF2C); (4) formation of early cardiomyocytes which can be characterised by alpha myosin heavy chain (α-MHC) expression or CTN1 (Mummery et al., 2012). Although the progenitor cell type may vary, cardiomyocyte formation from uncommitted mesoderm will follow this developmental cascade.

A combined use of chemical genetics and HTS have provided means of monitoring stem cell response to small molecule intervention (Sadek et al., 2008a; Willems et al., 2009b). In 2003 a phenotypic HTS was designed around human ESCs (hESCs): the uncommitted stem cells were transfected with GFP under the transcriptional control of the α-MHC promoter. HESCs that differentiated into cardiomyocytes emitted strong green fluorescence whereas those that remained uncommitted to the cardiac lineage were GFP- (Takahashi et al., 2003). In this system,

a library of 880 compounds was screened from which ascorbic acid **A (Figure 1.7)**, was found to significantly increase the number of cells expressing GFP in a dose dependent manner. The cardiogenic activity of ascorbic acid was confirmed by elevated expression of cardiomyocyte specific proteins. Ascorbic acid, an analogue of vitamin C, has antioxidative effects and is often used as a cofactor in biological systems. Several other antioxidants were examined in the same assay, none of which induced cardiomyocyte formation. Thus it was concluded that Ascorbic acids antioxidative effects are not related to its cardiogenic activity (Takahashi et al., 2003).

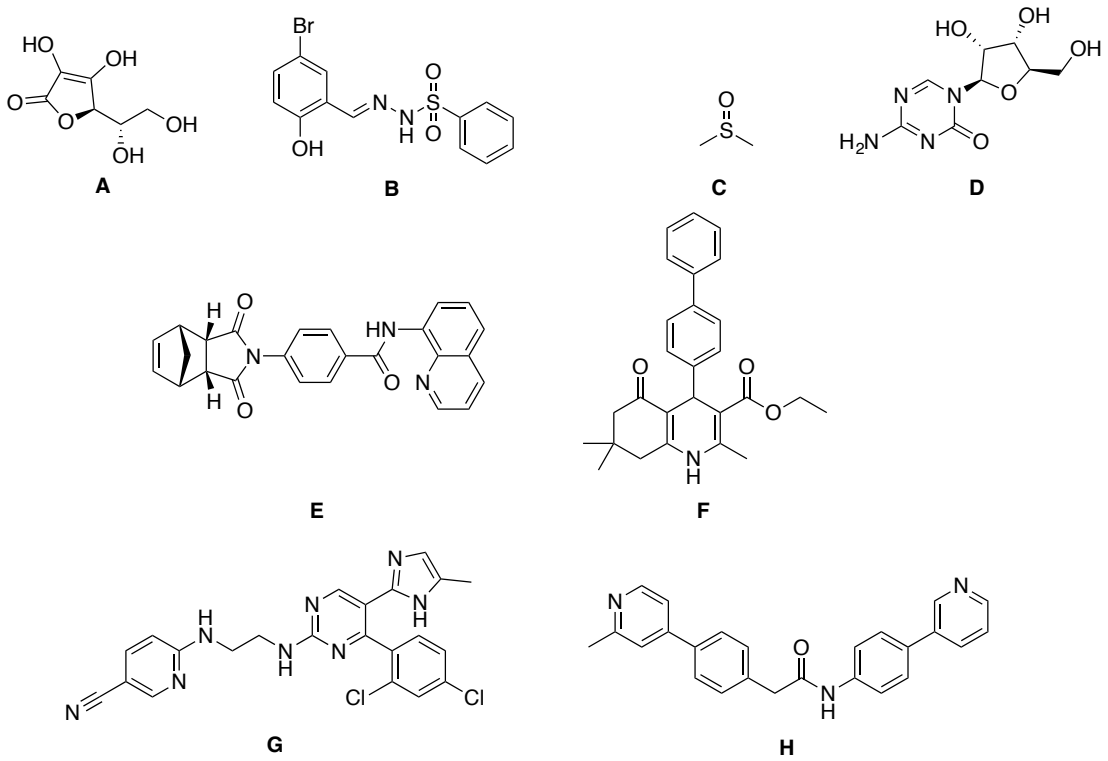


Figure 1.7 Cardiogenic small molecules identified from various phenotypic screening experiments (**A**) Ascorbic acid (**B**) Shz (**C**) DMSO (**D**)5-azacytidine (**E**) IWR-1 (**F**) Member of 1,4-dihydropyridine family (**G**) CHIR99021 (**H**)WNT C59.

Cardiogenic members of the sulfonyl-hydrazone (Shz) family **B (Figure 1.7)** were identified from an HTS screen of 150,000 small molecules in the mouse embryonic carcinoma (mEC P19) cell line stably transfected with an Nkx2.5-luciferase transgene. In secondary assays, the Shz compounds were also found to induce cardiac gene expression in human mobilised peripheral

blood mononuclear cells (M-PBMCs). M-PBMCs represent a clinically viable source of cells that avoid the ethical issues associated with cells from embryonic sources (Sadek et al., 2008b). Shz treated cells were injected into three different sites in cryoinjured rat hearts which showed significant improvements in function 7 days after treatment (Sadek et al., 2008b).

Early phenotypic experiments used the formation of beating cells from stem cell cultures as a primary read out for cardiogenesis. Using this read out, a number of groups reported that exposure to 1% dimethylsulfoxide (DMSO) **C** (**Figure 1.7**) can induce differentiation towards an immature cardiac fate in pluripotent cell lines including P19 and mouse ESCs (mESCs) (Dinsmore et al., 1996; Edwards et al., 1983; Lako et al., 2001). Combination of DMSO with 5-azacytidine **D** (**Figure 1.7**), was subsequently found to increase expression of proteins characteristic of late stage cardiogenesis in P19 cultures. Cardiomyocytes were derived from P19 cultures by treatment with 10 μM of 5-aza for 24 hours before nine days incubation in 1% DMSO and then transplanted into the retroperitoneal region of mice to assess their ability to structurally integrate *in-vivo* (Ohtsu et al., 2005). Pulsating tissue mass was found in each of the transplant locations, although the pulse rate was substantially less than the host heart rate (163/min and 360/min respectively). The cells had varied morphologies and heterogeneous expression of α-SMA which indicated some remained functionally immature. However, this was an early and promising example of the ability of ESC derived muscle to integrate into host tissue.

Full mechanistic understanding of the cardiogenic activity of **A**–**D**, and numerous other compounds has not been elucidated to-date, although DMSO has been reported to induced a transient increase in intracellular calcium levels which is postulated to trigger downstream initiation of cardiac differentiation (Heyden and Defize, 2003; Morley and Whitfield, 1993). Essential to improving the protocols that drive cardiomyocyte formation is an understanding of the underlying biology of myocyte commitment and differentiation, to which small molecule

contributions have been invaluable. Understanding what controls cardiogenesis at a molecular level could both divulge the MOA of cardiomyogenic compounds and help identify novel biological targets for therapy.

An interesting example of small molecules helping to elucidate the mechanisms of cardiomyogenesis are presented in the numerous publications by Willems *et. al.* from 2009 onwards (Willems et al., 2009b). The group initially sought to decipher the signalling processes that take partially differentiated mesodermal stem cells though the later stages of cardiomyogenesis to produce functioning cardiomyocytes (Willems et al., 2011). HESCs were differentiated into mesoderm then incubated with a collection of 305 agonists and antagonists of known molecular pathways. Only one compound, IWR-1 **E (Figure 1.7),** an inhibitor of the Wnt signalling pathway, was found to potently induce beating cells in the cultures. Wnt proteins have long been known to play a role in stem cell proliferation; the Wnt pathway controls transcriptional processes that enable embryonic stem cells to remain multipotent (Chen et al., 2009) and the natural inhibitor Dickkopf-related protein 1 (DKK1) is known to induce cardiogenesis (Willert et al., 2003). Subsequent investigations with other inhibitors that targeted different stages of the signalling cascade demonstrated that Wnt signalling must be disrupted in order for mesoderm cells to commit to cardiac fate. A role for transforming growth factor β (TGFβ) signalling pathway in cardiogenesis was also revealed with a similar approach (Willems et al., 2012)**.** The 1,4-dihydropyridine **F (Figure 1.7)** was found to potently induce beating cell clusters from T/BRA+ committed mesoderm in a small molecule phenotypic HTS. Interestingly **F** had a biphasic effect: if added before mesoderm formation it completely abolished cardiomyogenesis. To identify the target, a collection of known tyrosine kinase inhibitors was screened for cardiogenic activity: inhibitors of the Activin A and TGFβ signalling pathways promoted cardiogenesis from T/BRA+ mesoderm; subsequently **F** was found to strongly inhibit

the TGFβ2 signalling, suggesting that disruption of this cascade is responsible for its cardiogenic properties. Subsequently, the point of inhibition was investigated: in the normal cascade a TGFβ ligand binds to the type II (TGFβR2) receptor in the cell membrane, which then associates with the type I receptor (TGFβR1). The ligand receptor complex is then internalised, where it phosphorylates effector proteins within the cell (Discussed in detail in **Chapter 1.16**) (Wrana et al., 1992). Fluorescent tagging showed that **F** lowers the level of TGFβR2 both on the cell surface and internally: it is now known to both clear the receptor from the cell surface and target it for proteasome degradation.

The discovery of induced pluripotent stem cells (iPSCs) was a monumental step forward in the field of regenerative medicine. IPSCs are derived from adult terminally differentiated cells by forced expression of specific genes known as the 'Yamanaka Factors': octamer-binding transcription factor 4 (OCT4), (Sex Determining Region Y)-Box 2 (SOX2), Kruppel-like factor 4 (KLF4) and Myc proto-oncogene protein (MYC) (Takahashi and Yamanaka, 2006). These factors can induce pluripotency in terminally differentiated cells, which then closely resemble ESCs and have the ability to differentiate in to any of the three germ lines Originally, iPSCs were generated from cultures of mouse embryonic and adult fibroblasts; however, iPSCs can now be derived from human somatic cells including patient derived dermal fibroblasts, which can be readily expanded *in vitro* from a small skin biopsy (Hao et al., 2011; Park et al., 2008). In order for iPSC-derived cardiomyocytes to be used in a clinical setting, their production needs to be safe, efficient and relatively cost effective. The use of patient derived iPSCs potentially bypasses immunocompatibility problems associated with transplantation.

Several published methods of inducing cardiomyocyte formation from stem cells utilise various animal serums, animal cells or cytokines (Burridge et al., 2012; Messina et al., 2004). The use

of animal products can pose a risk of infection and recombinant cytokine technology is expensive. Furthermore, products from animal sources tend to experience batch variability and their contents are not chemically defined (Morrow and Felcone, 2004). These methods are therefore unsuitable for large-scale pharmaceutical production. Induced pluripotency cannot currently be conferred efficiently by chemical modulation alone, however derivation of cardiomyocyte populations from iPSCs can now be undertaken in chemically defined conditions (Burridge et al., 2014). Human derived iPSCs grown on synthetic matrices were differentiated into cardiomyocytes in 'CDM3' that consists of three components: RPMI 1640, a chemically defined media, L-ascorbic acid and recombinant human albumin. After seeding in CDM3, iPSCs were treated for two days with 6 μM of the glycogen synthase kinase 3 (GSK-3) inhibitor CHIR99021 **G (Figure 1.7)** that promotes Wnt signalling and ESC self-renewal (Ye et al., 2012), followed by two days of treatment with the small molecule Wnt inhibitor Wnt-C59 **H (Figure 1.7)** at 2 μM. Two days later the media was replaced with un-supplemented CDM3 and beating cell clusters were observed on day 7 of the differentiation; a similar protocol that negates the use of albumin has also recently been published (Lian et al., 2015).

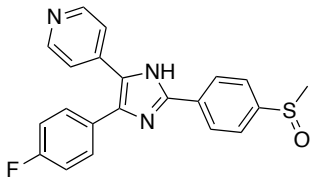
Whether the transplantation of stem cell derived cardiomyocytes will evolve into a successful therapeutic strategy is yet to be determined. However, it is clear that small molecules have and will continue to play an important role in the continued exploration of this field.

1.14 Recruiting resident cells for repair with small molecule compounds

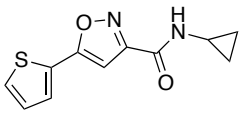
1.14.1 Cardiomyocyte proliferation

An alternative strategy applied to recruiting cells for functional cardiac repair is based upon stimulation of resident cell populations. The discovery that the zebrafish replenishes lost muscle after heart injury by division of existing cardiomyocytes, alongside the fact a that small numbers

of mammalian cardiomyocytes are also able to proliferate in response to injury (**Chapter 1.4**), generated interest in identifying small molecules that can amplify this response *in vivo*. During mammalian heart development, cardiac muscle is generated by the proliferation of existing cardiomyocytes: proliferative capacity rapidly decreases in the later stages of embryogenesis and there is a shift from hyperplastic to hypertrophic growth as the majority of cardiomyocytes become bi-nucleated, polypoloid and terminally exit the cell cycle (Pasumarthi and Field, 2002). Hypertrophic growth is associated with cardiomyocyte maturation and the formation of contractile sarcomeric machinery. Differentiation towards a mature cardiac fate is correlated with increased expression of the cell cycle inhibitors p21, p27 and p38 (Engel et al., 2005; Pasumarthi and Field, 2002). The p38 mitogen-activated protein (MAP) kinase phosphorylates signalling molecules essential for cardiac hypertrophy and differentiation. Proliferation experiments in adult rat cardiomyocytes *in vitro* demonstrated that stimulation with the growth factor FGF1 in combination with the small molecule p38 inhibitor SB203580 **I** (**Figure 1.7**) induced cardiomyocyte division via transient dedifferentiation (Engel et al., 2005, 2006). The same combination also induced cardiomyocyte proliferation, reduced scarring and improved function in rats after surgically induced MI (Engel et al., 2005, 2006).



I



J

Figure 1.8 Cardiogenic small molecules that target resident progenitor cells (**I**) SB203580 (**J**) Isx

1.14.2 Cardiac fibroblast reprogramming

Another resident cell population being targeted for cardiac repair are cardiac fibroblasts. Cardiac fibroblasts make up ~70% of the normal human heart making them the most prevalent cell type

(Song et al., 2012). As previously discussed, fibroblasts can be reprogrammed into IPS cells by forced expression of the Yamanaka factors (**Chapter 1.13**); more recently it has become apparent that direct reprogramming of fibroblasts to cardiomyocytes could be a novel therapeutic strategy (Schade and Plowright, 2015). Direct reprogramming has been achieved using by forced expression of developmental transcription factors GATA4, MEF2C, T-Box 5 (TBX5) and Heart- and neural crest derivatives-expressed protein 2 (HAND2) known as the GHMT cocktail, *in vitro*. Successful reprogramming was also achieved by retroviral transfection of GHMT *in vivo* that resulted in improved cardiac function and reduced fibrosis after MI (Ieda et al., 2010; Qian et al., 2012; Song et al., 2012). More recently still, human adult fibroblasts were directly differentiated into cardiomyocytes by forced expression of GATA4, TBX5, HAND2, Myocardin (MYOCD) and two micro RNAs miR-1 and 133 *in vitro* (Nam et al., 2013). Concerns about safety and accuracy of *in vivo* genetic reprogramming has driven investigation into direct reprogramming of fibroblasts with a cocktail of small molecules. Human foreskin fibroblasts transfected with GFP under the control of α-MHC were used in a series of consecutive experiments in which libraries of cardiogenic compounds, or compounds known to induce cell reprogramming, were screened in combination to assess their cardiogenic capacity (Cao et al., 2016). The result was a cocktail of 9 small molecules '9C' that efficiently reprogrammed cardiac fibroblasts in to a homogenous population of mature cardiomyocytes with distinct sarcomeric structure and calcium transients. Furthermore, transplantation of fibroblast derived cardiomyocytes to ischemic myocardium in mice partially remuscularised the damaged tissue (Cao et al., 2016). Further work is required to fully understand the mechanisms of reprogramming and ascertain the utility of '9C' in the treatment of human ischemic disease.

1.14.3 Recruiting epicardial progenitors

As previously discussed, it is now generally accepted that the heart contains a small population of resident stem cells with cardiogenic potential (**Chapter 1.5**). However, due to their relative rarity and the difficulties encountered with their isolation and characterisation no progress has yet been made towards recruiting them for repair (Schade and Plowright, 2015). However, although not a stem cell population due to their limited capacity to self-renew, the epicardium and activated EPDCs exist as a resident progenitor population that can potentially be targeted for repair. In 2012, a subset of epicardial cells were found to have active Notch signalling which is essential for cardiomyogensis and controls growth and differentiation of most cardiac lineages (Russell et al., 2011). The Notch activated EPDC (NEC) population was found to expand in response to cardiac injury and contributed to fibrotic repair. In an attempt to recruit NECs for functional repair, a series of compounds were screened for cardiogenic activity. The small molecule Isx **J** (**Figure 1.7**) was identified from a luciferase assay that screened compounds for activation of the early cardiac marker NKX2.5 (Russell et al., 2012a). Mice injected with Isx intraperitoneally once daily for a week showed upregulation of NKX2.5 levels in NEC populations as well as increased myocardial cell cycle activity; a promising result. However, treatment with Isx after surgically induced MI ameliorated this cardiogenic response, with the NEC population favouring fibrosis pathways; it was concluded that the inflammatory and paracrine effects of the endogenous wound healing response override the potential cardiogenic effects of Isx. Interestingly Isx was later shown to exert a cardioprotective effect by activation of a novel G-protein coupled receptor-68 (GPCR68): presence of the GPCR68 in cardiomyocytes at the injury border zone was correlated with cell survival and cardiogenic gene expression (Russell et al., 2012b).

Significantly more research is required for the identification of a pharmacological agent that can combat the endogenous fibrosis response triggered by MI. An alternative tactic could be developing combination therapies that combine inhibition of the pro-fibrotic response with agents that stimulate cardiogenesis and revascularization. In fact, in order to regenerate such a complex organ, successful therapy is likely to require this multifaceted approach. Collectively these studies illustrate the enormity of this challenge, and demonstrate that continued dedication to the field is required before therapeutic success will be realized.

1.15 Patient-derived human epicardium

As has previously been discussed (**Chapter 1.7**), the endogenous role of the adult epicardium in human MI and ischemia is hard to investigate, but it is believed to be activated in the failing heart as confirmed by expression of embryonic transcription factors WT1, TBX18 and RALDH2 (Braitsch et al., 2013). The study of human epicardium relies upon access to human heart samples that yield epicardium tissue from which to establish explant cultures. During coronary artery bypass graft surgery (CABG), in which a healthy artery or vein from the body is transplanted to the heart to bypass blood around a blocked portion of the coronary artery, blood flow must be temporarily redirected which is achieved by right arterial cannulation (Kertai et al., 2016). During surgery the right atrial appendage (RAA) (**Figure 1.9.A and B**) is often partially or fully excised to allow for cannulation (Omari et al., 1991); the RAA, also known as the right auricle, is a cone shaped, trabeculated pouch attached to the front of the right atrium (**Figure 1.9.A**). The RAA sits anterior and medial to the atrium and partially overlaps the root of the aorta; its role is to pump deoxygenated blood from the bloodstream into the right ventricle; with the permission of the patent, the RAA biopsies are donated to research to be used for *in vitro* study of human EPDCs (hEPDCs).

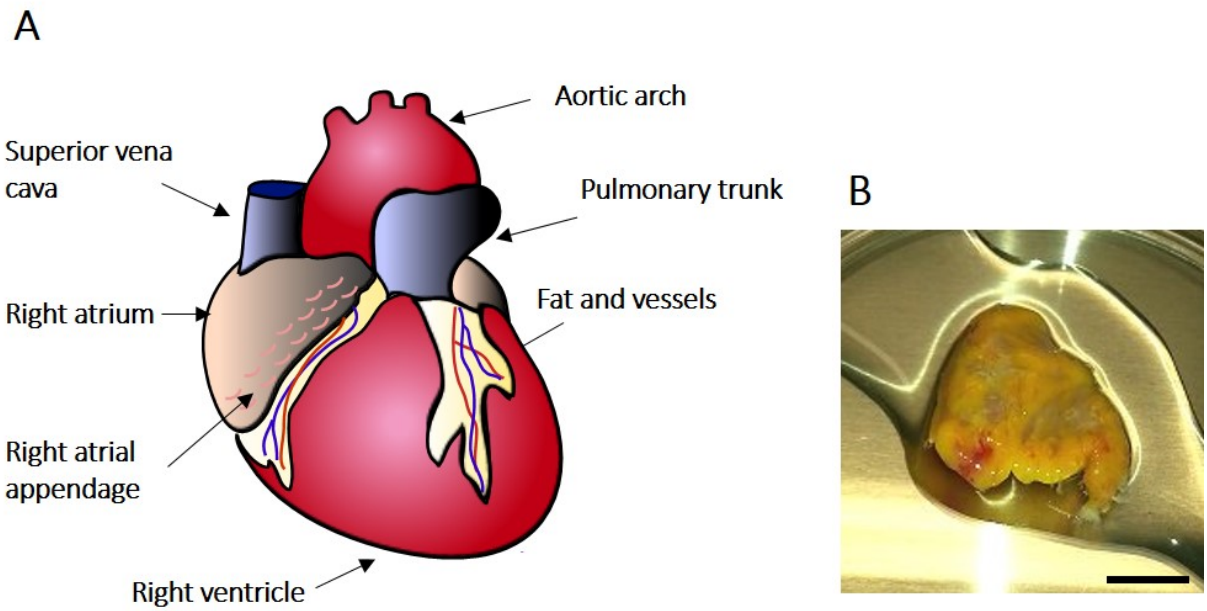


Figure 1.9 The right atrial appendage. (**A**) The right atrial appendage is attached anterior and medial to the right atrium; it also overlaps the root of the aorta. (**B**) Right atrial appendage samples excised from patient undergoing cardiac surgery. A layer of yellow epicardial fat can be seen across the surface of the muscle as can associated blood vessels. Scale bar 1 cm. Copyright © 2011 Pearson Education, Inc.

1.16 The role and characteristics of epithelial tissues

'Epithelia' refers to the single or multilayer 'sheet-like' membrane structures that line the cavities and surfaces of an organism, dividing it into separate organs and preventing free movement of molecules from one compartment to another. In humans, epithelial surfaces include the lining of the digestive and respiratory tracts, the surfaces of blood vessels, the outer layer of the skin the 'epidermis' and the epicardium (Madison, 2003; Nelson, 2009).

Epithelial cells exhibit apical-basal polarity, which refers to the asymmetric distribution of functional proteins within the cell which is essential to their proper function (**Figure 1.10 A**). (nature.com). The plasma membrane of epithelial cells is separated in to apical and basolateral segments by the presence of tight junctions. Tight junctions surround the perimeter of the cell: as well as dividing the apical and basal sides of the plasma membrane they act as a semi-

permeable barrier to paracelluar transport of solutes and ions between epithelial cells (Chiba et al., 2008). Tight junctions consist of two transmembrane proteins OCCLUDIN and CLAUDIN, which control junction stability and barrier function, and also contain cytoplasmic proteins such as ZONULA OCCLUDENS-1 (ZO-1) which link the junctions to the cell actin cytoskeleton (Hartsock and Nelson, 2008; Tsukita and Furuse, 2000).

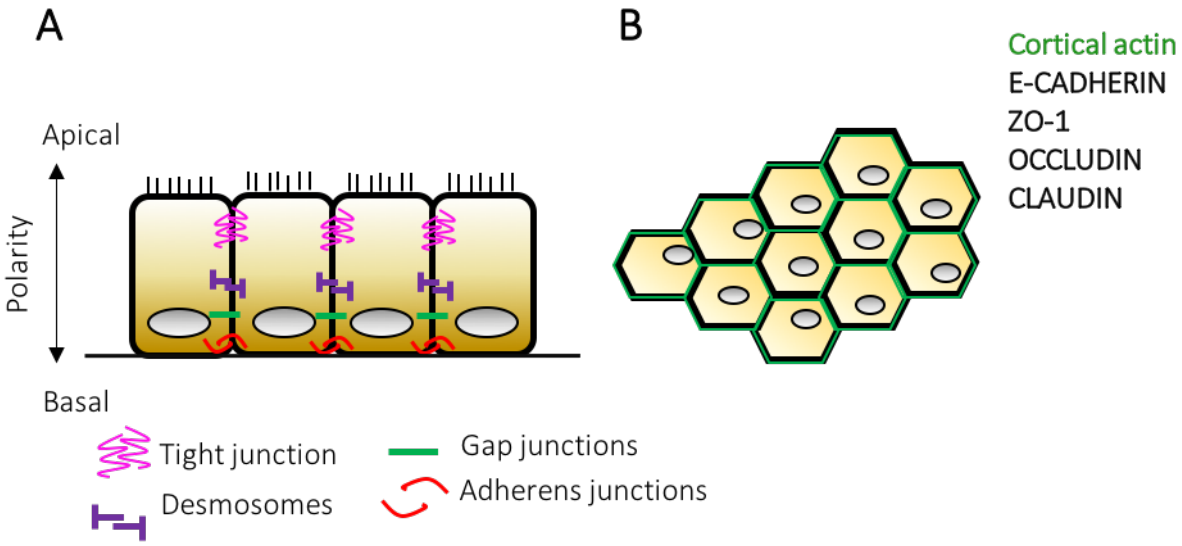


Figure 1.10 Characteristics of the epithelium (**A**) Epithelial cells have apical-basal polarity. They are connected by a number of protein junctions: tight junctions prevent paracellular movement of molecules between cells; desmosomes are localised patches that hold cells tightly together; gap junctions are intracellular ion transport channels; adherens junctions form strong mechanical attachments between cells. (**B**) Epithelial cells are characterised by the presence of E-CADHERIN ZO-1, OCCLUDINS and CLAUDINS. The cells exhibit regular polygonal morphology with a network of cortical actin rings. Adapted from (Rossier et al., 2015).

The apical surface faces the 'outside' of the organ or structure the epithelia is covering and communicates with the extracellular environment via microvilli and the primary cilium, mediating transcellular transport of molecules that travel through the cell passing both the apical and basal membranes (**Figure 1.10 A**) (Cao et al., 2012). The basolateral region consists of several essential components such as desmosomes, which are strong intercellular junctions that mediate cell-cell adhesion and link to the cytoskeleton which confers mechanical strength to epithelial tissues; gap junctions which are 'communication' junctions formed from six connexin

proteins which assemble to form a connexon, a protein channel that allows the passage of ions and solutes between neighbouring cells. (Nielsen et al., 2012). The final component are the adherens junctions, which are involved in cell adhesion and arrangement of the actin cytoskeleton as well as intracellular signalling and gene transcription (Hartsock and Nelson, 2008). The core transmembrane protein of the adherens junctions is E-CADHERIN; its extracellular domain interacts with the E-CADHERIN extracellular domains of neighbouring cells forming an adhesive interaction. In epithelial cells the cytoplasmic E-CADHERIN domain is tightly bound to the catenin proteins p120-CATENIN, α and β-CATENIN (Gumbiner, 2000; Hartsock and Nelson, 2008). Binding of p120-CADHERIN stabilises epithelial E-CADHERIN and its presence is thought to prevent endocytosis of the complex (Davis et al., 2003). The β-CATENIN protein has a dual role in that its presence in the cadherin-catenin complex helps stabilise the adherens junctions, however, it is also a key mediator of the Wnt signalling cascade, which will be discussed further in the next section (**Chapter 1.17**).

Initially α-CATENIN was thought form a bridge between the E-CADHERIN-β-CATENIN complex and the actin cytoskeleton but recent studies instead suggest a dynamic role in regulation of the F-ACTIN cytoskeleton (Drees et al., 2005; Hartsock and Nelson, 2008; Rimm et al., 1995). α-CATENIN exists in either a monomeric or homodimeric form whereby the monomeric form binds to the E-CADHERIN-β-CATENIN complex and the homodimeric form binds to actin. Increased α-CATENIN concentration at the membrane during assembly of the catenin-cadherin complex induces homodimer assembly. Binding of the homodimer to actin inhibits actin polymerisation, which prevents the formation of stress fibres, lamellipodium and filopodia (**Chapter 1.17**) characteristics of migrating cells. Instead F-ACTIN is reorganised into a contiguous ring of filaments that run parallel to the membrane contacts around the circumference of the epithelial cells (**Figure 1.10 B**). This contiguous ring of cortical actin,

regular ‘polygonal’ appearance (**Figure 1.10 B**) and membrane bound E-CADHERIN, are defining morphological features of tight epithelium (Smutny et al., 2010).

1.17 Epithelial to Mesenchymal Transition

EMT has been implicated in embryogenesis, tissue repair and disease. During EMT, cells lose their epithelial characteristics and instead adopt a migratory mesenchymal phenotype. The first stage of EMT involves disassembly of cell-cell contacts, via the breakdown of the desmosomes and the gap, tight and adherens junctions (**Figure 1.11 A**). This results in a loss of apical basal polarity: mesenchymal cells instead develop a front-rear axis polarity which is determined by their direction of migration (**Figure 1.11 B**) (Nelson, 2009). The loss of the cell-cell contacts also results in rearrangement of the actin cytoskeleton whereby the cortical actin ring is initially replaced by the formation of lamellipodium and filopodia. Lamellipodium is the membrane protrusion that projects forward from the front edge of migrating cells: the lamellipodium is filled with a complex actin network including the filamentous filopodia (**Figure 1.11,** green membrane extensions) that are dynamically formed by actin polymerization (Mattila and Lappalainen, 2008). In migrating cells, filopodia behave as ‘sensors’ extruding out from the cell edge to assess the surrounding microenvironment (Galbraith et al., 2007). Subsequently mesenchymal cells develop thick actin stress fibres that form the contractile machinery required for migration. Morphologically, EMT causes cells to lose their regular polygonal appearance, often referred to as ‘cobblestone’ and adopt a fibroid appearance often referred to as ‘spindle’ (**Figure 1.11**). This is also accompanied by the reduced expression of epithelial markers such as E-CADHERIN, ZO-1, OCCLUDIN and CLAUDIN. Instead the cells exhibit increased expression of mesenchymal markers which include: VIMENTIN, a filamentous protein that helps maintain cell shape and organise dynamic cytoskeletal interactions (Liu et al., 2015): FIBROBLAST SPECIFIC PROTEIN-1 (FSP1) another protein involved in cell motility (Okada

et al., 1997): and α-SMA, an actin isoform associated with the development of contractile machinery. The resulting mesenchymal cells have migratory capacity and can subsequently invade neighbouring or underlying tissues.

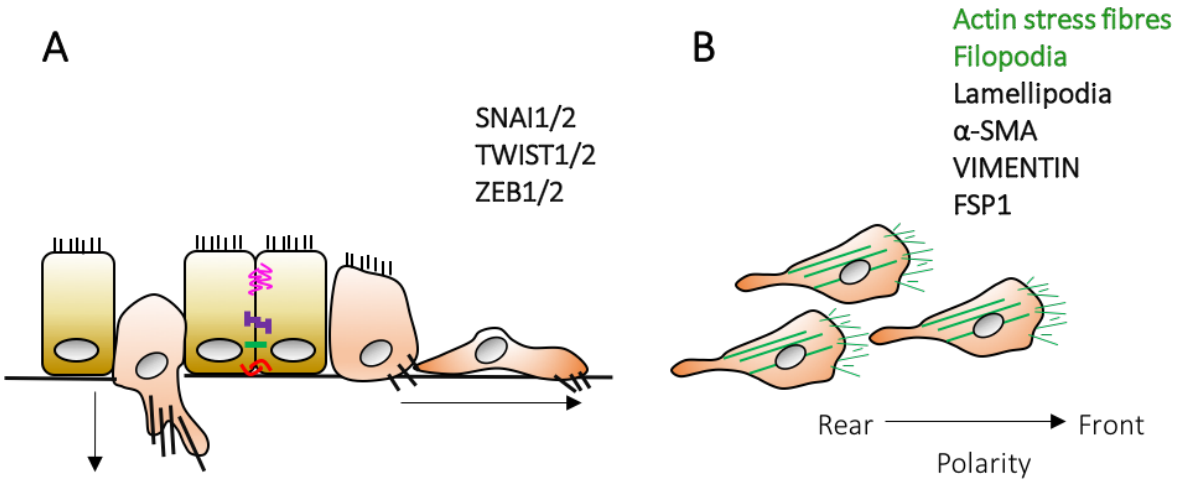


Figure 1.11 Epithelial to Mesenchymal Transition (A) During EMT epithelial cells lose cell-cell contact and develop invasive and migratory capacity**.** The first stage of EMT is the break-down of cell junctions mediated by the expression of a number of EMT transcription factors including SNA1/2, TWIST1/2 and ZEB1/2 which supress *Cdh1* expression. (**B**) Mesenchymal cells exhibit front-rear polarity determined by their direction of movement and develop a 'spindle' morphology with actin stress fibres, filopodia and lamellipodia. Epithelial markers are lost and replaced with mesenchymal markers such as α-SMA, VIMENTIN and FSP1. Adapted from (Rossier et al., 2015).

Several transcription factors directly induce EMT by inhibiting transcription of proteins associated with cell-cell adhesion. As already discussed (**Chapter 1.6**) SNAI1 and SNAI2 repress E-CADHERIN expression by binding to the *Cdh1* promotor region. The zinc finger e-box-binding homobox 1 and 2 (ZEB1/2) bind to E-box regions on either side of the *Cdh1* gene preventing transcription; ZEB1 also modifies histone proteins in the nucleus preventing binding of RNA polymerase to the *Cdh1* promoter region (Gonzalez and Medici, 2014). Other EMT inducing transcription factors include TWIST1/2 and lymphoid enhancer binding factor 1 (LEF-1).

Numerous cell signalling cascades contribute to the induction of EMT, which have been extensively reviewed elsewhere (Gonzalez and Medici, 2014; Lamouille et al., 2014). However, pathways of particular importance in epicardial EMT and in the subsequent findings of this thesis will be discussed.

Induction of EMT via the TGFβ signalling pathway is probably the best understood. Activation of the pathway is usually initiated by interaction of a range of ligands with TGFβ receptors present in the cell membrane. Several ligands are known to activate the signalling cascade including the three TGFβ isoforms 1, 2 and 3 and the bone morphogenetic proteins (BMP) 2–7 (Gonzalez and Medici, 2014). TGFβ signalling is initiated when an appropriate ligand binds a homodimer of the type II receptor (TGFβR2) at the cell membrane. This recruits a homodimer of the type I receptor (TGFβR1), forming an active and stable heterotetrameric complex. Binding of the ligand induces trans-phosphorylation of the TGFβR1 by TGFβR2 initiating its kinase activity (Zi et al., 2012). In mammals, seven type I and five type II receptors have been identified that combine to form a variety of complexes. The specific complexes formed will determine which extracellular ligands can interact and allow induction of different downstream signalling events from the same ligand (Derynck and Feng, 1997). The best characterised TGFβ signalling cascade involves the 'mothers against decapentaplegic homologs 2 and 3' (SMAD2/3) transcription factors. Phosphorylation of the TGFβR2 recruits and phosphorylates intracellular SMAD2/3; these subsequently form a complex with SMAD4 which enters the nucleus and binds to DNA activating expression of key EMT mediating transcription factors such as SNAIL and ZEB (**Figure 1.12 A** and **B**). TGFβ2 regulated SMAD signalling is essential for epicardial EMT in development (Huang et al., 2014a). The SMAD signalling cascade is not the only pathway activated by phosphorylation of the TGFβ receptor complex. Other signal transducers such as phosphatidylinositol-4,5-bisphosphate 3-kinase (PI3K) (Larue and

Bellacosa, 2005) and the various Ras proteins are activated by TGFβ, which also trigger signalling cascades that result in expression of EMT inducing transcription factors in the nucleus (Gonzalez and Medici, 2014).

Binding of growth factors such as the FGFs, PDGFs and epidermal growth factors (EGFs) to receptor tyrosine kinases (RTKs) at the membrane can also induce EMT via overlapping mechanisms. Growth factor binding stimulates intracellular phosphorylation of the receptor transducing the signal over the cell membrane and activating internal Ras and PI3K signalling pathways. (Kobayashi and Ozawa, 2013). FGF2 is expressed in the PE and drives development of the epicardial phenotype

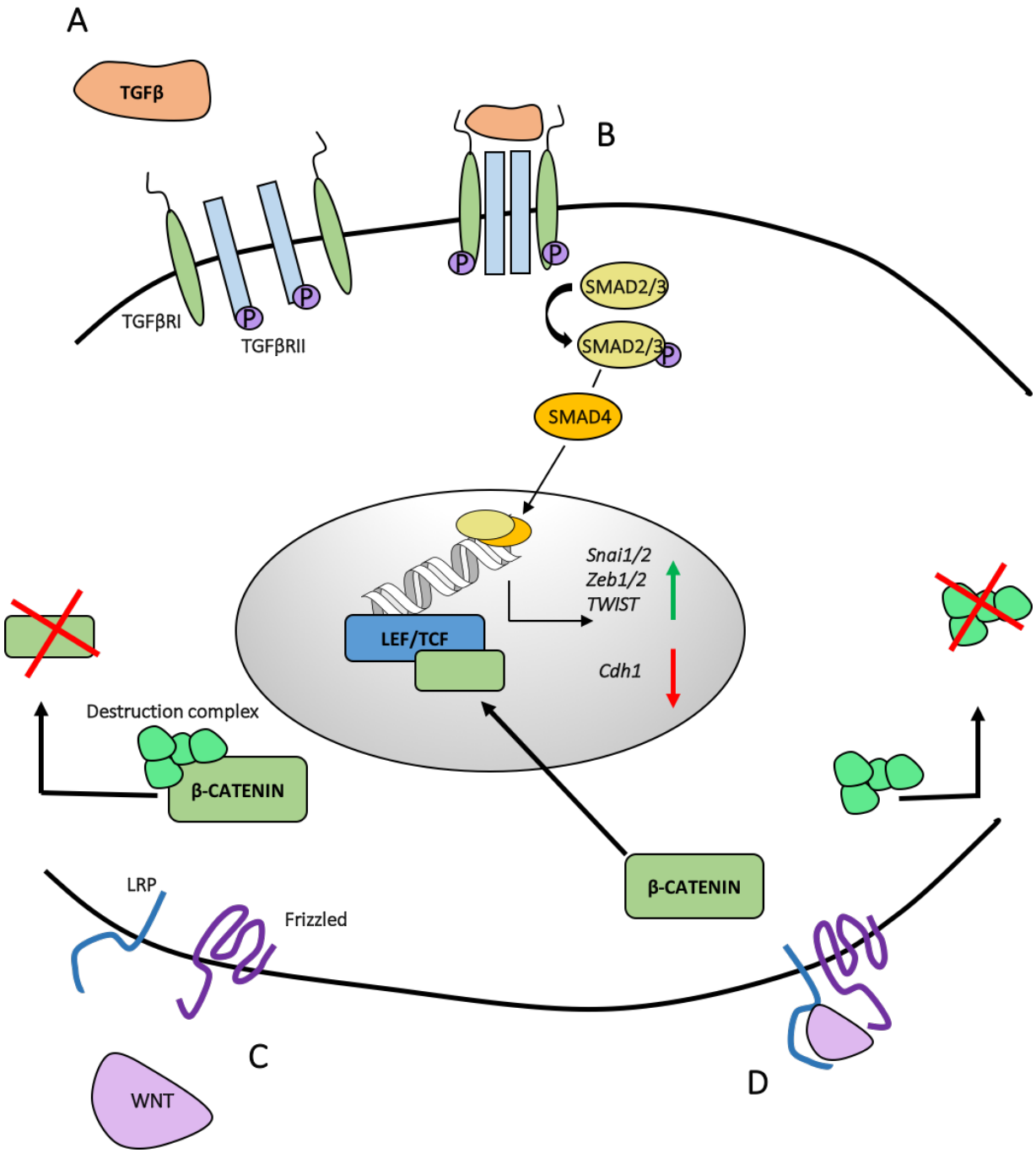


Figure 1.12 TGFβ and β-CATENIN signalling pathways in EMT (**A–B**) TGFβ signalling is initiated when an appropriate ligand binds a homodimer of the type II receptor (TGFβR2) at the cell membrane. This recruits and phosphorylates a homodimer of the type I receptor (TGFβR1). The heterotetrameric phosphorylates intracellular SMAD2/3 which form a complex with SMAD4 before being translocated to the nucleus. In the nucleus the complex binds to DNA initiating expression of EMT associated transcription factors. (**C–D**) In the absence of Wnt signalling cytoplasmic β-CATENIN is tagged for proteasomal degradation by a destruction complex. Binding of WNT ligands to the Frizzled and LRP receptors in the membrane inhibits the destruction complex. β-CATENIN is instead translocated to the nucleus where it forms a complex with LEF\TCF transcription factors and subsequently binds to DNA driving expression of key EMT transcription factors.

Several EMT inducing transcription factors are direct transcriptional targets of the WNT\β-CATENIN signalling cascade. The β-CATENIN protein has a dual biological role in that it is an essential structural component in adherens junctions but is also the fundamental mediator of WNT signalling. Association of newly synthesised E-CADHERIN with β-CATENIN occurs before both proteins leave the endoplasmic reticulum. This association is protective for both proteins and inhibits proteasomal degradation in the cytoplasm (Valenta et al., 2012). Signals from Wnt proteins are transduced by the frizzled and low-density lipoprotein receptor–related protein (LRP) receptors in the cell membrane. Without Wnt signalling, any free β-CATENIN protein in the cytoplasm is sequestered by a destruction complex that phosphorylates serine and threonine residues, marking it for ubiquitination and proteasomal degradation (Fodde and Brabletz, 2007). Receptor activation by Wnt proteins initiates a series of intracellular events that inhibit the degradation complex; β-CATENIN is subsequently translocated in to the nucleus where it binds to the Transcription factor 7 (TCF7)/LEF 1 transcription factors. The β-CATENIN-TCF/LEF complexes drive expression of the key EMT mediators SNAI1, SNAI2, ZEB and TWIST and the β-CATENIN-LEF complex can directly inhibit *Cdh1* transcription (**Figure 1.12 C** and **D**) (Kemler et al., 2004) (Kobayashi and Ozawa, 2013).

1.18 hEPDCs undergo spontaneous EMT

In 2007 a group from the Leiden University Medical Centre, The Netherlands, reported that epicardium explants dissected from RAA biopsies yield cultures of hEPDCs. Established cultures were described as having epithelial ‘cobblestone’ morphology and retained the ability to undergo spontaneous EMT as characterised by a switch from ‘cobblestone’ epithelial to ‘spindle’ mesenchymal morphology, relocalisation of the epithelial marker β-CATENIN and formation of actin stress fibres across the cell body (van Tuyn et al., 2007). In addition, treatment of hEPDC cultures with recombinant TGFβ stimulated EMT and induced expression of α-SMA

and smooth muscle myosin heavy chain (SM-MHC) (Bax et al., 2011). Together these data demonstrated that primary hEPDC cultures retain developmental plasticity: they are able to become 'activated', undergo EMT and differentiate toward a smooth muscle fate. As such, hEPDC cultures represent a potential system in which to examine the regenerative potential of the human epicardium.

1.19 High Throughput Phenotypic Screening in human EPDCs: Pilot Work

Previous work in the Riley lab has established the phenotypic plasticity of adult EPDCs *in vivo* and their ability to contribute small numbers of *de novo* cardiomyocytes after MI when primed with Tβ4 (**Chapter 1.7**) (Smart et al., 2007, 2011). This body of work, conducted in mouse, confirmed the widely held view that the epicardium is a resident progenitor population, but also reiterated that the endogenous regenerative response is not sufficient to restore lost heart tissue or heart function post MI. It was, therefore, postulated that small molecules may be able to optimally stimulate epicardial activation, thereby increasing their potential contribution to repair.

In order to identify small molecules capable of inducing hEPDC activation an appropriate screening assay was required. Prior to the start of this DPhil, a high throughput phenotypic screening (HTPS) protocol was designed by Dr Anke Smits, a postdoctoral researcher in the group, in collaboration with the Target Discovery Institute, Oxford. The screen was designed to probe the phenotypic plasticity of hEPDCs derived from RAA biopsy samples (**Chapter 1.15**).

The rational for the screen design was as follows: in embryogenesis EPDCs must undergo EMT in order to develop the migratory phenotype required for their contribution to the developing heart (**Chapter 1.6**). Furthermore, EPDCs activated by surgical induction of MI express the

EMT markers SNAI1 and α-SMA *in vivo* implicating the transition in the injury response (**Chapter 1.7**) (van Wijk et al., 2012; Zhou et al., 2011). If epicardial cells are to contribute to heart regeneration, it is logical that they must undergo EMT in order to lose their epithelial phenotype and become 'active' progenitors capable of migrating in to the underlying myocardium to give rise to cardiovascular derivatives, or to act a source of trophic signals. Therefore, EMT can serve as a surrogate read out for epicardial activation.

As previously discussed (**Chapter 1.7**), hEPDCs can be grown from RAA explant cultures and induced to undergo EMT by treatment with recombinant TGFβ; the induction of EMT can be confirmed visually by the morphological changes associated with the transition. Developing a suitable assay for phenotypic screening relies upon there being a biologically relevant and quantifiable change in the assay system that acts as a suitable read out of phenotypic change. Analysis of the pilot screen relied upon this characteristic switch from 'cobblestone' to 'spindle' morphology.

In the initial pilot screen hEPDCs were seeded in to 384 well plates for 48 hours before being treated with the Pharmakon1600 compound library at concentrations of 10, 2 and 0.4μM for 48 hours. The Pharmakon library is a collection of 1,600 known pharmacologically active drugs that have demonstrated activity against known targets, such as the kinases, proteases and G-protein coupled receptors (http://www.tdi.ox.ac.uk/small-compound-libraries). TGFβ and 0.5% DMSO were used as the positive and negative controls respectively. After 48 hours the plates were fixed and stained with the nuclear stain DAPI, the F-ACTIN stain phalloidin and cell mask plasma membrane stain. The cells were imaged using the Perkin Elmer Operetta High Content Imager (tdi.ox.ac.uk/high-content-imaging) and an analysis protocol was written to identify and quantify the percentage of cobble cells in each well; this was used to scan all of the images and

generate a data set documenting the hEPDC morphology associated with each individual compound. Analysis of this data set was the first task to be undertaken at the start of this DPhil project (**Chapter 3)**.

1.20 Hypothesis

1. The epicardium is a source of progenitor cells in the adult heart.

2. Adult human epicardial cells may be activated to contribute to heart repair.

3. EMT can be used as a surrogate marker for adult epicardial cell activation *in vitro*; the characteristic morphological switch in cell shape can be used as a read out for phenotypic screening.

4. Small molecules may be able to optimally stimulate epicardial activation with improved efficacy relative to known biological factors such as Tβ4.

1.21 Thesis aims

In order to test the above hypothesis, the following thesis aims were established:

1. Establish a robust protocol for the derivation and characterisation of primary hEPDC cultures.

2. Analyse data from the pilot phenotypic screen and validate the 'hits'.

3. Design and synthesise a range of small molecules based upon confirmed 'hits' from the pilot screen.

4. Determine hEPDC activation and differentiation capacity.

5. Build upon the original HTS protocol and carry out complementary genetic and chemical screens.

5. Validate hEPDC activating compounds into an animal MI model.

1.22 Chapter synopsis

Chapter 2

Chapter 2 outlines the general materials and methods used to perform the biological experiments described in chapters 3–8, and the hEPDC isolation and culture protocol established for generation of explant cultures.

Chapter 3

Chapter 3 describes the protocol established for derivation of hEPDC cultures and subsequent characterisation of hEPDC EMT *in vitro*. It also describes the methods used to analyse data from the pilot HTPS and the subsequent validation experiment.

Chapter 4

Chapter 4 describes attempts to establish a model of EMT and differentiation in an epicardial cell line derived from rat.

Chapter 5

Chapter 5 describes attempts to establish a model of EMT in an immortalised mouse EPDC cell line. Chapter 5 also describes the development of an automated scratch assay in which migration was used as a surrogate read out for epicardial activation.

Chapter 6

Chapter 6 describes the selection and synthesis of a targeted small molecule library that was used to test the newly designed automated scratch assay.

Chapter 7

Chapter 7 describes the methods used to analyse the automated scratch assay, and the subsequent validation of 'hit' compounds.

Chapter 8

Chapter 8 describes a subsequent scratch assay in which a panel of BET inhibitors, and the mimetic, were investigated to assess their effect on EPDC migration in a dose responsive manner. Finally, the compounds that increased the rate of mEPDC migration were tested at their 'effective' concentration in the previously established mouse EPDC model to investigate whether increased migratory capacity reflected EPDC EMT and differentiation.

Chapter 2

General Materials and Methods

2.1 Cell culture

2.1.1 Protocol for the isolation of epicardial tissue from RAA biopsies

Before beginning the isolation procedure, six well plates were coated with 0.1% gelatine, left in an incubator at 37°C in 5% CO_2 for 15 minutes and then aspirated. It was found that when plating epicardial explants, tissue pieces would detach from the bottom if the wells were too wet: to ameliorate this issue the plates were left to dry with the lid off for 2–3 minutes in a sterile environment before being used. Using pre-treated Corning Primaria tissue culture plates avoided this issue completely as they do not require gelatine coating. All tools and reagents used in the isolation were sterilised beforehand in 70% ethanol and all steps were performed in a laminar flow hood.

Once removed from the patient, RAA biopsies were stored and transported at 4°C in a sterile falcon tube filled with hEPDC culture medium consisting of: a 1:1 mixture of low glucose DMEM (Invitrogen) and M199 (Invitrogen), 10% FBS (Thermo Fischer) and 100U/mL penicillin with 100µg/mL streptomycin (pen/strep). To prepare the samples for culture they were removed from the media, transferred to a sterile petri dish, washed in Dulbecco's Phosphate Buffered Saline (DPBS) (Invitrogen) supplemented with pen/strep and transferred to a clean petri dish along with 1–2mL DPBS.

Using a stereomicroscope, the epicardial surface of the sample could easily be located (**Figure 2.1 A**, arrow); it is light pink in colour and sits atop a layer of epicardial adipose tissue (**Figure 2.1 A**, arrowhead). Using two pairs of forceps, one to steady the sample and one for dissection, the epicardium was pulled away from the myocardial surface (**Figure 2.1 B**) in white sheets that are easy to see, even at low magnification.

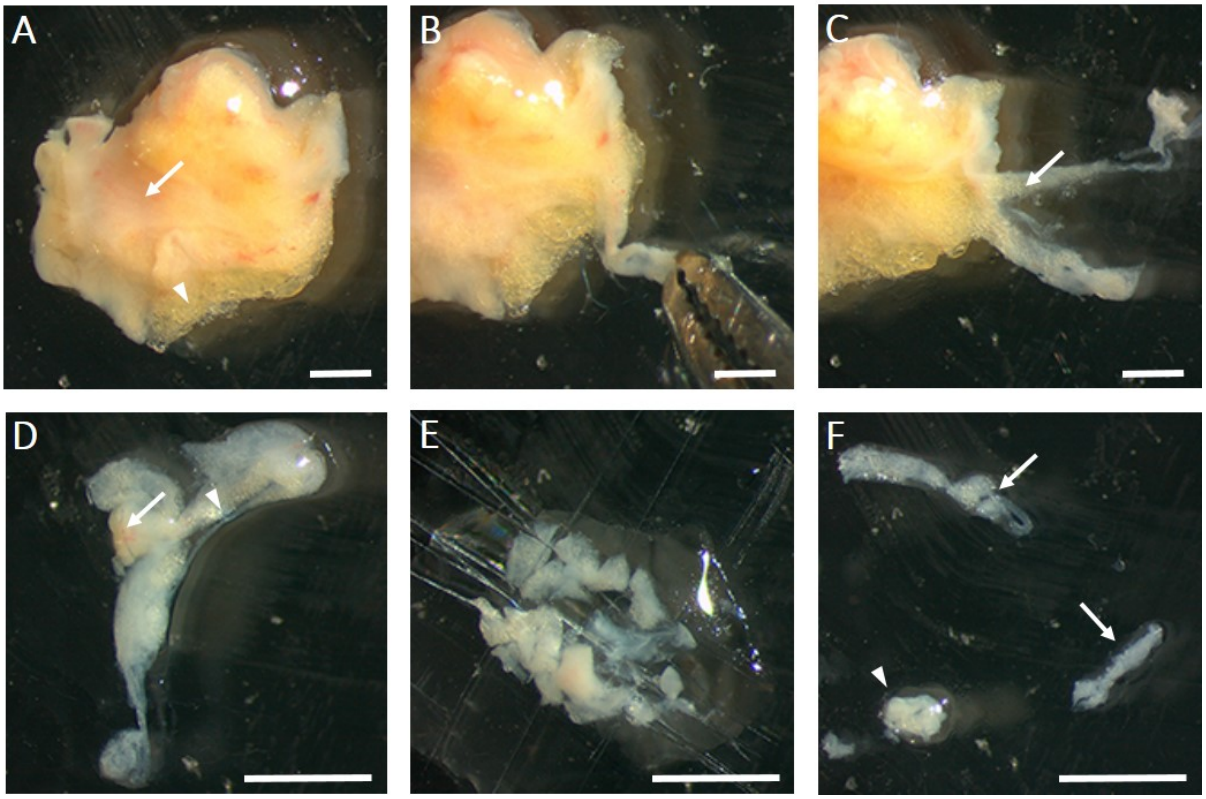


Figure 2.1 Isolation of human epicardium from right atrial appendage biopsy. (**A**) The outer epicardial surface (arrow) is smooth, light pink in colour and often sits over a thin layer of yellow epicardial fat (arrowhead). (**B**) Forceps are used to pull the epicardium tissue away from the underlying myocardium. (**C**) The epicardium should come away from the muscle in white sheets that are easy to locate with low magnification. Small amounts of contamination with fat (arrow) or blood vessels can occur at this stage. (**D**) Once removed, the tissue should be white and shiny. Contamination with red blood vessel (arrow) and yellow fat (arrowhead) is easily identified at this point and should be removed. (**E**) The epicardium is cut into pieces, but should not be minced. (**F**) The epicardium pieces are distributed between wells of a culture plate and topped with a coverslip. Forceps should be used to stretch the tissue pieces flat against the bottom of the well (arrows); the tissue should not be left as a heap (arrowhead). All scale bars 1mm.

Typically, the epicardium could be removed from the muscle quite easily, though sometimes a sharp tug was required to detach the tissue. As more samples were processed it became clear that epicardial tissue covering pink patches of viable myocardium was much easier to remove, so this was targeted as a starting point for the dissection. As the tissue was removed, some contamination from the underlying fat (**Figure 2.1 C**, arrow) and surrounding blood vessels would occur. Although this could be removed at a later stage, efforts were made to eliminate contamination in order to minimise heterogeneity in hEPDC cultures.

After all the epicardium was pulled off the sample, it was collected together and transferred to a clean petri dish with a few drops of DPBS (**Figure 2.1 D**). Epicardial tissue is white and shiny; fat and blood vessel contamination could be easily identified so at this point as much contamination as possible was removed using the forceps. Using a sterile scalpel, the tissue was then cut into pieces by cutting across the sample in parallel 2–3 times, rotating the sample by 90^{o} and repeating (**Figure 2.1 E**). It was important here not to mince the sample as it was necessary to spread the pieces flat across the bottom of the well when plating the explants; if explants were too small hEPDCs did not grow; 1–5 mm in length was ideal.

The pieces of epicardium were then spread between wells of the previously prepared tissue culture plate, usually four or five pieces of tissue per well. Preparing one well at a time, forceps were used to spread the pieces flat across the bottom of the plate (**Figure 2.1 F**, arrow); the tissue would not grow or adhere to the plate if it was left as a heap (**Figure 2.1 F**, arrowhead). The tissue pieces were then topped with a glass coverslip before moving onto the next well. At this point, it was noted that tissue pieces would not adhere to the bottom of the dish if they were too wet. However, it was also essential to work quickly during the plating procedure as the tissue would also dry out which made it sticky, difficult to work with and prevented hEPDC growth. When all the tissue was distributed the plate was placed into a humidified incubator at 37^{o}C with 5% CO_2 for 1 hour, after which 1mL of hEPDC medium was added to each well. The plates were then left in the incubator for 2–3 days to allow hEPDC growth; another 1mL of hEPDC media could be added to prevent explants from drying out; however, excessive movement of the plates resulted in the tissue pieces detaching from the bottom so was kept to a minimum. HEPDCs usually began to grow from the samples after 2–3 days and, even if no growth was observed, the coverslips were removed so that the cultures were fully exposed to the media.

2.1.2 hEPDC passage and culture

Once hEPDC explant cultures had been established it was necessary to expand the cell population for use in screening and characterisation experiments. HEPDC cultures were allowed to reach 95–100% confluency (i.e. an epithelial sheet) prior to passaging: passaging at lower densities resulted in spontaneous EMT. Patches of the explant cultures would sometimes develop a mesenchymal phenotype. Scratching away the differentiated cells with a p200 pipette tip and replacing with fresh media helped prevent EMT in the rest of the culture

Prior to passaging the hEPDCs, the appropriate sized culture plates were coated with a 0.1% gelatine solution in PBS and allowed to stand for 15 minutes at 37^{o}C before being aspirated. Culture media was aspirated from the cultures and the hEPDCs gently washed with DPBS; hEPDCs were incubated with 0.05% Trypsin-EDTA solution (trypsin) (200 µL/10 cm^2 of cells) (Invitrogen) for a maximum of 5 minutes at 37^{o}C to detach the cells. HEPDCs were washed off the plate using warm, fresh culture media supplemented with 10 µM of the ALK5 inhibitor SB-435142 (Sigma) and transferred to the prepared culture dish. A splitting ratio of 1:2 would maintain 'cobblestone' morphology, splitting at a higher ratio would induce spontaneous EMT. Cells would adhere to new culture dish as long at the final trypsin concentration was lower than 10%.

2.1.3 Culture of rEPDCs

Immortal rEPDCs were obtained from Dr Nicola Smart (DPAG, University of Oxford). REPDCs were seeded in standard DMEM (Invitrogen) with 10% FBS and pen/strep on 0.1% gelatine coated plates. When cells reached 80% confluency they were washed with DPBS and detached with trypsin solution (500 µL/10 cm^2 cells) for a maximum of five minutes for

passaging. Healthy cultures could be re-established with a splitting ratio of 1:3–1:6. All cells were maintained in humidified air with 5% CO_2 atmosphere at 37^{o}C.

2.1.4 Culture of mEPDCs

Immortalised mEPDCs were obtained from Dr Joaquim Vieira (DPAG, University of Oxford). In order to retain their immortalised state mEPDCs were cultured at 33^{o}C in 'immortalisation media' (IM) which consisted of standard DMEM supplemented with 10% FBS, 1:100 insulin transferrin-selenium (Thermo Fischer) and 10 units/mL of mouse gamma interferon (Peprotech). Cells were passaged following the same protocol as the rEPDCs when they reached 80% confluency. MEPDCs were maintained in humidified air with 5% CO_2.

2.2 EPDC EMT and differentiation protocol

2.2.1 HEPDC EMT and differentiation

HEPDCs were used for differentiation experiments if >80% of the cells retained a 'cobblestone' epithelial phenotype. HEPDCs were trypsinized, resuspended in warm media supplemented with 10 μM SB-435142 and seeded at a density of 20,000 cells/cm^2 into culture plates or on to glass coverslips coated with 0.1% gelatine as previously described. After 24 hours the media was aspirated and replaced with media supplemented with 2 ng/mL TGFβ; hEPDCs were left to differentiate for 72 hours before being collected for analysis.

2.2.2 REPDC EMT and differentiation

REPDCs were plated into 0.1% gelatine coated 6 well plates or on to coverslips in 24 well plates (2 cm^2) in standard medium. After 24 hours the media was replaced with low serum (0.5% FBS) media containing 10 ng/mL human recombinant FGF2 (Sigma). After a further 24 hours the medium was replaced with low serum media containing FGF2 and 2 ng/mL TGF-β (R & D

Systems) and the cells left to differentiate for a further 48 hours. In cell cultures differentiated with TGFβ alone the FGF2 and FGF2\TGFβ media was replaced with media supplemented with 2 ng/mL of TGFβ only at both time points.

2.2.3 MEPDC EMT and differentiation: differentiation media

MEPDCs were plated in to 0.1% gelatine coated tissue culture plates or on to glass coverslips in standard IM at 33^{o}C. After 24 hours the media was removed and replaced with differentiation media (DM) consisting of M199 media with 10% FBS and pen/strep, and the cells incubated at 37^{o}C. After a further 24 hours media was replaced with plain DM or DM containing 2 ng/mL TGFβ and the MEPDCs left to differentiate for 72 hours before being collected for analysis: the media was replaced on day two of the differentiation.

2.2.4 MEPDC EMT and differentiation in IM

MEPDCs were plated in to 0.1% gelatine coated tissue culture plates or on to glass coverslips in standard IM at 33^{o}C. After 24 hours the media was aspirated and replaced with plain IM or IM containing the growth factors or compounds of interest. MEPDCs were left to differentiate for between 1–7 days before being collected for analysis. In experiments with TGFβ the media was refreshed every two days: when mEPDCs were being treated with compounds the media was refreshed daily.

2.3 Molecular techniques

2.3.1 RNA Extraction

Cells were detached with trypsin, collected in their respective standard media and snap frozen as pellets. MRNA was extracted with an RNeasy® Plus Micro Kit (Qiagen) according to manufacturer's instructions. Cell pellets were homogenised in 350 μL of Buffer RLT Plus, transferred to a gDNA Eliminator spin column in a 2mL collection tube and centrifuged for 30

seconds (s) at 8000 x g. The flow through was mixed with 350 µL of 70% ethanol, transferred to an RNeasy MinElute spin column in a 2mL collection tube and centrifuged for 15s at 8000 x g. The flow-through was discarded and the RNA washed with 700 µL of Buffer RW1 by centrifuging for 15s at 8000 x g. The flow-through was discarded and the RNA washed with 500 µL of Buffer RPE in the same manner. The flow-through was again discarded and the RNA washed with 500 µL of 80% ethanol by centrifugation for 2 minutes at 8000 x g. The spin column was transferred to a dry 2mL collection tube and dried by centrifugation for 5 minutes at full speed. RNA was then eluted from the column in 16 µL of RNase free water. RNA quality and quantity was measured using a Nanodrop2000 (ThermoScientific, UK). Samples were stored at -80^{o}C.

2.3.2 cDNA synthesis

Complementary DNA was synthesised from the mRNA template by reverse transcription. Reactions were prepared in 0.6mL micro tubes (Corning). A maximum of 1µg of mRNA was added to each reaction tube and the volume made up to 8.5 µL with DEPC water. A mastermix containing 0.5 µL of random primers (20µg/ml; Promega); 1 µL dNTPs (from 10 mM GE Healthcare); 2 µL $MgCl_2$ (25mM, Thermo Scientific); 2 µL Dithiothreitol (DTT; 0.1M, Life Technologies); 1 µL RNasin® plus RNase inhibitor (Promega); 4 µL 5X FS Buffer (Life Technologies) and 1 µL of SuperScript® III Reverse Transcriptase (Life Technologies) was made for the number of samples (n) +2. 11.5 µL of this mix was added to each RNA sample tube giving a total volume of 20 µL per tube. The reaction tubes were then placed in a 96-well Veriti™ thermal cycler (Applied BioSystems) and cycled at 25°C for 10 minutes; 42°C for 50 minutes and 70°C for 15 minutes, before cooling to 4°C. Samples were diluted to 4 ng/µL in DEPC water and stored at 4°C short-term or -20°C long-term.

2.3.3 RT-PCR

Reverse transcription polymerase chain reactions were carried out using PCR beads (GD Healthcare) in a 96 well Veriti^{TM} thermal cycler (Applied Biosystems) cycled at 94°C for 2 minutes; 94°C for 30 seconds followed by 58^{o}C for 30 seconds which was repeated 35 times; 72°C for 45 seconds. 0.05pmol/ml of forward and reverse primers (**Table 2.1**) was added to 5µL of total cDNA in DEPC water to a total volume of 25µL.

Samples were run on agarose gels to determine the molecular weight of the DNA products. 2% weight by volume agarose gels were made by dissolving 2g agarose (Sigma Aldrich, UK) in 100ml of TBE buffer (40 mM Tris pH8.0; 20 mM Boric acid; 1 mM EDTA) and boiling in a microwave. 5 µL of Gel-Red (VWR) was added to the molten solution before pouring the gel. Plastic combs were used to create sample wells in the gel. 5 µL of orange DNA Loading Dye (Life Technologies) was added to samples prior to transferring to wells. A current of 120 V was passed through the gel for 45 minutes until the bands were suitably resolved. Gels were visualised using a UV box.

2.3.4 QPCR analysis

Q-PCR was used for the relative quantification of genes of interest. Reactions were performed in 0.1ml Fast 96-well plates on a ViiA™ 7 Real-Time PCR System. Each sample was tested in triplicate and each gene was run with a corresponding non-template control in which water replaced the cDNA. A master mix was made for each separate gene, so that each sample well would have the following: 6.25 µL SYBR® Green (Fast-mix; Life Technologies); 3.25 µL DEPC H_2O; and 0.25 µL of each respective primer, making a total volume of 11 µL. The master mix was pipetted into the plate followed by 4 ng (1 µL) of cDNA. The thermal cycles were 95°C for 15 minutes; 40 cycles of 95°C for 15 seconds and 60°C for one minute. A melt-curve to

detect non-specific amplification products was run where un-tested primers were included in the experiment. Cycle Threshold (Ct) values were determined using the ViiA™ 7 Software and values were exported to Microsoft Excel for manual analysis. Relative quantification of gene expression was determined using the comparative cycle threshold method ($2^{-\Delta\Delta CT}$). ΔCt values were calculated by normalisation of Ct values of genes of interest to a GAPDH (mouse) or β-ACTIN (human and rat) housekeeping sample. ΔΔCt values were calculated by calibrating values to control samples i.e. gene expression in TGFβ treated cells were calibrated against untreated samples. Primer sequences are in **Table 2.1**.

Table 2.1 Primer sequences

Gene	Forward	Reverse
Rat *β-Actin*	TGATTGTCAGAAGGCTTGGCTAAC	AAGTCCCTCACCCTCCCAAAAG
Rat *Snai2*	ATGCACATCCGAAGCCACAC	CAGGGAGAATGGCTTCTCAAT
Rat α-*SMA*	GTCCCAGACACCAGGGATGA	TCGGATACTTCAGGGTAAGGA
Rat *ZO-1*	AGCAAGCCTCCTGCACATA	TAGCATCAGTTTCGGGTTTC
Human *β-Actin*	CCTTGCACATGCCGGAG	GCACAGAGCCTCGCCTT
Human *Snai1*	TCGGAAGCCTAACTACAGCGA	AGATGAGCATTGGCAGCGAG
Human *Snai2*	CGAACTGGACACACATACAGTG	CTGAGGATCTCTGGTTGTGGT
Human *WT1*	CACAGCACAGGGTACGAGAG	CAAGAGTCGGGGCTACTCCA
Human *Acta2*	AGCCCAGCCAAGCACTG	CAAAGCCGGTTCCATAGAG
Human *TAGLN*	AGTGCAGTCCAAAATCGAGAAG	CTTGCTCAGAATCACGCCAT
Human *Tbx18*	CAAATGACATCCCAGCTTGA	CCTCCCCGGATGGAACAGGCT
Human *Tcf21*	TCCTGGCTAACGACAAATACGA	TTTCCCGGCCACCATAAAGG
Human *Myh7*	CTCTCCTGGGTCAGCTTCAG	TTCGACCTGCAGGAGAAGTT
Human *Tnnt2*	CGAGGAGAAGTTCAAGCAGC	AGCCAGGTCTATTTCCAG
Human *Cdh1*	CGAGAGCTACACGTTCACGG	GGGTGTCGAGGGAAAAATAGG

Mouse *ZEB1*	ACCCCTTCAAGAACCGCTTT	CAATTGGCCACCACTGCTAA
Mouse *WT1*	TTCAAGGACTGCGAGAGAAG	GGGAAAACTTTCGCTGACAA
Mouse *Tbx18*	ACGAAATAGGCACCGAGATG	TTGTCCACCGGCACAATATC
Mouse *Tcf21*	CGACAAGTACGAGAACGGTTAC	TGTAGTTCCACACAAGCGGTT
Mouse *GAPDH*	AGGTCGGTGTGAACGGATTTG	TGTAGACCATGTAGTTGAGGTCA
Mouse *FSP1*	TCCACAAAATACTCAGGCAAAGA	GCAGCTCCCTGGTCAGTA
Mouse *Snai1*	CTTGTGTCTGCACGACCTGT	CAGGAGAATGGCTTCTCACC
Mouse *Snai2*	CATTGCCTTGTGTCTGCAAG	CAGTGAGGGCAAGAGAAAGG
Mouse *TAGLN*	CAACAAGGGTCCATCCTACGG	ATCTGGGCGGCCTACATC
Mouse *Acta2*	TCGGATACTTCAGCGTCAGGA	GTCCCAGACATCAGGGAGTAA
Mouse *Cdh1*	ACT GTG AAG GGA CGG TCA AC	GGA GCA GCA GGA TCA GAA TC
Mouse *BVES*	GCTCTACTCACTCACTGAATGACC	TGGAGATCTGTGTGCAGAGG

2.3.5 Immunostaining

All coverslips were washed twice with PBS and fixed using 4% paraformaldehyde (PFA) for 20 minutes. Before staining, the fixed coverslips were washed with 0.1% Triton-X in PBS (PBT) for 5 minutes then permeabilised with 0.5% Triton X in PBS for 10 minutes. The coverslips were washed twice more in with PBT for 5 minutes and blocked in 0.1% Triton-X with 10% goat serum and 10% bovine serum albumin (BSA). The coverslips were incubated with primary antibodies overnight at appropriate concentrations at 4^{o}C in a wet chamber (**Table 2.2**). The coverslips were washed sequentially with PBT for a further 10, 20 and 10 minutes. Before being incubated with the appropriate secondary antibodies and/or stains in PBT for 1 hour at room temperature. Finally the coverslips were washed three more times, allowing 10 minutes for each wash, then incubated with DAPI (5 µg/mL in PBS) for 10 minutes before being mounted on glass slides in 50:50 glycerol/PBS. Slides were visualised on a Leica CTR6000.

Table 2.2 Antibodies and stains

Antibody/Stain	Supplier	Catalogue #	Source	Dilution
Alexa Fluor® 488 Phalloidin	Thermofisher	A12379	n/a	1:150
Alexa Fluor® 594 phalloidin	Invitrogen	A12381	n/a	1:150
Cell mask green	ThermoFischer	C37608	n/a	1:10000
CellTracker™ Red CMTPX	Thermo fischer	C34552	n/a	15μM
GAPDH	Abcam	ab8245	mouse	1:1000 (WB)
GATA 5	Novus biologicals	NBP1-51215	rabbit	1:100
Phosphohistone-H3	Santa Cruz Biotech	SC-8656-R	rabbit	1:100
P-SMAD3	Abcam	ab52903	rabbit	1:1000 (WB)
SM22-α	Abcam	ab14106	rabbit	1:100 (1:1000 WB)
TBX18	Millipore	MAB10084	mouse	1:100
VINCULIN	Sigma-Aldrich	V4505	mouse	1:100
WT1	Abcam	ab89901	rabbit	1:50
α-SMA	Sigma-Aldrich	A2547	mouse	1:1000 WB
α-SMA-Cy3™	Sigma Aldrich	c6198	mouse	1:100
β-CATENIN	Abcam	ab32572	rabbit	1:250

2.3.5 Western blot

Western blotting was performed using a standard Abcam protocol (http://www.abcam.com/protocols/general-western-blot-protocol). Proteins were visualised using ECL Western Blot detection reagents (GE Healthcare). Quantitative blot analysis by scanning densitometry was analysed using SPECTRstar nano software.

2.4 SMAD3 Phosphorylation assay

Both rEPDCs and mEPDCs were seeded into 0.1% gelatine coated 6 well plates at a concentration of 1 x 10^4 cells/cm^2 in their respective standard media. After 24 hours the cells were serum starved in their standard media which did not contain FBS for a further 24 hours. For the assay proper, cells were treated with their standard media supplemented with 2 ng/mL TGFβ for 60, 30, 20, 10, 5 or 0 minutes then collected into 100 µL of hot lamelli buffer. Western blot analysis was carried out using the standard protocol (http://www.abcam.com/protocols/general-western-blot-protocol).

2.5 High-Throughput Screening protocols

2.5.1 Original hEPDC phenotypic screening protocol

HEPDCs were seeded at a density of 750 cells/well into 0.1% gelatine coated 384 well plates in standard hEPDC media with 10µM SB-435142. After 24 hours this was replaced with plain hEPDC media. After a further 24 hours the cells were treated with compounds from the Pharmacon1600 library at concentrations of 15, 10 and 5 µM (Pilot screen), or with the 'hit' compounds identified from the pilot screen. Control cells were treated with either 2 ng/mL of TGF-β, 10µM SB-435142 or plain media. After 48 hours of incubation the media was removed, cells washed with PBS and fixed in 4% PFA for 30 mins. The cells were permabilised with PBT and stained with Phalloidin-594 (Invitrogen, 1:133). DAPI (1mg/ml 1:5000) and Cell Mask (Invitrogen,1: 25000). Images of cells were taken and analysed on the PerkinElmer Operetta High Content Imager (tdi.ox.ac.uk/high-content-imaging)**.**

2.5.2 rEPDC and mEPDC original phenotypic screening protocol

Cells were seeded into gelatine coated 384 well plates in their respective standard media. After 24 hours the cells were treated with plain media or plain media supplemented with 2 ng/µL of

TGFβ and left to differentiate for 72 hours. The cells were processed for analysis and data collected in the same manner as previously stated.

2.5.3 mEPDC automated scratch assay protocol

MEPDCs were plated into 0.1% gelatine coated 96 well plates at a concentration of 30,000 cells/ well in 100 µL of IM. After 16 hours the cells had formed a monolayer; the media was aspirated and the cells stained with 15µM CellTracker^{TM} in IM for 30 minutes. The media was aspirated and mEPDCs washed with plain IM for another 30 minutes. The IncuCyte WoundMaker^{TM} was used to make a scratch wound across the middle of each well. The media and cell debris was removed and replaced with 90 µL of IM and 10 µL of IM supplemented with the treatments of choice (10x concentration). Plates were incubated at 33^{o}C and imaged every six hours on the GE InCell 6000 High Content Imager. The stain and wash protocol was repeated 24 hours later. The cells were imaged every six hours until the scratch wounds closed, after which the plates were discarded.

2.6 Data analysis

Q-PCR data are presented throughout as mean ± SEM. Multiple group comparison was performed by one-way ANOVA followed by Tukey's multiple group comparisons of means using GraphPad Prism 6 (GraphPad Software, Inc.). Comparisons between two groups were performed using the unpaired Student's t-test or the Mann-Witney test using GraphPad Prism 6 (GraphPad Software, Inc.). *$P<0.05$ were considered statistically significant.

2.7 Compound purchase

All compounds purchased for screening experiments were bought from Sigma or Tocris. 'Hit' compounds from the mEPDC pilot scratch assay that had been sourced from in house libraries

were compared with solid samples purchased from Sigma or Tocris by low-resolution mass spectrometry on a Micromass Platform 1 spectrometer from solutions in MeOH.

Chapter 3

High Throughput Screening in primary human EPDCs

3.1. Establishing and characterising hEPDC cultures

3.1.1 Protocol for the isolation of epicardial tissue from RAA biopsies

The first undertaking was to establish a robust protocol for the derivation of hEPDCs from biopsy samples. Once this was in place, cultures needed to be expanded to generate suitable numbers of hEPDCs to complete full characterisation studies, to validate hits from the pilot screen and to use in additional high throughput screening experiments. With the aim being identification of compounds that activate the human *adult* epicardium, it was a prerequisite that the starting population be representative of the 'dormant' adult state. Thus, it was essential that the isolation and culture protocol produced epithelial hEPDCs. In collaboration with Dr Anke Smits, a post-doctoral fellow in the laboratory, a protocol was developed for the isolation and culture of cobblestone hEPDC cultures which is fully documented in **Chapter 2.1.1** (Clunie-O'Connor et al., 2015).

Briefly, epicardial tissue was dissected from the RAA samples using forceps and any blood or fat contamination was removed. The tissue was cut into pieces 1–5mm in length and separated between wells of a six-well tissue culture plate before being topped with a glass coverslip. The explants were incubated for one hour at 37^{o}C in 5% CO_2 to allow the coverslips to adhere, before 1mL of hEPDC media was added to the each well. The culture plates were then placed back in the incubator for two–three days before they were examined for hEPDC growth. In the duration of these studies, it was observed that only two or three pieces of tissue from each sample would yield cells. This was occasionally because the tissue pieces had not properly adhered to the plate, or because the tissue had adhered to the glass coverslip instead of the culture plate. Other possible reasons for this could be that some of the dissected tissue dried out during the plating procedure and therefore were no longer viable, or that sections of the biopsy had become damaged or begun to die in the process of removal, preparation and transport.

Once they had begun to grow, the morphology of hEPDC cultures was found to be highly varied: sometimes the cells would form a monolayer with polygonal 'cobblestone' morphology characteristic of epithelium (**Figure 3.1 A**, explant tissue top left) and sometimes the cells would have a mesenchymal 'spindle' appearance (**Figure 3.1 B**, explant tissue top left). As previously discussed (**Chapter 1.18**), in order to model epicardial activation and EMT the starting population of cells needed to be epithelial so as to mimic the adult *in vivo* epithelial phenotype; therefore, the 'spindle' cultures that had already undergone EMT were of no further use to us and generally were disposed of. On occasion, patches of 'cobblestone' cultures would start to spontaneously undergo EMT and develop mesenchymal morphology: continued growth resulted in the rest of the culture also undergoing the phenotypic switch. This was prevented by using a pipette tip to scratch away the patches of spindle cells, gently aspirating the debris and replacing with fresh media.

An interesting observation was that refreshing the media too frequently hindered cell growth and it was later found that rather than replacing the media entirely, removing half and topping up with fresh media better sustained hEPDC cultures. It is postulated that doing so retained a concentration of cell-secreted factors that promote hEPDC growth and survival.

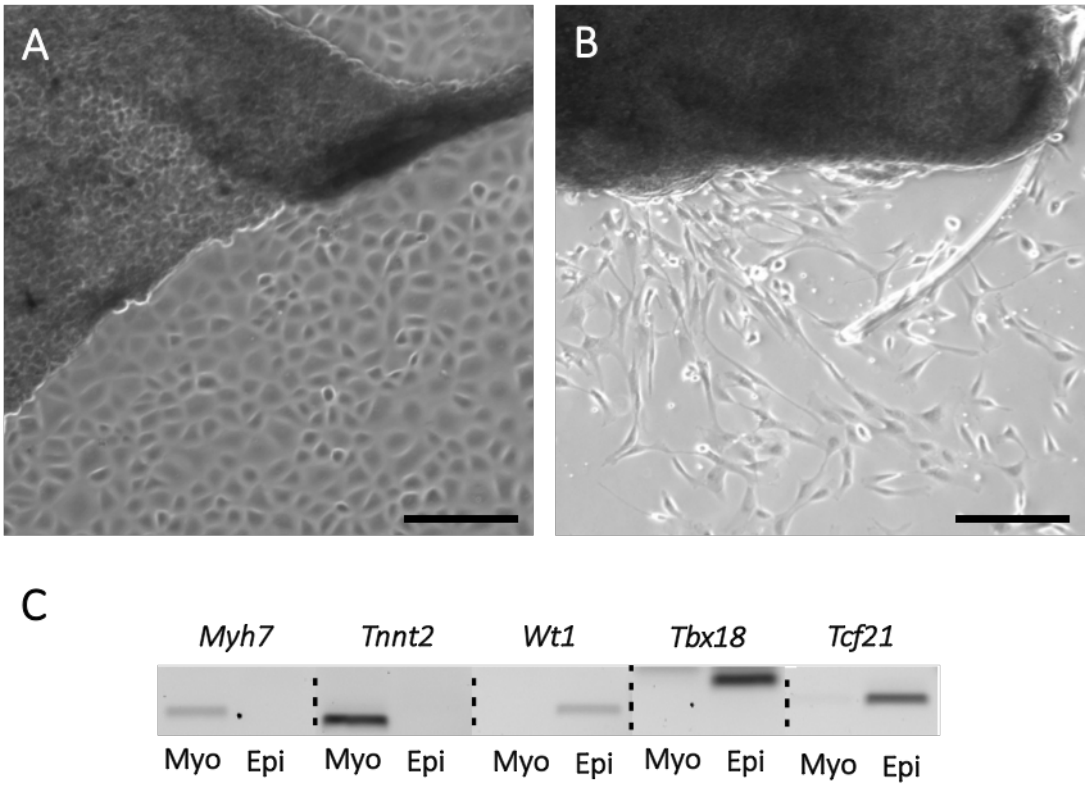


Figure 3.1 Human epicardium explants yield hEPDCs. RT-PCR confirms epicardial phenotype of isolated tissue. (**A**) After 2–5 days of culture hEPDCs began to grow from epicardium explants as an epithelial monolayer. (**B**) On occasion explants yielded mesenchymal cells. These cultures were not suitable for characterisation or screening experiments. (**C**) RT-PCR was used to compare gene expression between myocardium and isolated epicardial tissue from biopsy samples. Myocardium (**Myo**) expressed the muscle specific *Myh7* and *Tnnt2*, whereas epicardium tissue (**Epi**) expressed the epicardium specific genes *Wt1*, *Tbx18* and *Tcf21*. All scale bars 200µm.

RT-PCR was used to compare the gene expression profile of the epicardial tissue used for explant culture with that of the underlying myocardium (**Figure 3.1 C**). The myocardium (**Myo**) was positive for muscle markers *Myh*7 and cardiac troponin T (*Tnnt2*) but was negative for the epicardium markers *WT1*, *Tbx18* and *Tcf21*; the epicardium (**Epi**) tissue showed the opposite trend. This data confirmed that the tissue dissected from the RAA biopsies was indeed epicardium, and indicated that the cultures derived from this tissue were likely to be of epicardial origin.

3.1.2 Characterising hEPDCs

After establishing hEPDC cultures it was necessary to confirm an epicardial phenotype. Once the cultures were 95–100% confluent, hEPDCs were trypsinized and seeded on to coverslips or collected for analysis by RT-PCR. HEPDC growth is greatly affected by cell density: a splitting ratio of 1:2 was found to be effective for maintenance of epithelial 'cobblestone' hEPDCs (**Figure 3.2 A**); any higher than this and the switch to mesenchymal 'spindle' morphology would occur. Even with careful consideration of plating density, hEPDCs were prone to spontaneous EMT. As previously described (**Chapter 1.17**) TGFβ pathway activation occurs when the TGFβ ligand binds the TGFβ receptor II at the cell membrane which recruits and phosphorylates the TGFβ receptor I activin-like kinase 5 (ALK5), initiating downstream signalling (He et al., 2014; Shi and Massagué, 2003). In 2011 TGFβ induced hEPDC EMT was found to be ALK5 dependant (Bax et al., 2011): presence of the ALK5 inhibitor SB-435142 (SB) prevented the transition in the presence of the recombinant protein. During these studies it was found that supplementing the hEPDC media with 10μM of SB helped to maintain epithelial phenotype and prevent spontaneous EMT (Clunie-O'Connor et al., 2015).

After seeding on to coverslips, the cells were left to grow for three days in SB supplemented media before being fixed for analysis by ICC. 'Cobblestone' hEPDCs exhibited intense β-CATENIN staining at points of cell-cell contact; localisation of β-CATENIN to the membrane indicated the formation of adherens junctions, a hallmark of epithelia (**Figure 3.2 B**) (van Tuyn et al., 2007). Phalloidin staining revealed rounded epithelial morphology and that hEPDCs had begun to form a monolayer with a network cortical actin rings (**Figure 3.2 C**). During these investigations 'cobblestone' hEPDC explant cultures did not stain positive for the endothelial marker PECAM-1. HEPDCs stained positive for the epicardial markers WT1 and GATA binding protein 5 (GATA5) (**Figure 3.2 D–E**); RT-PCR confirmed expression of the epicardium

specific genes *WT1*, *Tbx18* and *Tcf21* and the epithelial marker *E-Cadherin* (**Figure 3.2 F**). Collectively this data confirmed that culture of RAA explants can generate epithelial epicardium cultures and validated the epicardium isolation protocol.

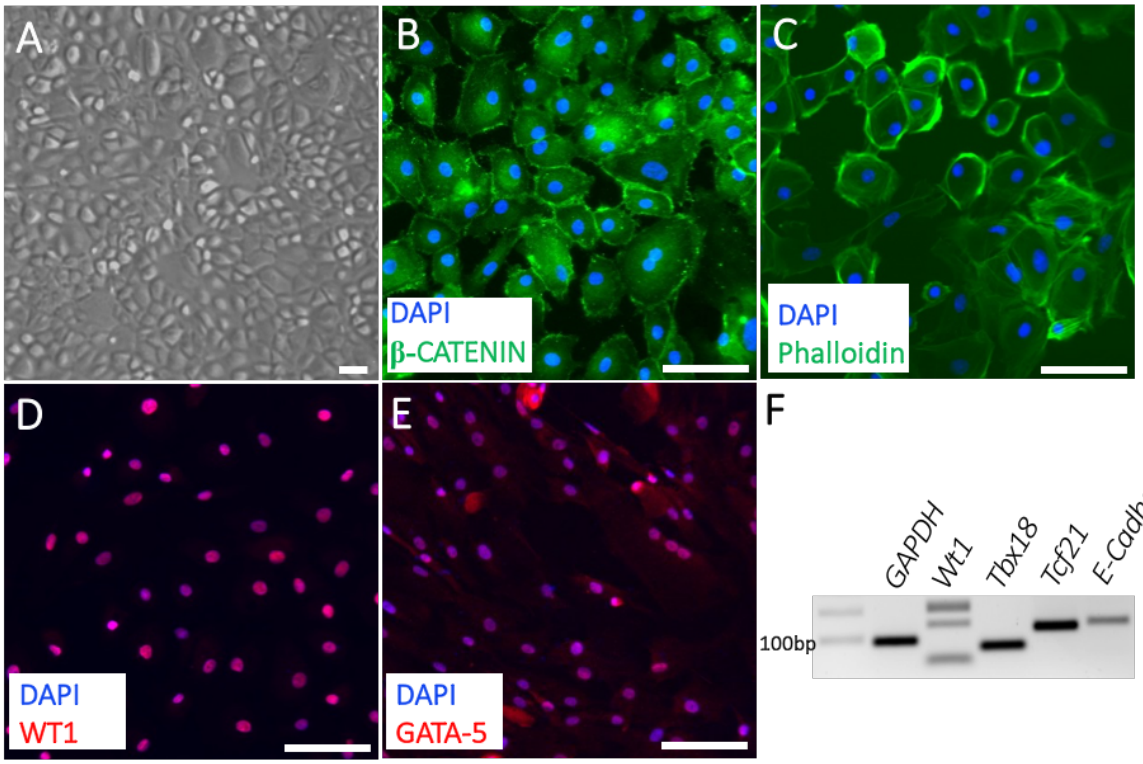


Figure 3.2 HEPDCs maintain epicardial phenotype in vitro. (**A**) Epicardial explants yielded cultures of hEPDCs with 'cobblestone' epithelial morphology. (**B**) HEPDCs stained positive for β-CATENIN, a component of the adherens junction, which was localised to the membrane at points of cell-cell contact. (**C**) Phalloidin staining revealed rounded epithelial morphology with cortical actin. (**D–E**) hEPDCs stained positive for epicardial markers WT1 and GATA5. (**F**) RT-PCR confirmed expression of epicardium specific genes *WT1, Tbx18 and Tcf21* and the epithelial marker *E-Cadherin* at their expected weights (**Chapter 2, Table 2.1**). All scale bars 50µm.

To complete the characterisation, a culture of hEPDCs that had migrated from the explant with 'spindle' morphology (**Figure 3.3 A**) were seeded on to coverslips and prepared for ICC as previously described. The 'spindle' cells were notably larger than the 'cobblestone' and phalloidin staining revealed dense stress fibre formation across the cell body, a hallmark of epicardial EMT (**Figure 3.3 B**) (Bax et al., 2011). 'Spindle' cells stained positive for the epicardial transcription factors WT1 and TBX18 (**Figure 3.3 C–D**) indicating that these too

were of epicardial origin. This data confirmed our own observations, as well as those stated in the literature, that hEPDCs can undergo spontaneous EMT whilst migrating from explants and in culture (Clunie-O'Connor et al., 2015; van Tuyn et al., 2007). Although this would clearly present a problem when it came to expanding the cultures for screening, it had the benefit of confirming hEPDC phenotypic plasticity, which was key if hEPDCs were to be targeted as source of cells for myocardial repair.

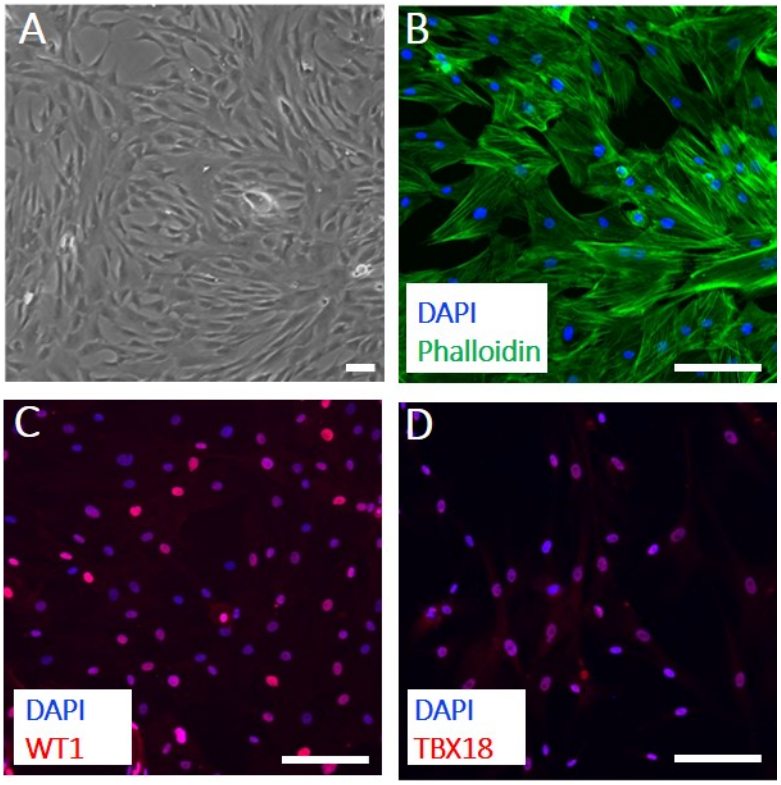


Figure 3.3 Spindle hEPDCs express epicardial markers. (**A**) Epicardial explants yielded cultures of hEPDCs with 'spindle' mesenchymal morphology. (**B**) Spindle hEPDCs had dense stress fibres across the cell body. (**C–D**) 'Spindle' hEPDCs stained positive for WT1 and TBX18 indicating they were of epicardial origin. All scale bars 50µm.

3.1.3 Characterising hEPDC EMT

In the pilot screen (**Chapter 1.19**), TGFβ induced EMT served as a positive control for hEPDC activation: therefore, a series of experiments were conducted in order to fully characterise this transition. Cultures of 'cobblestone' hEPDCs were trypsinized as previously described and seeded on to gelatine coated coverslips at a recommended density of 20,000 cells/cm^2 (Bax et al., 2011) in hEPDC media supplemented with 10μM SB. After 24 hours the media was replaced with SB, untreated hEPDC media (UT) or hEPDC media supplemented 2 ngmL of TGFβ. The cells were incubated for three days before being fixed for ICC or collected for analysis by western blot or quantitative PCR (Q-PCR).

HEPDCs cultured with SB generally appeared epithelial when examined by brightfield microscopy (**Figure 3.4 A**) whereas untreated cells had begun to undergo spontaneous EMT adopting mesenchymal morphology (**Figure 3.4 B**). TGFβ had induced culture wide EMT and hEPDCs were distinctly mesenchymal in appearance (**Figure 3.4 C**). This observation was validated with phalloidin staining: SB treated cells remained flat and polygonal with cortical actin (**Figure 3.4 D**), untreated cells had begun to develop stress fibres across the cell body (**Figure 3.4 E**) and TGFβ induced dense stress fibre formation (**Figure 3.4 F**). Interestingly all three hEPDC cultures expressed the epicardial marker GATA5 (**Figure 3.4 D–F**) indicating that although stress fibre formation suggested EMT in both untreated and TGFβ treated hEPDCs, the cells maintained an epicardial phenotype. β-CATENIN staining was clearly seen in cobble cultures particularly at the cell membrane (**Figure 3.4 G**); this was greatly reduced in untreated cultures although some could be seen at the membrane at points of cell-cell contact (**Figure 3.4 H**, arrowhead). Sporadic cytoplasmic β-CATENIN was seen in TGFβ treated cells: this relocalisation of β-CATENIN from the membrane indicated breakdown of the adherens junctions, a crucial stage in the progression of EMT (**Figure 3.4 I**).

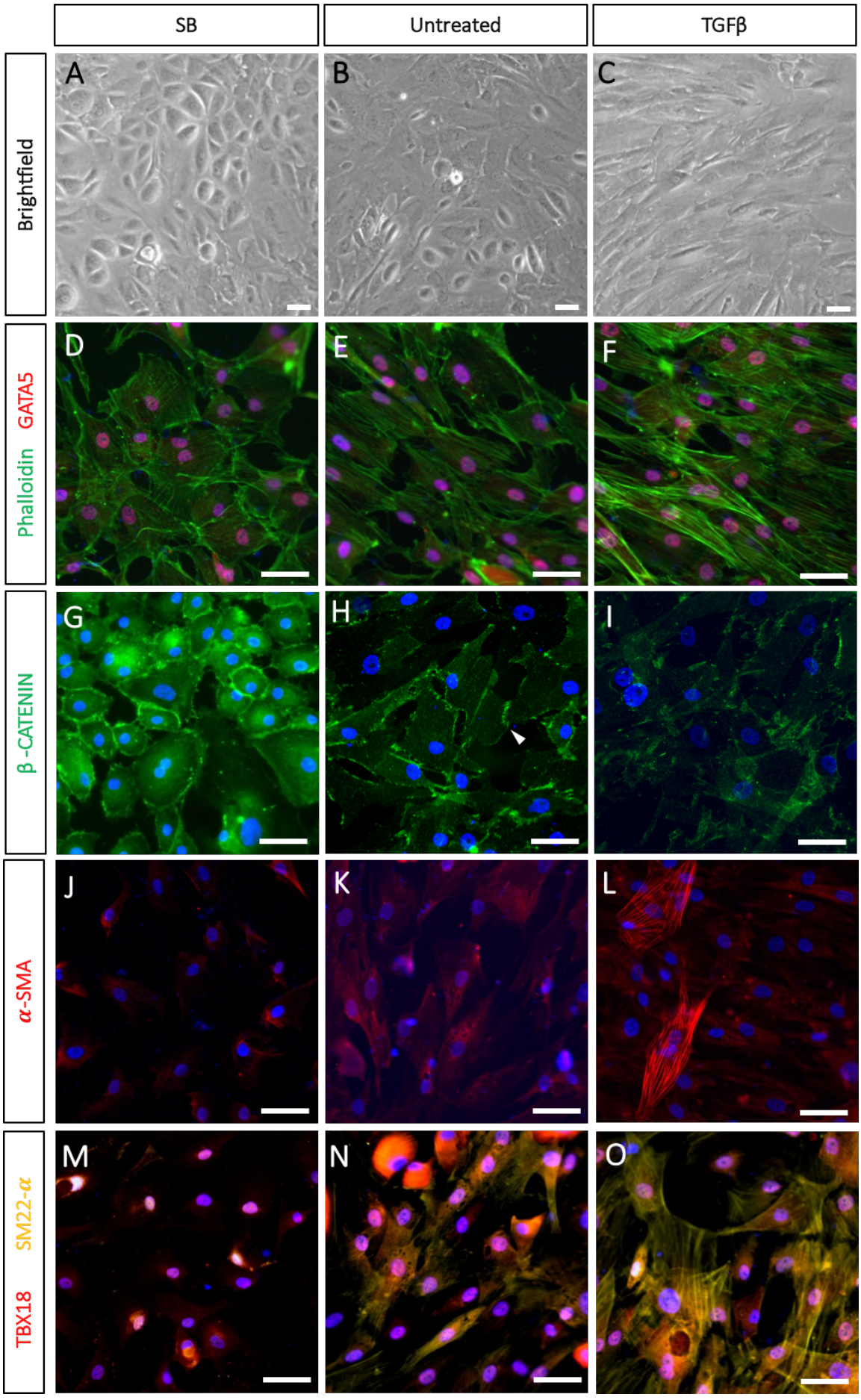

SB
Untreated
TGFβ
Brightfield
Phalloidin GATA5
β-CATENIN
α-SMA
TBX18 SM22-α
A
B
C
D
E
F
G
H
I
J
K
L
M
N
O

Figure 3.4 HEPDCs undergo EMT and differentiate in response to TGFβ treatment. (**A–C**) HEPDCs cultured with SB appeared epithelial when examined by brightfield microscopy. Untreated cells had begun to undergo spontaneous EMT and TGFβ induced culture wide EMT. (**D–F**) Phalloidin staining revealed SB treated cells remained polygonal with cortical actin, untreated cells had developed spindle morphology and begun to form stress fibres. TBFβ induced formation of dense stress fibres. All hEPDCs expressed the epicardial marker GATA5 irrespective of their treatment, indicating that both untreated and TGFβ treated cells retained an epicardial phenotype. (**G–H**) Membrane bound β-CATENIN was observed in SB treated cultures; this was mostly lost in both untreated and TGFβ treated cultures although it could be seen in some untreated cells at points of cell-cell contact (arrowhead). (**J–O**) SB treated cells did not express α-SMA or SM22-α. There appeared to be some expression in untreated cells however there were patches of α-SMA+ and SM22-α+ cells with defined striations in TGFβ treated cultures. All hEPDCs expressed the epicardial marker TBX18 again indicating that both untreated and TGFβ treated cells maintained an epicardial phenotype. All scale bars 50 μm.

SB treated cells did not express the EMT marker alpha smooth muscle actin (α-SMA, gene *Acta2*) (**Figure 3.4 J**), whereas a subset of α-SMA+ cells was identified in untreated and TGFβ treated cultures (**Figure 3.4 K** and **L**). α-SMA is an actin isoform found in vascular smooth muscle cells: *de novo* expression is associated with the development of contractile machinery and is commonly observed in cells undergoing EMT (Hinz et al., 2001; Sebe et al., 2008). The same pattern of expression was seen with Smooth Muscle Protein 22-Alpha (SM22-α, gene *TAGLN*), another protein associated with contractile machinery widely accepted to be smooth muscle specific (Lees-Miller et al., 1987; Li et al., 1996). Untreated cells did not express SM22-α (**Figure 3.4 M**); it was weakly expressed in untreated cultures (**Figure 3.4 N**) and defined striations had formed in response to TGFβ treatment (**Figure 3.4 O**). The formation of both α-SMA and SM22-α filaments in response to TGFβ treatment confirmed its ability to stimulate both epicardial EMT and differentiation toward a smooth muscle fate *in vitro*. It also confirmed the observation that inhibition of ALK5 by SB helps to preserve epithelial morphology by preventing spontaneous EMT. As had been observed with GATA5, all hEPDCs continued to express nuclear TBX18 (**Figure 3.4 M–O**) demonstrating that the cells had not fully differentiated away from their epicardial origin.

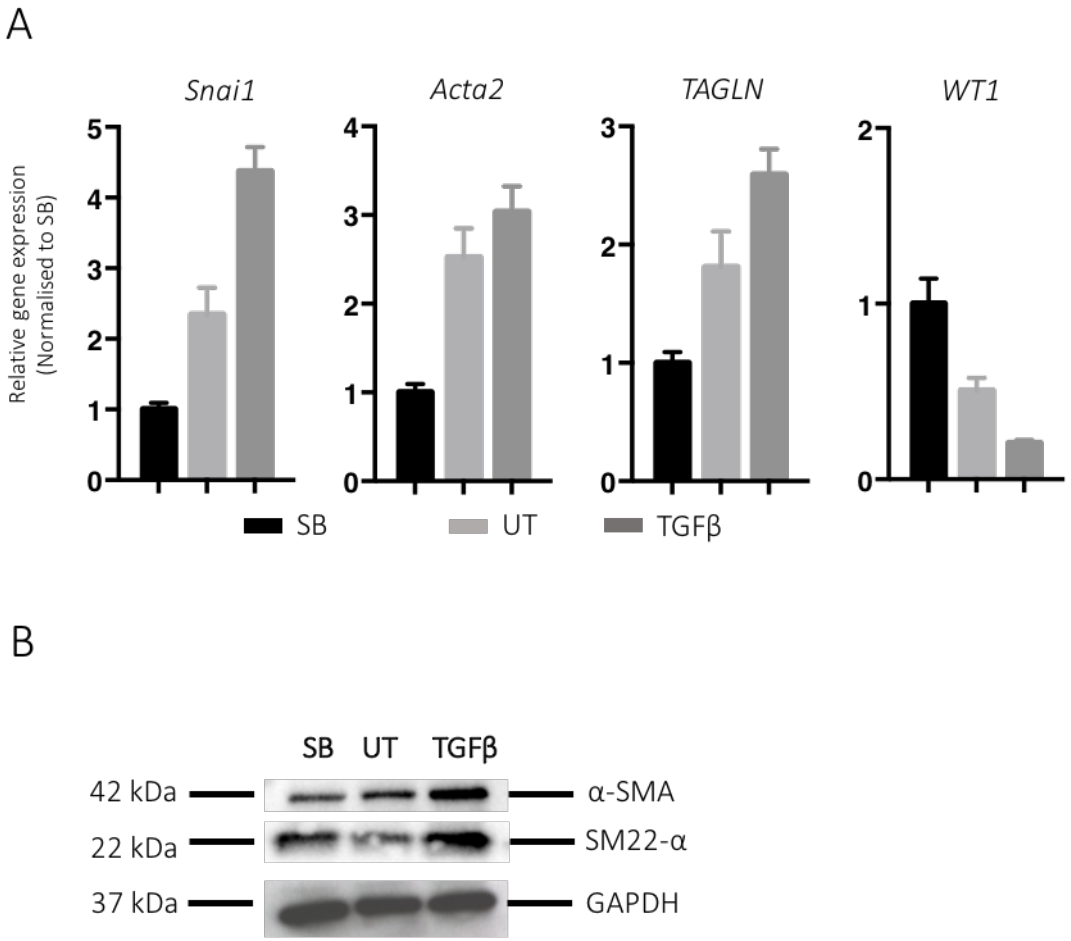


Figure 3.5 HEPDC EMT is confirmed by Q-PCR and western blot. (**A**) Increased expression of *Snai1*, *Acta2* and *TAGLN* confirmed spontaneous EMT in untreated cells relative to SB cultures. TGFβ increased levels of all three transcripts to a greater extent, confirming induction of EMT. There appeared to be in inverse correlation between induction of EMT and *WT1* expression possibly indicating differentiation away from the epicardial phenotype. (**B**) Increased expression of α-SMA and SM22-α was verified by western blot. In Q-PCR experiments n = 2 due to there being limited cells available for analysis from this sample batch, and difficulties in getting access to more tissue samples. Error bars reflect SEM. The experiment was conducted with hEPDCs derived from a single patient.

To further characterise the EMT model, samples of SB, untreated and TGFβ treated cells were analysed by Q-PCR and western blot. An increase in the EMT related transcription factor *Snai1* was seen in both untreated and TGFβ treated hEPDCs relative to SB cultures, by 2.3 and 4.2 fold respectively. This again confirmed the observation that inhibition of ALK5 kinase prevents hEPDC spontaneous EMT, and that TGFβ drives the transition (**Figure 3.5 A**). *Acta2* was upregulated in both untreated and TGFβ treated cultures relative to SB, as was *TAGLN,* further

corroborating ICC data (**Figure 3.5 A**). Interestingly, there appeared to be an inverse correlation between induction of EMT and expression of the epicardium marker *WT1*; this may reflect differentiation of hEPDCs away from an epicardial phenotype. Increased expression of α-SMA and SM22-α was verified by western blot (**Figure 3.5 B**).

3.1.4 Dynamic nuclear WT1 distribution

Whilst characterising hEPDC EMT a striking observation was made: nuclear distribution of the transcription factor WT1 appeared to vary depending upon hEPDC phenotype. In SB treated 'cobblestone' cells WT1 distribution was diffuse and filled the nucleus in a homogeneous manner (**Figure 3.6 A**, magnified in **B**). In contrast, both spontaneous and TGFβ induced EMT was associated with punctate WT1 staining, which appeared to be localised to several subnuclear compartments (**Figure 3.6 C** and **E,** magnified in **D** and **F.** Punctate staining highlighted by arrowheads in **D** and **F**). If WT1 localisation is dynamically associated with the progression of EMT, tracking its distribution might provide a quantitative and time dependant measure of hEPDC phenotypic change.

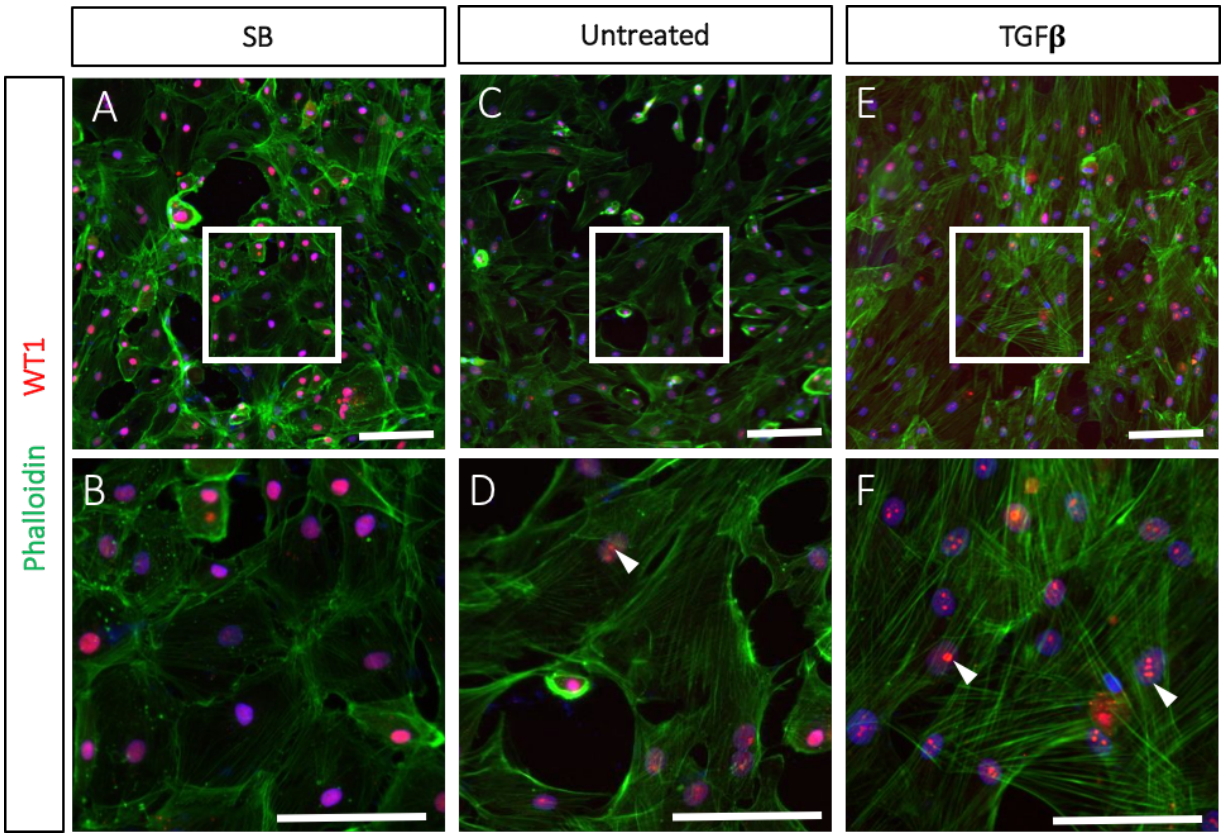


Figure 3.6 Dynamic nuclear distribution of WT1. (**A–B**) In SB treated cells WT1 distribution was diffuse and homogenous across the nucleus. (**C–F**) Both spontaneous and TGFβ induced EMT were associated with punctate WT1 localisation (arrowheads). White boxes in **A**, **C** and **E** are magnified in **B**, **D** and **E**. All scale bars 50 μm.

In 2006 Dutton *et al*. demonstrated the dynamic nature of WT1 patterning whilst investigating subnuclear location of two mammalian isoforms (Dutton et al., 2006). Variable splicing of exon 9 can result in a 9 base pair extension coding for lysine, threonine and serine (KTS) generating the WT1+KTS and WT1-KTS isoforms. WT1-KTS acts as transcription factor, directly binding to DNA and co-localising with other transcription factors (Hohenstein and Hastie, 2006). The WT1+KTS isoform is thought to bind to mRNA and may play a role in mRNA processing. In their study Dutton *et al.* transfected Cos7 cells with vectors encoding GFP tagged WT1-KTS or WT1+KTS isoforms; nuclear distribution was highly dynamic and both isoforms switched between 'diffuse' or 'discrete' patterning. WT1-KTS nuclear distribution was either diffuse; pertaining to even distribution of the protein across the nucleus with equal intensity; or had discrete staining of multiple irregular foci. WT1+KTS on the other hand was either seen

diffusely spread throughout the nucleus or as discrete patches of intense, punctate staining. The punctate pattern was found to be a result of accumulation of the +KTS isoform in the nucleolus, confirmed by co-localisation with the known nucleolar protein Ki67 (Dutton et al., 2006). When both WT1+KTS and WT1-KTS were transiently expressed in the same cells, a small number retained isoform specific distribution; however, most nuclei showed dispersed, complex WT1 staining with co-localisation of the two isoforms. Interestingly, treatment of these cells with actinomycin-D, an inhibitor of RNA synthesis that renders the cells transcriptionally inactive (Huang et al., 2000), resulted in separation of the two proteins: each reverted back to its previously described, isoform specific, nuclear patterning (Dutton et al., 2006).

3.1.5 Punctate WT1 is localised to the nucleolus in hEPDCs

To investigate whether the observed punctate WT1 patterning reflected its association with the nucleolus TGFβ treated hEPDCs were co-stained with WT1 and Ki67. Co-localisation of the two proteins was seen in Ki67+ hEPDCs (**Figure 3.7 A** and **B**). The Ki67 protein is most commonly used as a proliferation marker as is it only expressed during active phases of the cell cycle (Winking et al., 2004); its spatial and temporal patterning is highly dynamic and associated with several nuclear domains, including the nucleolus, which vary depending upon the stage of cell cycle (Schmidt et al., 2003). Therefore, to further support the observation that WT1 was associating with the nucleolus, TGFβ treated cells were stained for WT1 and the nucleolus marker NUCLEOLIN (**Figure 3.7 C**). Once again co-localisation of the two proteins was observed, corroborating the Ki67 data and confirming that in hEPDCs WT1 becomes associated the nucleolus during the process of EMT.

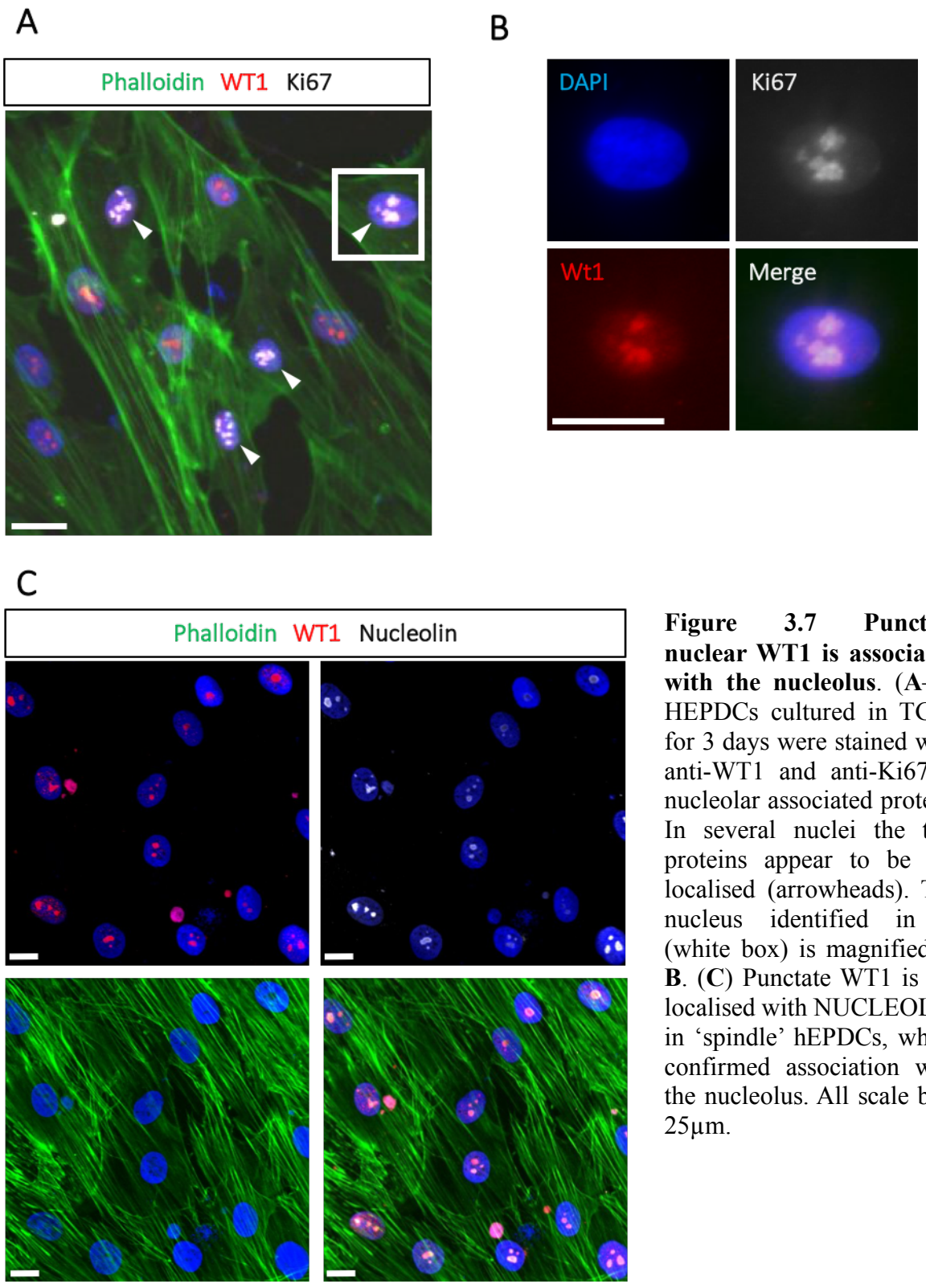


Figure 3.7 Punctate nuclear WT1 is associated with the nucleolus. (**A–B**) HEPDCs cultured in TGFβ for 3 days were stained with anti-WT1 and anti-Ki67, a nucleolar associated protein. In several nuclei the two proteins appear to be co-localised (arrowheads). The nucleus identified in **A** (white box) is magnified in **B**. (**C**) Punctate WT1 is co-localised with NUCLEOLIN in 'spindle' hEPDCs, which confirmed association with the nucleolus. All scale bars 25µm.

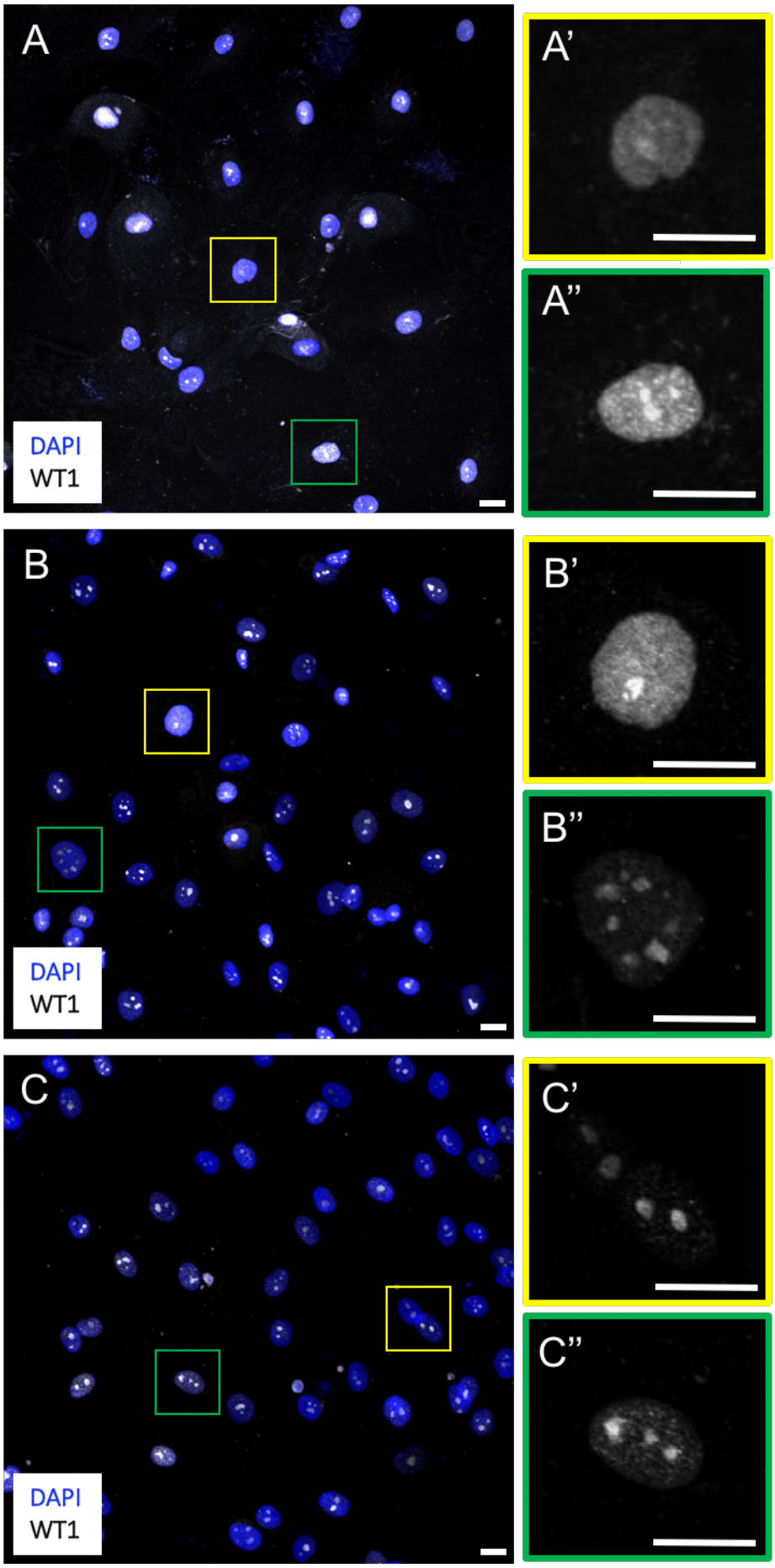


Figure 3.8 Dynamic WT1 localisation is observed in a second hEPDC EMT experiment. (**A**) In SB treated 'cobblestone' cells WT1 tended to be distributed throughout the whole nucleus. (**A'** and **A"**) WT1 was dispersed in a complex manner both at a number of intense foci throughout the nucleoplasm and also at the nucleolus. (**B**) In untreated hEPDCs WT1 signal is localised to the nucleolus. (**B'** and **B"**) Some nuclei retained complex patterning but a greater number exhibited punctate WT1 only. (**C**) In TGFβ treated cells WT1 was almost universally located at the nucleolus. All scale bars 25µm.

To assess whether this was a reproducible response the EMT experiment was repeated with a separate batch of hEPDCs and nuclear distribution of WT1 was examined using confocal microscopy. Once again in SB treated 'cobblestone' cells WT1 tended to be distributed throughout the whole nucleus (**Figure 3.8 A**). WT1 was dispersed in a complex manner both at a number of intense foci throughout the nucleoplasm and also at the nucleolus (**Figure 3.8 A'** and **A''**) reminiscent of the mixed isoform distribution described by Dutton *et al*. (Dutton et al., 2006). In untreated hEPDCs WT1 signal was localised to the nucleolus (**Figure 3.8 B**). Although some nuclei retained the complex patterning (**Figure 3.8 B'**) a greater number exhibited punctate WT1 only (**Figure 3.8 B''**). In TGFβ treated cells, as seen previously, WT1 was almost universally located at the nucleolus (**Figure 3.8 C** and **C'**); a few nuclei still had WT1 located at a number of small foci (**Figure 3.8 C''**).

This experiment replicated the previous observation that epithelial hEPDCs have diffuse nuclear distribution of WT1 that changes to a 'punctate' pattern as hEPDCs undergo TGFβ induced EMT; this relocalisation reflects association of WT1 with the nucleolus. An added point is that although diffuse WT1 nuclear distribution was seen across all nuclei in all SB treated cells in the first experiment; in the second experiment some SB treated nuclei had developed punctate WT1. These results probably reflect both experimental and biological variation in the hEPDC cultures, which were derived from different patient biopsies, and differences in the extent of spontaneous EMT that occurred before the experiment began.

3.2 Using hEPDCs for high throughput phenotypic screening

3.2.1 Analysis of the pilot screen data

As discussed previously, before the start of this project a pilot high throughput phenotypic screen was run by Dr Anke Smits in collaboration with the Target Discovery Institute, Oxford. HEPDCs were seeded in to 384-well plates for 48 hours before being treated with the Pharmakon1600 compound library at concentrations of 10, 2 and 0.4μM for 48 hours. The Pharmakon library is a collection of 1,600 known pharmacologically active drugs that have demonstrated activity against known targets, such as the kinases, proteases and G-protein coupled receptors (http://www.tdi.ox.ac.uk/small-compound-libraries). TGFβ and 0.5% DMSO were used as the positive and negative controls respectively: due to an error in the dilution the final concentration of TGFβ was 0.5 ng/mL rather than 2 ng/mL. The aim of the screen was to identify small molecule compounds that could 'activate' hEPDC EMT and differentiation: morphological changes induced by TGFβ would act as a surrogate read out for activation.

A

$$Z' = 1 - \frac{3(\sigma_p + \sigma_n)}{|\mu_p - \mu_n|}$$

σ = standard deviation
μ = mean

p = positive control
n = negative control

Z' factor	Assay quality
1	ideal
1< Z' > 0.5	excellent
0.5 > Z' > 0	marginal
0	poor

B

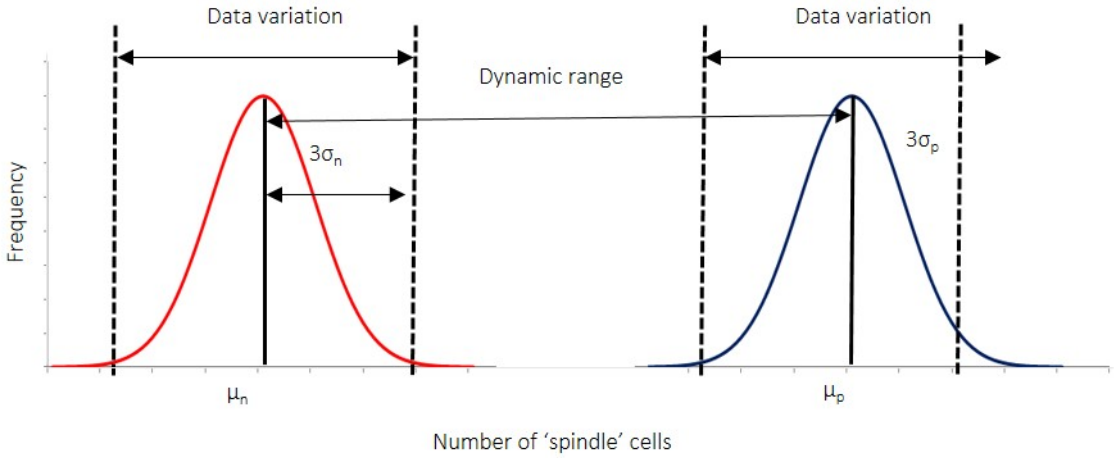


Figure 3.9 Calculating the Z-prime (Z') (**A**) The Z-prime (Z') is calculated using the average (μ) and standard deviation (σ) of both the positive (p) and negative (n) controls. A value of >0.5 is quoted for a robust assay. (**B**) Graphical representation of the Z', which compares the data variation within each control, with the dynamic range of the data set. Adapted from (Zhang et al., 1999).

After 48 hours the plates were fixed and stained with DAPI, phalloidin and cell mask plasma membrane stain. The cells were imaged using the Perkin Elmer Operetta High Content Imager (tdi.ox.ac.uk/high-content-imaging) and an analysis protocol was written to identify and quantify the percentage of cobble cells in each well; this was used to scan all of the images and generate a data set documenting the hEPDC morphology associated with each individual compound. The first step of the analysis was to calculate the Z-prime (Z') for the assay: a numerical evaluation that indicates whether there is sufficiently little overlap between distribution of the positive and negative control values for the rest of the assay data to be meaningful (Zhang et al., 1999). The Z' is calculated using the average (μ) and standard

deviation (σ) of both the positive (p) and negative (n) controls (**Figure 3.9 A**) and assumes a normal distribution of data. It compares the data variation within each control with the dynamic range: the difference between the average response of the positive and negative controls (**Figure 3.9 B**). A value of >0.5 is quoted for a robust assay. More careful interpretation of results is required for an assay with a lower Z', and this often necessitates an increased number of replicates (**Figure 3.9 A**). For this particular assay, a good Z' would correspond to there being more 'spindle' cells in the positive control than the negative control, but very little variation in cell morphology within each control population.

The pilot assay returned a Z' value of -0.295 when calculated using the percentage of spindle cells present in each control well. This low Z' value indicated that there was not enough difference in hEPDC phenotype between positive and negative control distributions which lead to a small dynamic range in the data. This was graphically represented by plotting the frequency distribution data of the number of spindle cells/well for the two control groups (**Figure 3.10 A**). In a robust assay the dynamic range of the data will be large and the variation within the two populations will be small in order to return a Z' as close to 1 as possible (**Figure 3.9**): this data illustrates that the two populations are beginning to overlap meaning the dynamic range of the data is insufficient. The high frequency of spindle cells in the negative control indicated that the hEPDCs had undergone spontaneous EMT, which had then lead to there being very little phenotypic difference between the two populations. This was confirmed by reviewing a set of images from the screen that demonstrated there to be very little difference in cell morphology between the different treatments (**Figure 3.10 B**)

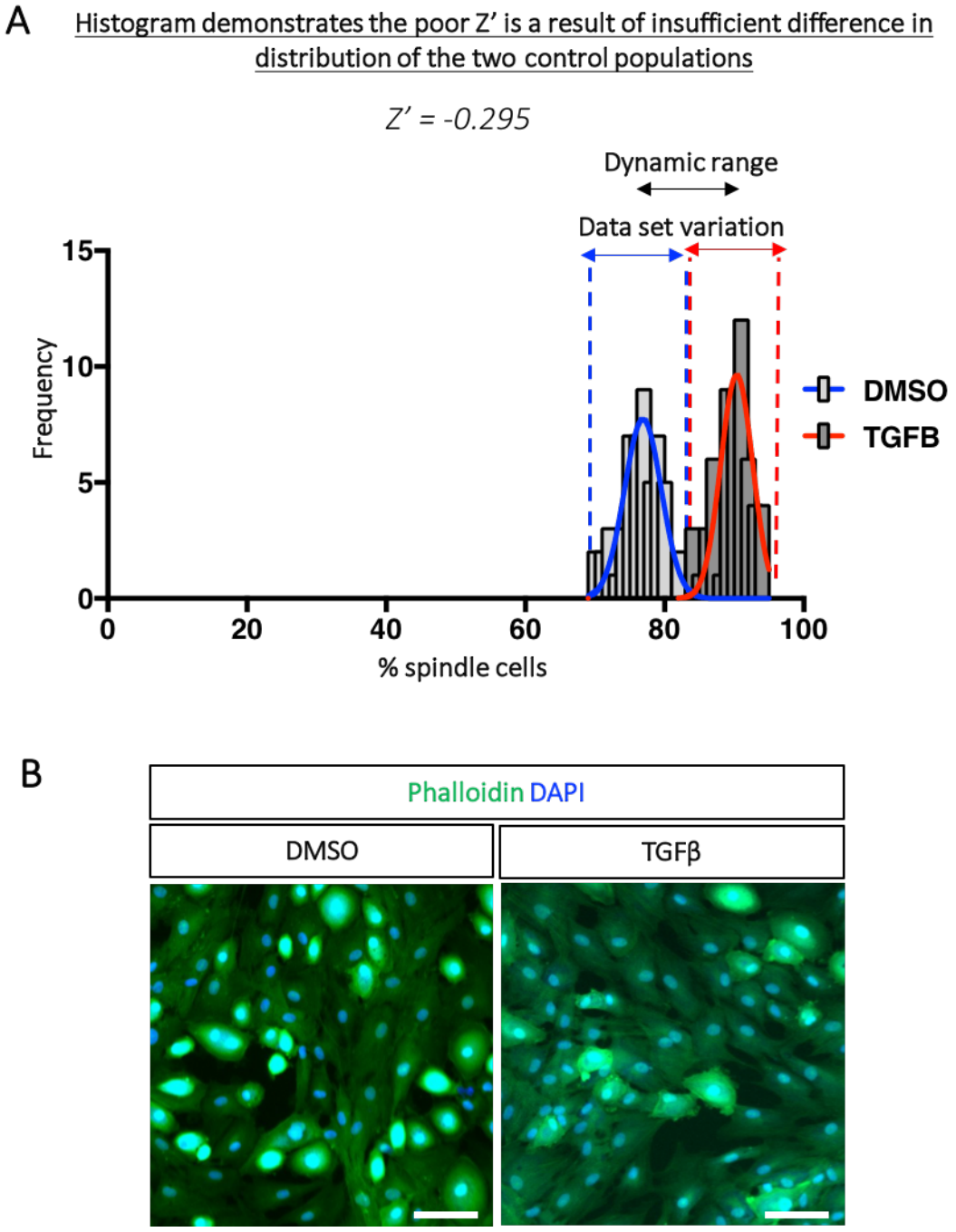
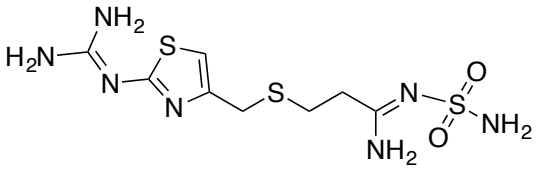
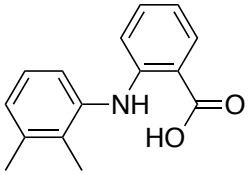
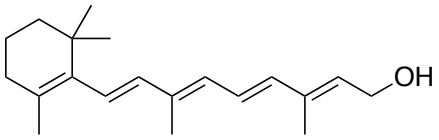
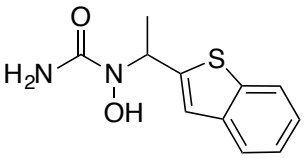
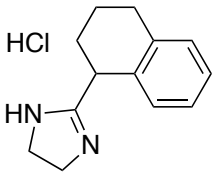
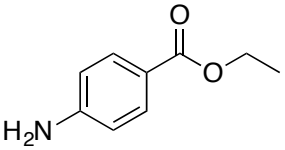


Figure 3.10 Histogram of HTPS control data and representative images from the controls. **(A)** Plotting control data from the pilot screen as a frequency histogram illustrates that a poor dynamic range (black arrow) between the two data sets has contributed to the return of a sub-optimal Z'. Ideally a robust assay has a large dynamic range and small data variation (data variation for DMSO illustrated with blue arrow, data variation for TGFβ illustrated with red arrow). (**B**) Images of the DMSO and TGFβ controls illustrate there to be minimal phenotypic difference between two conditions. Scale bars in **B** 50 µm.

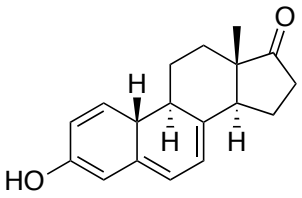
Despite the poor Z', there was an approximate 10% difference in the average percentage of spindle cells between the two controls, therefore the data was examined to see whether any putative hits could be derived, which could later be confirmed by additional assays. Each hEPDC treatment was ranked in order of its ability to induce spindle morphology in hEPDC cultures: the wells associated with the highest number of spindle hEPDCs had been treated with TGFβ (**Appendix Table A.3.1**); it was decided that a positive hit would constitute any compound that increased the number of 'spindle' cells above that of the DMSO controls. From the data, nine compounds were identified that appeared to induce hEPDC EMT. These were taken forward to be tested in a validation screen along with five extra compounds that either had the same target as an identified 'hit' or had been flagged as a negative 'hit' in the original screen. The full list of the 14 compounds selected for testing in the validation screen are listed in **Table 3.1** alongside details of their MOA.

Table 3.1 Putative hits from the pilot HTPS and extra compounds for the validation screen. Hits from the pilot HTPS and the additional compounds chosen for inclusion in the validation screen are listed along with their chemical structures and mechanisms of action (MOA). Drug indication and MOAs were taken from DrugBank (http://www.drugbank.ca/drugs/DB00812)

Compound and MOA	Structure
Famotidine Identified as the top hit from the HTPS. Famotidine is a competitive histamine H2-receptor antagonist. Used in the clinic for the treatment of gastrointestinal disorders.	
Mefenamic acid Identified as a hit from the HTPS. Mefenamic acid is a non-steroidal anti-inflammatory agent that inhibits prostaglandin synthesis. Used in the clinic to mediate pain in auto-immune diseases.	
Retinol Also known as vitamin A. Identified as a hit from the HTPS. Numerous essential roles in the body including controlling metabolic function in the retina, and binding to retinoid receptors that control epithelial migration and differentiation.	
Zileuton Identified as a hit from the HTPS. Inhibitor of the 5-lipoxygenase enzyme that catalyses the formation of leukotrienes from arachidonic acid. Leukotrienes are associated with the pathogenesis of asthma: Zileuton is prescribed to reduce symptoms.	
Tetryzoline Identified as a hit from the HTPS. Tetryzoline is an alpha-adrenergic agonist and constricts blood vessels. Used to treat eye redness.	
Benzocaine Identified as a hit from the HTPS. Benzocaine is a voltage dependent sodium channel blocker that prevents conduction of nerve impulses. Used as an anaesthetic and for pain relief.	

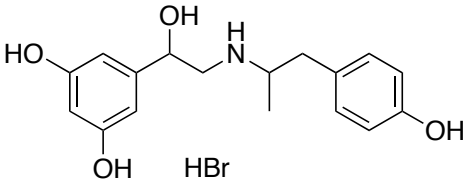
Equilin

Identified as a hit in the HTPS. Equilin is a horse estrogen and is widely used in hormone replacement therapy.



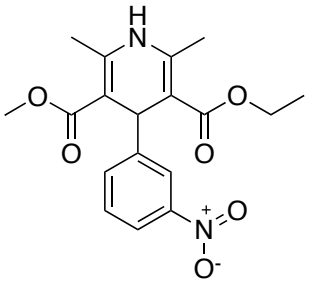
Fenoterol Hydrobromide

Identified as hit from the HTPS. A Beta(2)-receptor agonist used in the clinic to treat bronchoconstriction.



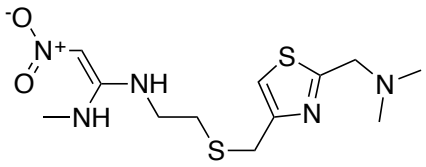
Nitrendipine

Identified as hit from HTPS. Calcium channel blocker that is used to treat vasoconstriction.



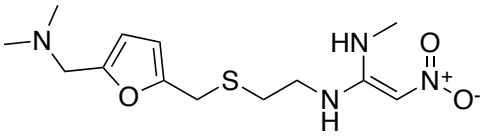
Nizatidine

Nizatidine has the same MOA as famotidine but was not identified as a hit. This was included in the validation screen for comparison.



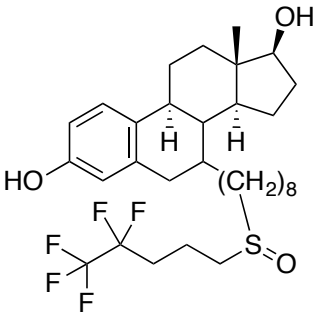
Ranitidine

Also the same MOA as Famotidine. Ranked as a 'negative' hit in the HTPS. Included in the validation HTPS for comparison.



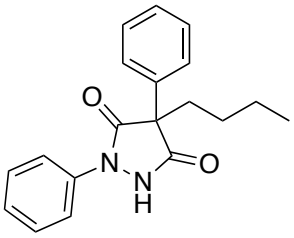
Fulvestrant

An anti-estrogen compound that was not identified as a hit in the original HTPS. Was included in the validation screen for comparison with Equilin



Phenyl Butazone

Same MOA as Mefenamic acid but not identified as a hit in the original HTPS. Was included in the validation screen for comparison.



3.2.2 HEPDC validation screen

The validation screen protocol was identical to that of the pilot screen; hEPDCs were treated with the 14 selected compounds (**Table 3.1**), in triplicate. In the pilot screen the Pharmakon1600 library had been screened at 10, 2 and 0.4 μM: no effects had been observed at the latter two. Therefore, for the validation screen the compounds were tested at concentrations of 5, 10 and 15 μM to investigate whether a dose response was observed. Analysing the data set with the old analysis protocol did not produce any coherent data. However, after examining the images, it was clear that the morphological changes induced by TGFβ treatment were much more defined then they had been in the pilot experiment. TGFβ treated hEPDCs were larger than the untreated controls and had developed stress fibres (**Figure 3.11 A** and **B**), a biological hallmark of EMT that had also been observed during hEPDC model characterisation (**Chapter 3.2**). Due to there being few observable differences between the positive and negative controls in the pilot screen, the original analysis protocol had been written to identify cell type by the intensity of the DAPI, a nuclear stain that binds A–T rich regions of DNA, which was seen to be greater in cobble cells. However, as the validation assay demonstrated biologically relevant hallmarks of EMT a new analysis was written that measured these features.

The images were first loaded in to the Perkin Elmer Operetta High Content Imaging System (tdi.ox.ac.uk/high-content-imaging). Using the DAPI channel the analysis protocol was first instructed to identify the nuclei in each image; then the cell mask plasma membrane stain was used to determine the area of the cytoplasm for each individual cell. The software was then instructed to assess a number of textural and morphological features from the phalloidin stain such as the presence of stress fibres.

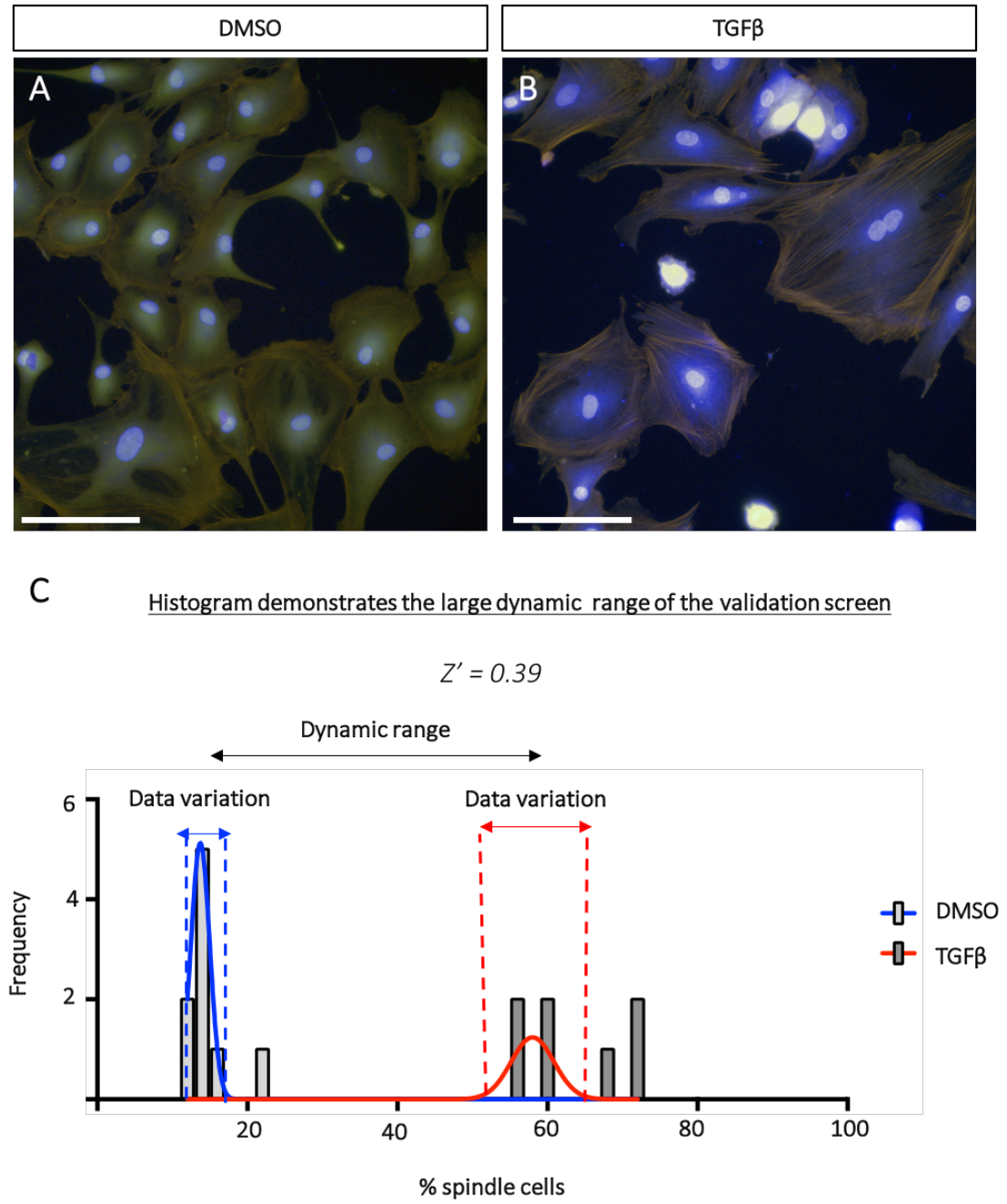


Figure 3.11 Validation screen produced improved Z' (**A**–**B**) Distinct morphological differences were observed between DMSO and TGFβ treated controls in the validation screen. (**C**) Histogram representing frequency of spindle cells in each control population illustrates the large dynamic range which resulted in an improved Z' of 0.39. Scale bars in **A** 50 µm.

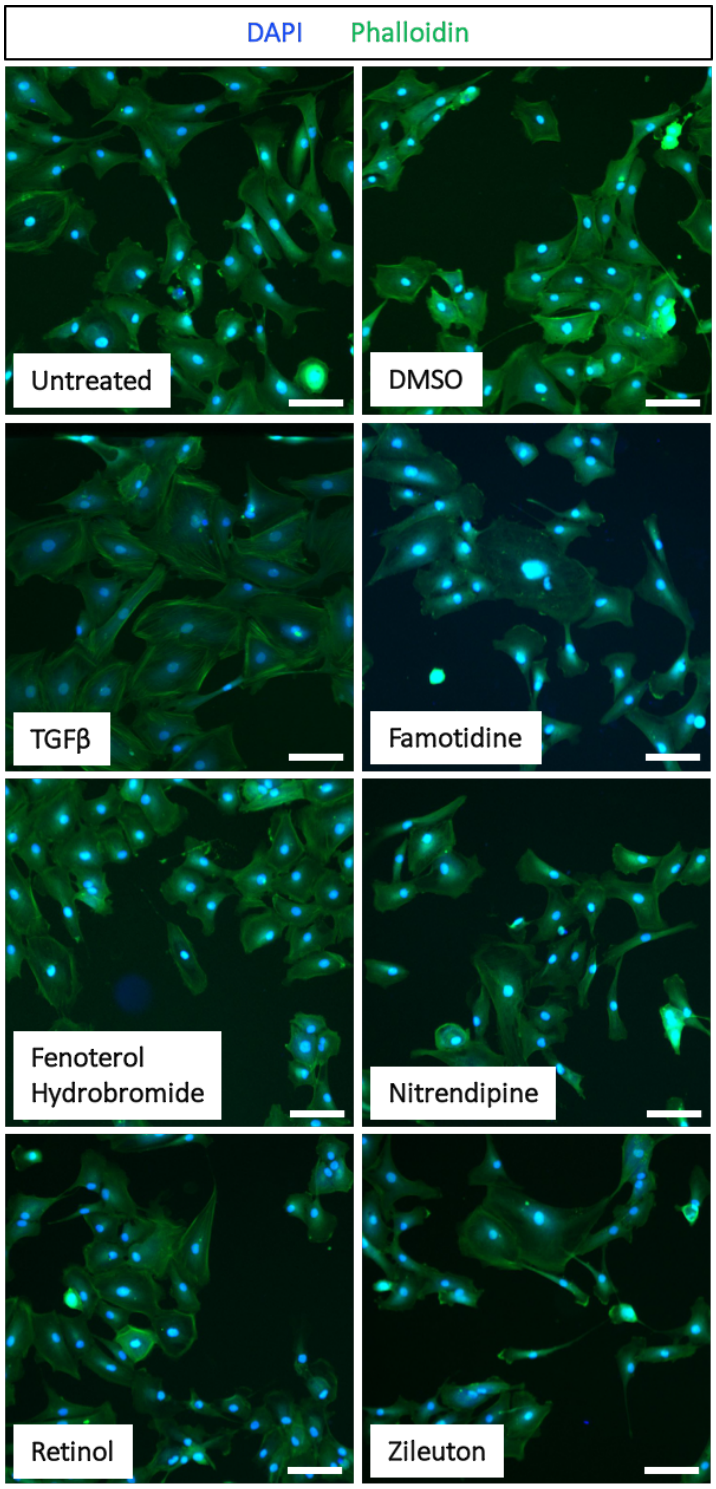


Figure 3.12 Representative images from validation screen. Images from the validation screen confirm induction of EMT in TGFβ treated cells compared with the untreated and DMSO controls. In representative images of hEPDCs treated with the 'hit' compounds hEPDCs do not appear to have undergone EMT. Scale bar 50 μm.

After the protocol had been written, cells that were good examples of 'cobblestone' and 'spindle' were manually selected so that the program was able to 'learn' which features were associated with each of the cell types. It was then able to scan the rest of the images and assign each cell as 'cobblestone' or 'spindle' (Screen shots documenting the analysis protocol are in the **Appendix, Figure A.3.1**). The resulting Z' for the validation screen was 0.39, a vast improvement upon the previous experiment. Due to there being far less replicates than there had been in the pilot screen, the histogram for each control is not normally distributed; however, what can be seen is that the dynamic range was much larger for this experiment and the control populations do not overlap (**Figure 3.11 C**). Unfortunately, despite improvements in the Z', after the operetta had analysed the images from the rest of the test wells it became apparent that none of the other compounds tested had induced a significant switch in cell morphology away from that of the untreated control; this was confirmed by reviewing the images from the screen (**Figure 3.12**).

3.3 Summary and discussion

3.3.1 Establishing hEPDC cultures and modelling EMT

This series of experiments demonstrated that cultures of hEPDCs can be derived from RAA epicardium explants. Explant cultures are highly variable: sometimes EPDCs migrate from explants with 'cobblestone' epithelial morphology; however, sometimes cells have already undergone an EMT and 'spindle' cultures are formed. In both cases hEPDCs stain positive for epicardial markers including WT1; however, for these studies, only cultures with epithelial morphology could be of use.

Next, hEPDC EMT was characterised *in vitro*. EMT was induced by treatment of cells with 2 ng/mL of TGFβ for three days, as confirmed by upregulation of genes associated with EMT and

differentiation by ICC, Q-PCR and western blot. This validated the continued use of TGFβ as a positive control in screening experiments. It also found that hEPDC cultures could be, to a degree, prevented from undergoing spontaneous EMT by treatment with 10μM of the ALK5 inhibitor SB-435142. These characterisation experiments (**Figures 3.4–3.6**) were conducted in hEPDCs established from a single RAA biopsy. Unfortunately, no statistics could be determined for the Q-PCR data as there were not sufficient cells; prior to the experiment the culture could not be expanded any further as patches of cells were beginning to undergo spontaneous EMT. Ideally a series of experiments would have been undertaken using a number of cultures isolated from different patients and the results compared/combined to better gauge sample variation and differential response. However, this was not possible due to consistent problems accessing a consistent supply of RAA samples: this will be discussed in detail later in this chapter.

3.3.2 Dynamic WT1 nuclear distribution

Characterisation of hEPDCs revealed that nuclear distribution of WT1 in hEPDC cultures is highly dynamic and its distribution appears to be correlated with EMT. In SB treated 'cobblestone' cultures WT1 tended to be diffusely spread throughout the nuclei. Spontaneous EMT and differentiation in untreated cultures was correlated with a mixture of diffuse and punctate WT1; in TGFβ treated cultures WT1 is universally punctate. By co-staining 'spindle' hEPDCs with WT1 and one of the two nucleolar markers Ki67 or NUCLEOLIN, it was shown that punctate patterning reflects association of WT1 with the nucleolus. For some time, it has been recognised that nuclear compartmentalisation of proteins is an important mechanism for regulating their function (Carmo-Fonseca, 2002). In particular the nucleolar sequestration of transcription factors, which restricts access to target genes, has been shown to repress activity. For example the initiation of trophoblast stem cell differentiation by the basic helix-loop-helix (bHLH) transcription factor heart and neural crest derivatives-expressed protein 1 (HAND1) is

inhibited by its sequestration in the nucleolus (Martindill et al., 2007) and the activity of the tumour suppressor gene p53 is controlled by localisation of its negative regulator to the nucleolus (Weber et al., 2000).

The WT1 protein has two major isoforms in humans: the WT1-KTS isoform acts as a transcription factor; it is known to upregulate *Snai1* and suppress the *Cdh1* promoter leading to EPDC EMT and migration in development (Martínez-Estrada et al., 2010). The +KTS isoform on the other hand has a limited role in transcription and instead is proposed to be involved with mRNA processing. The antibody used in these studies did not differentiate between the two KTS isoforms; however, the work of Dutton *et al.* suggests that this diffuse, nuclear wide staining may represent a mixture of both the WT1+KTS and WT1-KTS proteins. Their work, and the work of others, documented association of the +KTS, but not -KTS, isoform with the nucleolus, therefore, it could be the case that the punctate staining is representative of the non-transcriptionally active WT1+KTS isoform (Dutton et al., 2006).

Irrespective of whether the observed nucleolar sequestration is isoform specific or not, it points to suppression of WT1 transcriptional activity in hEPDCs that have undergone EMT. This observation appears counterintuitive due to the reported essential role of WT1 in epicardial EMT; however, the following reasoning is postulated: *in vivo* the adult epicardium is quiescent and does not express WT1; however, both ‘cobblestone’ and ‘spindle’ hEPDC explant cultures are WT1+. Thus it may be that in order for hEPDCs to migrate from the explants an activation event occurs that brings the epicardial cells out of their quiescent state. This activation includes re-expression of both WT1 isoforms that are seen in a complex pattern throughout the nucleoplasm. After cells have undergone EMT, either spontaneously or in response to TGFβ treatment, WT1 is localised to the nucleolus: whether this is the +KTS isoform or a mixture of

both it suggests that WT1 is no longer transcriptionally active. The WT1-KTS isoform is known to be essential for maintaining the undifferentiated state of progenitors in the heart during development (Hohenstein and Hastie, 2006) as well as for inducing the EMT; however, perhaps after the transition has been initiated transcriptional activity is no longer required and expression is decreased or the protein is 'inactivated' by translocation to the nucleolus.

In the absence of more RAA samples from which to derive new hEPDC cultures, discussed in details later in this chapter, deciphering the meaning behind the variable WT1 distribution has not been possible. Although our data suggests that the re-localisation is related to epicardial EMT, further experiments are required to determine how the events associate with one another. The experiments described reflect only a single time point: with access to more hEPDCs it would be imperative to investigate WT1 distribution over a time course so that the dynamic nature of WT1 distribution could be better understood. Furthermore, the Q-PCR data suggested that WT1 expression was decreased in untreated and TGFβ treated cells compared with the SB controls. Therefore, by extending the time window of the EMT experiment it would be possible to determine whether this is a permanent or transient response and quantify WT1 expression by ICC, Q-PCR and western blot. Finally, isoform specific WT1 antibodies or isoform specific Q-PCR primers could be used to confirm whether the distinct nuclear patterns do indeed reflect the different KTS isoforms.

3.3.3 High throughput phenotypic screening

Prior to the start of this project a pilot HTPS was run in collaboration with the Target Discovery Institute on hEPDCs using the Pharmakon1600 compound library. The aim was to identify small molecules that could activate the human adult epicardium: hEPDC EMT was to be used as a surrogate read out for activation. Analysis of the data from the pilot screen revealed that the

original experimental conditions had been suboptimal. The returned Z' of -0.295 indicated that there were not sufficient differences in hEPDC morphology between the 'cobblestone' DMSO and 'spindle' TGFβ treated controls and suggested that the hEPDCs had already undergone spontaneous EMT. Therefore, it was not possible to identify compounds that induced EMT purely by assessing their effect upon cell morphology. Despite the poor Z', it was decided that a series of 14 compounds that appeared to induce hEPDC morphological switch to a greater extent than the DMSO controls would be re-tested.

The validation screen was run with an identical protocol to the pilot HTPS. When examining the images at the end of the experiment it was evident that, unlike the pilot screen, TGFβ treated cells were markedly different to the DMSO controls and had formed distinct stress fibres, indicative of EMT. Therefore, a new analysis protocol was written that recognised the characteristics of EMT and then assessed whether any of the compounds had also induced this transition. The Z' returned from the validation screen was 0.39, a huge improvement upon that of the pilot screen. Unfortunately, none of the compounds identified from the pilot screen were found to induce EMT in hEDPCs in a manner similar to that of TGFβ in the validation experiment. Despite failing to provide any hits to take forward, the quality of the assay had been improved with the development of a new analysis sequence, as demonstrated by the higher Z'. This experiment demonstrated that it is possible to design a rigorous analysis protocol to identify hEPDC EMT based only upon biologically relevant morphological descriptors, so long as the starting population of cells are still epithelial and have not significantly undergone spontaneous EMT. In the pilot screen, a 1600 compound library was tested in triplicate: this required the generation of $9x10^6$ cells from a single biopsy sample. This equates to enough cells to cover 375 cm^2, which is a huge number considering that initial explant cultures generally yield a maximum of 20 cm^2 of cobble cells before the first passage. Generating sufficient cells required five

passages at a ratio of 1:2 which is highly problematic as hEPDC explant cultures are highly variable and prone to spontaneous EMT. Therefore, the starting population of the experiment was unlikely to have been entirely epithelial in morphology which would explain the poor Z' and apparent false hits. The preliminary HTS demonstrated the importance of having a robust experiment and analysis design as well as the limitations of pursuing experiments of this type under suboptimal conditions. Had the opportunity arisen, the improved analysis protocol would have been employed for any subsequent screens conducted in hEPDCs and efforts made to further improve upon the Z'.

3.3.4 Access to RAA biopsy samples

Continued efforts to characterise EMT in hEPDC cultures, as well as the opportunity to use the new analysis protocol to repeat the Pharmakon1600 screen or to screen other compound libraries, relied upon access to RAA samples from which explant cultures could be established. Shortly after the validation screen a series of problems were encountered with samples from our original source: The Hatter Cardiovascular Institute, London. Sample supply was always infrequent, averaging out to about one a month over the course of the first year which was not a sufficient supply to undertake all the experiments described. Despite the presence of antibacterial agents in the hEPDC media used for storage and transport and the use of sterile techniques for the isolation protocol, a number of RAA biopsies delivered for explant culture were contaminated; 2–3 days after plating the explants the culture medium was cloudy indicating presence of a bacterial or fungal infection. In these circumstances the cultures had to be thrown away. As previously discussed, the sample variability meant that often hEPDCs would migrate out of explants having already undergone EMT; these cells also could not be used in experiments. Furthermore, Dr Abdul Malik, the PhD student who supplied RAA samples, finished his degree meaning there was no longer anyone available to recruit patients.

Subsequently, investigation into the availability of tissue from Oxford hospitals was explored. The lab of Professor Charalambos Antoniades were able to supply some RAA biopsies. however, the supply of biopsies from Oxford was also very infrequent and, unlike samples from London, the tissue samples available were very small. This was problematic again due to sample variability and only three viable epithelial hEPDC cultures from the Oxford samples were established from >15 samples collections. It was not possible to expand these cultures to generate epithelial cells suitable for further high throughput experiments due to the small initial yield of cells and the large number of passages required. Due to limited access to primary human tissue and the numerous problems experienced during isolation and culture of hEPDCs, it was decided that an alternative cell line would be investigated with the hope of providing a complementary model in which to study EPDC activation *in vitro* which is described in **Chapters 3** and **4**.

3.3.5 Future work

The failure of the 'hit' compounds to repeat in the validation assay illustrated an important caveat of performing experiments in primary hEPDCs. The dynamic nature of hEPDC cultures and their tendency to undergo spontaneous EMT was problematic both for characterisation and screening experiments particularly because the supply of tissue was infrequent and the biopsy samples tended to be very small. Further development of this work is dependent upon acquiring a consistent supply of human tissue. For future screening experiments, dividing the compound libraries into smaller sub-libraries could would been a good way to minimise the number of cells needed from each explant and increase the likelihood of generating an epithelial hEPDC starting population. This approach could be used to repeat the Pharmakon1600 library screen, or used to screen any number of other compound or fragment libraries.

When a patient undergoes a MI, the ventricle is the site of ischemic injury. Recently a study from the Riley lab demonstrated distinct differences in the behaviour and contribution of the atrial and ventricular epicardium to the developing human heart (Risebro et al., 2015). WT1+ epicardium over the atria formed a single layer structure, whereas over the ventricle a multilayer WT1+ structure was formed that also expressed the EMT markers ZEB1 and VIMENTIN. *Ex vivo*, ventricular but not atrial EPDCs were found to undergo spontaneous EMT and express α-SMA. This finding raises the question of whether EPDCs derived from an atrial epicardial population are a relevant system to study when attempting to recruit EPDCs for repair. As RAA tissue samples are available from routine CABG surgery and because hEPDC explants retain differentiation potential, RAA epicardium explant cultures present a relevant model for preliminary studies. However, the implications of this finding must be appreciated when interpreting data derived from RAA samples. Furthermore, if it were possible to gain access to an alternate source of human epicardium, for example from whole heart donations, it would be imperative to compare behaviour of hEPDCs derived from both atrial and ventricular tissue.

Chapter 4

High Throughput Screening in rat EPDCs

4.0 Introduction: rat EPDC cell line

In 1992 Eid *et al.* generated an EPDC line from rat epicardial/mesothelial cells whilst developing an *in vitro* model for the study of cardiac muscle (Eid et al., 1992). Isolated primary adult myocytes rapidly adapt to culture and undergo cytoskeletal remodelling which results in loss of their characteristic sarcomere and myofibril structure. Eid *et al.* observed that small patches of their primary rat myocyte cultures maintained their mature phenotype and began synchronised contractions: in each case these patches of mature myocytes were adjacent to a collection of non-muscle cells. These polygonal non-muscle cells were positive for the epicardial marker WT1, negative for fibroblast and pericyte markers and grew with 'cobblestone' epithelial morphology. Suspecting these cells to be epicardium derived, a protocol for the isolation of EPDCs from whole rat hearts was successfully established. When these isolated rat EPDCs (rEPDCs) were co-cultured with adult rat myocytes they prevented, and even reversed, cytoskeletal remodelling and maintained myocyte contractility *in vitro* (Eid et al., 1992, 1994).

Recognising that this rEPDC line could provide an *in vitro* system in which to explore epicardial development and differentiation Wada *et al.* subsequently characterised rEPDC phenotype and behaviour (Wada et al., 2003). Epithelial phenotype was confirmed by localisation of the cell junction proteins E-CADHERIN, ZO-1 and β-CATENIN along the cell membrane at points of cell-cell contact. RT-PCR confirmed expression of the epicardial markers *Tbx18,* blood vessel epicardial substance (*BVES*) and *WT1*; nuclei stained positive for WT1 (Wada et al., 2003). Culture of rEPDCs with 10 ng/mL of FGF2, previously shown to induce epicardial EMT in explant cultures (Morabito et al., 2001b), resulted in slower formation of epithelia, disrupted E-CADHERIN localisation and induced stress fibre formation. This demonstrated that the rEPDCs retained their ability to respond to growth factor cues and undergo EMT. Furthermore, after 48

hours of treatment with a range of growth factors, including EGF, patches of rEPDCs began expressing SM-MHC, a marker for smooth muscle. This demonstrated that, despite long term culture, the rEPDC cell line remained a progenitor population able to differentiate toward a coronary vasculature fate (Wada et al., 2003). In the establishment of the rEPDC cell line Eid at al. did not report any modification or selection process made to the cell line which would ensure unrestricted growth: they reported use of the rEPDCs up to passage 30, and Wada *et al*. kept rEPDCs in culture for >3 years. It is somewhat remarkable that this cell line remained epicardial throughout numerous passages when primary both primary human and mouse EPDCs so readily undergo spontaneous EMT (Clunie-O'Connor et al., 2015; Smart and Riley, 2009).

4.1 Model development

In light of the restricted access to human RAA biopsy samples (**Chapter 3**), it was recognised that the rEPDC cell line might provide an excellent system in which to model epicardial EMT *in vitro*. Therefore, their suitability for HTPS was explored. REPDCs were cultured in DMEM with 10% FBS and pen/strep as described in the literature (Wada et al., 2003). Examination of confluent cultures with brightfield microscopy confirmed characteristic 'cobblestone' morphology (**Figure 4.1 A**).

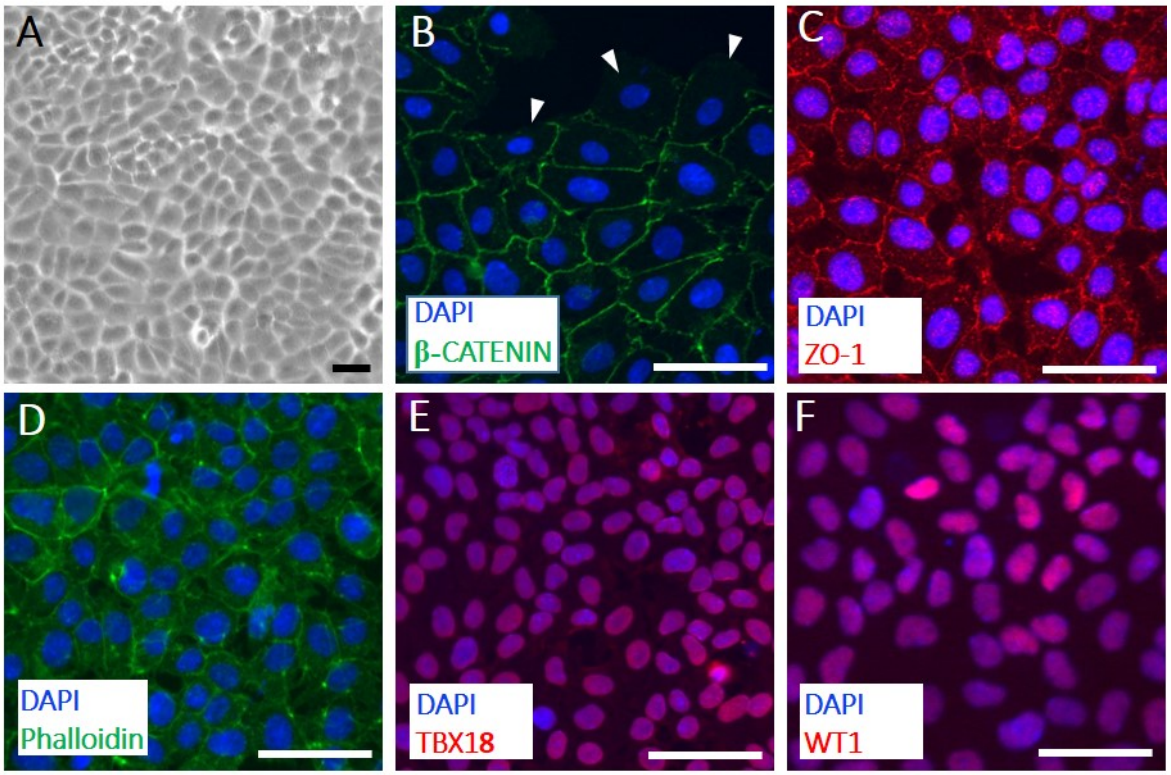


Figure 4.1 REPDCs maintain an epicardial phenotype *in vitro*. (**A**) Brightfield image of rEPDC culture with 'cobblestone' epithelial morphology. (**B**) β-CATENIN is localised to the cell membrane at points of cell-cell contact but is not detected at the free cell surface forming the edge of the epithelial sheet (white arrowheads). (**C–D**) REPDCs express the tight junction protein ZO-1 and a network of cortical actin. (**E–F**) REPDC cultures stain positive for epicardial markers TBX18 and WT1. All scale bars 50µm.

To further confirm an epicardial phenotype the cells were trypsinized, seeded on to glass coverslips and allowed to form sheets for 12–24 hours before being fixed with PFA in preparation for phenotypic evaluation by ICC. Several attempts were made to get an E-CADHERIN antibody working on the rEPDCs but this failed: it is possible that antibodies tested were not specific for the E-CADHERIN isoform expressed in these cells. In the absence of this widely recognised epithelial marker, distribution of β-CATENIN in the rEPDC cultures was investigated (**Figure 4.1 B**). The β-CATENIN protein has a dual role: it forms part of the E-CADHERIN/β-CATENIN complex that stabilises cell-cell contacts and is also a key regulator of WNT signalling. The WNT family of glycoproteins are responsible for regulating a huge array of cellular process involved in cell differentiation and migration. In the absence of

extracellular WNT signalling cytoplasmic β-CATENIN is tagged for proteolytic degradation; pathway activation by the WNT ligand results in β-CATENIN stabilisation and nuclear translocation, where it acts as a transcriptional co-activator on its target genes many of which stimulate cell migration and invasion. TGFβ induced EMT stimulates release of β-CATENIN from the cell membrane and stabilises it for nuclear translocation (Hülsken et al., 1994; Tian et al., 2011a).

In the rEPDC cultures, β-CATENIN was not localised to the cell membrane on free edges of the cell sheet (**Figure 4.1 B**, white arrowheads) only at points of cell-cell contact, consistent with a potential interaction with E-CADHERIN at the adherens junction. Therefore, it was used as an epithelial marker in this model. ICC also revealed membrane localisation of the tight junction protein ZO-1 (**Figure 4.1 C**), which along with β-CATENIN confirmed the formation of mature polarised epithelium (Wada et al., 2003; Zhang et al., 2005). Phalloidin staining revealed that rEPDCs formed a tight monolayer with cortical actin (**Figure 4.1 D**) and nuclear TBX18 and WT1 staining confirmed epicardial phenotype (**Figure 4.1 E-F**).

Subsequently rEPDC EMT and differentiation was examined to determine whether the model would be suitable for use in HTPS. Spontaneous differentiation of rEPDCs has previously been reported (Wada et al., 2003). Culture in standard DMEM with 10% FBS was shown to result in sporadic distribution of α-SMA+ and SM-MHC+ cells (<5% of cells). Serum free DMEM was used in the published rEPDC differentiation protocol presumably intended to minimise the effect of unknown, unspecified growth factors present in FBS.

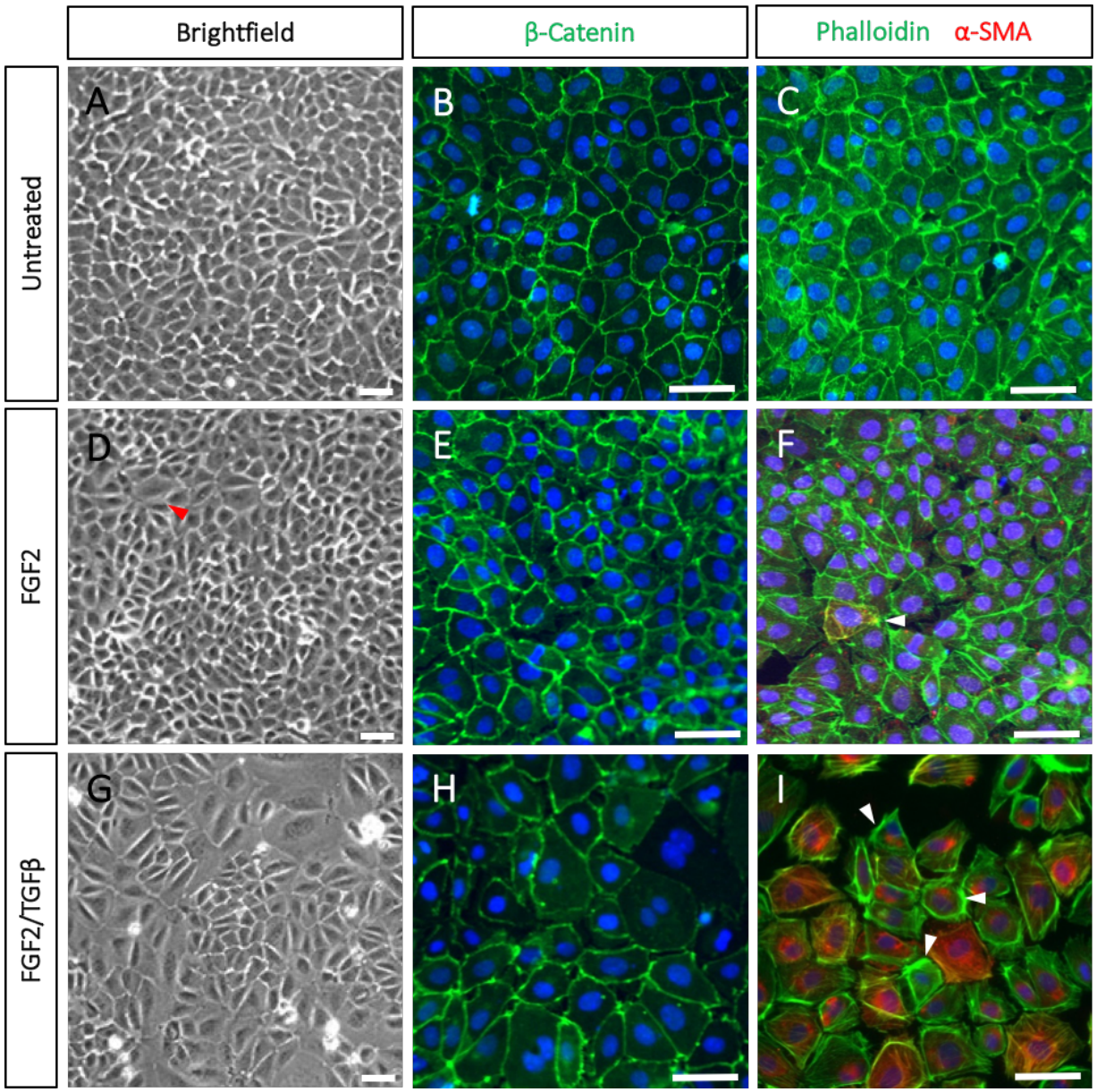


Figure 4.2 REPDCs underwent EMT and differentiated in response to FGF2/TGFβ treatment. (**A–C**) Untreated cultures formed tight epithelia as confirmed by uniform β-CATENIN distribution and cortical actin. (**D–F**) FGF2 alone was not sufficient to induce gross morphological changes in rEPDCs, although enlarged cells (**D**, red arrowhead) and sporadic α-SMA+ cells were identified (**F**, white arrowhead). (**G–I**) FGF2/TGFβ induced EMT in rEPDCs. Cultures contained patches of enlarged cells and exhibited irregular β-CATENIN patterning at the cell membrane. FGF2/TGFβ treatment also resulted in actin remodelling which formed stress fibres across the cell body and bundles at the cell edge (**I**, white arrowheads). Furthermore, FGF2/TGFβ induced expression of the EMT marker α-SMA in a subset of rEPDCs (**I**). All scale bars 50μm.

Preliminary experiments utilised the published protocol: rEPDCs were seeded at 2 x 10^4 cells/cm^2 in DMEM with 10% FBS for 24 hours before switching to FBS free media supplemented with 10 ng/mL FGF2 or 2 ng/mL TGFβ for differentiation. However, in our hands, culture without serum resulted in widespread cell death that rendered the cultures useless for further analysis by the end of the differentiation protocol. Fortunately, a successful rEPDC differentiation protocol using low serum DMEM (LS-DMEM) had previously been established in the lab by Dr Nicola Smart, whereby addition of just 0.5% FBS to the standard DMEM prevented cell death over the duration of the EMT experiment. In the revised protocol, cells were seeded at 2 x 10^4 cells/cm^2 in DMEM with 10% FBS. After 24 hours the cells were treated with LS-DMEM supplemented with 10 ng/mL FGF2 which was replaced after a further 24 hours with LS-DMEM containing 10 ng/mL FGF2 and 2 ng/mL of TGFβ. TGFβ is a central mediator of EMT (Zhou et al., 2012b) and has been shown to induce the transition in a range of epithelial cells including epicardium (Bax et al., 2011; Clunie-O'Connor et al., 2015; Huang et al., 2014b); FGF2 signalling is also involved in EPDC EMT and differentiation in development (Morabito et al., 2001b; Rosenblatt-Velin et al., 2005). The cells were allowed to differentiate for 48 hours before being collected for analysis. REPDCs cultured for 3 days in LS-DMEM appeared healthy and formed an epithelial sheet, as confirmed by the uniform distribution of β-CATENIN at the cell membrane and characteristic cortical actin patterning throughout the culture (**Figure 4.2 A–C**). After 3 days incubation with FGF2 a small number of rEPDCs had doubled in size (**Figure 4.2 D**, white arrowhead) but treatment did not grossly affect cell morphology. β-CATENIN and phalloidin patterning was analogous to that of untreated cells which indicated that in our hands FGF2 treatment alone was not sufficient to induce EMT (**Figure 4.2 E–F**). Differentiating in LS-DMEM with FGF2/TGFβ, however, resulted in culture wide patches of enlarged cells indicating that treatment had either prevented formation or induced the disassembly of mature, tight, epithelia (**Figure 4.2 G**). This observation was confirmed by irregular β-CATENIN

staining (**Figure 4.2 H**) and actin remodelling which was organised in to stress fibres and thick actin bundles concentrated at the cell edge (**Figure 4.2 I**, white arrowheads). To further probe rEPDC phenotype the cultures were co-stained with the EMT marker α-SMA: sporadic α-SMA+ cells were identified with FGF2 treatment whereas widespread α-SMA expression was induced by FGF2/TGFβ. No α-SMA+ cells were identified in untreated controls (**Figure 4.2 C, F, I**). In combination these results indicated that FGF2 alone was not sufficient to induce significant EMT in rEPDC cultures; however, this could be achieved with FGF2/TGFβ in combination.

The next step was to investigate whether FGF2/TGFβ induced EMT was reflected at the level of transcription. Comparing expression of a number of epithelial and EMT markers by Q-PCR revealed little difference in relative transcript levels between untreated and FGF2/TGFβ treated cells (**Figure 4.3**). If FGF2/TGFβ had induced EMT and either prevented formation or induced disassembly of cell-cell junctions a decrease in levels of tight junction protein *ZO-1* would be expected. Our analysis revealed a nominal decrease in *ZO-1* transcription; however, this failed to reach significance. A similar observation was made in the case of the EMT regulating transcription factor *Snai2* (Gonzalez and Medici, 2014); once again there appeared to be a slight increase in expression which would correlate with induction of EMT, but this was not significant. There was also a small increase in *Acta2* transcription (encoding α-SMA) but this was not found to be significant.

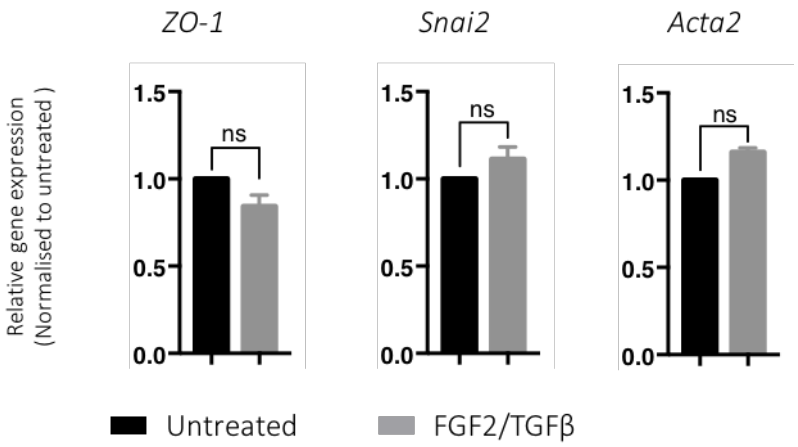


Figure 4.3 REPDC EMT was not reflected at the level of transcription. Q-PCR data of rEPDCs treated with FGF2/TGFβ relative to untreated controls. Analysis revealed no significant changes in *ZO-1*, *Snai2* or *Acta2* mRNA levels between the two groups. Statistics calculated using student's unpaired t-test; *p<0.05; **p<0.01; ***p<0.001; ****p<0.0001, n=3.

The rEPDC differentiation protocol was then repeated with a new batch of cells in order to increase n numbers and assess the reproducibility of the model. This was highly problematic and on several occasions rEPDCs failed to undergo EMT or differentiate all together. It appeared that it was possible to induce EMT in rEPDCs, however, the response was variable. It was postulated that this may be a result of contact inhibition in which formation of epithelium reduced EPDC response to growth factor stimulation (Grazia Lampugnani et al., 2003); therefore it was decided that an alternate protocol would be explored.

It was decided that plating the cells at a lower starting density may be beneficial for two reasons: firstly, because high cell density may confer some form of contact inhibition (Grazia Lampugnani et al., 2003): secondly, with phenotypic screening in mind, the cells required space to ensure that any morphological changes could be easily observed. In addition to the reduced cell density, it was decided that a range of treatments would be investigated to identify the most effective. The first differentiation condition explored was the combination of FGF2/TGFβ previously described. Next, differentiation with TGFβ at 2 and 4 ng/mL: the use of TGFβ alone

would simplify the differentiation protocol and correlate the experimental conditions with those used for hEPDC experiments (**Chapter 3**). 2 ng/mL of TGFβ (Huang et al., 2014b) had been successful in inducing EMT in the human model, however the TGFβ concentration was also doubled to investigate dose dependency. The final differentiation condition utilised the non-selective DNA-hypomethylating agent 5-azacytidine, which been reported to induce myogenic and cardiomyogenic gene programs in several stem cell lines with an effective concentration between 5–15 μM (Choi et al., 2004; Supokawej et al., 2013; Taylor and Jones, 1979). In addition there has been shown to be an inverse correlation between DNA methylation and transcription of *Snai1* and *Snai2*, key regulators of EMT (Chen et al., 2013; Medici et al., 2008). An added consideration was that a potent small molecule could have provided a cheaper, more stable positive control for use in screening than recombinant TGFβ. For these reasons the effect of 5-azacytdine was investigated in the rEPDC model at 10 μM. Treatment with FGF2 alone was excluded from the experiment, as it had not previously shown any significant effects.

Cells were plated at a reduced density of 2 x 10^3 cells/cm^3 in DMEM with 10% FBS for 24 hours. LS-DMEM was used to differentiate the cells, supplemented with the additives described above. After 3 days of incubation with their respective supplemented media rEPDC morphology was inspected with a brightfield microscope. Despite being seeded at low density the untreated cells formed ‘islands’ of smooth edged epithelia with uniform cell shape and size (**Figure 4.4 A**). REPDCs treated with FGF2/TGFβ, TGFβ and 2x TGFβ appeared clustered together but were heterogeneous in shape and size and several cells had failed to establish cell-cell contact (**Figure 4.4 A**, cells detached from sheet indicated by white arrowheads). 0.5% DMSO was included as a control for the 5-azacytidine treatment as it was used as the solvent at the same concentration. DMSO control appeared to have no effect on the formation of epithelia over the

3-day time course whereas cells treated with 5-azacytidine exhibited morphology comparable to that of the growth factor treated cells (**Figure 4.4 A**).

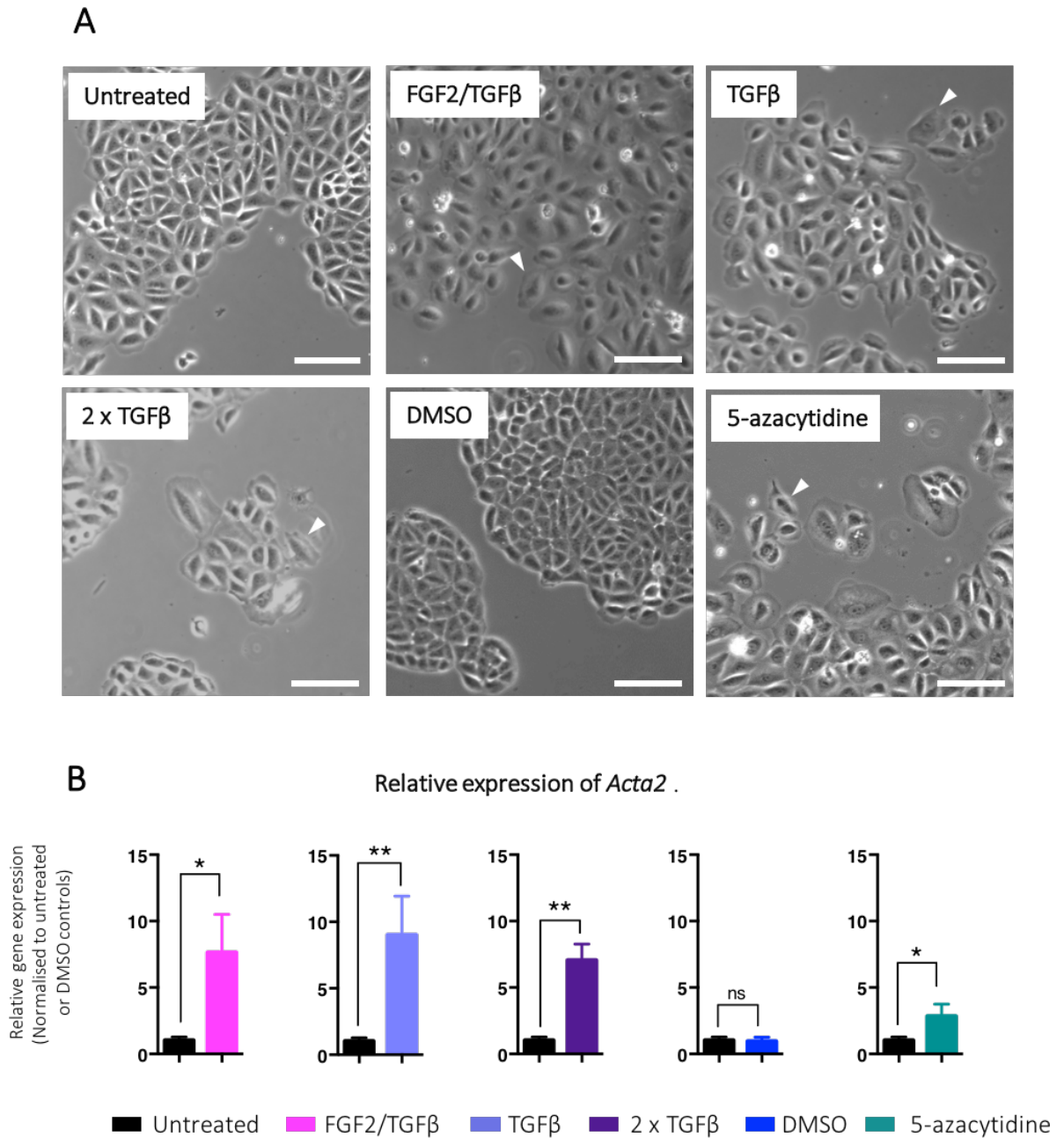
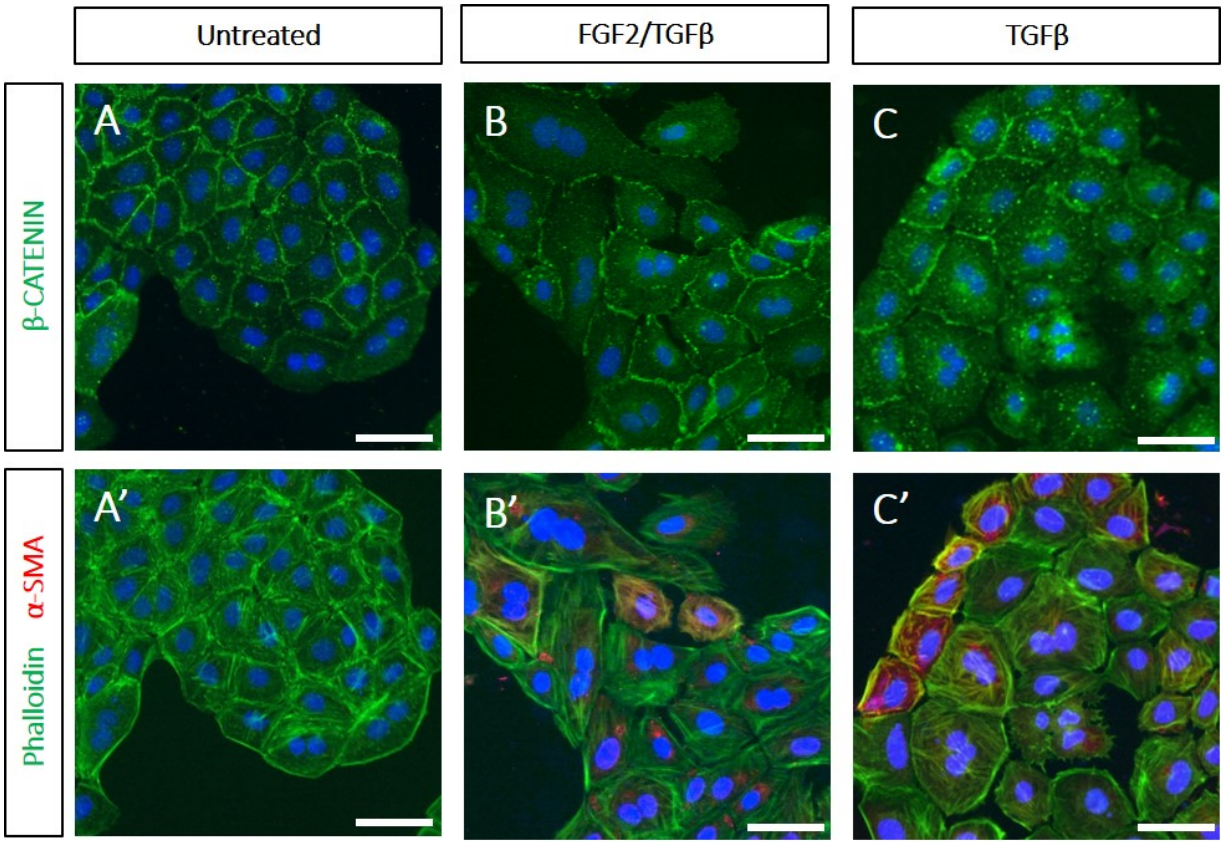
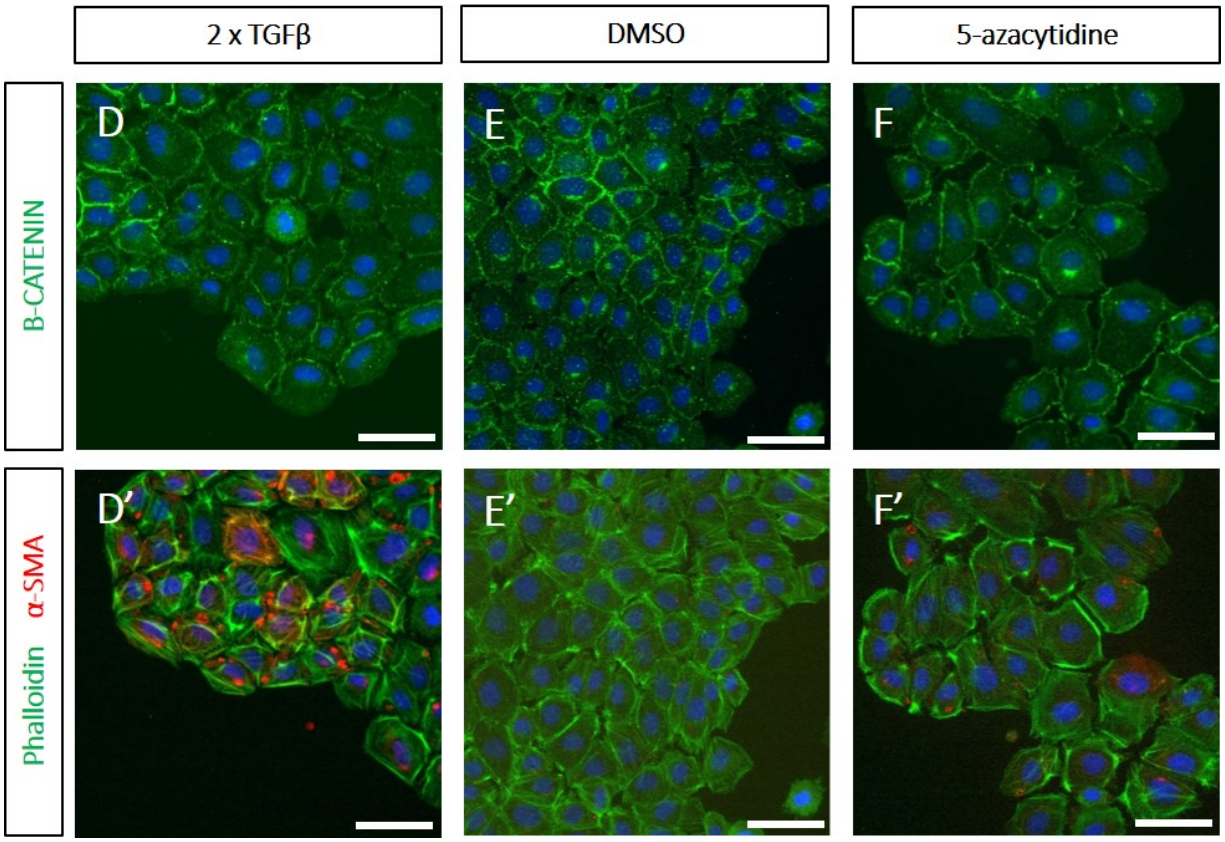


Figure 4.4 At low cell density rEPDC EMT is reflected at the level of transcription. (**A**) Treatment of rEPDCs with FGF2/TGFβ, TGFβ, 2 x TGFβ and 5-azacytidine induced morphological changes in rEPDCs compared with untreated and DMSO controls. Several cells failed to establish cell-cell contacts (highlighted by white arrowheads). (**B**) Relative expression of *Acta2* was significantly upregulated with all growth factor combinations. TGFβ resulted in the biggest change with a nine-fold increase relative to the untreated control. 0.5% DMSO did not affect expression levels of *Acta2*, whereas 5-azacytidine increased it by nearly three-fold. n = 3. Scale bar 100µm. Statistics calculated using student's unpaired t-test; *p<0.05; **p<0.01; ***p<0.001; ****p<0.0001.

Q-PCR analysis was used to interpret these observations at a molecular level (**Figure 4.4 B**). Unlike the previous experiments, at lower cell density rEPDCs demonstrated consistent and significant upregulation of the EMT marker *Acta2*. All growth factor combinations significantly increased *Acta2* expression; 2 ng/mL TGFβ induced the highest expression with 9-fold increase relative to the untreated control. Comparison of *Acta2* transcript levels in untreated and 0.5% DMSO treated cells confirmed that the latter had little to no effect on rEPDC phenotype. Interestingly, 10μM of 5-azacytidine increased *Acta2* by nearly threefold compared with DMSO alone. No significant changes were seen in expression levels of *Snai2* or *ZO-1* (**Appendix figure 4.1**).

ICC was used to further investigate rEPDC morphology and determine whether the observed increase in *Acta2* expression was correlated with morphological changes indicative of EMT. In untreated cells β-CATENIN was again localised to the cell membrane at cell-cell contacts (**Figure 4.5 A**); the distribution was less uniform then had been observed previously (**Figure 4.2**), suggesting the sparser cultures had not yet formed a tight monolayer. β-CATENIN localisation was markedly different to the control in all growth factor treated cultures, distributed sporadically at points of cell-cell contact but also throughout the cytoplasm (**Figure 4.5 B–D**). In addition to cytoplasmic presence, β-CATENIN appeared to be localised around and inside the nucleus particularly after TGFβ treatment. This likely reflects the dual role of β-CATENIN in Wnt signalling (Hülsken et al., 1994; Zhou et al., 2012b). Phalloidin staining revealed the formation of thick stress fibres, bundles of actin and failure to establish cell-cell contact in growth factor treated cultures compared with the untreated control (**Figure 4.5 A'–D'**).


Untreated
FGF2/TGFβ
TGFβ
β-CATENIN
Phalloidin α-SMA
A
B
C
A'
B'
C'


2 x TGFβ
DMSO
5-azacytidine
B-CATENIN
Phalloidin α-SMA
D
E
F
D'
E'
F'

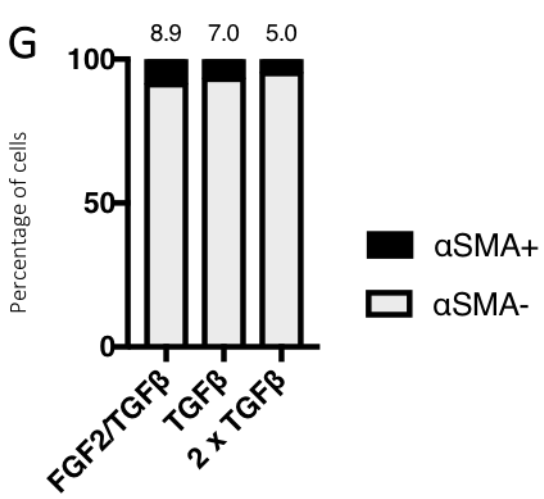


Figure 4.5 Immunostaining confirms rEPDC EMT at low cell density. (**A–D**) rEPDCs treated with FGF2/TGFβ, TGFβ and 2x TGFβ expressed lower levels of β-CATENIN at the cell membrane compared with untreated controls. In response to TGFβ treatment β-CATENIN appeared to be distributed throughout the cytoplasm and in the nucleus. (**A'–D'**) Untreated cells grew as smooth edged epithelia and actin appeared to form cortical rings. Exposure to all three growth factor combinations prevented the formation of epithelia, induced gaps in the cell sheet and increased the density of actin stress fibres across the cell body and actin bundles at the cell edges. In response to growth factor treatment a subset of rEPDCs began expressing α-SMA. (**E–F**) Treatment with 0.5% DMSO appeared to affect the formation of tight junctions as β-CATENIN was unevenly distributed at the cell membrane. 5-azacytidine treatment also resulted in irregular β-CATENIN distribution at the cell membrane. (**E'–F'**) DMSO treated cells had begun to form a cortical actin network whereas 5-azacytidine inhibited formation of an epithelial sheet and increased the incidence of actin bundles at the cell edge. (**G**) The percentage of α-SMA+ cells in growth factor treated cultures were calculated, percentage of α-SMA cells is printed at the top of each bar, n = 2. All scale bars 50μm.

A small number of treated rEPDCs have developed α-SMA+ filaments across the cell body, indicating formation of contractile machinery for migration (**Figure 4.5 A'–D'**), which corroborated the Q-PCR data that showed increased *Acta2* expression in response to all growth factor treatments. Counting the cells across two coverslips for each treatment revealed 8.9, 7.0 and 5.0% of α-SMA+ rEPDCs in FGF2/TGFβ, TGFβ and 2 x TGFβ treated cultures respectively (**Figure 4.5 G**).

Interestingly, 0.5% DMSO appeared to affect the formation of tight junctions as β-CATENIN was unevenly distributed at the cell membrane and remained in the cytoplasm; this too was the case for 5-azacytidine (**Figure 4.5 E–F**). However, DMSO appeared to slow rather than impair the establishment of epithelium as rEPDCs had clustered together and actin appeared to be forming the beginning of a cortical ring (**Figure 4.5 E'**). Conversely, 5-azacytidine treatment resulted in stress fibres, bundled actin and clear gaps between cells (**Figure 4.5 F'**). Despite a

three-fold increase in *Acta2* expression by Q-PCR analysis, no α-SMA+ cells were identified by ICC after treatment with 5-azacytidine (**Figure 4.5 F'**).

After reviewing the data, it was clear that a greater EMT response was induced in rEPDC cultures when the seeding density was reduced. Using TGFβ at 4 ng/mL or in combination with FGF2 did not appear to induce EMT to any greater extent than 2 ng/mL TGFβ, thus this was used as the positive control. Although 5-azacytidine had some effect on rEPDC morphology and increased *Acta2* expression at transcript level this was not as effective as the use of TGFβ. 5-azacytidine is toxic in a number of cell lines at higher concentrations and showed toxicity in rEPDCs at 20 μM (Hossain et al., 1997) therefore, this compound was not pursued further.

Our final task was to perform a quantitative western blot to determine whether the recombinant TGFβ ligand successfully activated the receptor complex and determine whether the canonical signalling pathway was functional and likely to be responsible for the observed phenotypic changes. As previously discussed (**Chapter 1.17**) TGFβ signalling is initiated when the TGFβ ligand binds a homodimer of the type II receptor at the cell membrane. This recruits a homodimer of the type I receptor, forming an active and stable heterotetrameric complex that phosphorylates intracellular SMAD2 and SMAD3 proteins (Zi et al., 2012). REPDCs were plated for 24 hours in DMEM with 10% FBS at a concentration of 1 x 10^4 cells/cm^2, then serum starved for 24 hours. Cells were treated with TGFβ for 0, 5, 10, 20, 30 and 60 minutes before being collected for analysis by western blot. The membrane was probed for phospho-SMAD3 (P-SMAD3) and quantitative analysis showed a transient increase in intracellular P-SMAD3 relative to a GAPDH loading control between 5 and 20 minutes of incubation with TGFβ, confirming pathway activation. (**Figure 4.6 A–B**).

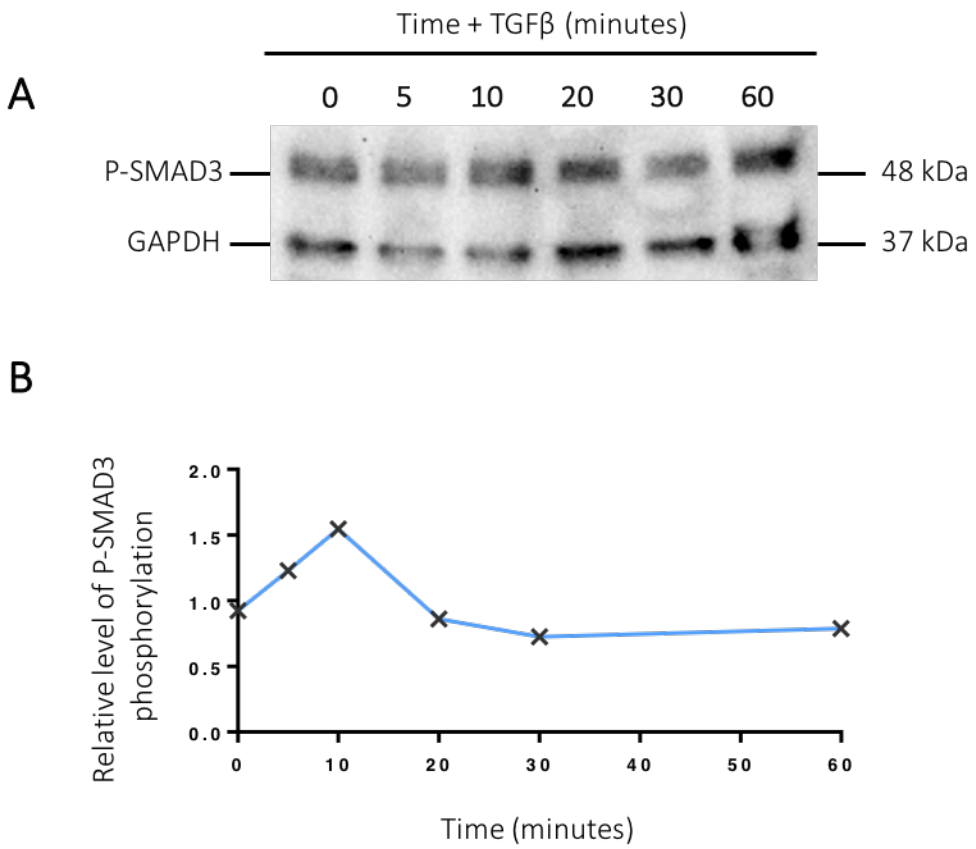


Figure 4.6 TGFβ activates the SMAD3 signalling pathway in rEPDCs. (**A**) Western blot of cell lysates from rEPDCs incubated with TGFβ for 0, 5, 10, 20, 30 and 60 minutes, probed for phosphorylated SMAD3 and GAPDH. (**B**) Quantitative scanning densitometry revealed an increase in SMAD3 phosphorylation in rEPDC cultures after 5–10 minutes incubation with TGFβ. This confirmed TGFβ receptor activation.

4.2 Utilising rEPDCs for high throughput phenotypic screening

4.2.1 REPDCs are not suitable for the previously established HTPS protocol

As discussed in **Chapter 3**, the suitability of a model for high content screening relies on the ability of the positive control to induce distinct morphological changes that can be recognised by the analysis software. To investigate whether the rEPDCs could be used in an analogous HTPS to that of the primary hEPDCs an appropriate cell density for screening was first established. REPDCs were seeded into a 384-well plate at concentration of 500, 1000, 1500 and 2000 cells/well and differentiated with TGFβ according to the previously established protocol (**Chapter 4.1**). After three days the plates were fixed; stained with phalloidin, cell mask membrane stain and DAPI; then imaged on the PerkinElmer Operetta high content imager

(tdi.ox.ac.uk/high-content-imaging). After examining the images it was clear that a seeding density of 500 cells/well was too low and few cells has survived the protocol (**Figure 4.7 A**). Plating the cells at 2000 cells/well appeared too many as the cultures were almost confluent making it difficult to observe morphological features in individual cells. There appeared to be little difference between the culture density when 1000 and 1500 cells were seeded (**Figure 4.7 A**). A feature of all the cultures was clustering of rEPDCs at the well edge that left the middle sparsely populated (**Figure 4.7 A**). After analysing the culture density, the analysis protocol established on the PerkinElmer Operetta for the hEPDC HTPS (**Chapter 3**) was used to try and distinguish between the treated and untreated rEPDC cultures. This unfortunately proved unsuccessful: detailed inspection of the images revealed that the morphological differences between the two 'populations' were much less distinct in the rat cells (**Figure 4.7 B, LHS**) as compared to the human (**Figure 4.7 B, RHS**) meaning the computer was unable to distinguish between the two. At this point it was decided that a selection of other EMT markers would be examined to see if they could be used, in combination with phalloidin, to produce a set of features on which to base the high content image analysis.

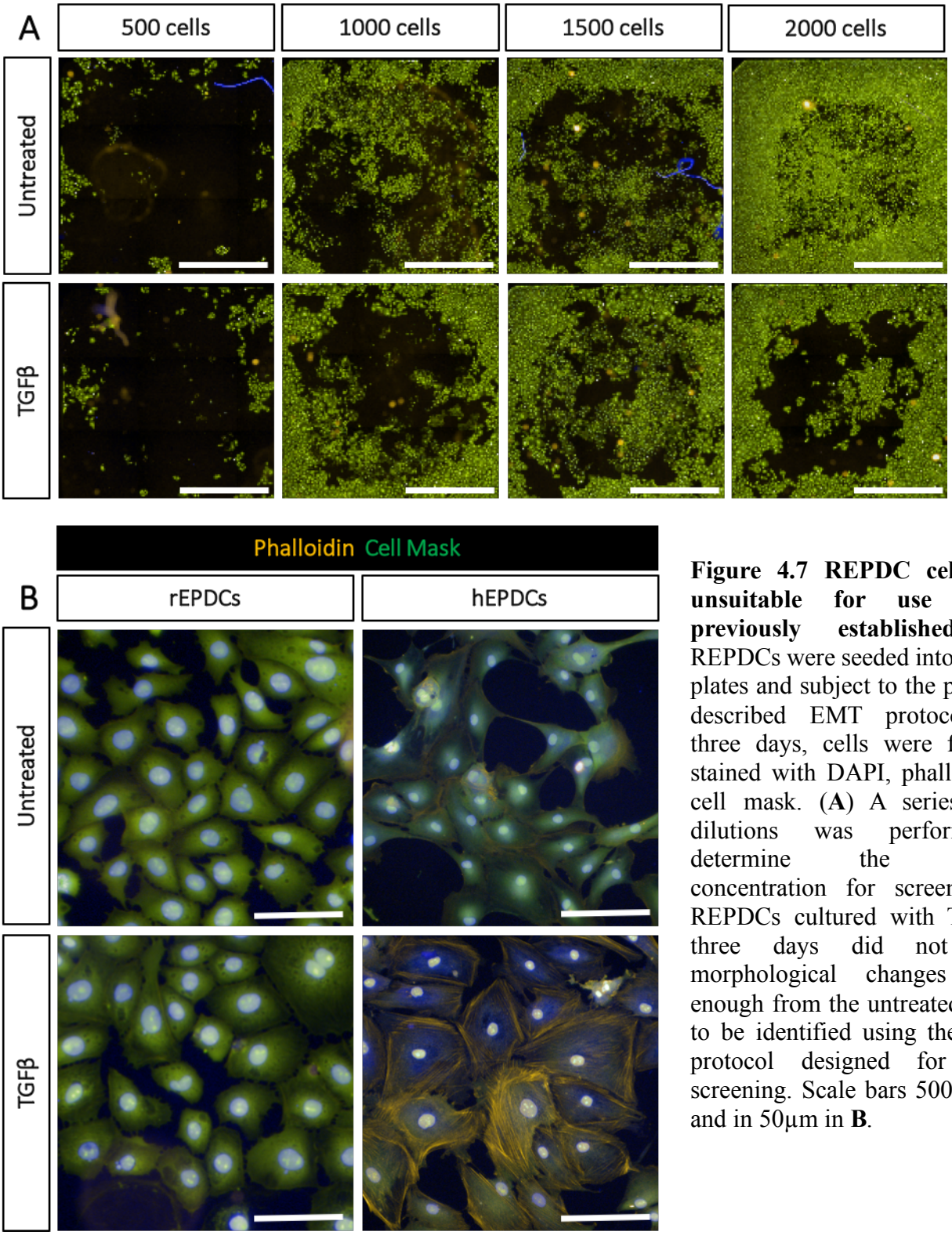


Figure 4.7 REPDC cell line is unsuitable for use in the previously established HTS. REPDCs were seeded into 384-well plates and subject to the previously described EMT protocol. After three days, cells were fixed and stained with DAPI, phalloidin and cell mask. (**A**) A series of cell dilutions was performed to determine the optimum concentration for screening. (**B**) REPDCs cultured with TGFβ for three days did not exhibit morphological changes distinct enough from the untreated controls to be identified using the analysis protocol designed for hEPDC screening. Scale bars 500 µm in **A** and in 50µm in **B**.

4.2.2 Quantifying VINCULIN 'speckles'

Due to the problems encountered whilst applying the previously established analysis protocol to rEPDCs, additional protein markers that might produce quantifiable measures of phenotypic change were investigated.

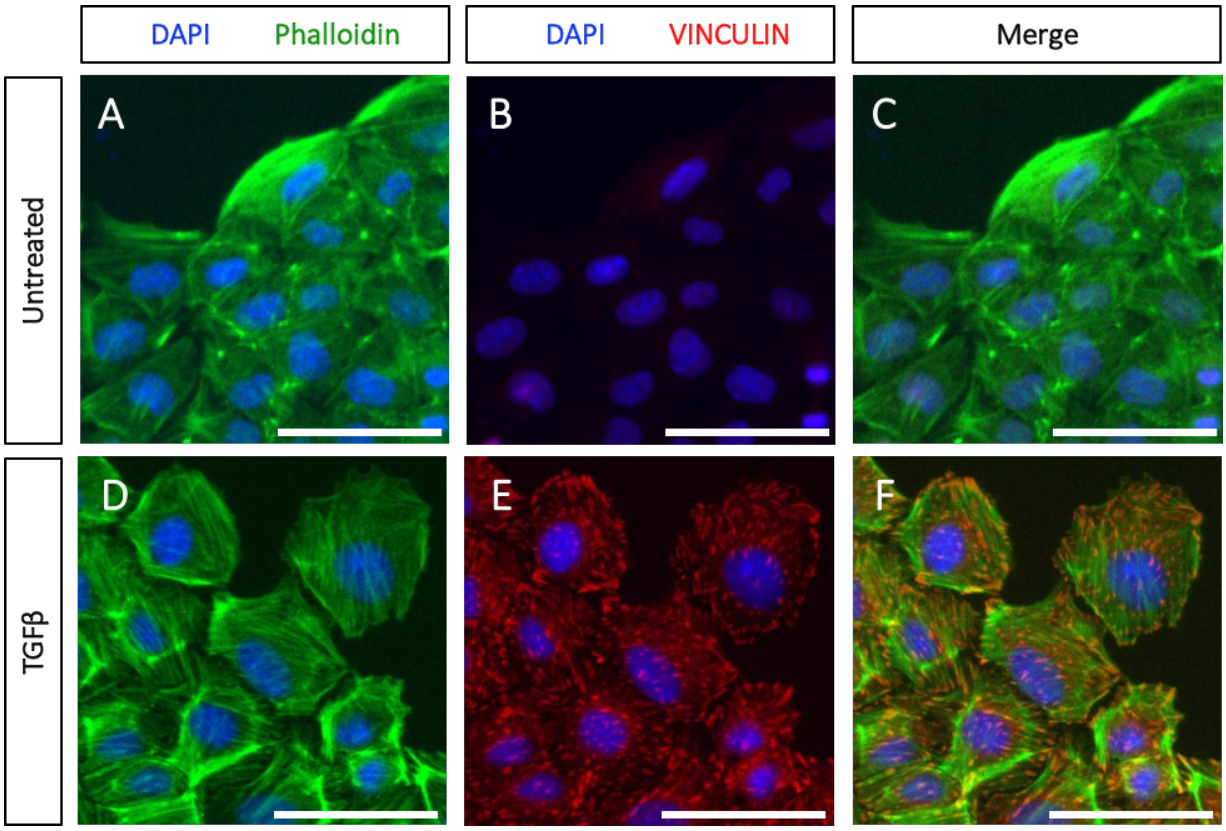


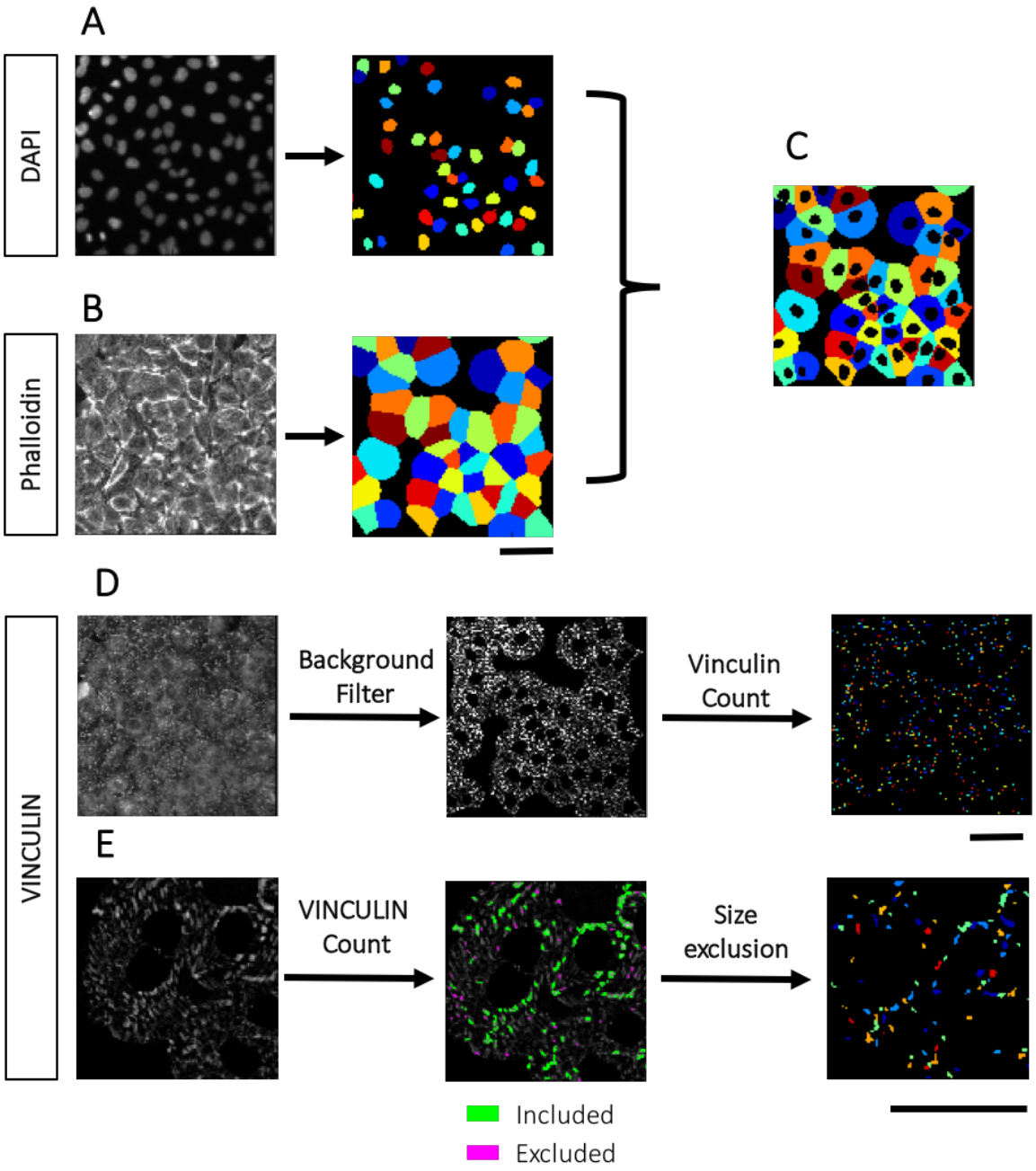
Figure 4.8 TGFβ induced formation of VINCULIN speckles. (**A-C**) Untreated cells begin to form epithelia and do not stain positive for VINCULIN. (**D-F**) TGFβ treated rEPDCs have formed stress fibres across the cell body and express high levels of VINCULIN that is localised to the ends of the actin stress fibres. All scale bars 50 µm.

VINCULIN is a member of the integrin family of proteins and an essential component of focal adhesions that link filamentous F-ACTIN to the ECM (Thievessen et al., 2015). When rEPDCs were grown on coverslips +/- 2 ng/mL TGFβ as previously described, ICC revealed striking differences in VINCULIN localisation. As previously seen, untreated cells began to form an epithelial sheet over the course of the experiment and this corresponded with little to no visible VINCULIN after 3 days of culture (**Figure 4.8 A–C**). However, TGFβ induced EMT, as

characterised by failure to form epithelia and stress fibre formation (**Figure 4.8 D**), was accompanied by the formation of numerous VINCULIN 'speckles' across the cell body (**Figure 4.8 E**). After merging the image channels, it was clear to see that VINCULIN was located at the end of the actin stress fibres which presumably represented its contribution to the focal adhesions (**Figure 4.8 F**). Due to there being such a distinct difference in VINCULIN expression between the untreated and TGFβ treated cells, investigation in to whether automated counting of the speckles could be used to quantify the extent of EMT in the cultures began.

CellProfiler is free, open source image analysis software (http://cellprofiler.org) that can be used to automatically assess cell phenotypes and has been widely used in peer reviewed publications (Carpenter et al., 2006; Roshanbin et al., 2016). By adapting a freely available analysis pipeline that counts speckles present in cell nuclei (http://cellprofiler.org/examples.html), a customised protocol was developed that could count the number of VINCULIN speckles in the cytosol of each cell in an image. Briefly, the DAPI channel was used to identify and count the nuclei (**Figure 4.9 A**). Using the phalloidin channel and nuclei location the software was able to segment the image to identify individual cells (**Figure 4.9 B**); the area of the nuclei was then subtracted from the whole cell leaving a measurement of the cytoplasm area (**Figure 4.9 C**). An additional analysis step was added in to the protocol before quantification of VINCULIN speckles that removed the background fluorescence (**Figure 4.9 D**). The protocol was further adapted so that it would measure VINCULIN expression in the cytoplasm region rather than the nucleus; the program was then trained to identify 'speckles' based on their size (**Figure 4.9 E**). Those that were too small were rejected from the count (**Figure 4.9 E**, denoted by green and purple highlights). Finally, the software assigned each VINCULIN 'speckle' to an individual cell so that an average number of speckles per cell could be calculated (**Figure 4.9 F**).

From these preliminary investigations it appeared as though VINCULIN was a suitable marker to use as a read out for rEPDC EMT as TGFβ treated cells, on average, contained 18 ‘speckles’ whereas untreated cells only contained 5 (**Figure 4.9 F**). Despite what appeared to be some success, further development of this protocol and attempts to increase experimental repeats in order to validate the analysis technique were hindered by a series of inconsistencies in the model, that will be described in the following section.



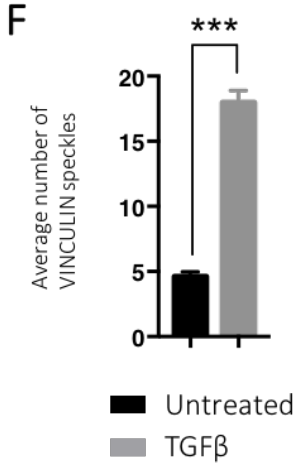


Figure 4.9 Automated quantification of VINCULIN 'speckles'. Using CellProfiler software an analysis protocol was written that could identify nuclei (**A**), segment the cell population (**B–C**) and identify the number of VINCULIN speckles per cell (**D–E**). TGFβ treatment resulted in a higher number of 'speckles' per cell, as quantified automatically (**F**) Statistics calculated using student's unpaired t-test; ***p<0.001; n = 9 images but account for only one experimental repeat, error bars denote SEM. All scale bar 50μm.

4.2.3 Quantifying α-SMA+ rEPDCs

Whilst exploring other proteins that could serve as reliable markers of EMT, the TGFβ induced differentiation protocol described in **Chapter 4.2** was repeated on several coverslips and probed again for α-SMA. It was thought that staining for VINCULIN and α-SMA expression in combination might provide two easily identifiable features upon which to design an image analysis protocol. To do so, cells were seeded on to coverslips at 2 x 10^3 cells/cm^2 and differentiated with 2 ng/mL TGFβ. On this occasion a series of time points were investigated: 24 hours was chosen to see whether α-SMA expression occurred at an earlier time point than previously investigated, 48 hours to compare with the previous experiments and 96 hours to allow for further differentiation. It was postulated that if α-SMA expression reflected EMT and subsequent differentiation the effect should be time dependent and increasing the length of the differentiation protocol should result in more α-SMA+ cells. Furthermore, a time course might have revealed an optimum time point at which morphological changes were more pronounced and thus easier to identify. The coverslips were fixed and stained for α-SMA as before; each coverslip for imaging was then 'divided' in to nine arbitrary regions so that a representative number of cells from the whole coverslip could be imaged (**Figure 4.10 A**). On this occasion no α-SMA+ cells were seen on any coverslips at any of the three time points (**Figure 4.10 B**, representative images). The experiment was then repeated using a new vial of cells at lower passage number in case prolonged culture had affected rEPDC phenotype, but again no rEPDCs developed α-SMA filaments. The experiment was also repeated with a new batch of TGFβ in case the previous samples had degraded in storage but once again rEPDCs did not express α-SMA in response to TGFβ treatment: Q-PCR data confirmed this observation and no *Acta2* expression was observed. Another four vials of rEPDCs from separate frozen batches were then thawed in order to try and identify a batch that would respond as had previously been documented. These growth rate of the thawed cells was much lower than the previous batches

and they did not form smooth epithelial islands as has been seen before (**Figure 4.4 A**) and instead appeared to be differentiating (**Figure 4.10 C**), furthermore, after a few weeks in culture the rEPDCs began to die suddenly. At this time, due to the issues that has arisen in generating reproducible data from the rEPDC model throughout our investigations, it was decided that an alternate cell model would be investigated with the aim of developing a more reliable system.

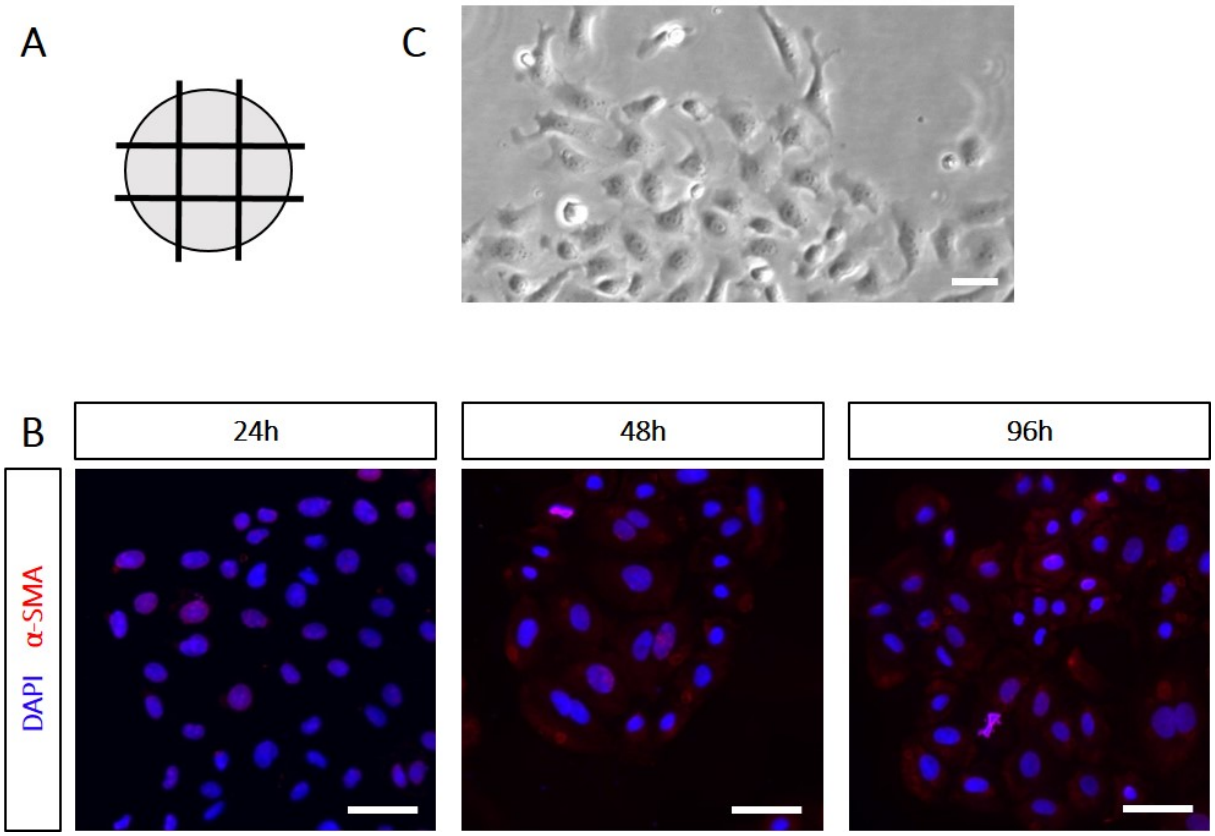


Figure 4.10 REPDC cell line failed to reproducibly undergo EMT and differentiate in response to TGFβ treatment. (**A**) Coverslips were divided in to nine segments for quantification of α-SMA+ cells. (**B**) REPDC cultures treated with TGFβ for 24–96 hours failed to express α-SMA filaments. (**C**) Several batches of thawed rEPDCs failed to grow with 'cobblestone' epithelial morphology under normal culture conditions. All scale bars 50µm.

4.3 Summary and discussion

This section describes efforts to establish an *in vitro* model of EPDC EMT in a cell line derived from rat epicardial/mesothelial cells. To begin investigations rEPDCS were subject to a published differentiation protocol (Wada et al., 2003); unfortunately, the use of serum free media in the described differentiation protocol resulted in mass cell death. Switching to a

protocol established in the lab by Dr Nicola Smart, rEPDC EMT and differentiation was achieved using LS-DMEM with FGF2 and TGFβ in combination. EMT was characterised by disrupted β-CATENIN localisation, cytoskeletal remodelling and sporadic expression of α-SMA+ filaments in growth factor treated cultures. Several attempts were made to fully characterise the model; however, at this point rEPDC response was found to be highly variable and on several occasions no EMT was observed despite identical experimental conditions. In their paper, Wada *et al.* discussed a 'time dependency' of growth factor induced EMT: after 24 hours of rEPDC differentiation they observed the formation of stress fibres and noted that E-CADHERIN patterning was disturbed; conversely, at 48 hours they observed that these features had reversed and the cells once again appeared to have formed tight epithelia (Wada et al., 2003). With this in mind, it was postulated that the rEPDC phenotypic plasticity described may have been inhibited or reversed under dense culture conditions. It was decided that rEPDCs would be assayed at a lower density using a range of growth factors to establish the most effective at inducing EMT. Our experiments revealed that rEPDCs could be induced to undergo EMT in response to the original combination of FGF2/TGFβ, TGFβ alone and TGFβ at double the original concentration. Morphological changes observed by brightfield microscopy indicated an EMT response, confirmed by significant upregulation of *Acta2* transcripts. ICC further supported this evidence, clearly demonstrating that treated cultures did not form tight epithelium, underwent cytoskeletal rearrangement and expressed α-SMA+ filaments. The greatest EMT effect was seen with 2 ng/mL TGFβ therefore this was taken forward as the positive control. At this time, the effect of the myogenic small molecule 5-azacytidine was also investigated which, despite appearing to increase *Acta2* expression, did not result in expression of α-SMA+ filaments and gross morphology was not significantly altered. Although 5-azacytidine has been reported to induce myogenic gene programs in stem cell populations, it did not appear to induce rEPDC differentiation. Furthermore, because 5-azacytidine is toxic at

higher doses and treatment with 10 μM did not significantly induced morphological changes useful for use HTPS this compound was not investigated further.

The next stage was to transfer the EMT model to a high throughput setting to assess its suitability for phenotypic screening. The HTPS analysis protocol, established to measure hEPDC differentiation, was not able to distinguish between positive and negative controls in the rEPDC model. When differentiated in the 384 well format, TGFβ induced EMT in rEPDCs was not associated with morphological changes distinct enough for the computer to identify, thus it could not distinguish two separate phenotypes. This failure to differentiate may have reflected the 'immortalised' state of the rEPDC cell line: it had already been reported that phenotypic plasticity is reversible and perhaps the cells were unable to properly differentiate away from the epicardial phenotype (Wada et al., 2003). Whilst investigating other proteins that might have served as useful EMT markers, the focal adhesion protein VINCULIN was found to be highly expressed in cells treated with TGFβ but not in untreated controls. Subsequently, an analysis protocol that quantified VINCULIN expression was written that measured the 'average' number of VINCULIN 'speckles' per cell.

To establish a second phenotypic marker it was decided that changes in α-SMA expression would be quantified over a time-course so as to fully characterise the model and to serve as validation of TGFβ induced EMT. In this experiment the rEPDCs completely failed to undergo EMT expressing no VINCULIN or α-SMA. This was the case in several further experiment repeats using various TGFβ, cell and serum batches. Furthermore, multiple vials of rEPDCs thawed for culture grew at a much slower rate than had previously been seen, no longer grew in epithelial islands and began to die in culture.

There could be several reasons why the rEPDC cell line proved so problematic to work with. The rEPDCs has not been immortalised and although Wada *et al.* reported successful culture of the rEPDCs for >three years it could perhaps be the case that extended culture cycles has caused the rEPDC phenotype to change. Although the rEPDCs used in this study were at a relatively low passage number, being used between passages 18–21, there have been numerous reports of repeated passage and cell competition effects causing genetic drift in cell lines (Hughes et al., 2007). Alternately it may have been that the cell freeze/thaw technique was suboptimal which could have resulted in rEPDC differentiation away from their original phenotype (Naaldijk et al., 2012). Furthermore, as the rEPDCs had not been immortalised genetically or by clonal selection they may have lost their ability to grow in an unrestricted fashion. Although increased *Acta2* expression was observed, no increased expression of the EMT transcription factor *Snai2* was observed neither was reduced expression of the tight junction protein *ZO-1*. Activation of TGFβ signalling was confirmed by a quantitative western blot, however perhaps ineffective signalling downstream of the SMAD proteins resulted in incomplete stimulation of EMT. TGFβ is also known to stimulate fibrosis, resulting increased expression of α-SMA (Desmoulière et al., 1993), so perhaps fibrotic mechanisms were activated instead. At this point, due to the ongoing problems encountered with the cell line and the necessity of finding a reliable model upon which to design future HTPS assays, an alternative mouse epicardial cell line was sourced.

Chapter 5

High Throughput Screening in mouse EPDCs

5.0 Introduction: immortalised mouse EPDCs

Primary somatic cells are limited in the number of times they can divide before entering senescence, which restricts their utility for *in vitro* study (Ouellette et al., 2000). Numerous techniques have been employed to immortalise cell lines and delay the onset of senescence (Irfan Maqsood et al., 2013). One such technique involves transfection of the cells with an oncogene which silences the checkpoints that regulate the normal cell cycle. Such mutations can exert an effect on other normal functions of the cell, and both the phenotype and behaviour of cell lines relative to primary cells must be carefully assessed. Nonetheless, immortalised cell lines have contributed extensively to research projects worldwide.

In 1998, a mouse line was generated containing the temperature dependent tumour virus 'Simian Virus 40' (SV40) that immortalises cells but only at temperatures suitable for viral activity (Ahuja et al., 2005; Jat et al., 1991). Using the mutant mouse, a conditionally immortalised line of EPDCs was generated from mouse epicardium (mEPDCs) (Austin et al., 2008). MEPDCs cultured at 33^{o}C in 'immortalisation media' (IM) consisting of DMEM supplemented with 10% FBS, insulin transferrin-selenium and mouse gamma interferon are immortal. Culture at 37^{o}C in 'differentiation media' (DM) consisting of M199 media with 10% FBS inactivates the oncogene restoring the cells to their 'natural' state; the mEPDCs formed tight epithelia, confirmed by expression of the tight junction protein ZO-1, and expressed the epicardial marker WT1. Furthermore, mEPDCs underwent EMT in response to TGFβ treatment, confirmed by the loss of ZO-1 and increased expression of SM22-α (Austin et al., 2008).

The rEPDC line discussed in **Chapter 4** had not been actively immortalised; the lack of reproducible data generated from these cells may have been a result of the cells drifting away from their *in vivo* phenotype. It was postulated that use of the immortalised mEPDC line could

circumvent this problem as well as the issue of spontaneous EMT experienced whilst working with primary human cells (**Chapter 3**).

5.1. Model development

Initially the published protocol for mEPDC differentiation was replicated to assess whether the cell line would respond to TGFβ treatment as described and to determine whether the cells expressed the appropriate epicardial markers (Austin et al., 2008). MEPDC cultures were kept in an immortalised state in 33^{o}C as recommended. For differentiation, the cells were plated at a range of densities in IM. After 24 hours the media was removed, replaced with the DM and the cells incubated at 37^{o}C. After a further 24 hours the media was replaced with plain DM or DM containing 2 ng/mL TGFβ and the cells left to differentiate for 72 hours before being collected for analysis by Q-PCR (**Figure 5.1**).

Examining the cells with brightfield microscopy, it was immediately obvious that the plating density was too high. Cultures were extremely dense and it was not possible to see whether EMT and subsequent differentiation had been stimulated by assessing cell morphology (**Figure 5.1 A**). Nevertheless, preliminary Q-PCR analysis indicated that TGFβ upregulated the EMT mediating transcription factors *Snai1* and *Snai2,* and the EMT and differentiation markers *α-SMA* and *SM22-α* relative to untreated controls, confirming a response to TGFβ treatment at transcript level (**Figure 5.1 B**). The biggest response was observed at day three in all genes except for *Snai2*. This could have been because the untreated cells were themselves beginning to spontaneously differentiate after five days in the differentiation media thus reducing the relative difference in gene expression. The three-day time point was taken forward for future experiments. RT-PCR analysis of untreated cells revealed expression of *WT1*, *Tbx18* and *Tcf21* confirming epicardial phenotype (**Figure 5.1.i C**).

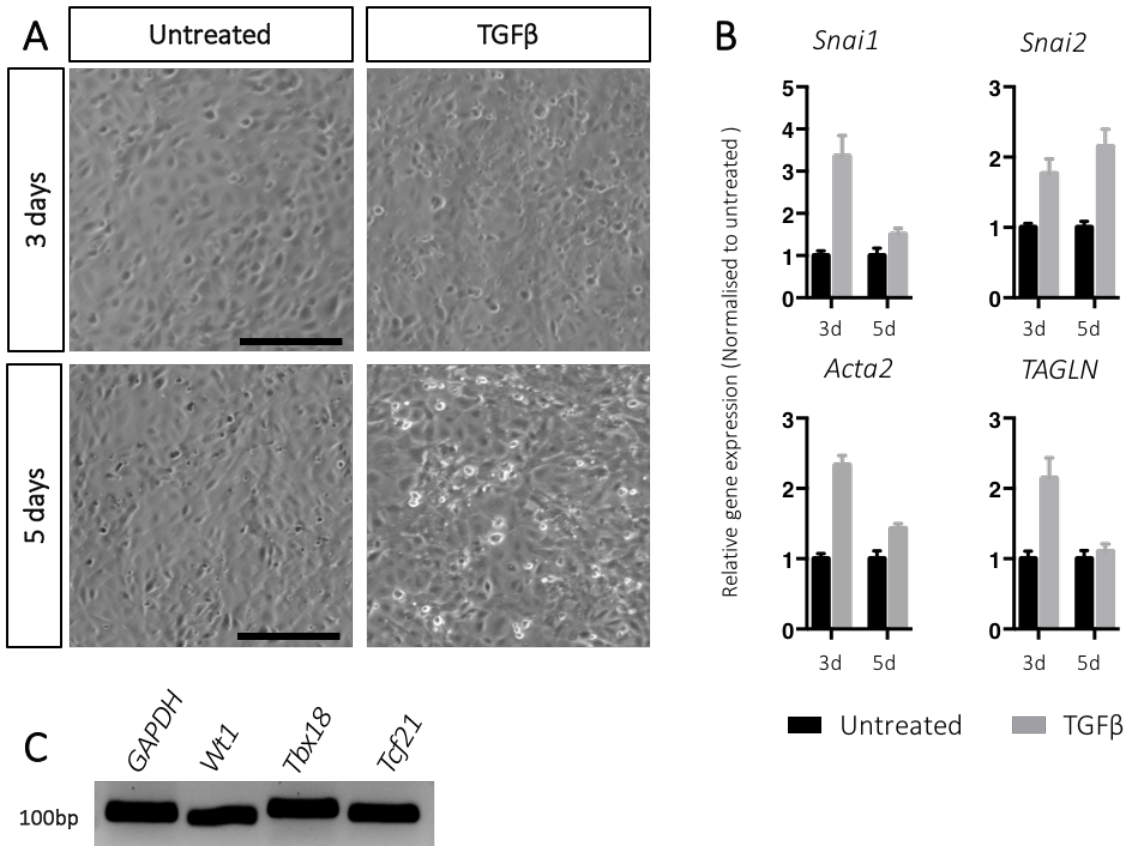


Figure 5.1 MEPDC cultures express epicardial markers and appear to undergo EMT in response to TGFβ treatment. (**A**) MEPDCs plated at a seeding density of $2.5x10^4$ cells/cm^2 were too dense to exhibit morphological signs of EMT in response to TGFβ treatment. (**B**) Despite the high density, cells were collected after three days and five days of treatment for analysis by Q-PCR. Preliminary data indicated that TGFβ induced mEPDC EMT and differentiation as confirmed by increased expression of *Snai1*, *Snai2*, *a-SMA and SM22-a* compared with the untreated control. The greatest response was seen at the three-day time point. (**C**) RT-PCR analysis of untreated cells confirmed expression of epicardial markers *Wt1*, *Tbx18* and *Tcf21*. Scale bar 200 μm in **A**. In preliminary Q-PCR experiments n=1.

With some evidence that the mEPDCs were responsive to TFGβ treatment the protocol was repeated at lower seeding densities of 1.25, 2.5 and 5 x 10^3 cells/cm^2; to investigate whether the expression of EMT related genes was reproducible and also to assess whether this expression was associated with observable morphological changes. At all three seeding densities the Q-PCR analysis revealed upregulation of *Snai1*, *Acta2* and *TAGLN* (**Figure 5.2 A**). At the lowest seeding density, gene expression between replicates was variable and the relative changes did not reach significance; however, at both 2.5 and 5 x 10^3 cells/cm^2 significant upregulation of

EMT genes by TGFβ was seen over all four replicates. This data supported the use of a higher starting cell density: there was negligible difference between expression levels when cells were plated at 2.5 or 5 x 10^3 cells/cm^2 although TGFβ appeared to have induced the greatest effect by a marginal amount in the former; consequently, this cell density was taken forward for future experiments. This data set was encouraging as it demonstrated that the mEPDCs responded to TGFβ and did so in a reproducible manner. Furthermore, a panel of EMT markers was upregulated (*Snai1*, *Acta2*, *TAGLN*), increasing confidence that this was a biologically relevant response. Unlike with the primary human cells, TGFβ induced EMT could not be easily identified just by examining the cultures using brightfield microscopy (**Figure 5.2 B**). Notably, untreated cells appeared more heterogeneous and were less uniform in size and shape than epithelial hEPDCs or rEPDCs; therefore, the morphological differences between the anticipated epithelial versus mesenchymal populations were not as defined.

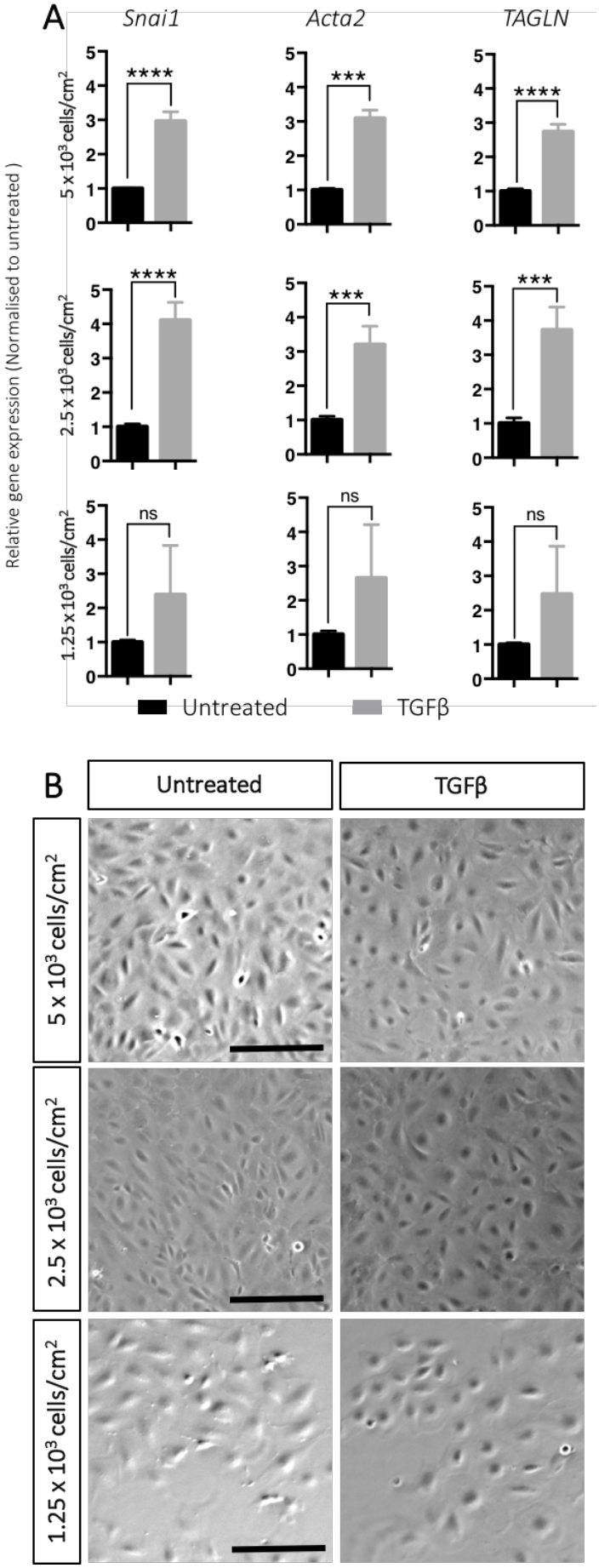


Figure 5.2 Q-PCR confirms mEPDC EMT at transcript level. Morphological changes were not observed by brightfield microscopy. (**A**) Q-PCR analysis revealed upregulation of *Snai1*, *Acta2* and *TAGLN* in TGFβ treated cells at all concentrations. Gene expression data at the lowest seeding density was variable and did not reach significance; however, at both 2.5 and 5 x 10^3 cells/cm^2 significant upregulation of EMT genes by TGFβ was seen over all four replicates. Cells seeded at 2.5 x 10^3 cells/cm^2 appeared to have experienced the greatest effect, therefore, this cell concentration was taken forward for future experiments. (**B**) TGFβ induced EMT was not evident when mEPDC cultures were examined by brightfield microscopy. n = 4; All scale bars in **B** 200µm. Statistics calculated using student's unpaired t-test; *p<0.05; **p<0.01; ***p<0.001; ****p<0.0001

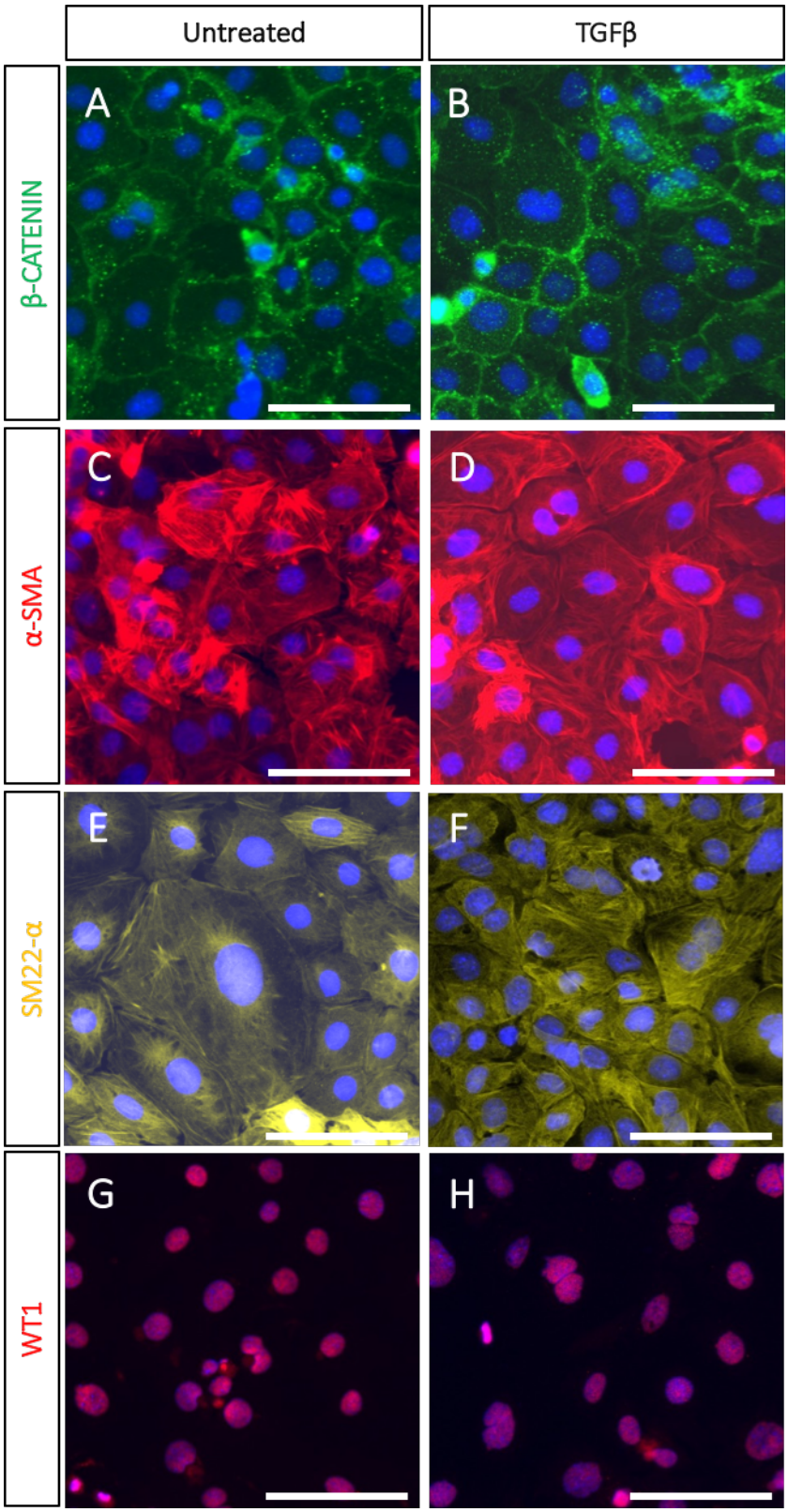


Figure 5.3 Protein expression indicates spontaneous EMT and differentiation in untreated mEPDCs and confirms TGFβ response. WT1 does not display dynamic nuclear distribution. (**A–B**) MEPDCs appear to have formed tight epithelia as confirmed by β-CATENIN staining at the cell membrane. (**C–D**) Several mEPDCs are α-SMA+ in untreated cultures indicating that spontaneous EMT has occurred. TGFβ has induced universal expression of α-SMA filaments. (**E–F**) Untreated cells also express SM22-α, further supporting the observation that spontaneous EMT and differentiation are occurring. All mEPDCs are expressing SM22-α in response to TGFβ treatment. (**G–H**) Unlike the human primary cells, nuclear distribution of WT1 does not appear to be dynamically associated with EMT. All scale bars 100μm.

Protein expression was then examined to validate the Q-PCR data. Cells were seeded onto glass coverslips at a density of 2.5 x 10^3 cells/cm^2 and subject to the same differentiation protocol. β-CATENIN was localised to the cell membrane in both untreated and TGFβ treated cells, indicating the formation of epithelium (**Figure 5.3 A** and **B**); it was also seen distributed throughout the cytoplasm. As previously discussed (**Chapter 1.17**), TGFβ induced EMT releases β-CATENIN from the cell membrane where it then plays a role in WNT signalling (Zhou et al., 2012b). Multiple TGFβ treated cells demonstrated both cytoplasmic and nuclear localisation of β-CATENIN which indicated the induction of EMT in these cultures. However, cytoplasmic distribution was also seen in the untreated cultures which suggested that mEPDCs may be undergoing spontaneous EMT over the duration of the experiment. This observation was confirmed with ICC probing for α-SMA and SM22-α, both proteins are associated with the development of contractile machinery in epicardial cells undergoing EMT and differentiation. Several mEPDCs were α-SMA+ in untreated cultures and TGFβ induced universal α-SMA expression. (**Figure 5.3 C–D**). Numerous untreated cells expressed SM22-α whereas all mEPDCs expressed SM22-α in response to TGFβ treatment (**Figure 5.3 E–F**). Unlike the human primary cells, in which WT1 was seen to localise to the nucleolus, mEPDC WT1 nuclear distribution did not appear to be dynamically associated with EMT meaning that, in this model, it could not be used to monitor the transition. (**Figure 5.3 G–H).** Collectively, this data confirmed that the mEPDC cell line responded to TGFβ treatment in a manner analogous to primary epicardial cells. Unlike the rEPDC cell line, in which only *Acta2* expression was found to increase, mEPDC EMT was associated with upregulation of a panel of characteristic markers, namely *Snai1*, *Snai2* and *TAGLN*. Relocalisation of β-CATENIN and the universal expression of α-SMA and SM22-α in TGFβ treated cells further supported this observation.

In light of this positive data, it was necessary to next assess whether the mEPDC cell line was appropriate for high throughput screening experiments. Keeping in mind that the HTPS protocol required the untreated and TGFβ treated cell populations to be morphologically distinct from one another, it was hypothesised that the spontaneous EMT in untreated cultures might provide an obstacle to image analysis. Therefore, an analogous experiment was conducted in the IM to determine whether TGFβ could induce EMT in the immortalised cells and whether the corresponding differentiated morphology was distinct as compared to the untreated control. MEPDCs were subject to the same differentiation protocol as previously described, except they were not transferred to DM prior to their respective treatments. The relative increases in *Snai1*, *Acta2* and *TAGLN* between untreated and TGFβ treated cells were 1:12.7, 1:7.7 and 1:7.1 respectively (**Figure 5.4**). The ratios of increased expression were much larger than they had been in the experiment conducted in differentiation media (**Figure 5.2**). This data indicated that TGFβ could still induce EMT when the cells were kept in immortalisation media, but that perhaps the two resulting cell populations were more distinct from one another. There was also a small but significant decrease in expression of *Cdh1* (encoding the cell adhesion molecule E-CADHERIN), which further confirmed induction of EMT. TGFβ treated mEPDCs appeared larger than the untreated controls when examined with brightfield microscopy, however this change was not as defined as that observed in primary human cultures (**Figure 5.4 B**). These findings suggested that performing the HTPS protocol on mEPDCs kept in the IM may result in two cell populations with greater morphological contrast, and therefore enable the analysis protocol to identify and differentiate between the untreated and TGFβ treated population.

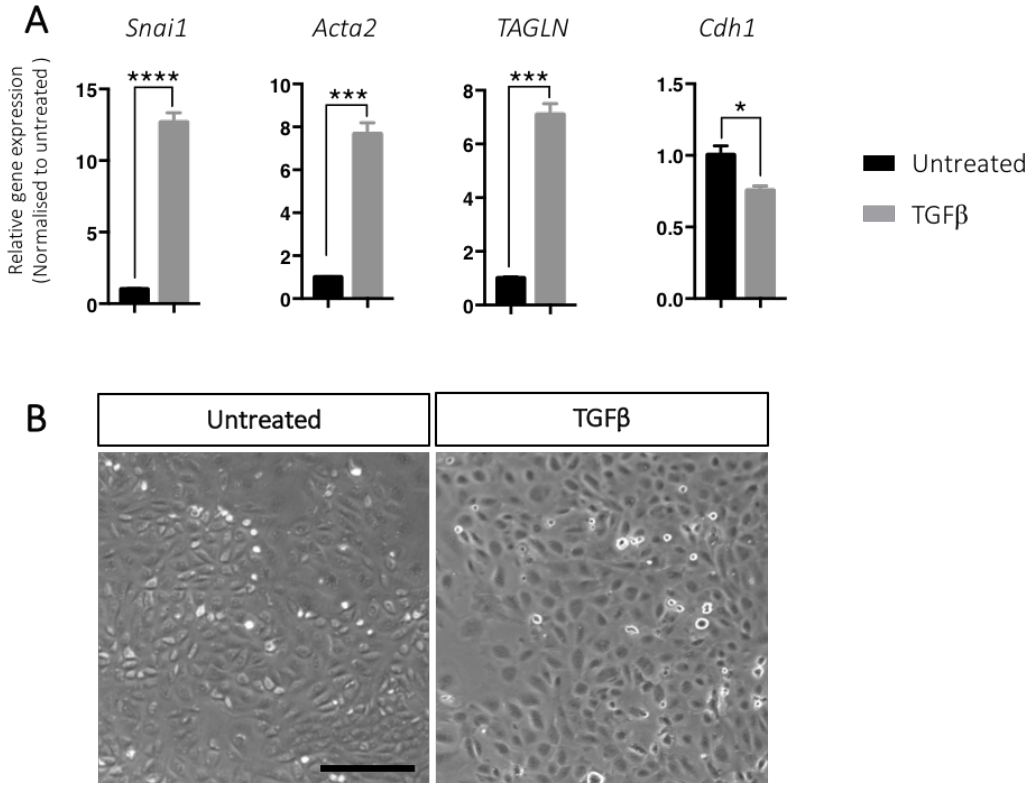


Figure 5.4 Increased expression of EMT markers in TGFβ treated mEPDCs differentiated in immortalisation media. (**A**) Relative increases of *Snai1*, *Acta2* and *TAGLN* between untreated and TGFβ treated cells in IM were much larger than they had been in the experiment conducted in DM. A small but significant decrease in *Cdh1* further confirmed mEPDC EMT. (**B**) Brightfield images of mEPDC cultures differentiated in IM revealed enlarged cells in TGFβ treated populations. Scale bar in **B** 100μm. Statistics calculated using student's unpaired t-test, *p<0.05; **p<0.01; ***p<0.001; ****p<0.0001

To further confirm and characterise EMT in immortalised mEPDCs, the same ICC analysis of EMT marker expression was conducted (**Figure 5.5**). As with the rEPDC cultures, β-CATENIN-was not located along the cell membrane at the edge of the cell sheet (**Figure 5.5 A,** arrowhead) again indicating its role in stabilising cell-cell contacts (Tian et al., 2011b). Untreated immortal mEPDCs had formed tight epithelia as confirmed by β-CATENIN staining at the cell membrane. Conversely, β-CATENIN was not uniformly distributed at the membrane in TGFβ treated cells and was also located around the nuclei (**Figure 5.5 B,** arrowhead) suggesting a role in cell signalling. Several α-SMA+ cells were identified in the untreated

cultures (**Figure 5.5 C**); α-SMA fibres were thicker and more abundant in treated cells (**Figure 5.5 D**). Once again, untreated cells were expressing SM22-α, however it was strongly expressed in all mEPDCs in response to TGFβ treatment (**Figure 5.5 E–F**). Cortical actin staining confirmed epithelial morphology in untreated cells. In contrast, TGFβ had induced stress fibre formation across the cell body and revealed ether the dissolution of, or failure to form, a continuous cell sheet. Cells in the TGFβ treated cells were also larger than those in the control.

Both the Q-PCR and ICC data indicated that immortalised mEPDCs were able to undergo TGFβ induced EMT and differentiation, despite not being transferred to the differentiation media. Furthermore, performing the EMT experiment on immortalised cells resulted in more defined morphological differences between the two cell populations which could potentially be used by an automated analysis protocol to differentiate between the two phenotypes.

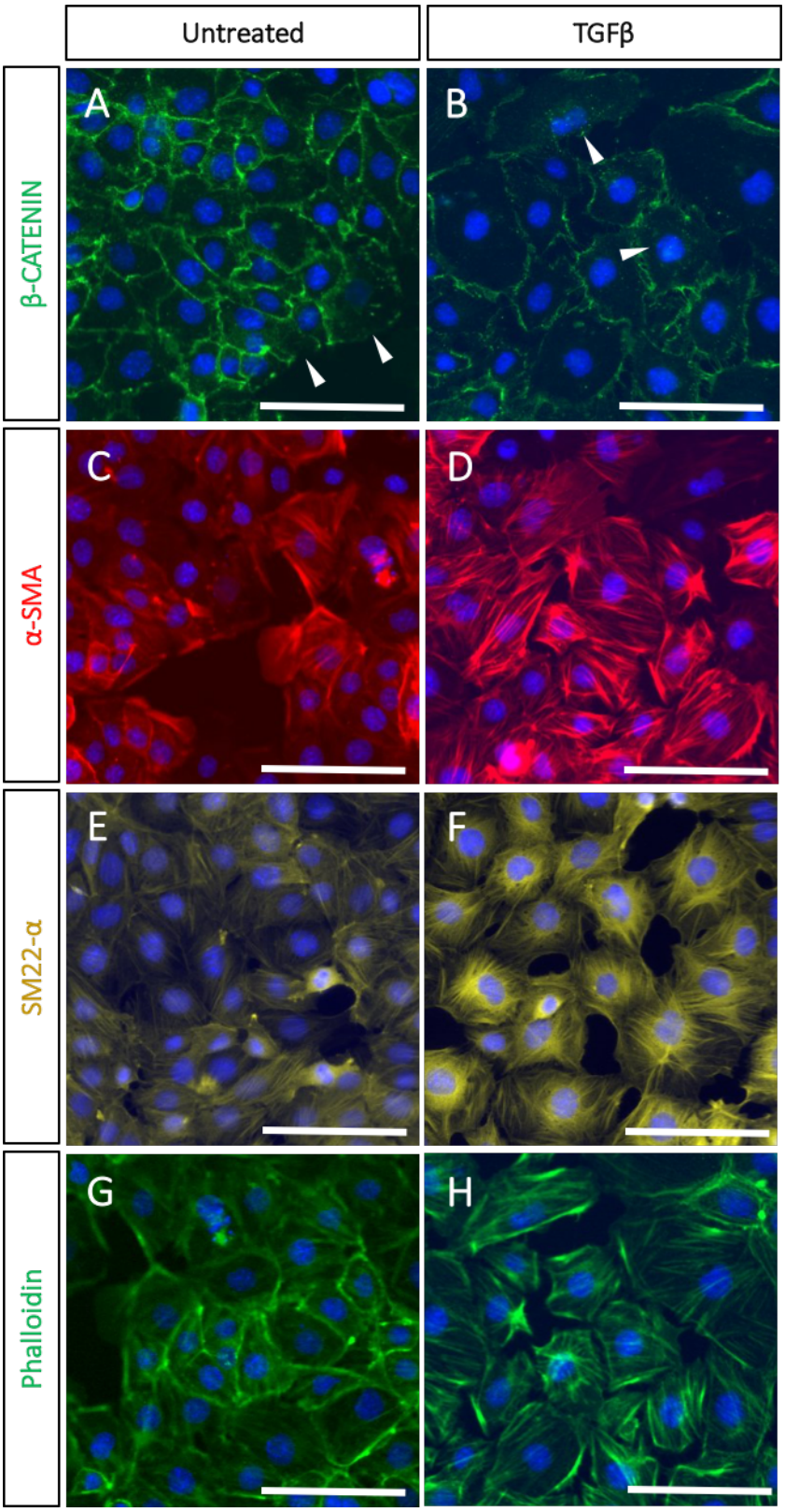


Figure 5.5 TGFβ can induce EMT in immortalised mEPDCs. (**A**) Untreated mEPDCs have begun to form tight epithelia as confirmed by β-CATENIN staining at the cell membrane: none is observed at the edge of the cell sheet (arrowhead) (**B**) β-CATENIN distribution is less uniform in TGFβ treated cultures; some protein localisation was seen surrounding the nuclei suggesting a role in cell signalling (arrowhead). (**C–D**) Several mEPDCs are α -SMA+ in untreated cultures. TGFβ has induced formation of thick α-SMA+ filaments across the cell body. (**E–F**) Untreated cells express some SM22-α. All mEPDCs are strongly expressing SM22-α in response to TGFβ treatment. (**G–H**) Phalloidin staining confirms formation of a tight epithelial monolayer in untreated cells; in contrast TGFβ treatment has induced stress fibre formation across the cell body. All scale bars 100 μm.

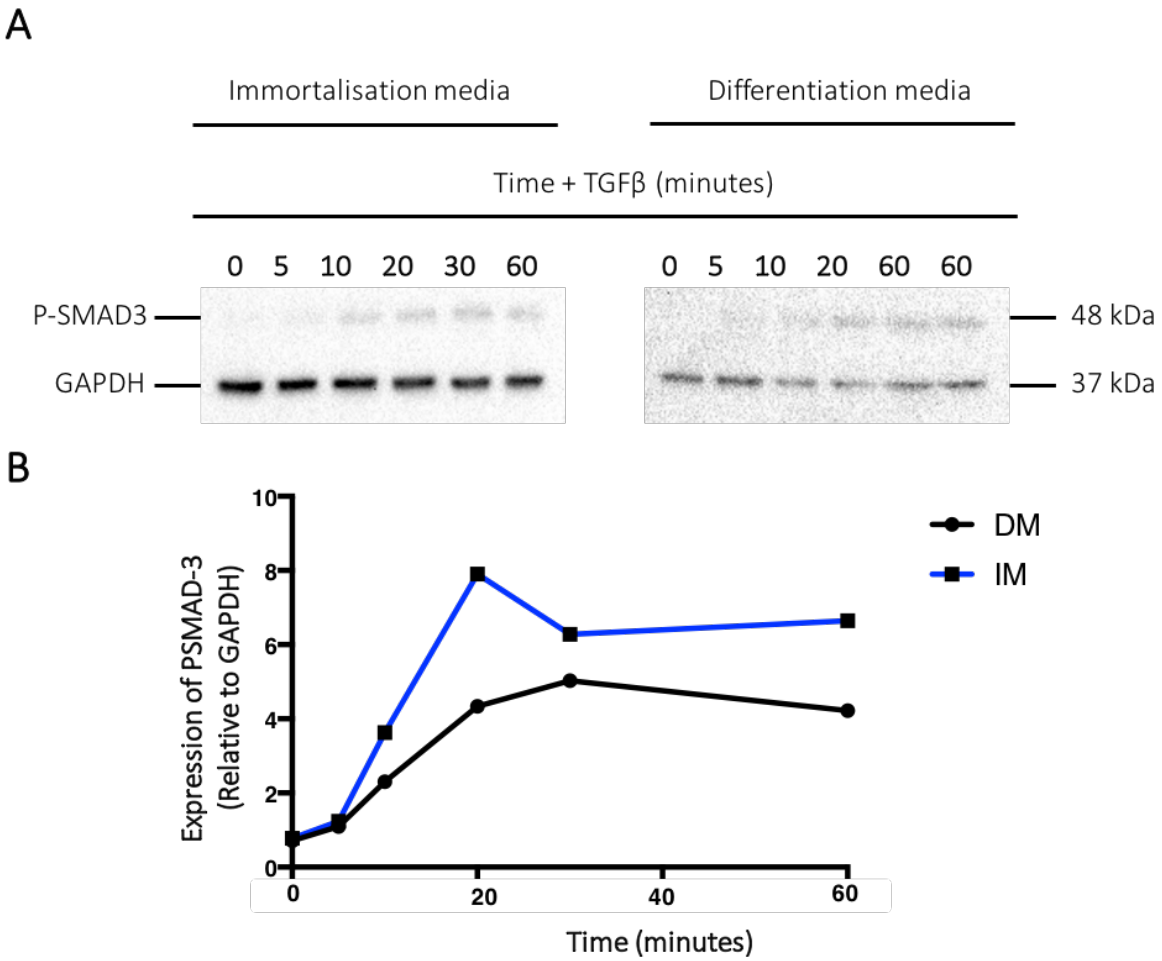


Figure 5.6 Quantitative western blot confirms TGFβ pathway activation. (**A**) mEPDCs in both immortalisation and differentiation media were treated with 2 ng/mL of TGFβ for 0, 5, 10, 20, 30 and 60 minute. Western blot confirmed increased expression of P-SMAD3 after 10 minutes of incubation with TGFβ in both experiments. (**B**) Quantitative analysis revealed higher P-SMAD3 expression, relative to GAPDH, in the immortalised cells compared to the differentiation media.

The final experiment to characterise the mEPDC EMT model was to perform a western blot, probing for P-SMAD3, in order to confirm activation of the TGFβ pathway. In an experiment analogous to the one performed in the rEPDCs (**Chapter 4.1**), mEPDCs were serum starved for 24 hours then treated with 2 ng/mL of TGFβ for 0, 5, 10, 20, 30 and 60 minutes before being collected for analysis. The phosphorylation assay was performed in both immortalisation media and differentiation media for comparison. The western blot confirmed increased expression of P-SMAD3 after 10 minutes of incubation with TGFβ in both immortalisation and differentiation

media. This demonstrated that recombinant TGFβ was successfully activating the signalling pathway and thus was likely responsible for the observed phenotypic changes characteristic of EMT (**Figure 5.6 A**). Quantitative analysis by scanning densitometry revealed higher P-SMAD3 expression, relative to GAPDH, in the immortalised cells compared to the differentiation media (**Figure 5.6 B**). This supported the Q-PCR and ICC data in suggesting that the differentiation media induced spontaneous EMT in mEPDC cultures, resulting in fewer observed morphological differences between the untreated and TGFβ treated populations.

5.2 Utilising mEPDCs for high throughput screening

After successfully establishing a reproducible model of epicardial EMT in the immortalised mEPDC cell line, as determined by QPCR and ICC, the next task was to assess whether it could be used for automated phenotypic screening. MEPDCs were plated into 384-well plates in IM: a cell titration was performed at three densities, 1.25, 2.5 and 5 x 10^3 cells/cm^2, to gauge which would be the most suitable for assessing EMT in high throughput experiments. The lowest cell concentration was too sparse and cultures failed to grow efficiently so it was not considered further. The remaining cells were cultured for three days in untreated IM or IM + TGFβ before being fixed and stained with DAPI, cell mask and phalloidin. Samples were treated for either three or 7 days to see whether a greater effect was exerted by TGFβ by extending the time frame. After staining, the plates were imaged on the PerkinElmer High Content Imager (tdi.ox.ac.uk/high-content-imaging) and then analysed using the previously established protocol (**Chapter 3.3**). After 7 days the cultures were very dense and this time point was not thought to be useful for further investigations. At three days there appeared to be some variation in cell morphology (**Figure 5.7**); at the lower cell density stress fibres and cortical actin were seen in both untreated and TGFβ treated cells; however, this was more pronounced in treated cells which also appeared to be larger (**Figure 5.7 A–B**). At the higher plating density treated and

untreated cells looked very similar and it was difficult to differentiate between the two (**Figure 5.7 C–D**).

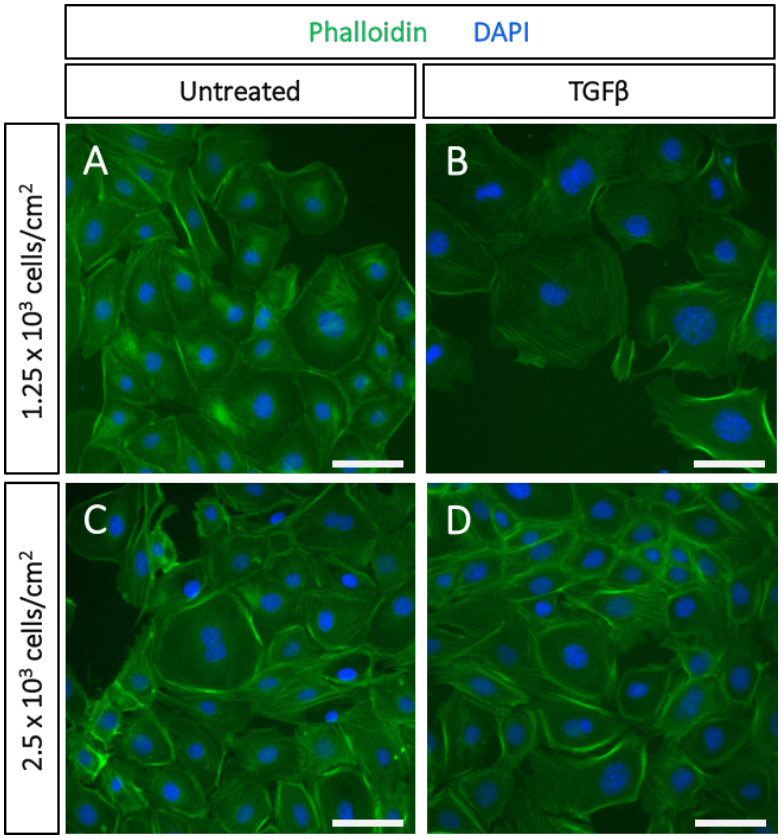


Figure 5.7 MEPDCs are not suitable for analysis with high content screening. MEPDCs were seeded into 384-well plates at 1.25 and 2.5 x 10^3 cells/cm^2 and subject to the previously established differentiation protocol before being fixed, stained with DAPI, Phalloidin and cell mask and imaged on the PerkinElmer High Content Imager. (**A–B**) Despite enlarged cells and stress fiber formation in TGFβ treated cells, the analysis program was not able to distinguish between the populations. (**C–D**) At higher cell density morphological differences between untreated and TGFβ treated cells were less distinct. All scale bars 50 µm. Cells were fixed after three days of differentiation.

Unfortunately, once again the automated analysis protocol was unable to distinguish between treated and untreated cells in this system. Looking through the images it appeared that mEPDC morphology was highly dependent on the cell density not only of the well as a whole well but of the local surrounding area. Patches of cells that had clumped together were small and resembled tight epithelium irrespective of whether they had been treated with TGFβ or not. Conversely, patches of the cultures that were less dense exhibited stress fibre formation and

appeared mesenchymal. Considering the options moving forward, other morphological features that could be used markers of EMT were considered.

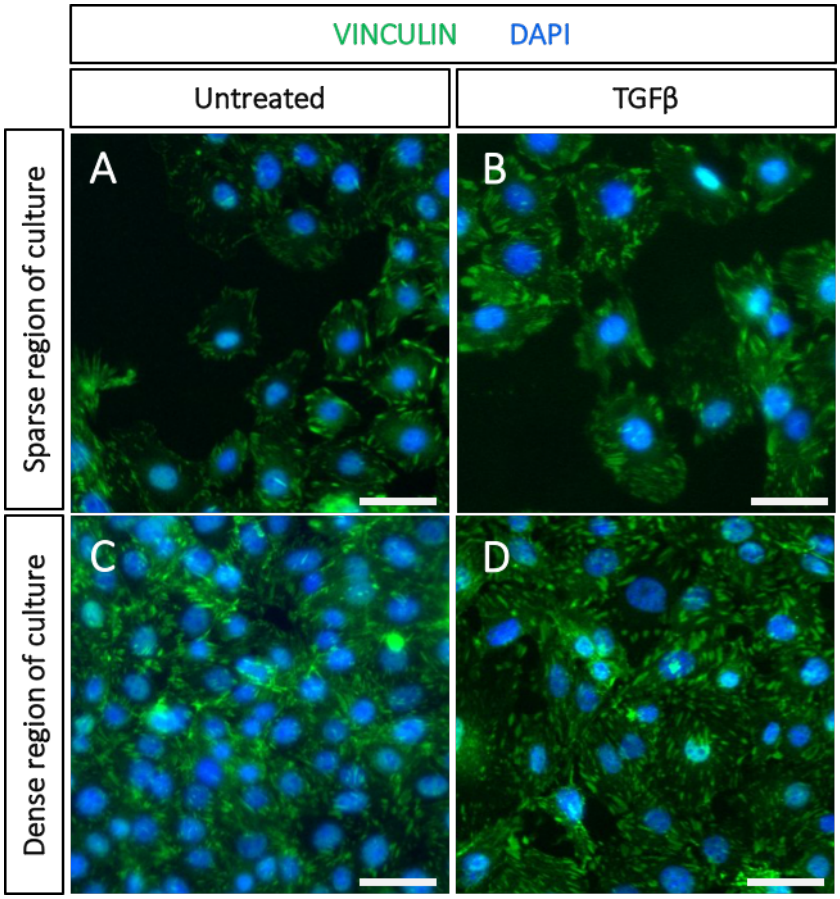


Figure 5.8 MEPDC VINCULIN expression was not a suitable marker of EMT. Both untreated and TGFβ treated mEPDCs expressed VINCULIN both in sparse (**A–B**) and dense (**C–D**) patches of the culture, meaning it was not a suitable marker for EMT in this model. All scale bars 50 μm.

Characterisation studies had already revealed that WT1 relocalisation was not seen during mEPDC EMT (**Figure 5.3**), so this could not be used as a marker. Furthermore, because untreated cultures still contained both α-SMA+ and SM22-α+ cells it did not appear that either of these would be useful. As a final resort the mEPDCs were stained for the adhesion molecule VINCULIN, which was found to be highly expressed in TGFβ treated rEPDCs but not in the untreated controls (**Chapter 4.2.2**). However, in the mEPDCs VINCULIN expression was observed in TGFβ treated and untreated cultures in both dense and sparse areas of the same coverslips; therefore, it was not deemed a suitable marker for EMT in this model (**Figure 5.8**).

Collectively, this data suggested that although mEPDC phenotype is variable between TGFβ and untreated cultures, it is also affected by culture density. As had already been demonstrated in both the human and rat studies, a rigorous assay protocol for the HTPS required a 'definitive' readout of EPDC activation. After investigation, it was thought that utilising this method of phenotypic screening in the mEPDC model would be too ambiguous. Thus, it was decided that other characteristics of cell behaviour exhibited by cells undergoing EMT would be investigated, to ascertain whether they could be used as an alternative read out for epicardial activation.

5.3 Developing an mEPDC Scratch Assay

5.3.1 Investigating mEPDC migration in low throughput

Of the numerous phenotypic changes that occur when a cell has undergone an epithelial to mesenchymal transition, increased migratory capacity is one of the most associated traits. In heart formation this ability is essential to EPDC invasion and population of the myocardium. It stands to reason that in order to contribute cells to a regenerative response EPDCs derived from the adult also require migratory capacity. Therefore, it was postulated that rather than use morphological changes associated with cell shape arising from EMT as a positive read out for activation, an experiment could be designed that identified increased mEPDC migration which is itself likely encompasses EMT. To do so, investigations began in to the possibility of setting up a high throughput scratch assay. The *in vitro* scratch assay is a simple method of analysing cell migration (Liang et al., 2007). Cells of interest are grown to a monolayer before a thin scratch 'wound' is made in the cell sheet: this is often done by scraping away the cells with a pipette tip. The cells are then imaged at regular intervals, or tracked via live cell imaging, and the rate of wound closure compared between different experimental conditions.

To determine whether this technique could be of use to us, preliminary experiments were performed at low throughput. To begin mEPDCs were seeded at a density of 6.25 x 10^4 cells/cm^2 in IM. MEPDC migration was assessed under a range of conditions: 1) migration in plain IM media; 2) migration in IM supplemented with 2 ng/mL of TGFβ; 3) migration in IM supplemented with 1 mM or 2 mM of hydroxyurea; 4) IM supplemented with 1 mM or 2 mM hydroxyurea with 2 ng/mL of TGFβ. TGFβ was included in the experiments as a possible positive control: it had already been confirmed that TGFβ stimulates mEPDC EMT *in vitro* so it was assumed this might also confer increased migratory capacity. Hydroxyurea is an inhibitor of ribonuclease reductase which is involved in dNTP synthesis: inhibition of this enzyme prevents DNA synthesis and thus arrests the cell cycle at early S phase (Koç et al., 2004). The aim of the assay was to assess cell migration and not proliferation, therefore, hydroxyurea was included to determine whether suppressing mEPDC proliferation would alter the rate of wound closure and if so, to act as a control to focus the assay on migration.

24 hours after seeding the cells has formed a monolayer; a P1000 pipette tip was used to make scratch in the middle of the well. The scratch wounds were then imaged every 12 hours and the extent of wound closure compared for each treatment group. Upon initial comparison it appeared as though TGFβ increased the rate of wound closure in mEPDCs compared with untreated (**Figure 5.9**). This appeared true whether or not the cells were also treated with hydroxyurea. Scratch wounds in mEPDCs treated with hydroxyurea (data shown for 1mM concentration) appeared to be close at a slower rate than those without; this suggested that cell proliferation contributed to wound closure of the latter.

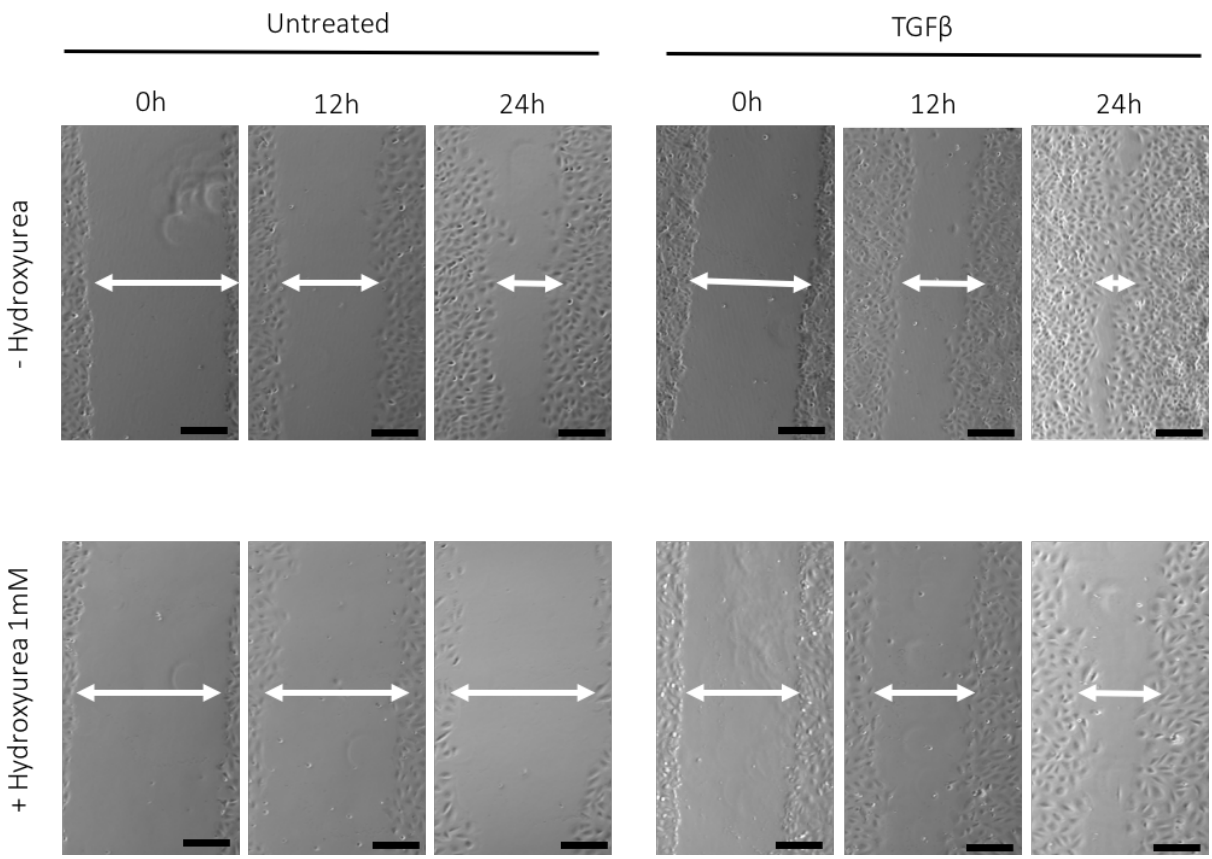


Figure 5.9 TGFβ appears to increase rate of mEPDC wound closure over 24 hours. MEPDCs were allowed to form a monolayer before a scratch wound was made in the culture with a P1000 tip. TGFβ appeared to increase the rate of wound closure in treated cells both with and without hydroxyurea (data shown for 1mM). Hydroxyurea appeared to slow down the rate of wound closure compared to untreated cells suggesting that cell proliferation was contributing to wound closure. All scale bars 200 μm.

To investigate whether hydroxyurea was indeed inhibiting cell proliferation, cells that had been grown on coverslips and treated with the same combinations for 24 hours were fixed and stained with phalloidin and anti-Ki67. Ki67 is a protein phosphatase-1 binding protein that is only present in the nucleus during active phases of the cell cycle, thus it is widely used as a proliferation marker. Its exact functional activity is still not entirely understood; however, recently it was found to act as a scaffolding protein helping numerous nucleolar proteins associate to the reassembling nucleolus after mitosis (Booth et al., 2014; Scholzen and Gerdes, 2000). Nuclear distribution of Ki67 is highly dynamic and associated with specific stages of the cell cycle; during G_1, when the cell is synthesising mRNA and proteins essential for division,

Ki67 is seen at a number of discrete foci throughout the nucleus. During S phase, when DNA is replicated in the nucleus, Ki67 is exclusively nucleolar. This is then replaced by diffuse nuclear staining throughout the G_2 phase where the cell grows and synthesises more proteins in preparation for mitosis (Kill, 1996; Manoir et al., 1991). Hydroxyurea inhibits cell proliferation by preventing DNA synthesis hence the cell cycle is arrested at G_1/early S boundary (Koç et al., 2004).

MEPDCs treated +/-TGFβ but with no hydroxyurea and stained with anti-Ki67 displayed a range of nuclear Ki67 patterning indicating that the cells were at various different stages of the cell cycle (**Figure 5.10 A–B**). Interestingly, in a number of TGFβ treated cells Ki67 was localised to a number of discrete foci, characteristic of G_1 (Manoir et al., 1991). TGFβ is also known to be a potent anti-mitogenic that prevents S-Phase entry: this discrete patterning may identify mEPDCs stuck at this G_1-S boundary (**Figure 5.10 B**, arrowheads) (Hocevar and Howe, 1998). In both hydroxyurea treated cell cultures, if present in the nucleus, Ki67 was primarily seen localised to large subnuclear compartments which may have represented the nucleoli (Manoir et al., 1991). This indicated that the cells were stuck in the early S phase and suggested that hydroxyurea was indeed inhibiting cell proliferation.

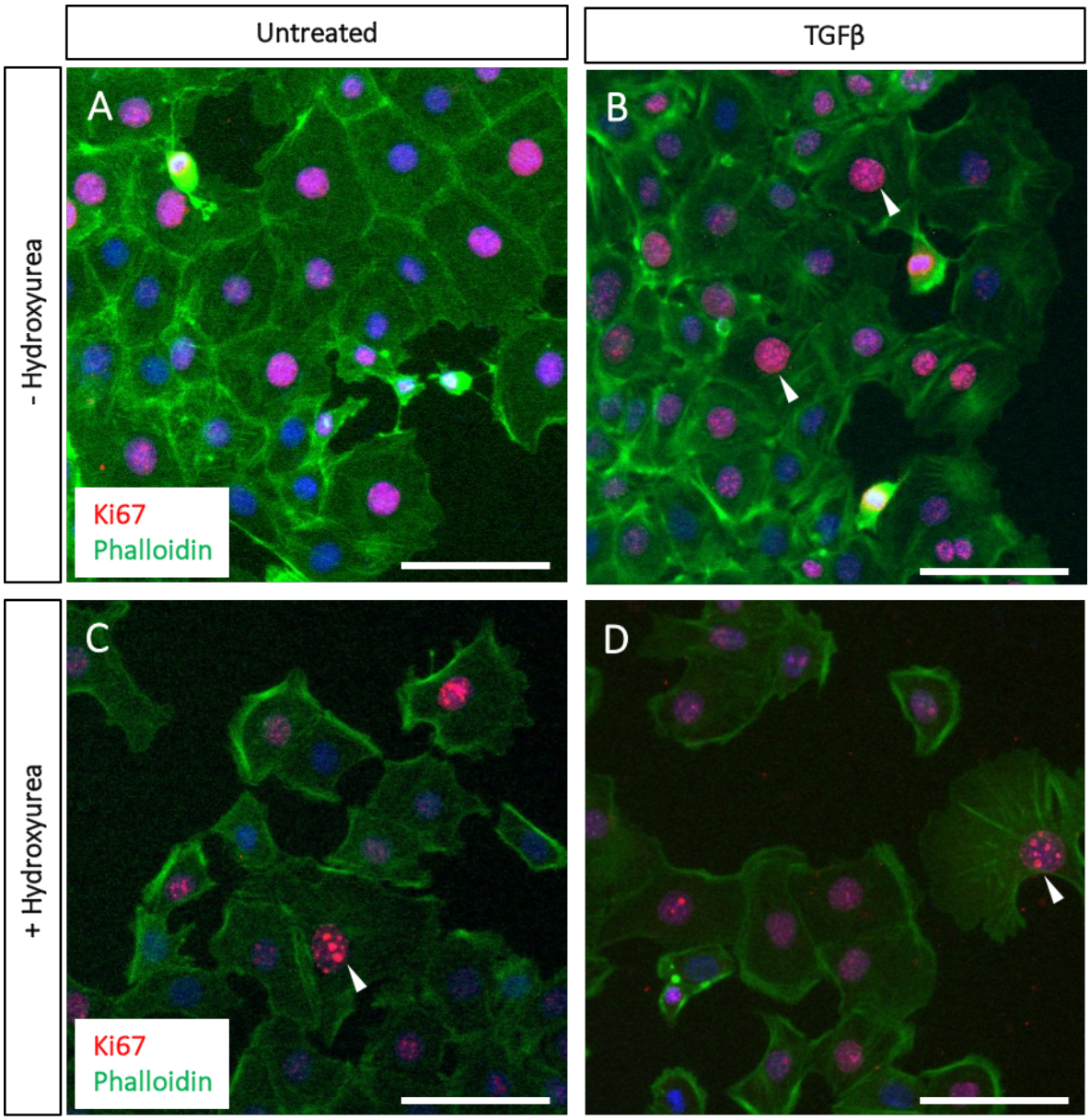


Figure 5.10 Hydroxyurea arrests the cell cycle at early S phase. (**A**) Untreated mEPDCs exhibit varied nuclear Ki67 patterning representative of various stages of the cell cycle. (**B**) A number of TGFβ cells display Ki67 at a number of discrete foci (arrowhead) indicating they have been prevented from exiting G_1. (**C–D**) In cells treated with hydroxyurea Ki67 appears to be localised at the nucleolus (white arrows). This confirms that hydroxyurea treatment has inhibited DNA synthesis thus the cells are stuck at the G1/S boundary and cannot undergo mitosis. All scale bars 100 μm.

From the preliminary data, it appeared as though mEPDCs were able to migrate to close a scratch wound, and that TGFβ increased the rate of closure. Hydroxyurea was found to inhibit mEPDC proliferation and thus would allow measurement of only migratory contribution to wound healing. However, while performing these experiments it became clear that an automated

procedure was required if the experiment were to be useful for screening in high throughput for several reasons. Firstly, the current protocol was conducted in 12-well plates and imaged by hand, which is not a suitable design in which to test hundreds or thousands of small molecules. Secondly, the scratch wounds were made by hand, meaning that despite best efforts they were not of uniform size and shape. The rate of cell migration can be affected by their proximity to other cells (Jonkman et al., 2014), thus a procedure that created equal scratch wound in all wells was required. When using the in house Leica microscope for live imaging there was not a suitable magnification setting that could measure the whole wound. This meant that several images of each scratch were taken at each time point and, despite taking the stage coordinates of each picture, it was not possible to image the exact same area of the scratch as it closed. Finally, an automated image analysis protocol was required in order to remove subjectivity from the analysis protocol. To address these issue an automated scratch assay was established with the help of the Target Discovery Institute, Oxford (tdi.ox.ac.uk).

5.3.2 Developing an automated Scratch Assay

With the assistance of Alison Howarth, a research assistant at the Target Discovery Institute, a 96-well automated scratch assay was developed. The first task was to find an appropriate cell density to ensure mEPDCs formed a complete monolayer ~16 hours after plating. Cells were plated in to gelatine coated 96 well CellCarrier plates in IM at densities of 2, 2.5, 3 and 3.5 x 10^4 cells/well. After 12 hours, cells seeded at 3 x 10^4 had formed a single monolayer, thus this density was taken forward for future experiments. A scratch was made across each well using the a IncuCyte WoundMaker™ (essenbioscience.com). The wound maker tool consists of 96 pins that are inserted into the cell culture plates; a uniform scratch is made across each well when the pins are moved across the culture surface by depression of a lever. The media and cell debris were removed using an automated liquid handler and replaced with either plain IM, IM

with 2 ng/mL TGFβ, IM with 1mM hydroxyurea or IM with 1mM hydroxyurea with TGFβ. The cells were imaged every 6 hours on the PerkinElmer Operetta High Content Imager and on the GE InCell 6000 High Content Imager (tdi.ox.ac.uk/high-content-imaging) until the wounds closed at between 42–48 hours.

The first observation made was that cells treated with hydroxyurea died between 30–36 hours which was before the scratches had closed. Hydroxyurea is known to be cytotoxic in several cells lines, via several mechanisms including generation of free radicals which react with and deactivate numerous cellular macromolecules (DeSesso, 1979). Unfortunately, it appeared that extended culture in hydroxyurea had cytotoxic effects on the mEPDCs which were exerted prior to closure of the scratch wound, therefore, its use was deemed unsuitable for this assay.

To analyze the preliminary automated experiment, two sets of images were captured, one from each of the imaging systems. The PerkinElmer Operetta takes images of the experiment wells from underneath the plate and, even at its lowest magnification, could only capture a third of the scratch at a time. This meant that large data sets were generated as each treatment at each time point had three images that required stitching together. The mEPDCs are flat, adherent and transparent which resulted in poor image contrast, which was likely to be particularly poor because the images were taken through one growth plane (Drey et al., 2013). The poor contrast between the cells and the scratch surface, meant the operetta was not able to accurately measure the scratch area (**Figure 5.11 A**).

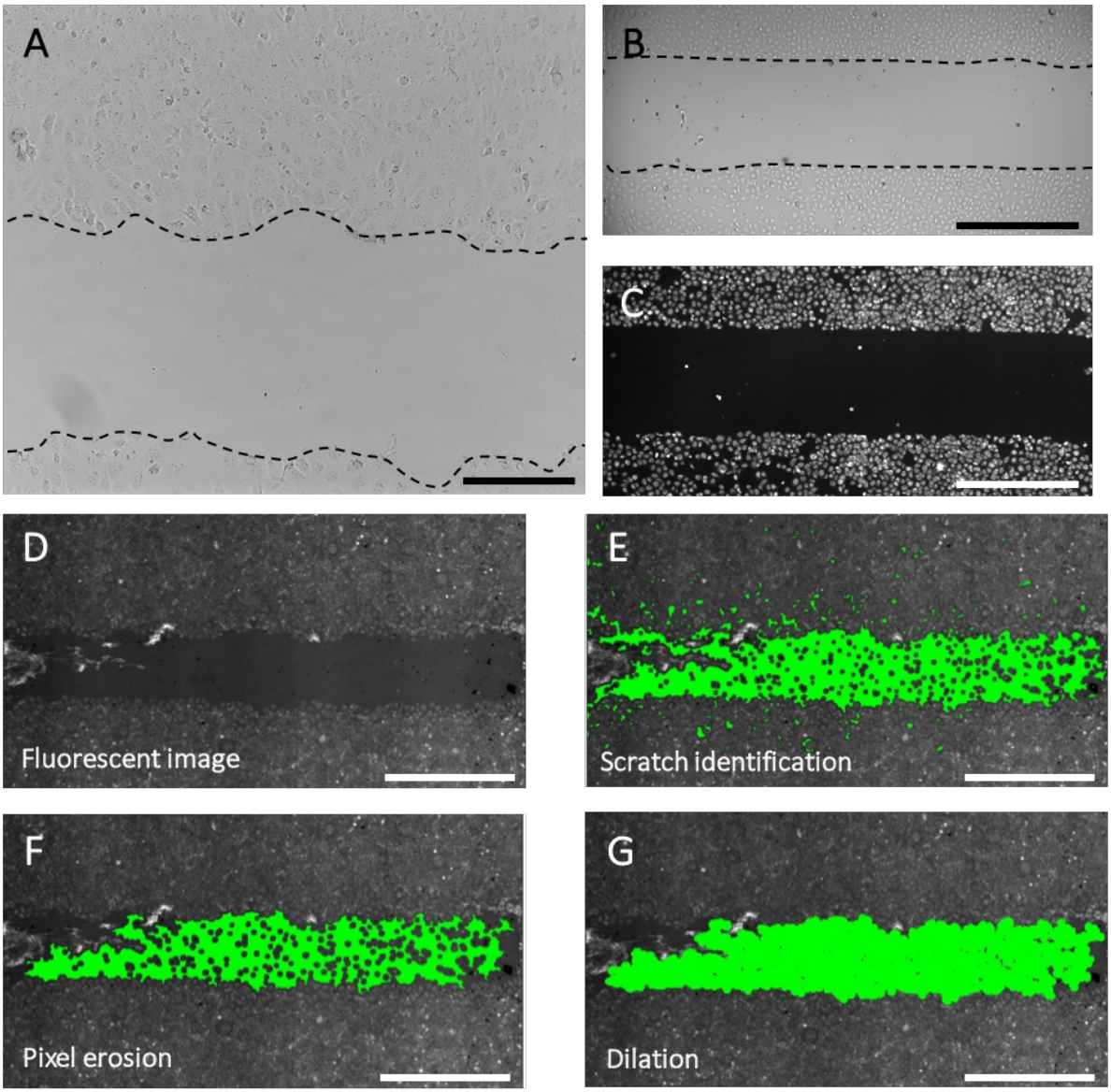


Figure 5.11 Development of a fluorescent, automated mEPDC scratch assay. (**A–B**) Brightfield images taken on the PerkinElmer (**A**) and InCell High Content imager (**B**) did not have sufficient contrast for automated measurement of the scratch wound. (**C**) MEPDCs dyed with the fluorescent probe CellTracker™ could be imaged with fluorescence which produced images with clearly defined scratches. (**D–F**) An automated analysis protocol was developed to measure the area of the scratch, identified by pixel intensity. A series of pixel erosion and dilation steps ensured correct measurement. (**H**) Comparing the scratch wound areas over time indicated that in TGFβ treated cells the scratch wound closed faster than the untreated controls. N = 3 for TGFβ and 2 for untreated.

Images from the InCell were much better: the 4x magnification allowed the whole scratch to be captured and thus greatly reduced the amount of data generated (**Figure 5.11 B**). Unfortunately, the InCell Analyzer software also had trouble distinguishing the scratch area from the cells due to a lack of contrast. Therefore, the assay was repeated with an additional step: prior to making the scratch wound, the cells were stained for 30 minutes with CellTracker™ (thermofisher.com). CellTracker™ is a stable, cell permeable, non-toxic fluorescent dye that contains a thiol-reactive chloromethyl group. Once in the cytoplasm CellTracker™ reacts with free thiols residues of amino acids forming a covalent linkage (Hayat, 2006), or reacts with glutathione in the cell forming a membrane impermeable adduct (http://www.biocenter.hu/pdf/CellTrackergreen.pdf). After being stained, the mEPDCs could be imaged using the InCell fluorescent microscope: this generated images in which the area of the scratch was clearly defined (**Figure 5.11 C**). After the images had been collected, an analysis protocol was designed that could measure the area of the scratch wound based upon the pixel intensity (**Figure 5.11 D–E**). The measured area could be adjusted by a series of pixel erosion and dilation steps to ensure only the scratch area was being calculated (**Figure 5.11 F–G**). Despite the fact that CellTracker™ is supposedly unable to exit the cell, the dye leached out over time making the scratch less defined (Compare **Figure 5.11 C** and **D** scratch intensity). As the images were captured every six hours over the duration of the experiment the contrast in fluorescent intensity between the cells and the scratch/ surrounding media became successively less defined. To help circumvent this issue the media was replaced every 24 hours which removed the background signal; however, the analysis protocol still required slight adjustment for each time point as the intensities changed.

The InCell Analyzer measured the scratch wound area and returned a value for each time point in mm^2; the raw data was plotted as area (mm^2) against time which revealed that TGFβ scratch wounds closed faster than the untreated controls. Unfortunately, one of the original scratch

wounds made in the untreated wells was half the size of the other replicates and had to be discounted, meaning there were not enough replicates to assess statistical significance of the differences in wound closure.

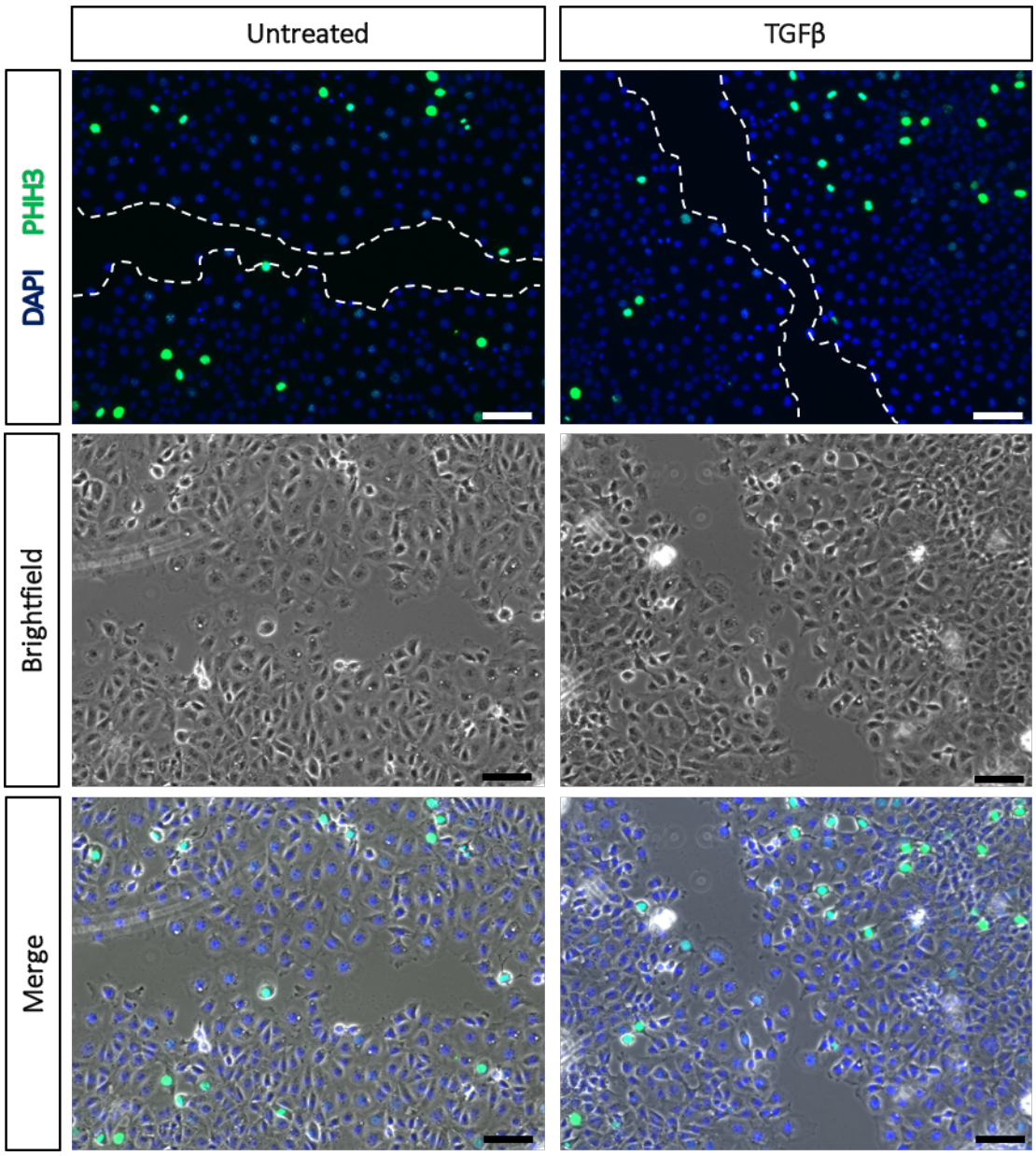


Figure 5.12 MEPDC wound closure is a result of migration, not proliferation. MEPDCs were plated on to glass coverslips in IM. After formation of a monolayer a scratch wound was made through the centre of the culture with a pipette tip. Cells were treated with either plain IM or IM with TGFβ and fixed after 24 hours. Staining for the proliferation marker PHH3 revealed minimal cell division at the leading edge irrespective of the treatment received. This indicated that proliferation was having minimal contribution to wound closure. All scale bars 100 μm.

The final experiments in the development of the scratch assay were designed to ensure that the wound closure observed in mEPDC scratch wounds was a result of cell migration not proliferation. This was an essential study because hydroxyurea was found to be cytotoxic over the length of the scratch assay and thus could not be used to suppress cell proliferation. MEPDCs were seeded on to coverslips in 12-well plates and a pipette tip used to make a scratch across the centre of culture after the cells had formed a monolayer. The cells were treated +/- TGFβ for 24 hours before being fixed and stained for the proliferation marker Phosphohistone-H3 (PHH3) (**Figure 5.12.v**). Phosphorylation of histone three is mitosis specific: chromatin phosphorylation can occur at different stages of cell division but metaphase chromosomes are always highly phosphorylated (Hans and Dimitrov, 2001; Veras et al., 2009). Imaging of the scratch wound in both untreated and treated mEPDCs revealed sporadic PHH3+ cells at the leading edge thus proliferation appeared to be minimally contributing to the closure of the wound. Some dividing cells were seen further back in the cultures away from the scratch wound.

The mEPDCs were also stained with α-SMA and β-CATENIN to allow further phenotypic analysis of cells at the leading edge: the scratch area in each image is along the bottom edge (**Figure 5.12**). α-SMA staining revealed that cells at the leading edge of both untreated and TGFβ treated scratch wounds mEPDCs had begun to form lamellipodia and filopodia, both hallmarks of cell migration (Machesky, 2008). Lamellipodium is the membrane protrusion observed to be projected in to the scratch area from the front edge of the cells (**Figure 5.13**, arrowheads): the lamellipodium is filled with a complex actin network including the filamentous filopodia that are dynamically formed by actin polymerization (**Figure 5.13**, arrow) (Mattila and Lappalainen, 2008). In migrating cells, filopodia behave as ‘sensors’ extruding out from the cell edge to assess the surrounding microenvironment (Galbraith et al., 2007). Their presence at the leading edge indicated that the mEPDCs have migratory capacity when cultured in untreated

media as well as when treated with TGFβ, although more cells in the TGFβ cultures had a dense filopodia network than in the untreated.

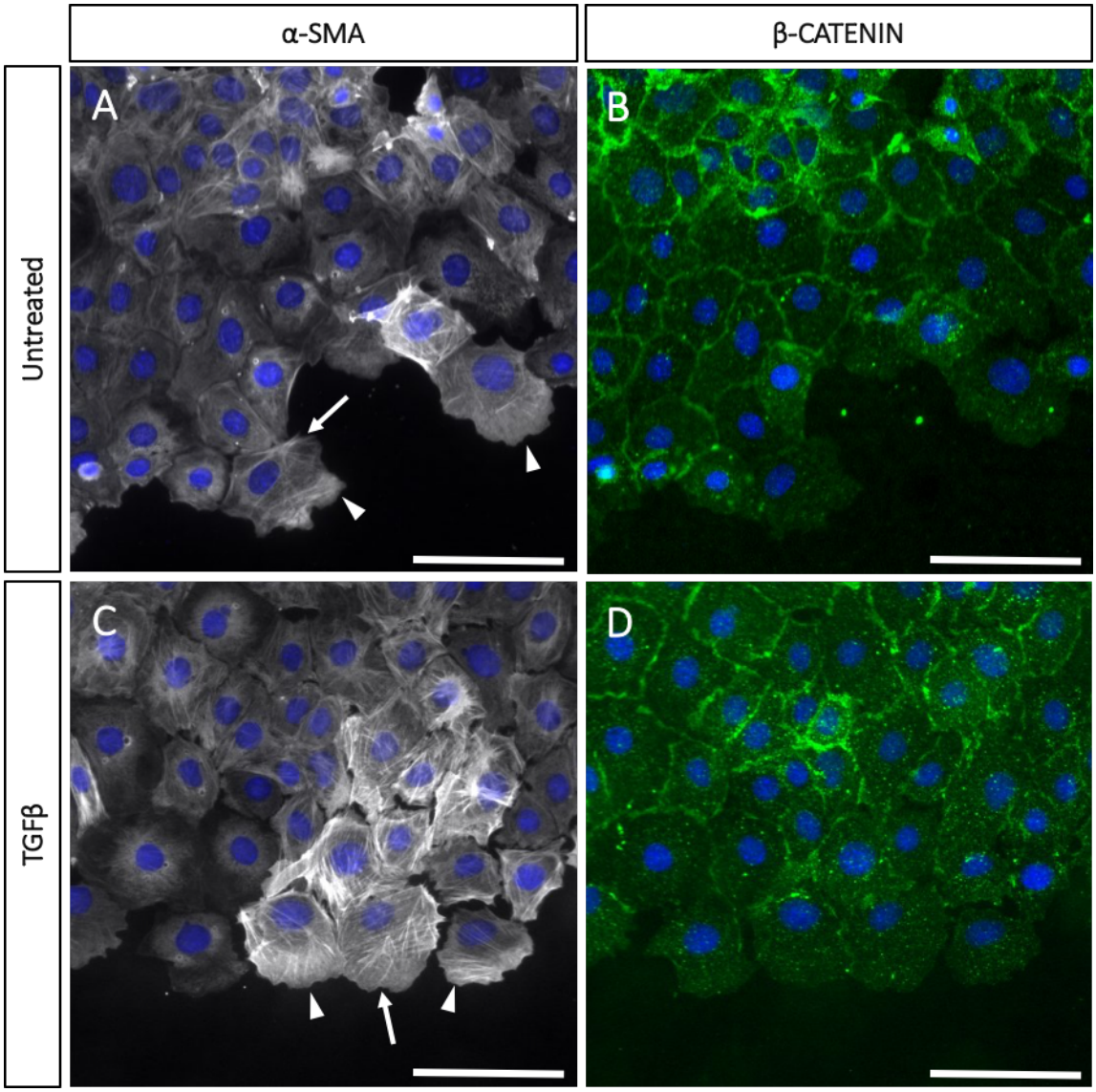


Figure 5.13 Observation of α-SMA and β-CATENIN expression at the leading edge is indicative of mEPDC migration in to the scratch wound. (A and **C)** α-SMA staining of untreated and TGFβ treated mEPDCs 24 hours after induction of a scratch wound revealed formation of lamellipodia (arrowhead) and filopodia (arrow) at the leading edge. (**B** and **D**) β-CATENIN was uniformly located along the cell membrane in untreated cells including in those towards the edge of the cell sheet. TGFβ has induced cytoplasmic β-CATENIN distribution and dissolution of the characteristic membrane patterning associated with epithelium. Scratch area is at the bottom of each image. All scale bars 100 μm.

β-CATENIN staining was seen uniformly distributed along the cell membrane in untreated cells at points of cell-cell contact, indicative of a role in cell-cell adhesion: this was lost at the leading

edge and cytoplasmic staining was also seen which was indicative of EMT (Valenta et al., 2012). In TGFβ treated cells, cytoplasm-wide distribution of β-CATENIN was seen in every cell; protein distribution at the cell membrane was much less uniform than the untreated control and towards the scratch wound most cells had lost the characteristic patterning associated with cell adhesion. This staining suggested that creation of the scratch wound had induced mEPDC migration and EMT in untreated cultures. The addition of TGFβ appeared to enhance this response causing increased filopodia formation and breakdown of the adherens junctions. This is likely to have conferred greater migratory capacity to the cells at the leading edge which explains why the TGFβ treated scratch wounds had closed at a faster rate.

5.4 Summary and discussion

5.4.1 Establishing an EMT model in immortalised mEPDCs

This chapter describes the development of an EMT model in immortalised mEPDCs. In preliminary experiments mEPDCs were cultured in an immortalisation medium, to retain their epicardial phenotype, and then switched to a differentiation medium for experiments (Austin et al., 2008). MEPDCs in DM underwent EMT in response to treatment with TGFβ, confirmed by the increased expression of EMT related genes *Snai1*, *Snai*2, *Acta2* and *TAGLN*. This was further confirmed by relocalisation of β-CATENIN and increased expression of α-SMA and SM22-α. However, untreated mEPDCs were also found to undergo spontaneous EMT and differentiation when switched to the DM. As spontaneous differentiation in hEPDCs had previously impeded automated image analysis, the differentiation protocol was repeated on mEPDCs kept in IM. It was reasoned that if TGFβ could induce EMT in immortalised mEPDCs, the phenotypic differences between untreated and treated cells might be more distinct. This idea was confirmed by Q-PCR analysis in which the relative expression of EMT related genes in treated cultures were found to be several times higher than untreated control: the fold increase

when mEPDCs were differentiated in IM were 2–3 times larger than they had been when the experiment was conducted in DM. The cells were stained to investigate protein markers: untreated cells appeared to be less differentiated and maintained epithelial characteristics, including membrane bound β-CATENIN and cortical actin. There were, however, still a number of α-SMA+ and SM22-α+ cells in untreated cultures. In both DM and IM activation of the TGFβ signalling pathway was confirmed by western blot.

5.4.2 High throughput screening with immortalised mEPDCs

The EMT experiment was next converted to 384-well format; mEPDCs were cultured for three days in IM +/- TGFβ before being fixed and stained with DAPI, phalloidin and cell mask. The cells were imaged and the images subject to the analysis protocol established for hEPDC screening. Unfortunately, despite confirmation of EMT and differentiation by Q-PCR and ICC, the morphological differences between the two populations could not be identified by the analysis software. The experiments so far had confirmed that the mEPDC cell line reliably responded to TGFβ treatment at a molecular level; however, it was not suitable for the previously established HTPS protocol. In light of this discovery, an alternative assay was sought that could measure epicardial activation using another read out.

Epicardial EMT *in vivo* is associated with increased migratory capacity: therefore, the possibility of designing a scratch assay that was capable of measuring the rate of mEPDC migration was explored. Cells were plated and allowed to form a monolayer before a scratch wound was made with a pipette tip. The cell debris was aspirated and cells treated with plain IM, IM plus TGFβ, IM with 1mM hydroxyurea or IM with 1mM hydroxyurea and TGFβ. The scratch wounds were imaged over time in order to compare the rate of closure under each condition. Hydroxyurea is a small molecule that inhibits cell proliferation: in mEPDCs

hydroxyurea decreased the rate of wound closure compared with untreated controls. Addition of TGFβ increased the rate of wound closure compared with untreated: this effect was seen both in cells that had been treated with hydroxyurea and those that had not. Moving forward the assay needed to be converted to a high throughput format which would allow for screening of large compound libraries.

In collaboration with the TDI the assay was translated to a 96-well, automated format. MEPDCs were plated in to 96-well plates at a range of concentrations and left to form a monolayer over 16 hours: a seeding concentration of 3 x 10^4 cells/well was found to be most suitable. Using the IncuCyte WoundMaker™ a scratch was made across the centre of every well, the cell debris was aspirated and the mEPDCs treated as previously described. In this experiment, mEPDCs treated with hydroxyurea died between 30–36 hours of treatment: cell death occurred before the scratch wounds had healed, therefore, this condition was not included in any further assays. Imaging in the brightfield channel on both the PerkinElmer and InCell imaging systems revealed that the contrast between the cell layer and the scratch was not well defined: this meant that image analysis software was not able to accurately measure the wound area.

The protocol was then adjusted so that prior to making the scratch wounds cells were stained with CellTracker™ a fluorescent dye that allows for live fluorescent cell imaging. With the protocol suitably modified the InCell Analyzer software was able to measure the area of each scratch every 6 hours. The InCell Analyser was preferable to the PerkinElmer imaging software as it was able to capture the whole scratch wound at 4x magnification, thereby reducing the number of images accumulated in the acquisition. After combining the data for the controls, it appeared that TGFβ increased the rate of wound closure. The experiment was repeated on glass coverslips for analysis by ICC: at the leading edge few mEPDCs were PHH3+ indicating that

migration, and not proliferation, was largely responsible for the wound closure. α-SMA expression revealed formation of cell migratory machinery: lamellipodia and filopodia: in both untreated and TGFβ treated mEPDCs at the edge of the cell sheet. Untreated cells displayed membrane bound β-CATENIN and some cytoplasmic localization: TGFβ induced widespread relocalisation of β-CATENIN to the cytoplasm. Together this data demonstrated that mEPDCs migrate to heal a scratch wound made in the epithelial layer: TGFβ treatment appeared to increase the speed of migration, which is likely due to EMT related disassembly of cell junctions and increased α-SMA expression.

In light of these results, it was decided that a small library of compounds would be screened in the newly developed high throughput scratch assay as a proof of principle. This would give the opportunity to increase control replicates and identify whether TGFβ was indeed increasing the rate of wound closure. Furthermore, screening a small library of compounds and validating the resulting hits would determine whether the assay was sensitive enough to identify changes in the rate of wound closure. Finally, there was the possibility of identifying a hit molecule from the compound library to take forward into differentiation assays and SAR studies. Therefore, the next task was the design and synthesis of a small compound library to be used in pilot automated scratch assay, which is discussed in **Chapter 6**.

Chapter 6

Small molecule library design and synthesis

6.0 Introduction: small molecule selection

In order to test the newly developed high throughput mEPDC migration assay (**Chapter 5**), it was decided that a library of compounds would be screened alongside the DMSO and TGFβ experimental controls to determine whether the assay was able to correctly identify both positive and negative modulators of mEPDC migration. Traditionally, high throughput screening utilises 'unbiased' chemical libraries of biologically active compounds that encompass a large range of chemotypes and mechanisms of action; the Pharmakon1600 compound series which was screened in the hEPDC pilot screen (**Chapters 1.19** and **3.2**) is an example of such a library. An alternative strategy is to screen a smaller targeted library that contains compounds predicted to induce change in the assay system. A successful examples of this approach was the design of the small molecule libraries used to identify the compound cocktail '9C' which differentiates cardiac fibroblasts in cardiomyocytes (**Chapter 1.14 2**) (Cao et al., 2016).

The costs of screening large compound libraries is anywhere from hundreds to thousands of pounds and it requires a fully automated procedure to allow swift and efficient reading of all experiment plates at the correct time points (Macarron et al., 2011). Unfortunately, transfer of the plates from the incubator to the InCell Analyser for the duration of the mEPDC scratch assay had to be done manually. For this reason, and due to the preliminary nature of the experiment, it was decided that a small library would be designed utilising the in house libraries available to the Russell lab. The selection criteria for the pilot library was varied but generally the compounds chosen had been reported to induce myogenic or cardiomyogenic gene programs in other *in vitro* experimental systems, such as 5-azacytidine that induces cardiac differentiation in ECSs (**Chapter 1.13**) (Ohtsu et al., 2005). In addition to the stock compounds, a small number of interesting molecules were identified from the literature and either purchased or synthesised.

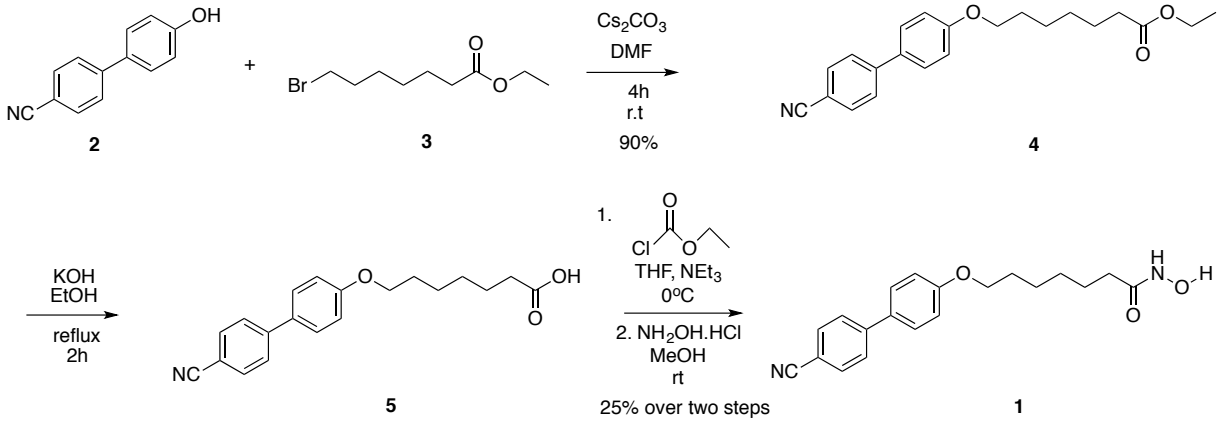
This chapter will detail the compounds chosen for the screen and also document the synthesis of a small selection of compounds that were not commercially available.

6.1 TGFβ mimetic synthesis

The multiple biological functions of the TGFβ protein has led to widespread interest in developing chemical modulators of its activity. The biaryl hydroxamic acid A-161906 **1** (**Scheme 1**) was found to increase luciferase activity in a Mv1Lu cells transfected with a plasminogen activator inhibitor-1 (PAI-1) promoter-luciferase (Glaser et al., 2002). PAI-1 is a downstream target of the TGFβ/SMAD3 signalling pathway which regulates the proteasomal degradation of extracellular matrix components; its activity was found to be essential for epithelial wound healing *in vitro* (Providence and Higgins, 2004). A-161906 mimicked several TGFβ functions including induction of fibronectin deposition and inhibition of collagenase production from human dermal fibroblasts *in vitro*. A-1618906 did not competitively displace TGFβ from its receptor and exerted activity in cells with mutated TGFβ receptors suggesting its function is exerted downstream of receptor binding and later in the signalling pathway. It was also found to be an inhibitor of the histone deacetylases (HDAC), which was unsurprising as the hydroxamic acid motif is commonly observed in HDAC inhibitors (Min et al., 2015). Due to the reported interaction of A-161906 with processes affecting cell migration and adhesion it was synthesised for use in the pilot scratch assay.

A protocol for the general synthesis of biphenyl hydroxamic acids (**Scheme 6.1**) was adapted for the synthesis of **1** (Fesik et al., 1997; Mai et al., 2001). A base mediated displacement reaction between ethyl-7-bromoheptanoate **2** and 4'-hydroxy-[1,1'-biphenyl]-4-carbonitrile **3** gave **4** in good yield. Hydrolysis of the ester was achieved by the reflux of **4** in KOH for two hours which yielded the crude acid **5**. To form the hydroxamic acid **5** was first refluxed with

$SOCl_2$ to generate the acid chloride; this was then treated with hydroxylamine hydrochloride in a mixture of water, THF and 4-methylmorpholine. Unfortunately, this reaction was found to return the starting material; which may have been due to a failure to form the acid chloride or due to rapid hydrolysis of the acid chloride occurring before the hydroxamic acid could form. Instead an alternative protocol was utilised, adapted from a synthesis for the closely related HDAC inhibitor SAHA (Mai et al., 2001). The acid **5** was dissolved in in THF and cooled to 0^{o}C before addition of ethyl chloroformate and trimethylamine. The resulting mixture was filtered and added to freshly prepared hydroxylamine in methanol which gave A-161906 in 25% yield. Both the **1** and its precursor **5** were included in the screen: the acid analogue was not found to exhibit TGFβ mimetic activity and thus was included as a negative control.

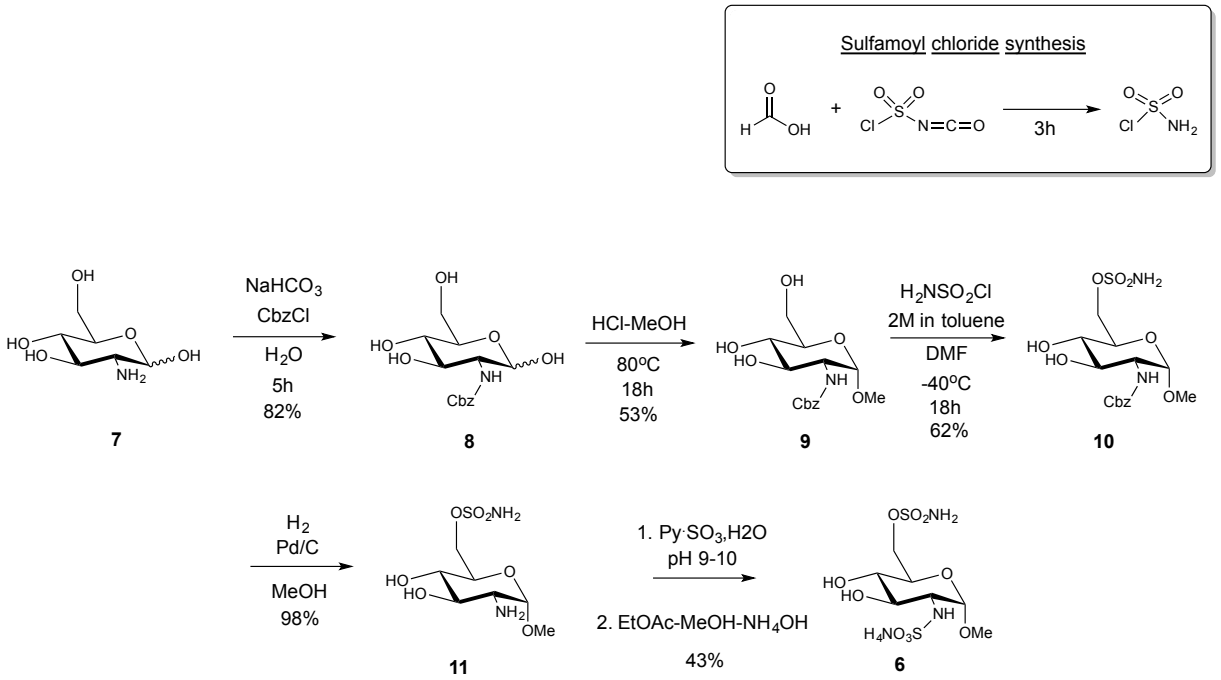


Scheme 6.1 Synthesis of the TGFβ mimetic A-161906.

6.2 Synthesis of small molecule sulfatase inhibitors

The heperan sulfate proteoglycans (HSPGs) are an essential component of the ECM: these membrane-bound glycoproteins act as co-receptors for TGFβ, FGF and other signalling molecules (Sahota and Dhoot, 2009). Away from the receptor sites, HSPGs can sequester macromolecules affecting active ligand concentration and activity (Ramsbottom et al., 2014). The function of HSPG is dependent upon 6-*O* sulfation of the polysaccharide chains (Sahota and Dhoot, 2009). Desulfation is carried out by the sulfatases, a family of 17 enzymes of which

SULF1 and SULF2 are able to edit HSPG sulfation state at the cell surface. Both SULF1 and 2 are expressed in the epicardium and, although their role is yet to be fully elucidated, expression is negatively correlated with epicardial EMT and migration in development (Bochmann et al., 2010; Smart, unpublished). Furthermore, siRNA knock down of both SULF1 and SULF2 was found to induce EMT and increase migration in in rEPDCs *in vitro* (Smart, unpublished). The glucosamine sulfate analogue **6** is a reported inhibitor of both Sulf enzymes (Miller et al., 2015). A sample of **6** was synthesised for inclusion in the automated scratch assay (**Scheme 6.2**).



Scheme 6.2 Synthesis of the small molecule sulfatase inhibitor

Cbz protection of D-glucosamine **7** gave **8** in 82% yield as a mixture of anomers. **8** was then heated to reflux with methanolic HCl yielding **9** as a mixture of α/β anomers with a ratio of 6:1, respectively; the α anomer was isolated by column chromatography with a yield of 53%. For the sulfamoylation of the 6-O, a 2 M solution of sulfamoyl chloride in toluene was first prepared, then added to **9** in DMF at -40^{o}C. The original protocol recommended one equivalent of sulfamoyl chloride solution for sulfamoylation; however, in our hands this reaction was low yielding (~30%) returning a mixture of **10** and starting material **9**. By increasing the sulfamoyl

chloride to three equivalents the yield of **10** could be doubled to 62%. Cbz deprotection by palladium catalysed hydrogenolysis returned **11** in near quantitative yield. The final product **6** was generated by sulfation of the amine with pyridine sulfur trioxide complex and purified by column chromatography in a mixture of EtOAc-MeOH-NH_4OH generating **6**. Both **6** and the primary amine **11** were included in the library for screening, as was an additional reported sulfatase inhibitor OKN 007 (**Appendix table A 6.1 S'**).

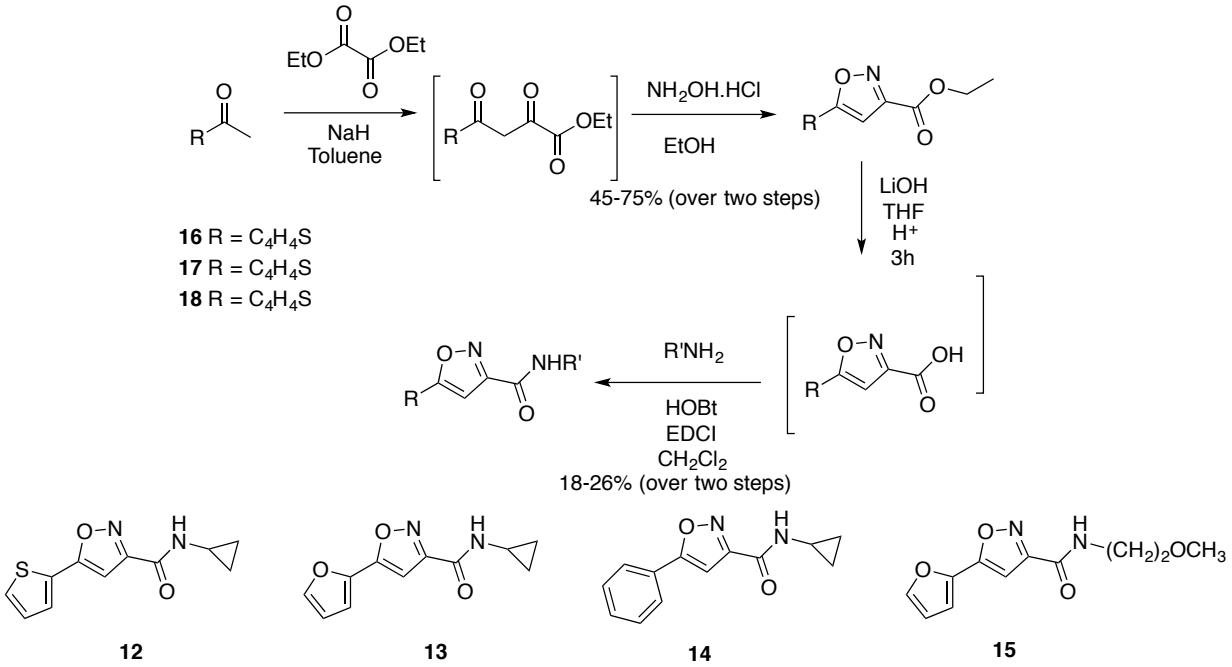
6.3 Isoxasole synthesis

In 2012, the small molecule Isx **12** (**Scheme 6.3**) was found to increase expression of NKX2.5, a protein expressed in cardiac progenitors and their myogenic progeny, in P19 embryonal carcinoma cells (Discussed in detail in **Chapter 1.14.3**) (Russell et al., 2012a). *In vivo*, Isx was found to drive expression of cardiac genes in Notch activated EPDCs, however, cardiac injury ameliorated this response favouring the fibrosis pathways. As Isx had been found to activate cardiac gene expression in a relevant EPDC model, it was synthesised for inclusion in the mEPDC scratch assay. Alongside Isx, three further analogues **13–15** were also synthesised for SAR exploration.

The four isoxazole compounds included in the scratch assay were synthesised via the same general route (**Scheme 6.3**). The parent starting material (**16–18**) was reacted with diethyloxalate and NaH to form the corresponding 4-substituted ethyl-2,4-dioxobutanoates. Generation of the isoxazole moiety was achieved by reflux of the crude dioxobutanoate with hydroxylamine hydrochloride with yields of 45–75% over the two steps. Synthesis of the isoxazole moiety from 4-substituted ethyl-2,4-dioxobutanoates can lead to formation of two possible regiosisomers: the isoxazole-3-carboxylate shown here, or the isoxazole-5-carboxylate. In acidic conditions the isoxzole-3-carboxylate is preferentially formed from nucleophilic attack

of the hydroxylamine at the α-carbon, a 98:2 mixture was reported by Lepage *et al*. (Lepage et al., 1992), however, it is likely that a small amount of the other isomer was present in the final product.

Ester hydrolysis followed by HOBt and EDCI mediated amide coupling returned the final compounds **12–15** with yields of 18–26% over the final two steps.



Scheme 3 General synthesis of the 3,5-disubstituted isoxazoles

6.4 Readily available compound selection

A number of test compounds were chosen from in-house chemical libraries available in the Russell group. The libraries contain a wide variety of known biologically active compounds with targets that span the druggable genome. When selecting the library, an attempt was made to encompass a variety of potential protein targets in order to increase the likelihood of identifying a novel target implemented in epicardial EMT or differentiation.

The first group of compounds selected for screening are known epigenetic modulators. The term ‘epigenetics’ refers to the study of varied gene expression that is not regulated by changes to the underlying DNA sequence. Enzymatic modifications to the basic chromosome structure, such as DNA methylation and histone acetylation, affect DNA packaging which in turn can alter which genes are accessible to RNA polymerases, co-factors and other transcriptional machinery. Epigenetic modifications can both activate and deactivate gene transcription which helps to govern cell fate decisions, an essential process in development and the maintenance of normal tissue homeostasis; aberrant epigenetic modifications have also been implicated in a number of disease states (Filippakopoulos and Knapp, 2014). Inhibition of proteins that regulate epigenetic state will in turn affect a cells transcriptional programming. Included in the screen were a number of compounds that modulate proteins responsible for the addition or removal of epigenetic modifications (**Table 6.1 and Appendix Table A.6.1 A–N**).

Bromodomains (BRDs) are motifs present within a number of proteins, such as transcription factors, that recognise and bind acetylated lysine residues and act as ‘readers’ of chromatin modification. Inhibition of the BRD binding site can prevent or modulate protein-protein interactions which in turn will alter transcription (Muller et al., 2011). A large number of proteins with varied functions contain BRDs: a selection of small molecule inhibitors with selectivity across the various families of BRD containing proteins were included in the screen (**Table 6.1 and Appendix Table A.6.1 N–W**).

The hedgehog (Hh) signalling pathway plays a role in cell growth, differentiation and survival in almost all mammalian cell lineages and tissues (Varjosalo and Taipale, 2008). Time dependent expression of the Hh proteins controls organ morphogenesis and more recently it was shown that Hh signalling from the cardiac outflow tract helps guide ventricular epicardial

regeneration in zebrafish (Wang et al., 2015a). The small molecule SAG, a Hh pathway agonist was found to increase myocyte proliferation in zebrafish embryos during development (Choi et al., 2013) . SAG and three other Hh modulators was included in the small molecule library (**Table 6.1 and Appendix Table A.6.1. X–A'**).

Kinases are responsible for the transfer of phosphate groups from ATP to hydroxyl groups on numerous substrates such as proteins, lipids and amino acids (Fabbro et al., 2015). Phosphorylation of proteins is reversible and, once again, has a seminal role on controlling cell function and behaviour. Kinases constitute some of the most 'drugged' enzymes to date: the mitogen-activated protein (MAP) kinase family, which includes stress activated p38 kinase and extracellular signal-regulated kinases (ERK), have been implicated in heart development and are responsive to many growth signals including FGF (Wang, 2007). Inhibitors of the Rho-associated kinases (ROCK) were found to promote cardiac differentiation in ESC and iPSC cultures (Cheng et al., 2015). A selection of small molecule modulators of kinase inhibitors was included in the screen (**Table 6.1 and Appendix Table A.6.1. B'–I'**). The protein kinase C (PKC) family are also key in regulating numerous growth, differentiation and migration; increased PKC activity was found to correlate with decreased expression of E-CADHERIN motility and disrupt cell-cell contacts in human cancer cell lines (Ivanov et al., 2009; Masur et al., 2001). Two reported small molecule activators of PKC activity were included in the library (**Table 6.1 and Appendix Table A.6.1. J and K**).

Table 6.1 List of small molecules selected for screening

	Name	Mechanism of action	Reference
A	**GSK-J4**	histone lysine demethylase inhibitor	(Heinemann et al., 2014)
B	**(R)-PFI-2**	methyl transferase inhibitor	(Barsyte-Lovejoy et al., 2014)
C	**SB216763**	kinase inhibitors: promotes pluripotency in mouse cells	(Coghlan et al., 2000)s
D	**UNC0642**	lysine methyl transferase inhibitor	(Liu et al., 2013)
E	**A-366**	lysine methyl transferase inhibitor	(Pappano et al., 2015)

F	**BML-210**	histone deacetylase inhibitor	(Borutinskaitė and Navakauskienė, 2015)
G	**Trapoxin A**	irreversible inhibitor of histone deacetylase	(Kijima et al., 1993)
H	**M344**	histone deacetylase inhibitor	(Li and Chen, 2009)
I	**MS-275**	histone deacetylase inhibitor	(Rao-Bindal et al., 2013)
J	**MGCD0103**	histone deacetylase inhibitor	(Zhang et al., 2016)
K	**AMI-1**	methyl transferase inhibitor	(Bonham et al., 2010)am
L	**5-Azacytidine**	methyl transferase inhibitor	(Choi et al., 2004)
M	**S-(5'-Adenosyl)-L-methionine chloride dihydrochloride (SAM)**	methyl donor	(King et al., 2016)
N	**RG 108**	methyl transferase inhibitor	(Bonham et al., 2010)
O	**(+)-JQ1**	BET inhibitor	(Meng et al., 2014)
P	**(-)-JQ1**	inactive form of (+)-JQ1	(Meng et al., 2014)
Q	**PFI-1**	BET inhibitor	(Picaud et al., 2013a)
R	**GSK2801**	Inhibitor of BAZ2A and BAZ2B bromodomains	(Chen et al., 2016)
S	**I-CBP112**	CBP/p300 inhibitor	(Teo et al., 2005)
T	**SGC-CBP30**	CBP/p300 inhibitor	(Zucconi et al., 2016)
U	**Bromosporine**	pan-bromodomain inhibitor	(Picaud et al., 2016)
V	**PFI-3**	SMARCA bromodomains	(Vangamudi et al., 2015)
W	**OXF-BD-02**	BET inhibitor	(Hewings et al., 2013)
X	**Purmorphamine**	hedgehog signalling pathway	(Sinha and Chen, 2006)
Y	**SAG**	hedgehog signalling pathway	(Sasaki et al., 2013)S
Z	**TWS119**	hedgehog signalling pathway	(Wang et al., 2015b)
A'	**Cyclopamine**	hedgehog signalling pathway	(Chen et al., 2002)
B'	**SB203580**	inhibits upstream of MAPK	(Barancík et al., 2001)
C'	**FR180204**	ERK inhibitor	(Ohori et al., 2005)
D'	**SB202190**	p38 map kinases	(Barancík et al., 2001)
E'	**PF-3644022**	p38 map kinases	(Mourey et al., 2010)
F'	**PD98059**	MAPK/ERK	(Yamaguchi et al., 2002)
G'	**PD184352**	MEK inhibitor	(Allen et al., 2003)
H'	**5-Iodotubercidin**	adenosine kinase inhibitor	(Phillis and Smith-Barbour, 1993)
I'	**Y-27632**	p160 ROCK inhibitor	(Maldonado et al., 2016)
J'	**Indolactam V**	protein kinase c activator	(Haynes-Smith et al., 2016)
K'	**PMA**	protein kinase c activator	(Park et al., 2001)
L'	**OX12004**	Potential BMP agonists	Russell group
M'	**OX02129**	Potential BMP agonists	Russell group
N'	**OX02197**	Potential BMP agonists	Russell group
O'	**OX02268**	Potential BMP agonists	Russell group
P'	**ICG-001**	Wnt signalling modulator	(Sasaki et al., 2013)
Q'	**Gallocyanine**	Dkk1 inhibitor	(Iozzi et al., 2012)
R	**Cardiogenol**	Cardiogenic in	

The bone morphogenetic proteins (BMPs) are a group of growth factors that form part of the TGFβ superfamily. Downstream signalling of the BMP receptors is critical in development, including development of the heart, and important in normal tissue homeostasis (Chen et al., 2004; Wang et al., 2014). As part of another project, the Russell group has synthesised a series

of potentiation BMP agonists: a selection was included in the screen (**Table 6.1 and Appendix Table A.6.1. L–O**).

The small molecule ICG-001 (**Table 6.1 and Appendix Table A.6.1. P**) is a modulator of Wnt signalling: nuclear β-CATENIN recruits one of two co-activators the CREB binding protein (CBP) or the coactivator E1A binding protein p300: each activates a separate subset of Wnt controlled gene expression (Sasaki et al., 2013). ICG-001 inhibits interaction of β-CATENIN with CRB, promoting binding with p300 which has been shown to activate number of differentiation pathways in stem and progenitor cell populations (Teo et al., 2005). ICG-001 was found to induce EMT in both rat and mouse EPDCs *in* vitro; subsequently, in a mouse model of MI, ICG-001 improved cardiac contractile function and appeared to preserve cardiac morphology, however this effect was not found to be significant (Sasaki et al., 2013). As a 'known' modulator of EPDC EMT this compound was included in the library to probe whether mEPDC migration was a viable read out for EMT.

The DKK1 protein, a member of the Dickkopf family, is a negative regulator of Wnt signalling: its expression can be upregulated by β-CATENIN and it is thought to form part of a negative feedback loop modulating Wnt activity (Iozzi et al., 2012; Niida et al., 2004). The small molecule dye Gallocyanine (**Table 6.1 and Appendix Table A.6.1. Q**) inhibits DKK1 activity and was included in the library as a potential activator of Wnt signalling.

All of the compounds identified as hits from the pilot hEPDC phenotypic screen were also included in library (**Chapter 3 Table 3.1**), so as to verify that the negative results from the validation screen were accurate. The final compound included was the small molecule

cardiogenol, which has been found to induce cardiomyocyte differentiation from mouse embryonic stem cells (**Table 6.1 and Appendix Table A.6.1 R)** (Wu et al., 2004).

After the compounds had been synthesised or purchased accordingly they were diluted into 96-well deep-well plates in mEPDC immortalisation media at a concentration of 10 μM in preparation for use in the automated mEPDC scratch assay. With the advice of the Target Discovery Institute it was decided that for the preliminary mEPDC assay the compound library would be screened at a single concentration, which was chosen to be 1 μM to try and encompass an effective concentration for all of the compounds. Primary screening at one concentration is a common practice in HTS with the principle that 'true' hits not encompassed by this concentration will be identified by other compounds with a similar MOA or chemotype (Macarron et al., 2011).

Chapter 7

Screening a small molecule library in the automated mEPDC scratch assay

7.1 Pilot mEPDC automated scratch assay

7.1.1 Assay protocol

After the 70 compound library had been selected and the compounds synthesised, or purchased, as necessary a batch of mEPDCs were thawed and expanded to be used in a pilot mEPDC automated scratch assay. Based upon preliminary experiments (**Chapter 5**), the following protocol was established (**Figure 7.1).**

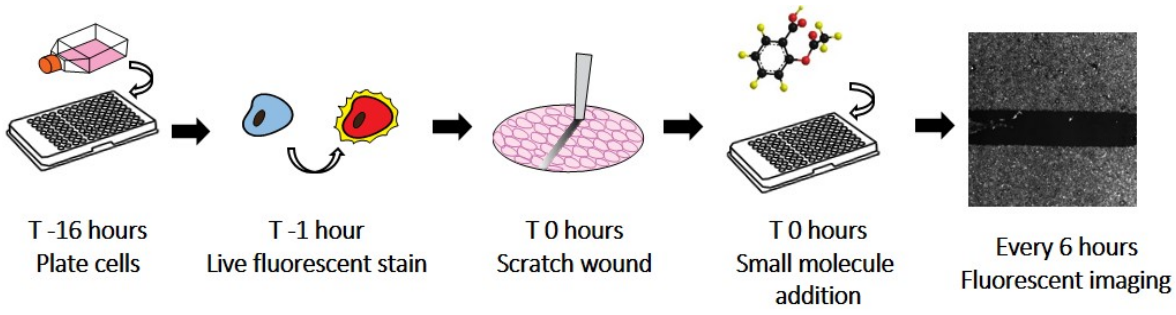


Figure 7.1 Protocol for the mEPDC automated scratch assay. MEPDCs were plated in to 96-well plates and left to form a monolayer overnight. Cells were stained with CellTracker™ for 30 minutes and a scratch made across the centre of each well with the IncuCyte WoundMaker™. The compound library was then added at a concentration of 1 µM and the cells imaged every six hours. The staining protocol was repeated after 24 hours to maintain strong fluorescence.

MEPDCs were seeded into 96-well plates at a concentration of $3x10^4$ cells/well and left in a 33^oC incubator overnight. After 15 hours the cells had formed a monolayer in the plates; the media was aspirated, the cells stained with CellTracker™ for 30 minutes, then washed in plain media for 30 minutes. The IncuCyte WoundMaker™ was used to make a scratch wound across the middle of each well before the media and cell debris were aspirated and replaced with the compound library at a final concentration of 1µM. The compound library was distributed one compound per well between two plates: each plate was assayed three times. No cells were plated in the outer wells to avoid edge effects (Lundholt et al., 2003). 'Edge effect' alludes to the varied response often seen in cells in the outer edges of HTS multiwall plates which occur due to numerous factors including thermal gradients; it is common place to avoid using these as experimental wells. MEPDCs were imaged on the InCell High Content Imager

(tdi.ox.ac.uk/high-content-imaging) in both the brightfield and red fluorescent protein channel every 6 hours for the duration of the experiment. The staining and wash protocol was repeated after 24 hours in order to maintain strong mEPDC fluorescence and remove background signal from the images: the compound library was then added back into the plates as previously described. After 54 hours all of the wounds were closed and the plates discarded. The images were then transferred in to the InCell Analyser software package and subject to the previously designed analysis protocol (**Chapter 5.3.2**) that measured the area of the scratch wound at each time point, returning a value in mm^2.

7.1.2 Data analysis

The first step of the data analysis was to compare the size of the starting scratches and remove those that were too large or too small. Cells migrate in response to a wide variety of stimuli including chemical signals from other cells (Jonkman et al., 2014; Petrie et al., 2009), variation in scratch size can create different *in vitro* 'environments' for the cells at the leading edge. To 'normalise' this the average starting scratch size and standard deviation of the data set was used to determine the 95% confidence interval: any scratches that did not fall between the limits of $1.336mm^{2} <$ to $< 2.651mm^2$ at 0 hours were excluded. For the subsequent analysis, any variation in the rate of wound healing was assumed to be solely related to individual treatments. Correct use of the scratch tool was essential if the resulting wounds were to be of equal width and length: if the WoundMaker™ was not properly inserted into the plate before use the pins did not reach the bottom and scratches were highly variable. Unfortunately, improper use of the scratch tool necessitated omission of one of the six replicate plates from the analysis.

Currently methods of scratch assay analysis are highly variable and, as of yet, a universal method has not been established (Jonkman et al., 2014). The technique originally chosen for analysis of

this assay was adapted from the 'Two Point Measurement' as described by Ibidi® (http://ibidi.com/fileadmin/support/application_notes/AN30_Wound_Healing_Data_Analysis.pdf). In the published protocol two images are taken from each well: one just after the scratch is made and one at a defined time point later in the assay; the difference between the sizes of the scratch wound in each images is then used to calculate rate of wound healing. The image selected for the latter time point should be taken before the curve reaches saturation, at a time when the cells are still migrating. To establish an appropriate time point to use as the 'end point' a growth curve was plotted of scratch wound area against time (**Figure 7.2 A**). The graph revealed that the TGFβ treated scratches were closing between 42–48 hours, whereas untreated and DMSO treated scratched were closing between 48–54 hours. The 36-hour time point was selected for analysis to ensure that the calculated rate of migration captured migrating mEPDCs. The average rate of wound closure at 36 hours (mm^2/hour) was calculated for each control treatment (**Figure 7.2.B**). The rate of wound closure in TGFβ treated cells appeared to be slightly faster than the untreated and DMSO controls; however, this was not found to be significant. Although TGFβ did not have a significant effect on mEPDC migration, wound healing in DMSO treated scratch wounds closely mimicked untreated cells (**Figure 7.2 A** and **B**). This meant that any changes in cell behaviour seen in mEPDCs treated with the small molecule library were likely to be a result of compound-cell interaction and not due to the presence of the DMSO vehicle.

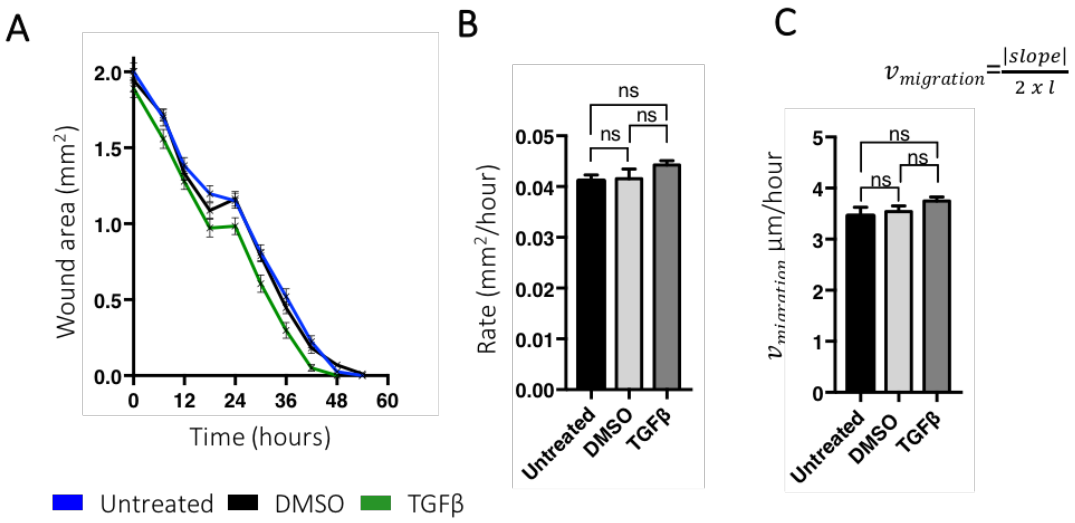


Figure 7.2 Control data from the pilot automated scratch assay. (**A**) A plot of the average wound size against time for each compound was made to determine when the scratch wounds closed. The 36-hour time point was chosen for rate analysis as this reflected a time at which all control groups were still migrating. (**B**) The rate of wound closure in mm^2/hour was calculated for the three control treatments at 36 hours. TGFβ treated scratch wounds appeared to be closing at a faster rate that the untreated and DMSO controls, however, this was not found to be significant. (**C**) An alternative measure of mEPDC migration, the $v_{migration}$, can be calculated from the slope of the growth curve and the length (l) of the scratch (Jonkman et al., 2014). There were no significant differences in $v_{migration}$ between the three controls. Statistics calculated using a one way ANOVA: n = 15.

For the rest of the data analysis in this experiment, and whilst evaluating data from subsequent assays, the same approach was taken: the growth curve of each experiment was fist plotted and an appropriate time point was chosen from which the rate of wound closure, in mm^2/hour, was determined. However, during the writing of this thesis a complementary approach to scratch assay analysis was identified that compares the rate of wound closure using an alternative measure: the $v_{migration}$ (Jonkman et al., 2014). To calculate the $v_{migration}$ the scratch area is first plotted as a function of time (as in **Figure 7.2 A**). A straight line fit is then used to determine the slope of the growth curve: for this data set only the slope between 0–36 hours was measured as after this time the wounds began to close and the growth curve reached a plateau. The $v_{migration}$ is calculated from the slope of the linear fit, which is equal to the change in wound area (A) over

time (t): $\frac{dA}{dt}$ in units of mm^2/hour. The area is equal to the length (l) x width (w) of the scratch; however, as the scratch is much longer than it is wide the length is assumed to be constant thus: $slope = \frac{l \times dw}{dt}$ which rearranges to: $\frac{slope}{l} = \frac{dw}{dt}$. Finally, because cells migrate from both sides of the scratch wound: $\frac{slope}{2 \times l} = \frac{dw}{dt}$. This method produces the rate of migration as the speed of cells moving in from the two edges of the scratch: $\frac{dw}{dt}$: in convenient units of mm/hour which can then be converted to μm/hour (**Figure 7.2 C**) (Jonkman et al., 2014). This new method was used to calculate the $v_{migration}$ for all control wells and once again no significant difference in the rate of wound closure between the three controls was found, although TGFβ appeared to increase the $v_{migration}$ slightly (**Figure 7.2 C**). Subsequent to this finding, the $v_{migration}$ method was also applied to all of the existing data sets for the purpose of validating the original analysis method. The trends identified by the two methods were closely correlated; the complementary $v_{migration}$ data sets are presented alongside the original analysis data in the appendix for comparison.

7.1.3 Z-score calculation and identification of positive hits

The next task was to investigate how the small compound library had affected mEPDC behaviour. The rate of wound closure at 36 hours for each individual well was first calculated and these values used to calculate the z-score (z_i) for each treatment in each replicate plate. The z_i is a commonly used statistical test in high throughput screening that calculates how many standard deviations (σ) away from the average ($\bar{v}$) a data point (v) lies (**Figure 7.3 A**) (Brideau et al., 2003). The z_i assesses variability within a set of results with the assumption that the majority of treatments will exert minimal effects. Hits are chosen by identifying 'outliers' that sit outside the bulk of the data: generally, a data point that sits >1.5 standard deviations outside the average is considered a 'hit' (**Figure 7.3 A**, outlier limits denoted by blue dashed line).

Control wells are excluded from z_i analysis so as not to skew the average value. Analysing each plate individually accounted for any plate to plate variation and permitted inter-plate comparison.

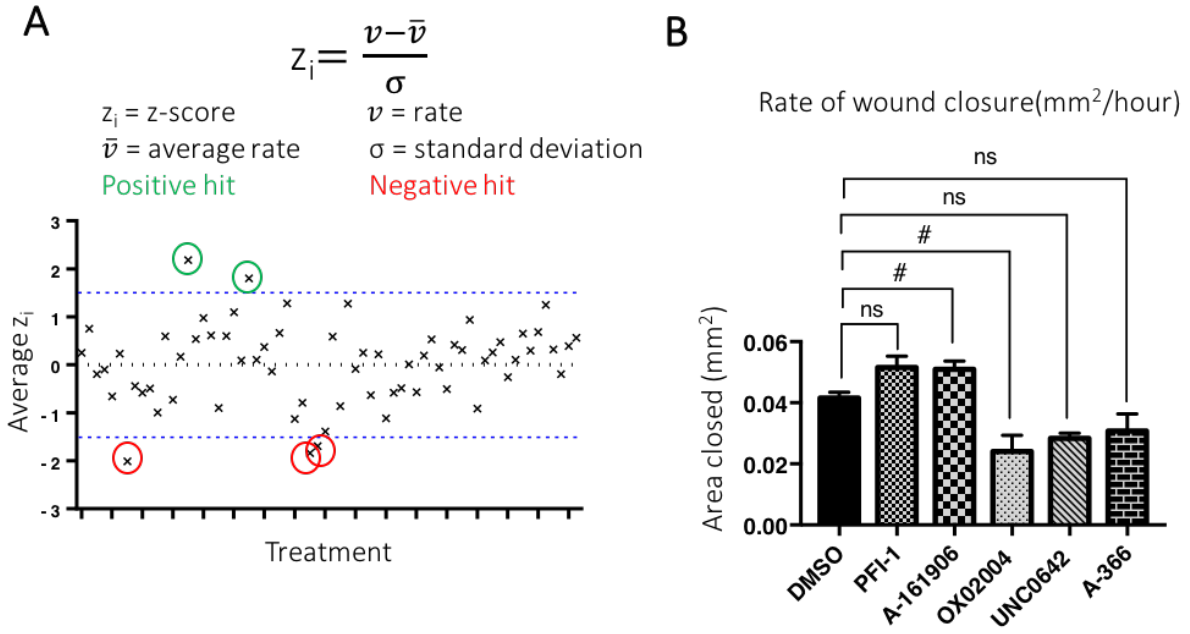


Figure 7.3 Calculating the z-score for each treatment from the rate of wound closure identified two positive and three negative hits. (**A**) The z-score (z_i) indicates how many standard deviations (σ) away from the average ($\bar{v}$) a data point (v) sits. Any treatment with z_i >1.5 standard deviations from the mean was classed as a 'hit (represented by blue dashed lines: positive hits circled in green and negative in red). (**B**) The rates of wound closure for each treatment were collated for comparison with the DMSO control. No significant difference was observed in rate of wound closure in cells treated with PFI-1, UNC0642 or A-366. There was not sufficient data to calculate statistics for A-161906 and OX02004. Statistics calculated using a one way ANOVA, n = 3 for DMSO, PFI-1, UNC0642 and A-366, n = 2 for A-161906 and OX02004, # indicates insufficient data to calculate significance.

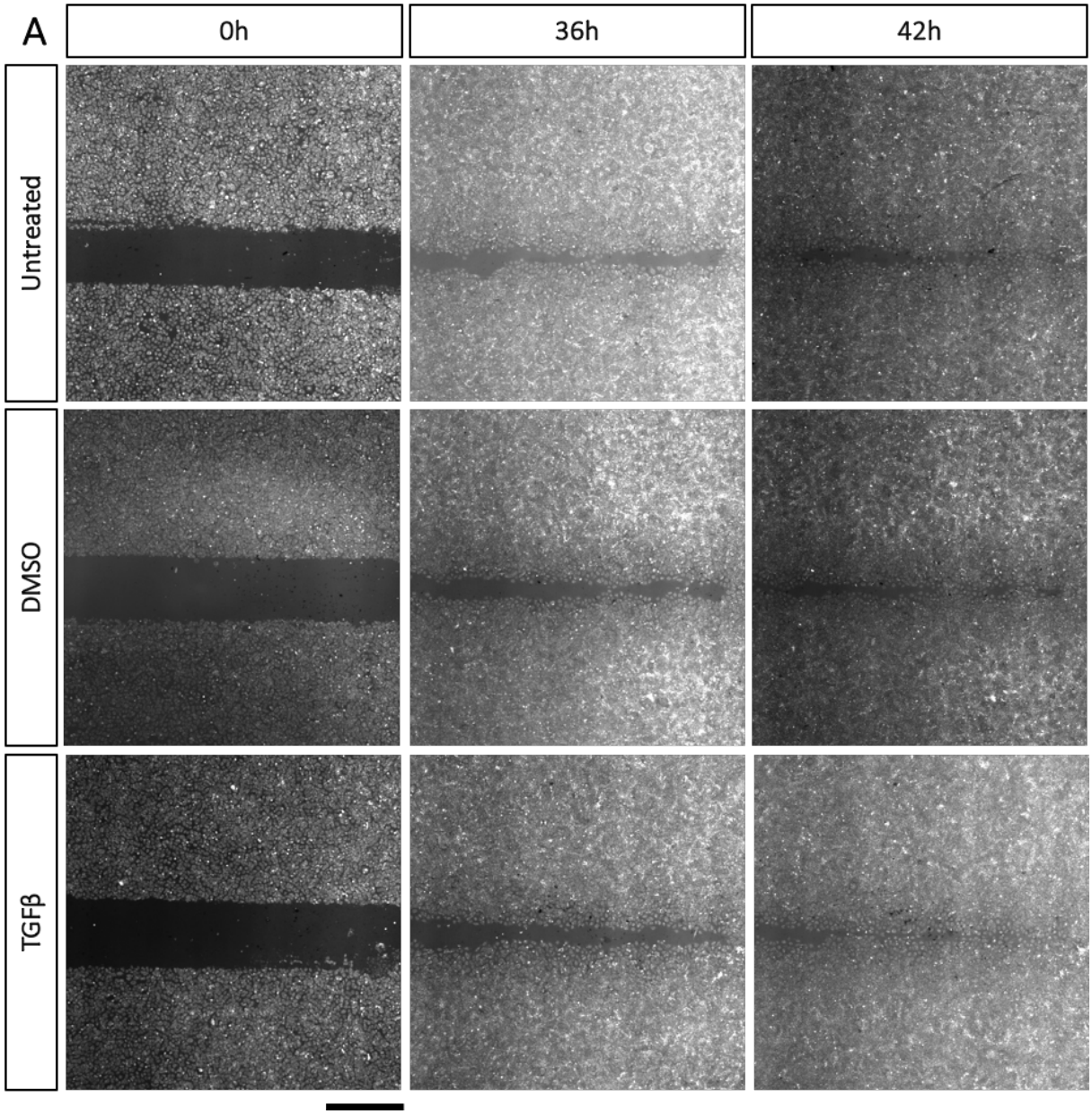
After the z_i values at 36 hours were calculated, the replicate data sets were compared to assess reproducibility (**Appendix Tables A.7.1 and A.7.2**); the z_i values were then averaged across the replicates and this value used to pick out 'hit' compounds. The pilot scratch assay identified two compounds with $z_i > 1.5$ which were considered to be 'positive hits': PFI-1, a broad and potent inhibitor of the Bromodomain and Extra Terminal Motif (BET inhibitor) and the TGFβ 'mimetic' A-161906 (**Figure 7.1.3 A**, positive hits are circled in green). Three negative 'hits' with $z_i < -1.5$ were also identified: UNC0642 and A-366, both inhibitors of lysine methyl

transferases, and OX02004 a reported BMP agonist. (**Figure 7.3 B**, negative hits are circled in red). The average z_i was also calculated using the $v_{migration}$ technique and the collated data returned the same five hits (**Appendix, Tables A.7.1 and A.7.2).**

The rates of migration for all the hit compounds at 36 hours were collected for comparison against the DMSO control (**Figure 7.3 B**). The average rate of migration of both PFI-1 and A-161906 were higher than the DMSO control and that of OX02004, UNC0642 and A-366 were lower. These differences were not found to be significant for PFI-1, UNC0642 or A-366. One scratch from each of the A-161906 and OX02004 data sets had to be excluded due to the starting scratch size being too small; as such there were not enough experimental repeats to determine significance for these treatments (**Figure 7.3 B**). Once again the data was also subject to $v_{migration}$ analysis. The data trends were the same as seen with the original analysis protocol; however, in this case the increased $v_{migration}$ in PFI-1 treated cells was found to be significantly more than the DMSO controls (**Appendix Figure A.7.1**).

After the hits had been identified, the corresponding images from the assay were examined to check whether they correlated with the automated analysis (**Figure 7.4**). Images from the 0, 36 and 42- hour time points were selected for comparison. To make an accurate visual comparison, experimental wells were selected that had equivalent starting scratch sizes. Starting scratch sizes were as follows (mm^2): untreated 1.82, DMSO 1.87, TGFβ 1.96, PFI-1 2.22, A-161906 1.90, OX02004 2.08, UNC0642 2.05, A 399 2.0.7. Visually there was little difference in the amount of wound closure between the three control groups, although at 42 hours the scratch wound treated with TGFβ was slightly smaller than the untreated and DMSO controls (**Figure 7.1.4 A**). Examining the images from the five 'hit' compounds on the other hand revealed distinct differences in the size of the scratch wound at both of the later time points. Scratch wounds treated with PFI-1 and A-161906 had closed by 42 hours and the wounds were smaller than the

corresponding DMSO controls at 36 hours (**Figure 7.4 B**). Scratch wounds treated with the three negative hits were clearly much larger at both 36 and 42 hours than the DMSO controls and the two positive hits (**Figure 7.4 B**). This data set indicated that the pilot scratch assay protocol and analysis was rigorous enough to correctly identify differences in the rate of mEPDC wound closure.



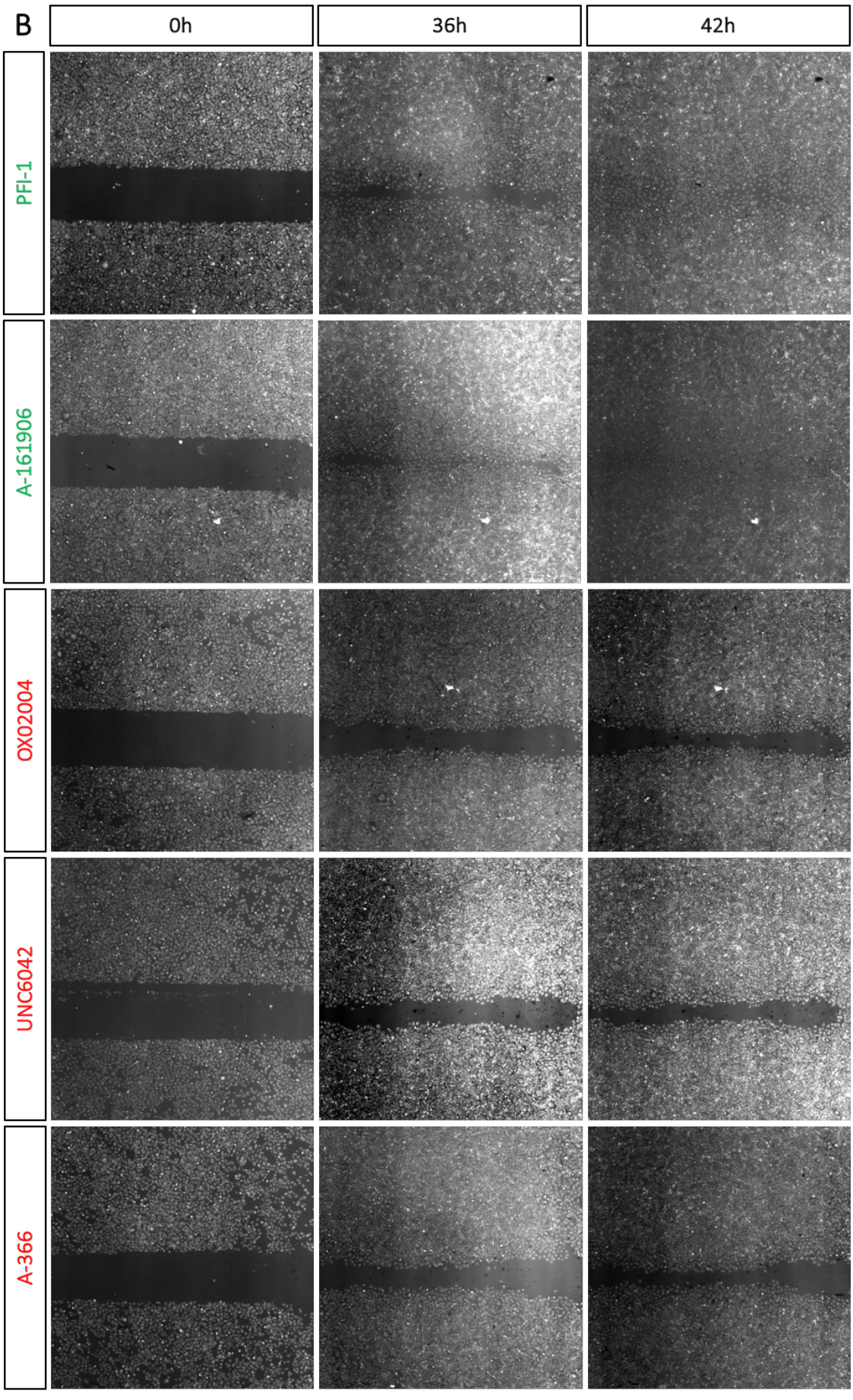

B
0h
36h
42h
PFI-1
A-161906
OX02004
UNC6042
A-366

Figure 7.4 Assay images confirm positive and negative hits. (**A**) As determined by the growth curves and the rate data, there was very little difference in wound healing rate between the three control groups. (**B**) The two positive hits PFI-1 and A-161906 (green) had closed faster that the DMSO counterparts. The three negative hits OX02004, UNC0642 and A-366 (red) appeared to prevent wound closure. In order to make a fair comparison scratches were chosen that had as similar a starting size as was possible. Starting sizes were as follows: Untreated 1.82 mm^2, DMSO 1.87 mm^2, TGFβ 1.96 mm^2, PFI-1 2.22 mm^2, A-161906 1.90 mm^2, OX02004 2.08 mm^2, UNC0642 2.05 mm^2, A 399 2.07mm^2. Scale bar 1mm in **A** and **B**.

7.2 Validation of primary 'hits'

To validate the hits from the original assay an analogous wound healing experiment was performed in which the five 'hits' from the primary screen were re-tested. Within the assay, compounds were tested across a range of concentrations to identify whether there was a dose response. Dose response curves are a plot of activity against concentration; usually with activity on the y-axis against the $\log_{10}$ dose on the x-axis. Biological responses induced by small molecules are often complex and can be variable depending upon the system; however, the effect should be directly related to the concentration of the drug at its site of action. In theory, a sigmoidal dose response curve should be observed if the compound is tested across an appropriate range of concentrations specific to drug potency. The curve represents minimal activity at low concentrations followed by an exponential increase in activity as the effective dose is reached; the slope then plateaus at higher concentrations as the system reaches saturation (DeLean et al., 1978). It must be noted, however, that while a sigmoidal curve is commonly seen in 'reductionist' assays, for example with direct inhibition of a purified enzyme, this may not be the case in more complex biological systems such as cell assays in which a compound may be exerting a number of off target effect (Shoichet, 2006). In the original assay compounds were tested at a 1μM: therefore, the dose response was based around this concentration. The final six concentrations, which varied from one another along a half $\log_{10}$ scale, were 0.03, 0.1, 0.3, 1, 3 and 10μM. Also included in the validation study was a dose response of the BET bromodomain inhibitor (+)-JQ1 to compare against the positive hit PFI-1. Both compounds are

inhibitors of the BET bromodomains but have different potency: PFI-1 has a reported IC_{50} of ~2 μM in cell based assays (Fish et al., 2012) whereas (+)-JQ1 is more potent with an IC_{50} of 0.03-0.1 μM (Devaiah et al., 2012). Furthermore, although both PFI-(1) and (+)-JQ1 inhibit BET proteins, they are structurally distinct from one another: if the increased rate of wound closure observed in PFI-1 treated cells was a result of this known target activity a similar response should be observed with (+)-JQ1 at lower dosages, irrespective of their contrasting structures.

The validation protocol mimicked exactly the protocol of the original screen. Each compound was tested at the six stated doses in duplicate within in each plate, and each plate was repeated three times giving a total of six replicates for each experimental condition. Despite not having a significant effect in the preliminary screen, TGFβ was included again as a 'positive' control and 0.5% DMSO and untreated cells were included as the negative controls.

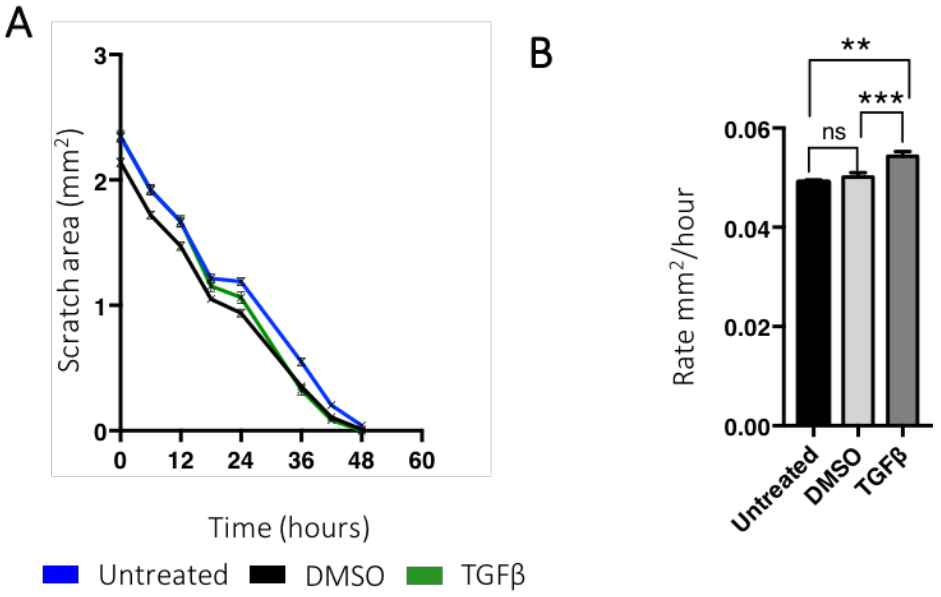


Figure 7.5 Control data from the validation screen. (**A**) MEPDC scratch wounds closed between 42–48 hours. (**B**) Rate analysis at 36 hours revealed that TGFβ treated scratches were closing significantly faster than untreated and DMSO treated controls. Statistics were calculated using a one way ANOVA, n = 13, *p<0.05; **p<0.01; ***p<0.001; ****p<0.0001

After the scratch data was collected, growth curves were plotted to assess the time of wound closure: once again scratches reached confluency between 42–48 hours, therefore the 36-hour time point was used as the experimental end point (**Figure 7.5 A**). Interestingly, in the validation assay the rate analysis revealed that TGFβ treated scratches were closing significantly faster than untreated and DMSO controls (**Figure 7.5 B**). This indicated that TGFβ acted as a suitable positive control in this experiment. Once again there were no significant differences between the rate of wound closure of untreated and DMSO treated scratch wounds, confirming DMSO to be an appropriate vehicle negative control. The $v_{migration}$ analysis method produced similar results (**Appendix A.7.2**). Dose response curves for each compound treatment were generated by calculating the rate (or the $v_{migration}$ **Appendix A.7.3**) at each concentration which was then plotted against the $\log_{10}$ dose. The data for the TGFβ and DMSO controls, which were tested at steady concentration, were included on the graphs for comparison (**Figure 7.6**). From here forward, when discussing the compound concentration, the equivalent $\log_{10}$ value will be quoted in brackets.

Between 0.1–3μM (-1 to 0.5) the rate of closure in scratch wounds treated with the BET inhibitor PFI-1 was higher than DMSO (**Figure 7.6 A**), this difference was found to be significant at 1 and 3 μM (0 and 0.5). It also appeared to be higher than the rate of wound closure in TGFβ treated cells at 1 and 3 μM (0 and 0.5), although this was not found to be significant. The general trend appeared to be an increase in activity with increased dosage up until 1μM (0), after which activity began to decline. At 10μM (1) the rate of wound closure had returned back to that of the control.

The dose response profile for (+)-JQ1was similar to that observed with PFI-1 treatment (**Figure 7.6 B**). From 0.03-3μM (-1.5 to 0) the rate of wound closure in scratch wounds treated with (+)-

JQ1 was found to be significantly higher than in DMSO. The rate was also significantly higher than the TGFβ positive control at 0.1, 0.3 and 1μM (-1, -0.5 and 0). Once again activity increased with increased dosage which then steeply declined at higher concentrations. The activity of (+)-JQ1 appeared to mimic that of PFI-1 but its greatest positive effect was seen at a lower concentration: this pattern in behaviour fitted with the known pharmacology of the two compounds, which have the same molecular targets but different potency. Both compounds demonstrated increased activity with increasing concentration, but activity was found to decline at higher doses. The similarity in dose response of the two inhibitors suggested a role of the BET bromodomain in mEPDC migration.

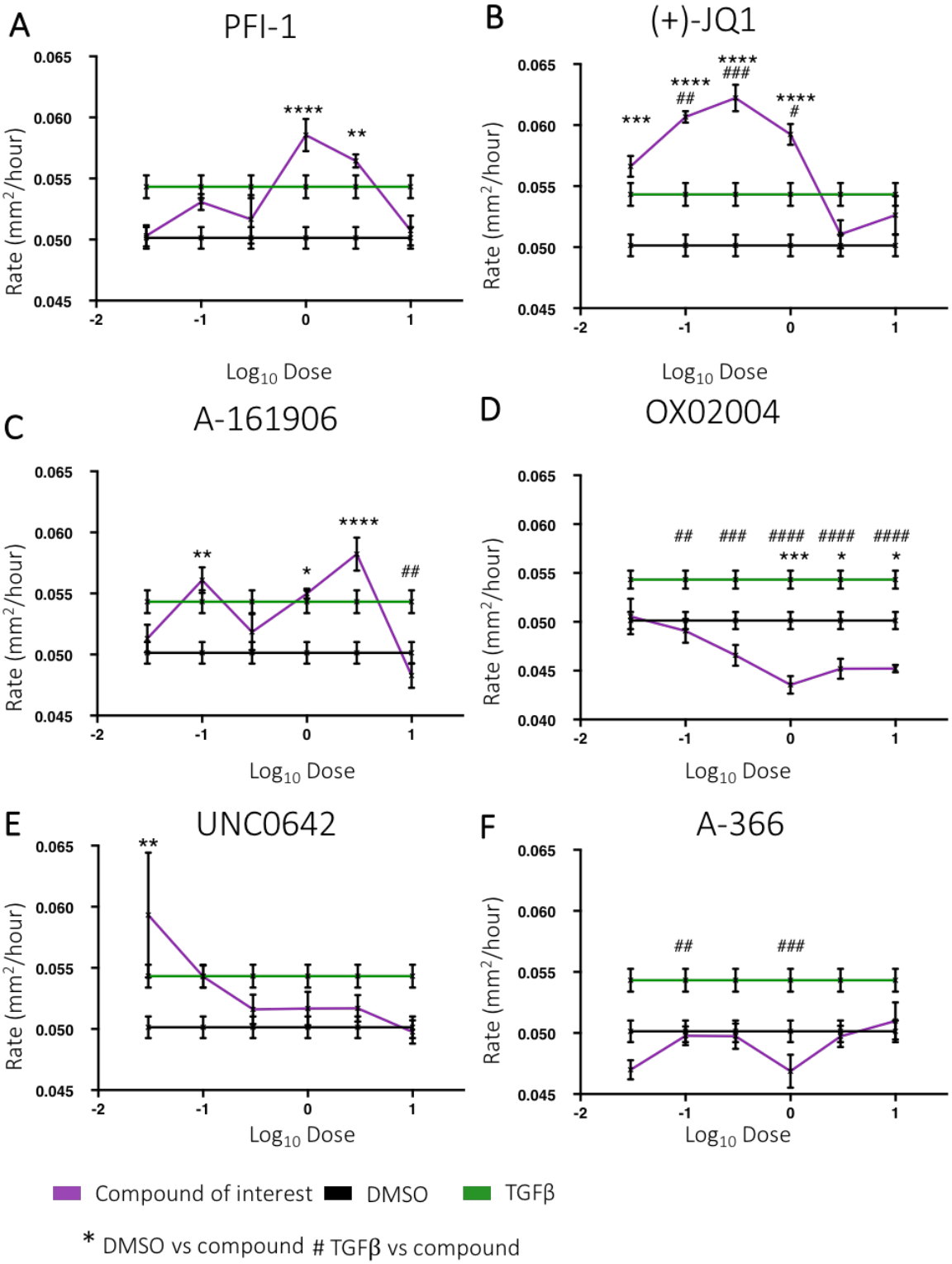


Figure 7.6 Validation screen dose response profiles. The six compounds chosen for our validation studies were screened over a range of doses at half $\log_{10}$ scale: 0.03, 0.1, 0.3, 1, 3 and 10µM. The rate of migration at 36 hours was calculated for each compound at each concentration and plotted against the $\log_{10}$ dose to generate dose response curves. A one way ANOVA was used to compare the rate of migration for each compound dose with the DMSO negative control and TGFβ positive control. N = 6, *p<0.05; **p<0.01; ***p<0.001; ****p<0.0001, # indicate identical significance boundaries.

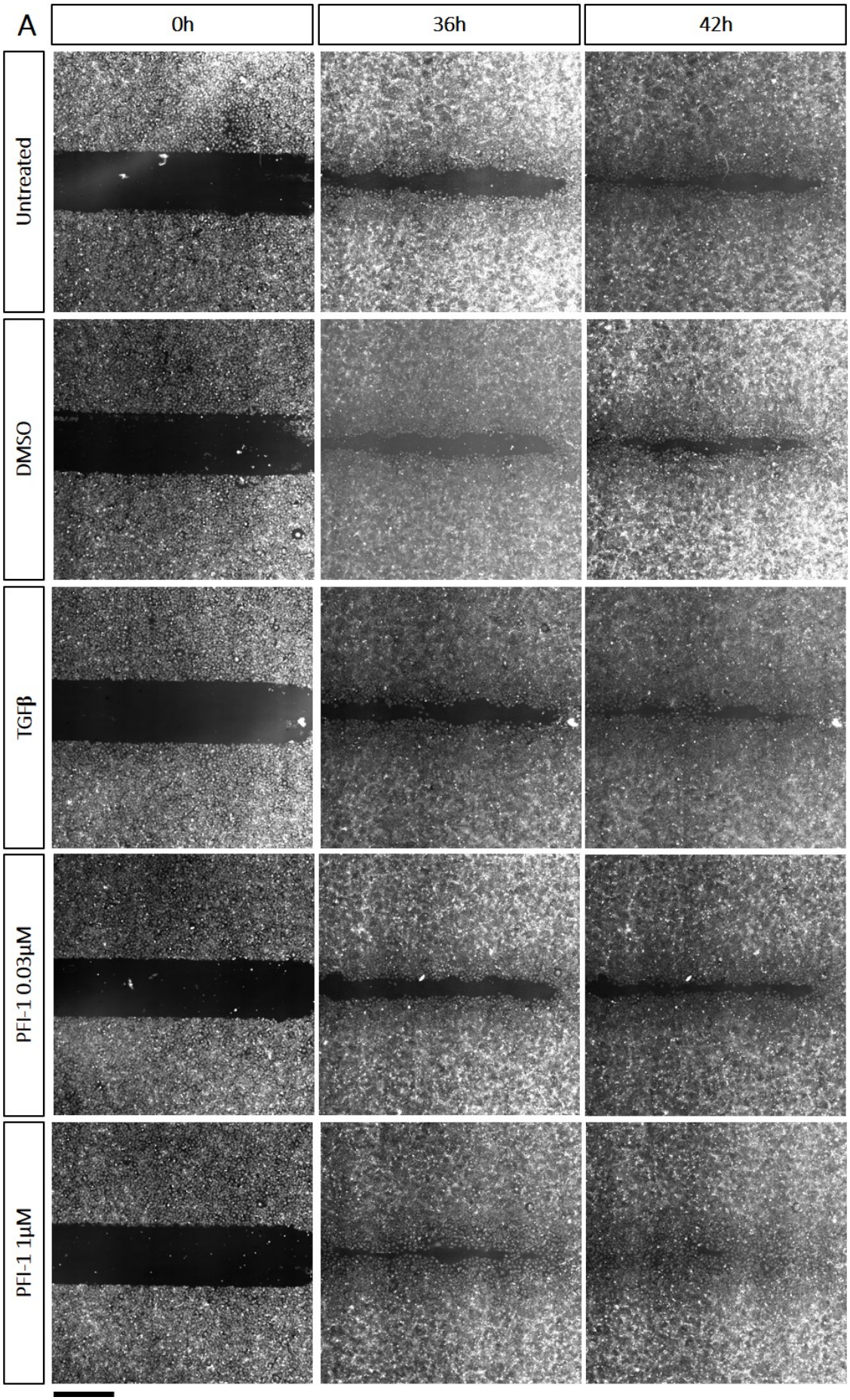
The dose response of the second positive hit from the preliminary screen, A-161906, did not follow such a convincing pharmacological profile (**Figure 7.6 C**). The rate of mEPDC migration appeared to increase with increasing concentration of A-161906; this was found to be significantly higher than DMSO and about equal to TGFβ treated cells at 0.1, 1 and 3μM (-1, 0 and 0.5). However, at both 0.3 μM and 10 μM (0.5 and 1) there was a dip in activity and the rate was about equal to the DMSO control.

The rate of wound closure in cells treated with OX02004 decreased as the dosage increased in a sigmoidal fashion, as would be expected with negative regulation of activity (**Figure 7.6 D**). The rate was significantly lower than in TGFβ treated cells at all concentrations except 0.03 μM (-1.5) and significantly lower than DMSO at 1, 3 and 10μM (0, 0.5 and 1). Treatment with UNCO642 at 0.03 μM (-1.5) appeared to increase the rate of migration to higher than that of the DMSO control: no significant differences were seen at any other concentration (**Figure 7.6 E**). The relationship between activity and dosage was unconvincing for A-366 and the rates of wound closure were not significantly different from the DMSO controls at any concentration (**Figure 7.6 F**).

Finally, images from the validation screen were reviewed to assess whether the rate calculations had accurately represented mEPDC behaviour. Images from the 36 and 42-hour time points were examined to see how wound healing progressed; representative scratches that had equivalent starting size were chosen for comparison. TGFβ treated scratches had closed more than the DMSO and untreated controls by 42 hours (**Figure 7.7 A**). The dose response of PF1-1 found a concentration of 1 μM (0) to be the most effective at increasing the rate of wound closure: at 0.03 μM (-1.5) the rate was equal to DMSO. Images from these two concentrations

confirmed the observed rate data: the 1μM treated scratch wound was much smaller than cells treated with 0.03μM (-1.5) at 36 and 42 hours (**Figure 7.7 A**). The rate at 10μM (1) was found to be similar to DMSO: when we reviewed the brightfield images it appeared that PFI-1 had begun to exert a toxic effect as by 42 hours and mEPDCs appeared to be dying, which explained the reduction in rate (**Appendix 7.4**).

The rate values calculated for (+)-JQ1 were higher than those of DMSO at all concentrations. The most effective concentration was shown to be 0.3μM (-0.5) which was significantly higher than both TGFβ and DMSO. Reviewing the scratch images for this concentration it was clear that at 36 and 42 hours the scratch wound had closed more than both controls (**Figure 7.7 B**). The rate was found to decline when cells were treated with (+)-JQ1 from 1-10μM (0-1); this was also confirmed by the image data (3μM data shown in **Figure 7.7 B**). Unlike PFI-1, (+)-JQ1 did not appear to be toxic at 10μM, however, it may be the case that at higher concentrations it had started to exert off target effects that affected mEPDC migration.


A
0h
36h
42h
Untreated
DMSO
TGFβ
PFI-1 0.03μM
PFI-1 1μM

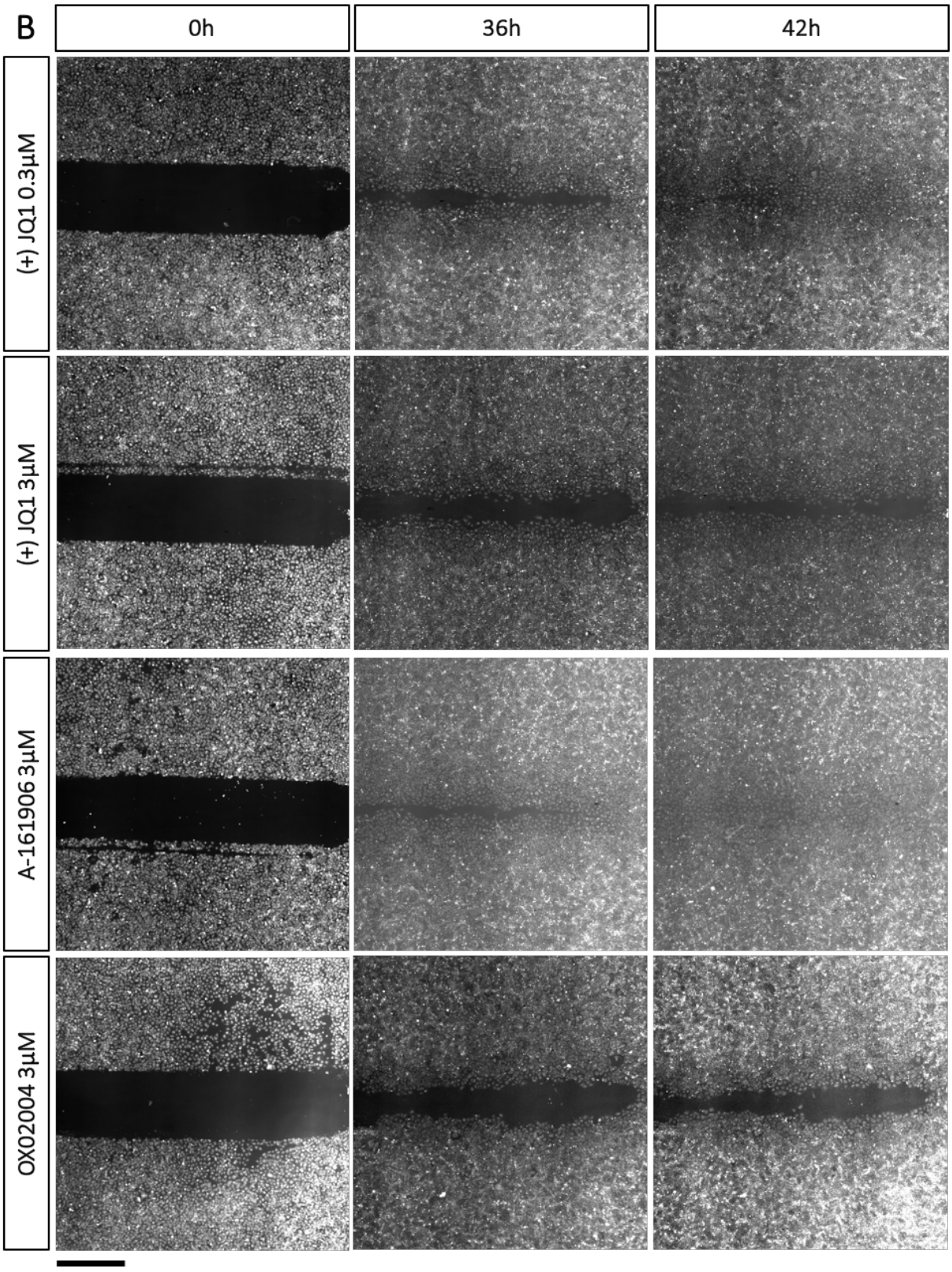


Figure 7.7 Representative scratch images of the validation assay. Starting scratch sizes (mm^2) untreated: 2.52, DMSO: 2.40, TGFB 2.53, PFI-1 0.03uM: 2.41, PFI-1 1μM: 2.51, JQ1 0.3μM 2.61, JQ1 3μM 2.53, A-161 2.44, OX02004 2.54. (**A**) Control wells confirm that TGFβ treated scratched closed quicker than untreated and DMSO. 1 μM of PFI-1 was found to be more effective than 0.03 μM. (**B**) 0.3 μM of (+)- JQ1 was found to be more effective than 3 μM. At 3

μM A-161906 treatment closed scratches faster than the than the DMSO control. OX02004 was confirmed to negatively regulate mEPDC migration.

The activity the TGFβ mimetic A-161906 did not appear to be as closely correlated with compound concentration. Reviewing the image data at 3μM indicated that the rate was higher than the DMSO control at this concentration as the scratch had closed by 42 hours (**Figure 7. B**); at 10 μM the rate of migration had decreased but A-161906 did not appear to be toxic at this concentration. The data for A-161906 was also manually analysed using ImageJ to calculate the wound areas, to see whether the dip in activity at 0.3μM (-0.5) was due to error in the automated image analysis; however, this was found not to be the case. At this point it was unclear whether the unusual profile reflected a pharmacological response or whether it was an anomalous data set.

The dose response curve for the negative hit OX02004 had shown decreased rate with increasing concentration. This observation was confirmed when reviewing the images (**Figure 7.7 B**). The dose response data for the negative hit UNC0642 was highly variable and this was confirmed when reviewing the images in which there was little correlation between experimental replicates. Scratch wounds treated with A-366 were not closed at any concentration by 42 or 48 hours and it appeared to be toxic at 10μM. It appeared as though A-366 was exerting a negative effect of mEPDC migration even at the lowest concentration as no changes in behaviour was observed with changing dose (Data for UNC0642 and A-366 not shown).

7.3 Summary and discussion

7.3.1 Pilot mEPDC scratch assay

In collaboration with the Target Discovery Institute (tdi.ox.ac.uk), a 70 compound library was screened in an automated fluorescent scratch assay. Cells were plated into 96-well plates and

left to form a monolayer before being stained with the live fluorescent dye CellTracker™. A scratch wound was made across the centre of each well and the cells imaged every 6 hours until the cultures reached confluency. The images were analysed using the InCell Analyser platform which measured the area of the scratch at each time point and returned a value in mm^2.

The initial method of data analysis was an adaptation of the 'Two Point Measurement' protocol recommended by Ibidi® (http://ibidi.com/fileadmin/support/application_notes/AN30_Wound_Healing_Data_Analysis.pdf). Images of the scratch at 0 and 36 hours were used to calculate a rate of wound closure (mm^2/hour) for each individual treatment. In addition to this, an alternative method described by Jonkman *et al.*, was later employed for the purpose of validating the original method. First, the raw data (mm^2) for each time point of each individual well was plotted against time and linear regression analysis was used to determine the slope (mm^2/hour). The slope was then used to calculate the $v_{migration}$ in mm/hour, which was then converted to μm/hour. Both methods of analysis revealed there to be no differences in the rate of wound closure between the controls; the data sets from both analyses have been documented in the appendix for comparison (**Figure A.7.1-A.7.3**).

To analyse the rate of wound closure in mEPDCs treated with the compound library the rate was first calculated for each individual well. These values were then used to determine a z_i for each individual treatment replicate. The z_i indicates how far away from the average an individual data point lies: it was assumed that the majority of experimental conditions would exert no biological effect; therefore, outliers with $z_i > 1.5$ standard deviations away from the average were identified as 'hits'. The z_i scores were averaged for each compound and the pilot assay returned two positive hits, the BET inhibitor PFI-1 and the reported TGFβ mimetic A-161906. The assay also identified three negative regulators of mEPDC migration: UNC0642 and A 336 both inhibitors

of lysine methyl transferases, and OX02004 a reported BMP agonist. Images from the assay were also visually analysed and were found to correlate with the calculated rate findings.

7.3.2 MEPDC validation screen

To determine whether the pilot screen had accurately identified positive and negative regulators of mEPDC migration an identical experiment was conducted to re-test the 'hit' compounds. In order to determine whether the effects were dose dependant the compounds were tested at a range of concentrations that increased at half $\log_{10}$ scale: 0.03, 0.1, 0.3, 1, 3 and 10μM. TGFβ, untreated and DMSO treated scratch wounds were included as controls. The potent BET inhibitor (+)-JQ1 was included as an additional experimental condition here to investigate whether similar effects were induced by two compounds with the same primary molecular target.

The control data was analysed in an identical manner to the pilot screen; interestingly, this revealed that TGFβ had significantly increased the rate of cell migration in this experiment: it had also appeared to increase the rate of migration in the pilot screen but this was not found to be significant.

To investigate dose response, the rate of migration for each compound concentration was calculated and plotted against the $\log_{10}$ dose. Once again PFI-1 appeared to increase the rate of mEPDC migration. At 1 and 3μM the rate of wound closure was significantly higher than the DMSO control. The rate of cell migration with PFI-1 treatment appeared to increase as the concentration increased up to 1μM after which it declined; PFI-1 was found to be toxic at 10μM. The second BET inhibitor (+)-JQ1 demonstrated a similar dose response profile increasing with increased dosage, followed by a decline at higher concentrations. At all concentrations, the rate

of closure was higher than that of the DMSO control, and at 0.1, 0.3 and 1μM the rate was found to be significantly higher than both the DMSO and TGFβ controls. These observations were also confirmed by the corresponding assay images. Unlike PFI-1, at higher concentrations (+)-JQ1 was not found to be toxic. It is postulated that at higher compound concentrations off target effects may have occurred that impeded any positive effect on mEPDC migration. The similarity in dose response exhibited by the two BET inhibitors was an encouraging observation. Firstly, the replicated hits indicated that the assay protocol was able to identify compounds that caused a change in the rate of wound closure. Secondly (+)-JQ1 activity appeared to correlate with its reported IC_{50} value of 0.03–0.1 (Devaiah et al., 2012), as did PFI-1 with an IC_{50} value of ~2 μM (Fish et al., 2012). As both compounds have the same primary molecular target, and their observed activity reflected their potency it appeared as though the BET bromodomains may have a role in mEPDC migration: this is further explored in **Chapter 8**.

The second positive hit A-161906 also increased mEPDC migration from 0.1–3μM relative to the DMSO control; this was significant at 0.1, 1 and 3μM. There was a dip in activity at 0.3μM which was confirmed by manual analysis of the scratch areas. At 10μM A-161906 had caused a reduction in the rate of wound closure but did not appear to be cytotoxic. Further investigation was required to determine whether the result at 0.3 μM was anomalous and to assess the pharmacological activity of the compound. This is also addressed in **Chapter 8**.

The negative hit OX02004 significantly decreased the rate of cell migration from 0.1 μM onwards. After 42 hours, the scratch wounds treated with OX02004 were much larger than the DMSO control, which confirmed that the assay design was sensitive enough to measure the variation in mEPDC migration. This compound was synthesised in the Russell lab as part of a series of potential BMP4 agonists; unfortunately, in a following assay that investigated

upregulation of BMP related genes in human hepatoma-derived cell line OX02004 was not found to be active. Further investigation would be required to decipher the activity of OX02004, however, as this was not our desired response we elected not to pursue investigations into this compound any further. Data from the second negative hit UNC0642 was highly variable and we concluded that this had been a false hit from the first screen. The final negative hit A-366 prevented wound healing at all concentrations and was toxic at 10μM. A-366 is an inhibitor of the G9a histone lysine methyl transferase enzyme: A-366 was found to induce growth inhibition and differentiation in various cancer cell lines (Pappano et al., 2015; Sweis et al., 2014). If A-366 stimulated mEPDC differentiation without EMT it may explain the negative regulation of migration. Once again, as this response was not our desired behaviour this compound was not investigated any further. Overall, these experiments confirmed that the newly designed assay was able to identify both positive and negative mediators of mEPDC migration.

All the rate data from both automated scratch assays was subject to a second analysis that calculated the rate of cell migration from the slope of each growth curve, so as to validate the original methodology. This analysis took into account the continuous behaviour of the cells at all time points from 0–36 hours rather than taking a 'snapshot' at one single time point. Both data sets however were found to produce very similar results, which confirmed the use of the original method against a second published protocol (Both data sets are presented in the appendix (**Figures A.7.1-A.7.3** and **Table A.7.1-A.7.2**). Either approach appears to be suitable; however, when screening compound libraries that are much larger than the one in the pilot screen a simpler approach may be preferred so as to minimise the volume of data. Therefore, the 'two-point measurement' method is recommended for analysis of future high throughput migration assays.

Chapter 8

Exploring the role of the BET bromodomains in mEPDC migration

8.0 Introduction to the BET bromodomains

In **Chapter 7** a small select library of compounds was screened in the newly developed mEPDC migration assay. From the pilot assay, a putative hit 'PFI-1' was found to significantly increase the rate of mEPDC wound closure at a concentration of 1 μM, relative to that of the DMSO control. PFI-1 is a reported inhibitor of the Bromodomain and Extra Terminal (BET) motif family of bromodomain containing proteins. Subsequently a validation screen was undertaken in which PFI-1 and (+)-JQ1, another BET inhibitor, were screened in the mEPDC migration assay over a range of concentrations. Both compounds were found to increase the rate of mEPDC migration in a dose dependent manner. BET domains are present within a number of proteins, such as transcription factors. They recognise and bind acetylated lysine (Kac) residues and acting 'readers' of chromatin modification.

In eukaryotic cells negatively charged genomic DNA is condensed in the nucleus by its interaction with positively charged histone proteins, forming the DNA-protein complex known as chromatin. Changes in gene transcription and gene silencing are governed by this interaction, which is tightly regulated by post-translational modification of the histones (Sanchez and Zhou, 2009). The basic unit of chromatin, the nucleosome, consists of an octamer of the core histone proteins: H2A, H2B, H3, and H4: around which is wrapped a 147 base-pair unit of DNA in two super-helical turns; each is connected to the next nucleosome via a linker DNA. The N-Terminal of the globular histone proteins project out from the nucleosome forming the 'histone tail': these N residues, and numerous other locations on the histone protein, are subject to a range of covalent modifications including methylation, acetylation, phosphorylation and ubiquitination (**Figure 8.1 A**). Histone modification affects chromatin either by disrupting nucleosome interactions causing DNA to 'unwind' or by recruiting other proteins to, or occluding them from, the site of modification (Kouzarides, 2007; Sanchez and Zhou, 2009). These modifications are

often enzymatically mediated, highly dynamic and are responsible for inducing a wide range of genomic activities (Kouzarides, 2007).

N-acetylation of the lysine (K) side chain (ε-*N*-acetylation) is one of the most commonly found and studied post translational protein modifications to date (Muller et al., 2011). Chromatin acetylation, most commonly seen on the N-terminal histone tail, is widely recognised as being associated with an open structure to which DNA and RNA polymerases and transcription factors are then recruited (Filippakopoulos and Knapp, 2014). Therefore, histone acetylation is generally associated with transcriptional activation and deacetylation with gene silencing (Muller et al., 2011). However, lysine acetylation has been found to occur on many other nuclear and non-nuclear proteins suggesting multiple roles of this modification in cell signalling and transduction events (Filippakopoulos and Knapp, 2014; Kouzarides, 2000).

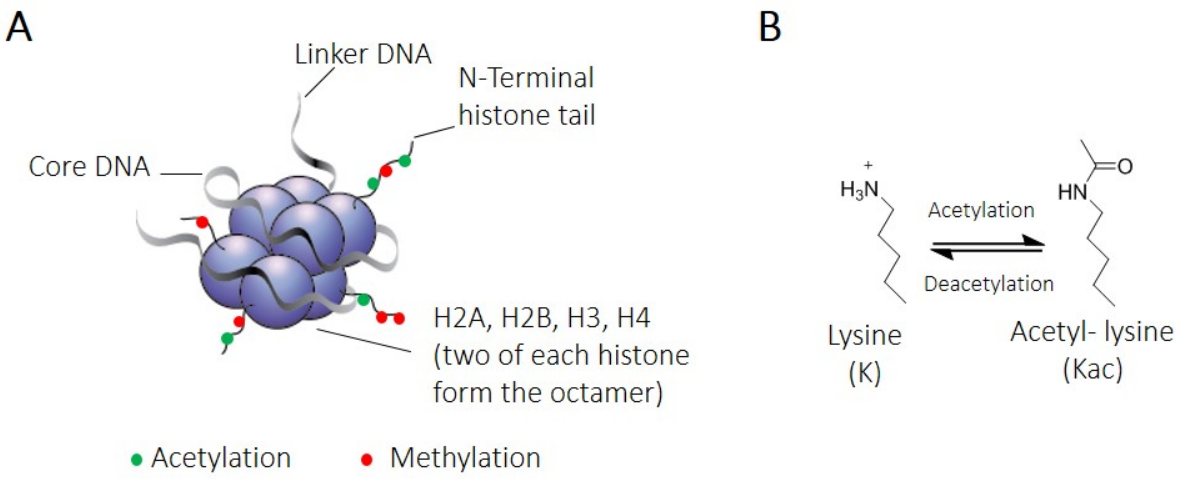


Figure 8.1 Chromatin organisation and lysine acetylation. (**A**) Human DNA is packaged in the nucleus by interaction with histone proteins. A 147 base-pair length of DNA is wound around an octamer of histone proteins H2A, H2B, H3 and H4 forming the main unit of chromatin: the nucleosome. Nucleosome are linked to one another via linker DNA. The N-Terminal of the histone projects out of the nucleosome and is subject to numerous post translational modifications such as acetylation and methylation. (**B**) N-acetylation of the Lysine side chain neutralises the positive charge altering its physiochemical properties. Adapted from (McGee and Hargreaves, 2011).

Lysine acetylation drastically alters its physiochemical properties by neutralising the positive charge (**Figure 8.1 B**) (Filippakopoulos et al., 2012). Acetylated lysine (Kac) motifs are specifically recognised by bromodomains (BRDs), evolutionarily conserved protein recognition sites that bind Kac via a hydrophobic pocket (Kac site). The BRD-Kac interaction is anchored through a series of water-mediated hydrogen bonds and a conserved asparagine residue that forms a hydrogen bond to the Kac oxygen through the amide nitrogen (Filippakopoulos et al., 2010; Owen et al., 2000). The role of BRDs is to recruit proteins to large macromolecules where they act as 'readers' of acetylation state and subsequently carry out a range of specific functions. Proteins that contain two N-terminal BRDs (BD1 and BD2) and an extra terminal domain form the BET bromodomain family, a group of nuclear localised epigenetic modifiers that regulate transcription and cell cycle progression.

The BET protein family consists of BRD2, BRD3, BRD4 and BRDT. BRDs 2–4 are ubiquitously expressed whereas BRDT is found only in germ cells (Chaidos et al., 2015). The BET family have particular affinity for acetylated tails of histones 3 and 4 and are transcriptional activators that regulate numerous cell growth, differentiation and apoptotic programs. Abnormal expression of BET proteins has been implicated in a number of cancers and inflammatory diseases (Belkina et al., 2013; Fu et al., 2015). This has led to the generation of a number of BET bromodomain inhibitors, including PFI-1 and (+)-JQ1, which were identified as positively regulating mEPDC migration in the previously described automated fluorescent scratch assay (**Chapter 7**). Reported inhibitors have varied specificity for the different BET proteins which is commonly represented by determination of the half maximal inhibitory concentration (IC_{50}) against the independent domains. Generally, the IC_{50} refers to how much of the compound is required to cause 50% inhibition of activity of a given protein *in vitro*; the lower the IC_{50} value the more potent the compound against that target. A common method of measuring the affinity

for compounds of the BET bromodomains is by measuring peptide displacement using an Amplified Luminescence Proximity Homogeneous Assay (AlphaScreen)
(Philpott et al., 2011). AlphaScreening utilises streptavidin-coated donor beads which are conjugated to biotinylated peptides (in this case tetracetylated histone H4 proteins) and 'acceptor' beads which contain a metal nickle ion to which histidine tagged BET proteins are conjugated (Philpott et al., 2011). Laser excitation of the donor bead converts oxygen to singlet oxygen. If interaction between the BET protein and the histone H4 has brought the beads close enough together, the singlet oxygen initiates a chemiluminescent reaction in the acceptor bead which emits light. By varying the concentration of an inhibitor, which will prevent BET-histone interaction, the concentration of an inhibitor required to supress the light signal by 50% can be quantified generating an IC_{50} value. Another common description of inhibitor potency is the dissociation constant (K_d). The K_d value is a measure of the propensity of the inhibitor (I) to associate with the target protein (P) and is defined as: $\frac{[I][P]}{[IP]}$, where [I] is the concentration of inhibitor, [P] is the protein concentration and [IP] is the concentration of the resulting complex. As such a lower K_d value represents greater affinity between the ligand and protein.

8.1 Compound selection for the BET inhibitor screen

The first BET inhibitor identified from the pilot automated scratch assay was PFI -1 (**Figure 8.2 A**). PFI-1 is a potent and selective BET inhibitor: a screen for Kac mimetics found that 6-bromo-3-methyl-3,4-dihydroquinazoline-2-one displaced tetra-acetylated histone 4 peptides from the BRD4 protein *in vitro*. A series of structure-activity relationship (SAR) studies then identified PFI-1 as one of a series of benzenesulfonamide-quinazolin-2-one BET inhibitors that displaced acetylated histones with IC_{50} of 98 nM for BRD2 and 200 nM for BRD4 (Picaud et al., 2013a). PFI-1 was found to have a higher affinity for the BRD4 BD1 (BRD4(1)) over BRD4 BD2

(BRD4(2)) with K_d values of 47 nM and 195 nM, respectively (Fish et al., 2012; Picaud et al., 2013a).

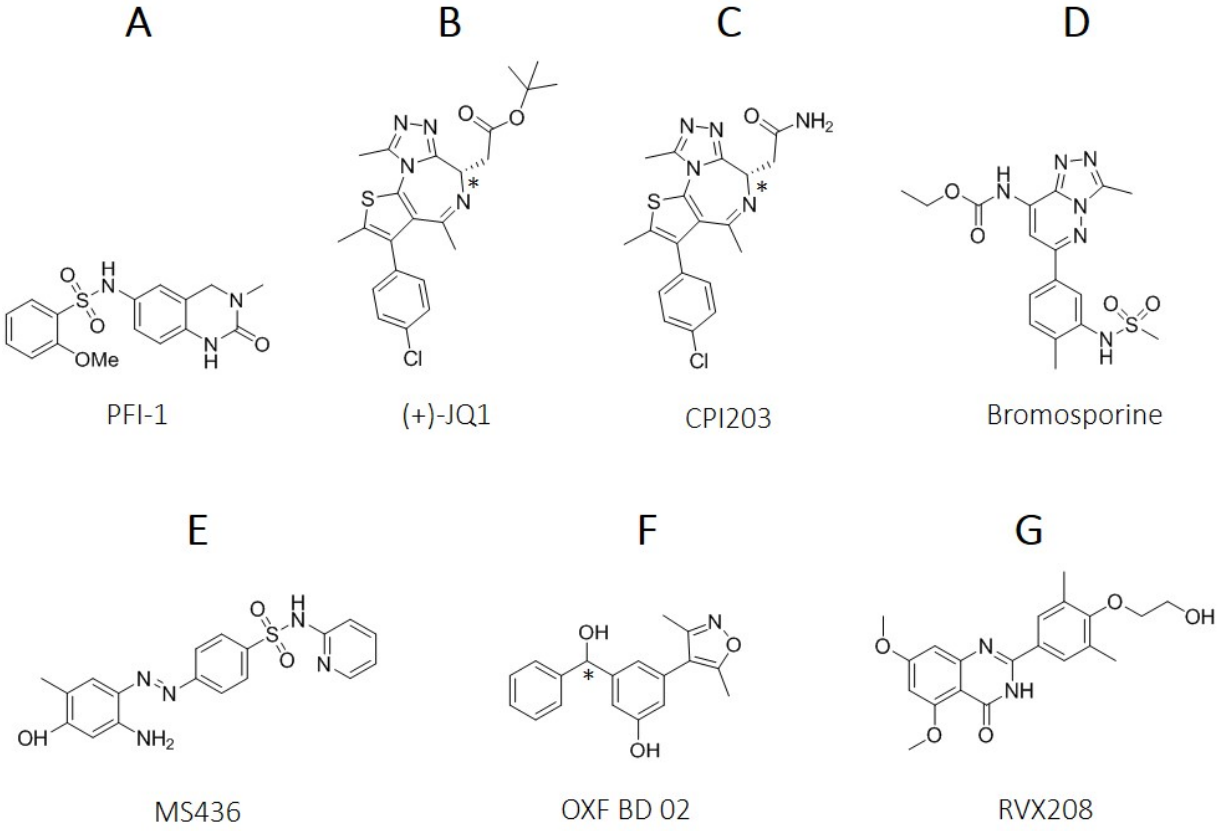


Figure 8.2 Library of small molecule BET inhibitors screened in an automated mEPDC scratch assay. A selection of small molecules with a range of BRD specificities were chosen for screening. (**A**) The first selective BET inhibitor to be identified as a positive hit from the automated scratch assay was PFI-1. (**B**) The potent broad BET inhibitor (+)-JQ1 was also found to positively regulate mEPDC migration. (**C**) CPI203, a structural analogue of (+)-JQ1, is selective for BRD(4). (**D**) The pan-bromodomain inhibitor Bromosporine. (**E**) MS436 demonstrates selectivity for BRD4(1) over BRD4(2). (**F**) OXF BD 02 demonstrates selectivity for BRD4(1) over BRD4(2). (**G**) RVX208 demonstrates selectivity for BRD3(2) over BRD3(1).

The second BET inhibitor identified as a positive regulator of mEPDC migration was (+)-JQ1 (**Figure 8.2 B**). Discovered in 2010, enantiomerically pure (+)-JQ1 was found to be a potent inhibitor of the BET bromodomains: K_d values of 50 nM and 90 nM were found for to BRD4(1) and BRD4(2), respectively, 59 nM and 82 nM for BRD3(1) and BRD3(2). Interestingly the binding affinity for BRD2 was approximately three-fold lower (Filippakopoulos et al., 2010).

(+)-JQ1 has a reported IC_{50} value of 22 nM against BRD4 as determine by AlphaScreen technology (Devaiah et al., 2012). The other enantiomer (-)-JQ1 was found to be inactive, which is predicted to be due to steric clash between the tertiary butyl group and the Kac binding site (Filippakopoulos et al., 2010).

In order to probe the implications of the BET bromodomains in mEPDC migration, it was decided that another scratch assay would be performed with a panel of BET inhibitors. Additional BET inhibitors from the literature were selected and screened, along with PFI-1 and (+)-JQ1. The range of compounds was chosen to encompass a variety of chemotypes (See **Figure 8.2**), varied specificity for both for the various BET proteins and also for the BD1 and BD2 subtypes in order to further confirm whether BET inhibition is related to epicardial migration and, if so, to map out whether one specific isoform is involved mEPDC migration.

The first compound selected for testing was CPI203 (**Figure 8.2 C**), a structural analogue of (+)-JQ1 with a primary amide in place of the tertiary butyl acetate. CPI203 is a selective and cell permeable inhibitor of the BET bromodomains and has a reported IC_{50} of 37 nM in BRD4 (Devaiah et al., 2012). CPI203 was included in our screen to provide some SAR information on mEPDC migratory response.

The next compound selected was the broad spectrum bromodomain inhibitor Bromosporine (**Figure 8.2 D**) with reported IC_{50} values of 410 nM, 290 nM, 122 nM and 17 nM for BRD2, BRD4, BRD9 and CECR2, respectively. The BRD9 protein is not part of the BET family, and is proposed to play a role in chromatin remodelling with the SW1/SNF complex, a collection of proteins that can alter DNA packaging including the movement of nucleosomes (Whitehouse et al., 1999). The cat eye syndrome critical region protein 2 (CECR2) is another non-BET

bromodomain containing protein involved in chromatin remodelling (Banting et al., 2005). Bromosporine was included in the pilot mEPDC scratch assay and was not identified as a hit when tested at 1μM **(Appendix Tables A.7.1** and **A.7.1**); it was included in the bromodomain screen to probe the effect of a promiscuous bromodomain inhibitor and to see whether adverse effects were observed compared with other more targeted compounds.

The diazobenzene-based BET inhibitor MS436 (**Figure 8.2 E**) was developed to probe the effect of selective inhibition of the two separate BRD4 bromodomains (Zhang et al., 2013). MS436 exhibits ten-fold increased selectivity for BRD4(1) over BRD4(2) with an estimated inhibitory constant (Ki) of 30–50 nM. Also included was OXF BD 02, another BRD4(1) inhibitor with K_d values of 360 nM and 390 nM for the (*R*)- and (*S*)- enantiomers respectively (**Figure 8.2 F)** (Hewings et al., 2013).

Finally the small molecule RVX208, currently undergoing clinical investigation for the treatment of atherosclerosis and other cardiovascular diseases, is a BET bromodomain inhibitor with selectivity for BD2 over BD1 (Nicholls et al., 2011; Picaud et al., 2013b) (**Figure 8.2 G**). This selectivity is particularly striking in BRD3 with a reported K_d of 4.06 μM for BD1 and 0.194 μM for BD2. BD2 selectivity was also seen across the other BET proteins but the differences were not as significant. MS336, OXF BD 02 and RVX203 were included to investigate whether selectivity between the BET BRDs affected mEPDC migratory response.

8.2 Screening the panel of BRD inhibitors

In the third automated mEPDC scratch assay, the 7 BRD inhibitors were tested at ten concentrations to determine a dose response. To decide upon an appropriate dosage, the cell based IC_{50} values of each compound were identified from the literature as a sensible starting

point. A number of assays have been used to measure inhibition of BET activity in cells. BET inhibition prevents expression of the MYC gene, that encodes a transcription factor, in MV4-11 acute myelogenous leukaemia cells; measurement of MYC mRNA expression can act as a read out of BET inhibition (Devaiah et al., 2012). BET inhibition also prevents release of interleukin 6 (IL-6) from leukaemia cells: IL-6 release can be measured by enzyme-linked immunosorbent assay (ELISA) which can measures the quantity of a an antigen in a sample by application of a specific antibody (Devaiah et al., 2012; http://www.elisa-antibody.com/ELISA-Introduction). It was decided that the highest dose tested would be 10-fold higher than the reported IC_{50} value for activity in cells, so as to hopefully encompass the point of saturation, and then decrease by a third of the $\log_{10}$ scale over a total of 10 concentrations. In addition to the 7 BRD inhibitors screened, a dose response of the reported TGFβ mimetic A-161906 was included at a range of concentrations based around the effective dose identified from the 'validation screen' (**Chapter 7.2**). The assay was performed following the same protocol as previously described.

In the BRD inhibitor screen, the scratch wounds closed approximately six hours earlier than the previous two experiments with TGFβ treated cells reaching confluency by 36 hours and untreated and DMSO by 42 hours (**Figure 8.3 A**).

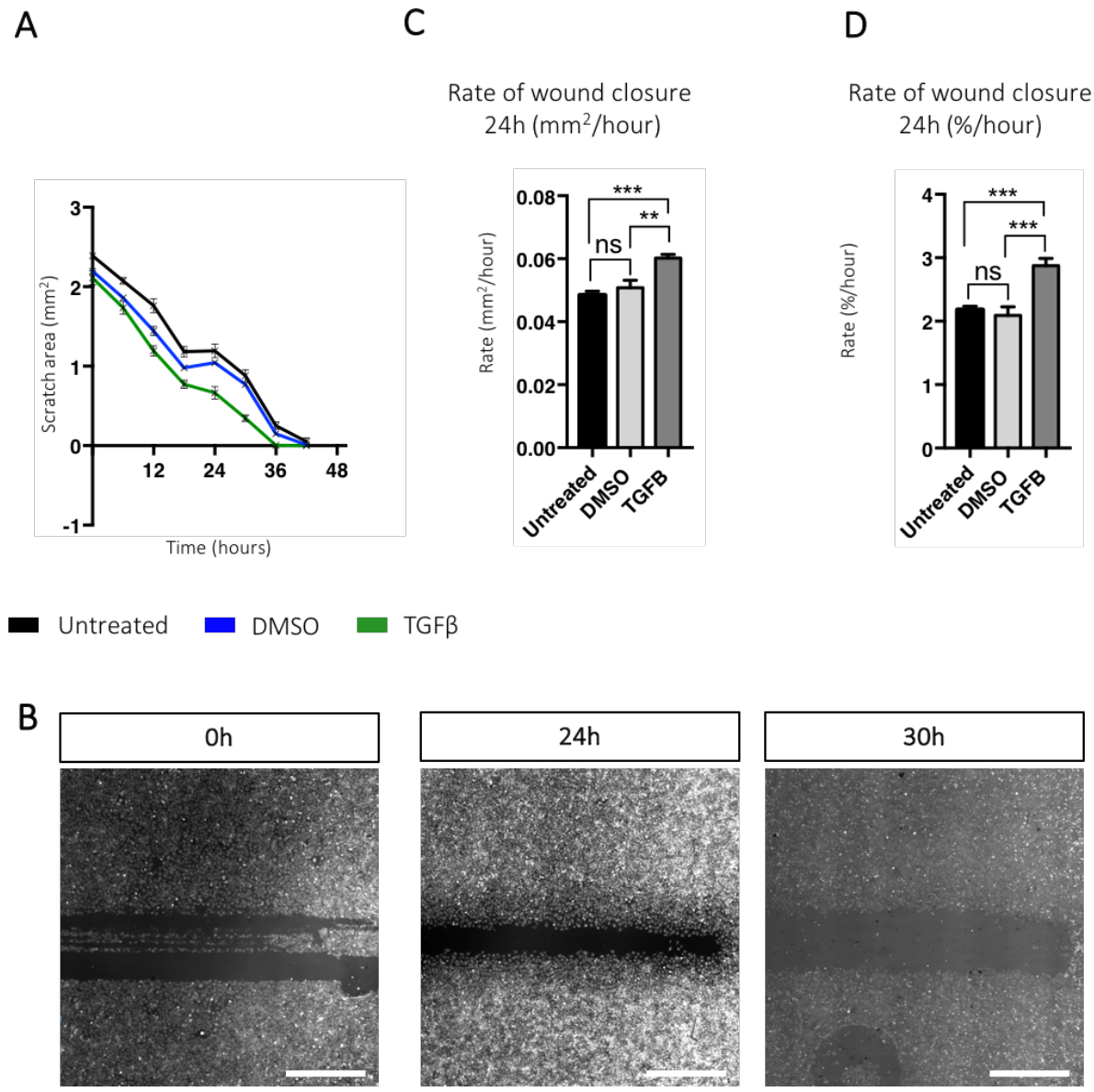


Figure 8.3 Control data for BRD inhibitor screen. (**A**) Plotting the growth curve for the three controls revealed that scratch wounds closed approximately six hours earlier than the previous experiment: TGFβ controls had closed by 36 hours and both untreated and DMSO by 42 hours. (**B**) Several wells had to be disregarded from the zero-hour time point due to inadequate wound formation. The 24-hour time-point was chosen over the 30-hour due to excess leaching of the Cell Tracker at 30 hours. (**C**) The rate of closure in TGFβ treated cells was significantly higher than the other controls at 24 hours. (**D**) To allow manual analysis the rate data was converted in to percentages. The percentage rate values of the controls were analysed and confirmed significant increase in rate of wound closure at 24 hours in TGFβ treated wounds. Statistics calculated using a one way ANOVA: n = 6, **p<0.01; ***p<0.001.

A number of problems were encountered during the BRD inhibitor screen that affected the method used for data analysis. In a number of zero-hour scratch wounds the cells had not been properly removed by the scratch tool leaving patches of mEPDCs in the middle of the well

(**Figure 8.3.1 B**): this meant that a number of wells had to be disregarded and so for several treatments there were not enough replicates for statistical analysis. A number of wells that were used for the analysis still had small patches of cells in the middle and in these cases the analysis protocol struggled to accurately measure the scratch. Originally, 30 hours was chosen as the 'end point' for the experiment, earlier than in the previous scratch assays due to the overall time taken for scratch wounds to close being shorter. However, during the data analysis, it became clear that leaching of the CellTracker^{TM} had resulted in fluorescent images with poor contrast between the scratch and the cells at 30 hours (**Figure 8.3 B**). Even when adjusting the parameters used to identify the scratch in the analysis protocol, the InCell Analyser struggled to identify the scratch. At 24 hours, immediately after the second stain, the contrast between cells and scratch was much more defined (**Figure 8.3 B**), therefore, we choose to analyse the data at this time point instead. When the rate of cell migration at 24 hours for each of the controls was calculated as before (**Chapter 7.1.2**), once again, the TGFβ treated scratch wounds had closed significantly faster than the untreated and DMSO treated controls (**Figure 8.3 C**). No significant differences were found between scratch wound closure in DMSO and untreated cells.

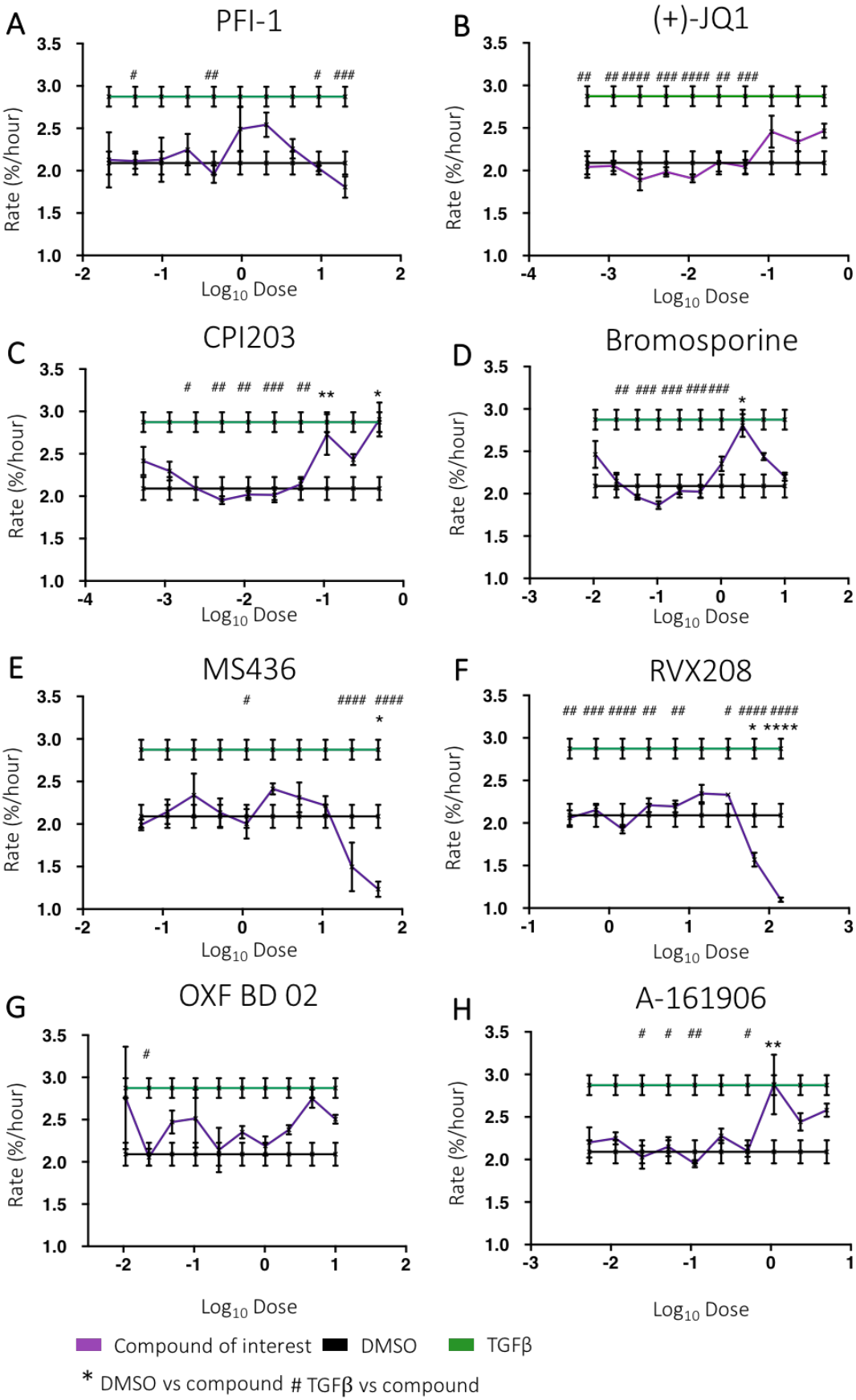

A
PFI-1
B
(+)-JQ1
C
CPI203
D
Bromosporine
E
MS436
F
RVX208
G
OXF BD 02
H
A-161906
Rate (%/hour)
Log10 Dose
Compound of interest
DMSO
TGFβ
* DMSO vs compound # TGFβ vs compound

Figure 8.4 Dose response profiles of the BRD bromodomains and the reported TGFβ mimetic A-161904. (**A**) The dose response of PF1-1 mimicked that seen in the validation screen: rate of migration increased with increasing concentration up to 2μM (0.3 on the log_{10} scale) after which the activity decreased. (**B**) The rate of migration for (+)-JQ1 was seen to increase as the concentration increased and the most effective concentration was found to 0.5μM (-0.3). (**C**) CPI203 was screened at the same dose range as (+)-JQ1: the most effective concentration was found to be 0.5 μM (-0.3). (**D**) The most effective concentration of Bromosporine was 2 μM (0.3) which was found to be significantly higher than the DMSO control (**E**) Treatment with MS436 at 2 and 5 μM (0.4 and 0.7) increased rate of migration to slightly higher than DMSO but this was not found to be significant. (**F**) The highest concentrations of RVX208 caused the rate of mEPDC migration to decrease: at 30 and 65 μM (1.5 and 1.8) the rate was greater than that of DMSO but this was not found to be significant. (**G**) At all but one concentration the rate of wound closure with OXF BD 02 was faster than DMSO control, however the data was variable and did not correlate neatly with dose. (**H**) At 1, 2 and 5 μM (0.04, 0.4, 0.7) of A-161906 the rate of migration was higher than that of DMSO: this was significant at 1 μM. Statistics calculated using a one way ANOVA: n = 6, *p<0.05; **p<0.01; ***p<0.001; ****p<0.0001, # indicate identical significance boundaries.

Due to a number of images from the zero-hour time point being sub-optimal and the small changes in migration being measured in this assay, it was felt that the automated data should also be checked manually to ensure that the results were accurate. All of the rate data was calculated manually in ImageJ for the control wells at every time point and for the compound data at 0 and 24 hours. For ease of comparing the area measurements on the InCell and ImageJ the rate of closure data was calculated as percentage wound closure/hour; comparison of the controls again confirmed that TGFβ treated cells were closing significantly faster that the untreated and DMSO controls (**Figure 8.3 D**). To analyse the compound treated data, the rate of migration (%/hour) was calculated for each treatment at each concentration and plotted against the log_{10} dose, along with the overall rate of migration in DMSO and TGFβ treated wells (at a steady dose) as previously described. This was done with the automated and manually analysed data: the two data sets returned the same results, which demonstrated that the InCell analyzer had been able to accurately measure the starting scratch despite some having not formed properly. The data presented here is from the automated analysis (**Figure 8.4**): the manual data is presented in the appendix (**Figure A.8.1**). Once again the equivalent log_{10} doses are quoted in brackets next to the concentration.

The reported IC_{50} value of PFI-1 in the IL-6 release assay is 2μM (Fish et al., 2012); therefore, the highest concentration tested was 20μM. The dose response curve for PF1-1 mimicked that seen in the validation screen: the rate of migration increased with increasing concentration up until 2μM (0.3 on the log_{10} scale) at which point activity declined (**Figure 8.4 A**). Between 1–4.3μM (0.3–0.64) the rate of migration appeared to be higher than that of DMSO however this was not found to be significant. At no point was the rate of wound closure in PFI-1 treated cells faster than that of TGFβ.

The reported IC_{50} of (+)-JQ1 in cells was 0.035 μM in the IL-6 assay , and 0.080μM in the MYC assay (Devaiah et al., 2012), thus 0.5μM was chosen as the highest test concentration. Once again the rate of migration was seen to increase as the concentration increased and the most effective concentration was found to be 0.5μM (-0.3) (**Figure 8.4 B**). This replicated the validation experiment in which the most effective concentration had been 0.3μM. There were no significant differences in the migration rates between any (+)-JQ1 concentrations and DMSO and at no point did the rate increase to greater than that of TGFβ treated wells.

The reported IC_{50} of CPI203 is similar to that of (+)-JQ1, with 0.03 μM in the IL-6 and 0.1μM in the MYC assay (Devaiah et al., 2012), therefore it was decided that the same test concentrations would be used. The dose response profile was very similar to that of (+)-JQ1 and migration rate was higher than DMSO at the same range of doses: 0.1–0.5μM (-1– -0.3). This was found to be significant at 0.1 and 0.5 μM (-1 and -0.3) and the most effective concentration was 0.5 μM (-0.03) (**Figure 8.4 C**). At no concentration was the rate faster than the TGFβ control.

The pan BRD inhibitor Bromosporine has a reported IC_{50} value of 1μM against BRD4 which was calculated in a fluorescence recovery after photobleaching (FRAP) assay (Structural Genomics Consortium, Bromosporine). In the FRAP assay, a small area of the cell nuclei that expressed mutant GFP tagged BRD4 protein was bleached out by a laser pulse. The time taken for the bleached area to recover is dependent upon the presence or lack of free GFP tagged protein. Inhibition of BRD4 should reduce chromatin binding and therefore decrease recovery time (Philpott et al., 2014). In the mEPDC scratch assay 10μM of Bromosporine was the highest test concentration. Bromosporine demonstrated increased activity with increased dose, followed by a decline at higher concentration. The most effective concentration was 2 μM (0.3) which was found to be significantly higher than the DMSO control (**Figure 8.4 D**). Once again, at no concentration was the rate faster than the TGFβ control.

The IC_{50} for MS436 is 5μM as measured in the IL-6 ELISA assay (Zhang et al., 2013), therefore the highest concentration screened was 50μM: at both 20 and 50 μM (1.4 and 1.7) the rate of migration was less than in DMSO. At 2 and 5 μM (0.4 and 0.7) the rate of migration appeared slightly higher than DMSO but this was not found to be significant (**Figure 8.4 E**). At no concentration was the rate of closure in treated cells faster than that of the TGFβ control.

The small molecule RVX208 is currently being investigated for the treatment of atherosclerosis: at 30 μM RVX208 enhances expression of Apolipoprotein A-1 (ApoA-1) in human hepatoma cells *in vitro*, which increases the ability of cells to efflux cholesterol (McLure et al., 2013). The reported IC_{50} for expression of ApoA-1 mRNA is approximately 1 μM however it was also tested at higher concentrations to encompass an effective concentration for initiating protein expression. The highest concentration required was 300 μM however the stock compound solutions were at 10mM and it was not possible to dilute the DMSO to less than 3% in the final

assay plate, therefore, this concentration was excluded from the dose response. At 140 μM (2.1), the highest dose, the final DMSO concentration was 1%: a 1% DMSO control was also included in the assay which showed no mEPDC toxicity or effect on rate of migration; therefore, the 140μM data was analysed. The dose response profile was very similar to that of MS436. At the highest concentrations of 65 and 140μM (1.8 and 2.1) mEPDC migration was decreased: at 14 and 30 μM (1.2 and 1.5) the rate was greater than that of DMSO but this was not found to be significant (**Figure 8.4 F**). At no concentration did the rate of migration exceed that of the TGFβ control.

The BRD inhibitor OXF BD 02 has a reported IC_{50} of 0.3μM against BRD4 and demonstrated an IC_{50} of 0.8μM in a cell based cytotoxicity assay (Hewings et al., 2013): 3μM was chosen as the highest concentration. At all but one concentration the rate of wound closure with OXF BD 02 was faster than the DMSO control, however, the data was very variable, failed to reach significance and did not follow a classical dose response (**Figure 8.4 G**) Once again, at no concentration did the rate of migration exceed that of the TGFβ control.

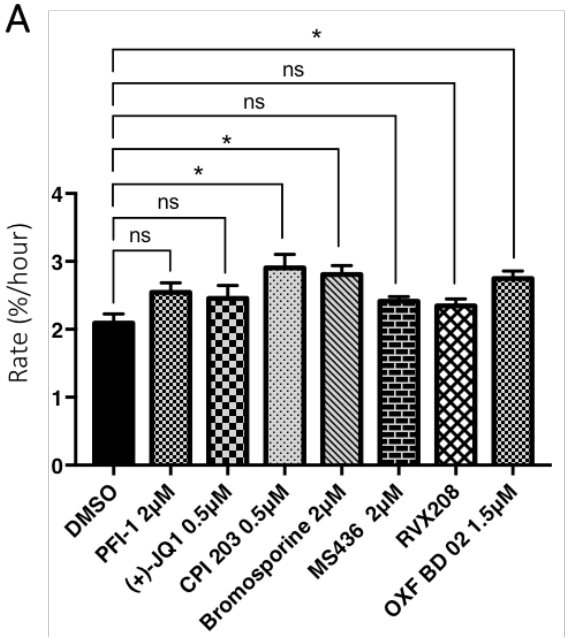
The final compound screened was the reported TGFβ mimetic A-161906. TGFβ mediates a range of processes involved in extracellular matrix degradation and deposition. *In vitro* human dermal fibroblasts treated with the cytokine interleukin one (IL-1) results in collagenase expression, an enzyme that destroys ECM components: this activity is inhibited by TGFβ. In the same system A-161906 inhibits IL-1 induced collagenase expression with a reported IC_{50} of 0.3μM (Glaser et al., 2002). In the validation assay 3μM was found to increase the rate of migration but at 10 μM the rate decreased again (**Chapter 7.2**). The highest concentration of A-161906 screened again along with the BRD inhibitors was 5μM. At 1, 2 and 5 μM (0, 0.3, 0.7)

the rate of migration was higher than that of DMSO and this was found to be significant at 1 μM (**Figure 8.4 H**).

The rate data calculated both from the automated and manual analysis produced the same dose response profiles (**Appendix, Figure A.8.1** and **A.8.2**), therefore, it was not necessary to re-examine the images to check they corresponded to the calculated rates. However, since PFI-1, Bromosporine, MS436 and RVX208 demonstrated a decrease in activity at higher concentrations these images were investigated to see whether this was due to cell toxicity. Indeed, all four appeared to be toxic at their highest concentrations as demonstrated by unhealthy cell cultures containing a number of rounded dead cells. Toxicity of the BET inhibitors at high concentration, possibly due to off target effects, was likely to be responsible for the appearance of a 'high dose hook effect', which describes a dose response curve in which a compound that appears demonstrate increased activity with increased concentration is then found to negatively regulate activity at higher concentrations (Agarwal et al., 2010).

After the dose response of each compound was calculated, the migration rate of the most effective concentration of each BET inhibitor was plotted against DMSO for easy comparison (**Figure 8.5**). From the graph it can be seen that Bromosporine, CPI203 and OXF BD 02 showed the greatest activity and significantly increased the rate of wound closure compared with the DMSO control: PFI-1, (+)-JQ1, MS436 and RVX208 were did not significantly increase the rate of wound closure The rate values were then used to calculate the percentage of the wound total that had closed with each individual treatment at 24 hours. 50% of the DMSO treated scratch wounds had closed after 24 hours, compared with 70, 67 and 66% with CPI203, Bromosporine and OXF BD 02, respectively.

A



B

Compound	Rate (%/hour)	Area closed (%)
DMSO	2.09	50
PFI-1	2.54	61
(+)-JQ1	2.45	59
CPI203	2.90	70
Bromosporine	2.81	67
MS436	2.41	58
RVX208	2.35	56
OXF BD 02	2.75	66

Figure 8.5 Combined rate data for the most effective concentration of each BET inhibitor. (**A**) The maximum rate of migration for each compound was plotted against the DMSO control. Bromosporine, CPI203 and OXF BD 02 significantly increased the rate of migration compared with the DMSO control. PFI-1, (+)-JQ1, MS436 and RVX208 were not found to increase the rate of wound closure by a significant amount. (**B**) The rata data (%/hour) was then used to calculate the percentage of scratch wound that had been closed by each treatment at 24 hours.

8.3 Investigating mEPDC EMT and differentiation

'Hits' from the automated scratch assay were selected based upon their ability to increase the rate of mEPDC migration, which was used as a surrogate read-out for activation. The overall aim was to identify small molecules that induce epicardial activation and EMT, producing a multipotent EPDC population with the potential to differentiate towards alternate cardiac fates. When conducting a phenotypic screen, it is essential that the read out selected, in this case migration, is biologically relevant to the desired cell behaviour. Therefore, it was imperative to investigate whether the increased cell migration observed after treatment with the BET inhibitors was associated with mEPDC EMT and differentiation, or whether the increased rate of migration in fact reflected an alternate biological response.

To do so, the BET inhibitors were tested in the same assay that was previously used to characterise TGFβ induced EMT and differentiation in the mEPDC cell line (**Chapter 5.1**). This assay was chosen because TGFβ induced EMT had already been well characterised both in the literature (Austin et al., 2008; Xu et al., 2009) and in the mEPDC characterisation studies (**Chapter 5.1**) and, therefore, could be used as a positive control. CPI203, Bromosporine and OXF BD 02 were found to significantly increase the rate of migration in the BET inhibitor screen at concentrations of 2, 0.5 and 1.5 μM, respectively, and so were included in the differentiation assay at these concentrations. The original hits PFI-1 and (+)-JQ1 were not found to significantly increase the rate of migration in the BET screen; however, these were also included for comparison. MS436 and RVX208 were not investigated further as they exhibited the least efficacy in the BET screen. MEPDCs were treated with the selected compounds for one, three or 7 days before being collected for analysis by Q-PCR and ICC; 0.5% DMSO and 2 ng/mL TGFβ were included as the negative and positive controls, respectively. The media was replenished every 24 hours in an effort to maintain a steady concentration of BET inhibitor, as the half-life of each compound in the assay system was unknown.

8.3.1 Morphology and gene expression of DMSO and TGFβ controls

Before investigating the effect of the BET inhibitors, the gross morphology and gene expression profile of the control conditions were examined. On day one, when the cultures remained sparse, the DMSO and TGFβ treated cells did not exhibit any obvious morphological differences. By day three the DMSO control has started to form epithelia; TGFβ treated cells were larger with a bigger cytoplasm to nucleus ratio and the cells had not formed a complete sheet. Both cultures were very dense by day 7, however, the TGFβ treated mEPDCs were not as small or rounded as those in the control and the nuclei appeared enlarged with numerous visible nucleoli (**Figure 8.6 A**).

Q-PCR analysis (**Figure 8.6 B**) revealed that the relative expression of the EMT associated transcription factor *Snai1* (Cano et al., 2000) had increased nearly six fold over the first 24 hours of exposure to TGFβ relative to the control, unlike *Snai2* which exhibited only small changes in expression until day 7. Interestingly, the DNA binding transcription factor *ZEB2* (Goossens et al., 2011), another regulator of EMT, was also found to increase but only at day 7. Expression of both *Acta2*, encoding α-SMA, and *TAGLN*, encoding SM22-α, incrementally increased over the duration of the experiment, indicating that mEPDCs continued to respond to TGFβ treatment over the 7 days and suggesting a phenotypic shift towards smooth muscle. No change in *WT1* expression was observed over the 7 days demonstrating that the cells were still epicardial in phenotype. Reduced activity of the E-CADHERIN gene *Cdh1* was observed in TGFβ treated cells after three days of treatment, as would be expected in cells undergoing EMT (Cano et al., 2000), although this was not found to be significant. However, this appeared to increase again at day 7. This observation perhaps reflects the immortalised mEPDCs retaining or reverting back to an epithelial phenotype at high density. This is postulated to be due to the immortalised state of the mEPDC cell line or perhaps due to contact inhibition, in which formation of cell-cell contacts reduces epithelial cell response to growth factor stimulation (Grazia Lampugnani et al., 2003).

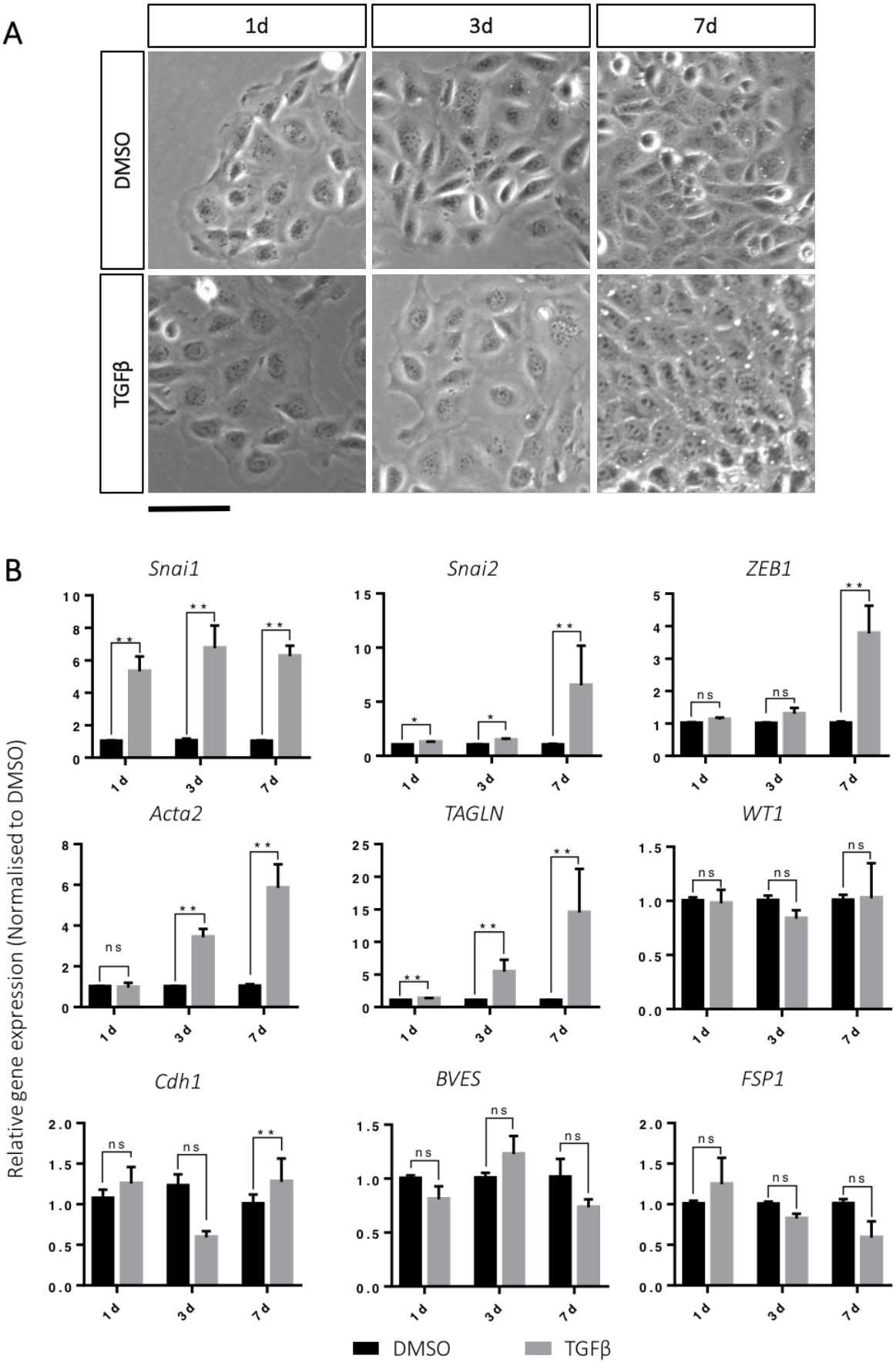

A
1d
3d
7d
DMSO
TGFβ
B
Snai1
Snai2
ZEB1
Acta2
TAGLN
WT1
Cdh1
BVES
FSP1
Relative gene expression (Normalised to DMSO)
1d
3d
7d
ns
DMSO
TGFβ

Figure 8.6 Brightfield images and gene expression panel of mEPDCs treated with TGFβ compared with the DMSO control. (**A**) Brightfield images of the two control conditions on days one, three and 7 of the differentiation experiment. DMSO treated cells appear to form epithelia over the time course. By day 7 TGFβ treated cultures are also dense, however, nuclei appear enlarged and the culture does not resemble uniform epithelia. (**B**) Q-PCR revealed increased expression of genes associated with epicardial EMT and differentiation**:** *Snai1, Snai2, ZEB1, Acta2 and TAGLN*. *Cdh1* expression was variable and was unexpectedly upregulated on day 7. No change was seen in expression of *WT1, BVES* or *FSP1*. Statistics calculated using a Mann-Whitney test, n = 5, *p<0.05; **p<0.01; ***p<0.001; ****p<0.0001. Scale bar 100 μm.

As has already been documented in the characterisation studies (**Chapter 5.1**), TGFβ induced expression of genes associated with epicardial EMT and differentiation towards a smooth muscle fate. However, the purpose of this work was not to find a compound that mimics the action of TGFβ but rather one that activates EPDCs with the potential to push them towards an alternate cardiac fate. therefore, two further genes related to epicardial activation and differentiation were investigated. Blood vessel epicardial substance (BVES) is known to regulate cell migration and adhesion (Benesh et al., 2013) and is expressed in the PE, migrating EPDCs and a number of related progeny including vascular smooth muscle (Reese et al., 1999). FSP1 is thought to be involved in the transition of epithelial cells to fibroblasts and is widely thought of as fibroblast marker, although more recently its specificity was questioned when it was also identified in both haematopoietic and endocardial cells of the injured heart (Kong et al., 2013; Strutz et al., 1995). FSP1 is also considered a mesenchymal marker. No significant changes in expression of either of these two genes was seen with TGFβ treatment. However, they were included in the gene expression panel for Q-PCR analysis as any observed change in their expression may have represented mEPDC activation by mechanisms different to that induced by TGFβ.

To further investigate mEPDC phenotypic switch, cells that had been fixed at each time point were stained with anti-β-CATENIN and phalloidin for imaging. As observed in **Chapter 5**, mEPDC morphology was variable depending upon the culture density and mEPDCs appeared

mesenchymal in morphology, irrespective of the treatment, in sparse areas of the culture. Therefore, at the one and three-day time points mEPDCs were imaged in denser areas of the culture to investigate how the compounds had affected the formation of epithelium.

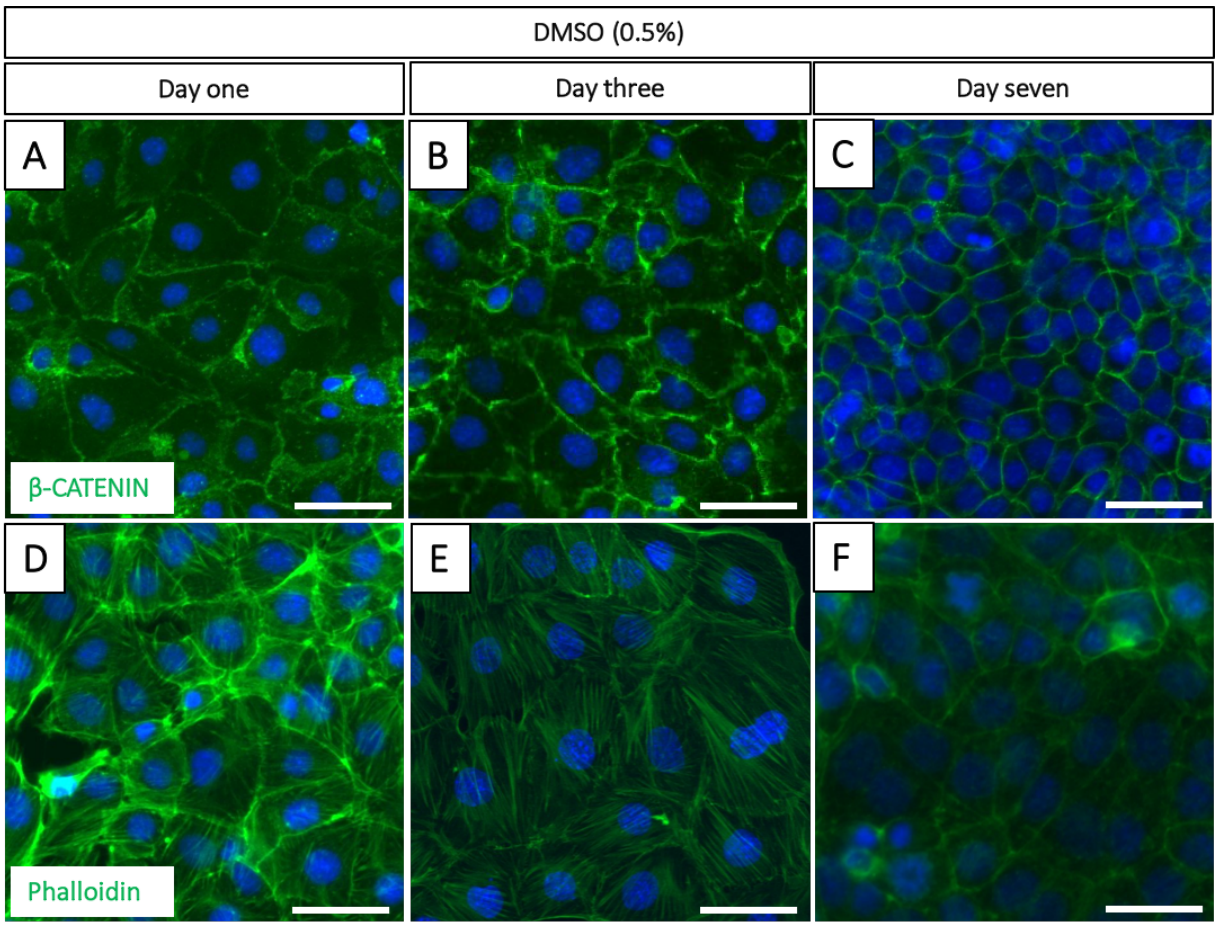


Figure 8.7 mEPDCs treated with DMSO for one, three and 7 days stained with β-CATENIN and phalloidin to assess morphology. (**A–C**) Over the time course β-CATENIN was seen to localise to the cell membrane indicating the formation of tight epithelia. (**D–F**) Phalloidin staining revealed formation of a cortical actin ring network; clearly defined stress fibres can also be seen on days one and three (**D** and **E**). Scale bars 50 μm.

First mEPDCs treated with the 0.5% DMSO control were examined (**Figure 8.7**). By day one the cells had begun to express β-CATENIN at the membrane and appeared to be forming epithelial sheets; cytoplasmic distribution was also observed **(Figure 8.7 A**). After three days β-CATENIN was seen at the membrane around every cell, although some cytoplasmic staining was still observed **(Figure 8.7 B**). By day 7, mEPDCs were very dense and β-CATENIN was neatly distributed around the periphery of every cell **(Figure 8.7 C**). On day one the mEPDCs

had begun to form a network of cortical actin rings which again indicated formation of epithelia, although stress fibres were also seen across the cell bodies **(Figure 8.7 D)**. Similar F-ACTIN staining was observed at day three and multiple stress fibres were observed across each cell body **(Figure 8.7 E)**. At day 7, the dense cultures were very tightly packed and definition between each cell was much less distinct **(Figure 8.7 F)**. Cortical actin rings had formed around the edges of the cells, however, it was not possible to bring the actin cytoskeleton into focus across the whole culture. It appeared that the cells had not been contact inhibited when they reached confluency and had begun to grow on top of each other. This staining indicated that the DMSO control had not impeded mEPDC growth and that they had been able to form tight epithelia.

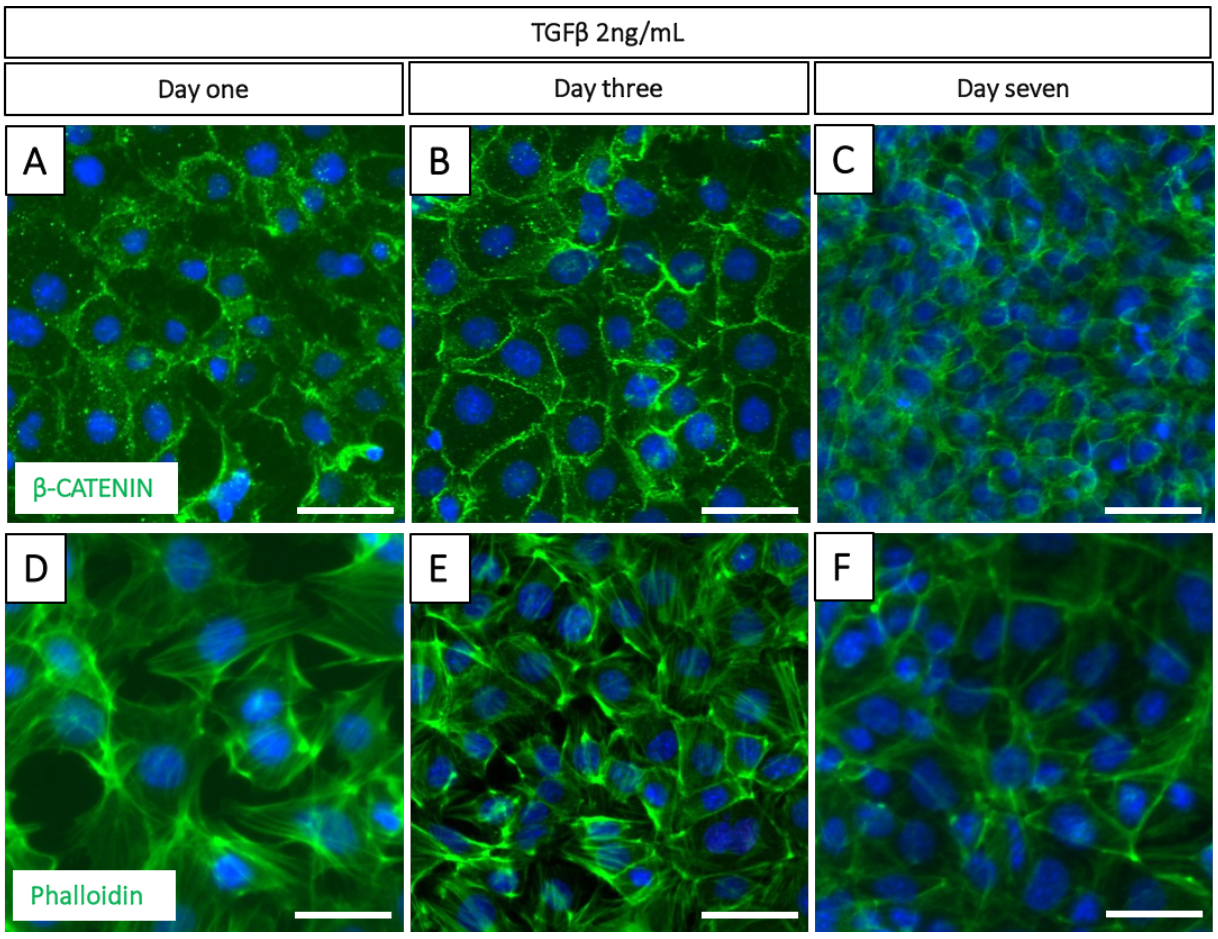


Figure 8.8 mEPDCs treated with TGFβ for one, three and 7 days stained with β-CATENIN and phalloidin to assess morphology. (**A**–**C**) β-CATENIN was seen to located at the membrane but also in the cytoplasm at all three time points. (**D**–**F**) Phalloidin staining revealed that TGFβ induced 'spindle' morphology on days one and three (**D** and **E**), however as the cultures became dense a cortical actin network formed (**F**). Scale bars 50 μm.

Next to be investigated were the TGFβ treated cultures (**Figure 8.8**). As had already been observed in the model characterisation, β-CATENIN staining was not uniformly distributed around the cell membrane on days one or three and was also observed in both the cytoplasm and the nuclei (**Figure 8.8 A** and **B**). On day 7 β-CATENIN was localised at the cell membrane, however it was also densely spread throughout the cytoplasm in a manner that made is difficult to distinguish the individual cells from one another **(Figure 8.8 C)**. On days one and three the phalloidin staining revealed distinct 'spindle' cell morphology and stress fibre formation across the cell body (**Figure 8.8 D** and **E**). By day 7 a cortical actin network had formed around the densely packed mEPDCs. However, the cells also contained stress fibres and did not appear to have formed a neat, uniform epithelium (**Figure 8.8 F**). Collectively this data indicated that mEPDCs responded to treatment with TGFβ but that they had not fully differentiated away from an epithelial phenotype as is demonstrated by the formation of a cortical actin network and presence of membrane bound β-CATENIN day 7.

8.3.2 Morphology and gene expression of PFI-1 treated mEPDCs

Next, the cell morphology and gene expression of mEPDCs treated with the BET inhibitors were examined. The first inhibitor to be examined was the original scratch assay hit PF1-1, which was used at a concentration of 2 μM. For all other differentiation experiments the mEPDCs were plated at a density of $2.5x10^3$ cells/cm^2. However, at this density, mEPDCs treated with PFI-1 one died between days one and three. Therefore, an identical experiment was conducted but with a cell density of $7.5x10^3$ cells/cm^2, at which the mEPDCs did not die. On day one the DMSO and PFI-1 treated cells appeared very similar (**Figure 8.9 A**). By day three the DMSO

cultures were dense whereas cells treated with PFI-1 were still large and flat. Both cultures had grown dense by day 7 but the PFI-1 treated cells were larger than the control and also appeared very rounded in shape.

Q-PCR was used to examine the gene expression profile of PFI-1 treated cells relative to DMSO. The only gene found to change significantly from the control in the duration of the experiment was *Cdh1*, however the general trends will still be discussed (**Figure 8.9 B**). There appeared to be a decrease in expression of the EMT markers *Snai1*, *ZEB1* and *Acta2* at each time point: *Snai2* appeared to be slightly upregulated on day one and also on day 7. *TAGLN, WT1* and *FSP1* expression was variable across the time points. *Cdh1* was significantly upregulated on day one, after which it decreased over the rest of the time course. *BVES* expression was incrementally downregulated over the course of the experiment. Generally, PFI-1 appeared to supress the markers of EMT and differentiation associated with TGFβ. This indicated that although both PFI-1 and TGFβ increased the rate of mEPDC migration, they did not do so via the same mechanisms.

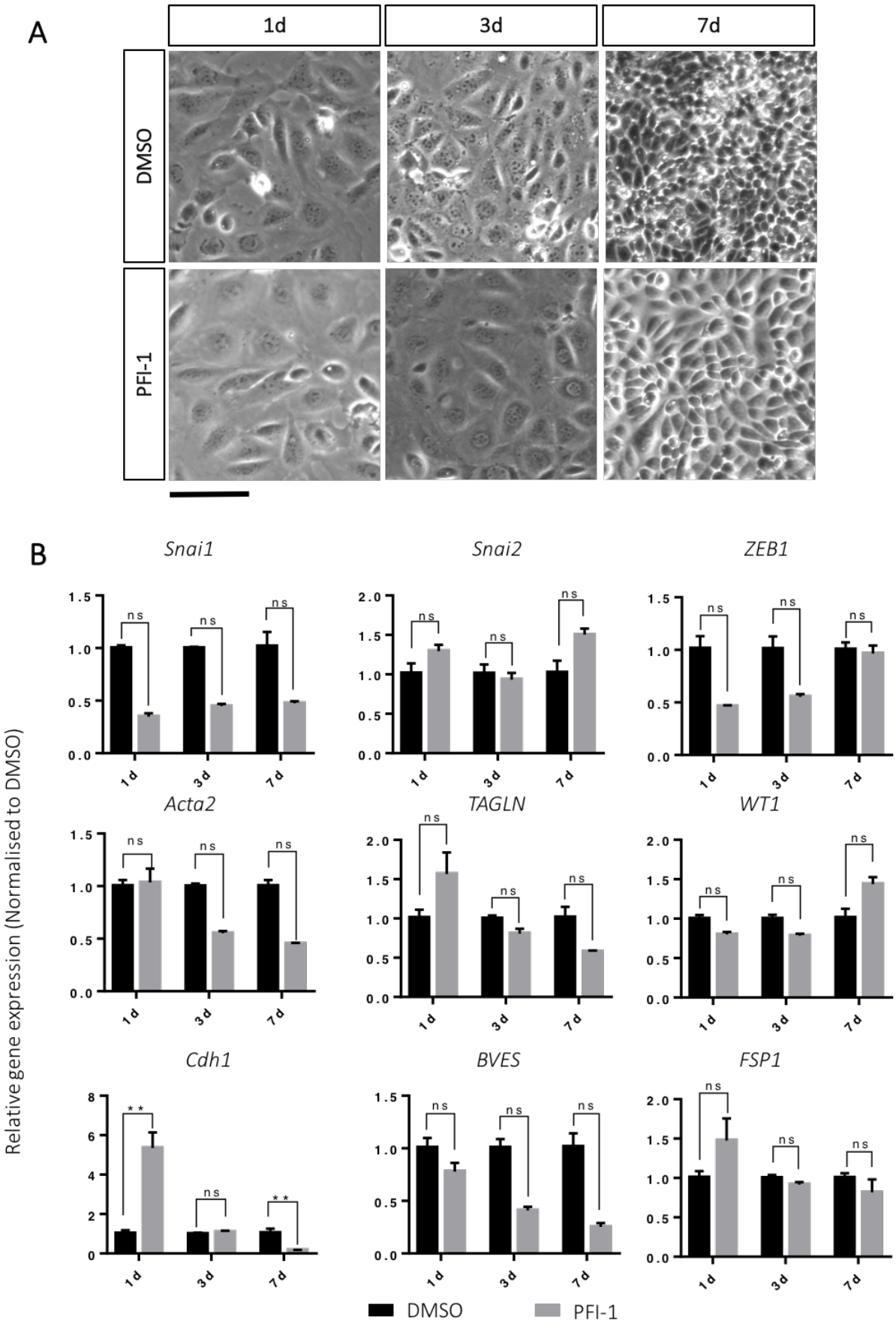

A
1d
3d
7d
DMSO
PFI-1
B
Snai1
Snai2
ZEB1
Acta2
TAGLN
WT1
Cdh1
BVES
FSP1
Relative gene expression (Normalised to DMSO)
ns
**
1d
3d
7d
DMSO
PFI-1

Figure 8.9 Brightfield images and gene expression panel of mEPDCs treated with PFI-1 compared with the DMSO control. (**A**) Brightfield images of cells treated with PFI-1 compared with the DMSO control. Treated mEPDCs appeared similar to the control on day one. On day three PFI-1 treated cells were much larger than the control; by day even both cultures were very confluent: PFI-1 cells appeared very rounded possibly forming more than one cell layer. (**B**) Q-PCR revealed decreased expression of genes associated with epicardial EMT and differentiation**:** *Snai1, ZEB1, Acta2*: relative to the control. *Snai2*, *TAGLN, WT1 and FSP1* expression was highly variable. *Cdh1* was significantly upregulated on day one after which is was found to decline. *BVES* expression was also downregulated. Statistics calculated using a Mann-Whitney test, n = 5, *p<0.05; **p<0.01; ***p<0.001; ****p<0.0001. Scale bar 100 µm.

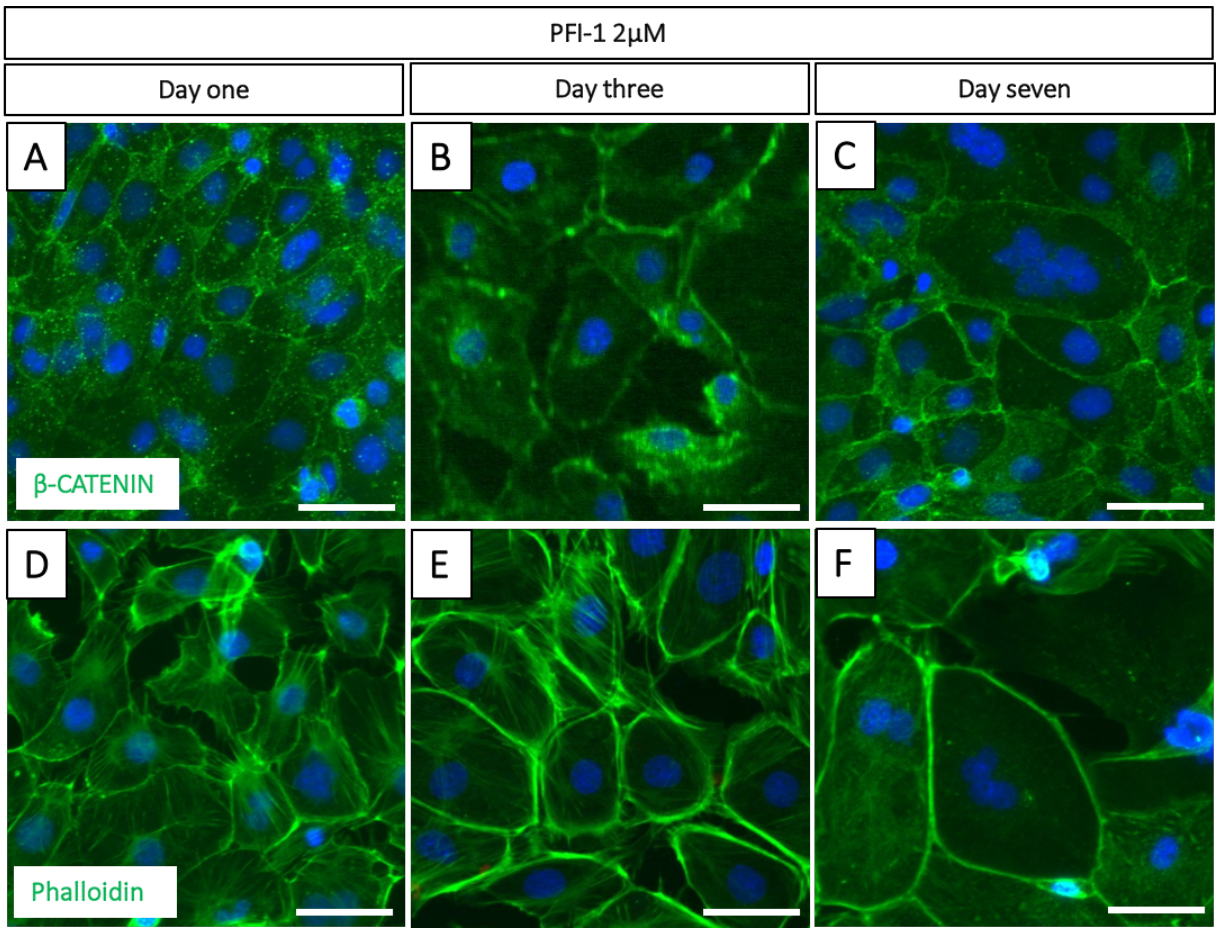


Figure 8.10 mEPDCs treated with PFI-1 for one, three and 7 days stained with β-CATENIN and phalloidin to assess morphology. (**A–C**) Cytoplasmic β-CATENIN was observed at all time points and was localised to the membrane at points of cell-cell contact. (**D–F**) Phalloidin staining revealed heterogeneous cell morphology on day one; smooth rings of actin formed around the mEPDCs which had become enlarged cells on days three and 7 (**E** and **F**) . Scale bars 50 µm.

Next PFI-1 treated mEPDCs were stained and imaged (**Figure 8.10**). After one day β-CATENIN was seen at the cell edge but this was less defined than in the DMSO control. 'Speckled' cytoplasmic β-CATENIN staining was seen in every cell on day one (**Figure 8.10 A**). On day

three β-CATENIN could be seen located in the cytoplasm and around the nucleus; the cells were enlarged and the cultures sparse, indicating some toxicity: this was not unexpected as complete cell death had already been observed when mEPDCs plated at low density were treated with PFI-1 (**Figure 8.10 B**). By day 7 the cells had started to reach confluency, however, they were heterogeneous in shape and much larger than the DMSO control (**Figure 8.10 C**).

Phalloidin staining revealed stress fibre formation and spindle morphology on day one, alongside gaps in the cell sheet (**Figure 8.10 D**). On day three the cells had become enlarged and smooth defined actin rings had formed around the cell edge: filopodia appeared to be extruding from the membrane towards neighbouring cells, however, the cultures did not resemble epithelia (**Figure 8.10 E**). Similar morphology was observed at day 7: mEPDCs were large with smooth actin rings surrounding the cytoplasm but did not have the homogenous polygonal morphology associated with epithelia and there were a number of binucleated cells. (**Figure 8.10 F**). In agreement with the QPCR data, PFI-1 did not appear to affect mEPDC morphology in the same manner as TGFβ over the time course. However, mEPDC morphology was distinct to that of the DMSO control (**Figure 8.7**). At all-time points β–CATENIN speckles were present in the cytoplasm suggesting it was not being recruited to the membrane to support the formation of adherens junctions. The increased cell size and rounded actin cytoskeleton was particularly striking as was the multinucleation (**Figure 8.10 E** and **F**). Knock down of BRD4 in a human cancer cell line suppressed cell proliferation and caused ‘mitotic catastrophe’, in which cells were unable to undergo cytokinesis resulting in multinucleation (You et al., 2009). It is postulated that continued treatment with PFI-1 may have induced a similar effect in the mEPDC which might have resulted in their unusual morphology.

8.3.3 Morphology and gene expression of (+)-JQ1 treated mEPDCs

The next cultures examined had been treated with 0.3 μM of (+)-JQ1. On day one, treated mEPDCs did not appear different from those treated with DMSO alone; however, on day three the treated mEPDCs appeared sparse and had not formed a continuous sheet (**Figure 8.11 A**). By day 7 (+)-JQ1 treated cultures were very dense and appeared unhealthy. A number of cells contained large numbers of vacuoles throughout the cytoplasm indicative of parapoptosis: non apoptotic cell death characterised by vacuolization of the endoplasmic reticulum and mitochondria (Palmeri et al., 2009; Zheng et al., 2016).

Q-PCR was used to examine the gene expression profile of (+)-JQ1 treated cells relative to DMSO (**Figure 8.11 B**). No significant differences were seen in *Snai1* expression although it appeared to be slightly reduced on days one and three. *Snai2* appeared to be upregulated on day one, however, this was not found to be significant and expression decreased to less than the DMSO control on days three and 7; no significant differences were observed in *ZEB1* expression on any day. *Acta2* was significantly decreased in (+)-JQ1 treated cells at every time point, as was *TAGLN* on days one and two: *TAGLN* expression was also reduced on day 7, however, this was not found to be significant. No significant change was observed in *WT1* expression indicating that mEPDCs were still epicardial in nature. *Cdh1* was significantly decreased on days one and three; it was also down on day 7. *BVES* expression was downregulated at all time points and this was significant on days one and three. No significant changes were seen in *FSP1* expression although it appeared to be slightly upregulated on day 7. Much like PFI-1, this data indicated that increased mEPDC migration conferred by treatment with (+)-JQ-1 was not through the same mechanisms associated with TGFβ induced EMT.

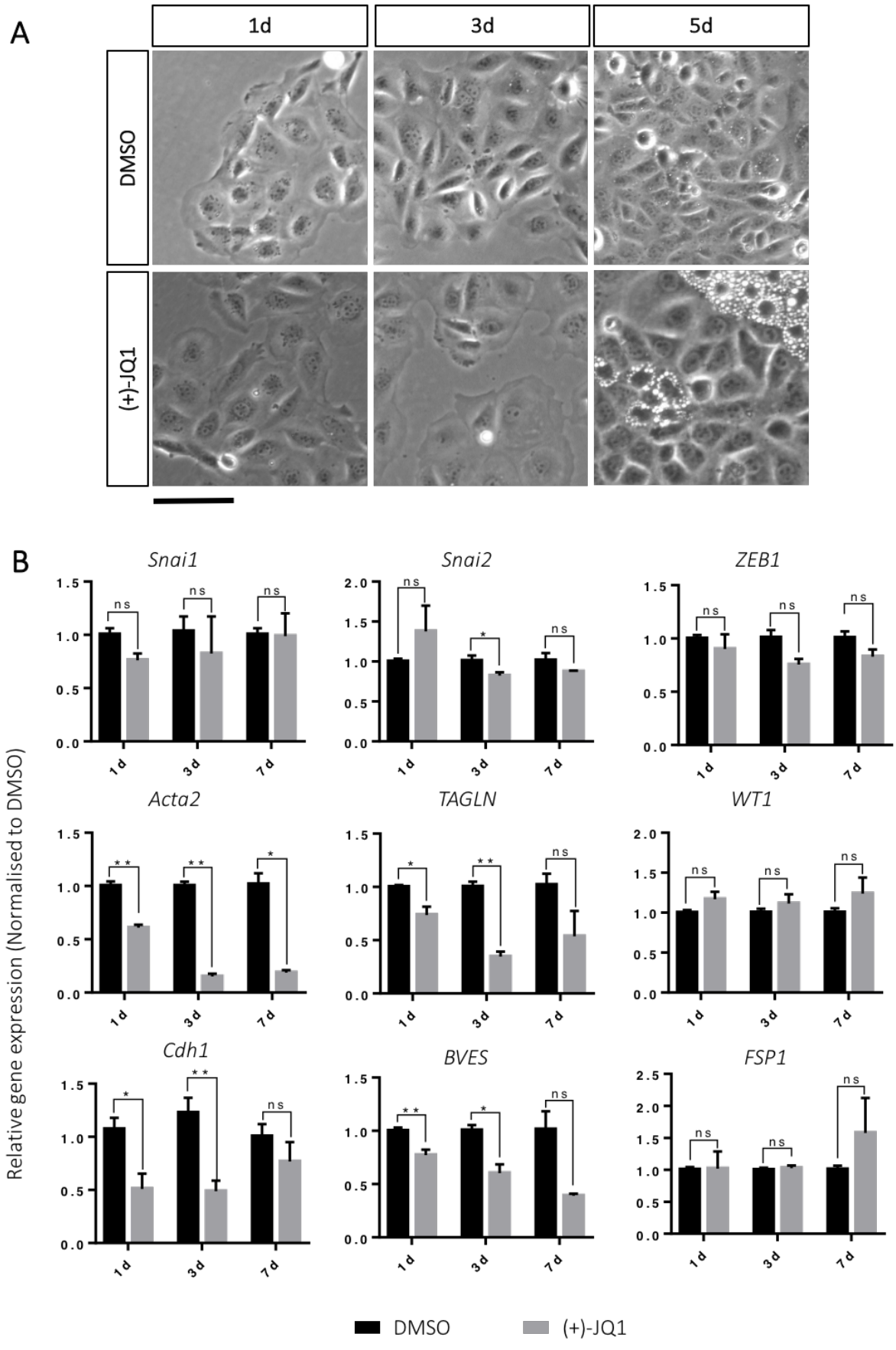

A
1d
3d
5d
DMSO
(+)-JQ1
B
Snai1
Snai2
ZEB1
Acta2
TAGLN
WT1
Cdh1
BVES
FSP1
Relative gene expression (Normalised to DMSO)
ns
1d
3d
7d
DMSO
(+)-JQ1

Figure 8.11 Brightfield images and gene expression panel of mEPDCs treated with (+)-JQ1 compared with the DMSO control. (**A**) Brightfield images of (+)-JQ1 treated cells compared with the DMSO control. Treated and untreated cultures appeared similar on day one; on day three (+)-JQ1 treated cells were sparser than the control. By day 7 treated cultures were dense but several cells had formed vacuoles throughout the cytoplasm indicating parapoptosis. (**B**) Q-PCR revealed decreased expression of genes associated with epicardial EMT and differentiation**:** *Snai1, Snai2, ZEB1, Acta2 and TAGLN*: relative to the control. *Cdh1* expression was down on days one and three but was upregulated on day 7. BVES expression was negatively regulated by (+)-JQ1 and no change was seen in the expression of *WT1, FSP1*. Statistics calculated using a Mann-Whitney test, n = 5, *p<0.05; **p<0.01; ***p<0.001; ****p<0.0001. Scale bar 100μm.

MEPDCs treated with (+)-JQ1 had similar β-CATENIN patterning to the DMSO control on day one (**Figure 8.12**). The cells were homogeneous in size and shape and the protein was located at the cell membrane. On day three some of the cells had become enlarged however the protein was still localised to the membrane. On day 7 the cultures were very dense: β-CATENIN was located at the membrane but speckles of the protein could also be seen in the cytoplasm. Interestingly, phalloidin staining on days one and three revealed stress fibre formation across the cell body, however, by day 7 these were gone and had been replaced by a smooth cortical actin network that appeared to connect the cells together. Much like in the DMSO control, the mEPDCs had started to grow on top of each other in the dense cultures. This suggested that (+)-JQ1 was having effect of mEPDC cytoskeletal arrangement on days one and three, but that this was reversed or inhibited in dense cultures. Perhaps, due to the density of cells by day seven 0.3 μM concentration of (+)-JQ1 was ineffective or that the cells had reverted back to an epithelial morphology.

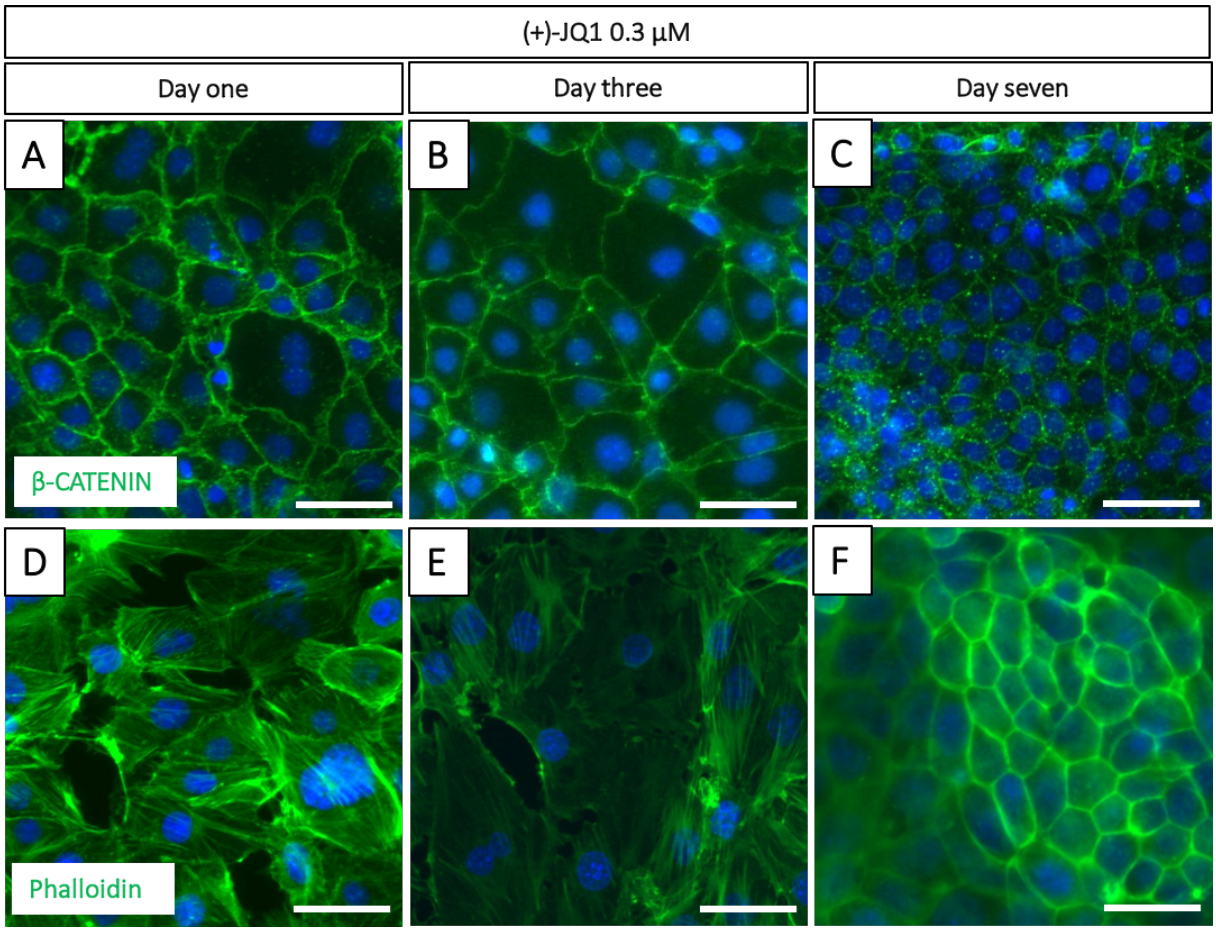


Figure 8.13 mEPDCs treated with (+)-JQ1 for one, three and 7 days stained with β-CATENIN and phalloidin to assess morphology. (**A**–**C**) β-CATENIN was observed at all time points located at the cell membrane: cytoplasmic 'speckles' were observed in the dense cultures at day 7 (**C**). (**D**–**F**) Phalloidin staining revealed 'spindle' like morphology and stress fibre formation on days one and three (**D** and **E**); interestingly by day 7 the stress fibres had disappeared and a smooth actin network connected the cells (**F**). Scale bars 50 µm.

8.3.4 Morphology and gene expression of CPI203 treated mEPDCs

The (+)-JQ1 analogue CPI203 was investigated next at a concentration of 0.5 µM. Brightfield microscopy revealed that the cells were morphologically different to the DMSO control at all time points (**Figure 8.14 A**). The treated mEPDCs appeared elongated on day one and were then much larger and flatter than the controls on days three and 7; as seen with (+)-JQ1 mEPDCs had not formed uniform epithelia and gaps were seen between the cells on day 7.

The Q-PCR results were then examined (**Figure 8.15 B**). With CPI203 treatment, the EMT transcription factors *Snai1* and *ZEB1* were found to be significantly downregulated on all days of the experiment. Conversely, *Snai2* expression was significantly upregulated on day one after which it decreased over the rest of the experiment. As with (+)-JQ1, *Acta2* expression was found to be significantly reduced on all days, whereas *TAGLN* expression was only found to be significantly less than the control on day three. No changes were seen in the level of *WT1* expression. *Cdh1* expression was again seen to be decreased compared with the DMSO control which was significant on days one and three, and both BVES and FSP1 expression was also reduced. Generally, CPI203 also appeared to be supressing the genes associated with TGFβ induced EMT and differentiation. The significant increase in *Snai2* expression at 24 hours was an interesting observation, as *Snai2* is an EMT associated transcription factor however it was not found to be upregulated in TGFβ treated cultures after 24 hours.

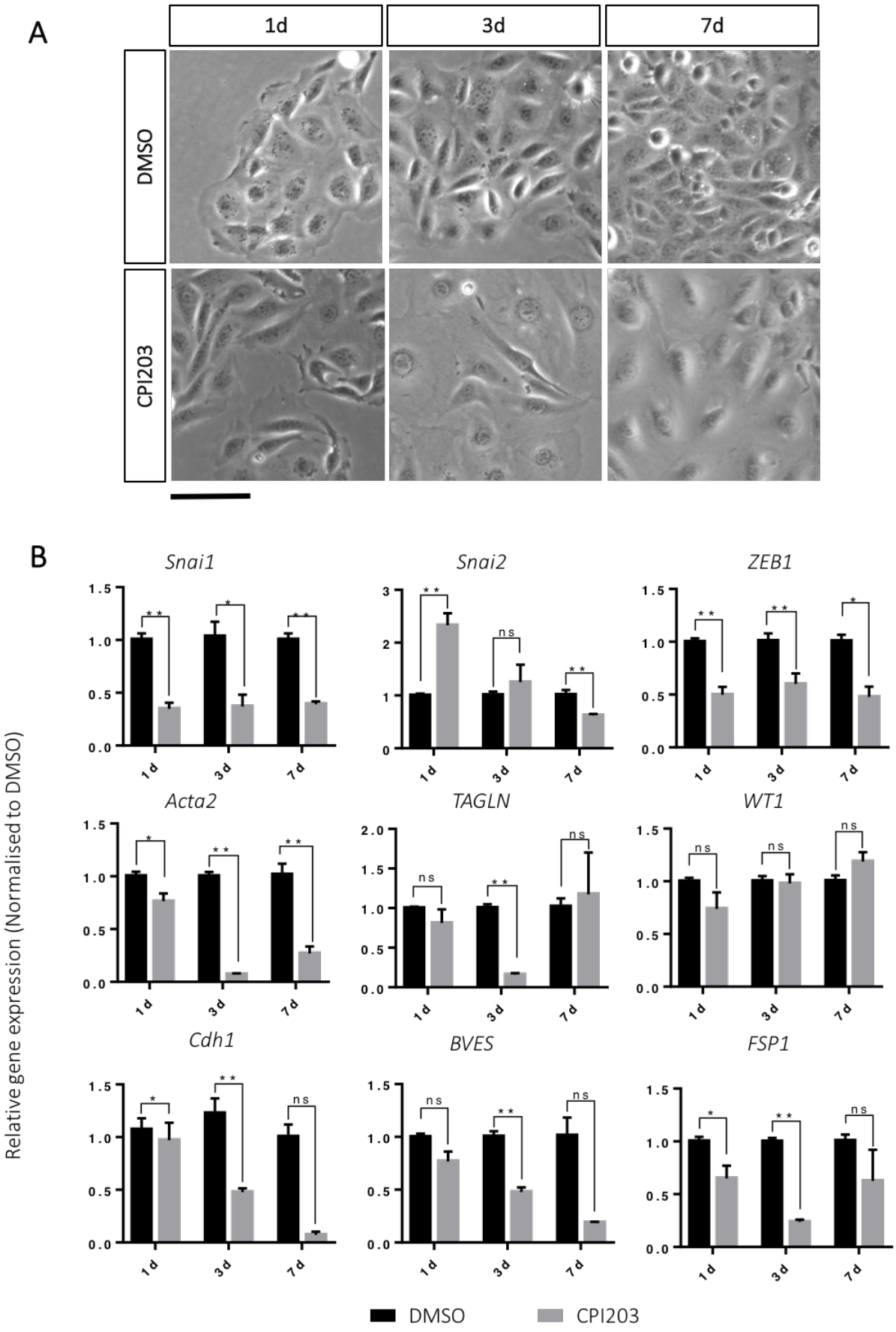

A
1d
3d
7d
DMSO
CPI203
B
Snai1
Snai2
ZEB1
Acta2
TAGLN
WT1
Cdh1
BVES
FSP1
Relative gene expression (Normalised to DMSO)
DMSO
CPI203

Figure 8.15 Brightfield images and gene expression panel of mEPDCs treated with CPI203 compared with the DMSO control. (**A**) Brightfield images of CPI203 treated cells compared with the DMSO control. Morphologically the treated mEPDCs looked very different from the control at all time points: cells were larger, elongated and did not appear to form a tight epithelial sheet. (**B**) Q-PCR revealed decreased expression of genes associated with epicardial EMT and differentiation**:** *Snai1, Zeb1, Acta2 and TAGLN*: relative to the control. Interestingly, *Snai2* expression was significantly upregulated on day one. *Cdh1*, *BVES,* and *FSP1* were negatively regulated by CPI203. No significant change was seen in *WT1* expression. Statistics calculated using a Mann-Whitney test, n = 5, *p<0.05; **p<0.01; ***p<0.001; ****p<0.0001. Scale bar 100 μm.

ICC revealed speckles of β-CATENIN located at the membrane but also throughout the cytoplasm and in the nucleus on day one **(Figure 8.16 A)**. On day three the mEPDCs had become enlarged and less cytoplasmic β-CATENIN was observed; however, there was also less of the protein at the cell membrane and the cells were not joined as a monolayer **(Figure 8.16 B)**. By day 7 the cultures were dense but the mEPDCs appeared heterogeneous in shape and size: β-CATENIN was observed at the membrane but also in the cytoplasm **(Figure 8.16 C)**. Phalloidin staining revealed stress fibre formation and enlarged 'spindle; morphology on days one and three **(Figure 8.16 D** and **E)**. By day 7 the cultures were also dense, however, they were highly heterogeneous in appearance, contained stress fibres and did not resemble uniform epithelium. The presence of cytoplasmic and nuclear β-CATENIN at day one suggested it may have been functioning as a signalling molecule at this time point, or that CPI203 was affecting its association with E-CADHERIN. This would correlate with increased expression of *Snai2* after 24 hours as the presence of β-CATENIN is known to stabilise *Snai2* mRNA (D'Uva et al., 2013). Much like the (+)-JQ1 treated cells, the mechanism of CPI203 induced stress fibre formation appeared to be ameliorated by day seven which again may have indicated that 0.5 μM of CPI203 was ineffective at high cell density although the heterogeneous appearance of the mEPDCs indicated that treatment had had some effect on mEPDC phenotype.

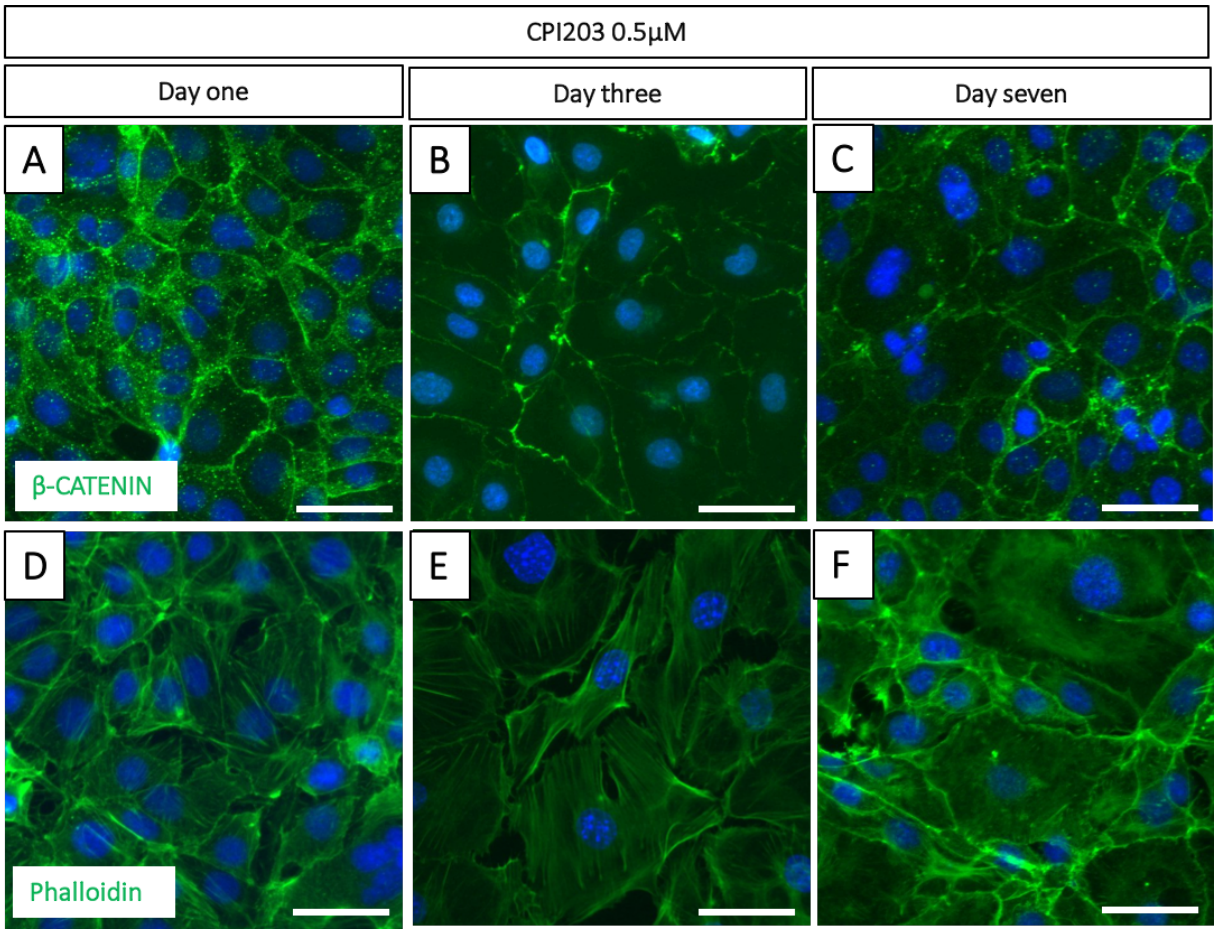


Figure 8.16 mEPDCs treated with CPI203 for one, three and 7 days stained with β-CATENIN and phalloidin to assess morphology. (**A**–**C**) Dense cytoplasmic β-CATENIN staining was observed on day one which was no longer present on days three and 7. β -CATENIN was also seen at the cell membrane at all three time points. (**D**–**F**) Phalloidin staining revealed 'spindle' morphology on day one which was more extreme on day three. MEPDCs in the day 7 cultures were heterogeneous and did not resemble epithelia. Scale bars 50 µm.

8.2.5 Morphology and gene expression of Bromosporine treated mEPDCs

Next to be examined was the pan BRD inhibitor Bromosporine, which was tested at 2μM. On day one of treatment the treated mEPDCs did not look much different to the control, whereas on day three the cells were again much larger and flatter. However, this was not the case on day 7 where cultures appeared very dense, more so than the control, and the cells were small and rounded in appearance (**Figure 8.17 A**).

Although morphologically the mEPDCs treated with Bromosporine appeared quite different to those treated with CPI203, changes in gene expression were found to be similar (**Figure 8.17 B**). Both *Snai1* and *ZEB1* were found to be increasingly downregulated, whereas *Snai2* was significantly upregulated nearly two fold on day one, followed by incremental decrease in expression over the time course. Both *Acta2* and *TAGLN* were significantly downregulated on days three and 7; no significant change in *WT1* expression was observed on days one or three, however it was upregulated on day 7. Despite the cultures appearing dense and 'cobblestone' like by day 7, *Cdh1* was found to be negatively regulated by Bromosporine, relative to the control, over the course of the experiment. Both *BVES* and *FSP1* expression was downregulated on days three and 7. Once again, increased mEPDC migration observed in Bromosporine treated cultures did not appear to be a result of the migratory mechanisms induced by TGFβ. Interestingly, significant increase in *Snai2* was observed again at 24 hours as had been observed with CPI203 which suggested some effect upon transcription of EMT related genes.

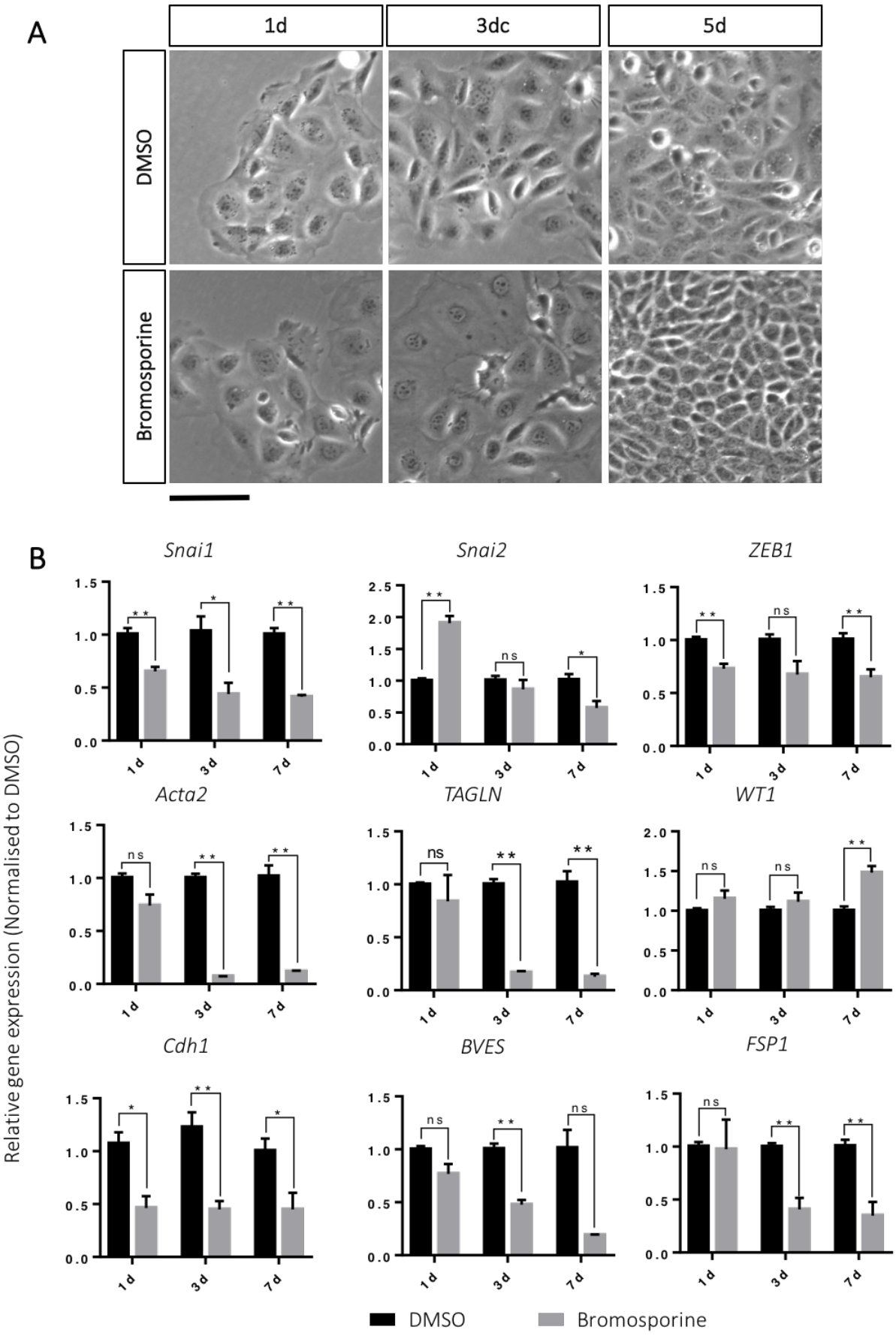

A
1d
3dc
5d
DMSO
Bromosporine
B
Snai1
Snai2
ZEB1
Acta2
TAGLN
WT1
Cdh1
BVES
FSP1
Relative gene expression (Normalised to DMSO)
1 d
3 d
7 d
ns
DMSO
Bromosporine

Figure 8.17 Brightfield images and gene expression panel of mEPDCs treated with Bromosporine compared with the DMSO control. (**A**) Brightfield images of Bromosporine treated cells compared with the DMSO control. Treated mEPDCs appeared similar to the control on day one, but were much larger and flatter on day three. By day 7 the cultures were very dense and the nucleus: cytoplasm ratio was large, as had been seen with TGFβ treatment. (**B**) Q-PCR revealed decreased expression of genes associated with epicardial EMT and differentiation**:** *Snai1, Zeb1, Acta2 and TAGLN*: relative to the control. Once again, *Snai2* expression was significantly upregulated on day one. *Cdh1*, *BVES,* and *FSP1* were negatively regulated by Bromosporine. No significant change was seen in *WT1* expression apart from day 7 where is appeared to be upregulated. Statistics calculated using a Mann-Whitney test, n = 5, *p<0.05; **p<0.01; ***p<0.001; ****p<0.0001. Scale bar 100 μm.

MEPDCs treated with Bromosporine had both membrane bound and cytoplasmic β-CATENIN on day one (**Figure 8.18 A**): on days three and 7 the cultures were heterogeneous and continued to express a mixture of both membrane bound and cytoplasmic β-CATENIN (**Figure 8.18 B** and **C**). At all three time points the cells contained actin stress fibres and had also started to form a cortical actin network (**Figure 8.18 E–F**). The presence of cytoplasmic and nuclear β-CATENIN on day one indicated that Bromosporine was affecting the binding of β-CATENIN to E-CAHERIN or causing it to be stabilised in the cytoplasm. This again was correlated with increased expression of *Snai2* at the one day time point. As had been seen with the other BET inhibitors, Bromosporine did not appear to inhibit the formation of a cortical actin network over the time course which may reflect a tendency of the mEPDCs to remain epithelial and high concentration or that the concentration was ineffective.

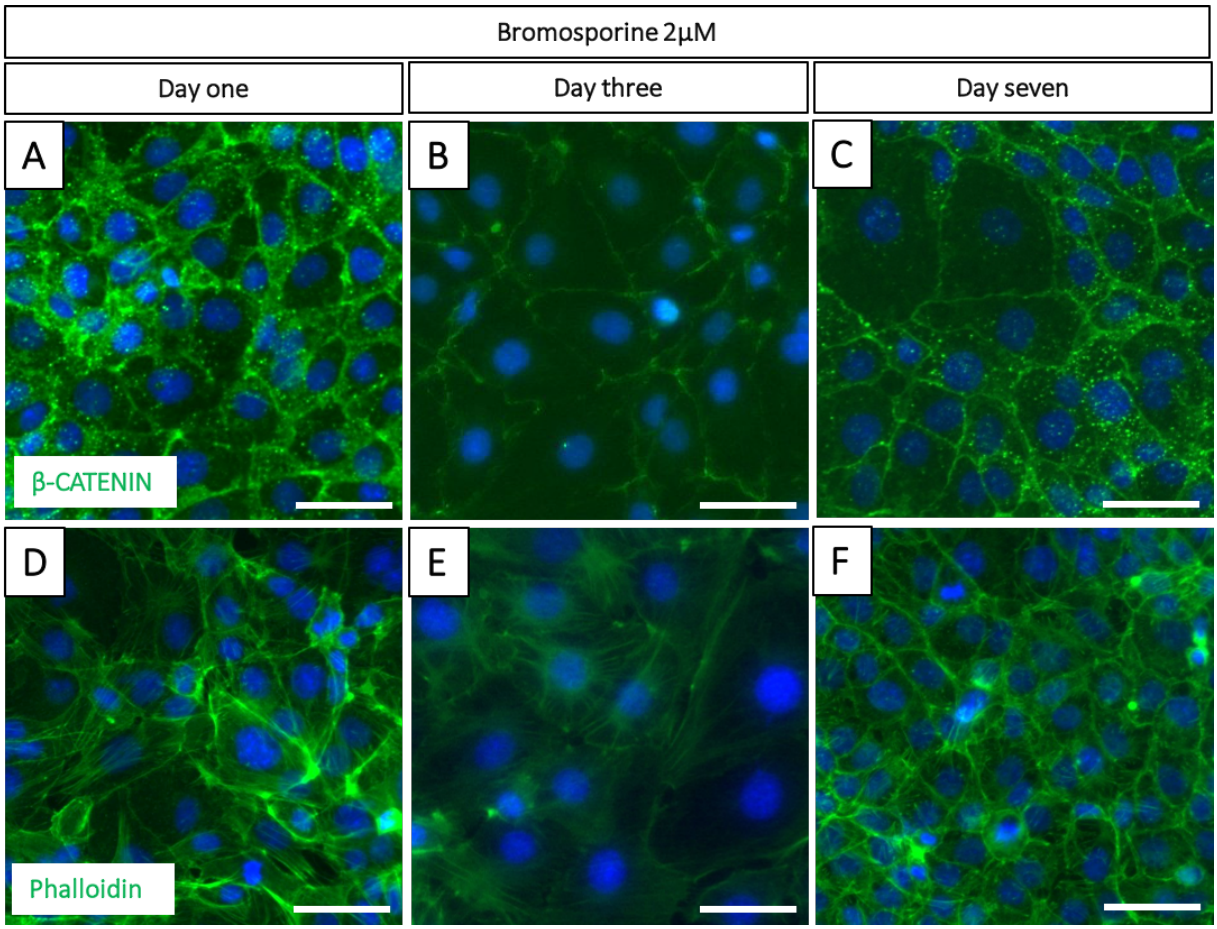


Figure 8.18 mEPDCs treated with Bromosporine for one, three and 7 days stained with β-CATENIN and phalloidin to assess morphology. (**A**–**C**) β-CATENIN was both cytoplasmic and membrane bound at all three time points. (**D**–**F**) Phalloidin staining revealed stress fibre formation at all three time points and the cells appeared to form an actin network. Scale bars 50 µm.

8.2.6 Morphology and gene expression of OXF BD 02 treated mEPDCs

The final BRD inhibitor examined was the selective BRD4(1) inhibitor OXF BD 02 which was tested at a concentration of 1.5µM. When examined by brightfield microscopy the mEPDCs did not appear much different to those treated with DMSO alone at any time point and by day 7 the cultures appeared confluent (**Figure 8.19 A**). Q-PCR found *Snai1* expression to be significantly downregulated on days three and 7, *ZEB1* was significantly lower than DMSO on day three only. Once again, *Snai2* expression was significantly increased on day one after which it decreased. Both *Acta2* and *TAGLN* were found to be negatively regulated by OXF BD 02 and WT1 expression had decreased by half on day one; however, no significant differences were

observed on days three and 7. Again *Cdh1* decreased relative to the DMSO control over the time course as did *BVES*; *FSP1* expression was downregulated on days one and three but no significant difference was found on day 7 (**Figure 8.19**). Collectively, OXF BD 02 had induced similar changes in gene expression as CPI203 and Bromosporine, supressing EMT and differentiation markers associated with TGFβ induced EMT, with the exception of *Snai2*.

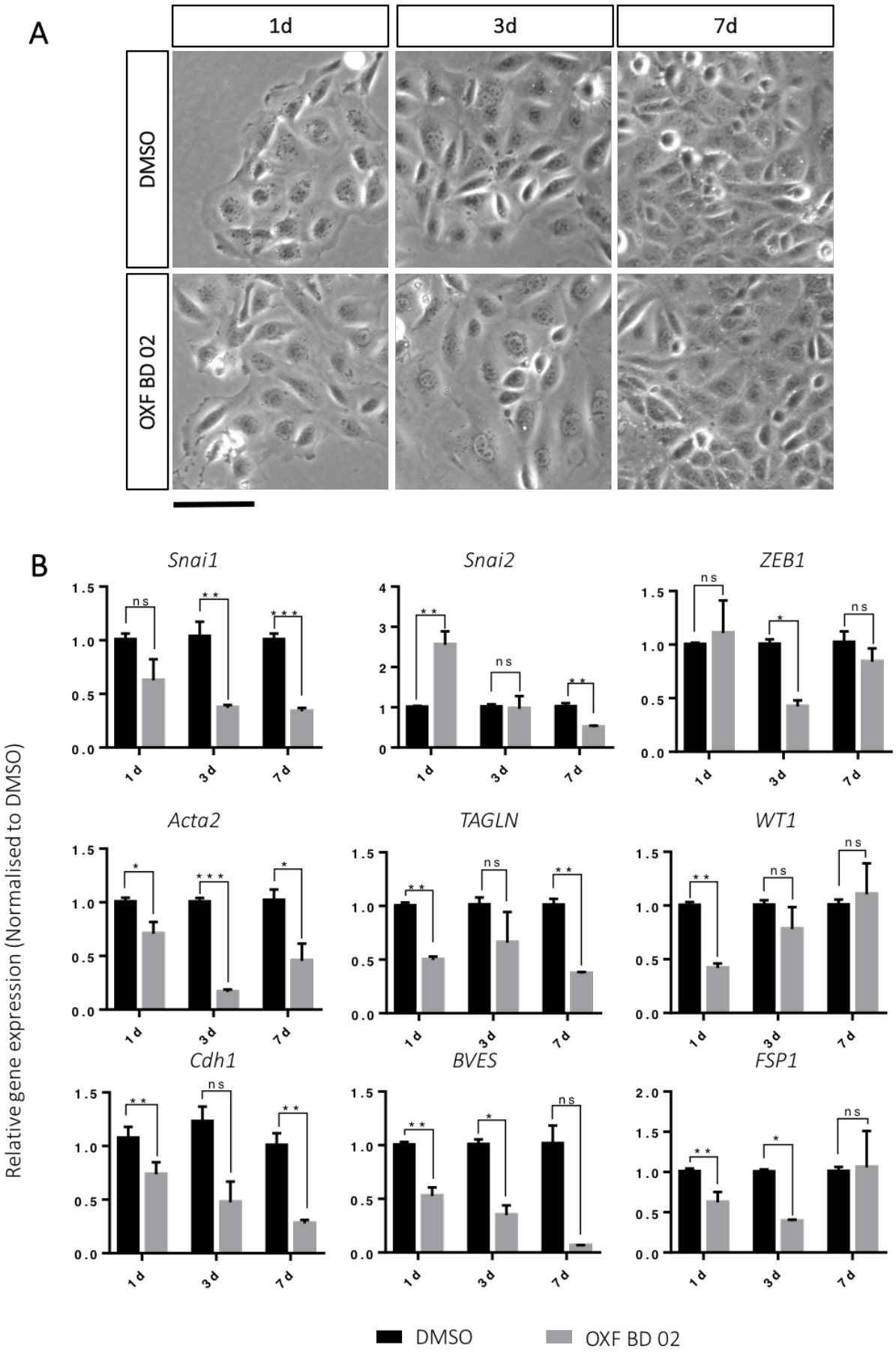

A
1d
3d
7d
DMSO
OXF BD 02
B
Snai1
Snai2
ZEB1
Acta2
TAGLN
WT1
Cdh1
BVES
FSP1
Relative gene expression (Normalised to DMSO)
DMSO
OXF BD 02

Figure 8.19 Brightfield images and gene expression panel of mEPDCs treated with OXF BD 02 compared with the DMSO control. (**A**) Brightfield images of cells treated with OXF BD 02 compared with the DMSO control. Treated mEPDCs appeared similar to the control at all time points. (**B**) Q-PCR revealed decreased expression of genes associated with epicardial EMT and differentiation**:** *Snai1, Acta2 and TAGLN*: relative to the control. Once again, *Snai2* expression was significantly upregulated on day one. There was no significant change in ZEB1 expression apart from day three, on which it was downregulated. *Cdh1*, *BVES,* and *FSP1* were negatively regulated by OXF BD 02. No significant change was seen in WT1 expression apart from day one where it was downregulated. Statistics calculated using a Mann-Whitney test, n = 5, *p<0.05; **p<0.01; ***p<0.001; ****p<0.0001. Scale bar 100 μm.

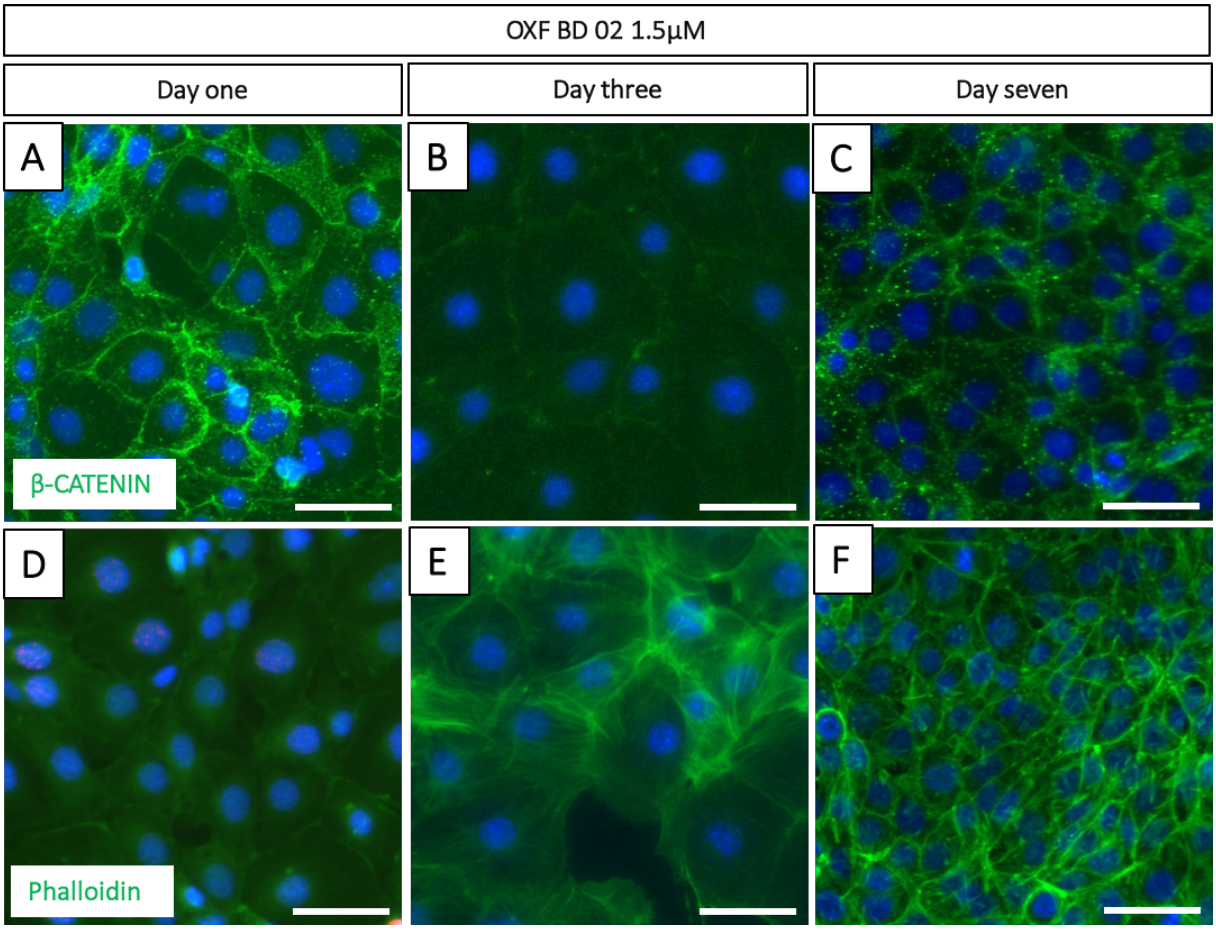


Figure 8.20 mEPDCs treated with OXF BD 02 for one, three and 7 days stained with β-CATENIN and phalloidin to assess morphology. (**A**–**C**) β–CATENIN was both membrane bound and located in the cytoplasm. (**D**–**F**) Faint phalloidin staining was observed on days one and three but a cortical actin network had formed by day 7. Scale bars 50 μm.

Finally, the OXF BD 02 treated mEPDCs were examined by ICC (**Figure 8.20**). On day one, β-CATENIN distribution was similar to what which had already been observed with the other BET inhibitors: it was both membrane bound and appeared in the cytoplasm, although this was

less uniformly distributed throughout the cytoplasm than the other cultures (**Figure 8.20 A**). On day three β-CATENIN was located at the membrane (**Figure 8.20 B**) and in the dense cultures on day 7 it could be seen both at the membrane and the in the cytoplasm (**Figure 8.20 C**). On day one the distribution of F-ACTIN was not well defined and it was not possible to focus the microscope upon a network of fibres or cortical actin (**Figure 8.20 D**). On day three the actin distribution was more visible (**Figure 8.20 E**) and by day 7 a cortical actin network could be seen surrounding the cells (**Figure 8.20 F**). Once again the presence of cytoplasmic β-CATENIN correlated with increased expression of *Snai2* suggesting an effect of BET inhibition on β-CATENIN activity and its interaction with the downstream target gene *Snai2*. The formation of an actin network over the seven days again suggested that the compound concentration had not effectively switched mEPDC phenotype away from that of epithelia.

8.2.7 Morphology and gene expression of A-161906 treated mEPDCs

In addition to the BET inhibitors the reported TGFβ mimetic A-161906 has also increased the rate of mEPDC migration in a dose responsive manner and therefore was also tested in the differentiation assay at a concentration of 1 μM. Morphologically the cells appeared very similar to the DMSO control at all time points (**Figure 8.21 A**). Negligible change in the EMT markers *Snai1*, *ZEB1*, *Acta2* and *TAGLN* were observed across the time course; *Snai2* was upregulated on days one and three but this was not found to be significant. No change was seen in *WT1* expression once again indicating that the cells remained epicardial in phenotype. *Cdh1* appeared to be upregulated on days three and 7, but this was not found to be significant. Expression of *BVES* and *FSP1* were significantly less than the DMSO control on days one and three, but had increased again by day 7 (**Figure 8.21 B**). This indicated that although A-16906 was a reported TGFβ mimetic it did not induce EMT or differentiation in the same manner as the recombinant protein.

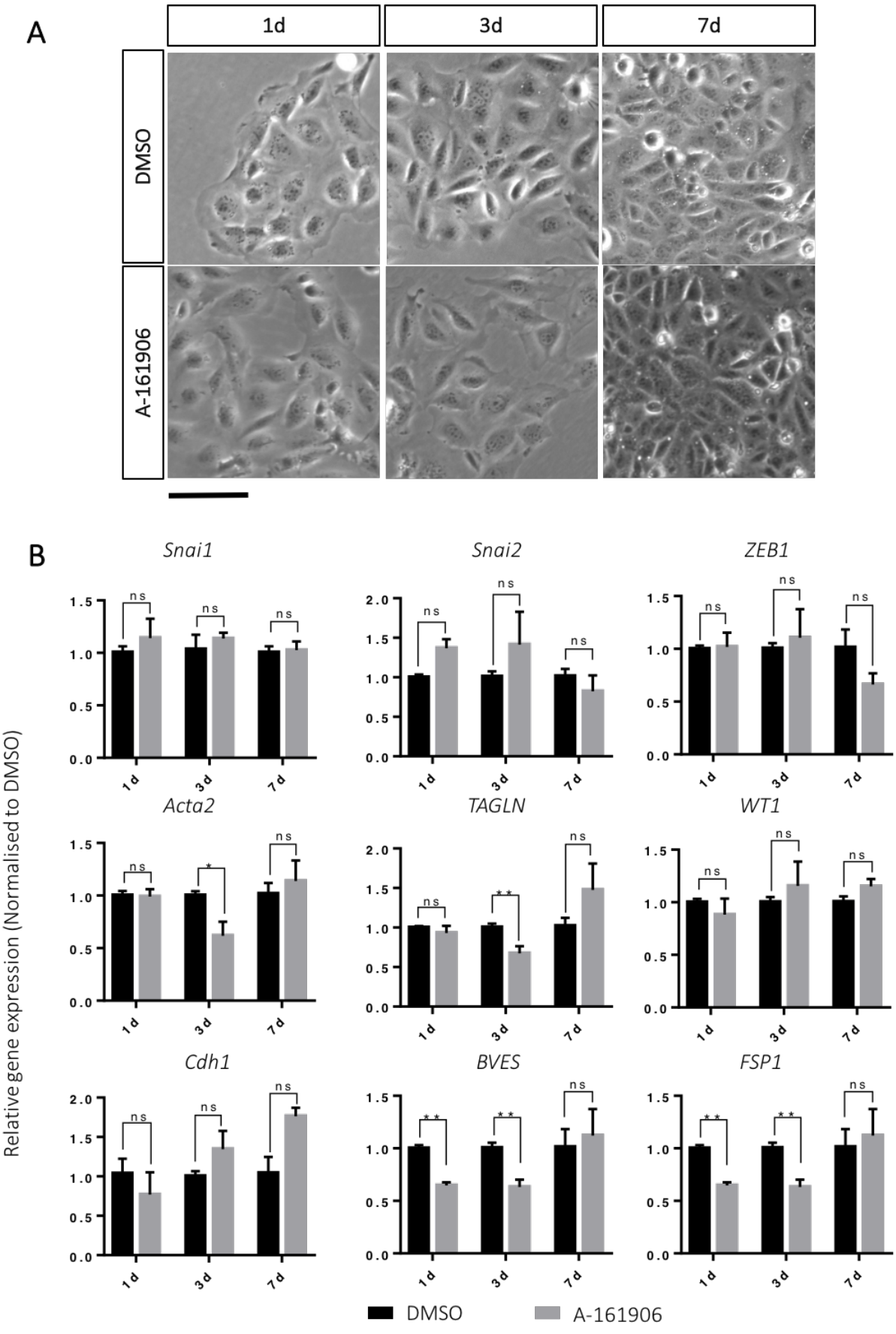

A
1d
3d
7d
DMSO
A-161906
B
Snai1
Snai2
ZEB1
Acta2
TAGLN
WT1
Cdh1
BVES
FSP1
Relative gene expression (Normalised to DMSO)
ns
*
**
1d
3d
7d
DMSO
A-161906

Figure 8.21 Brightfield images and gene expression panel of mEPDCs treated with A-161906 compared with the DMSO control. (**A**) Brightfield images of cells treated with A-161906 compared with the DMSO control. Morphologically, treated mEPDCs appeared similar to the control at all time points. (**B**) Q-PCR revealed negligible change in the EMT and differentiation markers *Snai1, ZEB1, Acta2* and *TAGLN* relative to the control. *Snai2* expression was upregulated on days one and three but this was not found to be significant. There was no significant change in WT1 at any time point. *Cdh1* appeared to be upregulated on days three and 7 but this failed to reach significance. *BVES,* and *FSP1* were negatively regulated by A-161906 on days one and three. Statistics calculated using a Mann-Whitney test, n = 5, *p<0.05; **p<0.01; ***p<0.001; ****p<0.0001. Scale bar 100 μm.

Finally, the A-161906 treated mEPDCs were stained with anti-β-CATENIN and Phalloidin (**Figure 8.22**). On days one and three β-CATENIN localisation was similar to that observed in the DMSO control with protein located at the cell membrane but also visible in the cytoplasm. Interestingly, on day 7 β-CATENIN was observed at the membrane but could also be seen densely spread throughout the cytoplasm. On days one and three phalloidin staining revealed dense stress fibre formation throughout the culture and a network of cortical actin had started to form. On day 7 the cultures were very dense with a network of cortical actin arranged in rings around the cell periphery. However, clearly defined thick stress fibres were also visible which had not been observed in the DMSO or TGFβ controls. Higher magnification revealed that the continuous cortical actin network that connected the cells together (**Figure 8.22 G**, arrowhead) was in a different plane to the dense stress fibre network (**Figure 8.22 H,** arrowhead). The presence of a dense stress fibre network suggested that although the TGFβ mimetic A-161906 was not inducing the same gene expression and TGFβ it was affecting the cytoskeleton which may be related to the increased mEPDC migration observed in the scratch assays.

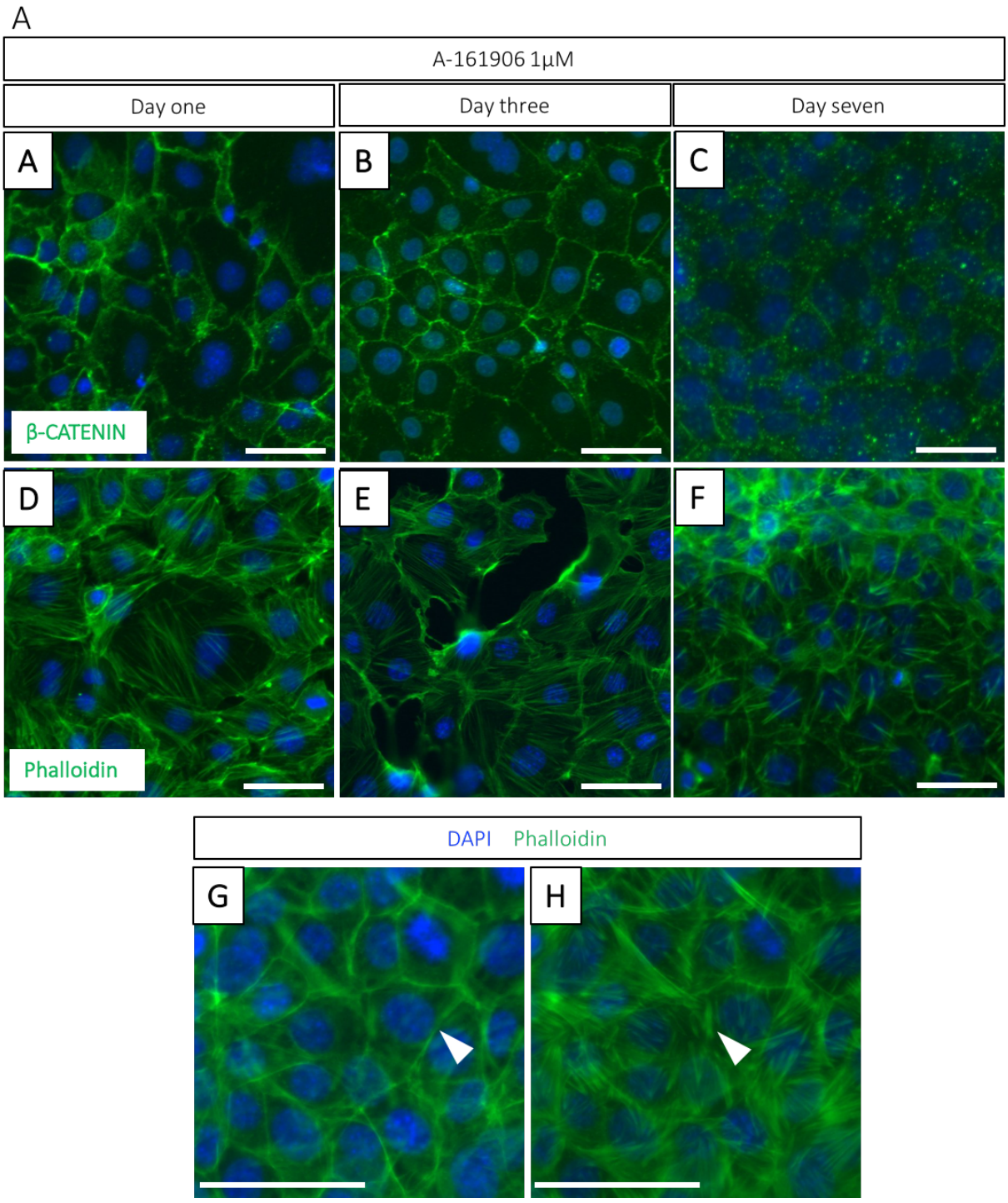


Figure 8.22 mEPDCs treated with A-161906 for one, three and 7 days stained with β-CATENIN and phalloidin to assess morphology. (**A–C**) β –CATENIN was both membrane bound and located in the cytoplasm on days one and three. On day 7 the cultures were dense and β-CATENIN was located both at the membrane and in speckles throughput the cytoplasm. (**D–F**) Phalloidin staining revealed the presence of actin stress fibres on days one and three; by day 7 the mEPDCs has formed a cortical actin network however thick stress fibres were still clearly visible. (**G–H**) Inspecting the cultures at higher magnification revealed that the cortical actin network (arrowhead **G**) was in a different plane to the stress fibres (arrowhead **H**). Scale bars 50 µm.

8.4 Summary and Discussion

8.4.1 Screening a panel of BET inhibitors in the automated mEPDC scratch assay

In **Chapter 7** two compounds, PFI-1 and (+)-JQ1, were found to increase the rate of mEPDC migration in the newly developed automated mEPDC migration assay: both compounds are known inhibitors of the BET bromodomains. To investigate whether BET bromodomains in general have a role in EPDC migration a series of reported BET inhibitors were screened in the automated mEPDC scratch assay. The 7 compounds tested were chosen to encompass a variety of chemotypes (See **Figure 8.2**) with varied selectivity for the various BET isoforms. The inhibitors were screened over a series of ten dilutions in order to determine a dose response: the dose range was chosen based upon effective concentrations that had been reported in the literature.

Scratch wounds in the BET inhibitor screen closed approximately six hours earlier than they had in the two previous screens. Therefore, the 'end point' chosen for analysis was changed to ensure that the rate calculations captured migrating mEPDCs. Originally, the 30-hour time point was chosen for analysis, however, at this time point the images captured had very poor contrast between the cells and the scratch area. It appeared that the CellTracker had leached to a greater degree that it had done in previous experiments and as a result the analysis software was unable to accurately identify the scratch area. It was postulated that the increase in migration rate may have correlated with increased cell metabolism, which led to faster expulsion of the dye from the cell body. At 24 hours the images were clearly defined because the cells had been freshly stained and washed. Therefore, data from the control wells at 24 hours was analysed to determine cell behaviour: the rate of migration in the TGFβ treated cells was found to be faster than the untreated and DMSO control at this time point. The mEPDCs used in this assay were of the same passage number as the previous two experiments, had been plated at the same

density and cultured in the same batches of serum and other media additives. The increased speed of migration may reflect biological variation between cultures, or the mEPDC batch may have been more proliferative. However, because the experimental controls behaved as expected, the 24-hour time point was deemed acceptable and the rest of the assay data was analysed.

Unfortunately, due to problems with the IncuCyte WoundMaker^{TM} tool, a number of wells did not have properly formed scratch wounds at the start of the experiment. As a result, the analysis protocol struggled to correctly identify the area of the scratch in some wells. Concerned that this would affect the results, it was decided that the assay would also be manually analysed using ImageJ software. To allow comparison between the two analysis methods, the wound healing data was converted from area (mm^2) to percentage coverage. The dose response graphs from both analysis methods were plotted as before, with the DMSO and TGFβ data included for comparison.

The original 'hit' compound PFI-1 behaved in a manner identical to that observed in the validation screen, with the rate of cell migration increasing with increased dosage up to 2μM after which it steeply declined. The effective dose was found to be 2μM, although the increase in migration rate was not found to be significant, and at 10μM PFI-1 was toxic. The structural analogues (+)-JQ1 and CPI203 both demonstrated increasing activity with increased concentration; effective concentrations were 0.3.and 0.5μM respectively; however, only CPI203 was found to significantly increase the rate of migration compared to the DMSO control. Bromosporine is a pan BRD inhibitor that is not specific for the BET bromodomains. Bromosporine was included in the pilot mEPDC scratch assay at a concentration of 1μM, but was not identified at a positive hit. However, at 2μM Bromosporine significantly increased the rate of mEPDC migration to almost that of the TGFβ control. As with PFI-1, at higher

concentrations the rate of cell migration decreased and Bromosporine was found to be toxic at 10μM. The dose response profiles of MS436 and RVX208 were similar: both marginally increased the rate of cell migration compared to the DMSO control and both were toxic at high concentrations. The BET inhibitor OXF BD 02 did not exhibit a classical dose response as the rate of migration fluctuated with increasing compound concentration. At 3μM the rate of migration was found to be significantly higher than the DMSO control. No compound at any concentration increased the rate of migration higher than that of the TGFβ positive control. This was in contrast to the validation screen (**Chapter 7.3**) in which (+)-JQ1 treated cells migrated significantly faster than both DMSO and TGFβ control at 0.1 and 0.3μM.

Collectively, these data suggested that inhibition of the BET bromodomains can increase migration of mEPDCs in a two-dimensional scratch wound assay. The compound with the greatest effect was the (+)-JQ1 analogue CPI203 at 0.5 μM. All the inhibitors screened in the BRD assay are specific inhibitors of BET proteins with the exception of Bromosporine which has a high affinity for the non-BET BRDs BRD9 and CERC2. However, Bromosporine can inhibit the BET proteins at higher concentrations.

8.4.2 Exploring the role of BET bromodomains mEPDC EMT and differentiation

After analysing the data from the BET inhibitor screen it appeared that a number of the compounds increased the rate of wound closure in a dose dependant manner. Across all three automated scratch assays performed TGFβ treatment increased the rate of wound closure compared with the DMSO and untreated controls; this was found to be significant in both the validation assay and the BET inhibitor screen. TGFβ induced epicardial EMT has been characterised extensively in the literature (Xu et al., 2009) as well as in the studies documented here (**Chapter 5.1**); it is postulated that the increased rate of migration is a result of the increased

migratory capacity conferred to the mEPDCs by TGFβ induced EMT. These differentiation studies sought to find out whether the same molecular mechanisms increased migration in cells treated with the BET inhibitors. The assay protocol was analogous to that which was employed in **Chapter 5** for the characterisation of TGFβ induced EMT and differentiation in mEPDCs: this was chosen because the model has already been well established and TGFβ could serve as the positive control.

MEPDCs were treated with their respective compounds for one, three or 7 days. The one-day time point was selected so as to reveal any 'immediate' changes in cell morphology and gene expression: this was also the time point at which the scratch assay has been analysed and reflected the time at which each treatment had been found to positively increase mEPDC migration. The three and 7-day time points were selected to investigate whether treatment of the mEPDCs for an extended period of time would result in differentiation away from an epicardial phenotype.

First, data from the DMSO and TGFβ controls was analysed. DMSO-treated cells formed uniform epithelium over the 7 days which was confirmed by localisation of β-CATENIN at the cell membrane and a network of cortical actin rings. The cultures were very dense by day 7 and although this was not associated with any observed cell death, phalloidin staining revealed that the cells had begun to grown on top of each other. Normally, epithelial cells would be expected to become 'contact inhibited' once a single cell monolayer had formed (Friedl and Gilmour, 2009). Upon reflection, the lack of contact inhibition in this model is likely because the mEPDCs were kept in the immortalisation media (IM) (discussed in **Chapter 5.1**) and, therefore, were not responding to normal stimuli that control proliferation.

The TGFβ treated mEPDCs also formed dense cultures over the 7 days although they appeared morphologically different to the DMSO control. Brightfield microscopy revealed that in the dense TGFβ treated cultures mEPDCs were less rounded and had large nuclei with numerous clearly visible nucleoli. A similar observation was made in another study in which TGFβ was used to induce EMT in AML12 line of mouse hepatocytes: after 36 hours of treatment with TGFβ the cells developed large nuclei and visible nucleoli which was found to reflect gross epigenetic changes to DNA during TGFβ induced EMT (McDonald et al., 2011). Continued treatment with TGFβ may have exerted a similar effect on chromatin packaging and epigenetic status in the mEPDCs.

Q-PCR data revealed that TGFβ treatment increased the expression of a panel of EMT and differentiation markers relative to the DMSO control. *Snai1* expression was dramatically increased on day one and expression levels remained high for the duration of the experiment: *Snai2* and *ZEB1* on the other hand were only found to be upregulated on day 7. Expression of *Acta2* and *TAGLN* increased over the time course indicating a phenotypic shift towards smooth muscle; however, *WT1* expression remained the same across all time points. This indicated that that mEPDCs had not fully differentiated away from the epicardial phenotype; *Cdh1* expression was downregulated on day three compared with DMSO however this had increased again by day 7 which further supported the observation that the mEPDCs were not fully differentiating. Two further genes known to be associated with epicardial differentiation, *BVES* and *FSP1*, were included in the panel of markers: neither were differentially expressed in TGFβ treated cells compared with the DMSO control.

On days one and three β-CATENIN was localised to the membrane but was also present in both the cytoplasm and nucleus; this indicated that the cytoplasmic protein was not being tagged for

proteasomal degradation and was likely involved in the transcriptional activation of EMT associated genes (**Chapter 1.17**) (Valenta et al., 2012). Phalloidin staining revealed mesenchymal morphology and multiple stress fibres which further indicated EMT and differentiation. However, on day 7 the dense cultures exhibited epithelial characteristics: mEPDCs had developed a cortical actin network and retained membrane bound β-CATENIN, indicating that the transformation was not complete. It is postulated that the cells were unable to fully differentiate away from the epicardial phenotype because they had been kept in the immortalisation media for the duration of the experiment; therefore, this model may not be ideal for the long term *in vitro* study of epicardial differentiation (Discussed further in **Chapter 8.5**).

Subsequently, mEPDCs that had been treated with the 'effective' concentration of BET inhibitors, as determined from the scratch assay dose response curves, were subject to the same analysis by QPCR and ICC as the TGFβ treated cultures. By day 7, with the exception of CPI203, all of the treated cultures had grown dense, exhibited β-CATENIN localised at the membrane and had developed a cortical actin network irrespective of how heterogeneous the cultures appeared. The retention of epithelial characteristics may again point to inability of the mEPDCs to differentiate away from the epicardial phenotype and therefore may not be a good time point for investigation in this model.

In order to better compare the general patterns of gene expression across the five different BRD inhibitor treatments, the results were tabulated and colour code (**Table 8.1**). Green fill indicates significantly increased expression, red fill indicates significantly decreased expression and grey fill indicated no significant change relative to the DMSO. Pale green or pink fill indicates increased or decreased gene expression respectively that was not found to be significant: it was included to allow observation of the general trends.

Gene	Day	TGFβ	PFI-1	(+)-JQ1	CPI203	Bromosporine	OXFBD02
	1d	**	ns	ns	**	**	ns
	3d	**	ns	ns	*	*	**
Snai1	7d	**	ns	ns	**	**	***
	1d	*	ns	ns	**	**	**
	3d	*	ns	*	ns	ns	ns
Snai2	7d	**	ns	ns	**	*	**
	1d	ns	ns	ns	**	**	ns
	3d	ns	ns	ns	**	ns	*
ZEB1	7d	**	ns	ns	*	**	ns
	1d	ns	ns	**	*	ns	*
	3d	**	ns	**	**	**	***
Acta2	7d	***	ns	*	**	**	*
	1d	**	ns	*	ns	ns	**
	3d	**	ns	**	**	**	ns
TAGLN	7d	**	ns	ns	ns	**	**
	1d	ns	ns	ns	ns	ns	**
	3d	ns	ns	ns	ns	ns	ns
WT1	7d	ns	ns	ns	ns	**	ns
	1d	ns	ns	**	ns	ns	**
	3d	ns	ns	*	**	**	*
BVES	7d	ns	ns	ns	ns	ns	ns
	1d	ns	ns	ns	*	ns	**
	3d	ns	ns	ns	**	**	*
FSP1	7d	ns	ns	ns	ns	**	ns
	1d	ns	*	*	*	*	**
	3d	ns	ns	**	**	**	ns
Cdh1	7d	**	ns	ns	ns	*	**

Increased expression Decreased expression No significant change

Increased expression: not significant Decreased expression: not significant

Table 8.1 Collated gene expression data exploring EMT and differentiation in mEPDCs treated with either TGFβ or BET inhibitors, relative to the DMSO control. Table indicates changes in gene expression relative to the DMSO control for each treatment at each time point. Green fill indicated significantly increased expression, red fill indicates significantly decreased expression. Pale green or pink fill indicates an increased or decreased gene expression that was not found to be significant. Grey fill indicated non-significant change that varied by less <0.1 from the DMSO control. Levels of significance are as follows: *p<0.05; **p<0.01; ***p<0.001; ****p<0.0001.

There was negligible change in WT1 expression with every treatment indicating that mEPDCs remained epicardial. As discussed, TGFβ universally upregulated the EMT transcription factors *Snai1*, *Snai2* and *ZEB1* and the EMT and differentiation markers *Acta2* and *TAGLN* over the 7-day time course. Collating the data together in **Table 8.1** revealed that although both treatment with TGFβ and BET inhibitors had stimulated an increase in the rate of mEPDC migration, the response at a molecular level was strikingly different. The BET inhibitors universally

suppressed expression of EMT markers with the exception of *Snai2*. The collective decrease in EMT markers and in *Acta2* and *TAGLN* expression demonstrated that BET inhibitors were not inducing a 'classic' epicardial EMT response or inducing mEPDCs to differentiate towards a smooth muscle fate in the same manner as TGFβ. Expression of *Cdh1* was consistently downregulated across the time course compared with the DMSO control, suggesting that the BET inhibitors had prevented the formation of tight epithelium. E-CADHERIN is the key component of the adherens junctions which are involved in cell-cell adhesion (Hartsock and Nelson, 2008) and presence of E-CADHERIN is a defining feature of epithelial tissue (**Chapter 1.16**) (Smutny et al., 2010). This observed downregulation of E-CADHERIN in BET treated cultures as compared with the DMSO control suggested that the BET bromodomains may play a role in EPDC cell-cell adhesion which might then in turn have affected migratory capacity.

CPI203, Bromosporine and OXF BD 02 all significantly increased *Snai2* expression by ~2-fold relative to the DMSO control on day one, after which it was seen to decrease. This was an interesting observation considering that at 24 hours CPI203, Bromosporine and OXF BD 02 had been found to significantly increase that rate of cell migration. Staining of DMSO treated mEPDCs with anti-β-CATENIN on day one revealed localisation of the protein at the cell membrane: it was also identified in the cytoplasm but this tended to be located toward the cell periphery rather than uniformly throughout the cell. In contrast, after 24 hours of treatment with CPI203 and Bromosporine ICC revealed extensive cytoplasmic and nuclear distribution. The β-CATENIN protein has a dual biological role: it associates with E-CADHERIN at the membrane helping to stabilise the adherens junctions, but it also acts as a signalling molecule and is a key mediator of WNT signalling (**Chapter 1.16 and 1.17**). In the nucleus, β-CATENIN acts as a transcriptional activator of several target genes including those associated with EMT such as SNAIL and ZEB (Kemler et al., 2004). The cytoplasmic and nuclear presence of β-CATENIN

suggested that at this time point β-CATENIN was not being trafficked to the membrane to help establish cell-cell contact in the same manner as in the DMSO control. If β-CATENIN were acting as a transcriptional activator in the nucleus it would be expected that a wider panel of its transcriptional targets, such as *Snai1* and *ZEB1* would also be upregulated and not just *Snai2,* so its function at this time point is currently unclear. However, β-CATENIN has been reported to directly stabilise *Snai2* mRNAs which may explain increased expression at day one (D'Uva et al., 2013).

The experiments described in **Chapter 8.3** indicated that increased mEPDC migration after treatment with the BET inhibitors was not a result of canonical EMT and differentiation through a TGFβ mediated mechanism. In a recent paper TGFβ-induced EMT in the A549 human lung carcinoma cell line was abolished by BRD4 inhibition (Chang et al., 2016), therefore it is logical that downstream mechanisms of TGFβ activation would not be stimulated by BET inhibitors. A huge area of scientific interest has been the aberrant expression of BET proteins in a variety of cancers, and their inhibition has been shown to ameliorate proliferation of numerous cancer models including pancreatic and ovarian (Sahai et al., 2014; Zhu et al., 2016). Furthermore, reduced migration and invasive capacity in a colorectal cancer cell line was found to be in part due to repression of EMT by inhibition of BRD4 (Hu et al., 2015). Although aberrant expression of BET proteins is associated with number of pathologies, they have also been shown to play a role in normal homeostasis (Bolden et al., 2014). In a mouse model, inducible *in vivo* silencing of BRD4 induced skin hyperplasia and suppressed normal haematopoiesis depleting the numbers of T-lymphoid cells and lineage negative haematopoietic stem cells (Bolden et al., 2014). There have also been reports of BET inhibition stimulating stem and progenitor cell differentiation. In mouse ESCs BRD4 expression was found to regulate pluripotency and selective inhibition resulted in ESC differentiation, increased expression of the EMT

transcription factors *Snai2* and *ZEB2* and repressed E-CADHERIN (Di Micco et al., 2014). Furthermore, small molecule BET inhibition was recently found to induce neurogenesis in neural stem and progenitor population *in vitro* (Li et al., 2016). Currently, no role has been established for BET proteins in heart development or in the injury response post MI, however, a role has been established for BRG1-associated factor 180 (BAF180) in heart development. BAF180 is a non-BET polybromo containing protein that forms part of the SWI/SNF-B (PBAF) complex. The SWI/SNF family of chromatin remodelling complexes direct spatial and temporal patterning of gene expression (Wang et al., 2004). In mice, genetic knock out of BAF180 in development was found to result in hypoplasia of the ventricle walls and septal defects (Wang et al., 2004). BAF180 is abundantly expressed in the proepicardium (PE) and epicardium at E9.5 and E12.5. In later studies it was shown that knock out of BAF180 does not prevent the formation of the PE or subsequent migration to cover the developing heart. However, after the epicardial layer is established epicardial EMT and subsequent EPDC invasion of the subepicardium is impaired, which results in improperly formed coronary vasculature. The role of the BET and other BRD containing proteins in development, tissue homeostasis and disease is both complex and variable. Clearly significantly more work is required to fully elucidate the mechanisms by which increased migratory capacity was conferred by the BET inhibitors and to determine whether this behaviour can prove useful in activating the epicardium in a therapeutic setting. This is discussed further in **Chapter 8.5**.

Finally, the TGFβ 'mimetic' A-161906 was also shown to increase the rate of wound closure in a dose responsive manner. In the differentiation experiment negligible change was seen in the EMT and differentiation markers *Snai1, ZEB1, Acta2* and *TAGLN* or in *WT1* and *Cdh1*. *Snai2* expression was upregulated on days one and three but this was not significant. *BVES* and *FSP1* were negatively regulated by A161906 on days one and three. Much like the BET inhibitors A-

161906 did not appear to be increasing the mEPDC migratory capacity via expression of genes associated with canonical EMT. However, an interesting observation was made on day seven: extensive stress fibre formation had occurred in every cell throughout the culture. Stress fibres form part of the contractile machinery that allow migration in mesenchymal, and other, cell types so this response may have been involved in increased mEPDC migration. A-161906 is a reported HDAC inhibitor: many studies in cancer cell lines have reported reduced migration in cells treated with HDAC inhibitors and they have also been known to suppress macrophage migration (Lin et al., 2012; Lugrin et al., 2009). Again, further work is required to assess the meaning of these results which is discussed in **Chapter 8.5**.

8.5 Future work

A prudent study moving forward is to determine whether the observed effects both on migration rate and *Snai2* expression are a result of BET inhibition. CPI203 was found to significantly increase the rate of mEPDC migration with respect to the DMSO control and increased *Snai2* expression by 2.3 fold. CPI203 has a stereospecific centre: the commercially available (*S*)-enantiomer was used in these experiments (**Figure 8.2**). BRD inhibition by the closely related analogue (+)-JQ1 is stereospecific: the (–)-JQ1 analogue is inactive which is predicted to be due to steric clash between the tertiary butyl group and the BRD binding site (**Figure 8.2**). Although CPI203 contains a primary amide in place of the tertiary butyl acetate group, it is postulated that inversion of the stereocenter may also result in decreased BRD inhibitory activity. Currently a postdoctoral researcher in the Russell lab is synthesising the (*R*)-enantiomer of CPI203: this enantiomer will be tested in parallel with the commercially available (*S*)-enantiomers in both the migration and differentiation assays to determine whether inverting the stereocenter ameliorates activity. (+)-JQ1 was found to significantly increase the rate of cell migration in the validation screen; in in the following BET screen (+)-JQ1 appeared to increase the rate of

migration in a dose dependent manner but this was not found to be significant at any concentration. The 1.3 fold increase in *Snai2* expression in (+)-JQ1 treated cells was also not found to be significant; however, both enantiomers of JQ1 would be screened alongside CPI203 for comparison. If either (*R*)-enantiomer resulted in supressed activity compared with the (*S*)-enantiomer this would give a good indication that the BET bromodomains play a role in mEPDC migration. To this end, another important parameter to determine is the stability of the various BET inhibitors in the assay system, so as to enable accurate compound dosing in future assays.

As it stands, little is known about the role of BET proteins in the heart therefore it is difficult to postulate what molecular mechanisms may be contributing to the observed increased in mEPDC migratory capacity. With the exception of Bromosporine, the inhibitors investigated in this thesis are reported to specifically inhibit proteins contains the BET motif over other known BRDs. Although these compounds have known target activity, it could be that in the mEPDC assay the inhibitors are associating with other BRD containing proteins present in the cells. Performing a cellular thermal shift assay (CETSA) could help identify the protein target (Schürmann et al., 2016). CETSA assays are based on the principle that the binding of a small molecule to a protein can lead to thermal stabilization or destabilisation which in turn can lead to a shift in melting temperature (Tm). By heating cells at a range of temperatures different proteins will remain stable or denature depending upon their thermal stability. When proteins are denatured they unfold and subsequently tend to aggregate; these can be precipitated by centrifugation. Stable soluble protein will remain in solution and can be quantified by immunoblotting (Schürmann et al., 2016). Subjecting mEPDCs to this protocol and immunoblotting for a number of BRD proteins could establish which potential target proteins are present and their respective Tm values. Subsequently the same experiment could be performed but with the addition of an active BET inhibitor: any proteins found to have varied

thermal stability in the presence of the chosen compounds might represent potential targets. Prior to undertaking the CETSA, performing RT-PCR on the mEPDC cell line probing for range of BRD mRNAs could help identify potential protein targets.

A number of additional biological assays could be employed to better understand the role of BET bromodomains in cell mEPDC activation and migration. After analysis of the 7-day time course, it became apparent that the differentiation model developed in **Chapter 5** for use in phenotypic screening may not have been appropriate for studying mEPDC differentiation. In **Chapter 5** the mEPDCs were differentiated in immortalisation media because a switch to the differentiation media was found to induce culture wide differentiation even in untreated cultures. However, the 7-day time course revealed that although TGFβ induced expression of EMT related transcription factors, the transition was not complete as the cells proliferated to form dense cultures and retained characteristics of epithelia. For future work, performing differentiation experiments in the differentiation media may allow the mEPDCs to respond fully to external stimuli and, therefore, provide a better model for assessing phenotypic changes.

The protocol employed in **Chapter 8.2** had been designed to explore mEPDC differentiation; however, the QPCR data collectively demonstrated suppression of genes associated with mEPDC differentiation. The experiments described were not representative of the scratch assay, in which mEPDCs responded to induction of a 'wound' in the cell sheet. A complementary assay would be to plate the cells at high density so that they form a monolayer overnight. After an epithelial sheet had been formed, a pipette tip could be used to make a scratch across the middle of the well. The mEPDCs would then be treated with DMSO, TGFβ or the effective concentration of the BET inhibitors. After 24 hours the cells could be collected for QPCR of fixed for ICC: using this model, the gene expression profile would better reflect the conditions

under which the BET inhibitors had induced a positive effect upon cell migration. ICC in this model would allow study of the cells at the leading edge; observing the phenotype and morphology of these cells may reveal more information about the mechanisms closing the scratch wound and would also allow for PHH3 staining in order to assess whether the response was proliferative. This model would also be good for investigating the phenotypic effects of A-161906: examination of cells at the leading edge might reveal further adaptations to the cytoskeleton in response to treatment. Another experiment that would make an interesting comparison would be to plate the cells at a high density and treat with the controls/BET inhibitors without induction of a scratch wound. This would allow investigation of whether cell-cell contact and epithelial architecture is disrupted by the BET inhibitors when the epithelial sheet has not been 'injured'.

As described previously, it is unlikely that a regenerative therapy to repair the myocardium will reply upon interaction with a single target. Therefore, although the BET inhibitors did not appear to induce mEPDC differentiation increasing EPDC motility might still contribute to wound healing. It would be interesting to see whether combination studies in which scratch wounded mEPDCs were treated with the active BET inhibitors alongside conditioned media, perhaps from cultured cardiomyocytes, had a synergistic effect upon migration. This could also be performed with other factors such as the FGFs or Tβ4. To perform these smaller scale studies, live cell imaging could be used in which cells at the leading edge could be individually monitored throughout the wound healing process. An experiment of this sort this would require access to a live imaging system such as the IncuCyte ZOOM™ system (http://www.essenbioscience.com/en/products/incucyte). An additional assay of interest would be to assess mEPDC invasive capacity in a 3D system, for example migration in to a collagen

matrix, a common assay which has been used before as a system to study EPDC behaviour (Rhee et al., 2009).

Due to the reported role of BRD4 in the control of ES cell pluripotency and subsequent EMT/differentiation (Di Micco et al., 2014; Li et al., 2016) it would be of interest to study the effect of the BET inhibitors on embryonic EPDC behaviour. Recently a protocol for the derivation of epicardium from human ESCs and iPSCs has been established (Iyer et al., 2015). These EPDCs retain migratory capacity and the ability to differentiate into smooth muscle cells both *in vitro* and i*n vivo,* thus could provide a relevant model for study. Explant cultures can be established from mouse E11.5 embryonic hearts (Ruiz-Villalba et al., 2013): it would also be interesting to compare embryonic EPDC migration from explant cultures *in vitro* +/- the BET inhibitors. A complementary experiment could utilise the protocol for establishing adult mouse EPDC cultures (Smart and Riley, 2009; Smart et al., 2007) to make a comparison between adult and fetal migratory response.

Finally, it would also be imperative to extrapolate these finding to an *in vivo* model to investigate how BET inhibition affects epicardial behaviour in development, and to establish whether increasing mEPDC migration can contribute to regeneration post MI. The zebrafish embryo provides an excellent system for the study of the heart (Gemberling et al., 2013). Large numbers of embryos can be generated by external fertilisation and their rapid maturation and permeability to small molecules has made them a popular tool for studying development *in vivo* (Morash et al., 2011). Three in house transgenic lines are available in the Riley lab in which epicardial cells and their progeny are fluorescently labelled. The epicardium can first be observed on day three post fertilization (Plavicki et al., 2013). Compound administration before this time point could be used to demonstrate their effect on initial epicardial formation and administration afterward

would probe how ‘activation’ of the newly formed epicardium alters further development of the heart. The tracing of labelled cell populations could be done using cryosectioning or live imaging technology, which can be conducted in a higher throughput setting with the zebrafish assay.

The fate of the epicardium in mice can also be traced using transgenic reporter lines that label EPDCs (Smart et al., 2011; Zhou et al., 2008). The neonatal MI model, in which full regeneration of surgically infarcted myocardium is seen on postnatal day 1 (P1) but lost by P7, could be utilised to examine how the regenerative response is affected by treatment with active BET inhibitors. Experiments would involve incubating the $WT1^{GFPCre}$ mouse with the compounds in question before or after surgically induced MI. Histological examination of the hearts could be carried out to assess heart morphology and the wound healing process; GPF+ cell distribution would demonstrate discrepancy in epicardial activation and cell migration in treated and non-treated animals. These experiments could also be extrapolated in to the adult MI model in both zebrafish and mouse.

Chapter 9

Final Summary

9.1 Final Summary

This thesis describes a body of work in which high throughput screening techniques were utilised to establish experimental protocols for the identification of small molecule compounds that activate the epicardium.

Prior to the start of this DPhil a high throughput phenotypic screen utilising human EPDCs was developed in collaboration with the Target Discovery Institute. Recombinant TGFβ was used to induce epithelial to mesenchymal transition (EMT) in hEPDC cultures, and the morphological changes indicative of EMT were used as a surrogate read out for hEPDC activation. A number of putative 'hits' were established from this screen: **Chapter 3** describes the efforts to establish hEPDC cultures in which to validate these 'hits'. A successful protocol was first established for the derivation of hEPDC cultures from human right atrial appendage biopsies; epicardial phenotype of hEPDC cultures was confirmed by RT-PCR and ICC. Whilst undertaking these studies it became apparent that hEPDCs are prone to undergoing spontaneous EMT *in vitro*; culturing hEPDCs with 10 μM of the ALK5 inhibitor SB-435142 helped to prevent spontaneous EMT and preserve epithelial phenotype. HEPDC cultures were used to characterise the morphological and phenotypic changes associated with TGFβ induced EMT which revealed a novel finding: nuclear patterning of the epicardial transcription factor WT1 is dynamically associated with the progression of EMT. The protein is found to be diffusely spread throughout the cytoplasm in 'cobblestone' epithelial cells but associates with the nucleolus in 'spindle' mesenchymal hEPDCs. Monitoring WT1 distribution could serve as a marker to monitor the progress of EMT in future work.

Unfortunately, none of the 'hits' from the pilot hEPDC screen were found to repeat in the validation assay. This was postulated to be because the staring population of cells in the pilot

screen had undergone spontaneous EMT prior to the start of the experiment, which had prevented accurate identification of compounds that induced the transition. The Z' from the original assay was found to be -0.295, this confirmed that there had not been sufficient differences between the positive and negative controls to write a rigorous analysis protocol. Although this was a disappointing finding, the cells used in the validation screen maintained epithelial morphology at the start of the experiment and TGFβ had induced distinct morphological changes as compared to the DMSO control. Based upon these morphological features another analysis protocol was written that returned a Z' of 0.39. Despite development of a rigorous analysis protocol, ongoing issues with access to primary human tissue led to investigation of an alternate *in vitro* model of epicardial EMT.

Chapter 4 describes a series of preliminary investigations into an EPDC line derived from rat. Although on a number of occasions rEPDCs appeared to undergo EMT and differentiate towards a smooth muscle fate in response to growth factor stimulation, this response was not reproducible and a series of inconsistencies necessitated use of an alternative cell line.

Success was found with an immortalised EPDC line derived from mouse (mEPDC), which is described in **Chapter 5**. MEPDCs reproducibly underwent EMT in response to TGFβ treatment as confirmed by expression of characteristic markers including α-SMA and SM22-α as well as increased expression of the EMT related transcription factor *Snai1*. However, mEPDC EMT was not accompanied by morphological changes as pronounced as in hEPDC cultures, thus the mouse line was deemed unsuitable for the previously described phenotypic screen. Subsequently, an automated mEPDC scratch assay, performed in 96-well plates, was developed in collaboration with the Target Discovery Institute in which cell migration was used as a surrogate read out for EPDC activation. In preliminary experiments, TGFβ treatment appeared

to increase the rate of mEPDC migration which was postulated to be due to induction of EMT. During assay development it became apparent that the mEPDCs could not be distinguished from the scratch area by the analysis software due to lack of contrast, therefore, prior to the start of the assay the cells were stained with the live fluorescent dye CellTracker™. With this addition, it was possible to conduct automated 2D migration assays: the plates were images every six hours and the InCell Analyser trained to measure the area of the scratch at each time point so as to track the rate of wound closure over time.

The design of a small, cherry picked, library is described in **Chapter 6.** The protocol used to screen the library and subsequent data analysis is described in **Chapter 7**. The pilot screen identified two positive regulators of mEPDC EMT: the BET inhibitor PFI-1 and the reported TGFβ mimetic A-161906. The pilot assay also identified three negative hits: the reported BMP agonist OX02004 and two lysine methyl transferase inhibitor UNC0642 and A-366. In a validation screen, both PFI-1 and A-161906 were found to increase the rate of wound migration in a dose dependant manner, which confirmed them as positive hits. An additional BET inhibitor (+)-JQ1 was screened in the validation assay which was also found to increase the rate of mEPDC migration is a dose dependant fashion: this result indicated a role for the BET bromodomains in regulation of mEPDC migration. The negative hit OX02004 was found to decrease the rate of wound closure in a dose dependant manner. This demonstrated that the newly designed automated mEPDC scratch assay was able to correctly identify positive and negative regulators of migration.

Chapter 8 describes a series of experiments that explored the role of the BET proteins in mEPDC migration. A panel of BET inhibitors were screened over a ten-point dose response and were found to increase the rate of wound closure in a dose dependent manner. Subsequently,

mEPDCs were treated for one, three or seven days with the most active compounds at their 'effective' concentration as derived from the dose response. This experiment sought to determine whether the increased rate of migration was associated with EMT and differentiation. DMSO and TGFβ were included in the experiment as the negative and positive controls. As expected, TGFβ induced expression of characteristic EMT and differentiation transcripts over the time course relative to DMSO. This was associated with stress fibre formation and presence of both nuclear and cytoplasmic β-CATENIN. Collectively, the BET inhibitors supressed expression of genes associated with EMT which suggested that increased migratory capacity was not a result of canonical EMT and differentiation through a TGFβ mediated mechanisms. However, three of the BET inhibitors CPI203, Bromosporine and OXF BD 02 were found to significantly upregulate expression of the EMT related transcription factor *Snai2* on day one and supress expression of *Cdh1* (encoding E-CADHERIN) which was correlated with the presence of cytoplasmic and nuclear β-CATENIN. Although the role of BET proteins in mEPDC migration is currently unclear, these results suggested that the BET bromodomains may play a role in EPDC cell-cell adhesion which might in turn affect migratory capacity. Although the BET inhibitors don't appear to push EPDCs towards alternate cardiac fates, migratory capacity is essential if they are to contribute to wound healing *in vivo* and as such a number of experiments that could further probe this response are also documented in **Chapter 8**.

To conclude, in relation to the initial aims of this thesis a number of important considerations for future high throughput screening experiments in EPDCs have been highlighted. The problems encountered with spontaneous EMT during the human studies demonstrated the caveats associated with performing large screens in primary cells. For future work, it would be necessary to modulate the experimental design to account for these problems. Alterations could include dividing compound libraries into smaller sub-libraries so as to minimise the number

times the cells must be passaged and thus increase the probability of maintaining an epithelial starting population. The issues encountered also demonstrated the necessity of having a rigorous and reproducible experimental protocol. In particular more careful analysis of hEPDC morphology prior the start of screening experiments might help to reduce the chance of another screen returning a poor Z'.

Although the immortalised mEPDC line may not be as biologically relevant as primary hEPDCs, these experiments have demonstrated its utility as a tool for preliminary investigations. The mEPDC line is robust and behaves in a reproducible manner. Furthermore, the design of the newly developed migration assay appeared rigorous, as was demonstrated by reproducible behaviour of the control conditions over the three experiments and its ability to successfully identify both positive and negative regulators of mEPDC migration. Currently, the assay protocol is somewhat laborious as there is no automated machinery to transfer the plates from the incubator to the imaging platform. This meant that for these studies, the plates have to be transferred manually every six hours for the duration of the experiment, which in turn makes the assay less amenable to screening libraries that consist of hundreds or thousands of compounds. However, analysis of mEPDC migration using the 'two point' method was revealed to produce the same data as determining the migration rate by linear regression. Therefore, in theory future assays would only require imaging at two time points which would vastly reduce the labour required and therefore increase feasibility of screening large compound libraries.

The compounds screened in the pilot mEPDC migration assay target only a small fraction of the druggable genome. There are thousands of compounds, divided in to a multitude of libraries, available for use in screening experiments all of which have the potential to identify new and unknown targets involved in EPDC activation. Without access to a constant supply of material

from which to derive hEPDCs, it would be difficult to screen large libraries in the hEPDC model in the near future. A sensible approach moving forward would be to utilise the mEPDC scratch assay for preliminary studies with large compound libraries and perform subsequent validation studies in hEPDCs at medium or low throughput. In combination, these techniques present a powerful set of tools to help identify small molecule compounds for activation of the epicardium and recruitment of resident EPDCs for endogenous repair of cardiac injury.

Chapter 10

Experimental

General Techniques: Reactions using moisture-sensitive reagents were carried out under a nitrogen atmosphere using standard vacuum line techniques and glassware that was oven-dried before use. Water was purified by an Elix® UV-10 system. All other solvents and reagents were used as supplied (analytical or HPLC grade) without prior purification. Organic layers were dried over $MgSO_4$. Brine refers to a sat. aq. solution of sodium chloride. *In vacuo* refers to the use of a rotary evaporator attached to a diaphragm pump. Petroleum ether refers to the fraction of petroleum spirit that boils between 30 and 40 °C.

Thin layer chromatography was performed on Merck aluminium plates coated with 60 F_{254} silica. Plates were visualised using UV light (254 nM) or 1% aq. $KMnO_4$ staining unless otherwise stated.

Flash column chromatography was performed on Kieselgel 60 silica in a glass column.

Melting points were recorded on a Gallenkamp Hot Stage apparatus and are uncorrected.

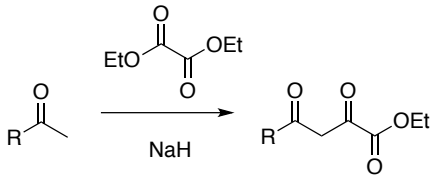
Infrared spectra were recorded on a Bruker Tensor 27 FT-IR spectrometer, as neat samples. Characteristic peaks are reported in wavenumbers (cm^{-1}).

NMR spectra were recorded on Bruker Avance spectrometers (DPX200, DQX400, AVIII400) in the deuterated solvent stated. The field was locked by external referencing to the relevant deuteron resonance. Chemical shifts (δ) are reported in parts per million (ppm). Coupling constants (*J*) are quoted in Hz and are reported to the nearest 0.1 Hz. The coupling constants were determined by analysis using ACD Labs software.

Mass Spectrometry Low-resolution mass spectra were recorded on either a VG MassLab 20-250 or a Micromass Platform 1 spectrometer from solutions of MeOH. Accurate mass measurements were run on either a Bruker MicroTOF internally calibrated with polyalanine, or a Micromass GCT instrument fitted with a Scientific Glass Instruments BPX5 column (15 m × 0.25 mm) using amyl acetate as a lock mass, by the mass spectrometry department of the Chemistry Research Laboratory, University of Oxford, UK. *m/z* values are reported in Daltons and followed by their percentage abundance in parentheses.

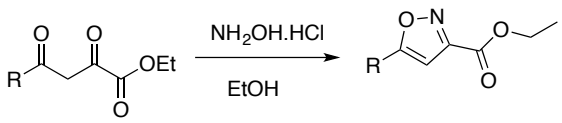
IUPAC names of all compounds are given.

General procedure 1: Synthesis of 4-substituted ethyl-2,4-dioxobutanoates



To a stirred solution of substituted ethanone (1.0 eq.) and diethyloxalate (2.0 eq.) in toluene was added NaH (3.0 eq.) and the reaction heated at reflux until completion, as indicated by TLC. The cooled reaction was extracted with EtOAc (3 x 10 mL), washed sequentially with HCl (1.0 M), water (3 x 10 mL) and brine (3 x 10 mL), dried and concentrated *in vacuo* yielding the 4-substituted ethyl-2,4-dioxobutanoate. The crude products were taken forward without further purification.

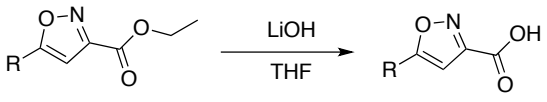
General procedure 2: Synthesis of isoxazole-3-carboxylates



The crude 4-substituted ethyl-2,4-dioxobutanoate (1.0 eq.) was refluxed in EtOH with hydroxylamine hydrochloride (3.0 eq.) until completion as indicated by TLC. The reaction was extracted with EtOAc (3 x 10 mL), washed sequentially with HCl (1.0 M), water (3 x 10 mL)

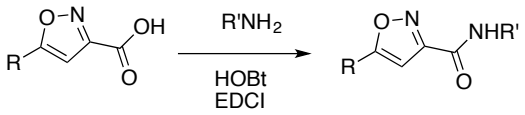
and brine (3 x 10 mL) dried and concentrated *in vacuo*. The crude isoxazole-3-carboxylates were purified by column chromatography.

General procedure 3: Ester hydrolysis



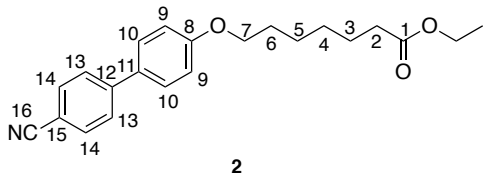
Isoxazole-3-carboxylates (1.0 eq.) were stirred with LiOH (4.0 eq.) in THF for 3 h at 50°C. The mixture was extracted with toluene and acidified to pH 1 with HCl (1.0 M). The crude product was extracted with EtOAc (3 x 10 mL), washed with water (3 x 10 mL) and brine (3 x 10 mL) dried and concentrated *in vacuo*. The acids were taken forward without further purification.

General procedure 4: Amide coupling



The crude acids (1.0 eq.) were stirred with HOBt (1.5 eq.) and EDCI (1.5 eq.) in CH_2Cl_2 for 10 min**.** The requisite amine (1.5 eq.) was added dropwise and the mixture stirred at room temperature until TLC indicated completion. The reaction was partitioned between EtOAc (3 x 10 mL) and water. The organic were washed with (3 x 10 mL) and brine (3 x 10 mL), dried and concentrated *in vacuo* yielding the crude amides.

Ethyl 7-((4'-cyano-[1,1'-biphenyl]-4-yl)oxy)heptanoate (4)

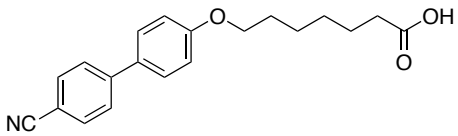


2

To a suspension of 4'-hydroxy-4-biphenylcarbonitrile (500 mg, 2.11 mmol, 1 eq.) and Cs_2CO_3 (1.03 g, 3.16 mmol, 1.5 eq.) in dry DMF (1 mL) was added ethyl 7-bromoheptanoate (616 µL, 3.16 mmol, 1.5 eq.) and the reaction mixture stirred for 4 h until TLC indicated reaction completion. The mixture was diluted with diethyl ether and acidified to pH 7. The organic phase was washed twice with brine (10 mL), dried and concentrated *in vacuo*. The

crude product was purified by silica column chromatography (increasing gradient of EtOAc:Petrol from 0:1 to 1:9) to yield **4** as an off-white solid (575 mg, 1.53 mmol, 73%); **mp** 84–85°C; **ν_{max} (film)** 2938 (C-H), 2229 (C≡N), 1720 (C=O); **δ_H (400 MHz, $CDCl_3$)** 1.26 (3H, t, *J* 7.0, Et C*H*$_3$), 1.37–1.47 (2H, m, C(4)*H*$_2$), 1.47–1.56 (2H, m, C(5)*H*$_2$), 1.68 (2H, app. qu, *J* 7.5, C(3)*H*$_2$), 1.78–1.88 (2H, m, C(6)*H*$_2$), 2.32 (2H, t, *J* 7.5, C(2)*H*$_2$), 4.01 (2H, t, *J* 6.5, C(7)*H*$_2$), 4.14 (2H, q, *J* 7.0, Et C*H*$_2$), 6.99 (2H, d, *J* 8.5, C(9)*H*), 7.53 (2H, d, *J* 8.5, C(10)*H*), 7.65 (2H, d, *J* 8.0, C(13)*H*), 7.70 (2H, d, *J* 8.0, C(14)*H*); **δ_C (400 MHz, $CDCl_3$)** 14.2 (C(2')), 24.8 (C(3)), 25.7 (C(5)), 28.8 (C(4)), 29.0 (C(6)), 32.2 (C(2)), 60.2 (C(1')), 68.0 (C(7)), 110.0 (C(16)), 115.0 (C(9)), 119.1 (C(15)), 127.1 (C(13)), 128.3 (C(10)), 131.3 (C(11)), 132.5 (C(14)), 145.3 (C(12)), 159.7 (C(8)), 173.7 (C(1)); ***m/z* (ESI$^+$)** 352 ([M+H]$^+$, 60%), 374 ([M+Na]$^+$, 100%); **HRMS (ESI$^+$)** $C_{22}H_{25}NNaO_3^+$ ([M+Na]$^+$) requires 374.1727, found 374.1720.

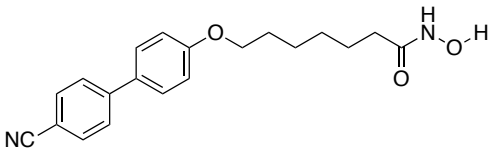
7-((4'-cyano-[1,1'-biphenyl]-4-yl)oxy)heptanoic acid (5)



5

KOH (320 mg, 5.70 mmol, 10 eq.) was added to a suspension of **4** (200 mg, 0.57 mmol, 1 eq.) in EtOH (7 mL) and stirred at reflux for 2 h. The cooled reaction mixture was extracted with EtOAc (3 x 20 mL), washed with brine (2 x 10 mL) and concentrated *in vacuo* yielding 157 mg of the crude acid **5; δH (400MHz, $CDCl_3$)** 1.37–1.57 (4H, m), 1.70 (2H, app. quin., *J* 7.4), 1.77–1.85 (2H, m), 2.38 (2H, t, *J* 7.4), 4.00 (2H, t, *J* 6.4), 6.98 (2H, d, *J* 8.7), 7.52 (2H, d, *J* 8.7), 7.63 (2H, d, *J* 8.5), 7.69 (2H, *J* 8.5).

7-((4'-cyano-[1,1'-biphenyl]-4-yl)oxy)-*N*-hydroxyheptanamide (1)



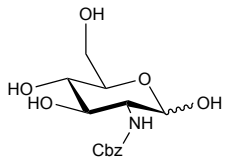
1

Hydroxylamine hydrochloride (110 mg, 1.58 mmol) was dissolved in ice cold MeOH (2.5 mL) and added to a mixture of KOH (90 mg, 1.60 mmol) in MeOH (2.5

mL) at 0°C. The crude acid (98 mg, 0.303 mmol, 1 eq.) was dissolved in THF (4 mL) and cooled to 0°C: to this was added ethyl chloroformate (38 μL, 0.40 mmol, 1.3 eq.) and trimethylamine (60 μL, 0.44 mmol, 1.4 eq.). The mixture was stirred for 15 min before being filtered, added to the freshly prepared hydroxylamine and stirred for a further 30 min. The solvent was evaporated and the residue purified by silica column chromatography (increased gradient of DCM: MeOH 1:0 to 0.9:0.1) yielding the hyroxamic acid **1** as an off white solid (26 mg, 0.076 mmol, 21% over two steps); **δ_H (400MHz, $CDCl_3$)** 1.34–1.57 (4H, m) 1.58–1.87 (4H, m), 2.17–2.24 (2H, m), 3.98 (2H, t, *J* 6.4), 6.97 (2H, d, *J* 8.6), 7.51 (2H, d, *J* 8.6), 7.58–7.71 (4H, m,); **δ_C (400MHz, $CDCl_3$)** 25.2, 25.7, 25.8, 28.8, 29.0, 67.9, 110.1, 115.1, 119.1, 127.1, 128.4, 131.4, 132.6, 145.2, 159.7, 171.5.

Data consistent with literature values (Fesik et al., 1997).

Benzyl ((3R,4R,5S,6R)-2,4,5-trihydroxy-6-(hydroxymethyl)tetrahydro-2H-pyran-3-yl)carbamate (8)

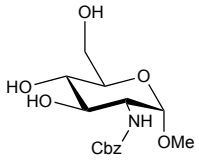


8

To a stirred solution of D-glucosamine hydrochloride (5.00 g, 23.19 mmol) and $NaHCO_3$ (5.85 g, 69.63 mmol) in H_2O (146 mL) was added benzyl chloroformate (3.60 mL, 25.22 mmol) portion wise over 30 min. The mixture was left to stir at room temperature for 24 h then the white precipitate filtered off, azeotroped with toluene (3 x 20 mL) and dried *in vacuo* at 50°C to give **8** as a white solid as a mixture of anomers (5.92 g, 18.91 mmol, 82%); **δ_H (400 MHz, CD_3OD)** 3.33–3.39 (1H, m); 3.53–3.82 (5H, m); 4.57 (0.2H, d, *J* 8.3, β *H*), 5.09 (2H, s), 5.12 (0.8H, d, *J* 3.3, α *H*); 7.23–7.40 (5H, m); **δ_C (400 MHz, CD_3OD)** 57.6, 62.8, 67.6, 72.4, 72.9, 73.1, 78.0, 92.9, 128.9, 129.4, 138.3, 158.8.

Data consistent with literature values (Miller et al., 2015).

Benzyl ((2S,3R,4R,5S,6R)-4,5-dihydroxy-6-(hydroxymethyl)-2-methoxytetrahydro-2H-pyran-3-yl)carbamate (9)

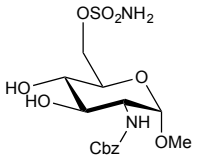


9

A suspension of **8** (5.01 g, 16.01 mmol) in a 1.25 M solution of HCl in methanol (45 mL) was refluxed at 80°C for 5 h. The solvent was removed *in vacuo* and the crude product purified by flash chromatography on SiO_2 with a gradient elution from 4–12% MeOH/CH_2Cl_2 to give a **9** as a white solid (3.24 g, 9.89 mmol, 63%); **δ_H (400 MHz, CD_3OD)** 3.37 (3H, s), 3.50–3.72 (5H, m) 3.82 (1H, dd, *J* 11.8 2.4), 4.68 (1H, d, *J* 3.0, α *H*) 5.09 (2H, s) 7.26–7.41 (5H, m); **δ_C (400 MHz, CD_3OD)** 55.5, 57.2, 62.7, 67.6, 72.2, 73.2, 73.7, 100.2, 128.9, 129.0, 129.4 138.3, 158.9.

Data consistent with literature values (Miller et al., 2015).

((2R,3S,4R,5R,6S)-5-(((Benzyloxy)carbonyl)amino)-3,4-dihydroxy-6-methoxytetrahydro-2H-pyran-2-yl)methyl sulfamate (10)



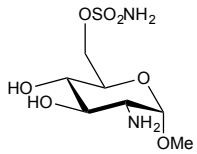
10

To generate sulfamoyl chloride formic acid (460 μL, 12 mmol, 1 eq.) was added dropwise to chlorosulfonyl isocyanate (1.05 mL, 12 mmol, 1 eq) at 0°C. The mixture was left to warm to room temperature and then stirred for 2 h until a white solid had formed. This was dissolved in toluene to form a 2 M solution. Once dissolved, the sulfamoyl chloride (3.23 mL, 2 M, 6.45 mmol, 3 eq.) was immediately added to **8** (800 mg, 2.15 mmol, 1 eq.) in DMF (8.6 mL) and the mixture was stirred at -40°C for 18 h. The mixture was quenched with water and extracted with EtOAc (3 x 50 mL). The organic layers were washed with saturated LiCl, dried over $MgSO_4$ and the solvent removed *in vacuo*. The solid was purified by column chromatography on SiO_2 with a gradient elution of 50% EtOAc: Petrol to 100% EtOAc to 10% MeOH:EtOAc. The product came off the column in 100% EtOAc and gave a white solid (543 mg, 1.34 mmol, 62%); **δ_H (400 MHz, CD_3OD)** 3.37 (3H, s), 3.55–3.87 (4H, m), 4.25 (1H, dd, *J* 10.7, 6.0), 4.40 (1H, dd, *J* 10.7, 2.0), 4.68 (1H,

d, *J* 3.0, α *H*), 5.09 (2H, s), 7.24–43 (5H, m); **δ_C (400 MHz, CD_3OD)** 55.9, 57.2, 67.8, 70.3, 71.4, 72.2, 73.2, 100.4, 129.1, 129.2, 129.6, 138.6, 159.1.

Data consistent with literature values (Miller et al., 2015).

((2R,3S,4R,5R,6S)-5-Amino-3,4-dihydroxy-6-methoxytetrahydro-2H-pyran-2-yl)methyl sulfamate (11)

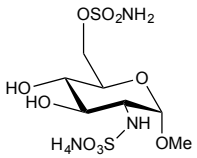


11

10 (366 mg, 0.90 mmol) was dissolved in dry MeOH (22.5 mL). After flushing with Argon, Pd/C (10% by wt.) was added, the mixture flushed with Argon once more and hydrogenated for 16 h at room temperature. The solvent was removed *in vacuo,* and the resulting oil azeotroped with toluene (3 x 20 mL) to yield **11** as a white solid (240 mg, 0.89 mmol, 98%); **δ_H (400 MHz, CD_3OD)** 3.33–3.50 (6H, m), 3.73–3.83 (1H,m) 4.20–4.32 (1H, m) 4.39 (1H, dd, *J* 10.7, 2.0), 4.68 (1H, d, *J* 3.6); **δ_C (400 MHz, CD_3OD)** 55.8, 57.0, 70.1, 71.2, 71.6, 75.93, 101.3.

Data consistent with literature values (Miller et al., 2015).

((2*S*,3*R*,4*R*,5*S*,6*R*)-4,5-Dihydroxy-2-methoxy-6-((sulfamoyloxy)methyl) tetrahydro-2*H*-pyran-3-yl)sulfamic acid (6)



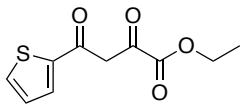
6

The amine **11** (100 mg, 0.37 mmol, 1 eq.) was dissolved in de-ionised water (2.14 mL) and the pH adjusted to between pH 9 and 10 with NaOH (2M). Pyridine-sulfur trioxide complex (64 mg, 0.40 mmol, 1.1 eq.) was added portion-wise at 30 min intervals and the pH adjusted to 9–10 with NaOH after each addition. The mixture was left to stir at room temperature for 2 h after which the solvent was removed *in vacuo*. The crude compound was then purified by silica chromatography using a gradient elution DCM:MeOH:NH_4OH from 70:30:3 (4 column volumes), 50:50:3 (4 column volumes) and 35:65:3 (2 column volumes). The product was dried *in vacuo* giving the product **6** as a white

solid (56 mg, 0.16 mmol, 43%); **δ_H (400 MHz, D_2O)** 3.24 (1H, dd, *J* 10.0, 3.6), 3.41 (3H, s), 3.52 (1H, app t, *J* 9.4), 3.59 (1H, app t, *J* 9.4), 3.95 (1H, ddd, *J* 9.8, 4.4, 2.5), 4.48–4.39 (2H, m), 5.02 (1H, d, *J* 3.6); **HRMS (ESI⁻)** $C_7H_{16}N_2O_{10}S_2$ requires 351.017, found 351.017.

Data consistent with literature values (Miller et al., 2015).

Ethyl 2,4-dioxo-4-(thiophen-2-yl)butanoate (19)

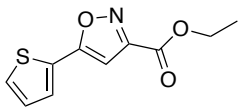


19

Following *General procedure 1*, using 2-acetylthiophene (1.60 mL, 11.88 mmol) and diethyloxalate (3.25 mL, 23.72 mmol) with NaH (783 mg, 32.63 mmol) in toluene (45 mL) afforded crude **19** as a brown solid which was used without further purification; **δ_H (400 MHz, $CDCl_3$)** 1.42 (3H, t, *J* 7.0), 4.41 (2H, q, *J* 7.0), 6.93 (1H, s) 7.20 (1H, dd, *J* 5.0, 4.0), 7.76 (1H, dd, *J* 5.0, 1.0), 7.86 (1H, dd, *J* 4.0, 1.0); ***m/z* (ESI⁺)** 249 ($[M+Na]^+$, 100%), 227 ($[M+H]^+$, 70%).

Data consistent with literature values (Pei and Wickham, 1993).

Ethyl 5-(thiophen-2-yl)isoxazole-3-carboxylate (20)

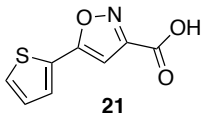


20

Following *General procedure 2*, using a solution of **19** (1.50 g, 6.63 mmol) and hydroxylamine hydrochloride (1.47 g, 21.19 mmol) refluxed in EtOH (30 mL) gave the crude reaction mixture. Purification *via* column chromatography on silica gel (Eluent EtOAc:Petrol, 1:9) gave **20** as a colourless crystalline solid (1.19 g, 5.33 mmol, 45%); **δ_H (400 MHz, $CDCl_3$)** 1.43 (3H, t, *J* 7.0), 4.48 (2H, q, *J* 7.0), 6.80 (1H, s), 7.16 (1H, dd, *J* 5.0, 4.0. C), 7.51 (1H, dd, *J* 5.0, 1.0. C), 7.58 (1H, dd, *J* 4.0, 1.0, C); ***m/z* (ESI⁺)** 469 ($[2M+Na]^+$, 100%).

Data consistent with literature values (Gardner and Wenis, 2002).

5-(thiophen-2-yl)isoxazole-3-carboxylic acid (21)

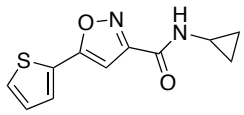


21

Following *General procedure 3*, using **20** (1.0 g, 4.48 mmol) with LiOH (431 mg, 17.99 mmol) in THF (50 mL) afforded crude **21** as a brown solid which was taken forward without further purification; δ_H **(400 MHz, DMSO-*d*$_6$)** 7.25 (1H, s), 7.27 (1H, dd, *J* 5.0, 4.0), 7.82 (1H, dd, *J* 4.0, 1.0), 7.88 (1H, dd, *J* 5.0, 1.0).

Data consistent with literature values (Schneider et al., 2007).

***N*-cyclopropyl-5-(thiophen-2-yl)isoxazole-3-carboxamide (12)**

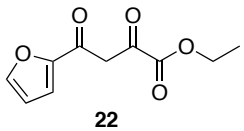


12

Following General procedure 4, using **21** (100 mg, 0.53 mmol) with HOBt (154 mg, 1.00 mmol), EDCI (239 mg, 1.25 mmol) and cyclopropylamine (70 μL, 1.02 mmol) in CH_2Cl_2 (5 mL) afforded crude **12** which was purified by column chromatography on silica gel (Eluent EtOAc:Hexane 1:5) affording a brown crystalline solid (57 mg, 0.23 mmol, 37%); δ_H **(400 MHz, DMSO-*d*$_6$)** 0.60–0.76 (4H, m), 2.83–2.91 (1H, m), 7.18 (1H, s), 7.28 (1H, dd, *J* 5.0, 3.5), 7.80 (1H, dd, *J* 3.5, 1.0), 7.88 (1H, dd, *J* 5.0, 1.0), 8.86–8.92 (1H, m); ***m/z*** **(ESI$^+$)** 235 ($[M+H]^+$ 100%), 257 ($[M+Na]^+$, 70%), 491 ($[2M+Na]^+$, 70%).

Data consistent with literature values (Schneider et al., 2007).

Ethyl 4-(furan-2-yl)-2,4-dioxobutanoate (22)

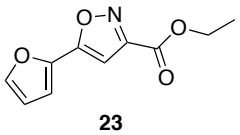


22

Following *General procedure 1*, using 2-acetylfuran (522 mg, 4.74 mmol) and diethyloxalate (0.93 mL, 6.81 mmol) with NaH (218 mg, 9.08 mmol) in toluene (15 mL) afforded crude **22** as a brown solid which was taken forward without further purification; δ_H **(400 MHz, $CDCl_3$)** 1.41 (3H, t, *J* 7.0), 4.40 (2H, q, *J* 7.0) 6.63 (1H, dd, *J* 3.5, 1.5), 6.95 (1H, s), 7.35–7.38 (1H, m), 7.69–7.72 (1H, m), 14.53 (1H, s); ***m/z*** **(ESI$^+$)** 443 ($[2M+Na]^+$, 100%).

Data consistent with literature values (Pei and Wickham, 1993).

Ethyl 5-(furan-2-yl)isoxazole-3-carboxylate (23)

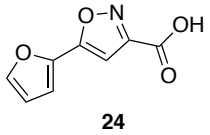


23

Following *General procedure 2*, using a solution of **22** (420 mg, 2.0 mmol) and hydroxylamine hydrochloride (460 mg, 6.61 mmol) refluxed in EtOH (10 mL) gave the crude reaction mixture. Purification *via* column chromatography on silica gel (Eluent EtOAc:Petrol, 1:5) gave **23** as a colourless crystalline solid (324 mg, 1.56 mmol, 78%); **δ_H (400 MHz, $CDCl_3$)** 1.37 (3H, t, *J* 7.0), 4.40 (2H, q, *J* 7.0), 6.50 (1H, dd, *J* 3.5, 1.5), 6.76 (1H, s), 6.92 (1H, d, *J* 3.5), 7.51 (1H, dd, *J* 1.5, 0.5); ***m/z*** **(ESI^+)** 437 ($[2M+Na]^+$, 100%).

Data consistent with literature values (Pei and Wickham, 1993).

5-(furan-2-yl)isoxazole-3-carboxylic acid (24)

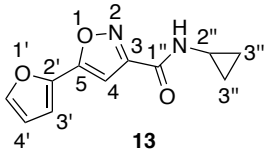


24

Following *General procedure* 3, using **23** (388 mg, 1.87 mmol) with LiOH (181 mg, 7.55 mmol) in THF (25 mL) afforded crude **24**; **δ_H (400 MHz, DMSO-*d_6*)** 6.77 1H, dd, *J* 3.5, 1.5), 7.12 (1H, s), 7.26–7.29 (1H, m), 7.99–8.02 (1H, m); ***m/z*** **(ESI^+)** 202 ($[M+Na]^+$, 100%), 180 ($[M+H]^+$, 45%).

Data consistent with literature values (Hwang et al., 2009).

***N*-cyclopropyl-5-(furan-2-yl)isoxazole-3-carboxamide (13)**

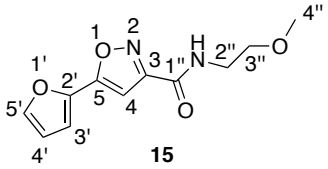


13

Following *General procedure* 4, using **24** (50 mg, 0.28 mmol) with HOBt (62 mg, 0.41 mmol), EDCI (85 mg, 0.45 mmol) and cyclopropylamine (29 μL, 0.42 mmol) in CH_2Cl_2 (3 mL) afforded crude **13** which was recrystallised from EtOH/H_2O yielding orange crystals (11 mg, 0.05mmol, 18%); **mp** 154–155°C; **ν_{max} (film)** 3292 (N-H), 3100 (C-H), 1647 (C=O); **δ_H (400 MHz, DMSO-*d_6*)**

0.52–0.67 (4H, m, CH_2), 2.75–2.83 (1H, m, C(2'')*H*), 6.69 (1H, dd, J 3.5, 2.0, (C(4')*H*), 6.99 (1H, s, (C(4)*H*), 7.15–7.20 (1H, m, (C(3')*H*), 7.90–7.93 (1H, m, (C(5')*H*), 8.82–8.88 (1H, m, N*H*); **δ_C (400 MHz, DMSO-*d_6*)** 6.1 (2 x C(3'')), 23.2 (C(2'')), 99.2 (C(4)), 112.6 (C(3')), 113.0 (C(4')), 142.0 (C(2')), 146.4 (C(5')), 159.6 (C(3)), 159.7 (C(5)), 162.2 (C(1'')); **HRMS (ESI$^+$)** $C_{11}H_{10}N_2NaO_3^+$ ([M+Na]$^+$) requires 241.0584, found 241.0581.

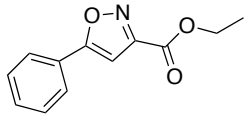
5-(furan-2-yl)-N-(2-methoxyethyl)isoxazole-3-carboxamide (15)



15

Following *General procedure 4*, using **24** (141 mg, 0.79 mmol) with HOBt (223 mg, 1.47 mmol), EDCI (322 mg, 1.68 mmol) and 2-methoxyethylamine (146 µL, 1.68 mmol) in CH_2Cl_2 (3 mL) afforded crude **15** which was purified by column chromatography on silica gel (Eluent EtOAc:Hexane 1:5) affording a light pink crystalline solid (43 mg, 0.18 mmol, 22%); **mp** 80–82^{o}C; **ν_{max} (film)** 3316 (N-H), 3150 (C-H), 1661 (C=O); **δ_H (400 MHz, DMSO-*d_6*)** 3.32 (3H, s, OCH_3), 3.47–3.53 (4H, m, CH_2), 6.82 (1H, dd, *J* 3.5, 2.0, C(4')*H*), 7.13 (1H, s, (C(4)*H*), 7.31 (1H, d, *J* 3.5, C(3')*H*), 8.05 (1H, d, *J* 2.0, C(5')*H*), 8.86–8.91 (1H, m, N*H*); **δ_C (400 MHz, DMSO-*d_6*)** 39.1 (*C*(3'')), 58.3 (*C*(4'')), 70.4 (*C*(2'')), 99.3 (*C*(4)), 112.6 (*C*(3')), 113.0 (*C*(4')), 142.0 (*C*(2')), 146.4 (*C*(5')), 158.5 (*C*(3)), 159.6 (*C*(5)), 162.2 (*C*(1'')); **HRMS (ESI$^+$)** $C_{11}H_{12}N_2NaO_4^+$ ([M+Na]$^+$) requires 259.0689, found 259.0686.

Ethyl 5-phenylisoxazole-3-*c*arboxylate (25)



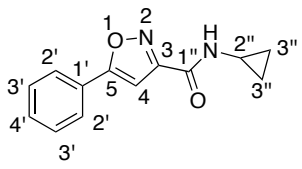
25

A mixture of ethyl 2,4-dioxo-4-phenylbutanoate (298 mg, 1.35 mmol) and hydroxylamine hydrochloride (328 mg, 4.72 mmol) was refluxed in EtOH (10 mL) for 2 h. The reaction was quenched with HCl (1 M, 10mL), extracted with EtOAc (3 x 10 mL). The organic layers were combined and washed with water (3 x 10 mL) and brine (3 x 10 mL), dried and concentrated *in vacuo*. Purification via column

chromatography on silica gel (Eluent EtOAc:Petrol, 1:5) yielded a **25** as a colourless solid (276 mg, 1.27 mmol, 94%); **δ_H (400 MHz, $CDCl_3$)** 1.46 (3H, t, *J* 7.0), 4.49 (2H, q, *J* 7.0), 6.94 (1H, s), 7.48–7.53 (3H, m), 7.80–7.85 (2H, m); ***m/z*** **(ESI^+)** 457 ($[2M + Na]^+$, 100%).

Data consistent with literature values (Tang et al., 2009).

_N_-cyclopropyl-5-phenylisoxazole-3-carboxamide (14)



14

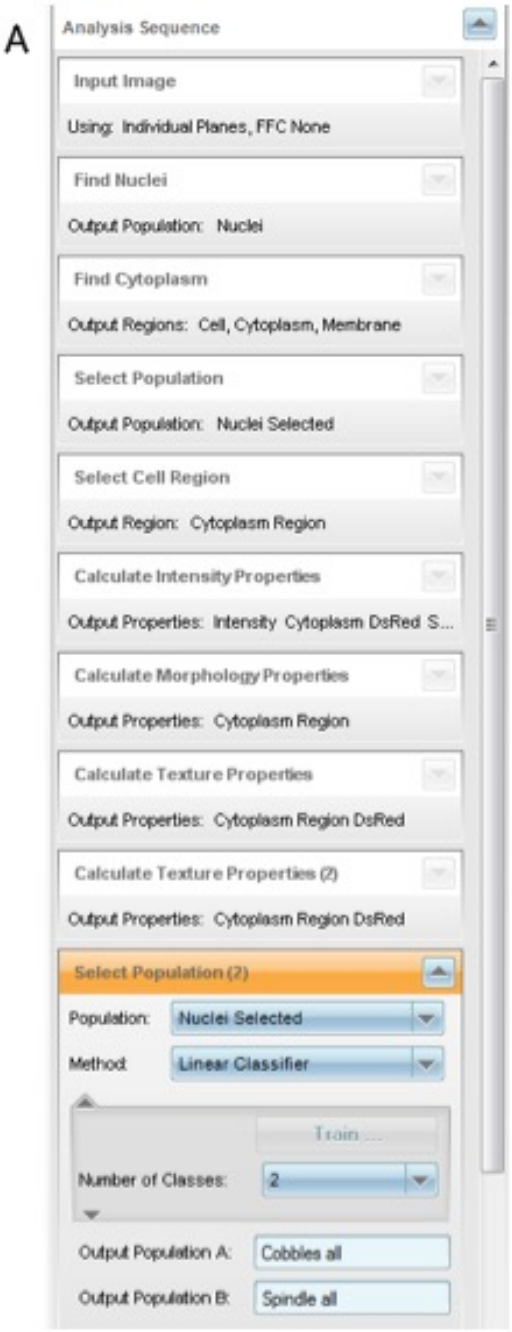
To a solution of ethyl 5-phenylisoxazole-3-carboxylate **25** (50 mg, 0.23 mmol) in EtOH (3 mL) was added cyclopropylamine (0.02 mL, 1.15 mmol) and the reaction heated at 80°C for 24 h. The mixture was extracted with EtOAc (3 x 10 mL), washed with water (3 x 10 mL) and brine (3 x 10 mL), dried and concentrated *in vacuo*. The product *14* was recrystallised from EtOH/H_2O (15 mg, 0.066 mmol, 26%); mp 135–136°C; **ν_{max} (film)** 3364 (N-H), 1657 (C=O); **δ_H (400 MHz, DMSO-d_6)** 0.58–0.75 (4H, m, C(3'')CH_2), 2.81–2.90 (1H, m, C(2'')*H*), 7.27 (1H, s, C(4)*H*), 7.52–7.59 (3H, m, *Ph*), 7.87–7.93 (2H, m, *Ph*), 8.89–8.93 (1H, m, N*H*); **δ_C (400 MHz, DMSO-d_6)** 6.1 (2 *C*(3'')), 23.2 (*C*(2'')), 100.0 (*C*(4)), 126.2 (*C*(2'& 6')), 126.7 (*C*(1'), 129.8 (*C*(3'& 5'), 131.4 (*C*(4')), 159.9 (*C*(5)), 160.3 (*C*(3)), 170.8 (*C*(1'')); **HRMS (ESI^+)** $C_{13}H_{12}N_2NaO_2^+$ ($[M+Na]^+$) requires 251.0791, found 251.0786.

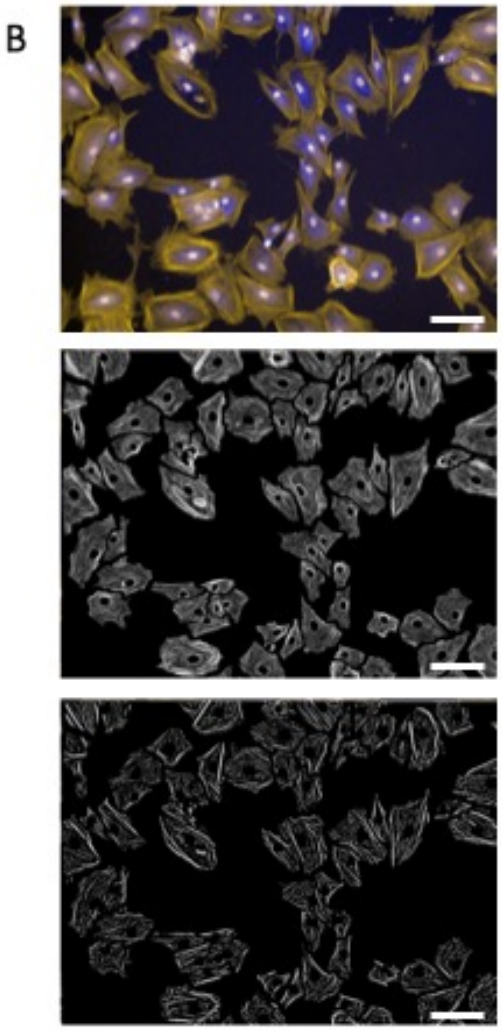
Chapter 11

Appendix

A.1 Figures

Figure A.3.1 Screen shots of the analysis protocol written on the Perkin Elmer Operetta High Content Imaging System (tdi.ox.ac.uk/high-content-imaging). The analysis protocol (**A**) was first taught to identify the cell nuclei from the DAPI stain. Images from the CellMask channel were used to identify the cytoplasm region of each cell. The phalloidin channel (**B**) was next employed to assess a number of intensity, textural and morphological features. Finally, a number of typical 'cobblestone' and 'spindle' cells were selected (**C**) to inform the program which features are associated with each phenotype. The analysis protocol was then able to scan through the remaining images and assign each cell as cobble or spindle accordingly.


A
Analysis Sequence
Input Image
Using: Individual Planes, FFC None
Find Nuclei
Output Population: Nuclei
Find Cytoplasm
Output Regions: Cell, Cytoplasm, Membrane
Select Population
Output Population: Nuclei Selected
Select Cell Region
Output Region: Cytoplasm Region
Calculate Intensity Properties
Output Properties: Intensity Cytoplasm DsRed S...
Calculate Morphology Properties
Output Properties: Cytoplasm Region
Calculate Texture Properties
Output Properties: Cytoplasm Region DsRed
Calculate Texture Properties (2)
Output Properties: Cytoplasm Region DsRed
Select Population (2)
Population: Nuclei Selected
Method: Linear Classifier
Train ...
Number of Classes: 2
Output Population A: Cobbles all
Output Population B: Spindle all


B

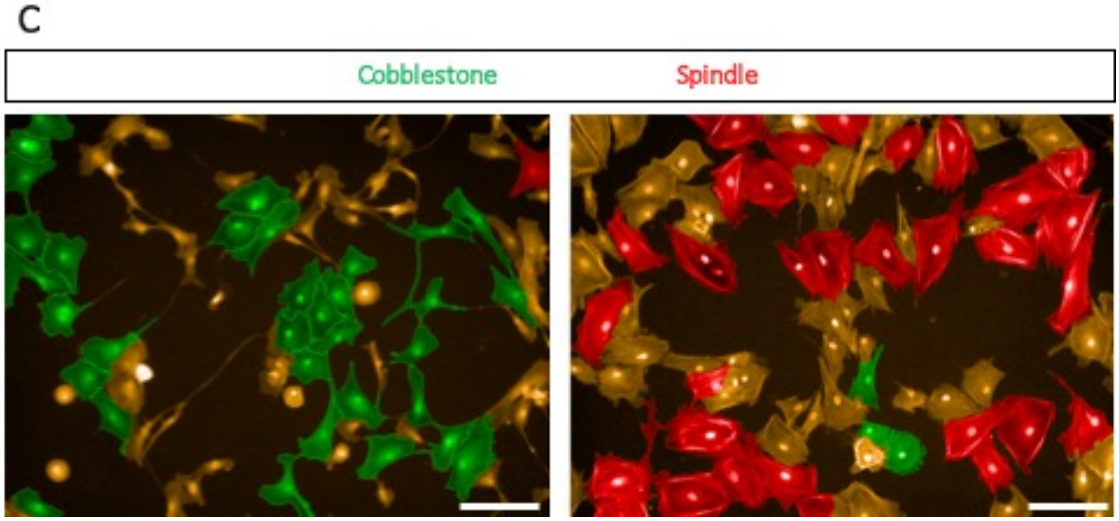

C
Cobblestone
Spindle

Figure A.4.1 QPCR analysis revealed no significant change in expression of *Snai2* or *ZO1* in response to any differentiation condition.

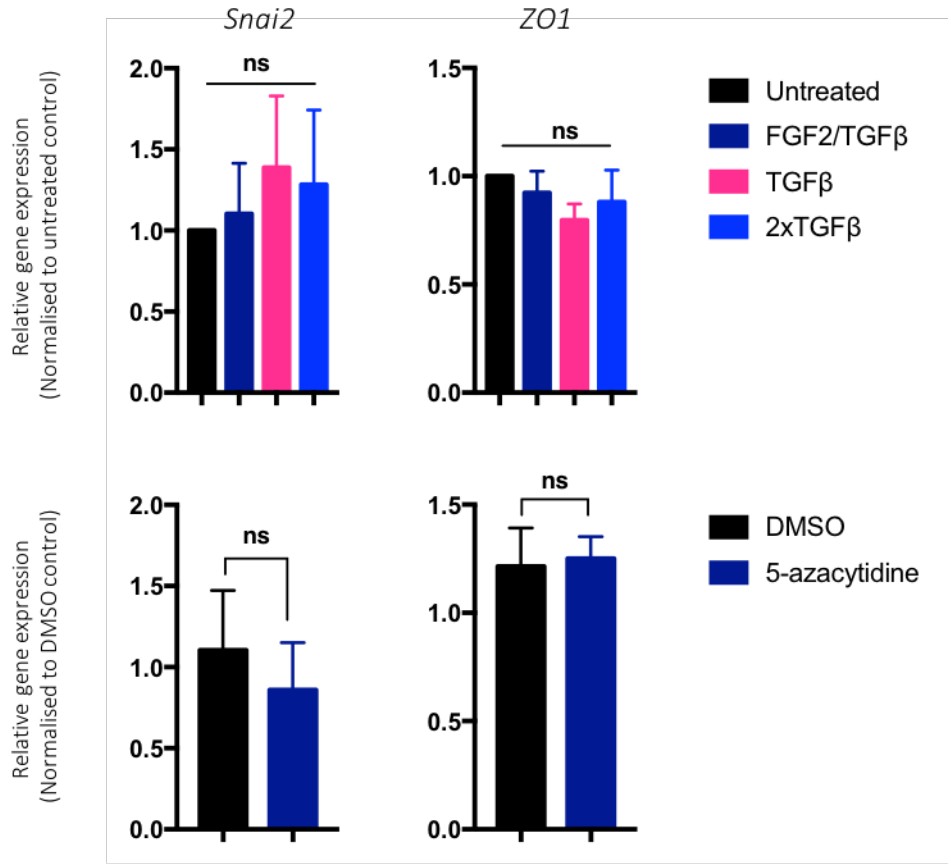


Figure A.7.1 Calculating the z_i for each treatment from the arte data dn the $v_{migration}$ data identified two positive and three negative hits. Both methods of analysis returned the same results. (A) Rate data calculated using original method (mm^2/hour) **(B)** The $v_{migration}$ data. Statistics calculated using a one way ANOVA, n = 3 for DMSO, PFI-1, UNC0642 and A 366, n = 2 for A-161906 and OXF2004, # indicates insufficient data to calculate significance.

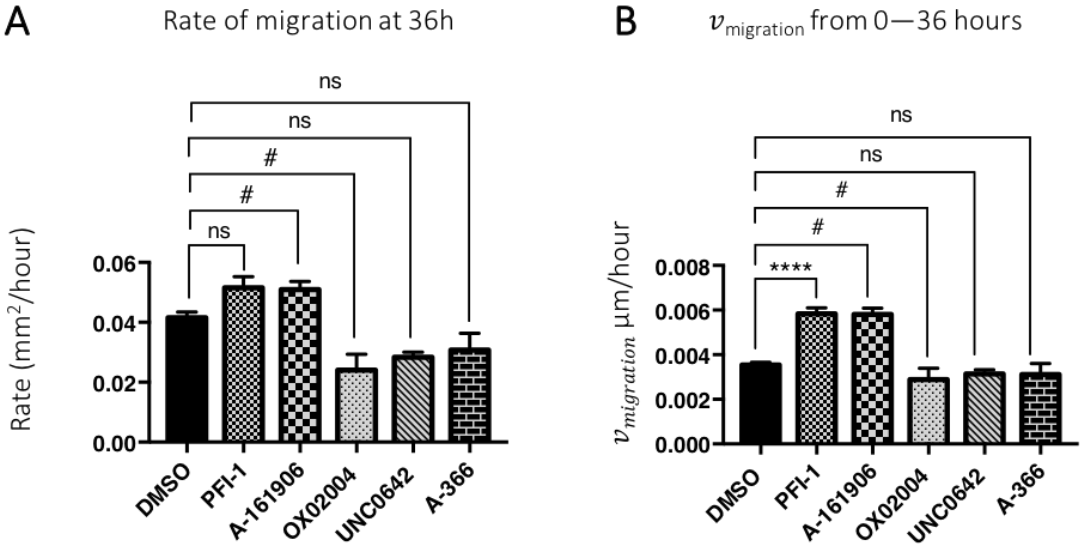


Figure A.7.2 Control data from validation screen reveals that TGFβ significantly increases the rate of mEPDC migration compared with the DMSO and untreated controls. Both methods of analysis return the same results. (A) Rate data calculated using original analysis method (**B**) $v_{\text{migration}}$ data.

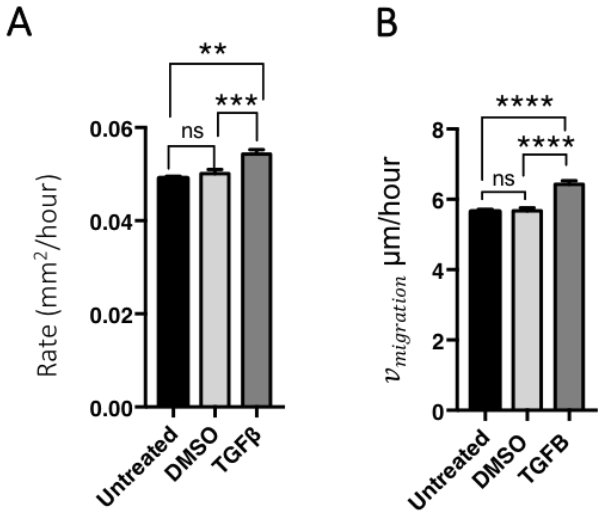
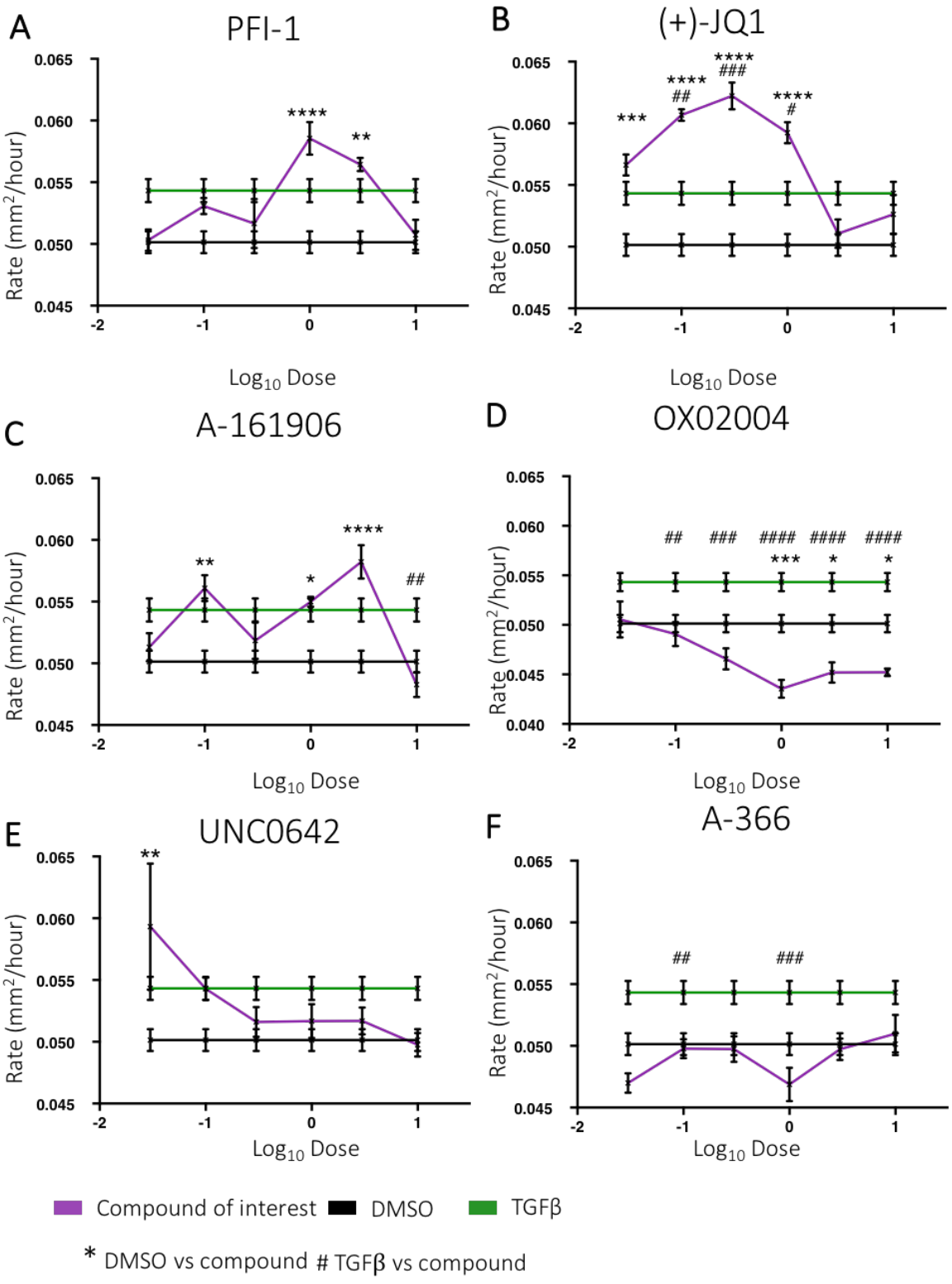


Figure A.7.3 Dose response curves generated from validation assay data. Both methods of analysis return the same results. (A-F) Data from original analysis. **(A'-F')** $v_{\text{migration}}$ data.


A
PFI-1
B
(+)-JQ1
C
A-161906
D
OX02004
E
UNC0642
F
A-366
Rate (mm²/hour)
Log10 Dose
Compound of interest
DMSO
TGFβ
* DMSO vs compound # TGFβ vs compound

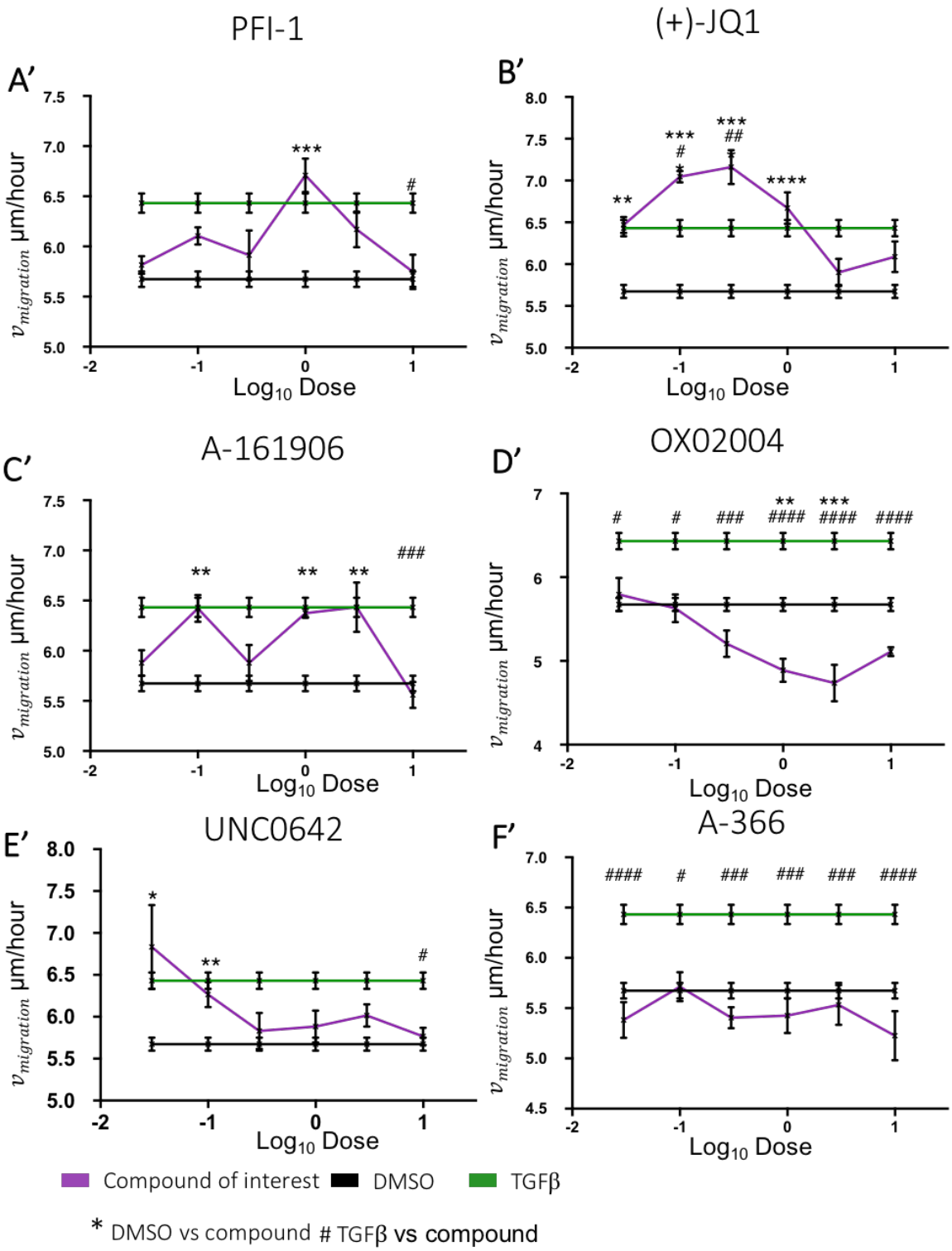

PFI-1
(+)-JQ1
A-161906
OX02004
UNC0642
A-366
A'
B'
C'
D'
E'
F'
$v_{migration}$ µm/hour
Log10 Dose
Compound of interest
DMSO
TGFβ
* DMSO vs compound # TGFβ vs compound

Figure A.7.4 PFI-1 appeared to be cytotoxic at 10 µM. PFI-1 treated cells appear to be dying at the 42-hour time point. Scale bar is 1mm.

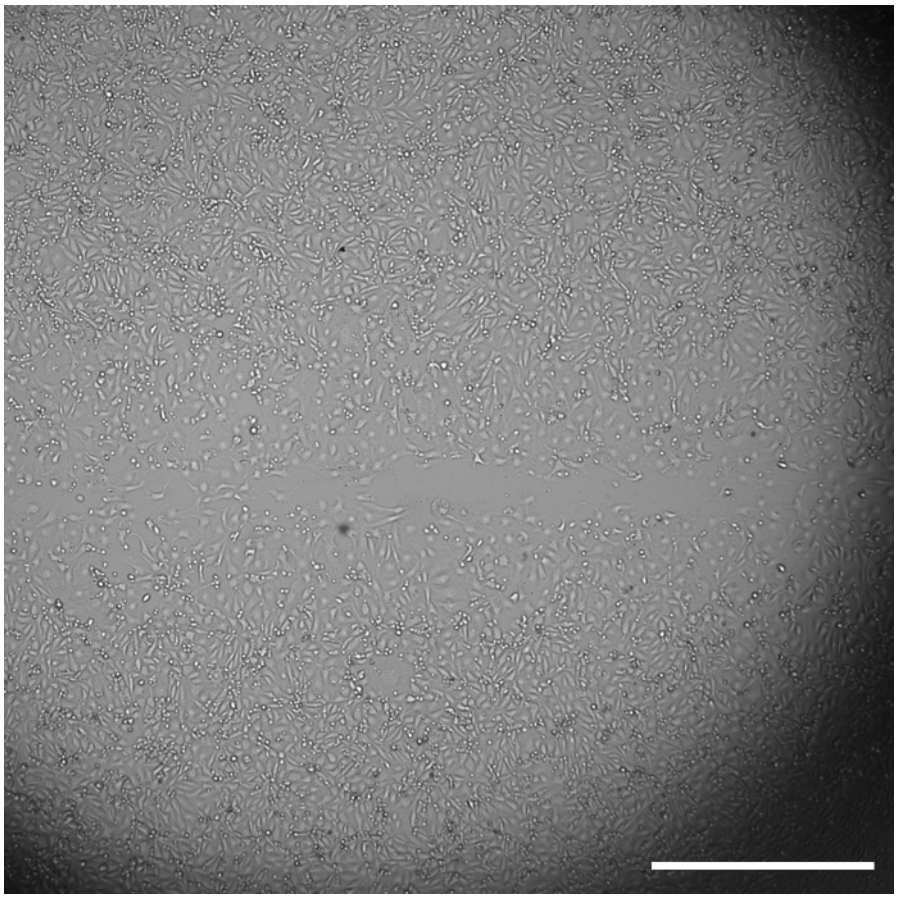
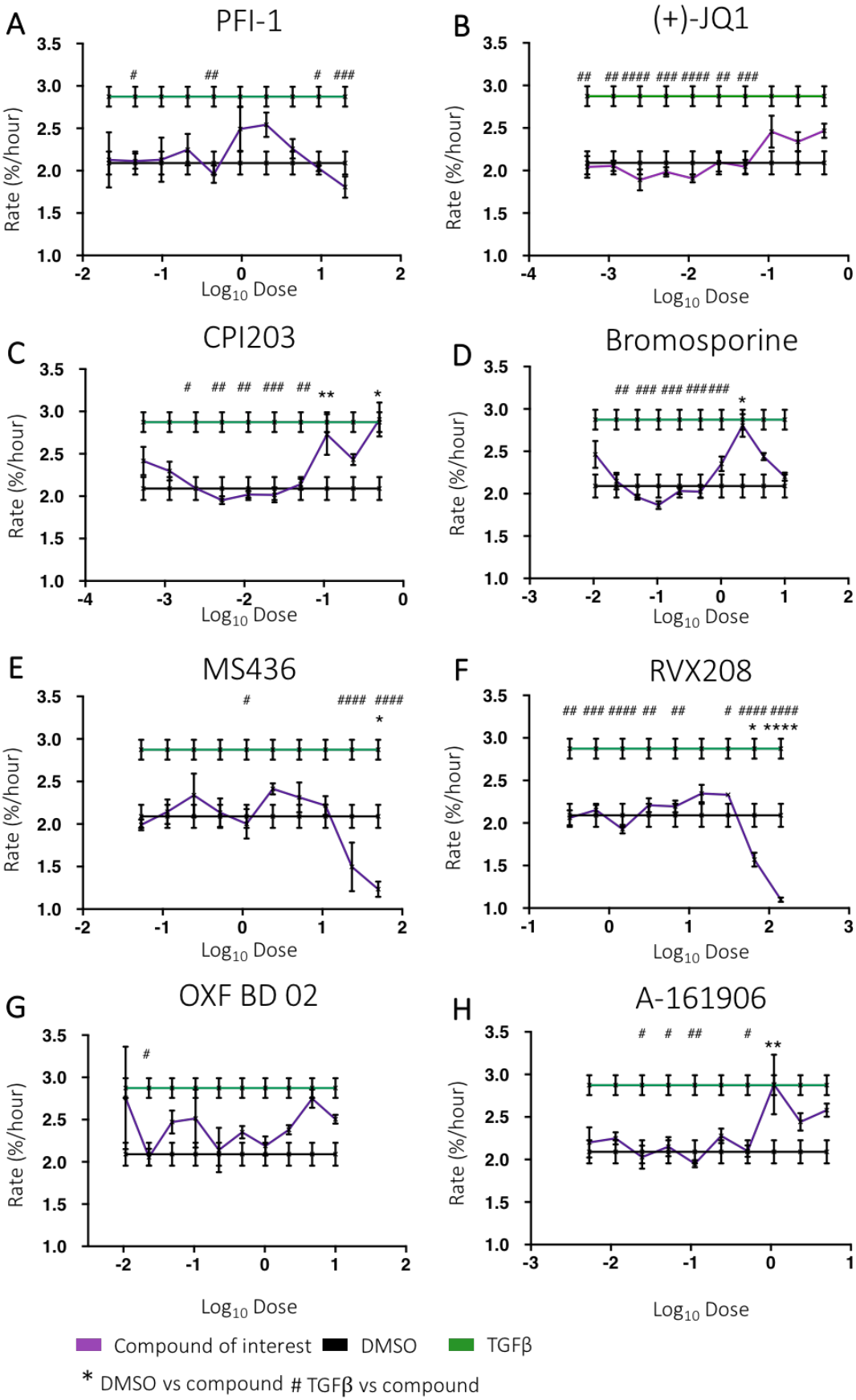
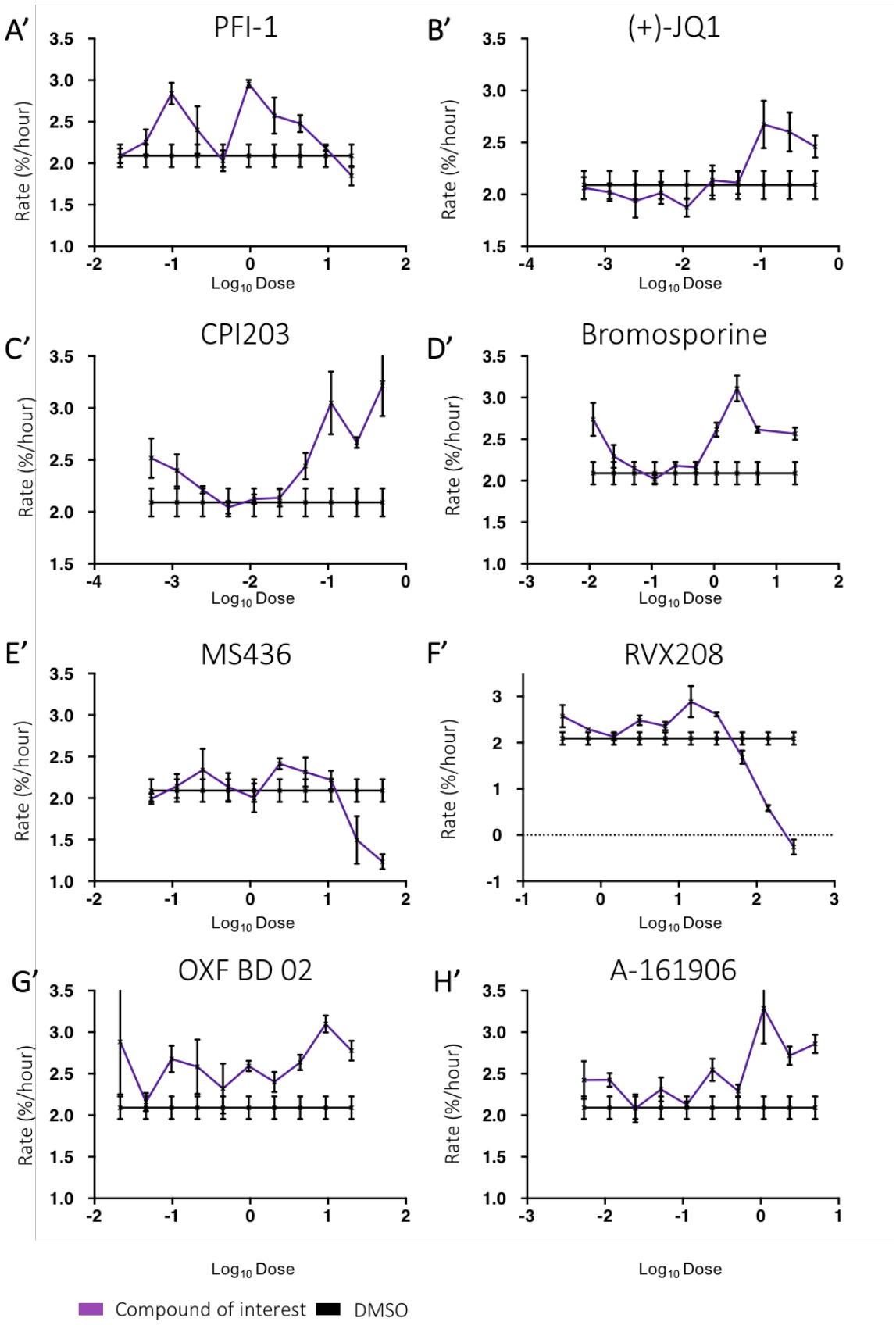


Figure A.8.1 Dose response curves from automated analysis (A–H) are the same as curves plotted from manual Image J calculations (A'–H').


A
PFI-1
B
(+)-JQ1
C
CPI203
D
Bromosporine
E
MS436
F
RVX208
G
OXF BD 02
H
A-161906
Rate (%/hour)
Log10 Dose
Compound of interest
DMSO
TGFβ
* DMSO vs compound # TGFβ vs compound


A'
PFI-1
B'
(+)-JQ1
C'
CPI203
D'
Bromosporine
E'
MS436
F'
RVX208
G'
OXF BD 02
H'
A-161906
Rate (%/hour)
Log10 Dose
Compound of interest
DMSO

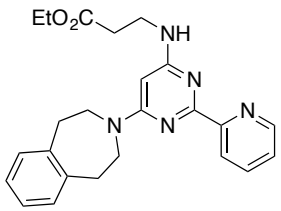
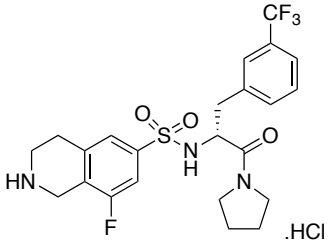
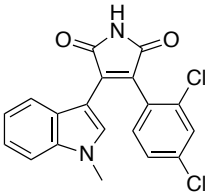
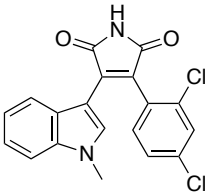
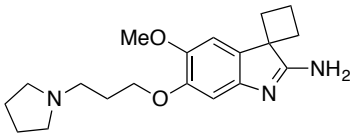
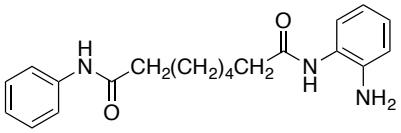
A.2 Tables

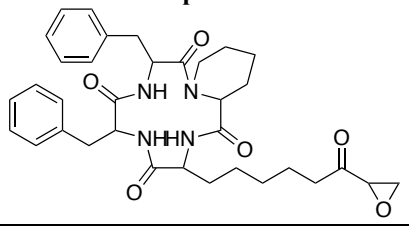
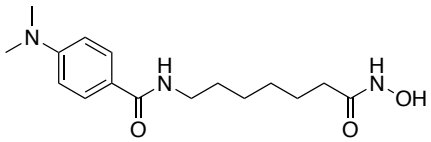
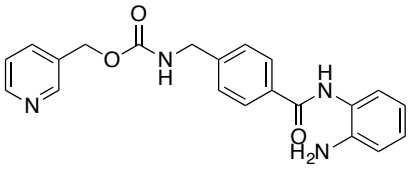
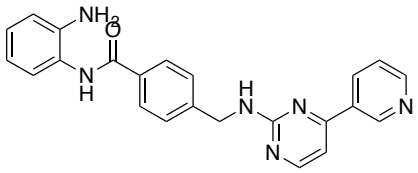
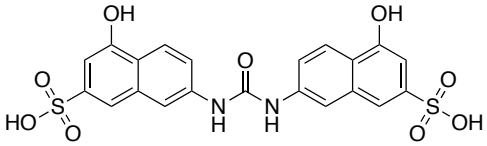
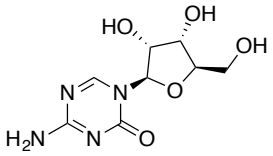
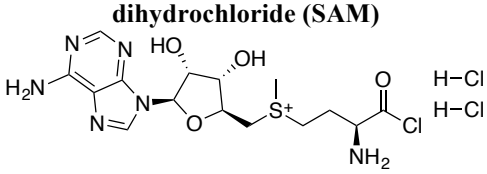
Table A.3.1 The top 72 treatments from the pilot HTPS ranked according to the number of spindle cells. The analysis protocol written on the Perkin Elmer Operetta High Content Imaging System (tdi.ox.ac.uk/high-content-imaging) which first calculated the number of spindled cells in each well and then assigned each well a 'Z-Score' which is a statistical measure of how far away from the average a data point sits (Full explanation see **Chapter 7, 7.1.3**) (Brideau et al., 2003). The higher the z-score the higher the number of spindle cells relative to the rest of the population. Compounds coloured in red were identified as hits but when viewing the images from the screen were found to be toxic or a falsely identified. The compounds highlighted in green were identified as hits and tested again in the validation screen. Despite the error in dilution in the pilot, hEPDCs treated with TGFβ appeared to have the highest Z-Score.

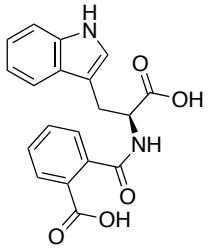
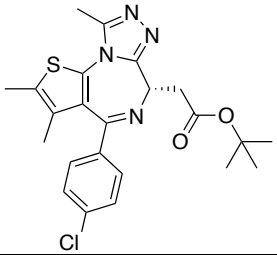
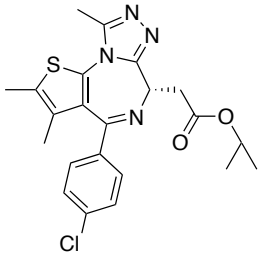
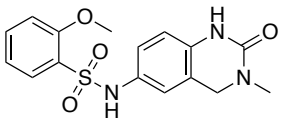
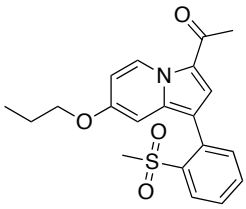
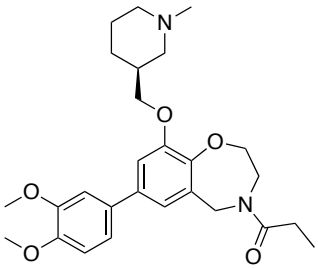
Number	Treatment	Average Z Score
1	TGFβ	1.80
2	COLFORSIN	1.60
3	TGFβ	1.51
4	TGFβ	1.51
5	TGFβ	1.50
6	TGFβ	1.50
7	TGFβ	1.47
8	TGFβ	1.44
9	TGFβ	1.42
10	TGFβ	1.42
11	TGFβ	1.41
12	EMPTY	1.39
13	TGFβ	1.39
14	DMSO	1.36
15	TGFβ	1.35
16	TGFβ	1.35
17	TGFβ	1.34
18	TGFβ	1.32
19	TGFβ	1.32
20	TGFβ	1.32
21	TGFβ	1.31
22	TGFβ	1.30
23	TGFβ	1.30
24	TGFβ	1.30
25	TGFβ	1.30
26	TGFβ	1.30
27	TGFβ	1.29
28	TGFβ	1.29
29	TGFβ	1.28
30	TGFβ	1.28
31	TGFβ	1.27
32	TGFβ	1.25
33	TGFβ	1.24
34	TGFβ	1.23

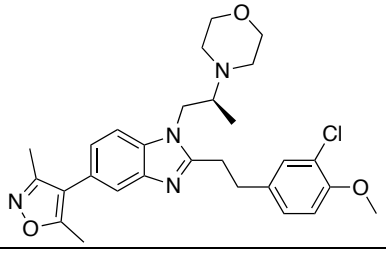
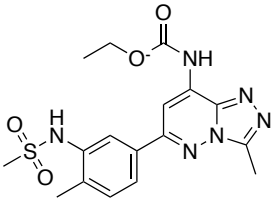
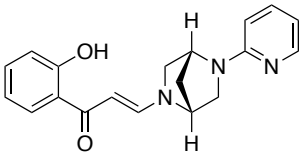
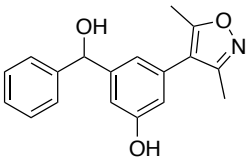
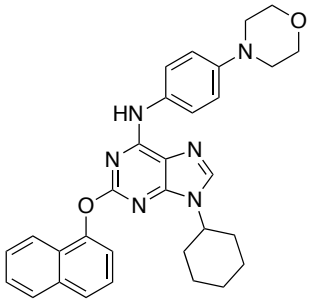
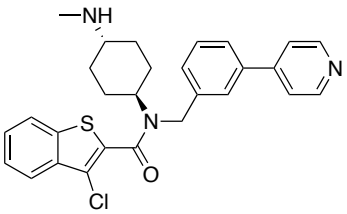
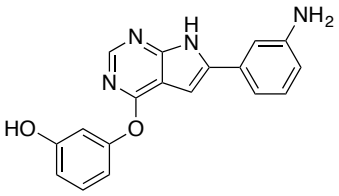
35	TGFβ	1.23
36	TGFβ	1.23
37	TGFβ	1.22
38	TGFβ	1.22
39	TGFβ	1.22
40	TGFβ	1.19
41	TGFβ	1.17
42	TGFβ	1.17
43	TRANYLCYPROMINE SULFATE	1.15
44	TGFβ	1.14
45	FAMOTIDINE	1.11
46	TGFβ	1.10
47	TGFβ	1.10
48	MEFENAMIC ACID	1.07
49	TGFβ	1.06
50	DMSO	1.06
51	TGFβ	1.05
52	TGFβ	1.00
53	RETINOL	1.00
54	TGFβ	1.00
55	ZILEUTON	0.99
56	TGFβ	0.98
57	TETRAHYDROZOLINE HYDROCHLORIDE	0.95
58	DMSO	0.94
59	BENZOCAINE	0.93
60	BENZETHONIUM CHLORIDE	0.93
61	FENOTEROL HYDROBROMIDE	0.91
62	TGFβ	0.90
63	TGFβ	0.90
64	TGFβ	0.90
65	NITRENDIPINE	0.90
66	METHYCLOTHIAZIDE	0.90
67	TGFβ	0.90
68	TGFβ	0.89
69	EQUILIN	0.86
70	DMSO	0.86
71	DMSO	0.85

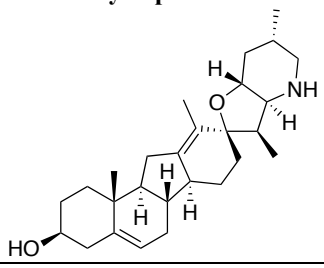
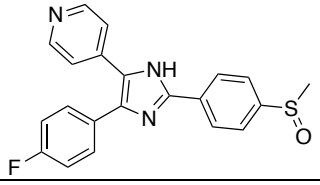
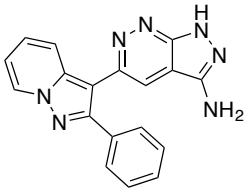
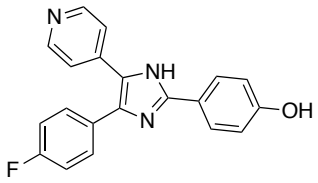
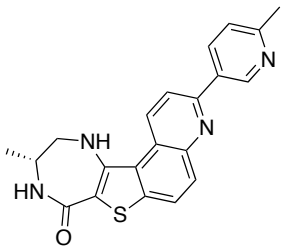
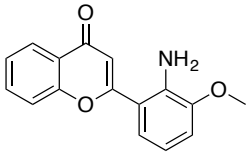
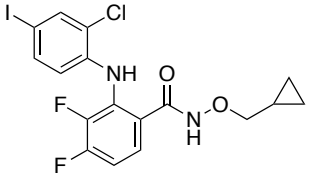
Appendix Table A.6.1 Small molecules screened in the mEPDC scratch assay

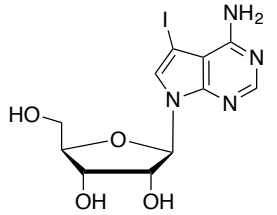
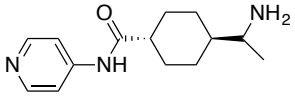
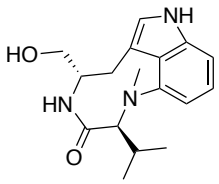
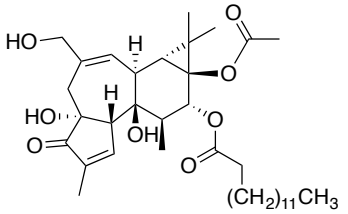
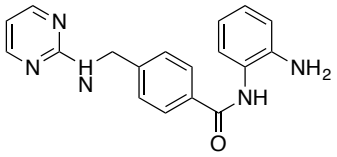
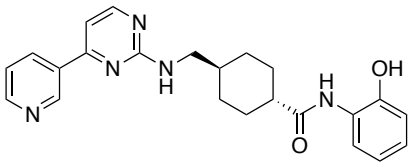
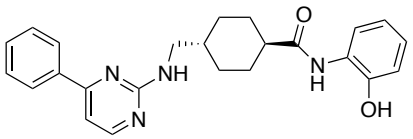
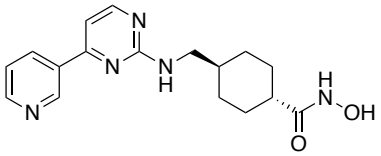
	Name and structure	Mechanism of action	Reference	Supplier
A	**GSK-J4** 	histone lysine demethylase inhibitor	(Heinemann et al., 2014)	Russell group library
B	**(R)-PFI-2** 	methyl transferase inhibitor	(Barsyte-Lovejoy et al., 2014)	Russell group library
C	**SB216763** 	kinase inhibitors: promotes pluripotency in mouse cells	(Coghlan et al., 2000)s	Russell group library
D	**UNC0642** 	lysine methyl transferase inhibitor	(Liu et al., 2013)	Russell group library
E	**A-366** 	lysine methyl transferase inhibitor	(Pappano et al., 2015)	Russell group library
F	**BML-210** 	histone deacetylase inhibitor	(Borutinskaitė and Navakauskienė, 2015)	Russell group library

G	**Trapoxin A** 	irreversible inhibitor of histone deacetylase	(Kijima et al., 1993)	Russell group library
H	**M344** 	histone deacetylase inhibitor	(Li and Chen, 2009)	Russell group library
I	**MS-275** 	histone deacetylase inhibitor	(Rao-Bindal et al., 2013)	Russell group library
J	**MGCD0103** 	histone deacetylase inhibitor	(Zhang et al., 2016)	Russell group library
K	**AMI-1** 	methyl transferase inhibitor	(Bonham et al., 2010)am	Russell group library
L	**5-Azacytidine** 	methyl transferase inhibitor	(Choi et al., 2004)	Russell group library
M	**S-(5'-Adenosyl)-L-methionine chloride dihydrochloride (SAM)** 	Methyl donor	(King et al., 2016)	Russell group library

N	**RG 108** 	methyl transferase inhibitor	(Bonham et al., 2010)	Russell group library
O	**(+)-JQ1** 	BET inhibitor	(Meng et al., 2014)	Russell group library
P	**(-)-JQ1** 	inactive form of (+)-JQ1	(Meng et al., 2014)	Russell group library
Q	**PFI-1** 	BET inhibitor	(Picaud et al., 2013a)	Russell group library
R	**GSK2801** 	Inhibitor of BAZ2A and BAZ2B bromodomains	(Chen et al., 2016)	Russell group library
S	**I-CBP112** 	CBP/p300 inhibitor	(Teo et al., 2005)	Russell group library

T	**SGC-CBP30** 	CBP/p300 inhibitor	(Zucconi et al., 2016)	Russell group library
U	**Bromosporine** 	BET inhibitor	(Structural Genomics Consortium, Bromosporine)	Russell group library
V	**PFI-3** 	SMARCA bromodomains	(Vangamudi et al., 2015)	Russell group library
W	**OXF-BD-02** 	BET inhibitor	(Hewings et al., 2013)	Conway group library
X	**Purmorphamine** 	hedgehog signalling pathway	(Sinha and Chen, 2006)	Russell group library
Y	**SAG** 	hedgehog signalling pathway	(Sasaki et al., 2013)S	Russell group library
Z	**TWS119** 	hedgehog signalling pathway	(Wang et al., 2015b)	Russell group library

A'	**Cyclopamine** 	hedgehog signalling pathway	(Chen et al., 2002)	Russell group library
B'	**SB203580** 	inhibits upstream of MAPK	(Barancík et al., 2001)	Russell group library
C'	**FR180204** 	ERK inhibitor	(Ohori et al., 2005)	Tocris
D'	**SB202190** 	p38 map kinases	(Barancík et al., 2001)	Tocris
E'	**PF-3644022** 	p38 map kinases	(Mourey et al., 2010)	Tocris
F'	**PD98059** 	MAPK/ERK	(Yamaguchi et al., 2002)	Tocris
G'	**PD184352** 	MEK inhibitor	(Allen et al., 2003)	Tocris

H'	**5-Iodotubercidin** 	adenosine kinase inhibitor	(Phillis and Smith-Barbour, 1993)	Russell group library
I'	**Y-27632** 	p160 ROCK inhibitor	(Maldonado et al., 2016)	Russell group library
J'	**Indolactam V** 	protein kinase c activator	(Haynes-Smith et al., 2016)	Russell group library
K'	**Phorbol 12-myristate 13-acetate (PMA)** 	protein kinase c activator	(Park et al., 2001)	Russell group library
L'	**OX12004** 	Potential BMP agonists	Russell group	Synthesised in the Russell lab
M'	**OX02129** 	Potential BMP agonists	Russell group	Synthesised in the Russell lab
N'	**OX02197** 	Potential BMP agonists	Russell group	Synthesised in the Russell lab
O'	**OX02268** 	Potential BMP agonists	Russell group	Synthesised in the Russell lab

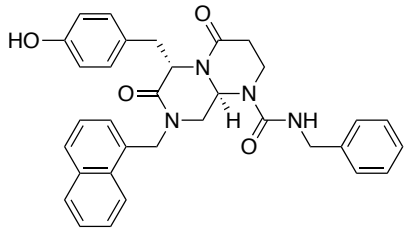
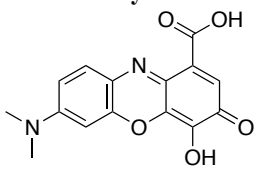
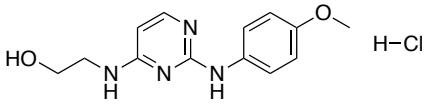
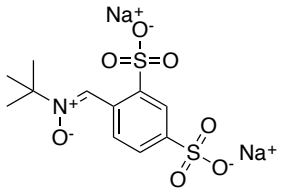
P'	**ICG-001** 	Wnt signalling modulator	(Sasaki et al., 2013)	Tocris
Q'	**Gallocyanine** 	Dkk1 inhibitor	(Iozzi et al., 2012)	Sigma
R'	**Cardiogenol** 			
S'	**OKN007** 	Human sulfatase 2 inhibitor	(Zheng et al., 2013b)	Synthesised in the Russell lab

Table A.7.1 Table contains the z_i calculated for each replicate plate and average z_i using the original rate calculation of area (mm^2)/time (hours) at the 36 hour time point. Green fill indicates z_i >1.5, orange fill indicates z_i <-1.5.

Treatment	z_i 1	z_i 2	z_i 3	Average z_i
(+)-JQ1	0.527	0.375	1.587	0.830
(-)-JQ1	0.806	0.017	-0.653	0.057
PFI-1	1.716	1.662	2.320	1.899
GSK-J4	0.103	0.192	0.673	0.323
GSK2801	0.373	0.417	0.413	0.401
I-CBP112	0.238	-0.402	-0.012	-0.059
SGC-CBP30	0.349	0.836	0.032	0.406
Bromosporine	1.518	1.792	1.094	1.468
PFI-3	-1.138	-0.505	-0.505	-0.716
(R)-PFI-2	-1.523	-0.745	0.276	-0.664
UNC0642	-2.110	-1.327	-1.679	-1.706
A-366	-1.172	-1.156	-3.037	-1.788
OXF-BD-02	-1.225	-0.280	-1.314	-0.940
BML-210	0.633	0.280	1.318	0.744
Trapoxin A	-0.683	-0.565	-2.496	-1.248
M344	0.517	1.354	1.591	1.154

SAG	-0.763	-1.723	-0.160	-0.882
TWS119	-0.171	-0.478	0.661	0.004
SB 216763	0.147	-0.071	-1.010	-0.311
MS275	0.522	0.307	0.353	0.394
MGCD0103)	-2.264	-1.034	-0.681	-1.327
cardiogenol	-0.031	-0.611	-0.116	-0.253
cyclopamine	0.681	-0.649	-0.517	-0.162
SB 203580	-1.013	0.055	-0.228	-0.395
AMI-1	-0.041	0.025	-0.024	-0.013
5-azacytidine?	0.777	-0.173	0.413	0.339
24346-00-7 S-(5′-Adenosyl)-L-methionine chloride dihydrochloride (SAM)	0.094	0.630	0.385	0.370
FR180204	1.047	-0.509	1.511	0.683
Sb202190	-1.567	-0.204	-1.038	-0.936
PF-3644022	0.455	0.577	-0.289	0.248
PD98059	0.643	0.600	0.096	0.446
PD184352	0.339	1.091	0.557	0.662
ICG-001	-0.229	-0.276	-1.118	-0.541
5-Iodotubercidin	0.060	0.017	-0.609	-0.177
RG 108	0.816	0.067	-0.084	0.266
Isx 12	-0.200	0.425	0.393	0.206
Isx 13	0.532	-0.448	0.320	0.135
Isx 14	2.048	0.169	0.220	0.813
Y-27632	0.200	0.684	0.441	0.441
Famotidine	-0.387	0.908	0.268	0.263
Nizatidine	0.647	0.889	0.497	0.678
Ranitidine	0.551	0.227	0.585	0.454
Mefenamic Acid	0.550	0.333	0.316	0.400
Phenyl Butazone		0.798	-0.523	0.137
Retinol		0.874	0.765	0.820
Zileuton		0.142	-0.632	-0.245
Fulvestrant		-0.720	0.934	0.107
Tamoxifen		-0.943	-0.649	-0.796
Fenoterol Hydrobromide		-0.151	0.123	-0.014
OX12004		-2.179	-2.259	-2.219
OX02129		-0.536	-0.626	-0.581
OX02197		-0.200	-0.311	-0.255
OX02268		-0.075	0.305	0.115
Indolactam v		-1.290	-1.517	-1.403

PMA		0.223	0.954	0.589
gallocyanine		-1.143	-0.165	-0.654
A-161906		2.560	1.266	1.913
SULF inhibitor 6		0.505	0.438	0.471
SULF inhibitor free amine (11)		0.560	1.047	0.804
OKN 007		0.505	0.298	0.402
A-161906 Acid		1.330	-2.007	-0.339

Table A.7.2 Table shown the z_i calculated for each replicate plate using the $v_{migration}$ analysis and the average z_i score. Green fill indicates z_i >1.5, orange fill indicates z_i <-1.5.

Treatment	z_i 1	z_i 2	z_i 3	Average z_i
(+)-JQ1	1.256	0.464	1.573	1.098
(-)-JQ1	0.623	0.041	-0.382	0.094
PFI-1	1.775	1.457	2.180	1.804
GSK-J4	-0.073	-0.060	0.439	0.102
GSK2801	0.459	0.278	0.375	0.371
I-CBP112	-0.008	-0.241	-0.162	-0.137
SGC-CBP30	0.871	0.799	0.327	0.666
Bromosporine	1.424	1.777	0.642	1.281
PFI-3	-1.280	-0.839	-1.261	-1.127
(R)-PFI-2	-1.296	-0.833	-0.247	-0.792
UNC0642	-2.597	-1.308	-1.611	-1.839
A-366	-0.613	-1.668	-2.800	-1.694
OXF-BD-02	-1.147	-1.078	-1.938	-1.388
BML-210	0.889	-0.153	1.033	0.589
Trapoxin A	-1.484	-0.548	-0.243	-0.758
M344	0.859	1.421	1.545	1.275
SAG	-0.185	-0.609	-0.660	-0.485
TWS119	0.096	0.028	-0.097	0.009
SB 216763	1.816-	0.126	-0.010	-0.567
MS275	-0.034	0.015	0.594	0.192
MGCD0103)	0.621	0.634	0.345	0.533
cardiogenol	-1.292	-0.306	1.445	-0.051
cyclopamine	-0.399	-0.241	-0.876	-0.505
SB 203580	0.925	0.517	-0.190	0.417
AMI-1	0.210	0.684	0.022	0.305
5-azacytidine?	1.210	0.960	0.635	0.935

24346-00-7 S-(5′-Adenosyl)-L-methionine chloride dihydrochloride (SAM)	-1.358	-0.222	-1.161	-0.914
FR180204	0.393	0.120	-0.230	0.094
Sb202190	0.548	0.148	0.068	0.255
PF-3644022	0.405	0.467	0.556	0.476
PD98059	-0.824	-0.357	0.406	-0.258
PD184352	0.006	-0.049	0.363	0.107
ICG-001	0.896	0.489	0.577	0.654
5-Iodotubercidin	-0.052	0.947	-0.016	0.293
RG 108	0.488	0.926	0.628	0.681
Isx 12	1.944	0.787	1.019	1.250
Isx 13	0.198	0.386	0.384	0.323
Isx 14	-0.290	0.240	-0.529	-0.193
Y-27632	0.792	0.537	-0.154	0.392
Famotidine	0.559	0.639	0.497	0.565
Nizatidine	-0.290	0.240	-0.529	-0.193
Ranitidine	0.792	0.537	-0.154	0.392
Mefenamic Acid	0.559	0.639	0.497	0.565
Phenyl Butazone		0.904	-0.401	0.251
Retinol		0.701	0.806	0.753
Zileuton		-0.099	-0.285	-0.192
Fulvestrant		-0.779	0.583	-0.098
Tamoxifen		-0.721	-0.591	-0.656
Fenoterol Hydrobromide		0.139	0.326	0.232
OX12004		-1.744	-2.286	-2.015
OX02129		-0.336	-0.545	-0.441
OX02197		-0.461	-0.705	-0.583
OX02268		-1.027	0.048	-0.489
Indolactam v		-0.742	-1.248	-0.995
PMA		0.210	0.985	0.597
gallocyanine		-1.361	-0.095	-0.728
A-161906		2.852	1.517	2.184
SULF inhibitor 6		0.714	0.356	0.535
SULF inhibitor free amine (11)		0.963	0.987	0.975
OKN 007		1.102	0.127	0.615
A-161906 Acid		-0.062	-1.731	-0.896

References

Abtan, J., Bhatt, D.L., Elbez, Y., Sorbets, E., Eagle, K., Ikeda, Y., Wu, D., Hanson, M.E., Hannachi, H., Singhal, P.K., et al. (2016). Residual Ischemic Risk and Its Determinants in Patients With Previous Myocardial Infarction and Without Prior Stroke or TIA: Insights From the REACH Registry. Clin. Cardiol. n/a-n/a.

Agarwal, M., Das, A., and Singh, A.S. (2010). High-dose hook effect in prolactin macroadenomas: A diagnostic concern. J. Hum. Reprod. Sci. *3*, 160–161.

Ahuja, D., Sáenz-Robles, M.T., and Pipas, J.M. (2005). SV40 large T antigen targets multiple cellular pathways to elicit cellular transformation. Oncogene *24*, 7729–7745.

Allen, L.F., Sebolt-Leopold, J., and Meyer, M.B. (2003). CI-1040 (PD184352), a targeted signal transduction inhibitor of MEK (MAPKK). Semin. Oncol. *30*, 105–116.

Andersen, D.C., Ganesalingam, S., Jensen, C.H., and Sheikh, S.P. (2014). Do Neonatal Mouse Hearts Regenerate following Heart Apex Resection? Stem Cell Rep. *2*, 406–413.

Ao, A., Hao, J., and Hong, C.C. (2011). Regenerative Chemical Biology: Current Challenges and Future Potential. Chem. Biol. *18*, 413–424.

Asai, Y., Tada, M., G. Otsuji, T., and Nakatsuji, N. (2010). Combination of Functional Cardiomyocytes Derived from Human Stem Cells and a Highly-Efficient Microelectrode Array System: An Ideal Hybrid Model Assay for Drug Development. Curr. Stem Cell Res. Ther. *5*, 227–232.

Ashley, E.A., and Niebauer, J. (2004). Cardiology Explained (London: Remedica).

Assmus, B., Walter, D.H., Seeger, F.H., Leistner, D.M., Steiner, J., Ziegler, I., Lutz, A., Khaled, W., Klotsche, J., Tonn, T., et al. (2013). Effect of shock wave-facilitated intracoronary cell therapy on LVEF in patients with chronic heart failure: the CELLWAVE randomized clinical trial. JAMA *309*, 1622–1631.

Austin, A.F., Compton, L.A., Love, J.D., Brown, C.B., and Barnett, J.V. (2008). Primary and immortalized mouse epicardial cells undergo differentiation in response to TGFβ. Dev. Dyn. *237*, 366–376.

Baell, J., and Walters, M.A. (2014). Chemistry: Chemical con artists foil drug discovery. Nature *513*, 481–483.

Balsam, L.B., Wagers, A.J., Christensen, J.L., Kofidis, T., Weissman, I.L., and Robbins, R.C. (2004). Haematopoietic stem cells adopt mature haematopoietic fates in ischaemic myocardium. Nature *428*, 668–673.

Banting, G.S., Barak, O., Ames, T.M., Burnham, A.C., Kardel, M.D., Cooch, N.S., Davidson, C.E., Godbout, R., McDermid, H.E., and Shiekhattar, R. (2005). CECR2, a protein involved in neurulation, forms a novel chromatin remodeling complex with SNF2L. Hum. Mol. Genet. *14*, 513–524.

Barancík, M., Bohácová, V., Kvackajová, J., Hudecová, S., Krizanová, O., and Breier, A. (2001). SB203580, a specific inhibitor of p38-MAPK pathway, is a new reversal agent of P-glycoprotein-mediated multidrug resistance. Eur. J. Pharm. Sci. Off. J. Eur. Fed. Pharm. Sci. *14*, 29–36.

Barsyte-Lovejoy, D., Li, F., Oudhoff, M.J., Tatlock, J.H., Dong, A., Zeng, H., Wu, H., Freeman, S.A., Schapira, M., Senisterra, G.A., et al. (2014). (R)-PFI-2 is a potent and selective inhibitor of SETD7 methyltransferase activity in cells. Proc. Natl. Acad. Sci. U. S. A. *111*, 12853–12858.

Bartunek, J., Behfar, A., Dolatabadi, D., Vanderheyden, M., Ostojic, M., Dens, J., El Nakadi, B., Banovic, M., Beleslin, B., Vrolix, M., et al. (2013). Cardiopoietic stem cell therapy in heart failure: the C-CURE (Cardiopoietic stem Cell therapy in heart failURE) multicenter randomized trial with lineage-specified biologics. J. Am. Coll. Cardiol. *61*, 2329–2338.

Bax, N.A.M., van Oorschot, A.A.M., Maas, S., Braun, J., van Tuyn, J., de Vries, A.A.F., Groot, A.C.G., and Goumans, M.-J. (2011). In vitro epithelial-to-mesenchymal transformation in human adult epicardial cells is regulated by TGFβ-signaling and WT1. Basic Res. Cardiol. *106*, 829–847.

Belkina, A.C., Nikolajczyk, B.S., and Denis, G.V. (2013). BET protein function is required for inflammation: Brd2 genetic disruption and BET inhibitor JQ1 impair mouse macrophage inflammatory responses. J. Immunol. Baltim. Md 1950 *190*, 3670–3678.

Beltrami, A.P., Urbanek, K., Kajstura, J., Yan, S.-M., Finato, N., Bussani, R., Nadal-Ginard, B., Silvestri, F., Leri, A., Beltrami, C.A., et al. (2001). Evidence That Human Cardiac Myocytes Divide after Myocardial Infarction. N. Engl. J. Med. *344*, 1750–1757.

Beltrami, A.P., Barlucchi, L., Torella, D., Baker, M., Limana, F., Chimenti, S., Kasahara, H., Rota, M., Musso, E., Urbanek, K., et al. (2003). Adult Cardiac Stem Cells Are Multipotent and Support Myocardial Regeneration. Cell *114*, 763–776.

Benesh, E.C., Miller, P.M., Pfaltzgraff, E.R., Grega-Larson, N.E., Hager, H.A., Sung, B.H., Qu, X., Baldwin, H.S., Weaver, A.M., and Bader, D.M. (2013). Bves and NDRG4 regulate directional epicardial cell migration through autocrine extracellular matrix deposition. Mol. Biol. Cell *24*, 3496–3510.

Bergmann, O., Bhardwaj, R.D., Bernard, S., Zdunek, S., Barnabé-Heider, F., Walsh, S., Zupicich, J., Alkass, K., Buchholz, B.A., Druid, H., et al. (2009). Evidence for Cardiomyocyte Renewal in Humans. Science *324*, 98–102.

van Berlo, J.H., Kanisicak, O., Maillet, M., Vagnozzi, R.J., Karch, J., Lin, S.-C.J., Middleton, R.C., Marbán, E., and Molkentin, J.D. (2014). c-kit+ cells minimally contribute cardiomyocytes to the heart. Nature *509*, 337–341.

Bleicher, K.H., Böhm, H.-J., Müller, K., and Alanine, A.I. (2003). Hit and lead generation: beyond high-throughput screening. Nat. Rev. Drug Discov. *2*, 369–378.

Bochmann, L., Sarathchandra, P., Mori, F., Lara-Pezzi, E., Lazzaro, D., and Rosenthal, N. (2010). Revealing New Mouse Epicardial Cell Markers through Transcriptomics. PLoS ONE *5*, e11429.

Bock-Marquette, I., Saxena, A., White, M.D., DiMaio, J.M., and Srivastava, D. (2004). Thymosin β4 activates integrin-linked kinase and promotes cardiac cell migration, survival and cardiac repair. Nature *432*, 466–472.

Bolden, J.E., Tasdemir, N., Dow, L.E., van Es, J.H., Wilkinson, J.E., Zhao, Z., Clevers, H., and Lowe, S.W. (2014). Inducible In Vivo Silencing of Brd4 Identifies Potential Toxicities of Sustained BET Protein Inhibition. Cell Rep. *8*, 1919–1929.

Bollini, S., Vieira, J.M.N., Howard, S., Dubè, K.N., Balmer, G.M., Smart, N., and Riley, P.R. (2014). Re-activated adult epicardial progenitor cells are a heterogeneous population molecularly distinct from their embryonic counterparts. Stem Cells Dev. *23*, 1719–1730.

Bonham, K., Hemmers, S., Lim, Y.-H., Hill, D.M., Finn, M.G., and Mowen, K.A. (2010). Effects of a Novel Arginine Methyltransferase Inhibitor on T Helper Cell Cytokine Production. FEBS J. *277*, 2096–2108.

Booth, D.G., Takagi, M., Sanchez-Pulido, L., Petfalski, E., Vargiu, G., Samejima, K., Imamoto, N., Ponting, C.P., Tollervey, D., Earnshaw, W.C., et al. (2014). Ki-67 is a PP1-interacting protein that organises the mitotic chromosome periphery. eLife *3*, e01641.

van den Borne, S.W.M., Diez, J., Blankesteijn, W.M., Verjans, J., Hofstra, L., and Narula, J. (2010). Myocardial remodeling after infarction: the role of myofibroblasts. Nat. Rev. Cardiol. *7*, 30–37.

Borutinskaitė, V., and Navakauskienė, R. (2015). The Histone Deacetylase Inhibitor BML-210 Influences Gene and Protein Expression in Human Promyelocytic Leukemia NB4 Cells via Epigenetic Reprogramming. Int. J. Mol. Sci. *16*, 18252–18269.

Brade, T., Pane, L.S., Moretti, A., Chien, K.R., and Laugwitz, K.-L. (2013). Embryonic Heart Progenitors and Cardiogenesis. Cold Spring Harb. Perspect. Med. *3*.

Braitsch, C.M., Kanisicak, O., van Berlo, J.H., Molkentin, J.D., and Yutzey, K.E. (2013). Differential expression of embryonic epicardial progenitor markers and localization of cardiac fibrosis in adult ischemic injury and hypertensive heart disease. J. Mol. Cell. Cardiol. *65C*, 108–119.

Brideau, C., Gunter, B., Pikounis, B., and Liaw, A. (2003). Improved statistical methods for hit selection in high-throughput screening. J. Biomol. Screen. *8*, 634–647.

British Heart Foundation https://www.bhf.org.uk/research/heart-statistics.

Bruneau, B.G. (2008). The developmental genetics of congenital heart disease. Nature *451*, 943–948.

Bryant, D.M., O'Meara, C.C., Ho, N.N., Gannon, J., Cai, L., and Lee, R.T. (2015). A systematic analysis of neonatal mouse heart regeneration after apical resection. J. Mol. Cell. Cardiol. *79*, 315–318.

Burn, S. (2012). Detection of β-Galactosidase Activity: X-gal Staining. In Kidney Development, O. Michos, ed. (Humana Press), pp. 241–250.

Burridge, P.W., Keller, G., Gold, J.D., and Wu, J.C. (2012). Production of De Novo Cardiomyocytes: Human Pluripotent Stem Cell Differentiation and Direct Reprogramming. Cell Stem Cell *10*, 16–28.

Burridge, P.W., Matsa, E., Shukla, P., Lin, Z.C., Churko, J.M., Ebert, A.D., Lan, F., Diecke, S., Huber, B., Mordwinkin, N.M., et al. (2014). Chemically defined generation of human cardiomyocytes. Nat. Methods *11*, 855–860.

Cai, C.-L., Martin, J.C., Sun, Y., Cui, L., Wang, L., Ouyang, K., Yang, L., Bu, L., Liang, X., Zhang, X., et al. (2008). A myocardial lineage derives from Tbx18 epicardial cells. Nature *454*, 104–108.

Cano, A., Pérez-Moreno, M.A., Rodrigo, I., Locascio, A., Blanco, M.J., del Barrio, M.G., Portillo, F., and Nieto, M.A. (2000). The transcription factor Snail controls epithelial–mesenchymal transitions by repressing E-cadherin expression. Nat. Cell Biol. *2*, 76–83.

Cao, N., Huang, Y., Zheng, J., Spencer, C.I., Zhang, Y., Fu, J.-D., Nie, B., Xie, M., Zhang, M., Wang, H., et al. (2016). Conversion of human fibroblasts into functional cardiomyocytes by small molecules. Science *352*, 1216–1220.

Cao, X., Surma, M.A., and Simons, K. (2012). Polarized sorting and trafficking in epithelial cells. Cell Res. *22*, 793–805.

Carmo-Fonseca, M. (2002). The Contribution of Nuclear Compartmentalization to Gene Regulation. Cell *108*, 513–521.

Carmona, R., Guadix, J.A., Cano, E., Ruiz-Villalba, A., Portillo-Sánchez, V., Pérez-Pomares, J.M., and Muñoz-Chápuli, R. (2010). The embryonic epicardium: an essential element of cardiac development. J. Cell. Mol. Med. *14*, 2066–2072.

Carpenter, A.E., Jones, T.R., Lamprecht, M.R., Clarke, C., Kang, I.H., Friman, O., Guertin, D.A., Chang, J.H., Lindquist, R.A., Moffat, J., et al. (2006). CellProfiler: image analysis software for identifying and quantifying cell phenotypes. Genome Biol. *7*, R100.

Chablais, F., Veit, J., Rainer, G., and Jaźwińska, A. (2011). The zebrafish heart regenerates after cryoinjury-induced myocardial infarction. BMC Dev. Biol. *11*, 21.

Chaidos, A., Caputo, V., and Karadimitris, A. (2015). Inhibition of bromodomain and extra-terminal proteins (BET) as a potential therapeutic approach in haematological malignancies: emerging preclinical and clinical evidence. Ther. Adv. Hematol. *6*, 128–141.

Chang, H., Liu, Y., Xue, M., Liu, H., Du, S., Zhang, L., and Wang, P. (2016). Synergistic action of master transcription factors controls epithelial-to-mesenchymal transition. Nucleic Acids Res. *44*, 2514–2527.

Chen, B., Dodge, M.E., Tang, W., Lu, J., Ma, Z., Fan, C.-W., Wei, S., Hao, W., Kilgore, J., Williams, N.S., et al. (2009). Small molecule–mediated disruption of Wnt-dependent signaling in tissue regeneration and cancer. Nat. Chem. Biol. *5*, 100–107.

Chen, D., Zhao, M., and Mundy, G.R. (2004). Bone Morphogenetic Proteins. Growth Factors *22*, 233–241.

Chen, J.K., Taipale, J., Cooper, M.K., and Beachy, P.A. (2002). Inhibition of Hedgehog signaling by direct binding of cyclopamine to Smoothened. Genes Dev. *16*, 2743–2748.

Chen, P., Chaikuad, A., Bamborough, P., Bantscheff, M., Bountra, C., Chung, C.-W., Fedorov, O., Grandi, P., Jung, D., Lesniak, R., et al. (2016). Discovery and Characterization of GSK2801, a Selective Chemical Probe for the Bromodomains BAZ2A and BAZ2B. J. Med. Chem. *59*, 1410–1424.

Chen, Y., Wang, K., Qian, C.-N., and Leach, R. (2013). DNA methylation is associated with transcription of Snail and Slug genes. Biochem. Biophys. Res. Commun. *430*, 1083–1090.

Cheng, Y.-T., Yeih, D.-F., Liang, S.-M., Chien, C.-Y., Yu, Y.-L., Ko, B.-S., Jan, Y.-J., Kuo, C.-C., Sung, L.-Y., Shyue, S.-K., et al. (2015). Rho-associated kinase inhibitors promote the cardiac differentiation of embryonic and induced pluripotent stem cells. Int. J. Cardiol. *201*, 441–448.

Chiba, H., Osanai, M., Murata, M., Kojima, T., and Sawada, N. (2008). Transmembrane proteins of tight junctions. Biochim. Biophys. Acta BBA - Biomembr. *1778*, 588–600.

Choi, S.-C., Yoon, J., Shim, W.-J., Ro, Y.-M., and Lim, D.-S. (2004). 5-azacytidine induces cardiac differentiation of P19 embryonic stem cells. Exp. Mol. Med. *36*, 515–523.

Choi, W.-Y., Gemberling, M., Wang, J., Holdway, J.E., Shen, M.-C., Karlstrom, R.O., and Poss, K.D. (2013). In vivo monitoring of cardiomyocyte proliferation to identify chemical modifiers of heart regeneration. Development *140*, 660–666.

Chong, J.J.H., Yang, X., Don, C.W., Minami, E., Liu, Y.-W., Weyers, J.J., Mahoney, W.M., Van Biber, B., Cook, S.M., Palpant, N.J., et al. (2014). Human embryonic-stem-cell-derived cardiomyocytes regenerate non-human primate hearts. Nature *510*, 273–277.

Christoffels, V.M., Grieskamp, T., Norden, J., Mommersteeg, M.T.M., Rudat, C., and Kispert, A. (2009). Tbx18 and the fate of epicardial progenitors. Nature *458*, E8-9-10.

Cleutjens, J.P.M., Blankesteijn, W.M., Daemen, M.J.A.P., and Smits, J.F.M. (1999). The infarcted myocardium. Cardiovasc. Res. *44*, 232–241.

Clunie-O'Connor, C., Smits, A.M., Antoniades, C., Russell, A.J., Yellon, D.M., Goumans, M.-J., and Riley, P.R. (2015). The Derivation of Primary Human Epicardium-Derived Cells. Curr. Protoc. Stem Cell Biol. *35*, 2C.5.1-2C.5.12.

Coghlan, M.P., Culbert, A.A., Cross, D.A., Corcoran, S.L., Yates, J.W., Pearce, N.J., Rausch, O.L., Murphy, G.J., Carter, P.S., Roxbee Cox, L., et al. (2000). Selective small molecule inhibitors of glycogen synthase kinase-3 modulate glycogen metabolism and gene transcription. Chem. Biol. *7*, 793–803.

Contreras, R.G., Shoshani, L., Flores-Maldonado, C., Lázaro, A., Monroy, A.O., Roldán, M.L., Fiorentino, R., and Cereijido, M. (2002). E-Cadherin and tight junctions between epithelial cells of different animal species. Pflüg. Arch. Eur. J. Physiol. *444*, 467–475.

Cooper, G., Kent, R.L., Uboh, C.E., Thompson, E.W., and Marino, T.A. (1985). Hemodynamic versus adrenergic control of cat right ventricular hypertrophy. J. Clin. Invest. *75*, 1403–1414.

Davis, M.A., Ireton, R.C., and Reynolds, A.B. (2003). A core function for p120-catenin in cadherin turnover. J. Cell Biol. *163*, 525–534.

De Herreros, A.G., Peiró, S., Nassour, M., and Savagner, P. (2010). Snail family regulation and epithelial mesenchymal transitions in breast cancer progression. J. Mammary Gland Biol. Neoplasia *15*, 135–147.

Deb, A., Wang, S., Skelding, K.A., Miller, D., Simper, D., and Caplice, N.M. (2003). Bone Marrow–Derived Cardiomyocytes Are Present in Adult Human Heart. Circulation *107*, 1247–1249.

DeLean, A., Munson, P.J., and Rodbard, D. (1978). Simultaneous analysis of families of sigmoidal curves: application to bioassay, radioligand assay, and physiological dose-response curves. Am. J. Physiol. - Gastrointest. Liver Physiol. *235*, G97-102.

Delewi, R., Piek, J.J., and Hirsch, A. (2013). Letter by Delewi et al regarding article, "Adult bone marrow cell therapy improves survival and induces long-term improvement in cardiac parameters: a systematic review and meta-analysis." Circulation *127*, e547.

Derynck, R., and Feng, X.-H. (1997). TGF-β receptor signaling. Biochim. Biophys. Acta BBA - Rev. Cancer *1333*, F105–F150.

DeSesso, J.M. (1979). Cell death and free radicals: a mechanism for hydroxyurea teratogenesis. Med. Hypotheses *5*, 937–951.

Desmoulière, A., Geinoz, A., Gabbiani, F., and Gabbiani, G. (1993). Transforming growth factor-beta 1 induces alpha-smooth muscle actin expression in granulation tissue myofibroblasts and in quiescent and growing cultured fibroblasts. J. Cell Biol. *122*, 103–111.

Dettman, R.W., Denetclaw, W., Ordahl, C.P., and Bristow, J. (1998). Common Epicardial Origin of Coronary Vascular Smooth Muscle, Perivascular Fibroblasts, and Intermyocardial Fibroblasts in the Avian Heart. Dev. Biol. *193*, 169–181.

Devaiah, B.N., Lewis, B.A., Cherman, N., Hewitt, M.C., Albrecht, B.K., Robey, P.G., Ozato, K., Sims, R.J., and Singer, D.S. (2012). BRD4 is an atypical kinase that phosphorylates Serine2 of the RNA Polymerase II carboxy-terminal domain. Proc. Natl. Acad. Sci. *109*, 6927–6932.

Di Micco, R., Fontanals-Cirera, B., Low, V., Ntziachristos, P., Yuen, S.K., Lovell, C.D., Dolgalev, I., Yonekubo, Y., Zhang, G., Rusinova, E., et al. (2014). Control of embryonic stem cell identity by BRD4-dependent transcriptional elongation of super-enhancer-associated pluripotency genes. Cell Rep. *9*, 234–247.

Dinsmore, J., Ratliff, J., Deacon, T., Pakzaban, P., Jacoby, D., Galpern, W., and Isacson, O. (1996). Embryonic stem cells differentiated in vitro as a novel source of cells for transplantation. Cell Transplant. *5*, 131–143.

Drees, F., Pokutta, S., Yamada, S., Nelson, W.J., and Weis, W.I. (2005). α-Catenin Is a Molecular Switch that Binds E-Cadherin-β-Catenin and Regulates Actin-Filament Assembly. Cell *123*, 903–915.

Drey, L.L., Graber, M.C., and Bieschke, J. (2013). Counting unstained, confluent cells by modified bright-field microscopy. BioTechniques *55*.

Druker, B.J., Tamura, S., Buchdunger, E., Ohno, S., Segal, G.M., Fanning, S., Zimmermann, J., and Lydon, N.B. (1996). Effects of a selective inhibitor of the Abl tyrosine kinase on the growth of Bcr-Abl positive cells. Nat. Med. *2*, 561–566.

Druker, B.J., Guilhot, F., O'Brien, S.G., Gathmann, I., Kantarjian, H., Gattermann, N., Deininger, M.W.N., Silver, R.T., Goldman, J.M., Stone, R.M., et al. (2006). Five-Year Follow-up of Patients Receiving Imatinib for Chronic Myeloid Leukemia. N. Engl. J. Med. *355*, 2408–2417.

Dutton, J.R., Lahiri, D., and Ward, A. (2006). Different isoforms of the Wilms' tumour protein WT1 have distinct patterns of distribution and trafficking within the nucleus. Cell Prolif. *39*, 519–535.

D'Uva, G., Bertoni, S., Lauriola, M., Carolis, S.D., Pacilli, A., D'Anello, L., Santini, D., Taffurelli, M., Ceccarelli, C., Yarden, Y., et al. (2013). Beta-Catenin/HuR Post-Transcriptional Machinery Governs Cancer Stem Cell Features in Response to Hypoxia. PLOS ONE *8*, e80742.

Edwards, M.K., Harris, J.F., and McBurney, M.W. (1983). Induced muscle differentiation in an embryonal carcinoma cell line. Mol. Cell. Biol. *3*, 2280–2286.

Eglitis, M.A., and Mezey, É. (1997). Hematopoietic cells differentiate into both microglia and macroglia in the brains of adult mice. Proc. Natl. Acad. Sci. U. S. A. *94*, 4080–4085.

Eid, H., Larson, D.M., Springhorn, J.P., Attawia, M.A., Nayak, R.C., Smith, T.W., and Kelly, R.A. (1992). Role of epicardial mesothelial cells in the modification of phenotype and function of adult rat ventricular myocytes in primary coculture. Circ. Res. *71*, 40–50.

Eid, H., de Bold, M.L., Chen, J.H., and de Bold, A.J. (1994). Epicardial mesothelial cells synthesize and release endothelin. J. Cardiovasc. Pharmacol. *24*, 715–720.

Ellison, G.M., Torella, D., Karakikes, I., Purushothaman, S., Curcio, A., Gasparri, C., Indolfi, C., Cable, N.T., Goldspink, D.F., and Nadal-Ginard, B. (2007). Acute β-Adrenergic Overload Produces Myocyte Damage through Calcium Leakage from the Ryanodine Receptor 2 but Spares Cardiac Stem Cells. J. Biol. Chem. *282*, 11397–11409.

Ellison, G.M., Vicinanza, C., Smith, A.J., Aquila, I., Leone, A., Waring, C.D., Henning, B.J., Stirparo, G.G., Papait, R., Scarfò, M., et al. (2013). Adult c-kitpos Cardiac Stem Cells Are Necessary and Sufficient for Functional Cardiac Regeneration and Repair. Cell *154*, 827–842.

Engel, F.B., Schebesta, M., Duong, M.T., Lu, G., Ren, S., Madwed, J.B., Jiang, H., Wang, Y., and Keating, M.T. (2005). p38 MAP kinase inhibition enables proliferation of adult mammalian cardiomyocytes. Genes Dev. *19*, 1175–1187.

Engel, F.B., Hsieh, P.C.H., Lee, R.T., and Keating, M.T. (2006). FGF1/p38 MAP kinase inhibitor therapy induces cardiomyocyte mitosis, reduces scarring, and rescues function after myocardial infarction. Proc. Natl. Acad. Sci. U. S. A. *103*, 15546–15551.

essenbioscience.com http://www.essenbioscience.com/en/products/peripherals/incucyte-cell-migration-kit/.

Evans, M. (2011). Discovering pluripotency: 30 years of mouse embryonic stem cells. Nat. Rev. Mol. Cell Biol. *12*, 680–686.

Fabbro, D., Cowan-Jacob, S.W., and Moebitz, H. (2015). Ten things you should know about protein kinases: IUPHAR Review 14. Br. J. Pharmacol. *172*, 2675–2700.

Fernandes, P.B. (1998). Technological advances in high-throughput screening. Curr. Opin. Chem. Biol. *2*, 597–603.

Ferrari, G., Cusella-De Angelis, G., Coletta, M., Paolucci, E., Stornaiuolo, A., Cossu, G., and Mavilio, F. (1998). Muscle regeneration by bone marrow-derived myogenic progenitors. Science *279*, 1528–1530.

Fesik, S., Summers, J., Davidsen, S., Sheppard, G., Steinman, D., Carrera, G., Florjancic, A., and Holms, J. (1997). Biphenyl Hydroxamate Inhibitors of Matrix Metalloproteinases.

Filippakopoulos, P., and Knapp, S. (2014). Targeting bromodomains: epigenetic readers of lysine acetylation. Nat. Rev. Drug Discov. *13*, 337–356.

Filippakopoulos, P., Qi, J., Picaud, S., Shen, Y., Smith, W.B., Fedorov, O., Morse, E.M., Keates, T., Hickman, T.T., Felletar, I., et al. (2010). Selective inhibition of BET bromodomains. Nature *468*, 1067–1073.

Filippakopoulos, P., Picaud, S., Mangos, M., Keates, T., Lambert, J.-P., Barsyte-Lovejoy, D., Felletar, I., Volkmer, R., Müller, S., Pawson, T., et al. (2012). Histone Recognition and Large-Scale Structural Analysis of the Human Bromodomain Family. Cell *149*, 214–231.

Fish, P.V., Filippakopoulos, P., Bish, G., Brennan, P.E., Bunnage, M.E., Cook, A.S., Federov, O., Gerstenberger, B.S., Jones, H., Knapp, S., et al. (2012). Identification of a chemical probe for bromo and extra C-terminal bromodomain inhibition through optimization of a fragment-derived hit. J. Med. Chem. *55*, 9831–9837.

Fodde, R., and Brabletz, T. (2007). Wnt/beta-catenin signaling in cancer stemness and malignant behavior. Curr. Opin. Cell Biol. *19*, 150–158.

Friedl, P., and Gilmour, D. (2009). Collective cell migration in morphogenesis, regeneration and cancer. Nat. Rev. Mol. Cell Biol. *10*, 445–457.

Fu, L., Tian, M., Li, X., Li, J., Huang, J., Ouyang, L., Zhang, Y., and Liu, B. (2015). Inhibition of BET bromodomains as a therapeutic strategy for cancer drug discovery. Oncotarget *6*, 5501–5516.

Galbraith, C.G., Yamada, K.M., and Galbraith, J.A. (2007). Polymerizing Actin Fibers Position Integrins Primed to Probe for Adhesion Sites. Science *315*, 992–995.

Gardner, T.S., and Wenis, E. (2002). Synthesis of 5-Substituted 3-Isoxazolecarboxylic Acid Hydrazides and Derivatives.

Gemberling, M., Bailey, T.J., Hyde, D.R., and Poss, K.D. (2013). The zebrafish as a model for complex tissue regeneration. Trends Genet. *29*, 611–620.

Glaser, K.B., Li, J., Aakre, M.E., Morgan, D.W., Sheppard, G., Stewart, K.D., Pollock, J., Lee, P., O'Connor, C.Z., Anderson, S.N., et al. (2002). Transforming growth factor beta mimetics: discovery of 7-[4-(4-cyanophenyl)phenoxy]-heptanohydroxamic acid, a biaryl hydroxamate inhibitor of histone deacetylase. Mol. Cancer Ther. *1*, 759–768.

Gonzalez, D.M., and Medici, D. (2014). Signaling mechanisms of the epithelial-mesenchymal transition. Sci Signal *7*, re8-re8.

González-Rosa, J.M., and Mercader, N. (2012). Cryoinjury as a myocardial infarction model for the study of cardiac regeneration in the zebrafish. Nat. Protoc. *7*, 782–788.

González-Rosa, J.M., Martín, V., Peralta, M., Torres, M., and Mercader, N. (2011). Extensive scar formation and regression during heart regeneration after cryoinjury in zebrafish. Dev. Camb. Engl. *138*, 1663–1674.

Goossens, S., Janzen, V., Bartunkova, S., Yokomizo, T., Drogat, B., Crisan, M., Haigh, K., Seuntjens, E., Umans, L., Riedt, T., et al. (2011). The EMT regulator Zeb2/Sip1 is essential for murine embryonic hematopoietic stem/progenitor cell differentiation and mobilization. Blood *117*, 5620–5630.

Grazia Lampugnani, M., Zanetti, A., Corada, M., Takahashi, T., Balconi, G., Breviario, F., Orsenigo, F., Cattelino, A., Kemler, R., Daniel, T.O., et al. (2003). Contact inhibition of VEGF-induced proliferation requires vascular endothelial cadherin, beta-catenin, and the phosphatase DEP-1/CD148. J. Cell Biol. *161*, 793–804.

Grounds, M.D., Garrett, K.L., Lai, M.C., Wright, W.E., and Beilharz, M.W. (1992). Identification of skeletal muscle precursor cells in vivo by use of MyoD1 and myogenin probes. Cell Tissue Res. *267*, 99–104.

Gumbiner, B.M. (2000). Regulation of Cadherin Adhesive Activity. J. Cell Biol. *148*, 399–404.

Hans, F., and Dimitrov, S. (2001). Histone H3 phosphorylation and cell division. Oncogene *20*.

Hao, J., Zhou, L., and C., C. (2011). Chemical Biology of Pluripotent Stem Cells: Focus on Cardiomyogenesis. In Embryonic Stem Cells - Recent Advances in Pluripotent Stem Cell-Based Regenerative Medicine, C. Atwood, ed. (InTech), p.

Hartsock, A., and Nelson, W.J. (2008). Adherens and Tight Junctions: Structure, Function and Connections to the Actin Cytoskeleton. Biochim. Biophys. Acta *1778*, 660–669.

Hasan, A., Khattab, A., Islam, M.A., Hweij, K.A., Zeitouny, J., Waters, R., Sayegh, M., Hossain, M.M., and Paul, A. (2015). Injectable Hydrogels for Cardiac Tissue Repair after Myocardial Infarction. Adv. Sci. *2*, n/a-n/a.

Hayat, M.A. (2006). Handbook of Immunohistochemistry and in situ Hybridization of Human Carcinomas: Molecular Genetics, Gastrointestinal Carcinoma, and Ovarian Carcinoma (Academic Press).

Haynes-Smith, J., Diaz, I., and Billingsley, K.L. (2016). Modular Total Synthesis of Protein Kinase C Activator (−)-Indolactam V. Org. Lett. *18*, 2008–2011.

He, Y., Zhang, H., Yung, A., Villeda, S.A., Jaeger, P.A., Olayiwola, O., Fainberg, N., and Wyss-Coray, T. (2014). ALK5-dependent TGF-β signaling is a major determinant of late-stage adult neurogenesis. Nat. Neurosci. *17*, 943–952.

Hefti, F.F. (2008). Requirements for a lead compound to become a clinical candidate. BMC Neurosci. *9*, S7.

Heinemann, B., Nielsen, J.M., Hudlebusch, H.R., Lees, M.J., Larsen, D.V., Boesen, T., Labelle, M., Gerlach, L.-O., Birk, P., and Helin, K. (2014). Inhibition of demethylases by GSK-J1/J4. Nature *514*, E1–E2.

Hewings, D.S., Fedorov, O., Filippakopoulos, P., Martin, S., Picaud, S., Tumber, A., Wells, C., Olcina, M.M., Freeman, K., Gill, A., et al. (2013). Optimization of 3,5-dimethylisoxazole derivatives as potent bromodomain ligands. J. Med. Chem. *56*, 3217–3227.

Heyden, M.A.G. van der, and Defize, L.H.K. (2003). Twenty one years of P19 cells: what an embryonal carcinoma cell line taught us about cardiomyocyte differentiation. Cardiovasc. Res. *58*, 292–302.

Hinz, B., Celetta, G., Tomasek, J.J., Gabbiani, G., and Chaponnier, C. (2001). Alpha-Smooth Muscle Actin Expression Upregulates Fibroblast Contractile Activity. Mol. Biol. Cell *12*, 2730–2741.

Hirt, M.N., Hansen, A., and Eschenhagen, T. (2014). Cardiac Tissue Engineering. Circ. Res. *114*, 354–367.

Ho, E., and Shimada, Y. (1978). Formation of the epicardium studied with the scanning electron microscope. Dev. Biol. *66*, 579–585.

Hocevar, B.A., and Howe, P.H. (1998). Mechanisms of TGF-beta-induced cell cycle arrest. Miner. Electrolyte Metab. *24*, 131–135.

Hohenstein, P., and Hastie, N.D. (2006). The many facets of the Wilms' tumour gene, WT1. Hum. Mol. Genet. *15*, R196–R201.

Hossain, M.M., Takashima, A., Nakayama, H., and Doi, K. (1997). 5-Azacytidine induces toxicity in PC12 cells by apoptosis. Exp. Toxicol. Pathol. Off. J. Ges. Für Toxikol. Pathol. *49*, 201–206.

Hsieh, P.C.H., Segers, V.F.M., Davis, M.E., MacGillivray, C., Gannon, J., Molkentin, J.D., Robbins, J., and Lee, R.T. (2007). Evidence from a genetic fate-mapping study that stem cells refresh adult mammalian cardiomyocytes after injury. Nat. Med. *13*, 970–974.

http://cellprofiler.org http://cellprofiler.org.

http://cellprofiler.org/examples.html http://cellprofiler.org/examples.html#Speckles.

http://ibidi.com/fileadmin/support/application_notes/AN30_Wound_Healing_Data_Analysis.pdf
http://ibidi.com/fileadmin/support/application_notes/AN30_Wound_Healing_Data_Analysis.pdf.

http://www.abcam.com/protocols/general-western-blot-protocol Western blot protocol | Abcam.

http://www.biocenter.hu/pdf/CellTrackergreen.pdf
http://www.biocenter.hu/pdf/CellTrackergreen.pdf.

http://www.drugbank.ca/drugs/DB00812 http://www.drugbank.ca/drugs/DB00812.

http://www.elisa-antibody.com/ELISA-Introduction http://www.elisa-antibody.com/ELISA-Introduction.

http://www.essenbioscience.com/en/products/incucyte IncuCyte® System.

http://www.tdi.ox.ac.uk/small-compound-libraries http://www.tdi.ox.ac.uk/small-compound-libraries.

http://www.who.int/mediacentre/factsheets/fs317/en/ WHO | Cardiovascular diseases (CVDs).

Hu, Y., Zhou, J., Ye, F., Xiong, H., Peng, L., Zheng, Z., Xu, F., Cui, M., Wei, C., Wang, X., et al. (2015). BRD4 inhibitor inhibits colorectal cancer growth and metastasis. Int. J. Mol. Sci. *16*, 1928–1948.

Huang, P., Sandoval, A., Van Den Neste, E., Keating, M.J., and Plunkett, W. (2000). Inhibition of RNA transcription: a biochemical mechanism of action against chronic lymphocytic leukemia cells by fludarabine. Leukemia *14*, 1405–1413.

Huang, T., Barnett, J.V., and Camenisch, T.D. (2014a). Cardiac Epithelial-Mesenchymal Transition Is Blocked by Monomethylarsonous Acid (III). Toxicol. Sci. *142*, 225–238.

Huang, T., Barnett, J.V., and Camenisch, T.D. (2014b). Cardiac Epithelial-Mesenchymal Transition Is Blocked by Monomethylarsonous Acid (III). Toxicol. Sci. *142*, 225–238.

Hughes, J., Rees, S., Kalindjian, S., and Philpott, K. (2011). Principles of early drug discovery. Br. J. Pharmacol. *162*, 1239–1249.

Hughes, P., Marshall, D., Reid, Y., Parkes, H., and Gelber, C. (2007). The costs of using unauthenticated, over-passaged cell lines: how much more data do we need? BioTechniques *43*, 575, 577–578, 581–582 passim.

Hülsken, J., Birchmeier, W., and Behrens, J. (1994). E-cadherin and APC compete for the interaction with beta-catenin and the cytoskeleton. J. Cell Biol. *127*, 2061–2069.

Hwang, S.G., Choi, S.R., Cho, J.W., Bae, S.J., Koo, T.S., Lee, S.Y., Cho, K.C., and Gwon, H.C. (2009). Pharmaceutical composition for preventintion and treatment of restenosis comprising isoxazole derivatives.

Ieda, M., Fu, J.-D., Delgado-Olguin, P., Vedantham, V., Hayashi, Y., Bruneau, B.G., and Srivastava, D. (2010). Direct Reprogramming of Fibroblasts into Functional Cardiomyocytes by Defined Factors. Cell *142*, 375–386.

Iozzi, S., Remelli, R., Lelli, B., Diamanti, D., Pileri, S., Bracci, L., Roncarati, R., Caricasole, A., and Bernocco, S. (2012). Functional Characterization of a Small-Molecule Inhibitor of the DKK1-LRP6 Interaction. Int. Sch. Res. Not. *2012*, e823875.

Irfan Maqsood, M., Matin, M.M., Bahrami, A.R., and Ghasroldasht, M.M. (2013). Immortality of cell lines: challenges and advantages of establishment. Cell Biol. Int. *37*, 1038–1045.

Ivanov, A.I., Samarin, S.N., Bachar, M., Parkos, C.A., and Nusrat, A. (2009). Protein kinase C activation disrupts epithelial apical junctions via ROCK-II dependent stimulation of actomyosin contractility. BMC Cell Biol. *10*, 36.

Iyer, D., Gambardella, L., Bernard, W.G., Serrano, F., Mascetti, V.L., Pedersen, R.A., Talasila, A., and Sinha, S. (2015). Robust derivation of epicardium and its differentiated smooth muscle cell progeny from human pluripotent stem cells. Development *142*, 1528–1541.

Jaenisch, R., and Young, R. (2008). Stem Cells, the Molecular Circuitry of Pluripotency and Nuclear Reprogramming. Cell *132*, 567–582.

Jat, P.S., Noble, M.D., Ataliotis, P., Tanaka, Y., Yannoutsos, N., Larsen, L., and Kioussis, D. (1991). Direct derivation of conditionally immortal cell lines from an H-2Kb-tsA58 transgenic mouse. Proc. Natl. Acad. Sci. U. S. A. *88*, 5096–5100.

Jeevanantham, V., Butler, M., Saad, A., Abdel-Latif, A., Zuba-Surma, E.K., and Dawn, B. (2012). Adult bone marrow cell therapy improves survival and induces long-term improvement in cardiac parameters: a systematic review and meta-analysis. Circulation *126*, 551–568.

Jeong, J.-O., Han, J.W., Kim, J.-M., Cho, H.-J., Park, C., Lee, N., Kim, D.-W., and Yoon, Y.-S. (2011). Malignant tumor formation after transplantation of short-term cultured bone marrow mesenchymal stem cells in experimental myocardial infarction and diabetic neuropathy. Circ. Res. *108*, 1340–1347.

Joensuu, H. (2002). Treatment of inoperable gastrointestinal stromal tumor (GIST) with Imatinib (Glivec, Gleevec). Med. Klin. Munich Ger. 1983 *97 Suppl 1*, 28–30.

Jonkman, J.E.N., Cathcart, J.A., Xu, F., Bartolini, M.E., Amon, J.E., Stevens, K.M., and Colarusso, P. (2014). An introduction to the wound healing assay using live-cell microscopy. Cell Adhes. Migr. *8*, 440–451.

Jopling, C., Sleep, E., Raya, M., Martí, M., Raya, A., and Izpisúa Belmonte, J.C. (2010). Zebrafish heart regeneration occurs by cardiomyocyte dedifferentiation and proliferation. Nature *464*, 606–609.

Journal of the Statistical Society of London (1839). First Annual Report of the Registrar-General on Births, Deaths, and Marriages in England, in 1837-8 ,.

Kajstura, J., Leri, A., Finato, N., Loreto, C.D., Beltrami, C.A., and Anversa, P. (1998). Myocyte proliferation in end-stage cardiac failure in humans. Proc. Natl. Acad. Sci. *95*, 8801–8805.

Kang, J., Gu, Y., Li, P., Johnson, B.L., Sucov, H.M., and Thomas, P.S. (2008). PDGF-A as an epicardial mitogen during heart development. Dev. Dyn. Off. Publ. Am. Assoc. Anat. *237*, 692–701.

Katz, A.M. (1995). The cardiomyopathy of overload: An unnatural growth response. Eur. Heart J. *16*, 110–114.

Kehat, I., Kenyagin-Karsenti, D., Snir, M., Segev, H., Amit, M., Gepstein, A., Livne, E., Binah, O., Itskovitz-Eldor, J., and Gepstein, L. (2001). Human embryonic stem cells can differentiate into myocytes with structural and functional properties of cardiomyocytes. J. Clin. Invest. *108*, 407–414.

Kemler, R., Hierholzer, A., Kanzler, B., Kuppig, S., Hansen, K., Taketo, M.M., de Vries, W.N., Knowles, B.B., and Solter, D. (2004). Stabilization of beta-catenin in the mouse zygote leads to premature epithelial-mesenchymal transition in the epiblast. Dev. Camb. Engl. *131*, 5817–5824.

Kent, R.L., Hoober, J.K., and Cooper, G. (1989). Load responsiveness of protein synthesis in adult mammalian myocardium: role of cardiac deformation linked to sodium influx. Circ. Res. *64*, 74–85.

Kertai, M.D., Qi, W., Li, Y.-J., Lombard, F.W., Liu, Y., Smith, M.P., Stafford-Smith, M., Newman, M.F., Milano, C.A., Mathew, J.P., et al. (2016). Gene signatures of postoperative atrial fibrillation in atrial tissue after coronary artery bypass grafting surgery in patients receiving β-blockers. J. Mol. Cell. Cardiol. *92*, 109–115.

Kijima, M., Yoshida, M., Sugita, K., Horinouchi, S., and Beppu, T. (1993). Trapoxin, an antitumor cyclic tetrapeptide, is an irreversible inhibitor of mammalian histone deacetylase. J. Biol. Chem. *268*, 22429–22435.

Kikuchi, K., Holdway, J.E., Werdich, A.A., Anderson, R.M., Fang, Y., Egnaczyk, G.F., Evans, T., Macrae, C.A., Stainier, D.Y.R., and Poss, K.D. (2010). Primary contribution to zebrafish heart regeneration by gata4(+) cardiomyocytes. Nature *464*, 601–605.

Kill, I.R. (1996). Localisation of the Ki-67 antigen within the nucleolus. Evidence for a fibrillarin-deficient region of the dense fibrillar component. J. Cell Sci. *109 (Pt 6)*, 1253–1263.

Kim, J., Wu, Q., Zhang, Y., Wiens, K.M., Huang, Y., Rubin, N., Shimada, H., Handin, R.I., Chao, M.Y., Tuan, T.-L., et al. (2010). PDGF signaling is required for epicardial function and blood vessel formation in regenerating zebrafish hearts. Proc. Natl. Acad. Sci. *107*, 17206–17210.

King, A.L., Mantena, S.K., Andringa, K.K., Millender-Swain, T., Dunham-Snary, K.J., Oliva, C.R., Griguer, C.E., and Bailey, S.M. (2016). The methyl donor S-adenosylmethionine prevents liver hypoxia and dysregulation of mitochondrial bioenergetic function in a rat model of alcohol-induced fatty liver disease. Redox Biol. *9*, 188–197.

Kira, Y., Kochel, P.J., Gordon, E.E., and Morgan, H.E. (1984). Aortic perfusion pressure as a determinant of cardiac protein synthesis. Am. J. Physiol. *246*, C247-258.

Kobayashi, W., and Ozawa, M. (2013). The transcription factor LEF-1 induces an epithelial–mesenchymal transition in MDCK cells independent of β-catenin. Biochem. Biophys. Res. Commun. *442*, 133–138.

Koç, A., Wheeler, L.J., Mathews, C.K., and Merrill, G.F. (2004). Hydroxyurea Arrests DNA Replication by a Mechanism That Preserves Basal dNTP Pools. J. Biol. Chem. *279*, 223–230.

Komiyama, M., Ito, K., and Shimada, Y. Origin and development of the epicardium in the mouse embryo. Anat. Embryol. (Berl.) *176*, 183–189.

Kong, P., Christia, P., Saxena, A., Su, Y., and Frangogiannis, N.G. (2013). Lack of specificity of fibroblast-specific protein 1 in cardiac remodeling and fibrosis. Am. J. Physiol. Heart Circ. Physiol. *305*, H1363-1372.

Kouzarides, T. (2000). Acetylation: a regulatory modification to rival phosphorylation? EMBO J. *19*, 1176–1179.

Kouzarides, T. (2007). Chromatin Modifications and Their Function. Cell *128*, 693–705.

Laflamme, M.A., Myerson, D., Saffitz, J.E., and Murry, C.E. (2002). Evidence for Cardiomyocyte Repopulation by Extracardiac Progenitors in Transplanted Human Hearts. Circ. Res. *90*, 634–640.

Laflamme, M.A., Chen, K.Y., Naumova, A.V., Muskheli, V., Fugate, J.A., Dupras, S.K., Reinecke, H., Xu, C., Hassanipour, M., Police, S., et al. (2007). Cardiomyocytes derived from human embryonic stem cells in pro-survival factors enhance function of infarcted rat hearts. Nat. Biotechnol. *25*, 1015–1024.

Lako, M., Lindsay, S., Lincoln, J., Cairns, P.M., Armstrong, L., and Hole, N. (2001). Characterisation of Wnt gene expression during the differentiation of murine embryonic stem cells in vitro: role of Wnt3 in enhancing haematopoietic differentiation. Mech. Dev. *103*, 49–59.

Lamouille, S., Xu, J., and Derynck, R. (2014). Molecular mechanisms of epithelial–mesenchymal transition. Nat. Rev. Mol. Cell Biol. *15*, 178–196.

Larue, L., and Bellacosa, A. (2005). Epithelial–mesenchymal transition in development and cancer: role of phosphatidylinositol 3′ kinase/AKT pathways. Oncogene *24*, 7443–7454.

Laugwitz, K.-L., Moretti, A., Caron, L., Nakano, A., and Chien, K.R. (2008). Islet1 cardiovascular progenitors: a single source for heart lineages? Development *135*, 193–205.

Lavine, K.J., Yu, K., White, A.C., Zhang, X., Smith, C., Partanen, J., and Ornitz, D.M. (2005). Endocardial and epicardial derived FGF signals regulate myocardial proliferation and differentiation in vivo. Dev. Cell *8*, 85–95.

Lee, J.H., Park, S., Hyun, H., Bordo, M.W., Oketokoun, R., Nasr, K.A., Frangioni, J.V., and Choi, H.S. (2013). High-throughput screening of small molecule ligands targeted to live bacteria surface. Anal. Chem. *85*, 3508–3514.

Lees-Miller, J.P., Heeley, D.H., and Smillie, L.B. (1987). An abundant and novel protein of 22 kDa (SM22) is widely distributed in smooth muscles. Purification from bovine aorta. Biochem. J. *244*, 705–709.

Lepage, F., Tombret, F., Cuvier, G., Marivain, A., and Gillardin, J. (1992). New N-aryl isoxazolecarboxamides and N-isoxazolylbenzamides as anticonvulsant agents. Eur. J. Med. Chem. *27*, 581–593.

Lepilina, A., Coon, A.N., Kikuchi, K., Holdway, J.E., Roberts, R.W., Burns, C.G., and Poss, K.D. (2006). A Dynamic Epicardial Injury Response Supports Progenitor Cell Activity during Zebrafish Heart Regeneration. Cell *127*, 607–619.

Leri, A., and Anversa, P. (2013). STEM CELLS Bone-marrow-derived cells and heart failure—the debate goes on. Nat. Rev. Cardiol. *10*, 372–373.

Li, X., and Chen, B.D. (2009). Histone Deacetylase Inhibitor M344 Inhibits Cell Proliferation and Induces Apoptosis in Human THP-1 Leukemia Cells. Am. J. Biomed. Sci. *1*, 352–363.

Li, J., Ma, J., Meng, G., Lin, H., Wu, S., Wang, J., Luo, J., Xu, X., Tough, D., Lindon, M., et al. (2016). BET bromodomain inhibition promotes neurogenesis while inhibiting gliogenesis in neural progenitor cells. Stem Cell Res. *17*, 212–221.

Li, L., Miano, J.M., Cserjesi, P., and Olson, E.N. (1996). SM22α, a Marker of Adult Smooth Muscle, Is Expressed in Multiple Myogenic Lineages During Embryogenesis. Circ. Res. *78*, 188–195.

Lian, X., Bao, X., Zilberter, M., Westman, M., Fisahn, A., Hsiao, C., Hazeltine, L.B., Dunn, K.K., Kamp, T.J., and Palecek, S.P. (2015). Chemically defined albumin-free human cardiomyocyte generation. Nat. Methods *12*, 595–596.

Liang, C.-C., Park, A.Y., and Guan, J.-L. (2007). In vitro scratch assay: a convenient and inexpensive method for analysis of cell migration in vitro. Nat. Protoc. *2*, 329–333.

Limana, F., Zacheo, A., Mocini, D., Mangoni, A., Borsellino, G., Diamantini, A., De Mori, R., Battistini, L., Vigna, E., Santini, M., et al. (2007). Identification of myocardial and vascular precursor cells in human and mouse epicardium. Circ. Res. *101*, 1255–1265.

Limana, F., Bertolami, C., Mangoni, A., Di Carlo, A., Avitabile, D., Mocini, D., Iannelli, P., De Mori, R., Marchetti, C., Pozzoli, O., et al. (2010). Myocardial infarction induces embryonic reprogramming of epicardial c-kit+ cells: Role of the pericardial fluid. J. Mol. Cell. Cardiol. *48*, 609–618.

Lin, K.-T., Wang, Y.-W., Chen, C.-T., Ho, C.-M., Su, W.-H., and Jou, Y.-S. (2012). HDAC inhibitors augmented cell migration and metastasis through induction of PKCs leading to identification of low toxicity modalities for combination cancer therapy. Clin. Cancer Res. Off. J. Am. Assoc. Cancer Res. *18*, 4691–4701.

Lindsay, M.A. (2003). Target discovery. Nat. Rev. Drug Discov. *2*, 831–838.

Lipinski, C.A., Lombardo, F., Dominy, B.W., and Feeney, P.J. (2001). Experimental and computational approaches to estimate solubility and permeability in drug discovery and development settings. Adv. Drug Deliv. Rev. *46*, 3–26.

Liu, B., Li, S., and Hu, J. (2004). Technological advances in high-throughput screening. Am. J. Pharmacogenomics Genomics-Relat. Res. Drug Dev. Clin. Pract. *4*, 263–276.

Liu, C.-Y., Lin, H.-H., Tang, M.-J., and Wang, Y.-K. (2015). Vimentin contributes to epithelial-mesenchymal transition cancer cell mechanics by mediating cytoskeletal organization and focal adhesion maturation. Oncotarget *6*, 15966–15983.

Liu, F., Barsyte-Lovejoy, D., Li, F., Xiong, Y., Korboukh, V., Huang, X.-P., Allali-Hassani, A., Janzen, W.P., Roth, B.L., Frye, S.V., et al. (2013). Discovery of an in vivo chemical probe of the lysine methyltransferases G9a and GLP. J. Med. Chem. *56*, 8931–8942.

Lugrin, J., Ding, X.C., Le Roy, D., Chanson, A.-L., Sweep, F.C.G.J., Calandra, T., and Roger, T. (2009). Histone deacetylase inhibitors repress macrophage migration inhibitory factor (MIF) expression by targeting MIF gene transcription through a local chromatin deacetylation. Biochim. Biophys. Acta BBA - Mol. Cell Res. *1793*, 1749–1758.

Lundholt, B.K., Scudder, K.M., and Pagliaro, L. (2003). A simple technique for reducing edge effect in cell-based assays. J. Biomol. Screen. *8*, 566–570.

Macarron, R., Banks, M.N., Bojanic, D., Burns, D.J., Cirovic, D.A., Garyantes, T., Green, D.V.S., Hertzberg, R.P., Janzen, W.P., Paslay, J.W., et al. (2011). Impact of high-throughput screening in biomedical research. Nat. Rev. Drug Discov. *10*, 188–195.

Machesky, L.M. (2008). Lamellipodia and filopodia in metastasis and invasion. FEBS Lett. *582*, 2102–2111.

Madison, K.C. (2003). Barrier function of the skin: "la raison d'être" of the epidermis. J. Invest. Dermatol. *121*, 231–241.

Mahdi, J.G., Mahdi, A.J., Mahdi, A.J., and Bowen, I.D. (2006). The historical analysis of aspirin discovery, its relation to the willow tree and antiproliferative and anticancer potential. Cell Prolif. *39*, 147–155.

Mai, A., Esposito, M., Sbardella, G., and Massa, S. (2001). A New Facile and Expeditious Synthesis of N-Hydroxy-N′-Phenyloctanediamjde, a Potent Inducer of Terminal Cytodifferecntiation. Org. Prep. Proced. Int. *33*, 391–394.

Maldonado, M., Luu, R.J., Ramos, M.E.P., and Nam, J. (2016). ROCK inhibitor primes human induced pluripotent stem cells to selectively differentiate towards mesendodermal lineage via epithelial-mesenchymal transition-like modulation. Stem Cell Res. *17*, 222–227.

Manoir, S.D., Guillaud, P., Camus, E., Seigneurin, D., and Brugal, G. (1991). Ki-67 labeling in postmitotic cells defines different Ki-67 pathways within the 2c compartment. Cytometry *12*, 455–463.

Markwald, R., Eisenberg, C., Eisenberg, L., Trusk, T., and Sugi, Y. (1996). Epithelial-mesenchymal transformations in early avian heart development. Acta Anat. (Basel) *156*, 173–186.

Martindill, D.M.J., Risebro, C.A., Smart, N., Franco-Viseras, M.D.M., Rosario, C.O., Swallow, C.J., Dennis, J.W., and Riley, P.R. (2007). Nucleolar release of Hand1 acts as a molecular switch to determine cell fate. Nat. Cell Biol. *9*, 1131–1141.

Martínez, J.L., Liu, L., Petranovic, D., and Nielsen, J. (2012). Pharmaceutical protein production by yeast: towards production of human blood proteins by microbial fermentation. Curr. Opin. Biotechnol. *23*, 965–971.

Martínez-Estrada, O.M., Lettice, L.A., Essafi, A., Guadix, J.A., Slight, J., Velecela, V., Hall, E., Reichmann, J., Devenney, P.S., Hohenstein, P., et al. (2010). Wt1 is required for cardiovascular progenitor cell formation through transcriptional control of Snail and E-cadherin. Nat. Genet. *42*, 89–93.

Mason, C., and Dunnill, P. (2008). A brief definition of regenerative medicine. Regen. Med. *3*, 1–5.

Masumoto, H., Nakane, T., Tinney, J.P., Yuan, F., Ye, F., Kowalski, W.J., Minakata, K., Sakata, R., Yamashita, J.K., and Keller, B.B. (2016). The myocardial regenerative potential of three-dimensional engineered cardiac tissues composed of multiple human iPS cell-derived cardiovascular cell lineages. Sci. Rep. *6*, 29933.

Masur, K., Lang, K., Niggemann, B., Zanker, K.S., and Entschladen, F. (2001). High PKC α and Low E-Cadherin Expression Contribute to High Migratory Activity of Colon Carcinoma Cells. Mol. Biol. Cell *12*, 1973–1982.

Mattila, P.K., and Lappalainen, P. (2008). Filopodia: molecular architecture and cellular functions. Ature Rev. Mol. Cell Biol. *9*, 446–454.

McDonald, O.G., Wu, H., Timp, W., Doi, A., and Feinberg, A.P. (2011). Genome-scale epigenetic reprogramming during epithelial to mesenchymal transition. Nat. Struct. Mol. Biol. *18*, 867–874.

McGee, S.L., and Hargreaves, M. (2011). Histone modifications and exercise adaptations. J. Appl. Physiol. *110*, 258–263.

McLure, K.G., Gesner, E.M., Tsujikawa, L., Kharenko, O.A., Attwell, S., Campeau, E., Wasiak, S., Stein, A., White, A., Fontano, E., et al. (2013). RVX-208, an Inducer of ApoA-I in Humans, Is a BET Bromodomain Antagonist. PLoS ONE *8*, e83190.

Medici, D., Hay, E.D., and Olsen, B.R. (2008). Snail and Slug Promote Epithelial-Mesenchymal Transition through β-Catenin–T-Cell Factor-4-dependent Expression of Transforming Growth Factor-β3. Mol. Biol. Cell *19*, 4875–4887.

Menasché, P., Alfieri, O., Janssens, S., McKenna, W., Reichenspurner, H., Trinquart, L., Vilquin, J.-T., Marolleau, J.-P., Seymour, B., Larghero, J., et al. (2008). The Myoblast Autologous Grafting in Ischemic Cardiomyopathy (MAGIC) Trial. Circulation *117*, 1189–1200.

Meng, S., Zhang, L., Tang, Y., Tu, Q., Zheng, L., Yu, L., Murray, D., Cheng, J., Kim, S.H., Zhou, X., et al. (2014). BET Inhibitor JQ1 Blocks Inflammation and Bone Destruction. J. Dent. Res. *93*, 657–662.

Merki, E., Zamora, M., Raya, A., Kawakami, Y., Wang, J., Zhang, X., Burch, J., Kubalak, S.W., Kaliman, P., Belmonte, J.C.I., et al. (2005). Epicardial retinoid X receptor α is required for myocardial growth and coronary artery formation. Proc. Natl. Acad. Sci. U. S. A. *102*, 18455–18460.

Messina, E., Angelis, L.D., Frati, G., Morrone, S., Chimenti, S., Fiordaliso, F., Salio, M., Battaglia, M., Latronico, M.V.G., Coletta, M., et al. (2004). Isolation and Expansion of Adult Cardiac Stem Cells From Human and Murine Heart. Circ. Res. *95*, 911–921.

Miller, D.C., Carbain, B., Beale, G.S., Alhasan, S.F., Reeves, H.L., Baisch, U., Newell, D.R., Golding, B.T., and Griffin, R.J. (2015). Regioselective sulfamoylation at low temperature enables concise syntheses of putative small molecule inhibitors of sulfatases. Org. Biomol. Chem. *13*, 5279–5284.

Min, A., Im, S.-A., Kim, D.K., Song, S.-H., Kim, H.-J., Lee, K.-H., Kim, T.-Y., Han, S.-W., Oh, D.-Y., Kim, T.-Y., et al. (2015). Histone deacetylase inhibitor, suberoylanilide hydroxamic acid (SAHA), enhances anti-tumor effects of the poly (ADP-ribose) polymerase (PARP) inhibitor olaparib in triple-negative breast cancer cells. Breast Cancer Res. BCR *17*, 33.

Moffat, J.G., Rudolph, J., and Bailey, D. (2014). Phenotypic screening in cancer drug discovery — past, present and future. Nat. Rev. Drug Discov. *13*, 588–602.

Moon, S.-H., Kang, S.-W., Park, S.-J., Bae, D., Kim, S.J., Lee, H.-A., Kim, K.S., Hong, K.-S., Kim, J.S., Do, J.T., et al. (2013). The use of aggregates of purified cardiomyocytes derived from human ESCs for functional engraftment after myocardial infarction. Biomaterials *34*, 4013–4026.

Morabito, C.J., Dettman, R.W., Kattan, J., Collier, J.M., and Bristow, J. (2001a). Positive and Negative Regulation of Epicardial–Mesenchymal Transformation during Avian Heart Development. Dev. Biol. *234*, 204–215.

Morabito, C.J., Dettman, R.W., Kattan, J., Collier, J.M., and Bristow, J. (2001b). Positive and negative regulation of epicardial-mesenchymal transformation during avian heart development. Dev. Biol. *234*, 204–215.

Morash, M.G., Douglas, S.E., Robotham, A., Ridley, C.M., Gallant, J.W., and Soanes, K.H. (2011). The zebrafish embryo as a tool for screening and characterizing pleurocidin host-defense peptides as anti-cancer agents. Dis. Model. Mech. *4*, 622–633.

Morley, P., and Whitfield, J.F. (1993). The differentiation inducer, dimethyl sulfoxide, transiently increases the intracellular calcium ion concentration in various cell types. J. Cell. Physiol. *156*, 219–225.

Morrow, T., and Felcone, L.H. (2004). Defining the difference: What Makes Biologics Unique. Biotechnol. Healthc. *1*, 24–29.

Mourey, R.J., Burnette, B.L., Brustkern, S.J., Daniels, J.S., Hirsch, J.L., Hood, W.F., Meyers, M.J., Mnich, S.J., Pierce, B.S., Saabye, M.J., et al. (2010). A benzothiophene inhibitor of mitogen-activated protein kinase-activated protein kinase 2 inhibits tumor necrosis factor alpha production and has oral anti-inflammatory efficacy in acute and chronic models of inflammation. J. Pharmacol. Exp. Ther. *333*, 797–807.

Muller, S., Filippakopoulos, P., and Knapp, S. (2011). Bromodomains as therapeutic targets. Expert Rev. Mol. Med. *13*.

Mummery, C.L., Zhang, J., Ng, E.S., Elliott, D.A., Elefanty, A.G., and Kamp, T.J. (2012). Differentiation of human embryonic stem cells and induced pluripotent stem cells to cardiomyocytes: a methods overview. Circ. Res. *111*, 344–358.

Murry, C.E., Soonpaa, M.H., Reinecke, H., Nakajima, H., Nakajima, H.O., Rubart, M., Pasumarthi, K.B.S., Virag, J.I., Bartelmez, S.H., Poppa, V., et al. (2004). Haematopoietic stem cells do not transdifferentiate into cardiac myocytes in myocardial infarcts. Nature *428*, 664–668.

Naaldijk, Y., Staude, M., Fedorova, V., and Stolzing, A. (2012). Effect of different freezing rates during cryopreservation of rat mesenchymal stem cells using combinations of hydroxyethyl starch and dimethylsulfoxide. BMC Biotechnol. *12*, 49.

Nadal-Ginard, B., Ellison, G.M., and Torella, D. (2014). The cardiac stem cell compartment is indispensable for myocardial cell homeostasis, repair and regeneration in the adult. Stem Cell Res. *13*, 615–630.

Nam, Y.-J., Song, K., Luo, X., Daniel, E., Lambeth, K., West, K., Hill, J.A., DiMaio, J.M., Baker, L.A., Bassel-Duby, R., et al. (2013). Reprogramming of human fibroblasts toward a cardiac fate. Proc. Natl. Acad. Sci. U. S. A. *110*, 5588–5593.

nature.com http://www.nature.com/subjects/cell-polarity.

Nelson, W.J. (2009). Remodeling Epithelial Cell Organization: Transitions Between Front–Rear and Apical–Basal Polarity. Cold Spring Harb. Perspect. Biol. *1*.

Nemolato, S., Cabras, T., Restivo, A., Zorcolo, L., Di Felice, E., Fanni, D., Gerosa, C., Messana, I., Castagnola, M., Faa, G., et al. (2013). Thymosin ß4 expression in colorectal polyps and adenomas. Clin. São Paulo Braz. *68*, 1220–1224.

Ngo, M.A., Müller, A., Li, Y., Neumann, S., Tian, G., Dixon, I.M.C., Arora, R.C., and Freed, D.H. (2014). Human mesenchymal stem cells express a myofibroblastic phenotype in vitro: comparison to human cardiac myofibroblasts. Mol. Cell. Biochem. 1–18.

Nicholls, S.J., Gordon, A., Johansson, J., Wolski, K., Ballantyne, C.M., Kastelein, J.J.P., Taylor, A., Borgman, M., and Nissen, S.E. (2011). Efficacy and Safety of a Novel Oral Inducer of Apolipoprotein A-I Synthesis in Statin-Treated Patients With Stable Coronary Artery Disease: A Randomized Controlled Trial. J. Am. Coll. Cardiol. *57*, 1111–1119.

Nielsen, M.S., Axelsen, L.N., Sorgen, P.L., Verma, V., Delmar, M., and Holstein-Rathlou, N.-H. (2012). Gap Junctions. Compr. Physiol. *2*.

Niida, A., Hiroko, T., Kasai, M., Furukawa, Y., Nakamura, Y., Suzuki, Y., Sugano, S., and Akiyama, T. (2004). DKK1, a negative regulator of Wnt signaling, is a target of the β-catenin/TCF pathway. Oncogene *23*, 8520–8526.

NISRA, N.I.S. and R.A. (1950). THE REGISTRAR-GENERAL'S ANNUAL REPORT FOR 1950.

Ohori, M., Kinoshita, T., Okubo, M., Sato, K., Yamazaki, A., Arakawa, H., Nishimura, S., Inamura, N., Nakajima, H., Neya, M., et al. (2005). Identification of a selective ERK inhibitor and structural determination of the inhibitor-ERK2 complex. Biochem. Biophys. Res. Commun. *336*, 357–363.

Ohtsu, Y., Johkura, K., Ito, K., Akashima, T., Asanuma, K., Ogiwara, N., Oka, T., Komuro, I., Sasaki, K., and Amano, J. (2005). Stimulation of P19CL6 with multiple reagents induces pulsating particles in vivo.

Okada, H., Danoff, T.M., Kalluri, R., and Neilson, E.G. (1997). Early role of Fsp1 in epithelial-mesenchymal transformation. Am. J. Physiol. - Ren. Physiol. *273*, F563–F574.

Omari, B.O., Nelson, R.J., and Robertson, J.M. (1991). Effect of right atrial appendectomy on the release of atrial natriuretic hormone. J. Thorac. Cardiovasc. Surg. *102*, 272–279.

Orlic, D., Kajstura, J., Chimenti, S., Limana, F., Jakoniuk, I., Quaini, F., Nadal-Ginard, B., Bodine, D.M., Leri, A., and Anversa, P. (2001). Mobilized bone marrow cells repair the infarcted heart, improving function and survival. Proc. Natl. Acad. Sci. *98*, 10344–10349.

Ott, H.C., Matthiesen, T.S., Goh, S.-K., Black, L.D., Kren, S.M., Netoff, T.I., and Taylor, D.A. (2008). Perfusion-decellularized matrix: using nature's platform to engineer a bioartificial heart. Nat. Med. *14*, 213–221.

Ouellette, M.M., McDaniel, L.D., Wright, W.E., Shay, J.W., and Schultz, R.A. (2000). The establishment of telomerase-immortalized cell lines representing human chromosome instability syndromes. Hum. Mol. Genet. *9*, 403–411.

Owen, D.J., Ornaghi, P., Yang, J.-C., Lowe, N., Evans, P.R., Ballario, P., Neuhaus, D., Filetici, P., and Travers, A.A. (2000). The structural basis for the recognition of acetylated histone H4 by the bromodomain of histone acetyltransferase Gcn5p. EMBO J. *19*, 6141–6149.

Palmeri, C.M., Petiti, J.P., del Valle Sosa, L., Gutiérrez, S., De Paul, A.L., Mukdsi, J.H., and Torres, A.I. (2009). Bromocriptine induces parapoptosis as the main type of cell death responsible for experimental pituitary tumor shrinkage. Toxicol. Appl. Pharmacol. *240*, 55–65.

Pappano, W.N., Guo, J., He, Y., Ferguson, D., Jagadeeswaran, S., Osterling, D.J., Gao, W., Spence, J.K., Pliushchev, M., Sweis, R.F., et al. (2015). The Histone Methyltransferase Inhibitor A-366 Uncovers a Role for G9a/GLP in the Epigenetics of Leukemia. PloS One *10*, e0131716.

Park, I.C., Park, M.J., Rhee, C.H., Lee, J.I., Choe, T.B., Jang, J.J., Lee, S.H., and Hong, S.I. (2001). Protein kinase C activation by PMA rapidly induces apoptosis through caspase-3/CPP32 and serine protease(s) in a gastric cancer cell line. Int. J. Oncol. *18*, 1077–1083.

Park, I.-H., Lerou, P.H., Zhao, R., Huo, H., and Daley, G.Q. (2008). Generation of human-induced pluripotent stem cells. Nat. Protoc. *3*, 1180–1186.

Pasumarthi, K.B.S., and Field, L.J. (2002). Cardiomyocyte Cell Cycle Regulation. Circ. Res. *90*, 1044–1054.

Patel, A.N., Henry, T.D., Quyyumi, A.A., Schaer, G.L., Anderson, R.D., Toma, C., East, C., Remmers, A.E., Goodrich, J., Desai, A.S., et al. (2016). Ixmyelocel-T for patients with ischaemic heart failure: a prospective randomised double-blind trial. The Lancet *387*, 2412–2421.

Pei, Y., and Wickham, B.O.S. (1993). Regioselective syntheses of 3-aminomethyl-5-substituted isoxazoles: A facile and chemoselective reduction of azide to amine by sodium borohydride using 1,3-propanedithiol as a catalyst. Tetrahedron Lett. *34*, 7509–7512.

Pennisi, D.J., Ballard, V.L.T., and Mikawa, T. (2003). Epicardium is required for the full rate of myocyte proliferation and levels of expression of myocyte mitogenic factors FGF2 and its receptor, FGFR-1, but not for transmural myocardial patterning in the embryonic chick heart. Dev. Dyn. Off. Publ. Am. Assoc. Anat. *228*, 161–172.

Pereira, D.A., and Williams, J.A. (2007). Origin and evolution of high throughput screening. Br. J. Pharmacol. *152*, 53–61.

Perin, E.C., Willerson, J.T., Pepine, C.J., Henry, T.D., Ellis, S.G., Zhao, D.X.M., Silva, G.V., Lai, D., Thomas, J.D., Kronenberg, M.W., et al. (2012). Effect of transendocardial delivery of autologous bone marrow mononuclear cells on functional capacity, left ventricular function, and perfusion in chronic heart failure: the FOCUS-CCTRN trial. JAMA *307*, 1717–1726.

Petrie, R.J., Doyle, A.D., and Yamada, K.M. (2009). Random versus directionally persistent cell migration. Nat. Rev. Mol. Cell Biol. *10*, 538–549.

Phillis, J.W., and Smith-Barbour, M. (1993). The adenosine kinase inhibitor, 5-iodotubercidin, is not protective against cerebral ischemic injury in the gerbil. Life Sci. *53*, 497–502.

Philpott, M., Yang, J., Tumber, T., Fedorov, O., Uttarkar, S., Filippakopoulos, P., Picaud, S., Keates, T., Felletar, I., Ciulli, A., et al. (2011). Bromodomain-peptide displacement assays for interactome mapping and inhibitor discovery. Mol. Biosyst. *7*, 2899–2908.

Philpott, M., Rogers, C.M., Yapp, C., Wells, C., Lambert, J.-P., Strain-Damerell, C., Burgess-Brown, N.A., Gingras, A.-C., Knapp, S., and Müller, S. (2014). Assessing cellular efficacy of bromodomain inhibitors using fluorescence recovery after photobleaching. Epigenetics Chromatin *7*, 14.

Picaud, S., Costa, D.D., Thanasopoulou, A., Filippakopoulos, P., Fish, P.V., Philpott, M., Fedorov, O., Brennan, P., Bunnage, M.E., Owen, D.R., et al. (2013a). PFI-1, a Highly Selective Protein Interaction Inhibitor, Targeting BET Bromodomains. Cancer Res. *73*, 3336–3346.

Picaud, S., Wells, C., Felletar, I., Brotherton, D., Martin, S., Savitsky, P., Diez-Dacal, B., Philpott, M., Bountra, C., Lingard, H., et al. (2013b). RVX-208, an inhibitor of BET transcriptional regulators with selectivity for the second bromodomain. Proc. Natl. Acad. Sci. *110*, 19754–19759.

Picaud, S., Leonards, K., Lambert, J.-P., Dovey, O., Wells, C., Fedorov, O., Monteiro, O., Fujisawa, T., Wang, C.-Y., Lingard, H., et al. (2016). Promiscuous targeting of bromodomains by bromosporine identifies BET proteins as master regulators of primary transcription response in leukemia. Sci. Adv. *2*, e1600760.

Pjanic, M., Miller, C.L., Wirka, R., Kim, J.B., DiRenzo, D.M., and Quertermous, T. (2016). Genetics and Genomics of Coronary Artery Disease. Curr. Cardiol. Rep. *18*, 102.

Plavicki, J., Hofsteen, P., Peterson, R.E., and Heideman, W. (2013). Dioxin Inhibits Zebrafish Epicardium and Proepicardium Development. Toxicol. Sci. *131*, 558–567.

Plavicki, J.S., Hofsteen, P., Yue, M.S., Lanham, K.A., Peterson, R.E., and Heideman, W. (2014). Multiple modes of proepicardial cell migration require heartbeat. BMC Dev. Biol. *14*, 18.

Porrello, E.R., Mahmoud, A.I., Simpson, E., Hill, J.A., Richardson, J.A., Olson, E.N., and Sadek, H.A. (2011). Transient Regenerative Potential of the Neonatal Mouse Heart. Science *331*, 1078–1080.

Porrello, E.R., Mahmoud, A.I., Simpson, E., Johnson, B.A., Grinsfelder, D., Canseco, D., Mammen, P.P., Rothermel, B.A., Olson, E.N., and Sadek, H.A. (2013). Regulation of neonatal and adult mammalian heart regeneration by the miR-15 family. Proc. Natl. Acad. Sci. U. S. A. *110*, 187–192.

Poss, K.D., Wilson, L.G., and Keating, M.T. (2002). Heart Regeneration in Zebrafish. Science *298*, 2188–2190.

Priest, B.T., and Erdemli, G. (2014). Phenotypic screening in the 21st century. Front. Pharmacol. *5*.

Providence, K.M., and Higgins, P.J. (2004). PAI-1 expression is required for epithelial cell migration in two distinct phases of in vitro wound repair. J. Cell. Physiol. *200*, 297–308.

Qian, L., Huang, Y., Spencer, C.I., Foley, A., Vedantham, V., Liu, L., Conway, S.J., Fu, J., and Srivastava, D. (2012). In vivo reprogramming of murine cardiac fibroblasts into induced cardiomyocytes. Nature *485*, 593–598.

Quaini, F., Urbanek, K., Beltrami, A.P., Finato, N., Beltrami, C.A., Nadal-Ginard, B., Kajstura, J., Leri, A., and Anversa, P. (2002). Chimerism of the Transplanted Heart. N. Engl. J. Med. *346*, 5–15.

Quinn, R. (2013). Rethinking Antibiotic Research and Development: World War II and the Penicillin Collaborative. Am. J. Public Health *103*, 426–434.

Radisic, M., Park, H., Shing, H., Consi, T., Schoen, F.J., Langer, R., Freed, L.E., and Vunjak-Novakovic, G. (2004). Functional assembly of engineered myocardium by electrical stimulation of cardiac myocytes cultured on scaffolds. Proc. Natl. Acad. Sci. *101*, 18129–18134.

Ramsbottom, S.A., Maguire, R.J., Fellgett, S.W., and Pownall, M.E. (2014). Sulf1 influences the Shh morphogen gradient during the dorsal ventral patterning of the neural tube in Xenopus tropicalis. Dev. Biol. *391*, 207–218.

Rao-Bindal, K., Koshkina, N.V., Stewart, J., and Kleinerman, E.S. (2013). The histone deacetylase inhibitor, MS-275 (entinostat), downregulates c-FLIP, sensitizes osteosarcoma cells to FasL, and induces the regression of osteosarcoma lung metastases. Curr. Cancer Drug Targets *13*, 411–422.

Reese, D.E., Zavaljevski, M., Streiff, N.L., and Bader, D. (1999). bves: A novel gene expressed during coronary blood vessel development. Dev. Biol. *209*, 159–171.

Rhee, D.Y., Zhao, X.-Q., Francis, R.J.B., Huang, G.Y., Mably, J.D., and Lo, C.W. (2009). Connexin 43 regulates epicardial cell polarity and migration in coronary vascular development. Development *136*, 3185–3193.

Rhee, Y.-H., Yi, S.-H., Kim, J.Y., Chang, M.-Y., Jo, A.-Y., Kim, J., Park, C.-H., Cho, J.-Y., Choi, Y.-J., Sun, W., et al. (2016). Neural stem cells secrete factors facilitating brain regeneration upon constitutive Raf-Erk activation. Sci. Rep. *6*, 32025.

Rimm, D.L., Koslov, E.R., Kebriaei, P., Cianci, C.D., and Morrow, J.S. (1995). Alpha 1(E)-catenin is an actin-binding and -bundling protein mediating the attachment of F-actin to the membrane adhesion complex. Proc. Natl. Acad. Sci. U. S. A. *92*, 8813–8817.

Risebro, C.A., Vieira, J.M., Klotz, L., and Riley, P.R. (2015). Characterisation of the human embryonic and foetal epicardium during heart development. Development *142*, 3630–3636.

Robinson, D.R., Wu, Y.M., and Lin, S.F. (2000). The protein tyrosine kinase family of the human genome. Oncogene *19*, 5548–5557.

Rosenblatt-Velin, N., Lepore, M.G., Cartoni, C., Beermann, F., and Pedrazzini, T. (2005). FGF-2 controls the differentiation of resident cardiac precursors into functional cardiomyocytes. J. Clin. Invest. *115*, 1724–1733.

Roshanbin, S., Lindberg, F.A., Lekholm, E., Eriksson, M.M., Perland, E., Åhlund, J., Raine, A., and Fredriksson, R. (2016). Histological characterization of orphan transporter MCT14 (SLC16A14) shows abundant expression in mouse CNS and kidney. BMC Neurosci. *17*.

Rossier, B.C., Baker, M.E., and Studer, R.A. (2015). Epithelial Sodium Transport and Its Control by Aldosterone: The Story of Our Internal Environment Revisited. Physiol. Rev. *95*, 297–340.

Rudat, C., and Kispert, A. (2012). Wt1 and epicardial fate mapping. Circ. Res. *111*, 165–169.

Ruiz-Villalba, A., Ziogas, A., Ehrbar, M., and Pérez-Pomares, J.M. (2013). Characterization of epicardial-derived cardiac interstitial cells: differentiation and mobilization of heart fibroblast progenitors. PloS One *8*, e53694.

Russell, J.L., Goetsch, S.C., Gaiano, N.R., Hill, J.A., Olson, E.N., and Schneider, J.W. (2011). A Dynamic Notch Injury Response Activates Epicardium and Contributes to Fibrosis Repair. Circ. Res. *108*, 51–59.

Russell, J.L., Goetsch, S.C., Aguilar, H.R., Frantz, D.E., and Schneider, J.W. (2012a). Targeting Native Adult Heart Progenitors with Cardiogenic Small Molecules. ACS Chem. Biol. *7*, 1067–1076.

Russell, J.L., Goetsch, S.C., Aguilar, H.R., Coe, H., Luo, X., Liu, N., van Rooij, E., Frantz, D.E., and Schneider, J.W. (2012b). Regulated Expression of pH Sensing G Protein-Coupled Receptor-68 Identified through Chemical Biology Defines a New Drug Target for Ischemic Heart Disease. ACS Chem. Biol. *7*, 1077–1083.

Ryan, T.J., Anderson, J.L., Antman, E.M., Braniff, B.A., Brooks, N.H., Califf, R.M., Hillis, L.D., Hiratzka, L.F., Rapaport, E., Riegel, B.J., et al. (1996). ACC/AHA Guidelines for the Management of Patients With Acute Myocardial Infarction:Executive Summary. Circulation *94*, 2341–2350.

Sadek, H., Hannack, B., Choe, E., Wang, J., Latif, S., Garry, M.G., Garry, D.J., Longgood, J., Frantz, D.E., Olson, E.N., et al. (2008a). Cardiogenic small molecules that enhance myocardial repair by stem cells. Proc. Natl. Acad. Sci. *105*, 6063–6068.

Sadek, H., Hannack, B., Choe, E., Wang, J., Latif, S., Garry, M.G., Garry, D.J., Longgood, J., Frantz, D.E., Olson, E.N., et al. (2008b). Cardiogenic small molecules that enhance myocardial repair by stem cells. Proc. Natl. Acad. Sci. *105*, 6063–6068.

Sahai, V., Kumar, K., Knab, L.M., Chow, C.R., Raza, S.S., Bentrem, D.J., Ebine, K., and Munshi, H.G. (2014). BET bromodomain inhibitors block growth of pancreatic cancer cells in three-dimensional collagen. Mol. Cancer Ther. *13*, 1907–1917.

Sahota, A.P., and Dhoot, G.K. (2009). A novel SULF1 splice variant inhibits Wnt signalling but enhances angiogenesis by opposing SULF1 activity. Exp. Cell Res. *315*, 2752–2764.

Sams-Dodd, F. (2005). Target-based drug discovery: is something wrong? Drug Discov. Today *10*, 139–147.

Sanchez, R., and Zhou, M.-M. (2009). The role of human bromodomains in chromatin biology and gene transcription. Curr. Opin. Drug Discov. Devel. *12*, 659–665.

Sasaki, T., Hwang, H., Nguyen, C., Kloner, R.A., and Kahn, M. (2013). The small molecule Wnt signaling modulator ICG-001 improves contractile function in chronically infarcted rat myocardium. PloS One *8*, e75010.

Schade, D., and Plowright, A.T. (2015). Medicinal Chemistry Approaches to Heart Regeneration. J. Med. Chem. *58*, 9451–9479.

Schenone, M., Dančík, V., Wagner, B.K., and Clemons, P.A. (2013). Target identification and mechanism of action in chemical biology and drug discovery. Nat. Chem. Biol. *9*, 232–240.

Schmidt, M.H., Broll, R., Bruch, H.-P., Bögler, O., and Duchrow, M. (2003). The proliferation marker pKi-67 organizes the nucleolus during the cell cycle depending on Ran and cyclin B. J. Pathol. *199*, 18–27.

Schneider, J., Hsieh, J., Frantz, D., Mcknight, S., and Ready, J.M. (2007). Isoxazole amides, derivatives and methods of chemical induction of neurogenesis.

Scholzen, T., and Gerdes, J. (2000). The Ki-67 protein: From the known and the unknown. J. Cell. Physiol. *182*, 311–322.

Schürmann, M., Janning, P., Ziegler, S., and Waldmann, H. (2016). Small-Molecule Target Engagement in Cells. Cell Chem. Biol. *23*, 435–441.

Seaberg, R.M., and van der Kooy, D. (2003). Stem and progenitor cells: the premature desertion of rigorous definitions. Trends Neurosci. *26*, 125–131.

Sebe, A., Leivonen, S.-K., Fintha, A., Masszi, A., Rosivall, L., Kähäri, V.-M., and Mucsi, I. (2008). Transforming growth factor-beta-induced alpha-smooth muscle cell actin expression in renal proximal tubular cells is regulated by p38beta mitogen-activated protein kinase, extracellular signal-regulated protein kinase1,2 and the Smad signalling during epithelial-myofibroblast transdifferentiation. Nephrol. Dial. Transplant. Off. Publ. Eur. Dial. Transpl. Assoc. - Eur. Ren. Assoc. *23*, 1537–1545.

Seif-Naraghi, S.B., Singelyn, J.M., Salvatore, M.A., Osborn, K.G., Wang, J.J., Sampat, U., Kwan, O.L., Strachan, G.M., Wong, J., Schup-Magoffin, P.J., et al. (2013). Safety and Efficacy of an Injectable Extracellular Matrix Hydrogel for Treating Myocardial Infarction. Sci. Transl. Med. *5*, 173ra25-173ra25.

Senyo, S.E., Steinhauser, M.L., Pizzimenti, C.L., Yang, V.K., Cai, L., Wang, M., Wu, T.-D., Guerquin-Kern, J.-L., Lechene, C.P., and Lee, R.T. (2013). Mammalian heart renewal by pre-existing cardiomyocytes. Nature *493*, 433–436.

Shi, Y., and Massagué, J. (2003). Mechanisms of TGF-β Signaling from Cell Membrane to the Nucleus. Cell *113*, 685–700.

Shoichet, B.K. (2006). Interpreting steep dose-response curves in early inhibitor discovery. J. Med. Chem. *49*, 7274–7277.

Sinha, S., and Chen, J.K. (2006). Purmorphamine activates the Hedgehog pathway by targeting Smoothened. Nat. Chem. Biol. *2*, 29–30.

Smart, N. (unpublished). Sulfatases: novel targets for enhancing regeneration by epicardium-derived cells?

Smart, N., and Riley, P.R. (2009). Derivation of epicardium-derived progenitor cells (EPDCs) from adult epicardium. Curr. Protoc. Stem Cell Biol. *Chapter 2*, Unit2C.2.

Smart, N., Risebro, C.A., Melville, A.A.D., Moses, K., Schwartz, R.J., Chien, K.R., and Riley, P.R. (2007). Thymosin β4 induces adult epicardial progenitor mobilization and neovascularization. Nature *445*, 177–182.

Smart, N., Bollini, S., Dubé, K.N., Vieira, J.M., Zhou, B., Davidson, S., Yellon, D., Riegler, J., Price, A.N., Lythgoe, M.F., et al. (2011). De novo cardiomyocytes from within the activated adult heart after injury. Nature *474*, 640–644.

Smart, N., Bollini, S., Dubé, K.N., Vieira, J.M., Zhou, B., Riegler, J., Price, A.N., Lythgoe, M.F., Davidson, S., Yellon, D., et al. (2012). Myocardial regeneration: expanding the repertoire of thymosin β4 in the ischemic heart. Ann. N. Y. Acad. Sci. *1269*, 92–101.

Smutny, M., Cox, H.L., Leerberg, J.M., Kovacs, E.M., Conti, M.A., Ferguson, C., Hamilton, N.A., Parton, R.G., Adelstein, R.S., and Yap, A.S. (2010). Myosin II isoforms identify distinct functional modules that support integrity of the epithelial zonula adherens. Nat. Cell Biol. *12*, 696–702.

Song, K., Nam, Y.-J., Luo, X., Qi, X., Tan, W., Huang, G.N., Acharya, A., Smith, C.L., Tallquist, M.D., Neilson, E.G., et al. (2012). Heart repair by reprogramming non-myocytes with cardiac transcription factors. Nature *485*, 599–604.

Strovel, J., Sittampalam, S., Coussens, N.P., Hughes, M., Inglese, J., Kurtz, A., Andalibi, A., Patton, L., Austin, C., Baltezor, M., et al. (2004). Early Drug Discovery and Development Guidelines: For Academic Researchers, Collaborators, and Start-up Companies. In Assay Guidance Manual, G.S. Sittampalam, N.P. Coussens, K. Brimacombe, A. Grossman, M. Arkin, D. Auld, C. Austin, B. Bejcek, M. Glicksman, J. Inglese, et al., eds. (Bethesda (MD): Eli Lilly & Company and the National Center for Advancing Translational Sciences), p.

Structural Genomics Consortium, Bromosporine Structural Genomics Consortium: Bromosporine.

Strutz, F., Okada, H., Lo, C.W., Danoff, T., Carone, R.L., Tomaszewski, J.E., and Neilson, E.G. (1995). Identification and characterization of a fibroblast marker: FSP1. J. Cell Biol. *130*, 393–405.

Stuckmann, I., Evans, S., and Lassar, A.B. (2003). Erythropoietin and retinoic acid, secreted from the epicardium, are required for cardiac myocyte proliferation. Dev. Biol. *255*, 334–349.

Sucov, H.M., Gu, Y., Thomas, S., Li, P., and Pashmforoush, M. (2009). Epicardial Control of Myocardial Proliferation and Morphogenesis. Pediatr. Cardiol. *30*, 617–625.

Supokawej, A., Kheolamai, P., Nartprayut, K., U-pratya, Y., Manochantr, S., Chayosumrit, M., and Issaragrisil, S. (2013). Cardiogenic and Myogenic Gene Expression in Mesenchymal Stem Cells After 5-Azacytidine Treatment. Turk. J. Hematol. *30*, 115–121.

Sürder, D., Manka, R., Cicero, V.L., Moccetti, T., Rufibach, K., Soncin, S., Turchetto, L., Radrizzani, M., Astori, G., Schwitter, J., et al. (2013). Intracoronary Injection of Bone Marrow–Derived Mononuclear Cells Early or Late After Acute Myocardial InfarctionClinical Perspective. Circulation *127*, 1968–1979.

Svensson, E.C. (2010). Deciphering the Signals Specifying the Proepicardium. Circ. Res. *106*, 1789–1790.

Sweis, R.F., Pliushchev, M., Brown, P.J., Guo, J., Li, F., Maag, D., Petros, A.M., Soni, N.B., Tse, C., Vedadi, M., et al. (2014). Discovery and development of potent and selective inhibitors of histone methyltransferase g9a. ACS Med. Chem. Lett. *5*, 205–209.

Swinney, D.C. (2013). Phenotypic vs. target-based drug discovery for first-in-class medicines. Clin. Pharmacol. Ther. *93*, 299–301.

Swinney, D.C., and Anthony, J. (2011). How were new medicines discovered? Nat. Rev. Drug Discov. *10*, 507–519.

Takahashi, K., and Yamanaka, S. (2006). Induction of Pluripotent Stem Cells from Mouse Embryonic and Adult Fibroblast Cultures by Defined Factors. Cell *126*, 663–676.

Takahashi, T., Lord, B., Schulze, P.C., Fryer, R.M., Sarang, S.S., Gullans, S.R., and Lee, R.T. (2003). Ascorbic Acid Enhances Differentiation of Embryonic Stem Cells Into Cardiac Myocytes. Circulation *107*, 1912–1916.

Takenaka, T. (2001). Classical vs reverse pharmacology in drug discovery. BJU Int. *88*, 7–10.

Tang, S., He, J., Sun, Y., He, L., and She, X. (2009). Efficient and Regioselective One-Pot Synthesis of 3-Substituted and 3,5-Disubstituted Isoxazoles. Org. Lett. *11*, 3982–3985.

Taylor, S.M., and Jones, P.A. (1979). Multiple new phenotypes induced in 10T1/2 and 3T3 cells treated with 5-azacytidine. Cell *17*, 771–779.

Taylor, D.A., Atkins, B.Z., Hungspreugs, P., Jones, T.R., Reedy, M.C., Hutcheson, K.A., Glower, D.D., and Kraus, W.E. (1998). Regenerating functional myocardium: Improved performance after skeletal myoblast transplantation. Nat. Med. *4*, 929–933.

tdi.ox.ac.uk http://www.tdi.ox.ac.uk/home.

tdi.ox.ac.uk/high-content-imaging http://www.tdi.ox.ac.uk/high-content-imaging.

Teo, J.-L., Ma, H., Nguyen, C., Lam, C., and Kahn, M. (2005). Specific inhibition of CBP/β-catenin interaction rescues defects in neuronal differentiation caused by a presenilin-1 mutation. Proc. Natl. Acad. Sci. U. S. A. *102*, 12171–12176.

Terstappen, G.C., Schlüpen, C., Raggiaschi, R., and Gaviraghi, G. (2007). Target deconvolution strategies in drug discovery. Nat. Rev. Drug Discov. *6*, 891–903.

The Longevity Science Advisory Panel (2012). Life expectancy: Past and future variations by gender in England & Wales.

Theise, N.D., Nimmakayalu, M., Gardner, R., Illei, P.B., Morgan, G., Teperman, L., Henegariu, O., and Krause, D.S. (2000). Liver from bone marrow in humans. Hepatol. Baltim. Md *32*, 11–16.

thermofisher.com https://www.thermofisher.com/order/catalog/product/C34552.

Thievessen, I., Fakhri, N., Steinwachs, J., Kraus, V., McIsaac, R.S., Gao, L., Chen, B.-C., Baird, M.A., Davidson, M.W., Betzig, E., et al. (2015). Vinculin is required for cell polarization, migration, and extracellular matrix remodeling in 3D collagen. FASEB J. Off. Publ. Fed. Am. Soc. Exp. Biol. *29*, 4555–4567.

Thorne, N., Auld, D.S., and Inglese, J. (2010). Apparent Activity in High-Throughput Screening: Origins of Compound-Dependent Assay Interference. Curr. Opin. Chem. Biol. *14*, 315–324.

Tian, X., Liu, Z., Niu, B., Zhang, J., Tan, T.K., Lee, S.R., Zhao, Y., Harris, D.C.H., Zheng, G., Tian, X., et al. (2011a). E-Cadherin/β-Catenin Complex and the Epithelial Barrier, E-Cadherin/β-Catenin Complex and the Epithelial Barrier. BioMed Res. Int. BioMed Res. Int. *2011*, *2011*, e567305.

Tian, X., Liu, Z., Niu, B., Zhang, J., Tan, T.K., Lee, S.R., Zhao, Y., Harris, D.C.H., Zheng, G., Tian, X., et al. (2011b). E-Cadherin/β-Catenin Complex and the Epithelial Barrier, E-Cadherin/β-Catenin Complex and the Epithelial Barrier. BioMed Res. Int. BioMed Res. Int. *2011*, *2011*, e567305.

Tsukita, S., and Furuse, M. (2000). The Structure and Function of Claudins, Cell Adhesion Molecules at Tight Junctions. Ann. N. Y. Acad. Sci. *915*, 129–135.

van Tuyn, J., Atsma, D.E., Winter, E.M., van der Velde-van Dijke, I., Pijnappels, D.A., Bax, N.A.M., Knaän-Shanzer, S., Gittenberger-de Groot, A.C., Poelmann, R.E., van der Laarse, A., et al. (2007). Epicardial Cells of Human Adults Can Undergo an Epithelial-to-Mesenchymal Transition and Obtain Characteristics of Smooth Muscle Cells In Vitro. STEM CELLS *25*, 271–278.

UNSW Embryology https://embryology.med.unsw.edu.au/embryology/index.php/Basic_-_Primitive_Heart_Tube.

Valenta, T., Hausmann, G., and Basler, K. (2012). The many faces and functions of β-catenin. EMBO J. *31*, 2714–2736.

Vane, J.R. (1971). Inhibition of Prostaglandin Synthesis as a Mechanism of Action for Aspirin-like Drugs. Nature *231*, 232–235.

Vangamudi, B., Paul, T.A., Shah, P.K., Kost-Alimova, M., Nottebaum, L., Shi, X., Zhan, Y., Leo, E., Mahadeshwar, H.S., Protopopov, A., et al. (2015). The SMARCA2/4 ATPase Domain Surpasses the Bromodomain as a Drug Target in SWI/SNF-Mutant Cancers: Insights from cDNA Rescue and PFI-3 Inhibitor Studies. Cancer Res. *75*, 3865–3878.

Varjosalo, M., and Taipale, J. (2008). Hedgehog: functions and mechanisms. Genes Dev. *22*, 2454–2472.

Veras, E., Malpica, A., Deavers, M.T., and Silva, E.G. (2009). Mitosis-specific marker phospho-histone H3 in the assessment of mitotic index in uterine smooth muscle tumors: a pilot study. Int. J. Gynecol. Pathol. Off. J. Int. Soc. Gynecol. Pathol. *28*, 316–321.

Verstovsek, S. (2007). New Hematological Indications for Imatinib. Oncol. Dis. *3*, 36–39.

Wada, A.M., Smith, T.K., Osler, M.E., Reese, D.E., and Bader, D.M. (2003). Epicardial/Mesothelial Cell Line Retains Vasculogenic Potential of Embryonic Epicardium. Circ. Res. *92*, 525–531.

Wagers, A.J., Sherwood, R.I., Christensen, J.L., and Weissman, I.L. (2002). Little Evidence for Developmental Plasticity of Adult Hematopoietic Stem Cells. Science *297*, 2256–2259.

Wagner, N., Panelos, J., Massi, D., and Wagner, K.-D. (2007). The Wilms' tumor suppressor WT1 is associated with melanoma proliferation. Pflüg. Arch. - Eur. J. Physiol. *455*, 839–847.

Wang, Y. (2007). Mitogen-activated protein kinases in heart development and diseases. Circulation *116*, 1413–1423.

Wang, H., Liu, Z., Li, D., Guo, X., Kasper, F.K., Duan, C., Zhou, J., Mikos, A.G., and Wang, C. (2012). Injectable biodegradable hydrogels for embryonic stem cell transplantation: improved cardiac remodelling and function of myocardial infarction. J. Cell. Mol. Med. *16*, 1310–1320.

Wang, J., Cao, J., Dickson, A.L., and Poss, K.D. (2015a). Epicardial regeneration is guided by cardiac outflow tract and Hedgehog signalling. Nature *522*, 226–230.

Wang, R.N., Green, J., Wang, Z., Deng, Y., Qiao, M., Peabody, M., Zhang, Q., Ye, J., Yan, Z., Denduluri, S., et al. (2014). Bone Morphogenetic Protein (BMP) signaling in development and human diseases. Genes Dis. *1*, 87–105.

Wang, W., Li, M., Wang, Y., Li, Q., Deng, G., Wan, J., Yang, Q., Chen, Q., and Wang, J. (2015b). GSK-3β inhibitor TWS119 attenuates rtPA-induced hemorrhagic transformation and activates the Wnt/β-catenin signaling pathway after acute ischemic stroke in rats. Mol. Neurobiol.

Wang, Z., Zhai, W., Richardson, J.A., Olson, E.N., Meneses, J.J., Firpo, M.T., Kang, C., Skarnes, W.C., and Tjian, R. (2004). Polybromo protein BAF180 functions in mammalian cardiac chamber maturation. Genes Dev. *18*, 3106–3116.

Weber, J.D., Kuo, M.-L., Bothner, B., DiGiammarino, E.L., Kriwacki, R.W., Roussel, M.F., and Sherr, C.J. (2000). Cooperative Signals Governing ARF-Mdm2 Interaction and Nucleolar Localization of the Complex. Mol. Cell. Biol. *20*, 2517–2528.

Wessels, A., and Pérez-Pomares, J.M. (2004). The epicardium and epicardially derived cells (EPDCs) as cardiac stem cells. Anat. Rec. A. Discov. Mol. Cell. Evol. Biol. *276*, 43–57.

Whitehouse, I., Flaus, A., Cairns, B.R., White, M.F., Workman, J.L., and Owen-Hughes, T. (1999). Nucleosome mobilization catalysed by the yeast SWI/SNF complex. Nature *400*, 784–787.

van Wijk, B., Gunst, Q.D., Moorman, A.F.M., and van den Hoff, M.J.B. (2012). Cardiac Regeneration from Activated Epicardium. PLoS ONE *7*, e44692.

Willems, E., Bushway, P.J., and Mercola, M. (2009a). Natural and Synthetic Regulators of Embryonic Stem Cell Cardiogenesis. Pediatr. Cardiol. *30*, 635–642.

Willems, E., Bushway, P.J., and Mercola, M. (2009b). Natural and Synthetic Regulators of Embryonic Stem Cell Cardiogenesis. Pediatr. Cardiol. *30*, 635–642.

Willems, E., Lanier, M., Forte, E., Lo, F., Cashman, J., and Mercola, M. (2011). A Chemical Biology Approach to Myocardial Regeneration. J Cardiovasc. Transl. Res. *4*, 340–350.

Willems, E., Cabral-Teixeira, J., Schade, D., Cai, W., Reeves, P., Bushway, P.J., Lanier, M., Walsh, C., Kirchhausen, T., Izpisua Belmonte, J.C., et al. (2012). Small Molecule-Mediated TGF-β Type II Receptor Degradation Promotes Cardiomyogenesis in Embryonic Stem Cells. Cell Stem Cell *11*, 242–252.

Willems, I.E., Havenith, M.G., De Mey, J.G., and Daemen, M.J. (1994). The alpha-smooth muscle actin-positive cells in healing human myocardial scars. Am. J. Pathol. *145*, 868–875.

Willems, I.E.M.G., Arends, J.-W., and Daemen, M.J. a. P. (1996). Tenascin and Fibronectin Expression in Healing Human Myocardial Scars. J. Pathol. *179*, 321–325.

Willert, K., Brown, J.D., Danenberg, E., Duncan, A.W., Weissman, I.L., Reya, T., Yates, J.R., and Nusse, R. (2003). Wnt proteins are lipid-modified and can act as stem cell growth factors. Nature *423*, 448–452.

Winking, H., Gerdes, J., and Traut, W. (2004). Expression of the proliferation marker Ki-67 during early mouse development. Cytogenet. Genome Res. *105*, 251–256.

Wrana, J.L., Attisano, L., Cárcamo, J., Zentella, A., Doody, J., Laiho, M., Wang, X.-F., and Massague, J. (1992). TGFβ signals through a heteromeric protein kinase receptor complex. Cell *71*, 1003–1014.

Wu, H., Lee, S.H., Gao, J., Liu, X., and Iruela-Arispe, M.L. (1999). Inactivation of erythropoietin leads to defects in cardiac morphogenesis. Dev. Camb. Engl. *126*, 3597–3605.

Wu, J., Zeng, F., Huang, X.-P., Chung, J.C.-Y., Konecny, F., Weisel, R.D., and Li, R.-K. (2011). Infarct stabilization and cardiac repair with a VEGF-conjugated, injectable hydrogel. Biomaterials *32*, 579–586.

Wu, X., Ding, S., Ding, Q., Gray, N.S., and Schultz, P.G. (2004). Small Molecules that Induce Cardiomyogenesis in Embryonic Stem Cells. J. Am. Chem. Soc. *126*, 1590–1591.

Xu, J., Lamouille, S., and Derynck, R. (2009). TGF-beta-induced epithelial to mesenchymal transition. Cell Res. *19*, 156–172.

Xu, Y., Shi, Y., and Ding, S. (2008). A chemical approach to stem-cell biology and regenerative medicine. Nature *453*, 338–344.

Yamaguchi, K., Tomita, H., Sugano, E., Nakazawa, T., and Tamai, M. (2002). Mitogen-activated protein kinase inhibitor, PD98059, inhibits rat retinal pigment epithelial cell replication by cell cycle arrest. Jpn. J. Ophthalmol. *46*, 634–639.

Yang, J.T., Rayburn, H., and Hynes, R.O. (1995). Cell adhesion events mediated by alpha 4 integrins are essential in placental and cardiac development. Dev. Camb. Engl. *121*, 549–560.

Ye, S., Tan, L., Yang, R., Fang, B., Qu, S., Schulze, E.N., Song, H., Ying, Q., and Li, P. (2012). Pleiotropy of glycogen synthase kinase-3 inhibition by CHIR99021 promotes self-renewal of embryonic stem cells from refractory mouse strains. PloS One *7*, e35892.

You, J., Li, Q., Wu, C., Kim, J., Ottinger, M., and Howley, P.M. (2009). Regulation of Aurora B Expression by the Bromodomain Protein Brd4. Mol. Cell. Biol. *29*, 5094–5103.

Zhang, G., Plotnikov, A.N., Rusinova, E., Shen, T., Morohashi, K., Joshua, J., Zeng, L., Mujtaba, S., Ohlmeyer, M., and Zhou, M.-M. (2013). Structure-guided design of potent diazobenzene inhibitors for the BET bromodomains. J. Med. Chem. *56*, 9251–9264.

Zhang, J., Betson, M., Erasmus, J., Zeikos, K., Bailly, M., Cramer, L.P., and Braga, V.M.M. (2005). Actin at cell-cell junctions is composed of two dynamic and functional populations. J. Cell Sci. *118*, 5549–5562.

Zhang, J., Wilson, G.F., Soerens, A.G., Koonce, C.H., Yu, J., Palecek, S.P., Thomson, J.A., and Kamp, T.J. (2009). Functional cardiomyocytes derived from human induced pluripotent stem cells. Circ. Res. *104*, e30-41.

Zhang, J.-H., Chung, T.D.Y., and Oldenburg, K.R. (1999). A Simple Statistical Parameter for Use in Evaluation and Validation of High Throughput Screening Assays. J. Biomol. Screen. *4*, 67–73.

Zhang, M., Methot, D., Poppa, V., Fujio, Y., Walsh, K., and Murry, C.E. (2001). Cardiomyocyte Grafting for Cardiac Repair: Graft Cell Death and Anti-Death Strategies. J. Mol. Cell. Cardiol. *33*, 907–921.

Zhang, Q., Sun, M., Zhou, S., and Guo, B. (2016). Class I HDAC inhibitor mocetinostat induces apoptosis by activation of miR-31 expression and suppression of E2F6. Cell Death Discov. *2*, 16036.

Zheng, H., Dong, Y., Li, L., Sun, B., Liu, L., Yuan, H., and Lou, H. (2016). Novel Benzo[a]quinolizidine Analogs Induce Cancer Cell Death through Paraptosis and Apoptosis. J. Med. Chem. *59*, 5063–5076.

Zheng, W., Thorne, N., and McKew, J.C. (2013a). Phenotypic screens as a renewed approach for drug discovery. Drug Discov. Today *18*, 1067–1073.

Zheng, X., Gai, X., Han, S., Moser, C.D., Hu, C., Shire, A.M., Floyd, R.A., and Roberts, L.R. (2013b). The human sulfatase 2 inhibitor 2,4-disulfonylphenyl-tert-butylnitrone (OKN-007) has an antitumor effect in hepatocellular carcinoma mediated via suppression of TGFB1/SMAD2 and Hedgehog/GLI1 signaling. Genes. Chromosomes Cancer *52*, 225–236.

Zhou, B., Ma, Q., Rajagopal, S., Wu, S.M., Domian, I., Rivera-Feliciano, J., Jiang, D., Gise, A. von, Ikeda, S., Chien, K.R., et al. (2008). Epicardial progenitors contribute to the cardiomyocyte lineage in the developing heart. Nature *454*, 109–113.

Zhou, B., von Gise, A., Ma, Q., Hu, Y.W., and Pu, W.T. (2010). Genetic Fate Mapping Demonstrates Contribution of Epicardium-Derived Cells to the Annulus Fibrosis of the Mammalian Heart. Dev. Biol. *338*, 251.

Zhou, B., Honor, L.B., He, H., Ma, Q., Oh, J.-H., Butterfield, C., Lin, R.-Z., Melero-Martin, J.M., Dolmatova, E., Duffy, H.S., et al. (2011). Adult mouse epicardium modulates myocardial injury by secreting paracrine factors. J. Clin. Invest. *121*, 1894–1904.

Zhou, B., Honor, L.B., Ma, Q., Oh, J.-H., Lin, R.-Z., Melero-Martin, J.M., von Gise, A., Zhou, P., Hu, T., He, L., et al. (2012a). Thymosin beta 4 treatment after myocardial infarction does not reprogram epicardial cells into cardiomyocytes. J. Mol. Cell. Cardiol. *52*, 43–47.

Zhou, B., Liu, Y., Kahn, M., Ann, D.K., Han, A., Wang, H., Nguyen, C., Flodby, P., Zhong, Q., Krishnaveni, M.S., et al. (2012b). Interactions Between β-Catenin and Transforming Growth Factor-β Signaling Pathways Mediate Epithelial-Mesenchymal Transition and Are Dependent on the Transcriptional Co-activator cAMP-response Element-binding Protein (CREB)-binding Protein (CBP). J. Biol. Chem. *287*, 7026–7038.

Zhu, H., Bengsch, F., Svoronos, N., Rutkowski, M.R., Bitler, B.G., Allegrezza, M.J., Yokoyama, Y., Kossenkov, A.V., Bradner, J.E., Conejo-Garcia, J.R., et al. (2016). BET Bromodomain Inhibition Promotes Anti-tumor Immunity by Suppressing PD-L1 Expression. Cell Rep. *16*, 2829–2837.

Zi, Z., Chapnick, D.A., and Liu, X. (2012). Dynamics of TGF-β/Smad signaling. FEBS Lett. *586*, 1921–1928.

Zucconi, B.E., Luef, B., Xu, W., Henry, R.A., Nodelman, I.M., Bowman, G.D., Andrews, A.J., and Cole, P.A. (2016). Modulation of p300/CBP Acetylation of Nucleosomes by Bromodomain Ligand I-CBP112. Biochemistry (Mosc.) *55*, 3727–3734.